Dieu Tien Bui · Anh Ngoc Do
Hoang-Bac Bui · Nhat-Duc Hoang
Editors

Advances and Applications in Geospatial Technology and Earth Resources

Proceedings of the International Conference on Geo-Spatial Technologies and Earth Resources 2017

Springer

Advances and Applications in Geospatial Technology and Earth Resources

Dieu Tien Bui · Anh Ngoc Do
Hoang-Bac Bui · Nhat-Duc Hoang
Editors

Advances and Applications in Geospatial Technology and Earth Resources

Proceedings of the International Conference on Geo-Spatial Technologies and Earth Resources 2017

Springer

Editors
Dieu Tien Bui
GIS group, Department of Business and IT
University College of Southeast Norway
Bo i Telemark
Norway

Hoang-Bac Bui
Department of Exploration Geology
Hanoi University of Mining and Geology
Hanoi
Vietnam

Anh Ngoc Do
Department of Underground and Mining Construction
Hanoi University of Mining and Geology
Hanoi
Vietnam

Nhat-Duc Hoang
Faculty of Civil Engineering
Duy Tan University
Da Nang
Vietnam

ISBN 978-3-319-68239-6 ISBN 978-3-319-68240-2 (eBook)
https://doi.org/10.1007/978-3-319-68240-2

Library of Congress Control Number: 2017956062

© Springer International Publishing AG 2018
This work is subject to copyright. All rights are reserved by the Publisher, whether the whole or part of the material is concerned, specifically the rights of translation, reprinting, reuse of illustrations, recitation, broadcasting, reproduction on microfilms or in any other physical way, and transmission or information storage and retrieval, electronic adaptation, computer software, or by similar or dissimilar methodology now known or hereafter developed.
The use of general descriptive names, registered names, trademarks, service marks, etc. in this publication does not imply, even in the absence of a specific statement, that such names are exempt from the relevant protective laws and regulations and therefore free for general use.
The publisher, the authors and the editors are safe to assume that the advice and information in this book are believed to be true and accurate at the date of publication. Neither the publisher nor the authors or the editors give a warranty, express or implied, with respect to the material contained herein or for any errors or omissions that may have been made. The publisher remains neutral with regard to jurisdictional claims in published maps and institutional affiliations.

Printed on acid-free paper

This Springer imprint is published by Springer Nature
The registered company is Springer International Publishing AG
The registered company address is: Gewerbestrasse 11, 6330 Cham, Switzerland

Preface

We would like to welcome you to International Conference on Geo-spatial Technologies and Earth Resources (GTER-2017), which will be held during October 5–6, 2017, at the Hanoi University of Mining and Geology (HUMG), Hanoi, Vietnam. GTER-2017 is co-organized by HUMG and International Society for Mine Surveying (ISM) to celebrate the 50th anniversary of Department of Mine Surveying (HUMG). The conference is financially supported by Vietnam Mining Science and Technology Association (VMSTA), Vietnam Association of Geodesy, Cartography and Remote Sensing (VGCR), Vietnam National Coal-Mineral Industries Holding Corporation Limited (VINACOMIN), and Dong Bac Corporation (NECO).

The main objective of the conference is to provide a platform for researchers, academicians, and engineers in the field of geospatial technologies and earth resources to present their recent research results. In addition, this conference provides a setting for them to exchange new ideas, innovative thinking, and application experiences face-to-face, to establish research or business relations, and to find partners for future collaboration.

The conference program was organized into three sessions covering topics of geospatial technologies, advance in mining and tunneling, and geological and earth sciences. Overall, the conference has attracted more than 288 papers, and among them, 57 high-quality papers were recommended to submit for this Springer proceedings book for peer-reviewing. Then, the double-blind review process was carried out for the 57 papers, in which each paper has been reviewed for its merit and novelty by at least two reviewers and one editor by matching the content areas. As a result, a total of 24 papers have been finally selected for this book. We believe that this proceedings book provides a broad overview of recent advances in the fields of geospatial technologies and earth resources for readers.

Finally, we would like to express our sincere thanks to (i) the President of ISM : Prof. Anatoly Okhotin; (ii) the Rector of HUMG : Assoc. Prof. Le Hai An; (iii) the Vice Rectors of HUMG : Assoc. Profs. Bui Xuan Nam, Tran Thanh Hai, and Tran Xuan Truong for their help in administrative works and other support. Special thanks go to Michael Leuchner and Bhavana Purushothaman at Springer

International Publishing AG for always responding promptly. We would like to thank all the reviewers for their timely and rigorous reviews of the papers and thank all the authors for their submissions.

October 2017

Dieu Tien Bui
Anh Ngoc Do
Hoang-Bac Bui
Nhat-Duc Hoang

List of Reviewers

Anh Tuan Nguyen	Hanoi University of Mining and Geology, Vietnam
Ataollah Shirzadi	University of Kurdistan, Iran
Binh Thai Pham	University of Transport Technology, Vietnam
Dinh Hieu Vu	Hanoi University of Mining and Geology, Vietnam
Dinh Sinh Mai	Le Quy Don Technical University, Vietnam
Phuong D. Dao	University of Toronto, Canada
Duc-Anh Nguyen	University College of Southeast Norway, Norway
Haijian Su	China University of Mining and Technology, China
Hanh Hong Tran	Hanoi University of Mining and Geology, Vietnam
Hong-Phuong Nguyen	Vietnam Academy of Science and Technology, Vietnam
Indra Prakash	Bhaskaracharya Institute for Space Applications and Geoinformatics, India
Kien-Trinh Thi Bui	Thuyloi University, Vietnam
Lien T.H Pham	Waikato University, New Zealand
Loi Huy Doan	Institute of Transport Science and Technology, Vietnam
Long Thanh Ngo	Le Quy Don Technical University, Vietnam
Pirat Jaroonpattanapong	Chiang Mai University, Thailand
Qian Yin	China University of Mining and Technology, China
Quoc-Phi Nguyen	Hanoi University of Mining and Geology, Vietnam
Quoc-Dinh Nguyen	Vietnam Institute of Geosciences and Mineral Resources
Ryszard Hejmanowski	AGH University of Science and Technology, Poland
Le Hoang Son	VNU University of Science, Hanoi
Tan Manh Do	Hanoi University of Mining and Geology, Vietnam
Thanh-Trung Duong	Hanoi University of Mining and Geology Vietnam
Thanh-Long Nguyen	Vietnam Institute of Geosciences and Mineral Resources
Thu-Trang Le	Hanoi University of Mining and Geology, Vietnam

Tien Dat Pham	University of Tsukuba, Japan
Tran Anh Quang Pham	IRISA/University of Rennes 1, France
Trong Trinh Phan	Vietnam Academy of Science and Technology, Vietnam
Tuan Quoc Vo	Can Tho University, Vietnam
Tuong-Thuy Vu	University of Nottingham, Malaysia
Trung Van Nguyen	Hanoi University of Mining and Geology, Vietnam
Vu Hien Phan	Ho Chi Minh University of Technology, Vietnam

Contents

A Computational Tool for Time-Series Prediction of Mining-Induced Subsidence Based on Time-Effect Function and Geodetic Monitoring Data 1
Nguyen Quoc Long, Xuan-Nam Bui, Luyen Khac Bui, Khoa Dat Vu Huynh, Canh Van Le, Michał Buczek, and Thang Phi Nguyen

Lightweight Unmanned Aerial Vehicle and Structure-from-Motion Photogrammetry for Generating Digital Surface Model for Open-Pit Coal Mine Area and Its Accuracy Assessment 17
Dieu Tien Bui, Nguyen Quoc Long, Xuan-Nam Bui, Viet-Nghia Nguyen, Chung Van Pham, Canh Van Le, Phuong-Thao Thi Ngo, Dung Tien Bui, and Bjørn Kristoffersen

Energy Analysis in Semiautomatic and Automatic Velocity Estimation for Ground Penetrating Radar Data in Urban Areas: Case Study in Ho Chi Minh City, Vietnam 34
Thuan Van Nguyen, Cuong Anh Van Le, Van Thanh Nguyen, Trung Hoai Dang, Triet Minh Vo, and Lieu Nguyen Nhu Vo

An Integration of Least Squares Support Vector Machines and Firefly Optimization Algorithm for Flood Susceptible Modeling Using GIS . . . 52
Viet-Nghia Nguyen, Dieu Tien Bui, Phuong-Thao Thi Ngo, Quoc-Phi Nguyen, Van Cam Nguyen, Nguyen Quoc Long, and Inge Revhaug

Estimation of Surface Parameters of Tidal Flats Using Sentinel-1A SAR Data in the Northern Coast of Vietnam 65
Si Son Tong, Jean Paul Deroin, Thi Lan Pham, and Xuan Cuong Cao

Reconstruction of Missing Imagery Data Caused by Cloudcover Based on Beyesian Neural Network and Multitemporal Images 89
Hien Phu La and Minh Quang Nguyen

Monitoring Mangrove Forest Changes in Cat Ba Biosphere Reserve Using ALOS PALSAR Imagery and a GIS-Based Support Vector Machine Algorithm 103
Tien Dat Pham, Kunihiko Yoshino, and Naoko Kaida

Detection and Prediction of Urban Expansion of Hanoi Area (Vietnam) Using SPOT-5 Satellite Imagery and Markov Chain Model 119
Trung Van Nguyen, Nam Van Nguyen, Ha Thu Thi Le, Hien Phu La, and Dieu Tien Bui

Analysis of Land Cover Changes in Northern Vietnam Using High Resolution Remote Sensing Data 134
Thanh Tung Hoang, Kenlo Nishida Nasahara, and Jin Katagi

Change Detection in Multitemporal SAR Images Using a Strategy of Multistage Analysis 152
Thu Trang Lê, Van Anh Tran, Ha Thai Pham, and Xuan Truong Tran

Understanding Factors Affecting the Outbreak of Malaria Using Locally-Compensated Ridge Geographically Weighted Regression: Case Study in DakNong, Vietnam 166
Tuan-Anh Hoang, Le Hoang Son, Quang-Thanh Bui, and Quoc-Huy Nguyen

A Novel Hybrid Model of Rotation Forest Based Functional Trees for Landslide Susceptibility Mapping: A Case Study at Kon Tum Province, Vietnam 186
Binh Thai Pham, Viet-Tien Nguyen, Van-Liem Ngo, Phan Trong Trinh, Huong Thanh Thi Ngo, and Dieu Tien Bui

Effects of Residual Soil Characteristics on Rainfall-Induced Shallow Landslides Along Transport Arteries in Bac Kan Province, Vietnam . . . 202
Do Minh Duc, Dao Minh Duc, and Do Minh Ngoc

Spatial Prediction of Rainfall Induced Shallow Landslides Using Adaptive-Network-Based Fuzzy Inference System and Particle Swarm Optimization: A Case Study at the Uttarakhand Area, India 224
Binh Thai Pham and Indra Prakash

GIS-Based Landslide Spatial Modeling Using Batch-Training Back-propagation Artificial Neural Network: A Study of Model Parameters 239
Nhat-Duc Hoang and Dieu Tien Bui

A Novel Hybrid Intelligent Approach of Random Subspace Ensemble and Reduced Error Pruning Trees for Landslide Susceptibility Modeling: A Case Study at Mu Cang Chai District, Yen Bai Province, Viet Nam 255
Binh Thai Pham and Indra Prakash

Recent Tectonic Movements Along the Coastal Zone of Tuy Hoa Area (Central Vietnam) and Its Significance for Coastal Hazards in the Case of Sea Level Rise 270
Hai Thanh Tran

Isotopic and Hydrogeochemical Signatures in Evaluating Groundwater Quality in the Coastal Area of the Mekong Delta, Vietnam 293
Tran Dang An, Maki Tsujimura, Vo Le Phu, Doan Thu Ha, and Nguyen Van Hai

Research Progress on Stabilization/Solidification Technique for Remediation of Heavy Metals Contaminated Soil 315
Yu Zhang, Cong Lu, Mengyi Xu, Lingling Pan, Nguyen Chau Lan, and Qiang Tang

Distribution and Reserve Potential of Titanium-Zirconium Heavy Minerals in Quang an Area, Thua Thien Hue Province, Vietnam 326
Nguyen Tien Dung, Bui Hoang Bac, Do Manh An, and Tran Thi Van Anh

Application of Land Subsidence Inversion for Salt Mining-Induced Rock Mass Movement 340
Ryszard Hejmanowski and Agnieszka A. Malinowska

Study on the Coupling Effect Between Surrounding Rock and Support Structures of Tunnels 355
Pham Thi Nhan, Guangsheng Zhang, Viet-Nghia Nguyen, and Viet Huy Le

Numerical Simulation of CFRA Pile Subgrade Reinforcement Based on Recycled Aggregate of Demolition Waste 367
Huanda Gu, Cong Lu, Guoqiang Xue, Huilong Wu, Nguyen Chau Lan, and Qiang Tang

Worthiness Assessment of New Mining Projects: The Case of Potash Mining in Bamnet Narong, Thailand 378
Kridtaya Sakamornsnguan and Jürgen Kretschmann

Author Index 395

A Computational Tool for Time-Series Prediction of Mining-Induced Subsidence Based on Time-Effect Function and Geodetic Monitoring Data

Nguyen Quoc Long[1(✉)], Xuan-Nam Bui[2], Luyen Khac Bui[3], Khoa Dat Vu Huynh[4], Canh Van Le[1], Michał Buczek[5], and Thang Phi Nguyen[1]

[1] Department of Mine Surveying,
Hanoi University of Mining and Geology, Hanoi, Vietnam
nguyenquoclong@humg.edu.vn
[2] Department of Surface Mining,
Hanoi University of Mining and Geology, Hanoi, Vietnam
[3] Department of Geodesy,
Hanoi University of Mining and Geology, Hanoi, Vietnam
[4] Norwegian Geotechnical Institute (NGI), Oslo, Norway
[5] Department of Engineering Surveying and Civil Engineering,
AGH University of Science and Technology, Kraków, Poland

Abstract. Underground mining-induced land subsidence may cause serious damage to engineering structures (e.g., buildings or roads) therefore, it is necessary to predict the subsidence with the highest possible accuracy. This paper proposes a new method for estimating preliminary values of the parameters to the modified Knothe time function, resulting in an improved capability of predicting land subsidence. A computational tool incorporating the proposed method has been developed to practically and numerically facilitate the time-series prediction of mining subsidence. A case study at the Mong Duong colliery at Quang Ninh province in Vietnam was considered and back-analyzed to validate the capability and accuracy of the tool. The accuracy of the subsidence prediction was evaluated using Root Mean Square Errors (*RMSE*), Mean Absolute Errors (*MAE*), and the Correlation coefficient (*r*). The result showed that the proposed method predicted reasonably well both the calibrating dataset (*RMSE* = 15 mm, *MAE* = 13 mm, $r = 0.996$) and the validating dataset (*RMSE* = 44 mm, *MAE* = 37 mm, $r = 0.857$). Based on the comparison results, it is concluded that the developed tool incorporating the proposed method is suitable for predicting underground mining-induced land subsidence.

Keywords: Computational tool · Time-series prediction · Modified knothe time function · Underground mining · Geodetic monitoring

© Springer International Publishing AG 2018
D. Tien Bui et al. (eds.), *Advances and Applications in Geospatial Technology and Earth Resources*, https://doi.org/10.1007/978-3-319-68240-2_1

1 Introduction

The rapid growths in the world's population and economy have resulted in continuous increase in energy and mineral consumption. To meet this high demand for minerals, mining activities have continuously and rapidly expanded over time, all over the world. Underground coal mining can cause serious damages, as a result of mining-induced land subsidence, to engineering structures such as buildings, roads, railways, and drainage systems [1–3]. It is important to note that mining-induced land subsidence can occur not only during active mining but also several decades after the completion of active mining. In Vietnam, damage caused by mine surface deformation is commonly observed and occurs in most of all underground mining areas, especially at the Quang Ninh coal basin [4]. For example, in 1991 mining-induced subsidence caused huge damage to the road at the Deo Nai mine [5]. In 2000, a subsidence observed at the Mao Khe coal mine caused serious damage for the fan station [4]. Several residential houses were heavily damaged and the 110 kV electricity line was destroyed because of a subsidence at the Mong Duong colliery [6, 7]. It is concluded that one of the main reasons of causing the above land subsidence phenomena in Vietnam was the lack of practical and sophisticated methods for accurately predicting mining-induced land subsidence.

Many methods have been developed and continuously improved to better predict and estimate land subsidence due to mining activities [1, 8, 9]. According to Bahuguna, et al. [10], subsidence prediction methods can be basically classified into three categories: empirical techniques, influence function and theoretical modelling. Among them, the Knothe time function (KTF) is considered to be the most effective and widely used [11, 12]. The major advantage of the KTF method is that it can describe the process of surface subsidence in time through a set of differential mathematical equations [13, 14]. By using the KTF method, land subsidence over time due to underground mining activity can be simply predicted through a subsidence curve. However, land subsidence is generally a complex and nonlinear process so that the application of the original KTF method is not able to correctly capture the whole process of surface subsidence. Wang [15] reported that the prediction accuracy of the KTF models could be low in many cases. Therefore, some modifications of KTF have been proposed [16–18], i.e. a modified function adding a constant parameter to the KTF [19]. Although many recent modified KTF models have made it possible to accurately predict land subsidence over time, it is still difficult and time-consuming to properly determine the function parameters due to the fact that these parameters heavily depend on the estimation of their preliminary values [19]. Therefore, research works are still needed to further improve the prediction accuracy of mining-induced land subsidence.

This research addresses the aforementioned limitation by proposing a new method for estimating the preliminary parameter values of the modified KTF model proposed by Chinh [19], leading to an improved capability of predicting land-surface subsidence. The proposed method was further used to develop a computational tool for time-series prediction of mining subsidence. It is noted that the computational tool was developed using Visual C.net programing language. A case study of the Mong Duong colliery at Quang Ninh province in Vietnam was considered to validate both the current model and the computational tool. The geodetic time-series data of mining subsidence

measured from 2013 to 2015 with 12 epochs were used as input to the modified KTF model. The subsidence prediction accuracy was assessed using Root Mean Square Error (*RMSE*), Mean Absolute Error (*MAE*), and the Correlation coefficient (*r*).

2 Methodology

2.1 Knothe Time Function and Its Modified Version

According to Knothe [13, 14], the relationship between a time parameter and land subsidence can be established using the following equation:

$$\frac{d\eta(t)}{dt} = b[\eta_{max} - \eta(t)] \tag{1}$$

where b is a parameter describing the influence of geological and mining conditions on the subsidence progress with time; η_{max} and $\eta_{(t)}$ are the final subsidence and the subsidence at the time t, respectively.

By integrating Eq. 1 with respect to t, the KTF model for surface dynamic subsidence could be written as below:

$$\eta^p(t_i) = \eta_{max}.\left[1 - e^{-bt_i}\right] \tag{2}$$

It is observed from Eq. 2 that there is only one parameter b which plays a significant role in predicting surface subsidence. This limitation could result in low prediction accuracy when using the KTF model in many cases [15]. To improve the prediction, Chinh [19] proposed a modified KTF model described as follows:

$$\eta^p(t_i) = \eta_{max}\left[1 - e^{-b(t_i)^c}\right] \tag{3}$$

where $\eta^p(t_i)$ is the predicted subsidence of the ith epoch; c is the fitting parameter.

Literature review indicates that the preliminary value of c equal to 2 is commonly assumed in various works [19]. The uncertainty in defining the fitting parameter c may result in large errors in some complex land subsidence. In some cases, it is even impossible to find c in a given dataset. Thus, the approach used for estimating the preliminary c-value needs to be improved in order to better determine the parameter c.

2.2 Method for Determination of Preliminary Parameters

From Eq. 3, the relation between $\eta^p(t_i)$ and the measured value $\eta(t_i)$ can be derived as:

$$\eta^p(t_i) = \eta(t_i) + V_{\eta(t_i)} \tag{4}$$

where $V_{\eta(t_i)}$ is residual value at the time t_i. The model parameters η_{max}, b, c are determined based on the least-squares principle using the following equations:

$$\begin{cases} \eta_{max} = \eta^0_{max} + \delta\eta_{max} \\ b = b^0 + \delta b \\ c = c^0 + \delta c \end{cases} \tag{5}$$

where η^0_{max}, b^0, c^0 are the preliminary values of the modified KTF; $\delta\eta_{max}, \delta b, \delta c$ are the residual ones.

Based on Eq. 4 and the system of Eq. 5, the residual equation can be rewritten as follows:

$$V_{\eta(t_i)} = \eta^p(t_i)\left(\eta^0_{max} + \delta\eta_{max}, b^0 + \delta b c^0 + \delta c\right) - \eta(t_i) \tag{6}$$

To estimate preliminary values for η^0_{max}, b^0, c^0, the following steps are proposed: Rewriting Eq. 3 as follows:

$$1 - \frac{\eta(t_i)}{\eta^0_{max}} = e^{-b^0(t_i)^{c^0}} \tag{7}$$

By taking the natural logarithm of the both sides of Eq. 7, the modified KTF model will become:

$$\ln\left[1 - \frac{\eta(t_i)}{\eta^0_{max}}\right] = -b^0(t_i)^{c^0} = > (t_i)^{c^0} = \frac{\ln\left[1 - \frac{\eta(t_i)}{\eta^0_{max}}\right]}{-b^0} \tag{8}$$

At the $(\mathrm{i}+1)^{\mathrm{th}}$ epoch, Eq. 8 is formed as:

$$(t_{i+1})^{c^0} = \frac{\ln\left[1 - \frac{\eta(t_{i+1})}{\eta^0_{max}}\right]}{-b^0} \tag{9}$$

Dividing Eqs. 8 and 9 gives the following equation for estimating preliminary parameter c^0:

$$c^0 = log_{\frac{t_i}{t_{i+1}}}\left[\frac{\ln\left[1 - \frac{\eta(t_i)}{\eta^0_{max}}\right]}{\ln\left[1 - \frac{\eta(t_{i+1})}{\eta^0_{max}}\right]}\right] \tag{10}$$

The value c^0 from Eq. 10 is substituted into Eq. (8), then b^0 can be determined as follows:

$$b^0 = -\frac{\ln\left[1 - \frac{\eta(t_i)}{\eta^0_{max}}\right]}{(t_i)^{c^0}} \tag{11}$$

2.3 Computation of Modified KTF Parameters

If the preliminary parameters are estimated sufficiently close to their desired values then the residuals are small. In this case, the residual value $V_{\eta(t_i)}$ in Eq. 4 can be approximated by a Taylor series expansion, retaining only the first order terms of $\partial_{\eta_{max}}, \delta b, \delta c$ as follows:

$$V_{\eta(t_i)} = \eta^p(t_i)\left(\eta^0_{max}, b^0, c^0\right) + \left(\frac{\partial \eta^p(t_i)}{\partial_{\eta_{max}}}\right)_0 \delta_{\eta_{max}} + \left(\frac{\partial \eta^p(t_i)}{\partial_b}\right)_0 \delta_b + \left(\frac{\partial \eta^p(t_i)}{\partial_c}\right)_0 \delta_c - \eta(t_i) \tag{12}$$

where $\frac{\partial \eta^p(t_i)}{\partial_{\eta max}} = 1 - e^{-b^0(t_i)^{c^0}}$; $\frac{\partial \eta^p(t_i)}{\partial_b} = \eta_{max}(t_i)^{c^0} e^{-b^0(t_i)^{c^0}}$;

and $\frac{\partial \eta^p(t_i)}{\partial_c} = \eta_{max} b^0 . e^{-b^0(t_i)^{c^0}} (t_i)^{c^0} \ln(t_i)$

The residual between the predicted values and their corresponding measured values is expressed as follows:

$$\ell_i = \eta^p(t_i)\left(\eta^0_{max}, b^0, c^0\right) - \eta(t_i) \tag{13}$$

Finally, the observation equation is derived as:

$$V_{\eta(t_i)} = \left(\frac{\partial \eta^p(t_i)}{\partial_{\eta_{max}}}\right)_0 \delta_{\eta_{max}} + \left(\frac{\partial \eta^p(t_i)}{\partial_b}\right)_0 \delta_b + \left(\frac{\partial \eta^p(t_i)}{\partial_c}\right)_0 \delta_c + \ell_i \tag{14}$$

The coefficients of Eq. 14 are symbolized as $\left(\frac{\partial \eta^p(t_i)}{\partial_{\eta_{max}, b, c}}\right)_0 = a_{ij}$, with $i = 1 \div n$ and $j = 1, 2, 3$, corresponding to the unknowns $\partial_{\eta_{max}}, \delta_b, \delta_c$. By doing so, a system of linear equations in Eq. 14 can be represented in matrix form as follows:

$$\boldsymbol{V} = \boldsymbol{A}.\boldsymbol{X} + \boldsymbol{L} \tag{15}$$

where $\boldsymbol{A}$ is the design matrix, $\boldsymbol{V}$ is the vector of discrepancies, $\boldsymbol{L}$ is the vector of observations, and $\boldsymbol{X}$ is the vector of unknowns.

$$\boldsymbol{A} = \begin{bmatrix} a_{1,1} & a_{1,2} & a_{1,3} \\ a_{2,1} & a_{2,2} & a_{2,3} \\ \cdots & \cdots & \cdots \\ a_{n,1} & a_{n,2} & a_{n,3} \end{bmatrix}; \boldsymbol{V} = \begin{bmatrix} V_1 \\ V_2 \\ \cdots \\ V_n \end{bmatrix}; \boldsymbol{L} = \begin{bmatrix} \ell_1 \\ \ell_2 \\ \cdots \\ \ell_n \end{bmatrix}; \boldsymbol{X} = \begin{bmatrix} \partial_{\eta_{max}} \\ \delta_b \\ \delta_c \end{bmatrix}. \tag{16}$$

The following normal equation can be derived from a set of different observation equations:

$$\left(\boldsymbol{A}^T\boldsymbol{A}\right)\boldsymbol{X} + \left(\boldsymbol{A}^T\boldsymbol{L}\right) = 0 \tag{17}$$

$$\boldsymbol{X} = -\left(\boldsymbol{A}^T\boldsymbol{A}\right)^{-1}\boldsymbol{A}^T\boldsymbol{L} \tag{18}$$

Considering these derived $\boldsymbol{X}$ values, parameters η_{max}, b, c of the prediction model can be firstly determined by Eq. 5, and then Eq. 3 is used to calculate the subsidence value of the ith epoch.

2.4 Accuracy Assessment

Accuracy of the current prediction model is assessed by comparing the predicted result with the measured data in terms of Root Mean Square Error (*RMSE*), mean absolute error (*MAE*) and correlation coefficient (r). The lower *RMSE* and *MAE* together with the higher r indicate the more accurate prediction of the model. More specifically, the following equations are used:

$$RMSE = \sqrt{\frac{1}{\mathrm{n}}\sum\nolimits_{i=1}^{n}\left[\eta^{p}(t_i) - \eta(t_i)\right]^2} \tag{19}$$

$$MAE = \frac{1}{n}\sum\nolimits_{i=1}^{n}\left|\eta(t_i) - \eta^{p}(t_i)\right| \tag{20}$$

$$r = \frac{\sum_{i=1}^{n}\left(\eta(t_i) - \bar{\eta}\right)\left(\eta^{p}(t_i) - \overline{\eta^{p}}\right)}{\sqrt{\sum_{i=1}^{n}\left(\eta(t_i) - \bar{\eta}\right)^2 * \sum_{i=1}^{n}\left(\eta^{p}(t_i) - \overline{\eta^{p}}\right)^2}} \tag{21}$$

where $\eta(t_i)$ and $\eta^{p}(t_i)$ are the measured and the predicted values at t_i; $\bar{\eta}$ and $\overline{\eta^{p}}$ are the corresponding medium values of measured and predicted values, respectively.

3 Computational Tool for Time-Series Prediction of Mining Subsidence

Based on the modified KTF method proposed in the Sect. 2, a computational tool for time-series prediction of mining subsidence was developed. It is noted that the tool was programmed in Visual Studio.Net 2013 Ultimate, an object-oriented programming language with Visual Studio DevExpress Universal 15.2.7 library package [20]. The tool can run in different versions of Microsoft Windows including the version 7, 8 and 10 and it is also compatible with both 32- and 64-bit environments.

Figure 1 presents a workflow for the determination of the preliminary parameters $(\eta^{0}_{max}, b^{0}, c^{0})$ of the modified KTF method. A workflow for the computation of the corresponding final parameters (η_{max}, b, c) based on the least-squares principle and accuracy assessment (*RMSE*, *MAE* and r) is illustrated in Fig. 2.

A Graphic User Interface (GUI) of the computational tool is shown in Fig. 3. Input data could be either entered directly through the GUI or imported from text or excel files. The computed results including the model's parameters and the predicted values, are stored both in txt and csv formats, which make them easier to be shared with and edited by other softwares. Furthermore, measurement data and prediction results can be exported/converted into a graphical file in Drawing Exchange Format (DXF). DXF is a

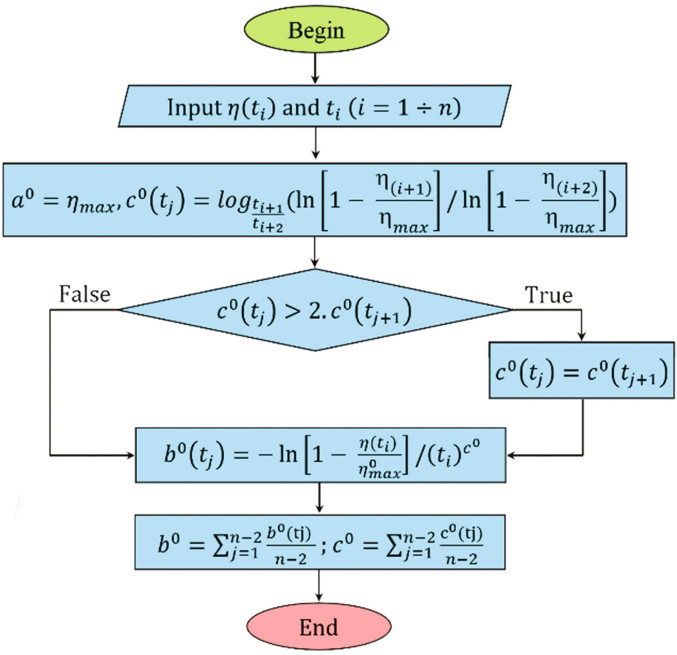

Fig. 1. Workflow used for estimating preliminary parameters of modified KTF

CAD data file format developed by Autodesk for enabling data interoperability between AutoCAD and other programs [21].

4 A Case Study of Mining Subsidence at Mong Duong Colliery, Quang Ninh Province in Vietnam

4.1 Description of the Study Site

Mong Duong colliery, a typical coal mine in Vietnam with more than 35-year operation, is selected as a case study for validating the modified KTF model. This mine is located about 10 km north of Cam Pha city, as shown in Fig. 4. The mine boundary was taken according to the Decision No. 1122/QD-HDQT dated on May 16, 2008, by the Chairman of the Vinacomin's Board of Directors on Approving the master plan for coal mines boundary of the Vietnam National Coal - Mineral Industries Holding Corporation Limited.

From explorations' results, there are in total 22 coal seams in the Mong Duong colliery. To date, the coal is excavated in various seams and multi-layer seams, mainly varying from −100 m to −250 m below the sea level. They consist of seams H10, G9 in the East Wing, G9 in the West Wing, G9 in Vu Mon area, II (11) and K8, etc. There are two shafts including the main shaft and the auxiliary shaft, which were built correspondingly from +18 m and +6.5 m down to −97.5 m.

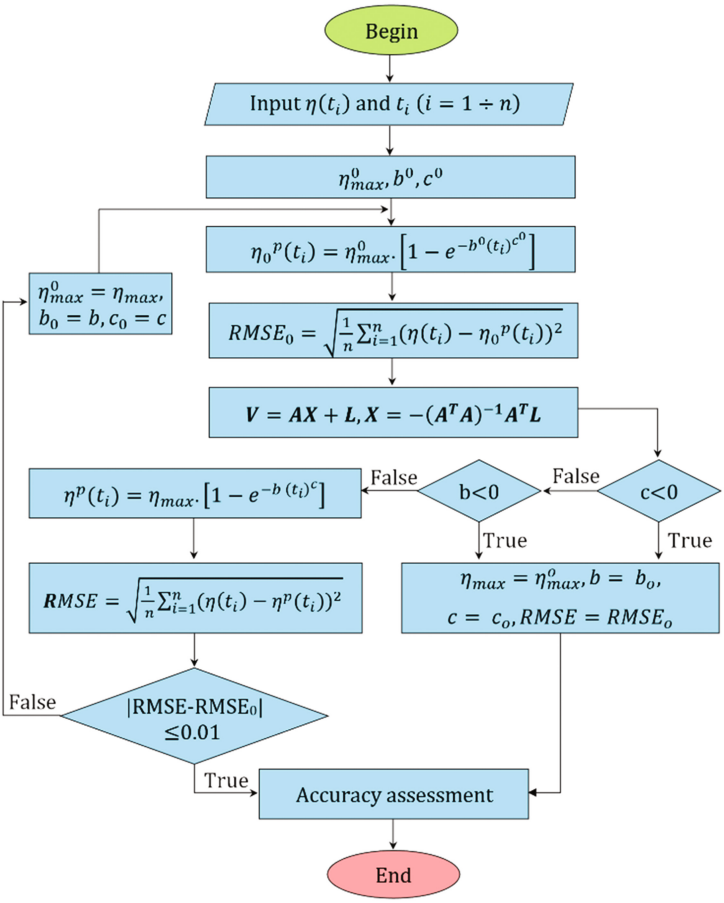

Fig. 2. Workflow used for the computing final parameters of modified KTF

Underground mining activity in the Mong Duong colliery has resulted in various subsidence problems that caused several damages to residential areas, the main shaft, the wind turbine station, the 110/35/6 kV substation and office buildings on the mine surface.

4.2 Data Collection and Processing

To assess and forecast potential land subsidence due to the underground mining at the Mong Duong colliery, a monitoring network has been established in the G9 BMD seam, where the Face No.2 was mined. The G9 BMD seam has an average thickness of 2.5 m with an average slope angle of 35°. The Face No.2 was commenced in the second quarter 2013 and finished in second quarter 2014. The panel was prepared along the seam strike and retreated, cutting coal by blasting and supporting the roof using hydraulic props (Fig. 5).

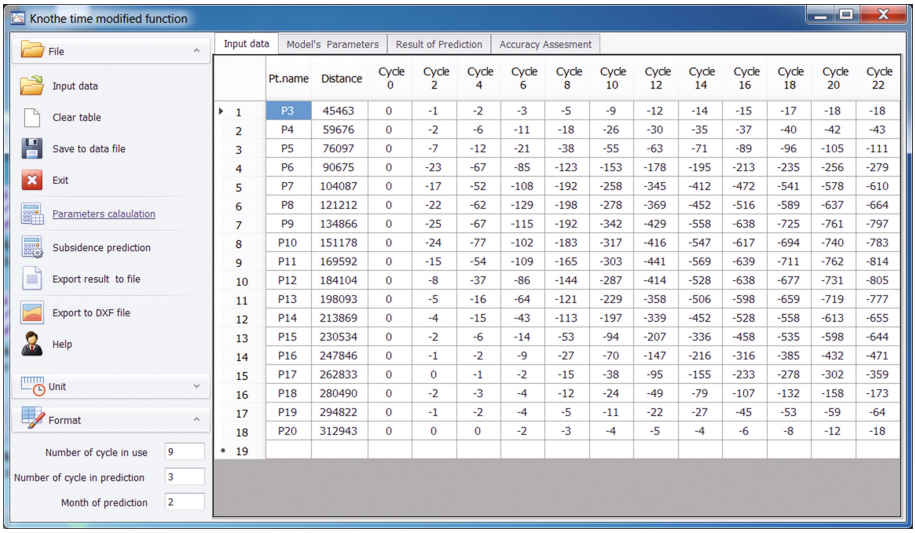

	Pt.name	Distance	Cycle 0	Cycle 2	Cycle 4	Cycle 6	Cycle 8	Cycle 10	Cycle 12	Cycle 14	Cycle 16	Cycle 18	Cycle 20	Cycle 22
1	P3	45463	0	-1	-2	-3	-5	-9	-12	-14	-15	-17	-18	-18
2	P4	59676	0	-2	-6	-11	-18	-26	-30	-35	-37	-40	-42	-43
3	P5	76097	0	-7	-12	-21	-38	-55	-63	-71	-89	-96	-105	-111
4	P6	90675	0	-23	-67	-85	-123	-153	-178	-195	-213	-235	-256	-279
5	P7	104087	0	-17	-52	-108	-192	-258	-345	-412	-472	-541	-578	-610
6	P8	121212	0	-22	-62	-129	-198	-278	-369	-452	-516	-589	-637	-664
7	P9	134866	0	-25	-67	-115	-192	-342	-429	-558	-638	-725	-761	-797
8	P10	151178	0	-24	-77	-102	-183	-317	-416	-547	-617	-694	-740	-783
9	P11	169592	0	-15	-54	-109	-165	-303	-441	-569	-639	-711	-762	-814
10	P12	184104	0	-8	-37	-86	-144	-287	-414	-528	-638	-677	-731	-805
11	P13	198093	0	-5	-16	-64	-121	-229	-358	-506	-598	-659	-719	-777
12	P14	213869	0	-4	-15	-43	-113	-197	-339	-452	-528	-558	-613	-655
13	P15	230534	0	-2	-6	-14	-53	-94	-207	-336	-458	-535	-598	-644
14	P16	247846	0	-1	-2	-9	-27	-70	-147	-216	-316	-385	-432	-471
15	P17	262833	0	0	-1	-2	-15	-38	-95	-155	-233	-278	-302	-359
16	P18	280490	0	-2	-3	-4	-12	-24	-49	-79	-107	-132	-158	-173
17	P19	294822	0	-1	-2	-4	-5	-11	-22	-27	-45	-53	-59	-64
18	P20	312943	0	0	0	-2	-3	-4	-5	-4	-6	-8	-12	-18
19														

Fig. 3. Illustration of Graphic User Interface of computational tool

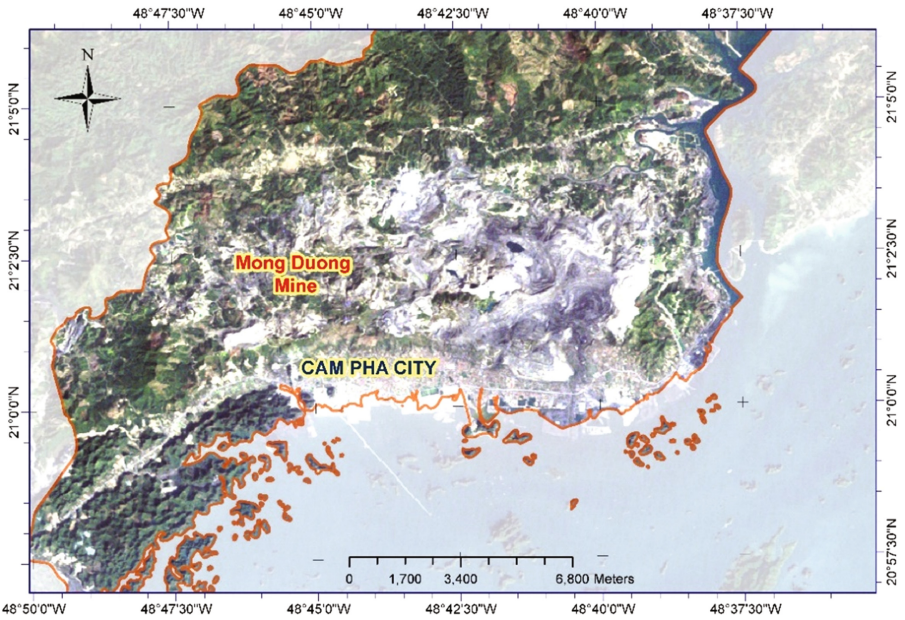

Fig. 4. Mong Dong colliery location

The measurements were carried out using Leica NAK2 automatic level instrument shown in Fig. 6. The observation network consists of 2 leveling lines - the line P was established in the strike direction and the line D is along the dip direction of the Face

Fig. 5. Face No.2 with hydraulic props (photo courtesy of Long Quoc Nguyen)

Fig. 6. Leica NAK2 level

No.2, as illustrated in Fig. 7. The land subsidence data have been continuously measured from 2013 to 2015 with 12 repeated epochs. The time interval between two successive epochs is approximately 2 months. Measurement precision satisfied the Vietnam National Specifications on Mine Surveying (closed loop misclosure is less than $20\sqrt{L}(\text{mm})$ [22] with L is the total length of the leveling route.

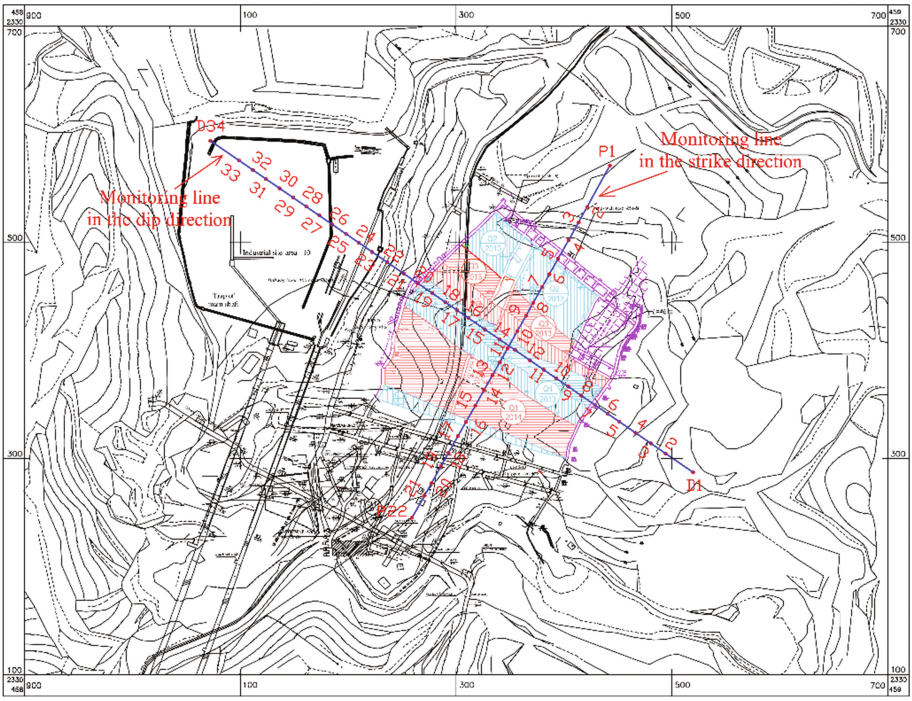

Fig. 7. The monitoring lines at the G9 BMD seam of the Mong Duong colliery

In order to detect and eliminate outliers, the difference in level between two adjacent benchmarks is determined from both forward and backward measurements. The difference in level between benchmarks is then taken equal to the average of the two values.

The monitoring observation results obtained from 16 benchmarks on the line P (see Fig. 7) were considered in the evaluation of the suitability of the algorithm used for determining the model parameters as well as the prediction accuracy of the modified KTF model. The datasets are summarized in Table 1.

Table 1. Measured subsidence (mm) with time from 16 benchmarks on line P

Point name	Cycle											
	1	2	3	4	5	6	7	8	9	10	11	12
P3	0	−1	−2	−3	−5	−9	−12	−14	−15	−17	−18	−18
P4	0	−2	−6	−11	−18	−26	−30	−35	−37	−40	−42	−43
P5	0	−7	−12	−21	−38	−55	−63	−71	−89	−96	−105	−111
P6	0	−23	−67	−85	−123	−153	−178	−195	−213	−235	−256	−279
P7	0	−17	−52	−108	−192	−258	−345	−412	−472	−541	−578	−610
P8	0	−22	−62	−129	−198	−278	−369	−452	−516	−589	−637	−664
P9	0	−25	−67	−115	−192	−342	−429	−558	−638	−725	−761	−797
P10	0	−24	−77	−102	−183	−317	−416	−547	−617	−694	−740	−783
P11	0	−15	−54	−109	−165	−303	−441	−569	−639	−711	−762	−814
P12	0	−8	−37	−86	−144	−287	−414	−528	−638	−677	−731	−805
P13	0	−5	−16	−64	−121	−229	−358	−506	−598	−659	−719	−777
P14	0	−4	−15	−43	−113	−197	−339	−452	−528	−558	−613	−655
P15	0	−2	−6	−14	−53	−94	−207	−336	−458	−535	−598	−644
P16	0	−1	−2	−9	−27	−70	−147	−216	−316	−385	−432	−471
P17	0	0	−1	−2	−15	−38	−95	−155	−233	−278	−302	−359
P18	0	−2	−3	−4	−12	−24	−49	−79	−107	−132	−158	−173

4.3 Land Subsidence Model and Its Performance Assessment

The data in the first nine cycles of 16 points were used to calibrate the subsidence model, whereas the remaining data (i.e. the data of cycles 10, 11 and 12) were used for validating the model as well as confirming its predictive capability. The algorithm described in Sect. 2 was applied to determine the parameters of the subsidence model for each point for the first 9 cycles. The calculated parameters are given in Fig. 8. The results show that the model performs well with the determining parameters set.

In this study, the authors did not use observation points such as points 1, point 2, point 19, and point 20 either to build the prediction model or to evaluate prediction results. As those points lying at the beginning and at the ending of monitoring lines, their settlement rules are not stable, hence, their subsidence curves do not match the curve for the modified KTF model.

To validate the predictive ability of the model, these calculated parameters have been used to predict the subsidence of points at the remaining cycles, i.e., the 10^{th}, 11^{th} and 12^{th} cycles. The subsidence calculated from the model was subsequently compared

Input data | Model's Parameters | Result of Prediction | Accuracy Assesment

	Point name	ηmax	b	c	RMSE (mm)	MAE (mm)	r
1	P3	-16,378	2,648	2,604	0	0	0,997
2	P4	-40,305	2,572	2,067	1	0	0,999
3	P5	-134,787	1,030	1,673	3	2	0,996
4	P6	-281,385	1,421	1,297	4	3	0,999
5	P7	-624,896	1,409	2,003	4	3	1,000
6	P8	-822,095	1,000	1,833	4	3	1,000
7	P9	-1031,594	1,022	2,145	12	10	0,999
8	P10	-867,376	1,279	2,269	15	13	0,998
9	P11	-776,726	1,796	2,694	14	11	0,998
10	P12	-722,038	1,945	2,917	9	6	0,999
11	P13	-730,788	1,739	3,219	6	5	1,000
12	P14	-586,518	2,337	3,545	5	4	1,000
13	P15	-601,833	1,437	4,298	5	4	0,999
14	P16	-476,517	1,077	4,000	4	3	0,999
15	P17	-326,077	1,246	4,713	3	2	1,000
16	P18	-144,227	1,361	4,129	1	1	1,000
▸▸ 17							

Fig. 8. Model parameters and its accuracy

with that of observations with a deviation between predicted and monitoring data calculated by Eq. 22.

$$\Delta_i = \eta_i - \eta_i' \tag{22}$$

where Δ_i is the difference between predicted value and its respective measurement of the ith point; η_i is the subsidence calculated from measurement data and η_i' is the value of prediction.

Small deviations shown in (Fig. 9) confirm a good model obtained. The biggest errors in prediction is at the point P9 with predicted errors at epochs 10, 11, 12 are

Input data | Model's Parameters | Result of Prediction | Accuracy Assesment

	Point name	Cycle 18 (η18)	Cycle 18 (η'18)	Δ18	Cycle 20 (η20)	Cycle 20 (η'20)	Δ20	Cycle 22 (η22)	Cycle 22 (η'22)	Δ22
1	P3	-16	-17	1	-16	-18	2	-16	-18	2
2	P4	-39	-40	1	-40	-42	2	-40	-43	3
3	P5	-96	-96	0	-105	-105	0	-111	-111	0
4	P6	-228	-235	7	-239	-256	17	-249	-279	30
5	P7	-520	-541	21	-556	-578	22	-581	-610	29
6	P8	-584	-589	5	-640	-637	-3	-685	-664	-21
7	P9	-755	-725	-30	-833	-761	-72	-895	-797	-98
8	P10	-704	-694	-10	-763	-740	-23	-805	-783	-22
9	P11	-711	-711	0	-747	-762	15	-765	-814	49
10	P12	-676	-677	1	-705	-731	26	-717	-805	88
11	P13	-673	-659	-14	-710	-719	9	-725	-777	52
12	P14	-570	-558	-12	-583	-613	30	-586	-655	69
13	P15	-546	-535	-11	-588	-598	10	-600	-644	44
14	P16	-392	-385	-7	-442	-432	-10	-466	-471	5
15	P17	-289	-278	-11	-317	-302	-15	-325	-359	34
16	P18	-128	-132	4	-140	-158	18	-143	-173	30
▸▸ 17										

Fig. 9. Differences between measured and predicted values

Input data | Model's Parameters | Result of Prediction | Accuracy Assesment

	Point name	RMSE (mm)	MAE (mm)	RMSE/Smax (%)	MAE/Smax (%)	r
1	P3	2	1	9	9	0,969
2	P4	2	2	6	5	1,000
3	P5	0	0	0	0	0,998
4	P6	21	18	7	6	0,996
5	P7	24	24	4	4	0,998
6	P8	13	9	2	1	0,994
7	P9	73	67	7	6	0,998
8	P10	20	19	2	2	0,997
9	P11	29	21	4	3	0,980
10	P12	53	39	7	5	0,948
11	P13	32	25	4	3	0,973
12	P14	44	37	7	6	0,962
13	P15	27	22	4	4	0,977
14	P16	7	7	2	1	0,989
15	P17	22	20	7	6	0,857
16	P18	20	17	14	12	0,993
17						

Fig. 10. Assessment of predicted results

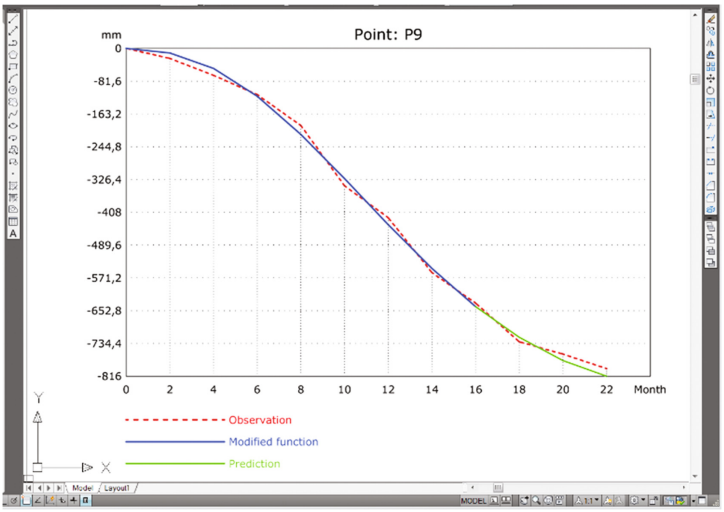

Fig. 11. Comparison of prediction and observation curves of point P9

−30 mm, −72 mm and -98 mm, respectively. These errors correspond to 4%, 8.6%, 11% of the actual subsidence magnitude of the corresponding measurement epochs. These errors are proportional to the temporal separation between the time of prediction and that of the last stage used for building prediction model, i.e., the 9th epoch. More strictly, the longer the temporal separation is, the higher error in prediction we get.

Statistical indicators including $RMSE$, MAE, $RMSE/\eta_{max}$, MAE/η_{max} and r were used to assess the accuracy of the modified KTF model in predicting subsidence

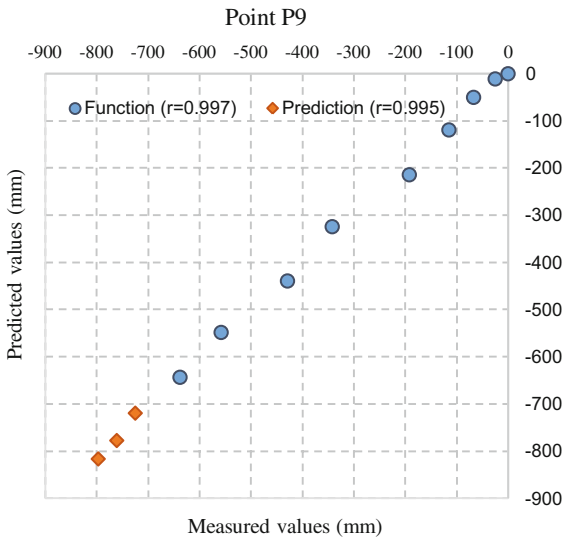

Fig. 12. Correlation between the measured and predicted values of point P9

monitored along the considered line P. The validation dataset is given in Fig. 10. It can be seen from the calculated results that the largest *RMSE* and *MAE* values are 44 mm and 37 mm, respectively, which are actually equivalent to 7% and 6% of maximum subsidence. The largest RMS/η_{max} and RMS/η_{max} values are obtained at point P18, which equal to 14% and 12%, respectively. This can be explained by the fact that this point is close to the trough subsidence edge so that the rule of point settlement has not been well-defined.

Figure 11 plots a comparison of the anticipated curve of point P9, which is calculated from Eq. (3), with the curve of actual values. It is seen from the figure that the model is able to predict very well the surface subsidence curve observed in the Mong Duong colliery.

The correlation coefficients between predicted and measured values for both cases of parameters determination and subsidence prediction are plotted in Fig. 12. With high values in the building model and the prediction results, it indicates that the predictive model is consistent with the measured data.

5 Conclusion

This research proposes a new method for calculating the preliminary values of the input parameters of the modified KTF model proposed by Chinh [19]. The method is basically based on the least-squares principle and observation data, which results in a more practical facilitation to the determination of model parameters. The computational tool has been developed incorporating a friendly user-interface and more flexibility for post-processing of the calculated results.

The functionality and accuracy of the tool were evaluated and validated against the measured subsidence values at 16 monitoring points along the observation line P which is located in the Face. No.2 at the Mong Duong colliery. The comparison result shows a very well agreement between the model prediction values and their corresponding geodetic monitoring data, where the largest *RMSE* and *MAE* are 44 mm and 37 mm, respectively. The smallest correlation coefficient r is calculated equal to 0.857, which indicates a high correlation between the monitoring measurements and their predicted values. It is concluded that the developed tool incorporating the modified KTF model is useful and suitable for predicting and evaluating potential mining-induced subsidence in the mining industry. Thereby, the tool can support appropriate strategy to prevent and minimize potential impact caused by land subsidence phenomenon.

A main limitation of this research work is that points lying at the beginning and at the end of the observation line have been excluded from the calculation model as they could have influenced by an irregular process of subsidence. The modified KTF applied in this research, therefore, cannot represent the subsidence of these points over time. More flexible prediction models are thus necessary.

Acknowledgement. This research was funded by the Mong Duong coal joint stock company and the Department of Mine Surveying, Hanoi University of Mining and Geology. The funding support is greatly appreciated.

Conflict of interest. The authors declare that there is no conflict of interest.

References

1. Reddish, D., Whittaker, B.: Subsidence: Occurrence. Prediction and Control. Elsevier, New York (1989)
2. Can, E., Kuşcu, Ş., Kartal, M.E.: Effects of mining subsidence on masonry buildings in Zonguldak hard coal region in Turkey. Environ. Earth Sci. **66**, 2503–2518 (2012)
3. Bozeman, M.: Underground Hard-Rock Mining: Subsidence and Hydrologic Environmental Impacts. Google Scholar (2002)
4. Phung, D.M.: Selection of Appropriate Technical and Technological Solutions for Exploitation in Areas Where Existing Historical, Cultural, Industrial and Civil Works. Vinacomin (2011)
5. Truc, K.K.: Defining land subsidence parameters of Thongnhat coal mine. Institute of Mining Science and Technology (1991)
6. Long, Q.N.: Sectional diagram of dynamic subsidence trough at the Mong Duong coal mine: evaluation and prediction. J. Min. Earth Sci. (JMES) **56**, 58–66 (2016)
7. Long, Q.N., My, C.V., Luyen, K.B.: Divergency verification of predicted values and monitored deformation indicators in specific condition of Thong Nhat underground coal mine (Vietnam). Geoinf. Pol. **15**, 15–22 (2016)
8. Jarosz, A., Karmis, M., Sroka, A.: Subsidence development with time—experiences from longwall operations in the appalachian coalfield. Geotech. Geol. Eng. **8**, 261–273 (1990)
9. Liu, X., Wang, J., Guo, J., Yuan, H., Li, P.: Time function of surface subsidence based on Harris model in mined-out area. Int. J. Min. Sci. Technol. **23**, 245–248 (2013)
10. Bahuguna, P., Srivastava, A., Saxena, N.: A critical review of mine subsidence prediction methods. Min. Sci. Technol. **13**, 369–382 (1991)

11. Hu, Q.F., Cui, X.M., Wang, G., Wang, M.R., Ji, Y.X., Xue, W.: Key technology of predicting dynamic surface subsidence based on knothe time function. JSW **6**, 1273–1280 (2011)
12. Zhang, Z., Zou, Y., Chen, J., Wang, Y.: Prediction model of land dynamic settlement in coal mining subsidence area. Trans. Chin. Soc. Agric. Eng. **32**, 246–251 (2016)
13. Lian, X.: Prediction model of dynamic subsidence caused by underground coal mining. Electron. J. Geotech. Eng. **21** (2016)
14. Hu, Q., Deng, X., Feng, R., Li, C., Wang, X., Jiang, T.: Model for calculating the parameter of the Knothe time function based on angle of full subsidence. Int. J. Rock Mech. Min. Sci., 19–26 (2015)
15. Wang, C.: Analysis on the improved time function model of surface subsidence. Electron. J. Geotech. Eng. **19** (2015)
16. Zhanqiang, C., Jinzhuang, W.: Study on the time function of surface subsidence - The Improved Knothe time function. Chin. J. Rock Mechan. Eng. **9**, 018 (2003)
17. Cui, X., Miao, X., Wang, J.A., Yang, S., Liu, H., Song, Y., Liu, H., Hu, X.: Improved prediction of differential subsidence caused by underground mining. Int. J. Rock Mech. Min. Sci. **37**, 615–627 (2000)
18. Han, H.L., Cui, B.: Modeling of surface subsidence based on time function. Adv. Mater. Res. **422**, 318–321 (2012)
19. Chinh, N.D.: Geodetic Methods for Geodynamics. Hanoi University of Mining and Geology, Hanoi (2003)
20. https://www.devexpress.com/
21. https://www.autodesk.com/techpubs/autocad/acadr14/dxf/dxf_reference.htm
22. Ministry of Information & Communications: Vietnam National Specifications on Mine Surveying, Vietnam (2015)

Lightweight Unmanned Aerial Vehicle and Structure-from-Motion Photogrammetry for Generating Digital Surface Model for Open-Pit Coal Mine Area and Its Accuracy Assessment

Dieu Tien Bui[1(✉)], Nguyen Quoc Long[2], Xuan-Nam Bui[3], Viet-Nghia Nguyen[2], Chung Van Pham[2], Canh Van Le[2], Phuong-Thao Thi Ngo[4], Dung Tien Bui[5], and Bjørn Kristoffersen[1]

[1] GIS and IT Group, Department of Business and IT, University College of Southeast Norway, Gullbringvegen 36, 3800 Bø i Telemark, Norway
Dieu.T.Bui@usn.no
[2] Department of Mine Surveying, Hanoi University of Mining and Geology, Hanoi, Vietnam
Nguyenquoclong@humg.edu.vn
[3] Faculty of Mining, Hanoi University of Mining and Geology, Hanoi, Vietnam
Buixuannam@humg.edu.vn
[4] Faculty of Information Technology, Hanoi University of Mining and Geology, Hanoi, Vietnam
Ngothiphuongthao@humg.edu.vn
[5] Center for the Development of Science and Technology, Hanoi University of Mining and Geology, Hanoi, Vietnam
BuiTienDung204@gmail.com

Abstract. Recent technological innovations have led to the available of lightweight Unmanned Aerial Vehicle (UAV) and Structure-from-Motion (SfM) photogrammetry that are successfully applied for 3D topographic surveys. However, application of UAV and SfM for complex topographic areas i.e. open-pit mine areas is still poorly understood. This paper aims to investigate and verify potential application of these techniques for generating Digital Surface Model (DSM) at open-pit coal mine area and assessing its accuracy. For this purpose, the Nui Beo open-pit coal mine located in northeast Vietnam is selected as a case study. Accordingly, a total of 206 photos were captured using DJI Phantom 3 Professional. In addition, 19 ground control points (GCPs) were established using Leica TS09 total station. The accuracy of DSM was assessed using root-mean-square error (RMSE) in X, Y, Z, XY, and XYZ components. The result showed that the DSM model has high accuracy, RMSE on the 12 calibrated GCPs for X, Y, Z, XY, XYZ is 1.1 cm, 1.9 cm, 0.8 cm, 2.2 cm, and 2.3 cm, respectively, whereas RMSE on the 7 checked GCPs is 1.8 cm, 2.4 cm, 3.2 cm, 3.0 cm, and 4.4 cm for X, Y, Z, XY, XYZ components, respectively. We concluded that small UAV and SfM are feasible and valid tools for 3D topographic mapping in complex terrains such as open-pit coal mine areas.

© Springer International Publishing AG 2018
D. Tien Bui et al. (eds.), *Advances and Applications in Geospatial Technology and Earth Resources*, https://doi.org/10.1007/978-3-319-68240-2_2

Keywords: UAV · Structure-from-Motion · Photogrammetry · Open-pit mine · Nui Beo · Quang Ninh · Vietnam

1 Introduction

Direct surveying techniques i.e. Electronic Distance Measurement (EDM) surveys or Total Station (TS) and RTK Global Navigation Satellite System (GNSS) are the most widely used in surveying engineering and volumetric computation at open pit mining due to ability to obtain observations with millimeter accuracy [1]. However, they are cost and time consuming techniques, and in some complex environments, these techniques may be unsafe to workers [2]. Recent technological innovations have provided new alternative techniques for topographic surveying such as Terrestrial Laser Scanning (TLS) and airborne Light Detection and Ranging (LiDAR) or airborne laser scanning (ALS).

For TLS, although this technique is quite straightforward to use and millimeter accuracy could be obtained for objects at short distances, the cost and survey time still are a critical issue because this technique requires many scanning stations. Therefore, TLS may not be suited in projects dealing with complex topographies such as open-pit mines [3]. Regarding LiDAR, the accuracy is heavily influenced by GNSS and Inertial Measurement Unit (IMU) systems. Although accuracy is reported 0.1–0.5 m for vertical and 0.1–0.5 m for horizontal, however, higher vertical errors could occur in areas with complex environments [4].

Recent advancements in robots and GNSS technologies have provided various Unmanned Aerial Vehicles (UAVs) that can be used for topographic surveying. Especially, small and low-cost UAVs with nonmetric digital cameras are becoming a valid and effective alternative surveying technique for topographic reconnaissance and volumetric computation. In addition, the fusion of computer vision and photogrammetry have provided various Structure-from-Motion (SfM) and Multi-View Stereo (MVS) algorithms that have been successfully used for automatic processing UAV images with high quality results [5].

Overall, the main advantage of lightweight UAVs is that they can fly at low altitude with slow speed providing captured photos with fine spatial resolution and users defined temporal resolutions. The SfM algorithms are capable to automatically process orientation and geometry of images as well as camera positions [6]. More specifically, these algorithms have included MVS techniques that enable us to generate various 3D productions from UAV overlapped images, i.e. 3D point cloud and Digital Surface Model (DSM). Consequently, UAV and SfM photogrammetry have successfully been used in various fields i.e. surveying earthwork projects [2], stockpile volumetric [7], topography reconstructions [8], gravel-pit surveying and change estimation [9], ice-cored moraine degradation [10], erosion monitoring [11], precision farming applications [12], and geological mapping [13]. Common conclusions from these works demonstrate that UAV and SfM are new and efficient tools. Nevertheless, accuracy of the topographic mapping and its generated DSM derived from small UAVs and SfM photogrammetry at open pit mines has been rarely assessed and is still poorly understood.

In this work, we extend the body of knowledge by assessing the utility of UAV and SfM photogrammetry for topographic mapping and DSM at complex terrain of open-pit coal mine, with a case study at the Nui Beo coal mine in Quang Ninh province (Vietnam). Accordingly, a DJI Phantom 3 Professional was used to capture images, whereas ground control points were measured by using a Leica TS09 total station. The image processing was carried out using Agisoft®PhotoScan Professional 1.0 (APP). Finally, accuracy assessment was performed and conclusions are given.

2 Materials and Methods

2.1 Study Site

The study area (Fig. 1) is the Nui Beo open-pit coal mine (107°7'46", 20°57'46"), one of the five largest open-cast mines in Vietnam (Nui Beo, Deo Nai, Ha Tu, Cao Son, and Coc Sau), located in the Ha Long city, Quang Ninh province (Vietnam), around 160 km east of the Hanoi city. This mine is operated by the Nui Beo coal joint stock company that belongs to Vietnam National Coal and Mineral Industries (VINACOMIN) group.

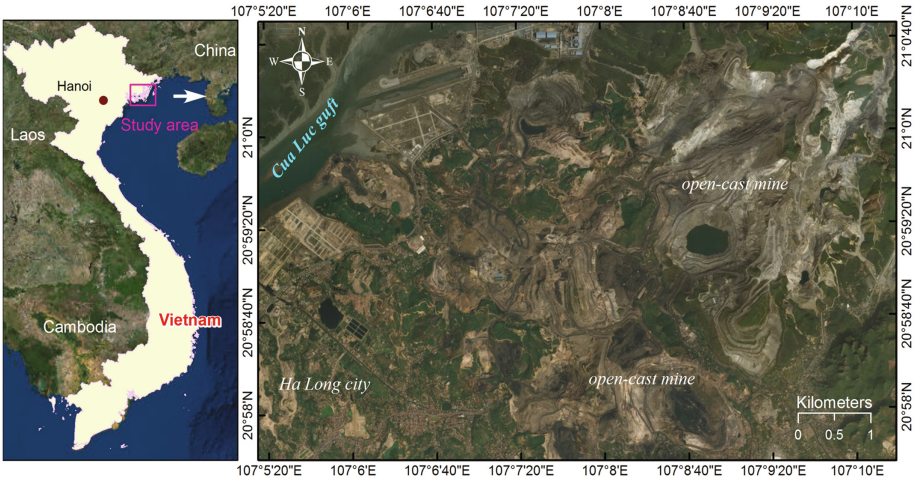

Fig. 1. Location of the Nui Beo coal mine.

It is noted that the Quang Ninh province produces 100% exported coals and nearly 90% domestic coals in Vietnam. The Nui Beo open-pit coal mine was designed in 1983 by the Giproruda Institute (former Soviet Union) and has officially operated since May 19, 1989. Total coal production is estimated around 32 million tons [14]. Total mineral coal area is around 3.75 km^2 for the open-pit coal mines and 5.6 km^2 for the underground coal mine.

Topographically, the Nui Beo coal mine presents complicated terrain conditions where the center is the opencast mining area, whereas the opening landfill is in the

north, industrial works locates in the south, and in the west is waste dumps and mining pits. Due to the surface mining activities, the high-end exploitation level reached −250 m (Fig. 2) [15].

Fig. 2. A photo of the Nui Beo open-pit coal mine (the photo was taken by Viet-Nghia Nguyen on January 6, 2017).

2.2 UAV and Camera

In this work, a lightweight DJI Phantom 3 professional (Fig. 3), which has been widely used for small surveying projects, was used to capture images due to its small size and weight, low-cost, ease of use, and still provides good image quality. This is a rotary wing quadcopter drone with four powerful motors that enable it to have high resistance wind and air pressure as well as higher stability [16]. The weight of the drone is approximately 1.3 kg including 0.75 kg payload. Flight time can reach 23 min with maximum speed 16 m/s in the no wind condition, whereas the highest altitude the drone can fly is 6 km [17].

The drone is equipped by nonmetric RGB Sony EXMOR camera with focal length is 3.61 mm and sensor size is 4.72 × 6.3 mm. This is called 4 K resolution camera (FC300X) where each image has a resolution of 4000 × 3000 pixels. Detailed characteristics of the DJI Phantom 3 professional and Sony EXMOR camera are summarized in Table 1.

Table 1. Characteristics of the DJI Phantom 3 professional and Sony EXMOR camera used in this research.

No.	Parameter	Characteristics
1	Total weight	1.28 kg
2	Height, length, width	18.5 cm, 28.9 cm, 28.95 cm
3	GNSS	GPS/GLONASS
4	Max. flight altitude	6 km
5	Max. flight time	~23 min
6	Max. speed	16 m/s
7	Operating temperature	0°C to 40°C
8	Camera sensor	Sony EXMOR 1/2.3", total pixels is 12.76 M
9	Camera lens	FOV 94° 20 mm f/2.8
10	Electronic shutter speed	8 s–1/8000 s
11	Image format	DNG, JPEG
12	Stabilization	3-axis (pitch, roll, yaw)

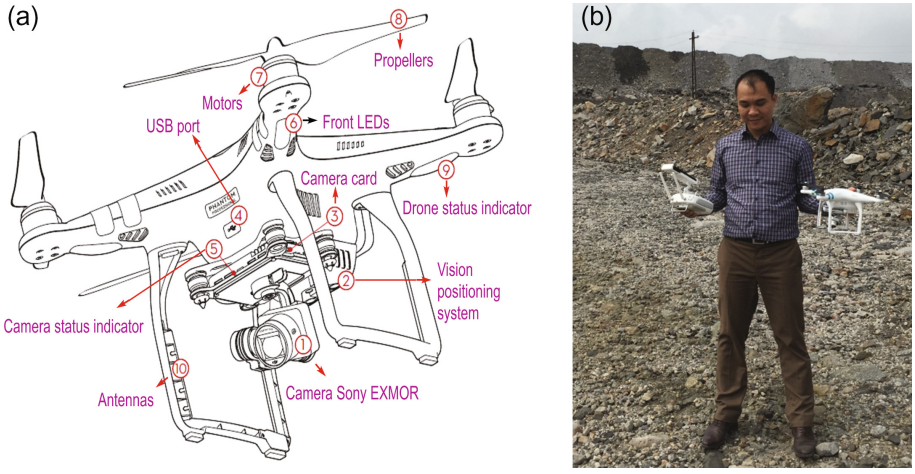

Fig. 3. (a) Description of components of a DJI Phantom 3 Professional (source http://www.dji.com/phantom-3-pro); (b) photo of a surveyor (Long-Quoc Nguyen) with the DJI Phantom 3 Professional used in this research.

2.3 Establishment of Ground Control Point

Before the image acquisition was carried out, it was necessary to place Ground Control Points (GCPs) for the study area surface. These GCPs are used for geo-referencing and evaluating the accuracy of the DSM model. Because the Nui Beo open-pit coal mine still is operating, field reconnaissance was conducted to select safe areas for placing these GCPs with a help of a handhold GPS i.e. iGeotrans [18] installed in iPhone 5. Accordingly, a total of 19 GCPs was established for a test area of 0.22 km^2 at the Nui Beo open-pit coal mine.

The GCPs were marked with a highly reflective material for enhancing the contrast in order for easier detecting in resulting images (Fig. 4a). The radius of the reflective material of 20 cm was used. In the next step, coordinates (x, y, z) for these GCPs were determined using a Leica TS09 total station (angular accuracy is 1" and distance accuracy is 1.5 mm + 2 ppm) and the available horizontal and vertical surveying network at the mine area. The measured coordinates (VN2000/UTM Zone 48 N) for these GCPs are shown in Table 2.

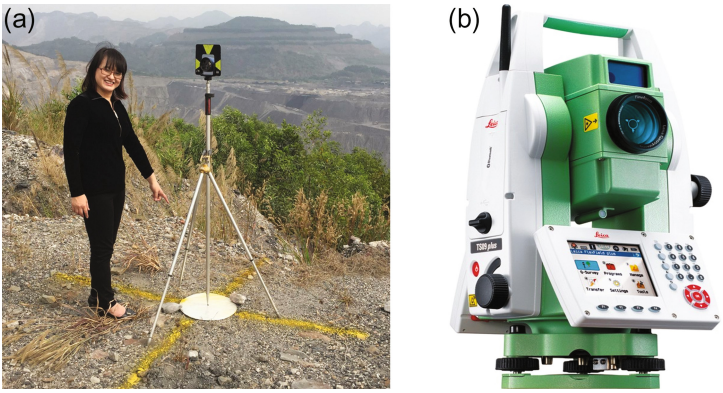

Fig. 4. (a) an example of established GCP and (b) Leica TS09 total station used for this work.

Table 2. XYZ coordinates of the Ground Control Points (GCPs) that measured by Leica TS06 total station for this study.

No.	Ground control point	X (m)	Y (m)	Z (m)
1	GCP1	722231.775	2319835.279	−42.683
2	GCP2	722175.977	2319988.738	−59.962
3	GCP3	722165.175	2320077.164	−69.634
4	GCP4	722148.859	2320112.948	−70.424
5	GCP5	722182.790	2320125.694	−74.195
6	GCP6	722325.858	2319730.317	−14.197
7	GCP7	722238.322	2319680.871	−5.625
8	GCP8	722150.193	2319657.720	3.110
9	GCP9	722198.746	2319720.943	−19.339
10	GCP10	722185.584	2319749.567	−20.668
11	GCP11	722152.108	2319776.945	−12.034
12	GCP12	722133.557	2319809.538	−7.448
13	GCP13	722122.263	2319871.090	−8.017
14	GCP14	722081.792	2319920.477	−7.439
15	GCP15	722076.996	2319993.553	−9.211
16	GCP16	721805.884	2319980.605	134.184
17	GCP17	721840.646	2319945.641	126.022
18	GCP18	721814.051	2319902.623	134.604
19	GCP19	721818.550	2319864.493	134.583

2.4 Image Acquisition

To design the flight plan, Pix4DCapture application installed in an Apple tablet was used. Accordingly, endlap and sidelap of images were selected as 80%. The application configured the flights, and then, the result was uploaded to the DJI Phantom 3 professional via telemetry. Due to the very high variation of the topography, a flying altitude of 90 m was selected and the flying speed was around 5 m/s. The auto and navigation modes were used for the flight project, and during flight, the drone could adjust its position and camera orientation automatically to ensure consistent images. As result, a total of 206 images were captured and used for deriving DSM. These images covered an area of 0.22 km^2.

When the flight project was done, these captured images were transferred from the drone into a personal computer for SfM analyses established in the Agisoft® PhotoScan Professional (APP). This photogrammetric software was used because it has proven to outperform other softwares in terms of accuracy [19]. Accordingly, the overall goal of the SfM analyses was to produce a high accurate and precise DSM for the project.

2.5 Photogrammetric Processing

Typically, the image processing using the SfM procedure consists of five steps: (i) photo alignment; (ii) bundle block adjustment; (iii) optimization, (iv) 3D surface reconstruction, (v) generation of Digital Surface Model (DSM).

In the first step, the captured images were aligned though a process named as selecting and triangulating the photos, also called "photo alignment". Using the function of "image quality" in APP, images with quality less than 0.5 were filtered and eliminated to ensure the high quality of the final 3D point cloud and the DSM models [20]. Position of these images that were initially estimated using the GNSS geographical coordinates was converted to the projected coordinate system (VN2000). Coordinates of these images were optimized in later processes. Feature detection process that used the Scale Invariant Feature Transform (SIFT) algorithm [21] was then carried out to detect tie points (also called key points) from overlapping areas (at least from 3 images), and in addition, other point across the body of images were also detected. These tie points and these GCPs were used later for the image matching and determining image and camera geometries.

Table 3. Camera-lens parameters used for this research.

No.	Parameter	Explanation
1	f	Focal length
2	Cx, Cy	Principal point offset of the image in x and y image coordinates
3	$K_1, K_2, K_3,$ and K_4	Radial distortion coefficient of $2^{nd,}$ 4^{th}, 6^{th}, 8^{th} -order, respectively
4	$P_1, P_2, P_3,$ and P_4	Tangential distortion coefficient
5	B_1 and B_2	Affinity and skew coefficients

In the second step, determination of the internal and external orientation parameters of the camera (including 13 parameters in Table 3) was carried out using these tie points and the GCPs, available information of the focal length and the camera parameters on the captured images, and the Camera Calibration tool in the APP software. Accordingly, the camera locations were determined using the greedy algorithm, and then, the camera positions, their orientation, and their distortion parameters were updated and adjusted via the bundle block adjustment process.

It is noted the RGB Sony EXMOR used in this study is frame type camera, therefore the calibration process was performed using the Brown's distortion model [22] to transform point coordinates in the local camera (X, Y, Z) to pixel coordinates (u, v) in the image frame using Eqs. 1, 2, 3 [23] as follows:

$$x^{'} = x(1 + K_1r^2 + K_2r^4 + K_3r^6 + K_4r^8) + (P_1(r^2 + 2x^2) + 2P_2xy)(1 + P_3r^2 + P_4r^4) \quad (1)$$

$$y' = y(1 + K_1r^2 + K_2r^4 + K_3r^6 + K_4r^8) + (P_2(r^2 + 2y^2) + 2P_2xy)(1 + P_3r^2 + P_4r^4) \quad (2)$$

$$u = 0.5 * w + Cx + x'f + x'B_1 + y'B_2;\ v = 0.5 * h + Cy + y'f \quad (3)$$

where $x = X/Z$; $y = Y/Z$; r = sqrt $(x^2 + y^2)$; w, h are the width and the height of the image in pixels; x', y' are the projected coordinates in the image plane; and u, v are pixel coordinates in the image frame.

Should be pointed out that although the internal and external parameters of the camera were found, however, in some cases, resulting DSM models may still show significant errors due to topographic complexity of the project and outliers points [20]. Therefore, an optimization process in step 3 was carried out. Accordingly, the tie points were manually inspected and outliers were removed. In addition, the number of GCPs was adjusted for possibly minimizing RMSE.

Once the optimization process was done and the optimized camera positions were derived, a dense surface reconstruction was carried out, in which depth maps for all the images were computed and combined, to generate 3D dense point cloud. Accordingly, the Mild depth filtering algorithm was adopted due to ability to eliminate outliers but still keep important features. This algorithm has proven suitable for poorly textured roofs areas [23], such as open-cash coal mine. Finally, the 3D dense point cloud was used to generate the final DSM for the study area.

2.6 Accuracy Assessment

Accuracy assessment of the Digital Surface Model (DSM) is an important task, and without this task, the DSM is useless. In this project, both the horizontal and vertical assessments were carried out by comparing DSM with the GCPs measured by the Leica total station in term of Root Mean Square Error (RMSE). More specifically, assessments in easting ($RMSE_X$), northing ($RMSE_Y$), vertical ($RMSE_Z$), horizontal

($RMSE_{XY}$), and all components ($RMSE_{XYZ}$) were used, as suggested in Agüera-Vega [24], using equations as follows:

$$RMSE_{\mathrm{X}} = SQRT\left[(1/n)\sum_{i=1}^{n}(X_{\mathrm{DSM}} - X_{\mathrm{GCPi}})^2\right] \quad (4)$$

$$RMSE_{\mathrm{Y}} = SQRT\left[(1/n)\sum_{i=1}^{n}(Y_{\mathrm{DSM}} - Y_{\mathrm{GCPi}})^2\right] \quad (5)$$

$$RMSE_{\mathrm{Z}} = SQRT\left[(1/n)\sum_{i=1}^{n}(Z_{\mathrm{DSM}} - Z_{\mathrm{GCPi}})^2\right] \quad (6)$$

$$RMSE_{\mathrm{XY}} = SQRT\left[(1/n)\sum_{i=1}^{n}((X_{\mathrm{DSM}} - X_{\mathrm{GCPi}})^2 + (Y_{\mathrm{DSM}} - Y_{\mathrm{GCPi}})^2)\right] \quad (7)$$

$$RMSE_{\mathrm{XYZ}} = SQRT\left[(1/n)\sum_{i=1}^{n}((X_{\mathrm{DSM}} - X_{\mathrm{GCPi}})^2 + (Y_{\mathrm{DSM}} - Y_{\mathrm{GCPi}})^2 + (Z_{\mathrm{DSM}} - Z_{\mathrm{GCPi}})^2)\right] \quad (8)$$

where X_{GCPi} and X_{DSM} are the X-coordinate component of GCP and corresponding coordinate in DSM, respectively; Y_{GCPi} and Y_{DSM} are the Y-coordinate component of GCP and corresponding coordinate in DSM, respectively; Z_{GCPi} and Z_{DSM} are the Z-coordinate component of GCP and corresponding coordinate in DSM, respectively.

3 Results and Discussion

3.1 Digital Surface Model and Its Accuracy

To determine the best camera-lens parameters in this research, an optimization process was carried out. For this task, the 19 GCPs were split in two subsets: (i) the first one is a calibrating dataset that accounts for 70% (12 GCPs) of the total GCPs and were used for the calibration of the camera-lens model and the bundle adjustment; the second one is a checking dataset that consists of the remaining GCPs (30%, 7 GCPs) were used for checking the final model and confirming it accuracy. Distribution of these GCPs in this study area is shown in Fig. 5. It could be seen that no GCP was placed at the lower left corner and the central of the study areas. This is because these were unsafe areas to reach due to the coal seams still were exploiting.

Using the detected tie points and 13 GCPs (Fig. 5), the optimization process was carried out with five runs to ensure a stable result. The final calibrated coefficients of the camera-lens model are shown in Table 4. It could be seen that the errors of these parameters are low, indicating good results.

Table 4. Camera-lens calibrated coefficients.

No	Parameter	Value	Error
1	f	2314.550	0.59
2	Cx	−22.8598	0.1600
3	Cy	11.4502	0.1000
4	B1	9.0365	0.2700
5	B2	2.7214	0.1500
6	K1	−0.006685	0.000110
7	K2	−0.008707	0.000390
8	K3	0.035100	0.000540
9	K4	−0.016010	0.000250
10	P1	−0.001735	0.000024
11	P2	0.000523	0.000009
12	P3	−0.767175	0.013000
13	P4	0.264946	0.008700

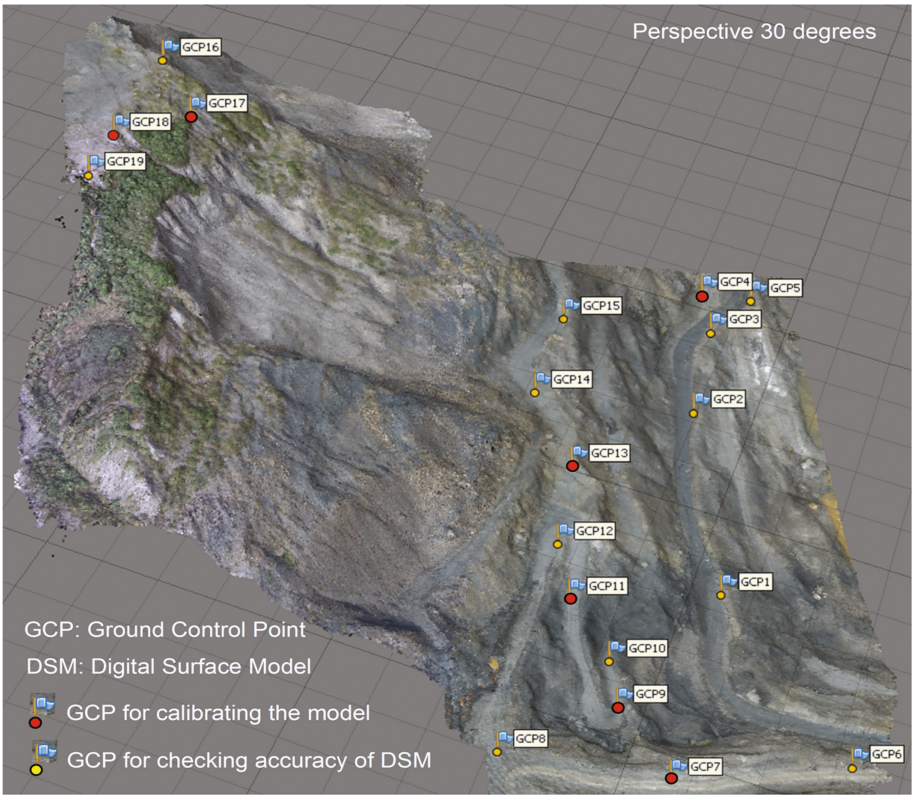

Fig. 5. 3D dense cloud and distribution of the GCPs in the study area.

Using the obtained coefficients, a 3-D dense cloud (Fig. 5) and a Digital Surface Model (DSM) (Fig. 6) for the study area were generated. Based on the DSM, a slope map (Fig. 7) was generated additionally. The goodness-of-fit of the DSM model with the calibrating dataset is shown in Table 5. It could be seen that RMSE for X, Y, Z, XY, XYZ is 1.1 cm, 1.9 cm, 0.8 cm, 2.2 cm, and 2.3 cm, respectively. The highest error for X is 2.9 cm and for Y is 3.1 cm (GCP1, Table 5). Whereas the highest error for Z is 1.7 cm (GCP14, Table 5) and the highest error for XY and XYZ are both 4.3 cm (GCPs 1 and 2, Table 5). These indicate that the fit of the DSM model with the calibrating dataset is very high.

Table 5. Error and RMSE in X, Y, Z, XY, and XYZ of GCPs used for the model calibration.

Calibration points	X error (m)	Y error (m)	Z error (m)	XY error (m)	XYZ error (m)
GCP1	0.029	0.031	−0.007	0.043	0.043
GCP2	−0.013	−0.041	−0.004	0.043	0.043
GCP3	0.009	0.025	0.004	0.026	0.027
GCP5	−0.006	−0.009	0.001	0.011	0.011
GCP6	−0.005	−0.009	0.002	0.010	0.011
GCP8	−0.005	−0.005	−0.012	0.007	0.014
GCP10	−0.013	0.017	0.007	0.022	0.023
GCP12	0.005	−0.024	0.008	0.024	0.025
GCP14	−0.002	−0.001	−0.017	0.002	0.017
GCP15	−0.005	0.009	0.012	0.011	0.016
GCP16	−0.002	0.001	−0.003	0.002	0.004
GCP19	0.002	0.001	0.000	0.002	0.002
RMSE	0.011	0.019	0.008	0.022	0.023

Since the calibrating dataset was used for both the optimization process and the goodness-of-fit, the result may be too positive. Therefore, the checking dataset that was not used in the calibration phase was used to assess the accuracy of the DSM model. The result is shown in Table 6. It could be seen that RMSE for X, Y, Z, XY, XYZ is 1.8 cm, 2.4 cm, 3.2 cm, 3.0 cm, and 4.4 cm, respectively. The highest error for X is 2.9 cm (GCP18), for Y is 4.4 cm (GCP7), for Z is 8.1 cm (GCP7), for XY is 4.9 cm (GCP18), and for XYZ is 9.2 cm (GCP7). These indicate that the accuracy of the DSM model is very high with the checked GCPs at hand.

Interpretation of the DSM model of the study area shows a complex topography. The maximum and minimum elevations are 137.5 m and −90.9 m, respectively. The difference between the highest point and the lowest point of the DSM model is 228.4 m (Fig. 6), whereas the mean and the standard deviation are 20.3 m and 64.3 m. For case of the slope map (Fig. 7) that was generated from the DSM, the maximum and the minimum slopes are 84.3° and 0.1°, respectively, whereas the mean and the standard deviations of the map are 25.4° and 14.7°, respectively.

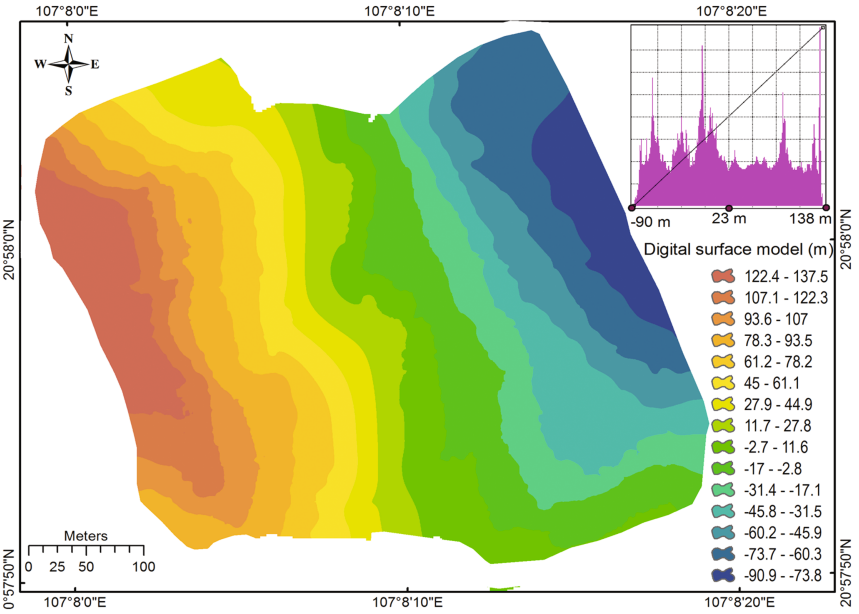

Fig. 6. Digital Surface Model (DSM) for the study area.

Table 6. Error and RMSE in X, Y, Z, XY, and XYZ of check points in this project.

Check points	X error (m)	Y error (m)	Z error (m)	XY error (m)	XYZ error (m)
GCP4	−0.010	−0.006	−0.021	0.012	0.024
GCP7	0.001	0.044	0.081	0.044	0.092
GCP9	−0.025	0.014	0.000	0.029	0.029
GCP11	0.012	0.017	−0.007	0.021	0.022
GCP13	−0.021	0.009	0.016	0.023	0.028
GCP17	0.004	0.001	0.002	0.004	0.005
GCP18	−0.029	0.040	0.002	0.049	0.049
RMSE	0.018	0.024	0.032	0.030	0.044

3.2 Influence of Ground Control Point and Its Distribution to the Accuracy of the DSM Model

To assess the influence of GCPs and its distribution to the accuracy of the DSM model, we varied the number of GCPs used for the calibration (camera-lens optimization and bundle block adjustment) and generated difference DSMs for this study area using the same captured images. Accordingly, six test cases were considered: Case 1, 3GCPs was selected among the 19 GCPs and used for the calibration (CAL), whereas the remaining 16 GCPs were used for the checking accuracy (CHC) of the resulting DSM; Case 2 with 5GCPs for CAL and 14 GCPs for CHC; Case 3 with 7 GCPs for CAL and 12 GCPs for CHC; Case 4 with 9 GCPs for CAL and 10 GCPs for CHC; Case 5 with 11

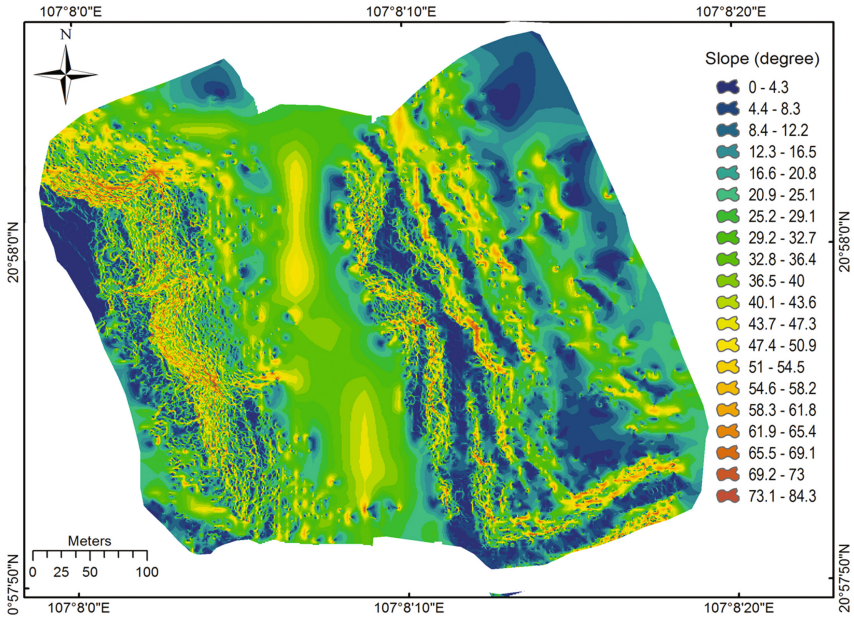

Fig. 7. Slope map generated from the DSM model for the study area.

GCPs for CAL and 10 GCPs for CHC; and Case 6 with 13 GCPs for CAL and 6 GCPs for CHC. The detailed GCPs used for CAL and CHS are shown in Table 7.

The detailed results of the accuracy of these DSMs are shown in Table 7 and errors of GCPs used in these DSMs are shown in Fig. 8. It could be observed that the goodness-of-fit of the DSM decreased when more GCPs were added to the CAL process. $RMSE_{XY}$ and $RMSE_{XYZ}$ are 0.005 m and 0.008, respectively, at Case 1 are increased to 0.021 m and 0.022 m, respectively, in Case 6. In addition, detailed errors

Table 7. RMSE (m) in X, Y, Z, XY, and XYZ of check points in this project (CAL: calibration; CHC: Checking; GCP: Ground control point).

Case	Task	$RMSE_X$	$RMSE_Y$	$RMSE_Z$	$RMSE_{XY}$	$RMSE_{XYZ}$	GCPused
1	CAL	0.001	0.005	0.006	0.005	0.008	3 GCPs:5,6,18
	CHC	0.785	0.597	0.911	0.986	1.343	16 GCPs:1-4,7-17,19
2	CAL	0.003	0.010	0.012	0.010	0.016	5 GCPs: 5,6,8,15,18
	CHC	0.139	0.212	0.497	0.253	0.558	14 GCPs:1-4,7,9-14,16,17,19
3	CAL	0.008	0.007	0.006	0.010	0.012	7 GCPs: 4,7,9,11,13,17,18
	CHC	0.075	0.175	0.291	0.190	0.348	12 GCPs: 1-3,5-7,8,10,12,14-16,19
4	CAL	0.006	0.014	0.006	0.016	0.017	9 GCPs: 1,2,5,6,8,12,15,16,19
	CHC	0.038	0.111	0.216	0.117	0.246	10 GCPs: 3,4,7,9-11,13,14,17,18
5	CAL	0.008	0.014	0.008	0.016	0.018	11 GCPs: 1,2,5,6,7,8,11,14,15,16,19
	CHC	0.038	0.060	0.051	0.071	0.088	8 GCPs: 3,4, 9,10,12,13, 17,18
6	CAL	0.013	0.016	0.007	0.021	0.022	13 GCPs: 1-3,5-9,11,14,15,16,19
	CHC	0.030	0.029	0.047	0.042	0.063	6 GCPs: 4,10,12,13, 17,18

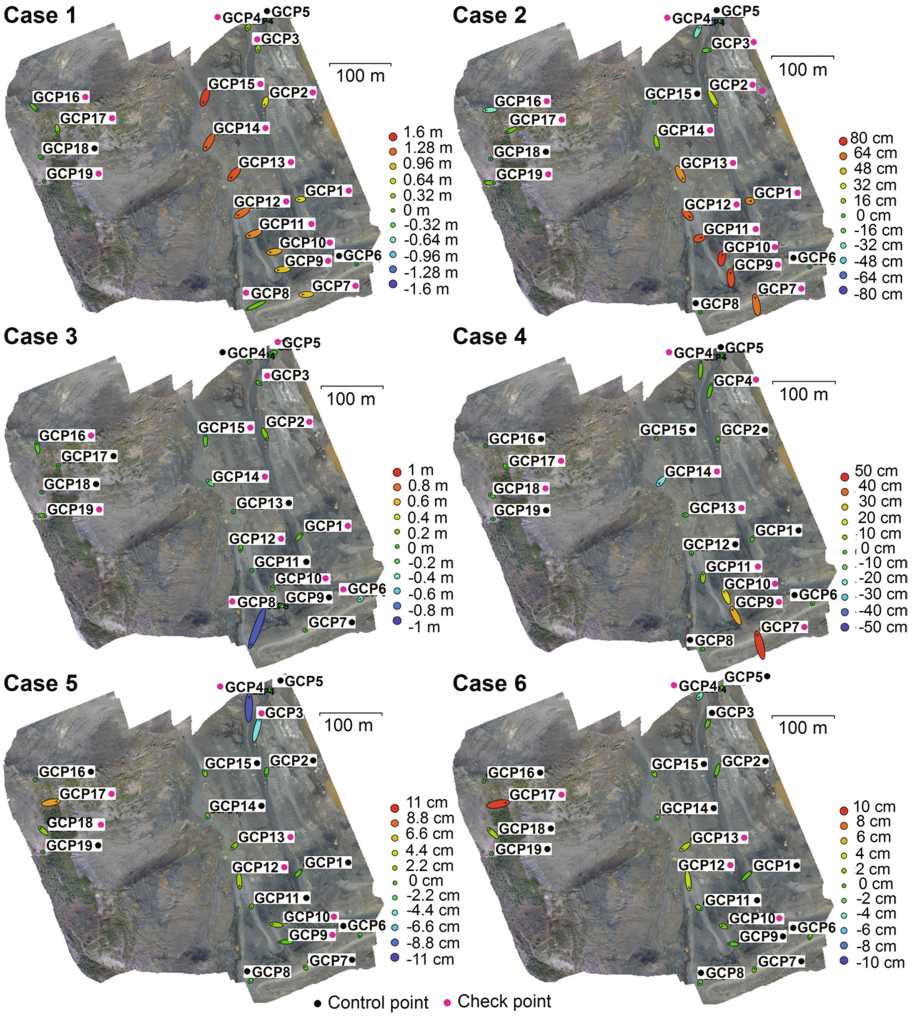

Fig. 8. Estimated errors of the calibrated GCPs and checked GCPs in the six testing cases in this study, in which Z error is represented by ellipse color, whereas X,Y errors are represented by ellipse shape.

in Z and XY components is shown in Fig. 8, in which ellipse color represents Z error, whereas ellipse shape represents for X,Y errors.

The checking results (Table 7) show that the accuracy of the DSM model is increased significantly, when more GCPs were added to the model. Specifically, RMSE in the Case 1 (Table 7, Fig. 8) for X (0.785 m), Y (0.579 m), Z (0.911 m), XY (0.986 m), and XYZ (1.343 m) significantly decreased in the Case 6, where RMSE for X, Y, Z, XY, and XYZ is 0.030 m, 0.029 m, 0.047 m, 0.042 m, and 0.063 m, respectively (Table 7, Fig. 8). This finding is in agreement with Tahar [25] and

Agüera-Vega et al. [24] who concluded that accuracy of the DSM increased when more GCPs were used in the bundle block adjustment.

4 Concluding Remarks

This research assesses potential application of small UAV, SfM photogrammetry for generating DSM and its accuracy assessment at open-pit coal mine area with a case study at the Nui Beo coal mine, Quang Ninh province, one of the largest open-pit coal mines in Vietnam. Accordingly, a lightweight and low-cost DJI Phantom 3 Professional equipped by the nonmetric RGB Sony EXMOR camera was used. A total of 206 images were captured, and in addition, 19 GCPs were established and determined XYZ coordination (VN2000/UTM Zone 48 N) using a Leica TS09 total station (1”angular accuracy and 1.5 mm + 2 ppm distance accuracy).

The result showed that the DSM model has high accuracy; RMSE in the calibrating dataset is 0.8 cm and 2.2 cm for vertical and horizontal, respectively indicating high success-rate of fit, whereas RMSE in the checking dataset is 3.2 cm and 3.0 cm for vertical and horizontal, indicating high accuracy. These indicate that the processes of capturing images, establishment of GCPs, and photogrammetric processing were carried out successfully.

Overall, one of the most interested issues in using UAV and SfM photogrammetry is how to increase the horizontal and vertical accuracy of UAV products. According to Agüera-Vega et al. [24], flight altitude and number of GCPs influences vertical accuracy significantly but not terrain morphology, whereas horizontal accuracy is not effected by flight altitude and terrain morphology. However, the optimal number of GCPs for a study area still is a questionable matter. Literature review shows that most studies only reported number of GCPs used without documenting the background used. To our knowledge, few works have investigated the correlation of number of GCPs and DSM accuracy with different conclusions, i.e. Tahar [25] and Agüera-Vega et al. [24] concluded that the number of GCP influence the horizontal accuracy of the DSM model significantly, whereas Mancini et al. [26] reported that decreasing the number of GCPs does not influence the accuracy of the DSM. The result in this study (Fig. 8 and Table 7) shows a different result compared to [26], where the horizontal and vertical errors were significantly reduced when more GCPs were added to the model.

A limitation of this research is related to the distribution of the GCPs, it could be observed that the central and low left corner areas have no GCP; therefore accuracy of the DSM model for these areas was not assessed. It is noted that these are unsafety areas for us to research and establish GCPs because the coal seams in these area were exploiting. Despite the limitation, based on the finding in this research, it could be concluded that small UAV and SfM photogrammetry are valid and efficient tools for topographic mapping at complex terrain areas such as open-pit coal mine.

Conflict of interest. The authors declare that there is no conflict of interest.

Acknowledgement. This research was supported by Department of Mine Surveying, Faculty of Geomatics and Land Administration, Hanoi University of Mining and Geology (Vietnam) and the Nui Beo coal joint stock company - VINACOMIN group.

References

1. Ogundare, J.O.: Precision Surveying: The Principles and Geomatics Practice. Wiley, Hoboken (2015)
2. Siebert, S., Teizer, J.: Mobile 3D mapping for surveying earthwork projects using an Unmanned Aerial Vehicle (UAV) system. Autom. Constr. **41**, 1–14 (2014)
3. Hugenholtz, C.H., Walker, J., Brown, O., Myshak, S.: Earthwork volumetrics with an unmanned aerial vehicle and softcopy photogrammetry. J. Surveying Eng. **141**, 06014003 (2014)
4. Carrivick, J.L., Smith, M.W., Quincey, D.J.: Structure From Motion in the Geosciences. Wiley, Handbook (2016)
5. Fernández-Hernandez, J., González-Aguilera, D., Rodríguez-Gonzálvez, P., Mancera-Taboada, J.: Image-based modelling from Unmanned Aerial Vehicle (UAV) photogrammetry: an effective. Low-Cost Tool Archaeol. Appl. Archaeometry **57**, 128–145 (2015)
6. Vasuki, Y., Holden, E.-J., Kovesi, P., Micklethwaite, S.: Semi-automatic mapping of geological structures using UAV-based photogrammetric data: an image analysis approach. Comput. Geosci. **69**, 22–32 (2014)
7. Cryderman, C., Mah, S.B., Shufletoski, A.: Evaluation of UAV photogrammetric accuracy for mapping and earthworks computations. Geomatica **68**, 309–317 (2014)
8. Clapuyt, F., Vanacker, V., Van Oost, K.: Reproducibility of UAV-based earth topography reconstructions based on Structure-from-Motion algorithms. Geomorphology **260**, 4–15 (2016)
9. Shahbazi, M., Sohn, G., Théau, J., Menard, P.: Development and evaluation of a UAV-photogrammetry system for precise 3D environmental modeling. Sensors **15**, 27493–27524 (2015)
10. Tonkin, T.N., Midgley, N., Cook, S.J., Graham, D.J.: Ice-cored moraine degradation mapped and quantified using an unmanned aerial vehicle: a case study from a polythermal glacier in Svalbard. Geomorphology **258**, 1–10 (2016)
11. Eltner, A., Baumgart, P., Maas, H.G., Faust, D.: Multi-temporal UAV data for automatic measurement of rill and interrill erosion on loess soil. Earth Surf. Proc. Land. **40**, 741–755 (2015)
12. Candiago, S., Remondino, F., De Giglio, M., Dubbini, M., Gattelli, M.: Evaluating multispectral images and vegetation indices for precision farming applications from UAV images. Remote Sens. **7**, 4026–4047 (2015)
13. Hugenholtz, C.H., Whitehead, K., Brown, O.W., Barchyn, T.E., Moorman, B.J., LeClair, A., Riddell, K., Hamilton, T.: Geomorphological mapping with a small unmanned aircraft system (sUAS): feature detection and accuracy assessment of a photogrammetrically-derived digital terrain model. Geomorphology **194**, 16–24 (2013)
14. Tuan, V.A.: Annual report of the Nui Beo coal joint stock company - VINACOMIN group. The Nui Beo coal joint stock compan (2013)
15. Nui Beo Joint Stock company: The environmental impact assessent report on the project of investments and construction of underground mining of the Nui Beo coal mine (2013)

16. Ajayi, O.G., Salubi, A.A., Angbas, A.F., Odigure, M.G.: Generation of accurate digital elevation models from UAV acquired low percentage overlapping images. Int. J. Remote Sens. **38**, 3113–3134 (2017)
17. Han, Y.-G., Jung, S.-H., Kwon, O.: How to utilize vegetation survey using drone image and image analysis software. J. Ecol. Environ. **41**, 18 (2017)
18. Tien Bui, D., Tran, C.T., Pradhan, B., Revhaug, I., Seidu, R.: iGeoTrans – a novel iOS application for GPS positioning in geosciences. Geocarto Int. (2014)
19. Sona, G., Pinto, L., Pagliari, D., Passoni, D., Gini, R.: Experimental analysis of different software packages for orientation and digital surface modelling from UAV images. Earth Sci. Inf. **7**, 97–107 (2014)
20. Leon, J.X., Roelfsema, C.M., Saunders, M.I., Phinn, S.R.: Measuring coral reef terrain roughness using 'Structure-from-Motion'close-range photogrammetry. Geomorphology **242**, 21–28 (2015)
21. Lowe, D.G.: Distinctive image features from scale-invariant keypoints. Int. J. Comput. Vision **60**, 91–110 (2004)
22. Fryer, J.G., Brown, D.C.: Lens distortion for close-range photogrammetry. Photogrammetric Eng. Remote Sens. **52**, 51–58 (1986)
23. Manual, A.P.U.: Professional Edition, Version 1.2. Russia: Agisoft LLC (2016)
24. Agüera-Vega, F., Carvajal-Ramírez, F., Martínez-Carricondo, P.: Accuracy of digital surface models and orthophotos derived from unmanned aerial vehicle photogrammetry. J. Surveying Eng. (2016). 04016025
25. Tahar, K.: An evaluation on different number of ground control points in unmanned aerial vehicle photogrammetric block. ISPRS J. Photogramm. XL-2 (W2) 93–98 (2013)
26. Mancini, F., Dubbini, M., Gattelli, M., Stecchi, F., Fabbri, S., Gabbianelli, G.: Using unmanned aerial vehicles (UAV) for high-resolution reconstruction of topography: the structure from motion approach on coastal environments. Remote Sens. **5**, 6880–6898 (2013)

Energy Analysis in Semiautomatic and Automatic Velocity Estimation for Ground Penetrating Radar Data in Urban Areas: Case Study in Ho Chi Minh City, Vietnam

Thuan Van Nguyen, Cuong Anh Van Le(✉), Van Thanh Nguyen, Trung Hoai Dang, Triet Minh Vo, and Lieu Nguyen Nhu Vo

Department of Geophysics, University of Science, Vietnam National University, Ho Chi Minh City, Viet Nam
lvacuong@hcmus.edu.vn

Abstract. Maps of underground construction works, such as water pipes and water drainage systems are necessary for expansion of urban areas. For shallow depths, Ground Penetrating Radar (GPR) can provide high-resolution subsurface images. Electromagnetic velocity is crucial in time-to-depth conversion and imaging of the structures from the GPR section. Shielded common-offset antennas can work in city surroundings due to superior noise isolation properties. We have implemented new automatic/semiautomatic strategies to define the electromagnetic velocity and locations of the construction works by using common offset GPR data. In our approach, Kirchhoff migration is employed to image underground objects by correcting the locations of subsurface reflectors (i.e. diffractors, dips). The automatic technique helps define the velocity and position of an object or a diffractor by targeting high-valued data points in the maximum energy difference section, which is calculated from multiple migrated GPR sections of different velocities. When migrated correctly, a collapsed diffractor will contain the majority of its energy at the peak of the diffraction hyperbola. If migrated using the wrong velocity, the peak of the diffraction hyperbola will contain the least energy, with the rest of the energy smeared over migration artefacts. In the semiautomatic technique, the calculated velocities and positions from the first strategy can help interpreters in judging focused zones and under/over migration artefacts from different migrated GPR sections by using a limited velocity band. We applied the techniques to 2D/3D visualizations of underground pipes from one numerical model and a case study in Ho Chi Minh City, Vietnam.

Keywords: Energy · GPR data processing · Diffraction · Kirchhoff migration

1 Introduction

The Ground Penetrating Radar (GPR) method can provide highly detailed image of underground structures at shallow depths depending on electromagnetic frequency. By solving the high-frequency component of Maxwell ‘s equations for electromagnetic wave propagation [1, 2], reflectivity characteristics of the subsurface are revealed. The

© Springer International Publishing AG 2018
D. Tien Bui et al. (eds.), *Advances and Applications in Geospatial Technology and Earth Resources*, https://doi.org/10.1007/978-3-319-68240-2_3

difference in electric permittivity of two different media can result in a reflection event, yielding information about the depth of that boundary and other physical properties (i.e., velocity). Analysing the reflection GPR data can utilise elements of various seismic processing techniques [3] to increase signal-to-noise ratio, and produce high-quality images. GPR can be quickly applied in many areas for characterizing shallow stratigraphy and/or detecting buried objects (i.e., electric pipes, water supply/drainage systems) and other subsurface objects as cracks, sinkholes and small factures [4–11].

Investigation depth is heavily dependent on antenna frequency and electrically conductivity of environments [11, 12]. Trusted GPR depth decreases when the environment conductivity is high because of clay or soluble salt existences in the soils [11]. Higher frequency antenna can provide higher resolution images in lower depth while the lower frequency one is able to map deeper structures or objects but low resolution [12].

1.1 Conventional Workflow

Figure 1 expresses a workflow for processing GPR data [3]. Firstly, time correction is applied for removing the gap between transmitting and receiving antennas. It is commonly a static shift from the first break to time zero. Secondly, filtering techniques, such as de-wow, bandpass filtering, and background removal are applied to increase the ratio between signal and noise. Applied signal gain compensates energy loss from wave front divergence and decay of amplitudes versus depth, caused by the geometric spreading of electromagnetic waves [13]. Then, several techniques as Normal move-out (NMO) correction applying to Common mid point (CMP) data and prior known depth of an anomaly are considered to estimate velocity [14–17]. Finally, migration technique can move dipping reflections to their actual positions and mitigate diffractions effects [14]. Note that the key factor to the success of migration is velocity information. Size and depth of an object can be achieved in the GPR migrated section.

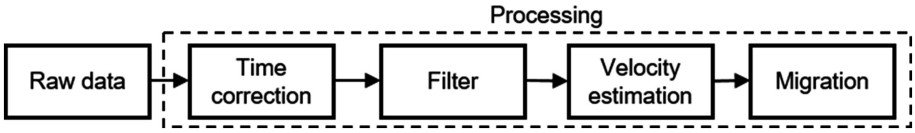

Fig. 1. Workflow for analyzing GPR data

1.2 Velocity Estimation

Several methods of estimating GPR velocity are overviewed by many authors (i.e., [14–17]) for the two different measurement settings as CMP and common offset (CO). A hyperbola expresses the relation between velocity, and the distance between transmitter and receiver antennas. The NMO approach can provide velocity information with the CMP data made by an unshielded tool. Unfortunately, CMP gather for GPR data is not common in urban areas because of noises coming from human activities and inconvenience of surveys although some separable shielded antennas which could be applicable to CMP surveys are developed (i.e., MALA tool). Shielded antenna type is

an effective tool for mitigating noise detriment to GPR data. In the CO data type from the shielded antennas, hyperbolic curves resulting from diffractors as electric conduits and water pipes are good indicators of subsurface velocity.

Migration techniques [14, 18] (i.e., Kirchhoff migration) is an effective technique for collapsing diffraction hyperbolae into localized high-energy zones. Kirchhoff migration conveys the idea of the diffraction summation method [14] in which summation of seismic amplitudes along a diffraction hyperbola whose shapes are controlled by environment velocity is put at the peak of the diffraction hyperbola. Sham and Lai [15] suggest the same approach to evaluate the velocity by dealing with the hyperbola curves recorded in the GPR CO section when they consider the curve shapes are function of two-way travel time, velocity, size of diffractor object, depth of the object, and distance between antennas. Meanwhile, Forte, Dossi, Pipan and Colucci [16] use the idea of the Snell's equation in calculating the velocity of the later layer if its previous layer velocity information, reflections coefficients and incident angles of the reflection layers are known.

Other approach applied for seismic reflective data like optimization of many objective functions can be potentially useful to GPR data. For example, optimization of flatness, local continuity and simplicity of migrated data can be an effective automatic tool for defining velocity in seismic case [18].

1.3 Object Recognition

Positions of hyperbolic curves resulting from diffractors, or subsurface anomalies, can be investigated by using pattern recognition and neural networks [19–21]. Supervised learning of a set of training data featuring hyperbolic diffractors is an effective tool for detecting targets of interest that sharing hyperbolic signature. Meanwhile, pattern recognition (i.e., Hough Transform [22]) takes advantage of the geometry associated with diffraction hyperbolae, and searches all of the possible cases relating to the hyperbolic equations.

2 Method

The idea of determining electromagnetic wave propagation velocity and anomaly depth comes from analysis of diffraction effects. Initially, shapes, sizes, and depths are unknown. Some assumptions require clarification before calculating the parameters. Firstly, a hyperbola must be symmetric for computing velocity. Secondly, applying a migration (i.e., Kirchhoff technique) with correct velocity will convert any hyperbola-like curves into points, and finally; the velocity for small anomalies are often more-correct than one for large anomalies.

Our approach for velocity estimation focuses on the convergence of a diffraction hyperbola after migration. For a diffraction point from a small-sized target, migration with correct velocity provides the highest energy point at the apex of its hyperbola, resulting from the summation of similar phase wave-like signals in many GPR traces [14]. Migration with wrong velocities creates downward or upward curves [14].

In the case of diffractions from larger objects, the convergence of their hyperbolic curve results in small points, reflecting the incorrect geometry of the object. To achieve the most-correct velocity, the second assumption shows that the flatter shape of the first 'strong' wiggles of the traces, nearby the apex of the hyperbola, can provide the best velocity estimation when geometry of the large sized objects, and their depths are unknown.

Our aims are to semi-automatically and automatically define positions of the underground targets, and calculate the subsurface electromagnetic velocity.

2.1 Automatic Strategy

Firstly, the approximate velocity and position of an object can be automatically specified using the maximum difference of energy focused from each diffraction event after migration. We apply Kirchhoff migration with a range of velocities to the GPR section (See Fig. 2a) to show the effect of velocity variation on our synthetic migrated sections (See Fig. 2b). Each energy section can be computed from square of each migrated section. For a specific data point (x,t) in the GPR section, the two extremums (minimum and maximum) can be derived from a set of migrated sections with different velocities (See Fig. 2c). Then, the maximum difference of energy in the data point is the subtract of the two extremes. The idea here is that, if a hyperbola exists, there will be a distinguishable energy difference in the apex of the hyperbola. The maximum energy difference section when formed from many data points (See Fig. 2d) is then rescaled into an integer range (i.e., unassigned 8 bit) for representing pixel amplitude [23, 24]. The next process will be done by automatically searching the distinguished energy difference points using the pixel recognition technique [25]. The recognition technique shows that the "salt and pepper" noise always appears in the data and one-pixel variation is its characteristics. The "true" local maximum amplitude should have more than one-pixel variation, in which the maximum energy difference can show its relations with diffraction hyperbola.

When the temporal and spatial locations are defined within the maximal energy difference section, the velocity which correlates to the maximum energy can be obtained through tracing back the migration parameter. In this case, all hyperbolae are considered as originating from point diffractors. The assumption for velocity estimation is violated when the diffractors are larger-sized anomalies.

2.2 Semiautomatic Strategy

In this strategy, the idea of velocity calculation of GPR data is to analyse 'flatness' level of the first wavelet and additionally the simplicity of the second wavelet from the diffraction event after migration. We suggest three cases can be visible for the large-sized objects. When the greater velocity is applied, the "smile" image can appear in the migrated section (see images with the velocities V4 and V5 in Fig. 2). For the lesser velocity, "frown/eyebrow" is visible in the migrated data (see images with the velocities V1 and V2 in Fig. 2). When the correct velocity is applied, the migrated section does not need to have the focused point, because of the large sized objects. We can choose the greatest flatness level of the first wavelet event (see the small grey rectangular in the

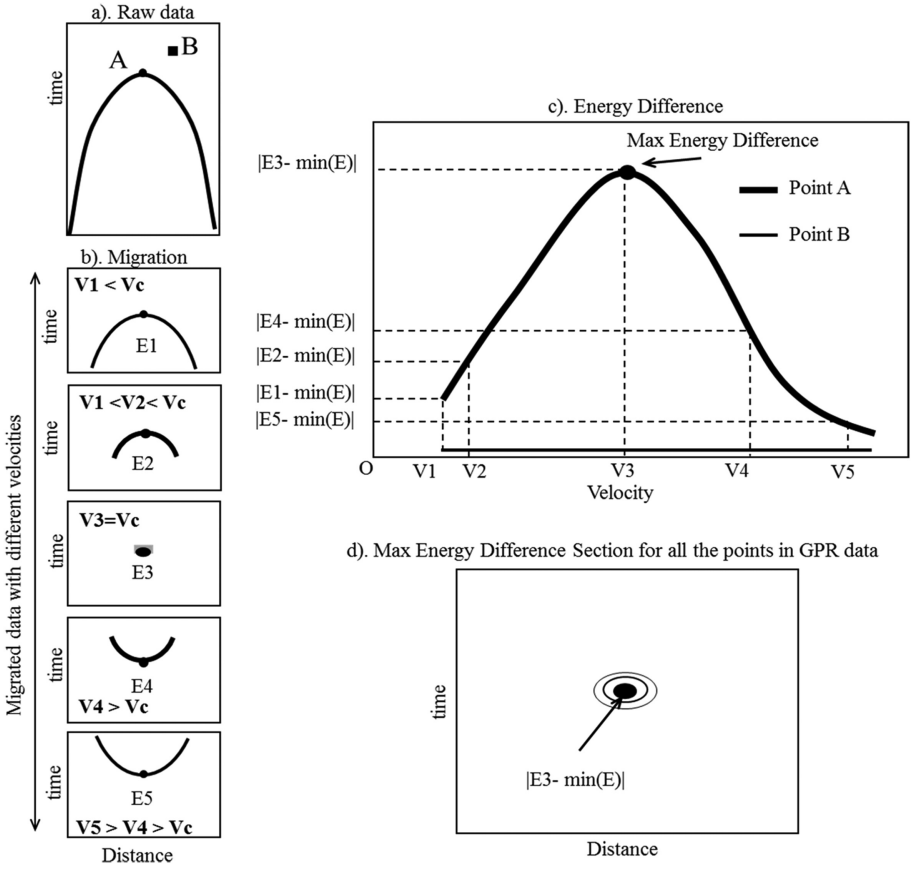

Fig. 2. Schematic of the automatic strategy. (a) Raw data. (b) Migration process to create different migrated sections from the raw data and different velocities. (c) Evaluation of energy difference at point A (the peak of the hyperbola) and at point B in the raw data image. min (E) and E3 for the data point are the minimum and maximum of the five energy values E1, E2, E3, E4 and E5, respectively. Note that the smaller size straight line for point B does show no interest because of no recorded reflection or diffraction events. (d) The max energy difference for the whole data points in the GPR data section

image with the velocity V3 in Fig. 2) and less chaotic, or 'smear tail', of the second wavelet (see the small black ellipse in the image with the velocity V3 in Fig. 2).

The information such as velocity and positions in time-distance domain which are collected from automatic strategy can support the procedure shown in the semiautomatic approach. That is, the velocity band for testing how their migration events change can vary within the velocity coming from the automatic strategy. We can then narrow the possible and realistic velocity ranges from the approximate calculated velocity.

3 Results

3.1 Numerical Model

Set up model. We have created a synthetic model with six anomalies, including three rectangular pipes, and three circle pipes (Fig. 3). The model is two-dimensionally illustrated in Cartesian coordinates. The background velocity (black zone in Figs. 3, 4, and 5) is 1.34×10^8 m/s and the anomalies 1.22×10^8 m/s (white zone in Figs. 3, 4, and 5). The anomalies can be represented within time - space domain in Fig. 4. We use the programs MATGPR [13, 26] to build the model and codes from CREWES [27] to compute conversion of velocity between time and depth domain. The two types of velocity models are also illustrated for interpretation purpose.

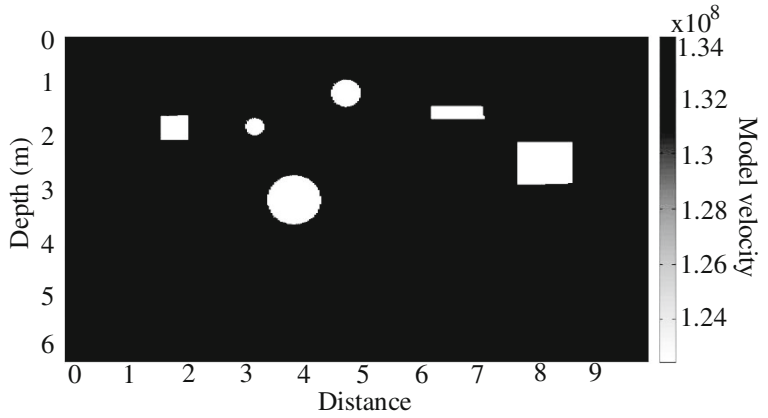

Fig. 3. Model of six anomalies in Cartesian coordinate

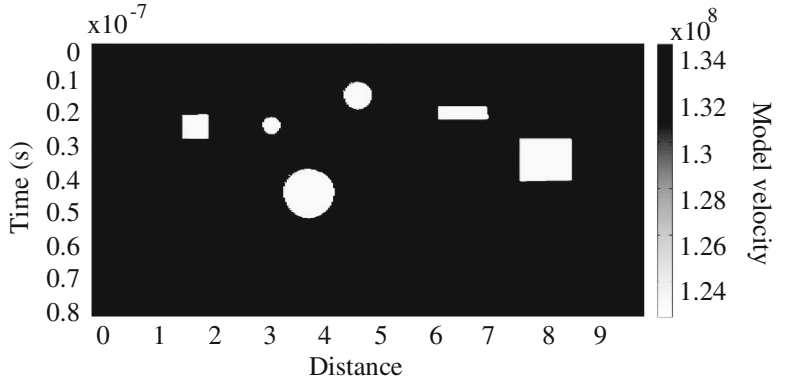

Fig. 4. Model of six anomalies in time and space domains

Root mean square (RMS) velocity model (see Fig. 5) is calculated from depth velocity model (see Fig. 4) [27]. It is the best velocity model for time migration method (i.e., Kirchhoff migration). However, the challenge is to establish the model when we have only one single zero-offset GPR section. Normally, we need to have many CMP sections to fully evaluate RMS velocity.

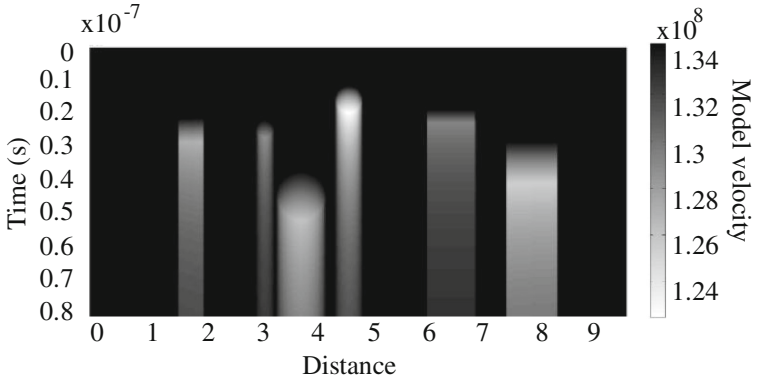

Fig. 5. Root mean square velocity model

Forward modelling. We have used the modelling tool of the source code MATGPR [13, 26] to create synthetic CO GPR data from the model (Fig. 3). This modelling tool applied the theory described by Bitri and Grandjean [1]. In their works, wavefield extrapolation is achieved using a phase-shift technique in the frequency-wavenumber (f-k) domain, and is dependent on the solution of the 2D Maxwell's equations.

The GPR synthetic section (see Fig. 6) expresses some remarks. Firstly, in location of a circle pipe (i.e., in x = 3, 4, 5 m), two distinguished hyperbola-like curves show the top and bottom. Moreover, many other hyperbolae with weak amplitudes are

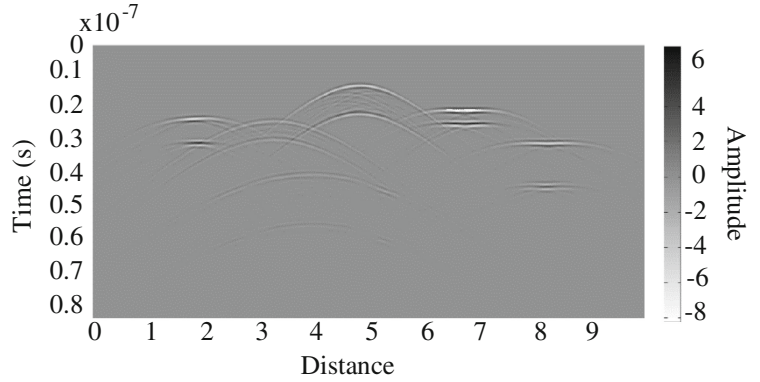

Fig. 6. Synthetic data of Model

created from small diffractors of the left and right edges of the pipe. Secondly, for a rectangular pipe case, two horizontal layers (top and bottom) are visible and four hyperbolae appear in each of the four corners.

Processing and result. Our automatic workflow helps identify all the objects illustrated and their relatively good velocities in the model. Specifically, the whole migrated sections are created from testing velocities from 0.8×10^8 m/s to 1.6×10^8 m/s. The next step is processing their energy sections and their max energy difference section (see Sect. 2.1 Automatic strategy). In the maximum energy difference (Fig. 7), the black dots related to the high values of energy difference indicate the positions of the top and bottom edges of anomalies (i.e., circle and rectangular objects) of the model (Fig. 4). The automatic process can estimate the approximate velocities and coordinates in time-space domain for each black dot. Note that only CO section with one main frequency GPR data is used to calculate the position and velocity information. Criterion for choosing the approximate velocity is picking the velocity with the largest energy at any data point (Fig. 8) in the GPR section. Overall, there is a tendency that velocity of the upper part (top boundary) of an anomaly (i.e., at the location x = 7.1 m) is larger than below-depth one (below boundary). This matches exceptionally well with the RMS velocity model trend (for example Figs. 7 and 8). That is, the background velocity is larger than any anomalies' velocities in the both model velocity and RMS velocity. One exception is the point in $x \sim 1.8$ m (velocities at the top and bottom are 1.25×10^8 m/s and 1.3×10^8 m/s, respectively). Additionally, the smaller size anomalies (i.e., velocity 1.3×10^8 m/s at x = 3.2 m) produce better top boundary velocities comparable with the background velocity 1.34×10^8 m/s.

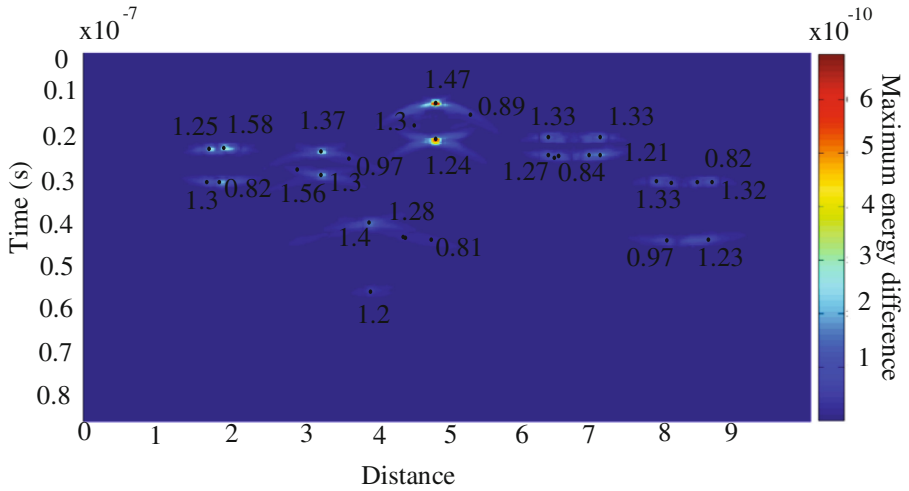

Fig. 7. The maximum energy difference section created by migration of the synthetic data (Fig. 6) and a range of velocities. The processed velocities estimated from the automatic strategy are multiplication of numbers put in the figure and the value 10^8 m/s

Velocity estimation value is manually analysed in the semiautomatic strategy. The interpretation process needs some locations of data points derived in the GPR section from the automatic strategy. The considered data points are shown in Fig. 9a. Five migrated sections with five different velocities are illustrated to determine the suitable velocity according to energy focus criterion of diffraction [14].

Shapes of diffraction events can be used for velocity estimation. The migrated section (Fig. 8d) with the correct velocity v = 1.34 $\times$ 10^8 m/s presents the most "focused" image of GPR data and also the best image comparable to the numerical model image (Fig. 3). Under-migration sections (see Fig. 8b and c) with velocity less than the correct velocity provide downward shape as "frown eyebrow" as discussed in Fig. 2. Over-migration sections (see Fig. 8e and f) with the larger velocities than the correct one provide the upward shape as "smile". Difference of the migrated sections between 1.32 $\times$ 10^8 m/s or 1.36 $\times$ 10^8 m/s and 1.34 $\times$ 10^8 m/s is small for the below boundary of each anomaly. However, checking the side boundaries of the five migrated cases (see black arrow for the small hyperbolae in Fig. 8), we can see the relatively meaningful difference.

Correct velocity estimation for the bottom boundary of one anomaly with only one CO GPR section is challenging. However, the automatic strategy is potentially able to show that the velocities of the six anomalies is smaller than the background one by defining the velocity of the bottom boundary smaller than the top boundary of each anomaly. Topic of true velocity calculation for the bottom boundaries will be our concern in the future.

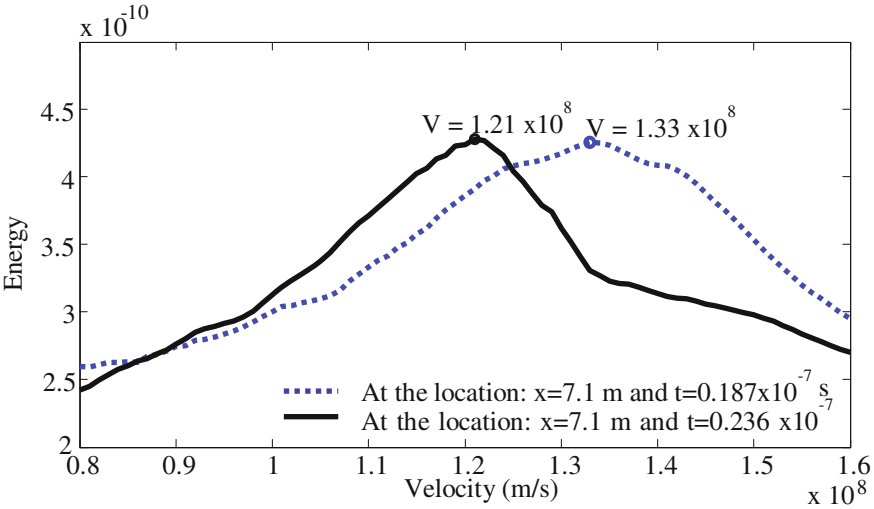

Fig. 8. Representation of energy versus velocity in two data points of the GPR section

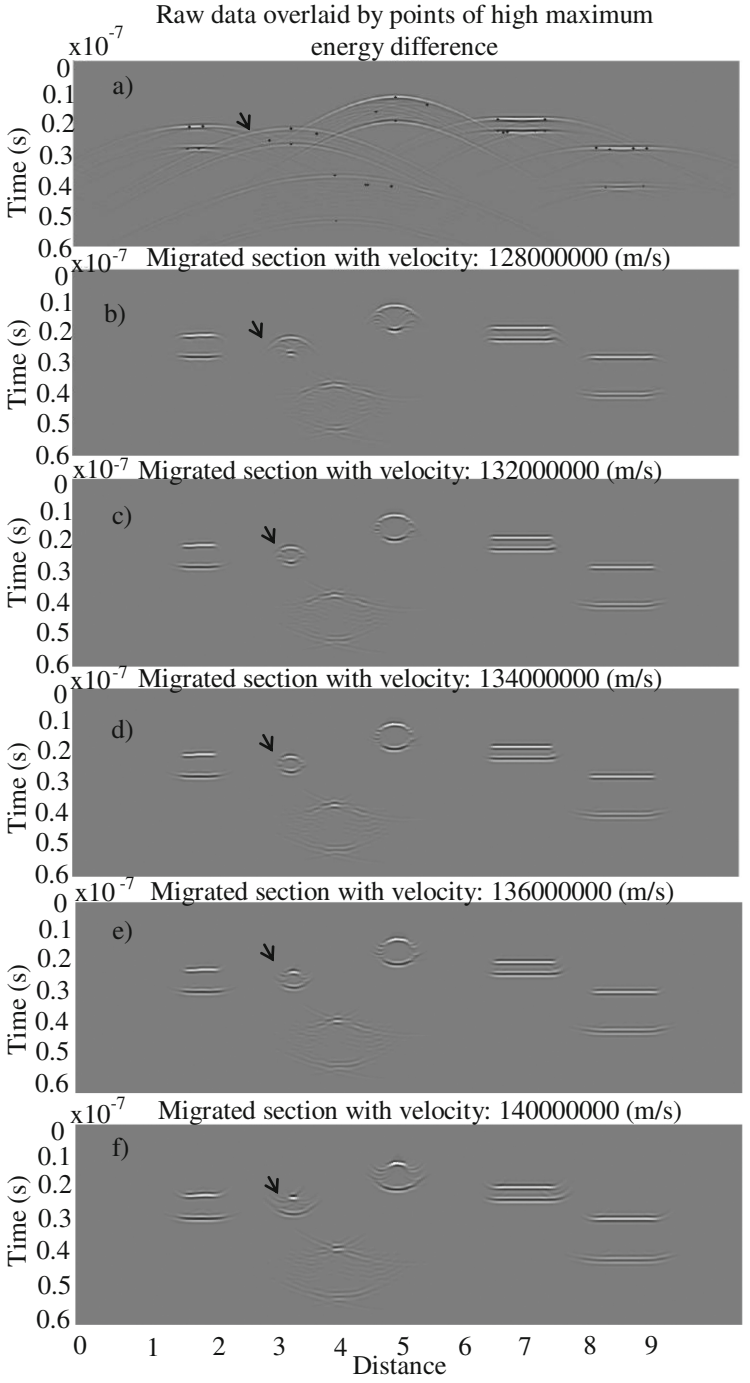

Fig. 9. Semiautomatic strategy in velocity evaluation from different migrated sections for the synthetic data

3.2 Field Data

Data Preparation. GPR data are measured in a street, District 10, Ho Chi Minh City, Vietnam by Detector Duo equipment with 700 MHz. Four 2D GPR profiles are conducted with the length 12 m and a distance from one to another is 1 m. The prior information from Enteco Company's courtesy shows that there are two water pipes for supply and drainage locating in the interest area (cyan zone in Fig. 10) but their geometry information such as sizes or positions are not properly documented. Some approaches as time correction, DC remove, and dewow are applied to have the processed data ready for migration (Fig. 11).

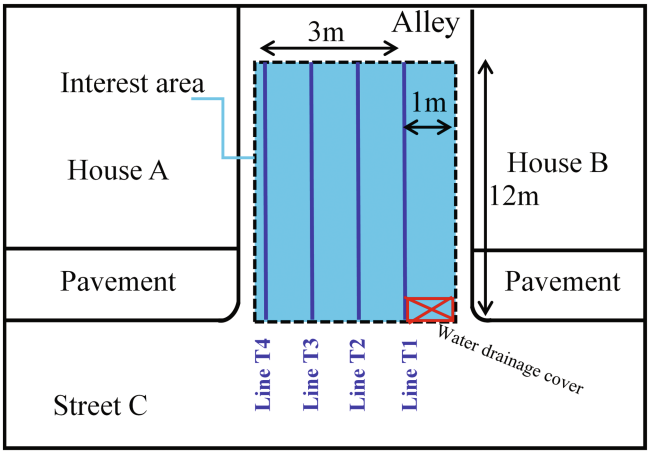

Survey location in District 10, Ho Chi Minh City, Vietnam

Fig. 10. Map of the four GPR lines carried in a street, District 10, Ho Chi Minh city, Vietnam

Processing and result. The steps in the automatic strategy are applied to the four GPR sections (See Sect. 2.1 Automatic strategy). The result shows their max energy difference sections for the four lines in Fig. 12. Some remarks for the whole field data are presented. Firstly, at approximately x = 1.4 m, two distinguished energy max difference could illustrate the top and bottom of one anomaly, fantastically matching with two hyperbolae for each GPR sections in Fig. 12. At x = 2.2 m, we can see one visible event appearing for three lines T1, T2, and T4 but line T3 does not show it. Existence of the two pipes correlates with the prior information from Enteco Company. The other point only locates at x = 5.7 m at the lines T3 and T4. Interestingly, many shallower depth points (Fig. 12) can form the horizontal layers at approximately times 0.8×10^{-8} s and 2×10^{-8} s, but they do not provide convincing unreliable velocity estimation because of their random curves in the field data (see Fig. 11).

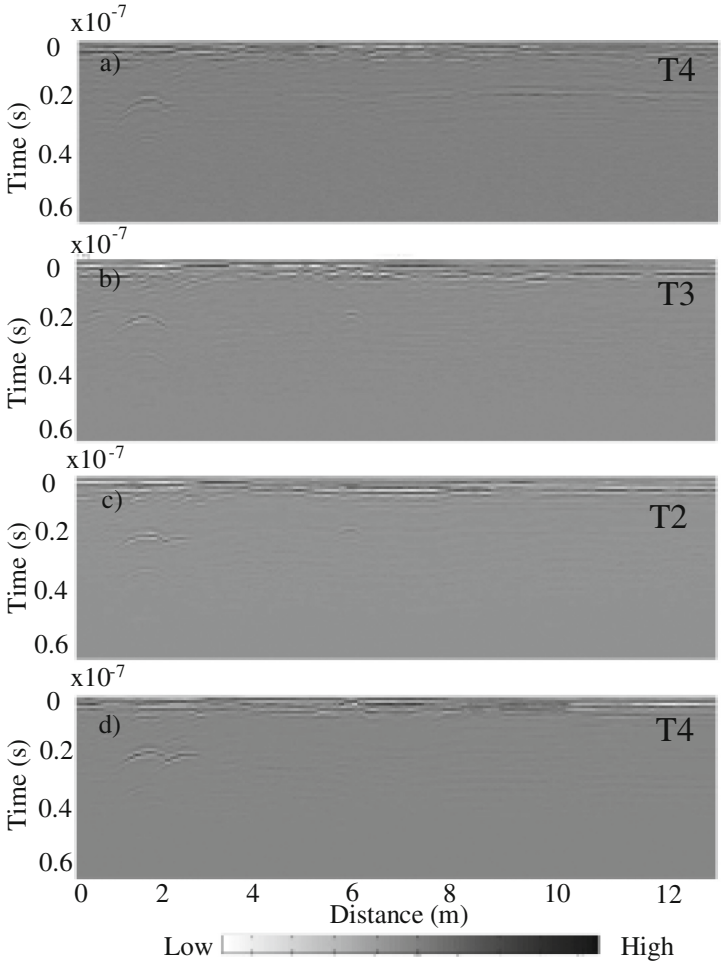

Fig. 11. The four processed GPR sections are ready for migration.

Figure 13 shows that velocity can range from 0.76×10^8 m/s to 1×10^8 m/s using the criteria of the highest energy in the automatic strategy. Two top and bottom positions of one anomaly are used for evaluating the relationship between velocity and energy from a set of migrated sections via two curves for each GPR profile (see Fig. 13).

The second strategy can be done to the four lines. In this paper, line T1 is chosen for velocity analysis because it has the most symmetric hyperbola-like curves (Fig. 14). Then, we choose its velocity result to migrate the whole four GPR sections (see the bottom image in Fig. 15). Following the same judging technique as "focus line" as shown in Fig. 2b, velocity evaluation of line T1 can produce the best result for the values 0.80×10^8 m/s in Fig. 14c. The small rectangular zones in Fig. 14 show the convergence level of the hyperbolae. Under- and over- migration phenomena occur in

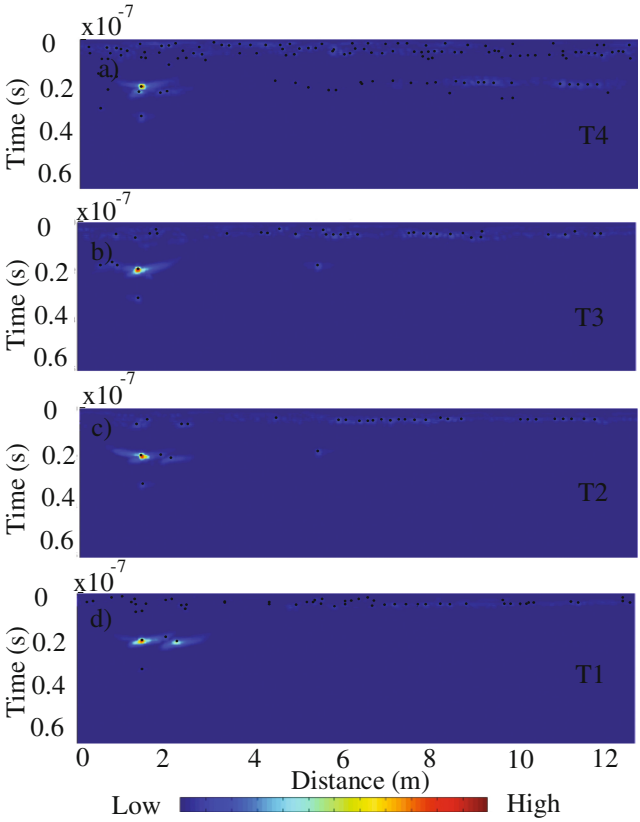

Fig. 12. The four max energy difference sections automatically processed from the GPR sections in Fig. 11.

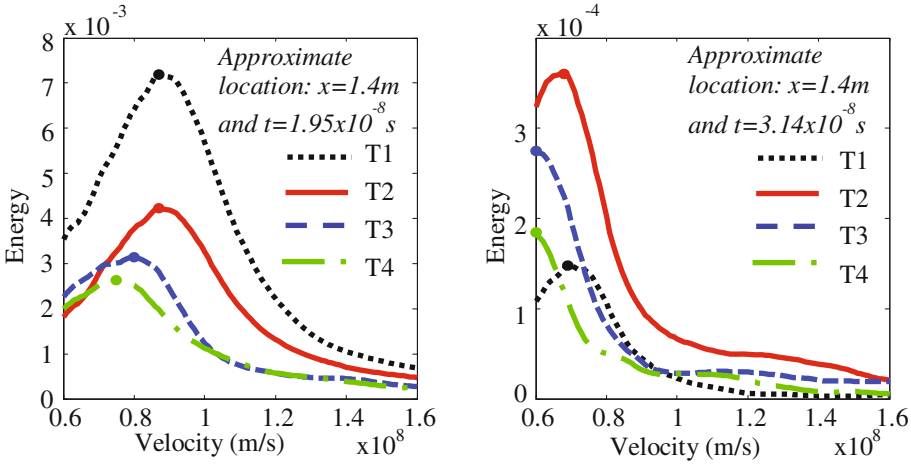

Fig. 13. Representation of energy versus velocity for the two approximate positions (top for left image and bottom for right image) of an anomaly in each GPR profile

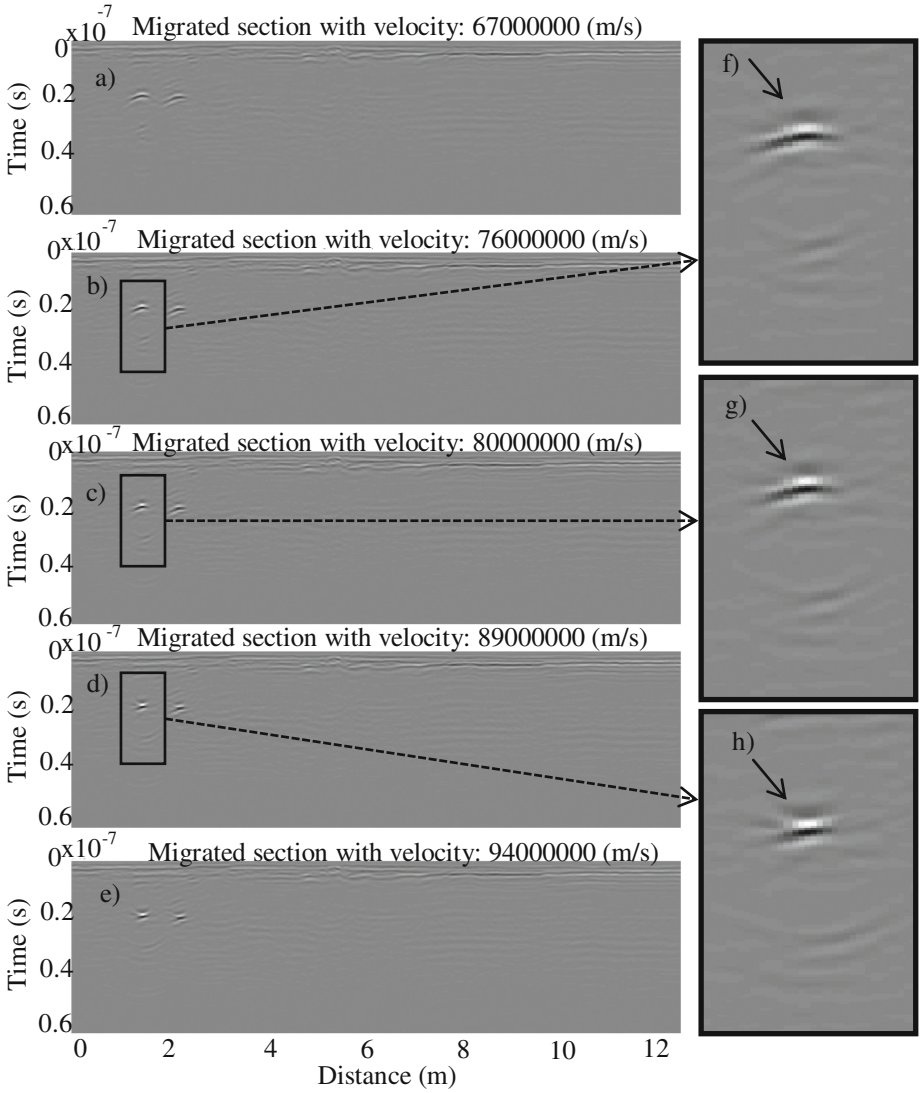

Fig. 14. Semiautomatic strategy in velocity evaluation from different migrated sections for the line T1 of the field data 2.

Fig. 14a, b, d, and e. To look closer into the rectangular zones of Fig. 14f, g and h as the larger scale of the figures Fig. 14b, c, d, respectively, interpretation could be done with flatness levels of the migrated event at x = 1.4 m and t = 1.95 $\times$ 10^{-8} s. It is clear that Fig. 14c represents the flattest first event (see the black arrow) and less smeared feature of the second event. Meanwhile, more stretched features for both events appear in the Fig. 14b, showing the "frown eyebrow" image. "Smile" image goes to Fig. 14d, expressing over-migration effect with higher migration velocity.

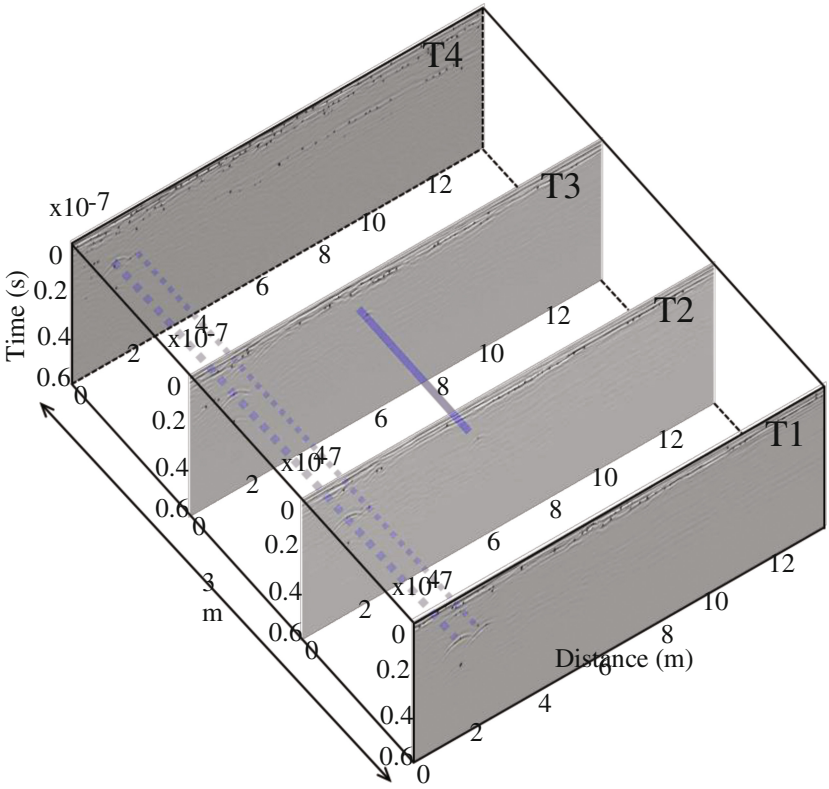

Fig. 15. 3D representation of the four processed lines T1-4 before migration. The larger dashed blue line is interpreted as drainage water pipe and the smaller dashed line are water pipe. The other blue line shows a different pipe

For better visualization of the whole field data, two 3D images are made for the GPR processed data before migration (Fig. 15) and the GPR migrated data (Fig. 16) with the constant velocity 0.80×10^8 m/s. There are two visible pipes (the dashed line in Figs. 15 and 16) with the depth approximately 0.8 m and their sizes around 0.4 m at x = 1.4 m and x = 2.2 m. The result is comparable with the prior information from Enteco Company. Also, a small line (the short blue line in Figs. 15 and 16) is visible in connecting between the profiles T3 and T4 at x = 5.7 m.

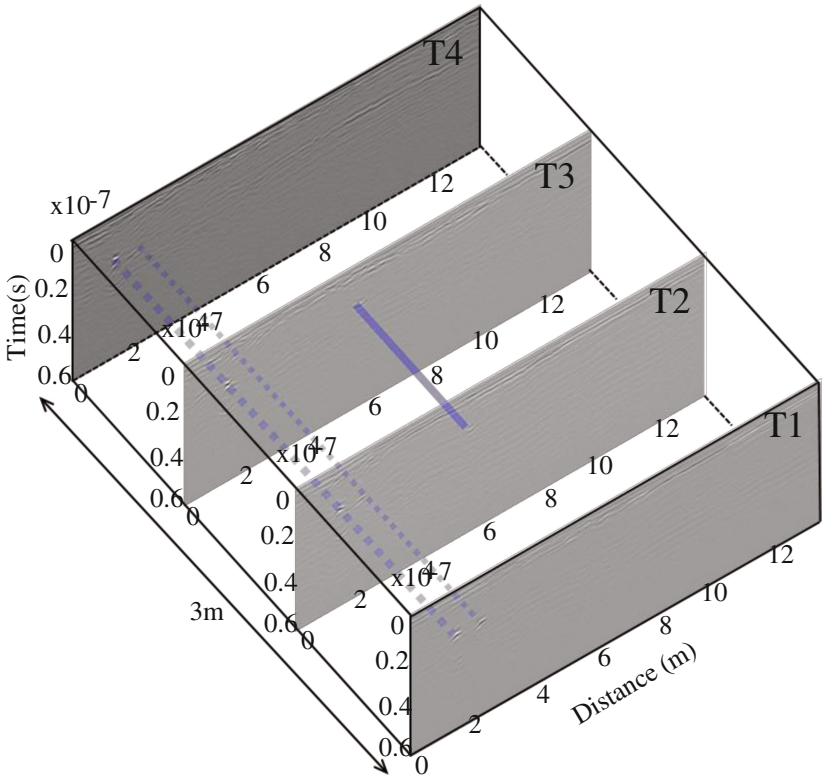

Fig. 16. 3D representation of the four migrated lines T1-4. The larger dashed blue line is interpreted as drainage water pipe and the smaller dashed line are water pipe. The other blue line shows a different pipe

4 Conclusion

Our strategies can be useful in automatically/semiautomatically estimating velocity of the urban environment and locations of underground anomalies. We have tested our methods for both cases numerical model and real datasets in which their objects are positioned or located. The automatic strategy using energy and max energy difference analysis can produce the reasonably acceptable results and it helps the interpreters in checking environment velocities from the suggested migrated velocity range as well as the suspected diffraction points in the GPR sections. The semiautomatic strategy could use information extracted from the first strategy to support the interpreter in narrowing the necessary environment velocity band and zones of underground targets. The shapes of upward or downward curves in the migrated sections of the different velocities are important to recognize the unsuitable velocity while the correct velocity leads to focused/flattest level of the objects. We believe that the techniques can be applicable in many case of GPR processing where lacking CMP gather velocity estimation. Meanwhile for urban construction, knowing underground structure before drilling or digging

is very necessary and the methods can reduce risks of incorrectly imaging the underground structure. We have believed that our strategies can help to reduce ambiguity of processing and interpreting this kind of data.

Acknowledgments. We are thankful for the helpful discussion and assistance given by Alex Costall, Michael Carson from Curtin University and Vu Lam. We would like to thank the Ho Chi Minh City Department of Science and Technology, the Ho Chi Minh City Department of Transport and Enteco Company for their supports.

References

1. Bitri, A., Grandjean, G.: Frequency–wavenumber modelling and migration of 2D GPR data in moderately heterogeneous dispersive media. Geophys. Prospect. **46**, 287–301 (1998)
2. Irving, J., Knight, R.: Numerical modeling of ground-penetrating radar in 2-D using MATLAB. Comput. Geosci. **32**, 1247–1258 (2006)
3. Fisher, S.C., Stewart, R.R., Jol, H.M.: Ground penetrating radar (GPR) data enhancement using seismic techniques. J. Environ. Eng. Geophys. **1**, 89–96 (1996)
4. Liner, C.L., Liner, J.L.: Application of GPR to a site investigation involving shallow faults. Lead. Edge **16**, 1649–1651 (1997)
5. Singh, K., Kumar, I., Singh, U.K.: Interpretation of voids or buried pipes using Ground Penetrating Radar modeling. J. Geol. Soc. India **81**, 397–404 (2013)
6. Toshioka, T., Tsuchida, T., Sasahara, K.: Application of GPR to detecting and mapping cracks in rock slopes. J. Appl. Geophys. **33**, 119–124 (1995)
7. Strobach, E., Harris, B.D., Dupuis, J.C., Kepic, A.W.: Waveguide properties recovered from shallow diffractions in common offset GPR. J. Geophys. Res. Solid Earth **118**, 39–50 (2013)
8. Liu, L., He, K., Xie, X., Du, J.: Image enhancement with wave-equation redatuming: application to GPR data collected at public transportation sites. J. Geophys. Eng. **4**, 139 (2007)
9. Nguyen, V.G., Marquis, G., Le, M.: EM and GPR investigations of contaminant spread around the Hoc Mon waste site, Vietnam. Acta Geophys. **58**, 1040–1055 (2010)
10. Nguyen, V.G., Ziętek, J., Nguyen, B.D., Karczewski, J., Gołębiowski, T.: Study of geological sedimentary structures of Mekong river banks by Ground Penetrating Radar: forecasting avulsion-prone zones. Acta Geophys. Polonica **53**, 167–181 (2005)
11. Doolittle, J.A., Collins, M.E.: Use of soil information to determine application of ground penetrating radar. J. Appl. Geophys. **33**, 101–108 (1995)
12. Smith, D.G., Jol, H.M.: Ground penetrating radar: antenna frequencies and maximum probable depths of penetration in Quaternary sediments. J. Appl. Geophys. **33**, 93–100 (1995)
13. Tzanis, A.: matGPR Release 2: a freeware MATLAB® package for the analysis & interpretation of common and single offset GPR data. FastTimes **15**, 17–43 (2010)
14. Yilmaz, O.: Seismic Data Analysis: Processing, Inversion, and Interpretation of Seismic Data. Society of Exploration Geophysicists, United States of America (2001)
15. Sham, J.F., Lai, W.W.: Development of a new algorithm for accurate estimation of GPR's wave propagation velocity by common-offset survey method. NDT E Int. **83**, 104–113 (2016)
16. Forte, E., Dossi, M., Pipan, M., Colucci, R.: Velocity analysis from common offset GPR data inversion: theory and application to synthetic and real data. Geophys. J. Int. **197**, 1471–1483 (2014)

17. Zhao, W., Tian, G., Forte, E., Pipan, M., Wang, Y., Li, X., Shi, Z., Liu, H.: Advances in GPR data acquisition and analysis for archaeology. Geophys. J. Int. **202**, 62–71 (2015)
18. Stinson, K., Crase, E., Chan, W., Levy, S.: Optimized determination of migration velocities. Recorder **30**, 5–6 (2005)
19. Maas, C., Schmalzl, J.: Using pattern recognition to automatically localize reflection hyperbolas in data from ground penetrating radar. Comput. Geosci. **58**, 116–125 (2013)
20. Al-Nuaimy, W., Huang, Y., Nakhkash, M., Fang, M., Nguyen, V., Eriksen, A.: Automatic detection of buried utilities and solid objects with GPR using neural networks and pattern recognition. J. Appl. Geophys. **43**, 157–165 (2000)
21. Szymczyk, P., Tomecka-Suchoń, S., Szymczyk, M.: Neural networks as a tool for georadar data processing. Int. J. Appl. Math. Comput. Sci. **25**, 955–960 (2015)
22. Illingworth, J., Kittler, J.: A survey of the Hough transform. Comput. Vis. Graph. Image Process. **44**, 87–116 (1988)
23. Le, C.V.A., Harris, B.D., Pethick, A.M., Takam Takougang, E.M., Howe, B.: Semiautomatic and automatic cooperative inversion of seismic and magnetotelluric data. Surv. Geophys. **37**, 845–896 (2016)
24. Samarasinghe, S.: Neural Networks for Applied Sciences and Engineering From Fundamentals to Complex Pattern Recognition. Auerbach Publications, New York (2006)
25. https://www.mathworks.com/matlabcentral/fileexchange/37388-fast-2d-peak-finder
26. Tzanis, A.: MATGPR: A freeware MATLAB package for the analysis of common-offset GPR data. In: Geophysical Research Abstracts (2006)
27. Margrave, G.F.: Numerical methods of exploration seismology with algorithms in Matlab. CREWES Toolbox Version 1006 (2003)

An Integration of Least Squares Support Vector Machines and Firefly Optimization Algorithm for Flood Susceptible Modeling Using GIS

Viet-Nghia Nguyen[1], Dieu Tien Bui[2(✉)], Phuong-Thao Thi Ngo[3], Quoc-Phi Nguyen[4], Van Cam Nguyen[5], Nguyen Quoc Long[1], and Inge Revhaug[6]

[1] Department of Mine Surveying, Hanoi University of Mining and Geology, Duc Thang, Bac Tu Liem, Hanoi, Vietnam
NguyenVietNghia@humg.edu.vn

[2] Geographic Information System Group, Department of Business and IT, University College of Southeast Norway, Gullbringvegen 36, 3800 Bø i Telemark, Norway
Dieu.T.Bui@usn.no

[3] Faculty of Information Technology, Hanoi University of Mining and Geology, Duc Thang, Bac Tu Liem, Hanoi, Vietnam
ngothiphuongthao@humg.edu.vn

[4] Faculty of Environmental Sciences, Hanoi University of Mining and Geology, Duc Thang, Bac Tu Liem, Hanoi, Vietnam
nguyenquocphi@gmail.com

[5] Institute of Geography, Vietnam Academy of Science and Technology, 18 Hoang Quoc Viet Road, Cau Giay, Hanoi, Vietnam
nguyencamvandl@gmail.com

[6] Department of Mathematical Sciences and Technology, Norwegian University of Life Sciences, PO.5003IMT, Aas, Norway
Inge.Revhau@nmbu.no

Abstract. The main aim of this research is to propose and evaluate a new hybrid intelligent approach (namely LSSVM-FA) based on Least Squared Support Vector Machines (LSSVM) and Firefly algorithm (FA) for flood susceptible modeling with a case study at a typical flood region in Central Vietnam. LSSVM and FA are current state-of-the art machine learning techniques that have rarely been explored for flood study. For this aim, a geospatial database of flood for the study area was constructed that consists of 76 historical flooded locations and 10 influencing factors. Using the database, the flood model was established using LSSVM, and then, the model was optimized where the best model's parameters were determined using FA. The goodness-of-fit and the prediction capability of the proposed model were evaluated using Receiver Operating Characteristic (ROC) curve and area under the ROC curve (AUC). The results showed that the proposed model performs well with the training data (AUC = 0.961) and the validation data (AUC = 0.934). Since the proposed model is better than benchmarks i.e. Neuron-fuzzy, support vector machines, and random forest, it could be concluded that the proposed model is a promising

© Springer International Publishing AG 2018
D. Tien Bui et al. (eds.), *Advances and Applications in Geospatial Technology and Earth Resources*, https://doi.org/10.1007/978-3-319-68240-2_4

tool that should be used for flood modeling. The result from this research is useful for land-use planning and management at flood-prone areas.

Keywords: Flood · Least-squares support vector machines · Firefly algorithm · Vietnam

1 Introduction

Quantification of areas with high susceptibility to flood is considered as a key element for flood risk assessment at flood-prone areas, therefore, various approaches have been proposed in literature, including physically based models and data-driven models [1]. Physically based models simulate hydrological processes through a set of mathematical equations of physical laws. They vary from simple 1D model i.e. flow computation in channels to more complicated 2D or 3D models that taken into account factors i.e. surface roughness, permeability, and topography [2]. Therefore, these models are capable to simulate floods in both space and time with different scenarios. The main disadvantage of these models is that detailed data are required. This is difficult when study areas are large. In addition, high-skill expertise is needed for the interpretation of the results [3].

Data-driven models used available datasets to obtain relationships between input and output variables, and then, functions or models are established and will be used to predict future scenarios. The main advantage of data-driven models is that they are easily and quickly developed and implemented [4], However, the accuracy of data-driven models is dependent on methods and techniques used.

Various data-driven methods have been explored for flood susceptibility modeling, such as logistic regression [5], artificial neural networks [6], M5 model trees [7], weights of evidence [8], analytic hierarchy process [9], k-nearest neighbors [10], neural fuzzy [11], support vector machines [12], and logistic model tree [13]. Literature review shows that although these models have proven to be able to simulate nonlinear and complex problem of flooding, however, accuracy of these models is still need improved by new approaches to reach reasonable conclusions. Therefore, explorations of new methods and techniques are highly necessary.

We address this issue by proposing and evaluating a new hybrid intelligent approach based on Least Squares Support Vector Machines (LSSVM) [14] and Firefly algorithm (FA) [15] for flood susceptible modeling with a case study at Tuong Duong district, a typical flood region of Central Vietnam [16]. According to current literature, they are current state-of-the art machine learning techniques have rarely been explored for flood study. LSSVM is used to create the flood model, whereas FA is adopted to optimize the model parameters. The rest of the paper is organized as follows: the second section describes the study area and data used; backgrounds of the method used are provided in the third section; the proposed model is depicted in the next section; the fifth section reports the experimental results; conclusion of this research is stated in the final section.

2 Study Area and Data

The case study is the Tuong Duong district (Fig. 1) that covers an area of 2803.1 km^2 and is a typical mountainous region lying on Nghe An province (Vietnam). Elevation of the study area varies from 2.9 m to 2122.2 m with the mean value is 527.8 m. Slope angle is ranged from 0^o to 84.66^o with the mean value is 19.27^o and the standard deviation value is 13.67^o. Around 68.2% of the study area has slopes larger than 10^o, whereas 21.3% are covered areas with slopes less than 5^o. Areas with slopes from 5^o to 10^o account for 10.4% of the total study area.

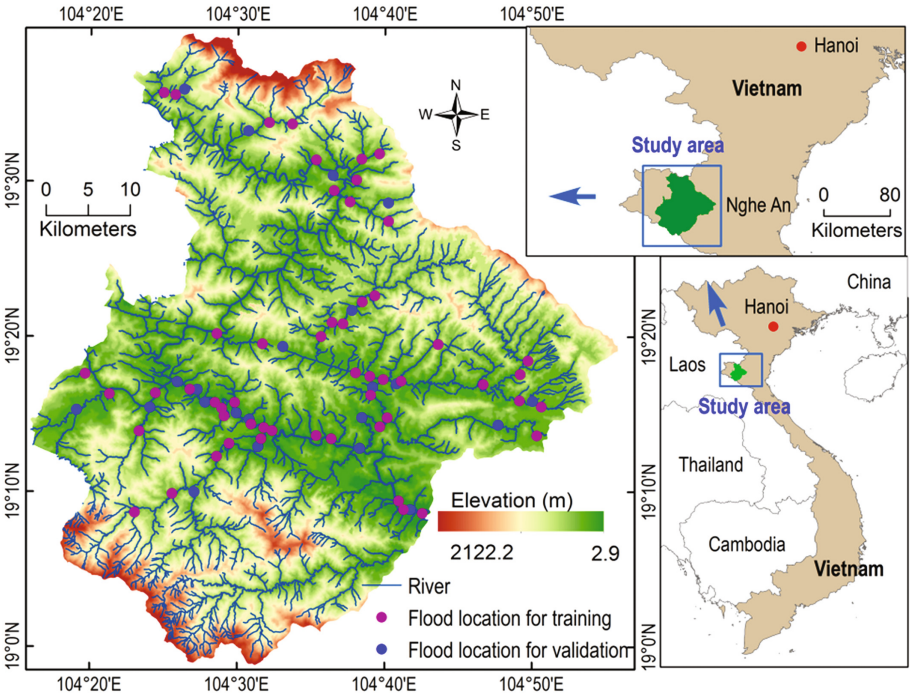

Fig. 1. Study area and flood locations

Rainfall is mainly concentrated from April to October (88.6–93.3% of the total rainfall per year), whereas from November to March rainfall is general low. Statistical analysis of rainfall from 1979 to 2010 showed that the highest total rainfall per year is 3259 mm whereas the lowest one is around 1679 mm. Temperature is also varied significantly among months, in the summer, the highest temperature may up to 42.7 °C in June and July, while the temperature may down to 0.5^o in the winter, such as in January and February [11].

Because flood modeling at regional scales is based on a statistical assumption that floods in the future will occur under the same conditions that produced them in the past. Therefore, it is necessary to collect historical flood locations. In this study, a flood

inventory map was created based on flood locations from: (i) sources of the Tuong Duong district; (ii) field works using handhold GPS; and (iii) interpretation of Landsat 8 OLI imagery with 30 m resolution that acquired in from 2010-2014. These images are available at the USGS archive at http://earthexplorer.usgs.gov. As results, a total of 76 flood locations were identified and these floods occurred during the last five years.

Flood modeling in this study is an indirect approach; therefore a large numbers of influencing factors should be collected. These factors could be determined based on analysis of flood locations and geo-environmental factors of the study areas. For this study, based on the previous analysis carried out in [11], a total of ten flood influencing factors (Table 1) were selected, including slope, elevation, curvature, topographic wetness index (TWI), stream power index (SPI), distance to river, stream density, NDVI, lithology, rainfall.

Table 1. Flood influencing factors and their classes for this study

Factors	Detailed classes
Slope (^{o})	0–0.5, 0.5–2, 2–5, 5–8, 8–13, 13–20, 20–30, >30
Elevation (x100 m)	<1, 1–2, 2–3, 3–4, 4–5, 5–6, 6–7, 7–10, 10–13, >13
Curvature	<-2; (−2) – (−0.05); (−0.05) – 0.05; 0.05 – 2; >2.
TWI	<6.5, 6.5–7.5, 7.5–8.5, 8.5–9.5, 9.5–10.5,10.5–11.5,11.5–12.5, >12.5
SPI (x100)	<1, 1–3, 3–5, 5–7, 7-10, 10–15, 15–20, 20-30, 30-50, >50
Distance to river (m)	<40, 40–80, 80–120, 120–200, 200–400, 400–700, 700–1500, >1500
Stream density (km/km^2)	<1, 1–3, 3–5, 5–7, 7–9, >9
NDVI	<0.3,0.3–0.35,0.35–0.4,0.4–0.45,0.45–0.50,0.50–0.55,0.55–0.60, > 0.60
Lithology	Q, Nkb, Jmh, T3npb, T2, C-bslk, D-ntdl, S2-D1hn, O3-S1sc3, O3-S1sc2, O3-S1sc1, PR2bk
Rainfall (x1000 mm)	<1.82, 1.82–1.92, 1.92–2.02, 2.02–2.12, 2.12–2.22, 2.22–2.32, 2.32–2.42, >2.42

First, a Digital Elevation Model for the study area was generated using national topographical maps at scale of 1:50,000. These maps have contour intervals of 10 m. Based on the DEM, slope, elevation, curvature, TWI, and SPI were extracted. Slope, elevation, and curvature were selected because slope and curvature influence runoff volumes; whereas elevation was used because floods are usually happen in lower elevations [17]. TWI and SPI were selected because they influence erosive powers and runoff volumes that related to occurrence of floods [18].

Distance from the river map and stream density map were generated based on the river network from the aforementioned national topographical maps. These maps were selected because they influence the spread and magnitude of flooding [19]. NDVI for the study area was estimated the Landsat 8 OLI imagery above using the equation belows [20]

$$\mathrm{NDVI} = (\mathrm{NIR} - \mathrm{RED})/(\mathrm{NIR} + \mathrm{RED}) \tag{1}$$

where NIR is the near-infrared reflectance and RED is the red reflectance.

NDVI was selected because it relates to characteristics of vegetation that influence flood disturbances [21]. Lithology was used for this analysis because it influences channel shape that relates floodplains [22]. Lithology map for this study was derived from Geological and Mineral Resources Map at 1:50,000 scale. For the case of rainfall, an average rainy season from 1979 to 2010 (available at https://www.ncdc.noaa.gov/) was used to construct the rainfall map for the study area.

3 Background of the Methods Used

3.1 Least Squares Support Vector Machines

In this section, LSSVM for classification is briefly described. Consider a training dataset $D = (x_k, y_k)_{k=1}^{n}$ with $x_k \in R^{10}$ is ten flood influencing factors, n is the number of training samples, and $y_k \in (1, 0)$ is the class label with '1' is for the flood class and '0' is for the non-flood class. LSSVM establishes a non-linear system by mapping the influencing factors into a high dimensional space, and then, solving linear equations for classifying these samples into the flood and non-flood classs. Thus, the classification function is expressed as belows:

$$y* = (w, \phi(x)) + b \tag{2}$$

where $\phi(x)$ is a mapping function; w is the weight vector; and b is the bias.

The two parameters w and b can be obtained through solving the optimization problem [23] as follows:

$$\begin{aligned} &\mathrm{Min} \quad J(w, e) = \frac{1}{2} w^T w + C \frac{1}{2} \sum_{k=1}^{h} e_k^2 \\ &\mathrm{Subject\ to}\ y_k = (w, \phi(x_k)) + b + e_k \ \mathrm{with}\ k = 1, \ldots, h \end{aligned} \tag{3}$$

where $J(w, e)$ is a loss function; e_k is error that is the difference between $y*$ and y; $C > 0$ is the regularization factor.

To avoid computational cost, a kernel function is used to map the input data to the feature space. For this research, the Radial Basis Function (RBF) is selected because it has proven better than other functions in various studies [24, 25]. The RBF is expressed as the following equation:

$$K(x_k, x) = \exp\left(-\frac{\|x_k - x\|}{\delta^2}\right) \tag{4}$$

where δ is the kernel parameter; $\|x_k - x\|$ is the Euclidean distance.

The Lagrangian function for solving the optimization problem in Eq. (3) is described as:

$$L(w, b, e, \alpha) = J(w, e) - \sum_{k=1}^{h} \alpha_k (y_k(w, \phi(x_k)) + b + e_k - y_k) \tag{5}$$

where α_k is the Lagrange multipliers.

The Karush–Kuhn–Tuker (KKT) conditions for optimality are written as:

$$\begin{cases} \frac{\partial L}{\partial w} = 0 \rightarrow w = \sum_{k=1}^{h} \alpha_k y_k \phi(x_k) \\ \frac{\partial L}{\partial b} = 0 \rightarrow \sum_{k=1}^{h} \alpha_k \\ \frac{\partial L}{\partial e} = 0 \rightarrow \alpha_k = Ce_k \\ \frac{\partial L}{\partial \alpha_k} = 0 \rightarrow (w, \varphi(x_k)) + b + e_k - y_k = 0 \end{cases} \tag{6}$$

The final LSSVM model for is expressed as follows:

$$y(x) = \text{sign}\left(\sum_{k=1}^{h} \alpha_k K(x_k, x) + b\right) \tag{7}$$

It could be seen that α_k and b are the solution from Eq. (6), whereas the regularization factor (C) and the kernel parameter (σ) are determined through the optimization using the Firefly algorithm.

3.2 Firefly Optimization Algorithm

Performance of the LSSVM model is strongly influenced by the pair (C, σ), therefore, these parameters should be carefully selected. Accordingly, the Firefly algorithm (FA) that is a population-based optimization algorithm developed by Yang [15] is proposed in this paper for searching the optimized values for the pair. The aim of the FA algorithm is to find the best firefly position that has the lowest RMSE between the flood inventory values and the output values from the model. Description of FA is briefly presented as follows:

Fireflies use their flashing light as the main signals for mating with rules [26] as follows: (i) all fireflies are unisex and they attract to other based on their flash lights; (ii) the degree of attractiveness of a firefly is proportional to its brightness; (iii) the attractiveness (β) of a firefly is determined by its light intensity (L(r)) that is derived from the objective function.

The light intensity L(r) and the attractiveness (β) of a firefly are defined using the equation as follows:

$$L(r) = L_o e^{-\gamma r}; \ \beta = \beta_o e^{-\gamma r^2} \tag{7}$$

where L_o is the original light intensity; γ is the absorption coefficient; r is the distance; β_o is the attractiveness of a firefly at r = 0.

The distance between two fireflies at position i and j is calculated as:

$$r_{ij} = \sqrt{\sum_{k=1}^{DS} (x_{ik} - x_{jk})^2} \tag{8}$$

where DS is the dimensional space.

The movement equation of firefly from position i to position j due to attraction of brighter firefly could be written as:

$$x_i = x_i + \beta_o e^{-\gamma r^2}(x_i - x_j) + \alpha\varepsilon_i \tag{9}$$

The detailed explanation of the FA algorithm could be seen in Yang [26].

4 Proposed Hybrid Intelligent Approach Based on Least Squares Support Vector Machines and Firefly Optimization Algorithm (LSSVM-FA) for Flood Susceptible Modeling

This section describes the proposed LSSVM-FA model for flood susceptible modeling. The source code of LSSVM is available at the LS-SVMlab toolbox [27], whereas the FA algorithm is programmed by the authors in Matlab environment. In this study, flood locations and influencing factors were processed and prepared using IDRISI Selva 17.01 and ArcGIS10.2.

4.1 Establishment of the Flood Database and Preparation of the Training and the Validation Datasets

At first, a geospatial database of flood for the study area was established using ArcCatalog 10.2 software. The database consists of 76 historical flooded areas and 10 influencing factors (slope, elevation, curvature, topographic wetness index (TWI), stream power index (SPI), distance to river, stream density, Normalized Difference Vegetation Index (NDVI), lithology, and rainfall). All the factors were converted in to a raster format with a pixel size of 30 m.

For flood susceptibility modeling, the historical floods were randomly split into two subsets with a ratio of 70/30 [28].The first subset with 54 locations was used for building model whereas the second subset with 22 locations was used for model validation. Modeling of flood susceptibility could be considered to be binary pattern recognition; therefore it is necessary to collect non-flood locations. Accordingly, the same amounts of non-flood locations for the two subsets were randomly sampled from free-flood areas. Finally, values of ten influencing factors were extracted for the flood and the non-flood locations, to build the training dataset and the validation dataset.

4.2 Configuration of Initial LSSVM Model and Object Function

A LSSVM model was initially created where the regularization parameter (C) and the RBF parameter (σ) were generated randomly in the searching space. Since C must be larger than 0, therefore, the lower and the upper boundaries for the searching space were selected as 0.001 and 10^3, respectively. The best values for C and σ for the data at hand were searched in the optimization process in the next step.

The best C and σ values were determined through the following object function

$$\text{Root Mean Squared Error (RMSE)} = \sqrt{\frac{1}{n}\sum_{i=1}^{n}(\text{Tag}_i - \text{Opt}_i)^2} \qquad (10)$$

where Tag is the target values; Opt is output values from the models; and *n* is the number of samples.

4.3 Optimization of the LSSVM Model Using the Firefly Algorithm

The goal of this step was to find best values for C and σ using the Firefly optimization algorithm. Since each firefly position in the searching space represents a possible solution for C and σ, therefore a population size of 50 fireflies were selected to ensure the sufficient diversity.

During the optimization process, various combinations of C and σ were explored. In each iteration, the FA algorithm guides these fireflies to the best position (the lowest RMSE). Thus, the fitness (RMSE) of each firefly in the training dataset was computed to eliminate fireflies with inferior combinations of C and σ. Only fireflies with robust combinations were passed to the next iteration. This is an iteration process and we used 1000 iterations as the stopping criteria.

Once the optimization process was terminated, the firefly with the lowest RMSE was determined, and the position in the searching space was used to derive the best C and σ for the flood susceptibility model.

4.4 Final Flood Susceptibility Model

Using the best C and σ in the previous step, the final flood susceptibility model was constructed, and then, the model was used to compute flood indices for all pixels in the study areas. The goodness-of-fit and the prediction capability of the flood susceptibility model were evaluated using the Receive Operating Characteristic (ROC) curve. The curve is a two dimensional graph that is constructed based on true-positive rate (sensitivity) and 1-specificity (false-positive rate), and is widely used to checked the global performance of predictive models, including flood susceptibility models [29]. A model is considered better if its curve closer to the upper left corner.

To quantify the global performance of the flood model, area under the ROC curve (AUC) was used. According to Kantardzic [30], the correlation of AUC with prediction models can be expressed as: poor (0.5–0.6), average (0.6–0.7); good (0.7–0.8), very good (0.8–0.9), and excellent (0.9–1).

5 Result and Discussion

Using the training dataset and the FA algorithm, the LSSVM-FA model for flood susceptibility modeling was established and optimized during the training phase. As result, the best values for the regularization parameter (C) and the RBF parameter (σ) were found as 19.903 and 6.229, respectively. The goodness-of-fit and statistical metrics of the flood model are shown in Table 2 and Fig. 2.

Table 2. Performance of the LSSVM-FA model in the training dataset and the validation dataset

Statistical measure	Training dataset	Validation dataset
True positive	48	16
True negative	48	21
False positive	6	6
False negative	6	1
Positive predictive value (%)	88.9	72.7
Negative predictive value (%)	88.9	95.5
Sensitivity (%)	88.9	77.8
Specificity (%)	88.9	94.1
Classification accuracy (%)	88.9	84.1
Kappa statistics	0.778	0.682

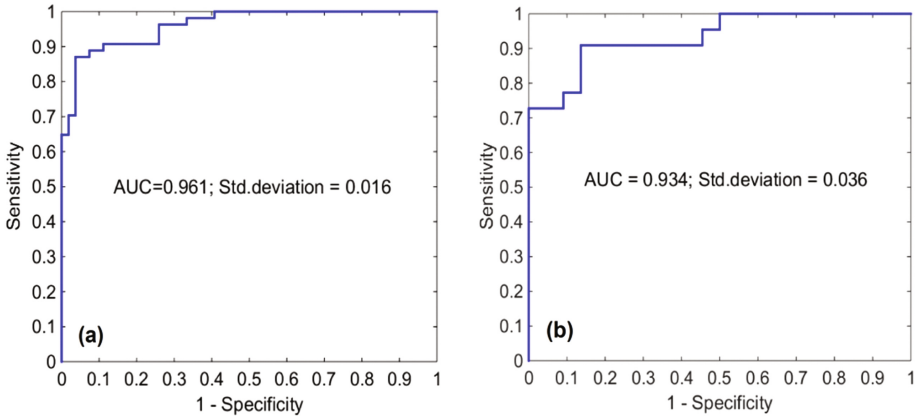

Fig. 2. ROC curve and AUC for the LSSVM-FA model using (a) the training dataset and (b) the validation dataset.

It could be observed that the classification accuracy (CA) is 88.9% indicating high classification accuracy. Positive predictive value (PPV) is 88.9% denoting that the probability the flood model correctly classifies pixels to the flood class is 88.9%. The same value of 88.9% is for negative predictive value (NPV), sensitivity, and specificity, indicating that the model has high performance with the training data. AUC of the

model is 0.961 (Fig. 2a) indicating that the global fit of the model is 96.1%. Kappa statistics is 0.778 indicating that the model perform 77.8% better than random, a high agreement between the flood model and the training data.

Using the validation dataset, the prediction capability and statistical metrics of the model were evaluated. CA is 84.1% indicating high accuracy. PPV is 72.7% denoting that the probability the flood model correctly classifies pixels to the flood class is 72.7%. NPV is 95.5% denoting that the probability the flood model correctly classifies pixels to the non-flood class is 95.5%. Sensitivity is 77.8% indicating that 77.8% the flood locations are classified to the flood class correctly. Specificity is 94.1% indicating that 94.1% the non-flood points are correctly classified to the non-flood class. AUC is 0.934 indicating that the prediction capability of the flood model is 93.4%. Kappa statistics is 0.682 indicating a satisfied result.

Because this is the first time the LSSVM-FA model is proposed for the flood susceptibility modeling. Therefore, the usefulness of the proposed model should be assessed by comparing with benchmark models such as neural fuzzy, support vector machines, and random forests using the same data. These models have been established and verified by the same authors in Tien Bui, Pradhan, Nampak, Quang Bui, Tran and Nguyen [11]. We see that the prediction capability of the proposed LSSVM-FA model (AUC = 0.934) is better than the neural fuzzy model (AUC = 0.911), the support vector machines model (AUC = 0.905), the random forests model (AUC = 0.894).

Since the LSSVM-FA model performed well for the study area, the model was used to compute flood indices for the entire pixel in the study area, and then, exported to ArcGIS 10.2 for producing the flood susceptibility map. The map was reclassified into six susceptible classes, such as very high (10%), high (10%), moderate (10%), low (10%), very low (10%), and no susceptible (50%). The threshold values for these classes were determined by overlaying the flood locations with the flood indices, and then, a graph was constructed and the threshold values were determined (Fig. 3).

Detailed descriptions of the six susceptibility classes are shown in Table 3. It could be seen that the very high class covers 280.3 km^2 (10%) of the study area, but accounts for 72.4% of the total flood locations, whereas the no susceptible class cover 50% of the total study area, but contains no flood location. These indicating that the LSSVM-FA model produced high accuracy result.

Table 3. Description of the flood susceptibility classes for the study area

Range of flood indices	Verbal expression	Flood location (%)	Areas (km^2)	Areas (%)
0.218–1.705	Very high	72.4	280.3	10
−0.043–0.217	High	13.2	280.3	10
−0.222–−0.044)	Medium	5.3	280.3	10
−0.368–−0.223	Low	5.3	280.3	10
−0.502–−0.369	Very low	4.0	280.3	10
−1.781–−0.503	No susceptible	0.0	1401.6	50

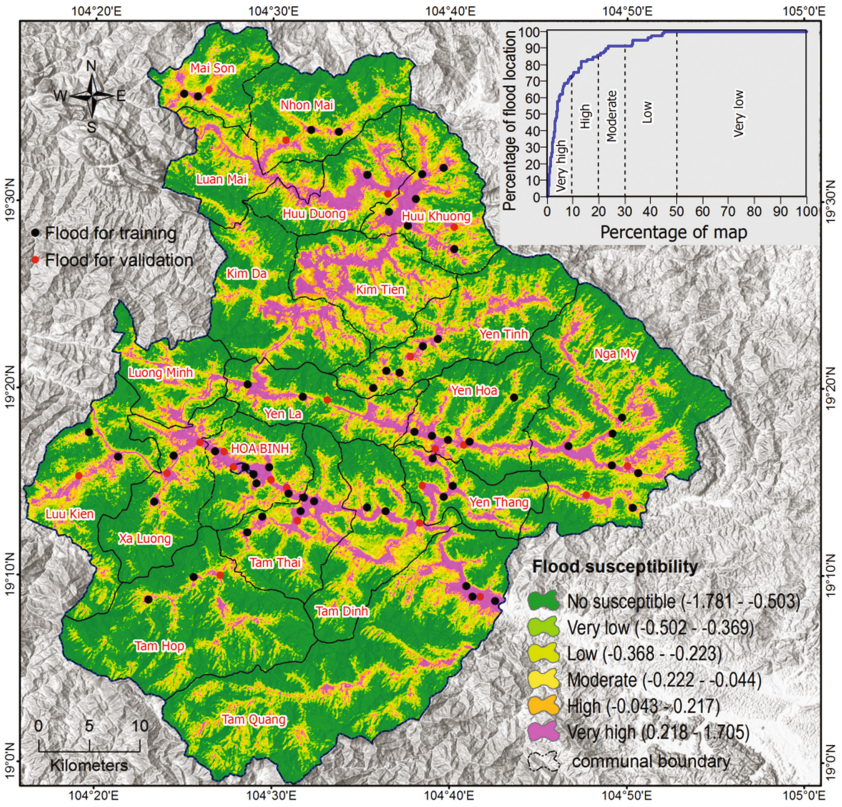

Fig. 3. Flood susceptibility map for the study area

6 Concluding Remarks

This research proposed and evaluated a new hybrid machine learning approach based on LSSVM and the FA algorithm (named as LSSVM-FA) for flood susceptibility modeling with a case study at an area in Central Vietnam. In the proposed modeling approach, LSSVM was used to create the flood model, whereas the FA algorithm was used to search the best model parameters through the optimization process. Accordingly, the geospatial database of flood for the study area was created and used to construct and assess the LSSVM-FA model. Probability of pixels belongs to the flood class was used as flood susceptibility indices. Experimental results showed that the LSSVM-FA model performs well with both the training and validation datasets.

Overall, conclusions from this research could be highlighted as follows: (i) performance of the flood model using LSSVM is heavily influenced by the regularization parameter (C) and the RBF parameter (σ). Therefore integration of a population-based optimization algorithm such as the FA algorithm is a good solution. The high goodness-of-fit and prediction capability of the flood model in this study indicate that the two parameters (C, σ) of has been successfully found by the FA algorithm; (ii) the

LSSVM-FA model perform better than benchmarks such as neural fuzzy, support vector machines, and random forests, therefore the proposed model is a promising tool that should be considered for flood susceptibility modeling in other areas; (iii) as final conclusion, the result from this research is useful for land-use planning and decision making at flood-prone areas

Acknowledgement. This research was supported by the Geographic Information System group, University College of Southeast Norway. The data for this research was provided by the Project No. B2014-02-21 (Ministry of Education and Training, Vietnam).

References

1. Werner, M.: A comparison of flood extent modelling approaches through constraining uncertainties on gauge data. Hydrol. Earth Syst. Sci. **8**, 1141–1152 (2004)
2. Vojinovic, Z., Hammond, M., Golub, D., Hirunsalee, S., Weesakul, S., Meesuk, V., Medina, N., Sanchez, A., Kumara, S., Abbott, M.: Holistic approach to flood risk assessment in areas with cultural heritage: a practical application in Ayutthaya. Thai. Nat. Hazards **81**, 589–616 (2016)
3. Nguyen, P.K.-T., Chua, L.H.-C., Son, L.H.: Flood forecasting in large rivers with data-driven models. Nat. Hazards **71**, 767–784 (2014)
4. Tiwari, M.K., Chatterjee, C.: Development of an accurate and reliable hourly flood forecasting model using wavelet–bootstrap–ANN (WBANN) hybrid approach. J. Hydrol. **394**, 458–470 (2010)
5. Fekete, A.: Validation of a social vulnerability index in context to river-floods in Germany. Nat. Hazards Earth Syst. Sci. **9**, 393–403 (2009)
6. Seckin, N., Cobaner, M., Yurtal, R., Haktanir, T.: Comparison of artificial neural network methods with L-moments for estimating flood flow at ungauged sites: the case of East Mediterranean River Basin. Turk. Water Res. Manage. **27**, 2103–2124 (2013)
7. Sattari, M.T., Pal, M., Apaydin, H., Ozturk, F.: M5 model tree application in daily river flow forecasting in Sohu stream. Turk. Water Res. **40**, 233–242 (2013)
8. Tehrany, M.S., Pradhan, B., Jebur, M.N.: Flood susceptibility mapping using a novel ensemble weights-of-evidence and support vector machine models in GIS. J. Hydrol. **512**, 332–343 (2014)
9. Kazakis, N., Kougias, I., Patsialis, T.: Assessment of flood hazard areas at a regional scale using an index-based approach and analytical hierarchy process: application in rhodope-evros region, Greece. Sci. Total Environ. **538**, 555–563 (2015)
10. Liu, K., Li, Z., Yao, C., Chen, J., Zhang, K., Saifullah, M.: Coupling the k-nearest neighbor procedure with the Kalman filter for real-time updating of the hydraulic model in flood forecasting. Int. J. Sedim. Res. (2016)
11. Tien Bui, D., Pradhan, B., Nampak, H., Quang Bui, T., Tran, Q.-A., Nguyen, Q.P.: Hybrid artificial intelligence approach based on neural fuzzy inference model and metaheuristic optimization for flood susceptibility modelling in a high-frequency tropical cyclone area using GIS. J. Hydrol. **540**, 317–330 (2016)
12. Tehrany, M.S., Pradhan, B., Mansor, S., Ahmad, N.: Flood susceptibility assessment using GIS-based support vector machine model with different kernel types. CATENA **125**, 91–101 (2015)

13. Chapi, K., Singh, V.P., Shirzadi, A., Shahabi, H., Bui, D.T., Pham, B.T., Khosravi, K.: A novel hybrid artificial intelligence approach for flood susceptibility assessment. Environ. Model Softw. **95**, 229–245 (2017)
14. Suykens, J.A., Vandewalle, J.: Least squares support vector machine classifiers. Neural Process. Lett. **9**, 293–300 (1999)
15. Yang, X.-S.: Nature-Inspired Metaheuristic Algorithms. Luniver Press (2010)
16. Wang, S.-Y.S., Promchote, P., Truong, L.H., Buckley, B., Li, R., Gillies, R., Trung, N.T.Q., Guan, B., Minh, T.T.: Changes in the autumn precipitation and tropical cyclone activity over central Vietnam and its east sea. Vietnam J. Earth Sci. **36**, 489–496 (2015)
17. Qi, S., Brown, D.G., Tian, Q., Jiang, L., Zhao, T., Bergen, K.M.: Inundation extent and flood frequency mapping using LANDSAT imagery and digital elevation models. GISci. Remote Sens. **46**, 101–127 (2009)
18. Wang, Z., Lai, C., Chen, X., Yang, B., Zhao, S., Bai, X.: Flood hazard risk assessment model based on random forest. J. Hydrol. **527**, 1130–1141 (2015)
19. Glenn, E.P., Morino, K., Nagler, P.L., Murray, R.S., Pearlstein, S., Hultine, K.R.: Roles of saltcedar (Tamarix spp.) and capillary rise in salinizing a non-flooding terrace on a flow-regulated desert river. J. Arid Environ. **79**, 56–65 (2012)
20. Tucker, C., Sellers, P.: Satellite remote sensing of primary production. Int. J. Remote Sens. **7**, 1395–1416 (1986)
21. Džubáková, K., Molnar, P., Schindler, K., Trizna, M.: Monitoring of riparian vegetation response to flood disturbances using terrestrial photography. Hydrol. Earth Syst. Sci. **19**, 195–208 (2015)
22. Heitmuller, F.T., Hudson, P.F., Asquith, W.H.: Lithologic and hydrologic controls of mixed alluvial–bedrock channels in flood-prone fluvial systems: Bankfull and macrochannels in the Llano River watershed, central Texas, USA. Geomorphology **232**, 1–19 (2015)
23. Suykens, J., Gestel, J.V., Brabanter, J.D., Moor, B.D., Vandewalle, J.: Least Square Support Vector Machines. World Scientific Publishing Co. Pte. Ltd, Singapore (2002)
24. Tien Bui, D., Pradhan, B., Lofman, O., Revhaug, I., Dick, O.B.: Application of support vector machines in landslide susceptibility assessment for the Hoa Binh province (Vietnam) with kernel functions analysis. In: iEMSs 2012 - Managing Resources of a Limited Planet: Proceedings of the 6th Biennial Meeting of the International Environmental Modelling and Software Society, pp. 382–389 (Year)
25. Tien Bui, D., Anh Tuan, T., Hoang, N.-D., Quoc Thanh, N., Nguyen, B.D., Van Liem, N., Pradhan, B.: Spatial prediction of rainfall-induced landslides for the Lao Cai area (Vietnam) using a novel hybrid intelligent approach of least squares support vector machines inference model and artificial bee colony optimization, Landslides (2016). doi:10.1007/s10346-016-0711-9
26. Yang, X.-S.: Nature-Inspired Computation in Engineering. Springer (2016)
27. De Brabanter, K., Karsmakers, P., Ojeda, F., Alzate, C., De Brabanter, J., Pelckmans, K., De Moor, B., Van de Walle, J., Suykens, J.: LS-SVMlab toolbox user's guide. ESAT-SISTA Technical report, pp. 10–146 (2011)
28. Tien Bui, D., Pradhan, B., Lofman, O., Revhaug, I., Dick, O.B.: Landslide susceptibility mapping at Hoa Binh province (Vietnam) using an adaptive neuro-fuzzy inference system and GIS. Comput. Geosci. **45**, 199–211 (2012)
29. Tien Bui, D., Le, K.-T., Nguyen, V., Le, H., Revhaug, I.: Tropical forest fire susceptibility mapping at the cat ba national park area, Hai Phong city, Vietnam, using GIS-based kernel logistic regression. Remote Sens. **8**, 347 (2016)
30. Kantardzic, M.: Data Mining: Concepts, Models, Methods, and Algorithms. Wiley, Hoboken (2011)

Estimation of Surface Parameters of Tidal Flats Using Sentinel-1A SAR Data in the Northern Coast of Vietnam

Si Son Tong[1,2(✉)], Jean Paul Deroin[3], Thi Lan Pham[4], and Xuan Cuong Cao[4]

[1] University of Science and Technology Ha Noi, 18 Hoang Quoc Viet, Cau Giay, Ha Noi, Vietnam
tongsison@gmail.com
[2] Institute of Space Technology, 18 Hoang Quoc Viet, Cau Giay, Ha Noi, Vietnam
tsson@sti.vast.vn
[3] GEGENAA Laboratory, Université de Reims Champagne-Ardenne, Reims, France
jean-paul.deroin@univ-reims.fr
[4] Ha Noi University of Mining and Geology, Ha Noi, Vietnam
phamthilanhdl23@gmail.com

Abstract. Tidal flat is a special environment which is submerged during flood tide and exposing the air during ebb tide. Tidal flats in the north coast in Vietnam surfer diurnal tide with tide range varying from 0.3 m to 3.5 m. Along 350 km coastline of the study area, the diversity of constituent conditions forms various tidal flats with different characteristics. Soil moisture and surface roughness are the key parameters for the studies concerning tidal flat environment. These surface parameters of tidal flats can be investigated using inversion models with SAR data. This study applies the inversion method of the Oh model 2004 to estimate vertical surface roughness and soil moisture. Two Sentinel-1A SAR data are acquired and preprocessed to yield backscattering coefficients of VV and VH polarizations of C band. In condition of missing co-polarization data (HH) for fully applying the Oh inversion model, a calibration function is generated to calibrate estimated roughness and soil moisture. This is the first time that the surface roughness and soil moisture of tidal flats are successfully estimated from SAR data in the study area. Even now, the applications of the Oh model for estimating surface parameters of tidal flat using Sentinel-1A SAR images have not found yet in literatures. Vertical roughness after calibrating is estimated with an accuracy of 0.09 cm. The accuracy of estimated soil moisture of tidal flats is not assessed due to lacking the referent data. However, the estimated soil moisture is good correlation with the real environmental conditions in the study area.

Keywords: Tidal flats · Surface parameters · Sentinel-1A SAR data · Oh model

© Springer International Publishing AG 2018
D. Tien Bui et al. (eds.), *Advances and Applications in Geospatial Technology and Earth Resources*, https://doi.org/10.1007/978-3-319-68240-2_5

1 Introduction

Tidal flats are sandwiched between land, freshwater, and marine environment in which tidal flats are characterized by regular alternations of exposure and flooding by tide [1–3]. In general, tidal flats are coastal wetlands, soft sediment habitats, non-vegetated. Soil moisture and surface roughness are key parameters for the studies concerning tidal flat environment [4, 5]. Surface of tidal flats is regularly covered by seawater in different duration depending on the tide cycle. Thus, it is hard to investigate surface parameters on the field, only remote sensing technique allows instantaneously mapping tidal flat surface at a large scale [6, 7]. On the basic of the specific interaction between Electromagnetic (EM) waves and the properties of natural surface, Synthetic Aperture Radar (SAR) data can be used to survey surface parameters. The backscatter of the EM waves from a surface is influenced by factors related to radar properties (incident angle, frequency, polarization) and surface characteristics (dielectric constant, soil moisture, surface roughness consisting of vertical roughness and correlation length) [8, 9]. In order to simulate the relationship between radar backscatter and the surface parameters, numerous models are proposed such as theoretical models (ex. Integral Equation Model (IEM) [8]), semi-empirical models (ex. Oh [10], Dubois model [11]) and empirical models [12, 13]. For each model, an inversion method is developed to estimate the parameters of bare soil surface (including tidal flats) from backscattering signals.

Surface parameters inverted from SAR data are deeply researched in the field of agricultural land [14–17]. In the fields related to geology, the estimation of soil surface parameters was carried out in numerous studies and obtained successful results [18–21]. These studies used different polarizations of various SAR image systems in the common conditions of relatively dry surface and non-saline soil. For a surface suffering the tide regime such as tidal flats, the issues of estimating surface parameters from SAR data were only carried out in few studies [4, 22], and gained mixed successes [9]. The theoretical backscattering model IEM was applied to characterize surface roughness of intertidal flats in Westerschelde, Netherland using C-band ERS SAR images by Van der Wal *et al*. [9]. The results denoted that the backscattering was mainly related to the vertical surface roughness and positively correlated with medium grain sizes, but it was negatively correlated with muddy area. Moreover, the moisture in tidal flats was too high to significantly affect the radar backscatter in the IEM model. Both IEM and semi-empirical model were applied for the tidal flats in Suncheon bay, South Korea by Park et al. [4]. This experiment successfully estimated Root Mean Square (RMS) height but failed to properly estimate the correlation length from the L band of AirSAR data. Ulaby et al. [23] found that the influence of saline soil to dielectric constant was negligible for the C band SAR. The case study of Gade et al. [24] produced the similar results obtained by Van der Wal et al. [9] when the vertical roughness well fitted with in-situ data, however, the correlation length was lower than that of field measured data. This study also suggested that the combination of L band with C band or X band for the IEM model could produce the highest accuracy of estimating roughness parameters. The application of semi-empirical or empirical model to characterize surface parameters of tidal flats is less popular than the IEM model.

Kim et al. [25] applied the IEM and Oh model using L band Alos Palsar and C band Radarsat-2 data for tidal flats in South Korea but the results were not deeply analyzed. The correlation between five soil types of tidal flats, roughness parameters and backscattering data of L band Alos Palsar and C band ERS-2 was investigated using empirical model in Baie de Veys, Normandy [22]. Generally, the previous studies denoted that the surface parameters of tidal flats were underestimated if the surface was covered by remnant water even applying any inversion models.

Tidal flats along the northern coast of Vietnam play an important role in environment and the livelihood of local people. However, there are no studies related to surface parameters in this area found in literatures. This study firstly applies the Oh inversion model for Sentinel-1A SAR data to estimate soil moisture and surface roughness of tidal flats. Subsequently, the correlation between surface parameters and radar backscatters, sediment size, tidal flat elevation in the study area is investigated. In addition, soil moisture and surface roughness of tidal flats represent both biogenic and physical depositional characteristics of sediments [26]. Thus, surface parameters are not only keys for describing the land-use characteristics but also supporting the valuable information for aquaculture planning in tidal flats along the northern coast of Vietnam.

2 Tidal Flats in the North Coast in Vietnam

The study focuses on tidal flats along 350 km coastal line in the north of Vietnam, next to the Gulf of Tonkin. The study area is the natural border of 15 coastal districts belonging 5 provinces: Ninh Binh, Nam Dinh, Thai Binh, Hai Phong and Quang Ninh. Located in the tropical zone and suffering the moon soon weather, this area consists of a rainy season in summer and a dry season in winter. Tidal flats in here experience the diurnal tide with the average of 3.5 m amplitude. High mountain terrain along with the intensive precipitation in rainy season in the northern part (Hai Phong, Quang Ninh) form numerous short, steep slope, temporary rivers along the coast. In addition, more than 2300 rocky islands parallel and 12 km far from the coastline protect coastal zones in Hai Phong, Quang Ninh from the influences of wind, waves. The high dynamic of rivers together with the tidal domination constitute the wide sandy tidal flats. As an example of tidal flats constituted by human activities, the coastal area in Cam Pha (the middle of the study area) has accumulated sediments from coal exploitation for more than 100 years. Coal sediments concentrate in near-shore water and form the black muddy tidal flats. Tidal flats in Ninh Binh, Nam Dinh, Thai Binh are fed by a huge amount of sediments from Red river system and Thai Binh river system. Each year, these river systems transport an average of about 77×10^6 tons of sediments to the coastal area [27]. The diversity of constituent conditions forms tidal flats with various surface characteristic. For convenience when mentioning about location, the district names (ex. Kim Son, Thai Thuy, Mong Cai..in Fig. 1) will be used as relative coordinates.

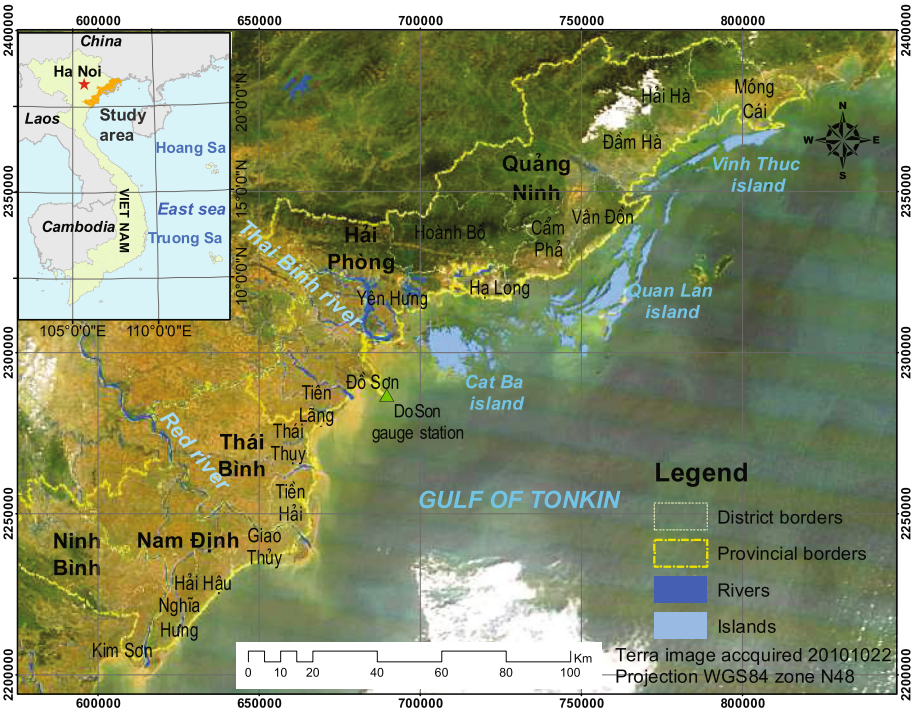

Fig. 1. Map of the study area

3 Materials and Methods

3.1 Radar Data

For the purpose of estimating the surface parameters of tidal flats, 2 scenes of Sentinel-1A processed at level-1 SLC are acquired covering fully the study area (Table 1). The scene in the orbit 006831 covers the southern coast of the study area from Kim Son to Cam Pha. This image is captured in the morning on 15th July 2015 at 5 h 50′ am local time. Along the coast from the South to the North, this SAR data is recorded following the incident propagation range of 36.2–33.0°. The weather condition at acquisition time is gentle wind speed, 25 °C air temperature, clear cloud, and at lowest tide level. The scene in the orbit 009227 covers 70% of the study area from Hai Hau to Mong Cai with the variation of incidence angle from 31.1 to 42.9°. This scene is

Table 1. General information of Sentinel-1A data in use.

Sensor/orbit	Acquisition date/time (local time)	Resolution (m)	Wave length	Polarization	Level processing	Tide level (m)	Tide period
S1/006813	20150715/05 h50′36″	5 × 20	C band, 5.54 cm	VV, VH	L1 SLC	0.64	Flood
S1/009227	20151227/17 h57′26″	5 × 20	C band, 5.54 cm	VV, VH	L1 SLC	0.37	Ebb

acquired at the sunset time (17 h 57′ local time) in winter with wind speed of 4 m/s and lowest tidal level (0.37 m). The tidal flats fully expose to the air on this image. Both images overlay each other in the area from Hai Hau to Cam Pha. The scene orbit 006831 is recorded in ascending flight and the other one is in descending direction.

3.2 In-Situ Data

Field measurements are performed at two test sites in Giao Thuy and Thai Thuy. The test site in Giao Thuy is a back-barrier tidal flat. The outer edge of tidal flat next to the sea is obstructed by a sand bar. There are 7 sample sites GT1, GT2, GT3, GT4, GT5, GT6, GT7 distributed along the cross section AB of the tidal flats (Fig. 2). Sediments at GT1, GT2 are characterized by clay and silt located at the lowest area of tidal flat. The samples from GT3 to GT5 gradually increase of sand content. The sample site GT7 is on the steep side of sand bar seaward. The GT6 is excluded in measuring roughness since its location is on the top of sand bar, very dry sand, rubbishes from sea concentrated on the surface, and not formed in a particular shape. The measurement is implemented during the low tide from 6 h 30′ to 9 h 00′ am on 15th July 2015 in the condition of gentle wind (2 m/s), clear cloud, 27 °C of air temperature. The test site in Thai Thuy is measured on 16th July 2015, one day after the Giao Thuy measurement and 40 km far from each other. Thai Thuy site is an open coast tidal flat with the width of 2200 m. The measurement is performed from 6 h 30′ to 8 h 30′ am. There are 5 sample sites TT1, TT2, TT3, TT4, TT5, are placed in Thai Thuy. The surface roughness and correlation length are measured using common ruler for each sample site defined by a block with 1 m x 1 m size. In-situ data in Giao Thuy and Thai Thuy are showed in Table 2. Soil samples are collected for every sample site to analyze grain size, carbonate content. In addition, the three field samples HH1, HH2, HH3 in Hai Ha in the northern part of the study area are also visited on 19th July, 2015.

Table 2. Vertical roughness (s) and correlation length (l) measured in the field

Location/ Visiting date	Name	Number observes	s (cm)			l (cm)		
			Min	Max	Average	Min	Max	Average
Giao Thuy/15th July 2015	GT1	7	0.06	0.14	0.10			
	GT2	12	0.97	1.68	1.42	9.6	13.2	11.5
	GT3	15	0.44	0.85	0.60	1.8	3.0	2.4
	GT4	10	0.49	0.96	0.76	2.2	3.7	2.8
	GT5	8	0.13	0.48	0.20	0.6	1.7	1.1
	GT7	16	1.79	2.5	2.24	9.3	14.9	12.6
Thai Thuy/16th July 2015	TT1	11	0.5	0.74	0.63	3.8	6.0	5.1
	TT2	10	0.47	0.66	0.54	5.7	7.2	6.4
	TT3	15	0.39	0.62	0.48	3.9	6.1	5.3
	TT4	9	0.34	0.58	0.44	4.1	5.4	4.8
	TT5	10	0.51	0.65	0.57	4.8	7.3	6.7

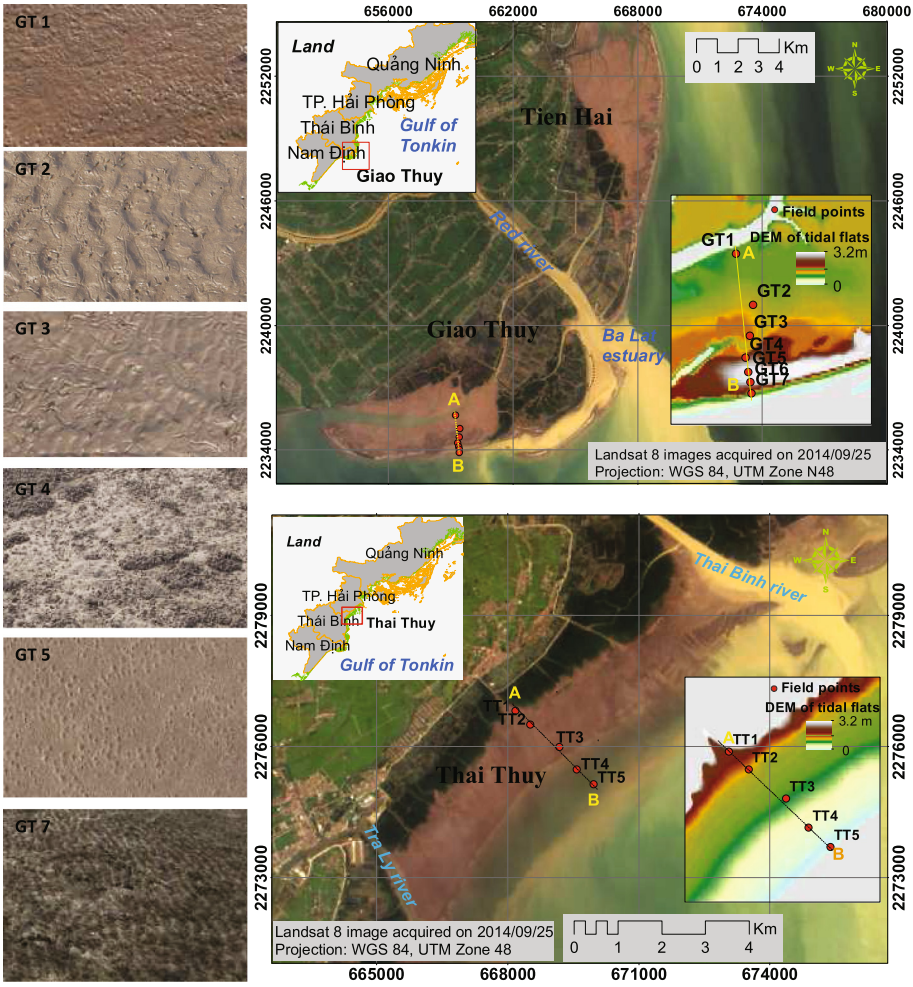

Fig. 2. Surface shape of sample sites in Giao Thuy (left photos), locations of sample sites in Giao Thuy (up right image), in Thai Thuy (low right image)

3.3 Method for Estimating Surface Parameters

Two main steps are implemented to estimate the surface roughness and soil moisture consisting of pre-processing Sentinel-1A SAR data, and the application of the inversion models. In addition, a calibration function is calculated to calibrate the estimated roughness and soil moisture values from the inversion model.

3.3.1 Pre-processing Sentinel-1A SAR Image

Sentinel-1A SAR data used in this study is already systematically processed at the level 1 SLC which is transformed from raw data by processes: internal calibration, Doppler centroid estimation, ranger processing and azimuth processing. Consequently, the level

1 SLC products consist of single look for each dimension using a full available signal bandwidth and complex sample (real and imaginary) keeping the phase information. These data are geo-referenced using the orbit and attitude data from the satellite and corrected for azimuth bi-static delay, elevation antenna pattern and ranger spreading loss. In order to apply the Sentinel-1A level 1 SLC data for the inversion surface model, it is necessary to process following steps: 1. Radiometric calibration, 2. Thermal noise removal, 3. TOPSAR deburst, 4. Multi look, 5. Speckle filter, 6. Geometric correction. All these pre-processing steps are implemented by Sentinel-1A Toolbox. After preprocessing, a Normalized Radar Cross Section (NRSC) image is simultaneously produced with an image of projected local incidence angle at the 14.3 m spatial resolution in WGS84 zone N48 projection. The preprocessing steps are repeatedly implemented for both VV and VH polarizations of two acquired Sentinel-1A scenes.

3.3.2 Estimating Surface Roughness and Soil Moisture

For this study, the Oh model is used for estimating surface roughness and soil moisture of tidal flats in the study area. The Oh model [28] is generated from ensemble-averaged differential Muller matrix that calculates electromagnetic scattering from bare soil surface. Series of radar data from truck-mounted scatterometer measurements and Airborne SAR observation combining with the measured surface profiles are used to define the parameters of the model. The predicted EM scattering from the Oh model is constrained to be consistent with known theoretical values then the functional form of the model is determined. The conversion model for estimating surface roughness and soil moisture from the backscatter coefficients is ultimately introduced in [10]. The semi-empirical Oh model 2004 is briefly presented as.

$$\sigma^0_{vh} = 0.11 m_v^{0.7} (\cos\theta)^{2.2} \left[1 - \exp\left(-0.32(ks)^{1.8}\right)\right] \tag{1}$$

$$p = \frac{\sigma^0_{hh}}{\sigma^0_{vv}} = 1 - \left(\frac{\theta}{90^0}\right)^{0.35 m_v^{-0.65}} .e^{-0.4(ks)^{1.4}} \tag{2}$$

$$q = \frac{\sigma^0_{vh}}{\sigma^0_{vv}} = 0.095(0.13 + \sin 1.5\theta)^{1.4} \left\{1 - \exp\left[-1.3(ks)^{0.9}\right]\right\} \tag{3}$$

The direct inversion model:

$$ks = \left\{\frac{-1}{1.3} \ln\left[1 - \frac{q}{0.095(0.13 + \sin 1.5\theta)^{1.4}}\right]\right\}^{1.111} \tag{4}$$

$$m_v = \left\{\frac{\sigma^0_{vh}}{0.11(\cos\theta)^{2.2}\left[1 - \exp\left(-0.32(ks)^{1.8}\right)\right]}\right\}^{1.4286} \tag{5}$$

where σ^0 is the backscatter coefficient, p, q are ratio of co- and cross polarizations of EM backscatter, θ is the incidence angle, k is free-space radar wave number, s is

surface roughness height, ks = k * s is used as RMS height of estimated roughness, and m_v is soil moisture.

Based on five Eqs. (1)–(5), an inversion process is generated to estimate m_v and *ks* (detailed in [10]) with a valid range of $s < 5.5$ cm and $0.01 < m_v < 0.35$ cm^3/cm^3. The surface parameters are estimated using the ENVI software in this study, thus, the inversion equations need to be transferred to the code style of the IDL programming language. The *ks* estimated from the Oh inversion is calibrated using in-situ roughness measured in Giao Thuy. The roughness data measured in Thai Thuy are used to assess the accuracy of *ks* after calibrating. Soil moisture is estimated using variables: surface roughness, local incident angle, and NRSC of VH polarization. All processes to estimate *ks* and m_v are initially applied for the Sentinel-1A radar image acquired on 15th July 2015 and then they are reapplied for the radar image acquired on 27th December 2015. The calibration of *ks* for image acquired on 27th December 2015 uses the calibration function defined from the SAR data acquired on 15th July 2015 due to the absence of appropriate field survey data. General steps of processing are illustrated in Fig. 3.

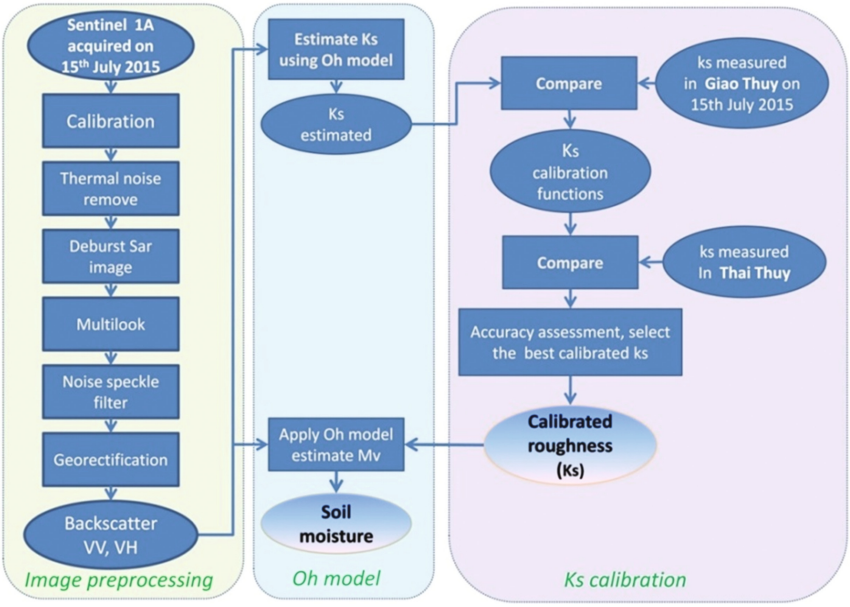

Fig. 3. Flow chat of estimating roughness (*ks*) and soil moisture (m_v) using Oh model

4 Results and Discussions

4.1 The Use of the Oh Inversion Model

There are various models estimating the surface parameters from the electromagnetic backscatter data. The theoretical model such as IEM is commonly used for estimating the surface parameters but it strongly depends on a known surface Autocorrelation Function (ACF) [29, 30]. However, with a given approximate function, the high

sensitivity of theoretical models to the selected ACF, even small deviations can cause the differences in the calculated backscatter on the order of several decibels [31]. In addition, for each single-scale roughness, a better fit between the theoretical and the experimental ACF should be obtained [32]. For tidal flats along 350 km of the coastline of the study area, the surface characteristic are so different, thus, it is difficult to define an ACF for operating IEM model. The semi-empirical model as Dubois directly estimates roughness and dielectric constant from co-polarization HH, VV but this study uses Sentinel-1A with VV and VH polarizations. Each empirical model is mostly only appropriated for a specific surface condition and radar data available [11, 33]. The inversion model Oh version 2004 [10] uses three polarization VV, HH, VH to estimate roughness and soil moisture using the combination of three equation components, in which the Eq. (3) can be independently used to estimate roughness from VV and VH polarizations. Moreover, Panciera et al. [34] compared three models IEM, Dubois and Oh and recognized that the Oh model exhibits the best agreement between the observed data and simulated results. The Oh model is only valid if the surface roughness is less than 5.5 cm, and the soil moisture is greater than 0.01 cm^3/cm^3. In the study area, the maximum of measured roughness parameter is 2.5 cm (Table 2). It is sure that the soil moisture of tidal flats is greater than 0.01 cm^3/cm^3. Thus, the Oh model is appropriate for estimating surface parameters of this study area. However, because of absent HH polarization to apply full Oh model, it is necessary to calculate a calibration function for *ks* estimated from Eq. (4).

The roughness properties of natural surface are described by RMS height and correlation length. However, the correlation length is not estimated from SAR data using the Oh model due to the insensitivity of the cross-polarization ratio on that parameter [10]. The very weak correlation between cross-polarization data and the correlation length was also confirmed by Dubois et al. [11]. Thus, the correlation length is not mentioned in this study although they are measured at some locations in the field. The complex dielectric constant is also ignored in the Oh model because the backscatter coefficients insignificantly depend on soil types comparing with its responses to surface roughness and soil moisture [10]. Moreover, the dielectric constant mostly depends on soil moisture [35]. The influence of dielectric constant to backscatter is even negligible with saline soil for C-band SAR [23]. Hence, the soil moisture is directly calculated from Eq. (5) instead of dielectric constant in this study.

4.2 Calibration Function and Accuracy Assessment of Estimated Roughness

The vertical roughness and correlation length measureded in Giao Thuy are used for calibrating the roughness estimated from radar data since the acquisition time of SAR image is approximate the time of field visit. The surface parameters measured in Thai Thuy (16th July) is just one day after acquiring SAR image (15th July). In addition, the weather conditions are similar in both days. Thus, it is assumed that the ripple orientation and geometry of tidal flat surface are persistent in the time-scale of 24 h. In this case, the surface parameters measured in Thai Thuy are used to assess the accuracy of surface parameters estimated from Sentinel-1A SAR data.

The SAR data acquired on 15th July 2015 is about 1 h before field measurement in Giao Thuy so that estimated *ks* is compared with the roughness measured on the field to calculate the calibration function. The estimated roughness values for comparing are averaged of 9 pixel values surrounding the sample sites. The comparison results between estimated roughness and measured roughness are presented in Table 3.

Table 3. Comparison of roughness estimated using Oh model and field measured data

Samples	Measured S (cm)	Measured *ks* (cm)	Estimated *ks* average (cm)	Residual (cm)
GT1	0.10	0.11	2.10	1.99
GT2	1.42	1.61	3.18	1.57
GT3	0.60	0.68	2.67	1.99
GT4	0.76	0.86	2.90	2.04
GT5	0.20	0.23	2.33	2.10
GT7	2.24	2.54	3.64	1.10

Table 4 shows that the *ks* inverted from ratio VH/VV backscatter using Oh model is much higher than the *ks* measured in the field. The highest residual between 2 data sets is at GT5 with 2.1 cm and lowest residual is at GT7 with 1.1 cm. There is a contrast in the variation of estimated *ks* and measured *ks*. The lowest residual at GT7 (1.1 cm) belongs to the highest roughness (2.54 cm of measured *ks*), and highest residual (2.1 cm) at GT5 belongs to almost lowest roughness (0.23 cm of measured *ks*). In general, the estimated *ks* data positively correlate to the measured *ks* data with 0.952 R-square (Fig. 4b). Because there is the bias between surface roughness estimated from the Oh model and the in-situ data so that it is necessary to calculate a calibration function for the estimated *ks*. Five potential interpolation methods are proposed consisting of exponential, linear, logarithmic, polynomial, and power methods. The results of calculating the calibration functions are presented in Fig. 4. It is clear that the R-square of the power and polynomial methods are highest with 0.979 and 0.992 respectively. Contrastingly, the three other methods produce much lower R-square with 0.912 of the logarithmic, 0.951 of the exponential, and 0.952 of the linear method. It is possible to consider two methods with highest R-square values supporting the highest potential for the calibration function. However, to ensure selecting the best appropriate method, both of the power and polynomial functions are applied to calibrate the estimated *ks* and assessing the accuracy of *ks* after calibration.

$$\text{Polynomial interpolation function: } y = 0.688x^2 - 2.336x + 1.965 \quad (6)$$

$$\text{Power interpolation function: } y = 0.001x^{5.766} \quad (7)$$

The estimated *ks* is calibrated using power and polynomial interpolation equations. The calibrated *ks* values are then compared with the measured roughness values in Thai Thuy to assess the accuracy. The better accuracy of calibrated *ks* represents the better calibration function. The comparison results of nine *ks* values surrounding five sample

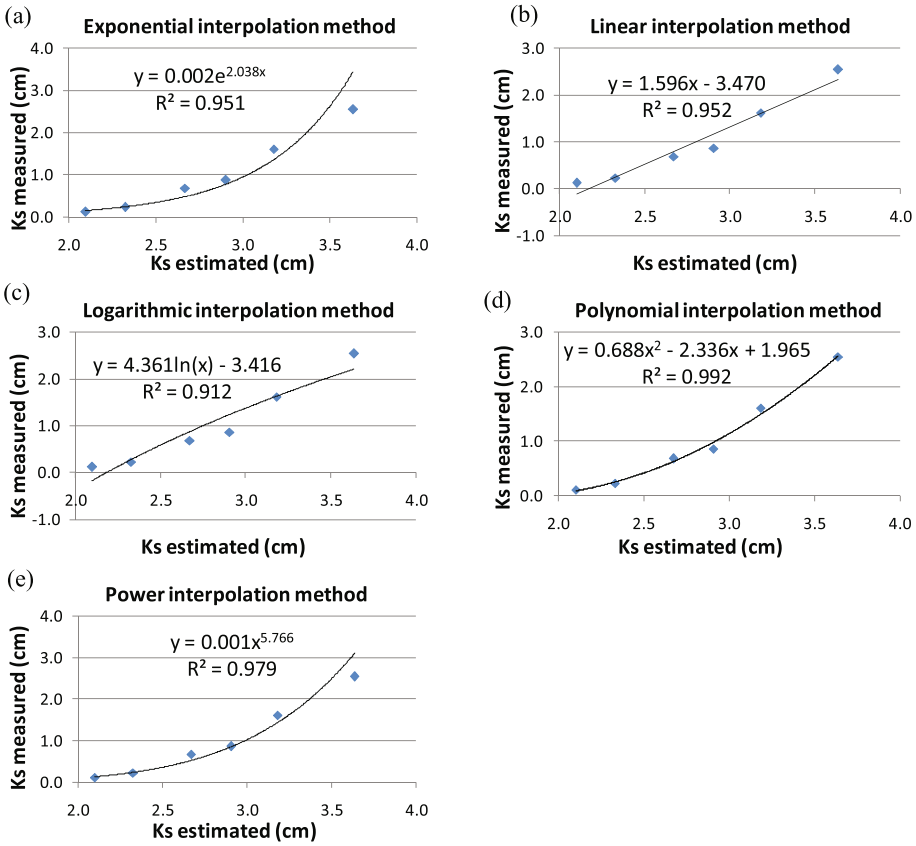

Fig. 4. Interpolation methods for calculating calibration function.

sites TT1, TT2, TT3, TT4, TT5 in Thai Thuy are presented in Table 4. It is obviously seen that the residuals of *ks* calibrated by the polynomial interpolation method are double less than residuals of *ks* calibrated by the power interpolation method. In addition, the RMS errors of the polynomial and the power function are 0.09 cm and 0.34 cm respectively. Consequently, the calibration using polynomial function produces the higher accuracy than the other functions. It can be concluded that the accuracy of *ks* estimated from Sentinel-1A in the study area is 0.09 cm. The general method applied for this study is suitable for the context of semi-empirical method. The *ks* calibrated by polynomial function is used to estimate soil moisture.

4.3 The Correlation Between Surface Parameters and Backscatter Coefficients

Figure 5 illustrates the correlations between surface parameters and backscattering coefficients of SAR data acquired on 15th July 2015 along 2 km long of the cross section in Giao Thuy (line AB in Fig. 2). It is clearly seen that both estimated *ks* and *ks*

Table 4. Comparison of calibrated *ks* using power function and polynomial (poly) function with the measured *ks* in Thai Thuy.

Pixels	TT1		TT2		TT3		TT4		TT5	
	ks (cm) poly	*ks* (cm) power	*ks* (cm) poly	*ks* (cm) power	*ks* (cm) poly	*ks* (cm) power	*ks* (cm) poly	*ks* (cm) power	*ks* (cm) poly	*ks* (cm) power
1	0.67	0.31	0.42	0.19	0.55	0.25	0.48	0.22	0.67	0.31
2	0.92	0.44	0.54	0.25	0.50	0.23	0.55	0.26	0.52	0.24
3	0.91	0.43	0.72	0.33	0.37	0.17	0.56	0.27	0.49	0.22
4	0.95	0.45	0.85	0.40	0.50	0.23	0.79	0.37	0.46	0.21
5	0.74	0.34	0.49	0.23	0.38	0.18	0.70	0.32	0.57	0.26
6	0.71	0.33	0.58	0.27	0.45	0.26	0.83	0.39	0.47	0.22
7	0.60	0.27	0.48	0.22	0.48	0.22	0.48	0.22	0.59	0.27
8	0.69	0.31	0.49	0.22	0.58	0.26	0.63	0.23	0.45	0.21
9	0.75	0.34	0.56	0.26	0.46	0.21	0.52	0.24	0.53	0.24
Average	0.77	0.36	0.57	0.26	0.47	0.22	0.62	0.28	0.53	0.24
Measured *ks*	0.71		0.61		0.54		0.50		0.65	
Residual	−0.06	0.35	0.04	0.35	0.07	0.32	−0.12	0.22	0.12	0.41
Polynomial RMS error: 0.09					Power RMS error: 0.34					

after applying calibration function (Fig. 5a, b) are relatively weakly correlated with the backscattering coefficients of vertical-horizontal (VH) polarization. The R-squares in this case are 0.002 and 0.017 corresponding to the estimated *ks* and the calibrated *ks*. Similarly the *ks*, the correlation between soil moisture (m_v) and VH polarization is insignificant with 0.039 R-square (Fig. 5c). In contrast, the VV polarization has the good agreement to the estimated *ks* (0.768 R-square) and more correlative to the calibrated *ks* with 0.790 R-square (Fig. 5d, e). The calibrated *ks* gradually increases by 1.6 cm from 0.2 cm to 1.8 cm when the VV backscatter increases by 18 Db from −22 Db to −4 Db (Fig. 5e). Especially, the significant correlation is seen in the scatter plot of ratio VH/VV and calibrated *ks* with 0.992 R-square (Fig. 5h). This behavior is well agreement with the experiments of Oh [10] and Oh et al. [12]. The results of correlation assessment depict that the calibration function is well calculated in this study.

The estimated soil moisture is independent from VH polarization (0.039 R-square) but it relatively strongly depends on VV polarization with 0.521 R-square (Fig. 5f).

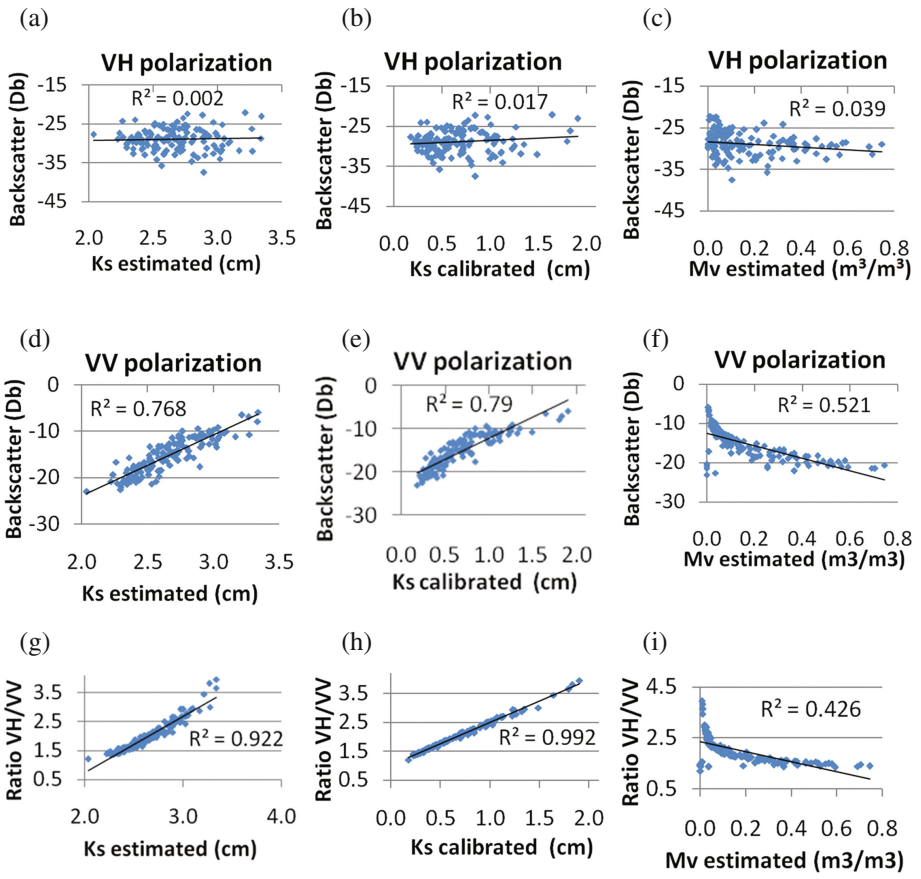

Fig. 5. Backscattering coefficients of VH, VV polarization and ratio VH/VV versus the estimated *ks*, calibrated *ks*, and m_v along cross section in Giao Thuy.

The role of VH in estimating m_v is represented through the ratio VH/VV. In the valid range of the Oh model ($0.01 < m_v < 0.35$ cm^3/cm^3), the correlation between m_v and VH/VV (0.672 R-square) is greater than that of m_v and VV (0.553 R-square) (in the whole range of m_v, R-squares of VV and VH/VV are 0.521 and 0.426, respectively in Fig. 5f, k). Figure 5k presents the relationship between estimated m_v and ratio VH/VV. The estimated m_v may not be accurate if outside the valid range. There is a sharply dropping of ratio VH/VV from 4 to 2.25 in the range of m_v from 0 to 0.01 cm^3/cm^3. Soil moisture increases from 0.01 to 0.35 cm^3/cm^3, the ratio VH/VV gradually reduces from 2.25 to 0.79. This decrease scale of VH/VV corresponds to the gradual decrease of about −7 Db of VV backscatter. In case m_v is greater than 0.35 cm^3/cm^3, the variations of both ratio VH/VV and VV backscatter are negligible. The behavior of m_v with the ratio VH/VV in this study relatively agrees with results of Oh [10] and Holah et al. [36] who believed that the cross-polarized ratio VH/VV have weak dependence on soil moisture.

In other case study, Wang et al. [33] applied modeled cross-polarization q and co-polarization p to estimate surface parameters but the good results were obtained in only a small percentage of pixels of a large area. For this study area, the correlations between surface parameters and backscattering coefficients are investigated in a location far from the position of calibrated field data to test the confidence of the method. Kim Son is located 70 km far southward from of Giao Thuy. The testing area in Kim Son is a tidal flat connecting a sandbar in front of Day river mouth. The correlations between surface parameters and backscattering coefficients in Kim Son are presented in Fig. 6. It is clear that the correlations of calibrated *ks*, m_v with ratio VH/VV are similar to the relations of that in Giao Thuy. The very high correlation (0.995 R-square) between calibrated *ks* and ratio VH/VV proves that the application of this method produces good results for not only in the field measurement site but also in the whole of the extent of the SAR data in use. However, the correlation between soil moisture and ratio VH/VV in Kim Son is lower than that in Giao Thuy. Several pixels (11 in total 159 pixels of cross section in Kim Son) are out of the general trend of correlative curve (Fig. 6b). These pixels appear on the top of the sandbar and can be counted as random errors. In overall, the estimated soil moisture in the valid range of the Oh method ($0.01 < m_v < 0.35$ cm^3/cm^3) is good achievement in all scene of Sentinel image.

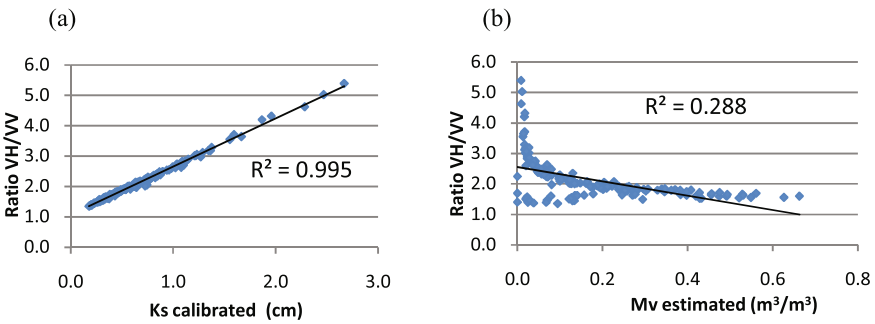

Fig. 6. Ratio VH/VV versus calibrated *ks* and m_v along cross section in Kim Son

4.4 The Comparison of Surface Parameters Estimated on Two SAR Images

In the whole steps of estimating surface parameters in this study, the lowest confidence is the application of the same calibration function for both SAR images which acquired on 15th July (summer) and on 27th December (winter). Two Sentinel-1A SAR images overlay each other in the extent of about 100 km along the coast from Hai Hau to Cam Pha. In order to assess the capacity of using one calibration function for both images, *ks* and m_v profiles along Giao Thuy cross section estimated on 2 SAR images are extracted for comparison (Fig. 7) (Giao Thuy is the middle of overlaid area). The vertical roughness estimated on two SAR images relatively agrees with each other in general. The highest residual is the area from pixel number 60 to 110 with an average *ks* difference of 0.5 cm, and the maximum of 0.96 cm (Fig. 7a). This area is surrounding a small creek in tidal flat so that it is highly dynamic of sediment transport due to the seasonal variation. Hence, the roughness is significantly different between two dates. The stable surface roughness is the area from pixel number 1 to 60. This area is shell fields where all the land parcels are separated with each other by net systems. The net keeps the stable surface and reducing the influences caused by the change of environment over time scale from July to December. Vertical roughness estimated on 2 SAR images in shell fields are relatively close to each other with the maximum residual less than 0.4 cm (an average of 0.11 cm). The differences between two SAR images are not only the acquisition time but also the flight directions (ascending of image on 15th July and descending of image on 27th December). At the same location, the backscatter is recorded in the different incident angle and opposite side. The radar look direction related to the periodic row direction strongly affects the radar cross section [37]. Moreover, the local acquisition time also contributes to the increase of the residuals. The SAR image acquired on 15th July was recorded at 5 h 50′ am when the influences of human activities on the surface roughness are less than that of image acquired at 5 h 57′ pm on 27th December.

Similarly to the case of *ks*, the m_v profiles (Fig. 7b) estimated on 2 SAR images in the shell fields are relatively close to each other. However, the area from pixel number 60 to 140 is a heterogeneous appearance. The ebb tide at the acquisition time of image in December remains the remnant water in tidal flat surface. The lower evaporation in winter (December) than that in July (summer) supports the higher moisture in tidal flat. Subsequently, the soil moisture estimated on SAR image acquired in December is much higher than that of SAR image acquired in July in this area. Consequently, the comparison results of *ks* and m_v estimated on 2 Sentinel-1A SAR images support the evidences to confirm the applicability of the same calibration function for both images. The application of the same calibration equation is a suitable solution in the case of lacking reference data.

4.5 Surface Roughness of Tidal Flats in the Study Area

The surface roughness estimated on 2 Sentinel-1A SAR images are merged to fully cover the tidal flats in the study area. The full surface roughness data are then stratified into 8 classes using Geometrical intervals algorithm (Fig. 8). This method defines the

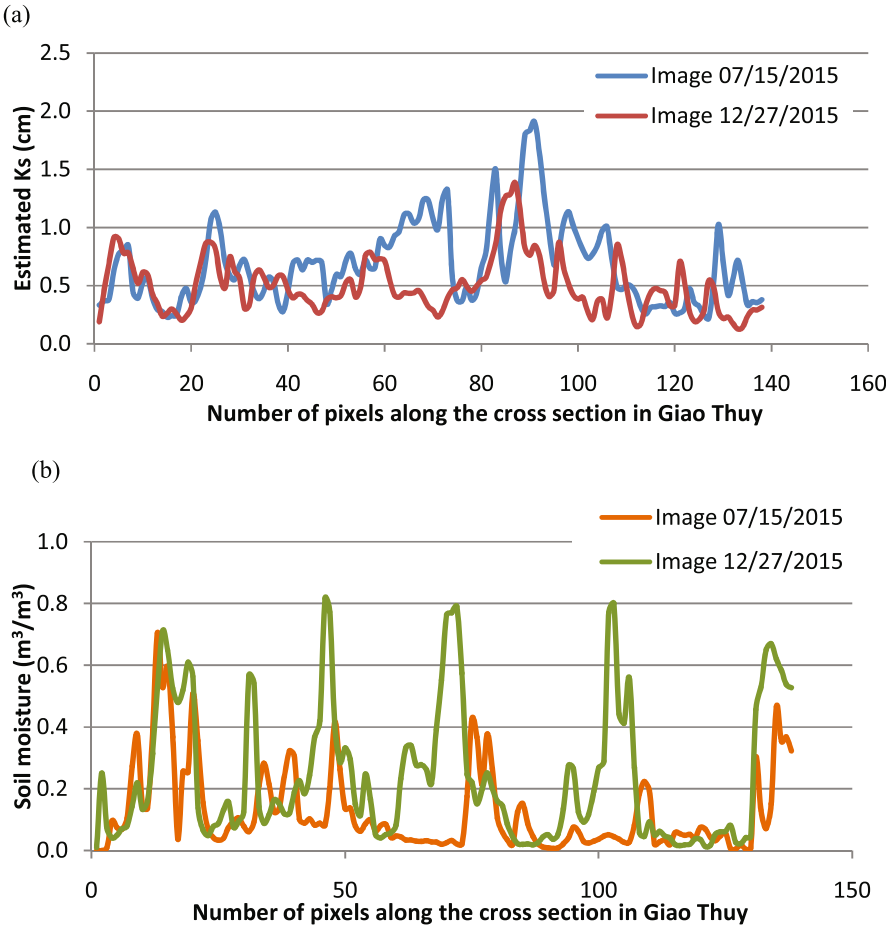

Fig. 7. (a) The comparison of *ks* and (b) m_v estimated on 2 SAR images along Giao Thuy cross section.

interval for each class by minimizing the square sum of the number of pixels in the class. It is ensured that each class range has approximately the same number of values with each class and that the change between intervals is fairly consistent. In all 8 roughness classes, the first 5 classes in the range of $0.01 < ks < 3.25$ cm are estimated in best accurate [10]. The *ks* class number 6th in the ranger of 3.25–8.24 cm distributes as small groups at the top of sandbars in front of river mouths (tiny area in light orange color in Kim Son (Fig. 8). The class 6th appears only in the South of the study area from Kim Son to Do Son where the highest influence of wind and waves. Another 2 classes (class 7th, 8th) are rarely seen in the study area, they appear in some scattering pixels and may ignore in statistic. The first class is the smallest *ks* in the range of 0.01 −0.28 cm that the vertical roughness "s" (with C band) is 0.008−0.24 cm respectively. In this range of RMS high, the nature surface of tidal flats is possible to occur in

2 cases. Firstly, SAR images are acquired with the incident angle from 31.1–42.9° that the smooth surface is defined as RMS high less than 0.23 cm for C band [37]. Consequently, the first class of *ks* is the smooth surface. The other case, this class may be covered by remnant water. Because the penetration depth of the microwave C band is the maximum of around 2 cm deep in seawater at 20 °C [23] so that the insignificant backscatter causes the confusion between very low roughness and shallow remnant water. In both cases, the backscattering electromagnetic is very weak, even negligible due to the specular reflectance of smooth surface or absorption of seawater. It is true that it is impossible to discriminate the smooth surface or remnant water on the tidal flat surface in the study area. In overview, there is a gradual decrease of surface roughness following the direction from south to north. In the South, sediments from Red river system and Thai Binh river system concentrate in tidal flats with the mixture of sandy particles and fine particles [38]. If the ratio of sand and mud approaches approximately to 1, the wavy bedding tends to be created [1]. In addition, water flow in wave motion makes sediment ripples with generally symmetrical cross section [39]. Thus, the roughness is relatively high in the tidal flats in the southern coast and the *ks* classes are clearly discriminated with each other (Fig. 8, block A, B, C). Tidal flats in the north of the study area are uniquely formed by sands (more than 45% is coarse sand in Hai Ha) [38]. Surface roughness in the north is the intermixture of classes thus it is hard to define the boundaries between classes (Hai Ha, Mong Cai in Fig. 8, block E). The intermixture of roughness classes is caused by the modification of natural surface in tidal flats due to the human activities. In Hai Ha, the exposure tidal flat is dug to collect

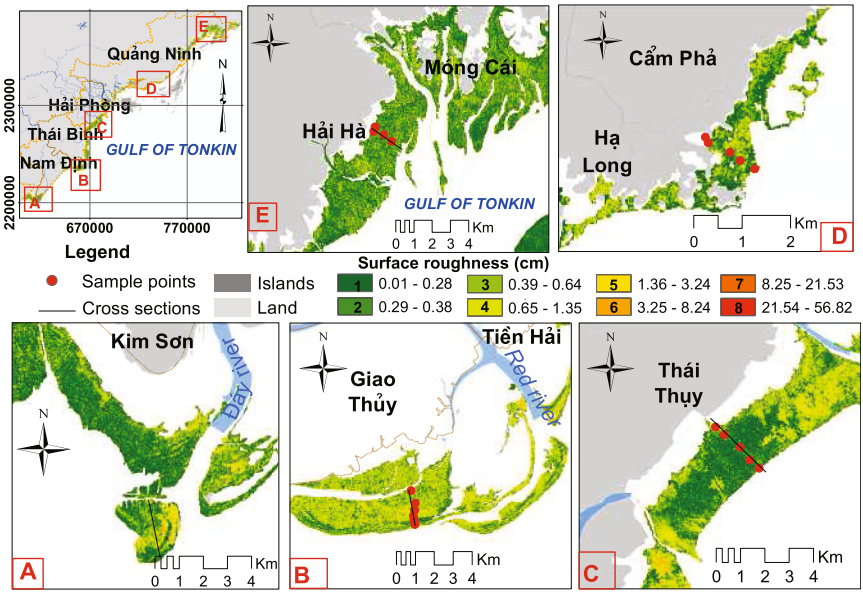

Fig. 8. Map of surface roughness of tidal flats estimated from Sentinel-1A SAR image acquired in 2015

benthos by local people. The digging activities create holes with full water and sandy mounds in random location. These activities disturb the natural form of tidal flat surface. The new mounds are formed in 30 cm diameter, 15 cm high and then they are gradually lower and enlarger after time. Because of the insignificant wave motions, the holes and sandy mounds are usually kept over several tide cycles. One hand, this disturbed surface decreases the accuracy of estimating surface roughness. In the other hand, it causes the intermixture of classes of surface parameters. Figure 9a, b illustrates the tidal flat surface in Giao Thuy (the south of the study area) and disturbed tidal flat in Hai Ha (the northern part of the study area). The roughness in the study area is the results of the synthesis impacts of natural factors and human activities.

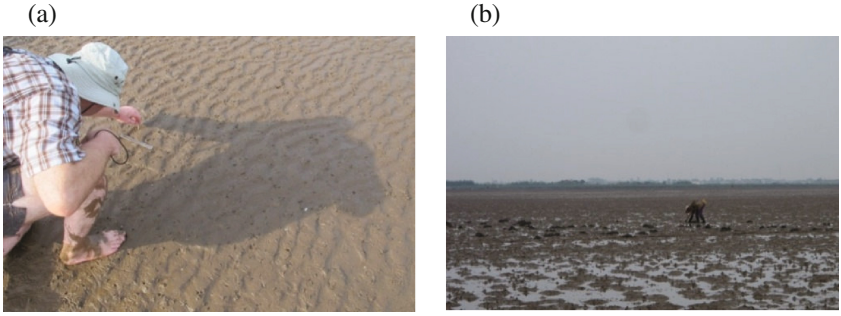

Fig. 9. (a) Natural tidal flat surface in Giao Thuy and (b) disturbed tidal flat due to human activities in Hai Ha

4.6 Soil Moisture of Tidal Flats in the Study Area

Soil moisture of tidal flats in the study area is classified into 6 classes using geometric intervals method. The map of soil moisture is presented in Fig. 11. In the overview, the driest class with the range of 0–0.07 m^3/m^3 is highlighted in light red. This class is distributed on the top of sandbars or on the highest area of tidal flats. Similarly to the distribution of roughness classes, the driest classes gather in the southern part of the study area (Kim Son, Giao Thuy, Thai Thuy in Fig. 11 block A, B, C), but they scatter in small groups in the northern part (Cam Pha, Hai Ha in Fig. 11, block D, E). Four moisture classes from 0.08 to 0.4 m^3/m^3 are intermixed and scattered distribution all over the tidal flats. These classes are clearly recognized in the map as the transition area between the driest and wettest classes. The highest soil moisture (class 6th) is defined with m_v greater than 0.4 m^3/m^3 indicated in sea blue. This layer is obviously discriminated with other classes by homogeneous segments in the southern part of the study area. However, the class 6th interposes with the other classes in the northern coast. Although the highest soil moisture is out of the valid range (0.01–0.35 m^3/m^3) of the Oh model but it needs to be understood as the lowest accuracy comparing with other classes. However, the class with $m_v > 0.4$ m^3/m^3 well correlates with the morphology of tidal flats in the southern part of the study area. The tidal flats in the southern area are formed in the highly influence of wind, waves along with the mixture

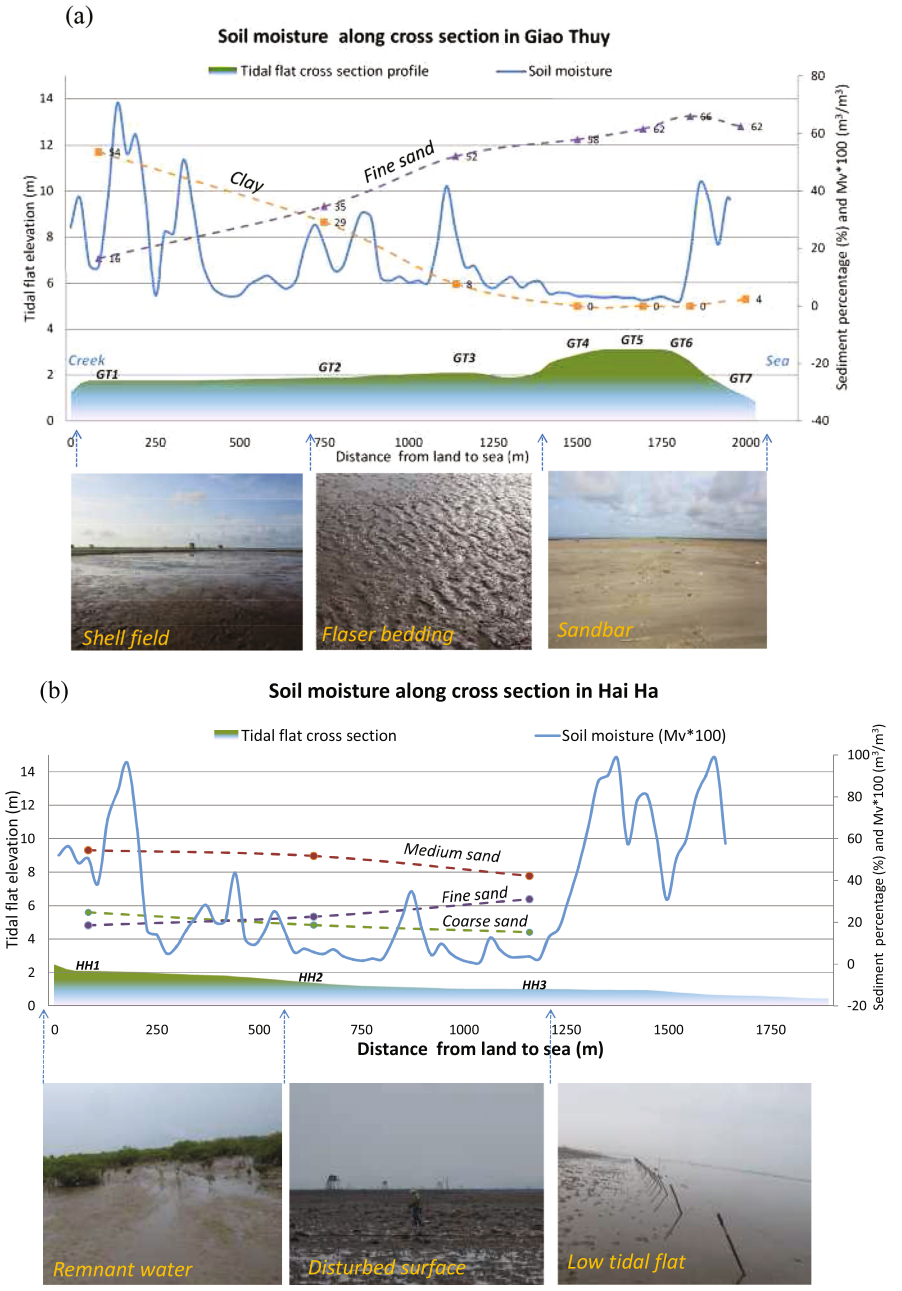

Fig. 10. Correlation between soil moisture, tidal flat morphology, and sediment grain size in (a) Giao Thuy and (b) Hai Ha.

of sand and mud [38]. Thus, along the cross section, the elevation transition consists of a high sandbar, and then passes an extremely low flat surface. The discrete morphology is the main reason which causes the clear distinction between low moisture layer and higher soil moisture layers. On the other side, the tidal flats in the north are characterized by simple morphology (open coast tidal flats), only sandy sediment concentration (in Hai Ha), random distribution of water remnant, and the surface is disturbed by human activities. These conditions cause the intermixture between classes of soil moisture in the north of the study area.

Figure 10a,b illustrates the correlation between soil moisture, sediment type, and tidal flat elevation along the cross sections in Giao Thuy and Hai Ha. The left axis of the scatter plot indicates the elevation of tidal flat. The right axis is the percentage of sediment types, and also the soil moisture (m_v *100) in cm^3/cm^3 unit. Elevation data are extracted from Digital Elevation Model (DEM) of tidal flats which is built in previous study [40]. In Giao Thuy, the surface of tidal flats is generally higher than 1.4 m that lengthens the exposure time and dries surface than tidal flats in other locations (Fig. 11). The amount of water content in surface layer of tidal flat in Giao Thuy (Fig. 10a) is separated in different levels. The highest soil moisture (up to 0.7 cm^3/cm^3) is around GT1 which contains the highest percentage of clay (54%). In contrast, the area on sandbar (field points GT5, GT6) is lowest moisture which corresponds to the highest percentage of sand (66%). Generally, the reduction of soil moisture from GT1 to GT6 well correlates with the gradual decrease of clay but negative correlation with sandy particle content in tidal flat. This correlation of soil moisture and sediment sizes

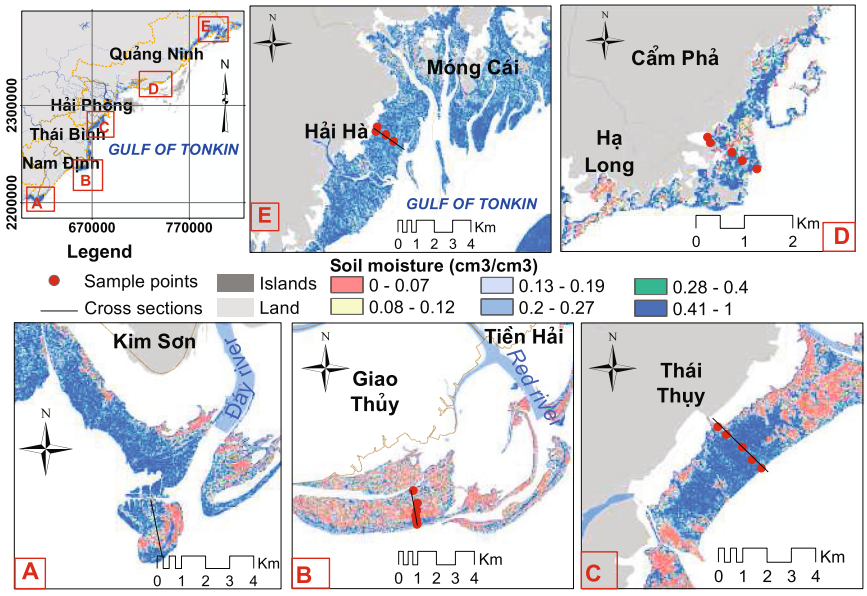

Fig. 11. Soil moisture map of tidal flats estimated from Sentinel-1A SAR image acquired in 2015

well agrees with reports of Deroin [22]. In addition, Van der Wal et al. [9] denoted that high moisture content is associated with finer sediments then smoother surface and negative correlation with backscatter. In the mid area from GT2 to GT3, soil moisture is relatively high because the surface tends to form the Flaser bedding (Fig. 10a). This type of surface structure is constituted since the ratio of sand/mud greater than one [1]. The Flaser bedding is characterized by small, hollow holes with similar distance between each other in the flat surface. During water saturation in tidal flats, saline water fills up these holes and increases the soil moisture estimated on SAR data. Tidal flats in Hai Ha (Fig. 10b) are fed only by sandy sediments. The area from HH1 to HH3 is in range of middle tidal flat, further seaward than HH3 is the area of low tidal flats. Thus, it is clear that the soil moisture is highest in low tidal flat. The area surrounding HH1 is on the high part of tidal flat but the moisture is extremely high with up to 0.9 m^3/m^3. This unusual behavior can be explained by remnant water. High tidal flat zone in Hai Ha is covered by mangrove forest which stores water and little by little spreads to the sandy surface even when tidal flat has fully exposed to the air. Soil moisture in the mid part of cross section (distance from 250 m to 1200 m) is in the valid range of the Oh model (0.01–0.35 m^3/m^3) corresponding to disturbed area of tidal flat.

Soil moisture is successfully estimated in this study using SAR data and Oh model. However, the fact that it is difficult to assess the accuracy of estimated soil moisture due to the very quickly change of tidal flat environments. This study is not an exception because of lacking reference data, but there is a good correlation between estimated soil moisture and sediment distribution, and real conditions of tidal flats in the study area.

5 Conclusions

This study successfully applies the Oh inversion model version 2004 to estimate vertical surface roughness and soil moisture of tidal flats in the northern coast of Vietnam. Two Sentinel-1A SAR L1 SLC images are acquired and preprocessed to yield backscattering coefficients of VV and VH polarizations of C band. In the case of lacking co-polarization data (HH) for fully applying the inversion model, one part of the Oh inversion model has been used. The roughness parameter estimated from cross-polarization backscatter is compared with the field measured roughness to calculate the calibration function. The calibrated roughness produces a good agreement with the other series of field data in Thai Thuy. The surface roughness after calibration gives the accuracy of 0.09 cm. The use of the same calibration function for two SAR images which acquired 5 month difference is the lowest confidence step of the method. However, the comparison results between roughness parameter estimated on 2 images after calibration support well agreement in the stable surface in shell field area in Giao Thuy.

The study denotes that the roughness classes in the range 0.01–0.35 cm are clearly discriminated with other classes in the southern part of the study area. The roughness classes in the range of greater than 0.35 cm appear scattered in the top of sandbars. Tidal flats in the northern part present an intermixture of roughness layers due to the human activities. The correlation of soil moisture with the sediment sizes and morphology of tidal flats in Giao Thuy and Hai Ha is analyzed in this study. The moisture

of tidal flats is positively correlated with the fine sediment content (clay) but negative correlation with the sandy sediments. High moisture in the center of tidal flat in Giao Thuy are caused by the water remnant at the surface due to the Flaser bedding which develops in the higher amount of sand content than mud in the mixed grain size environment. The sandy sediment close to land is higher moisture than the middle area of tidal flat since the water spreading from mangrove forest is seen in Hai Ha. Consequently, although the surface parameters are successfully estimated from SAR images, but as a true that it is difficult to map soil moisture content from radar data with high accuracy [17]. In this study, the soil moisture estimated from Sentinel-1A SAR images shows the correlation with real conditions and good agreement with the reports of other studies. This is the first time the surface roughness and soil moisture of tidal flats are successfully estimated on SAR data in the study area. Even until now, report about application of the Oh model for estimating surface parameters of tidal flat using Sentinel-1 SAR image has not been found yet in literatures.

Acknowledgement. This study is implemented in GEGENAA laboratory, funded by the cooperation between University of Science and Technology Ha Noi, Vietnam and Université de Reims Champagne-Ardenne, France. We express heartfelt thanks to these valuable supports. We also many thank to Space Technology Institute, VAST has trained us the advantage experiences in processing satellite images.

References

1. Klein, G.d.V.: Intertidal flats and intertidal sand bodies. In: Coastal Sedimentary Environments, pp. 187–224 (1985)
2. Jackson, J.A., Bates, R.L.: Glossary of Geology. American Geological Institute (1997)
3. MacKinnon, J., Verkuil, Y.I., Murray, N.: IUCN situation analysis on East and Southeast Asian intertidal habitats, with particular reference to the Yellow Sea (including the Bohai Sea). In: Occasional Paper of the IUCN Species Survival Commission, No. 47, 70 (2012)
4. Park, S.-E., Moon, W.M., Kim, D.-j.: Estimation of surface roughness parameter in intertidal mudflat using airborne polarimetric SAR Data. IEEE Trans. Geosci. Remote Sens. **47**, 1022–1031 (2009)
5. Barrett, B.W., Dwyer, E., Whelan, P.: Soil moisture retrieval from active spaceborne microwave observations: an evaluation of current techniques. Remote Sens. **1**, 210–242 (2009)
6. Cracknell, A.P.: Remote sensing techniques in estuaries and coastal zones an update. Int. J. Remote Sens. **20**, 486–496 (1999)
7. Deroin, J.-P., Shimada, M.: The importance of local mean time in remote sensing for mapping megatidal zones. C. R. Geosci. **342**, 11–18 (2010)
8. Fung, A.K.: Microwave scattering and emission models and their applications. Artech House (1994)
9. Van der Wal, D., Herman, P.M.J., van den Dool, A.W.: Characterisation of surface roughness and sediment texture of intertidal flats using ERS SAR imagery. Remote Sens. Environ. **98**, 96–109 (2005)
10. Oh, Y.: Quantitative retrieval of soil moisture content and surface roughness from multipolarized radar observations of bare soil surfaces. Trans. Geosci. Remote Sens. **42**, 596–601 (2004)

11. Dubois, P.C., Zyl, J.V., Engman, T.: Measuring soil moisture with imaging radars. Geosci. Remote Sens. **33**, 915–926 (1995)
12. Oh, Y., Sarabandi, K., Ulaby, F.T.: An empirical model and an inversion technique for radar scattering from bare soil surfaces. Trans. Geosci. Remote Sens. **30**, 370–381 (1992)
13. Zribi, M., Dechambre, M.: A new empirical model to retrieve soil moisture and roughness from C-band radar data. Remote Sens. Environ. **84**, 42–52 (2003)
14. Rakotoarivony, L., Taconet, O., Vidal-Madjar, D., Bellemain, P., Benallègue, M.: Radar backscattering over agricultural bare soils. J. Electromagn. Waves Appl. **10**, 187–209 (1996)
15. Davidson, M.W.J., Toan, T.L., Mattia, F., Satalino, G., Manninen, T., Borgeaud, M.: On the characterization of agricultural soil roughness for radar remote sensing studies. Trans. Geosci. Remote Sens. **38**, 630–640 (2000)
16. Baghdadi, N., King, C., Bourguignon, A., Remond, A.: Potential of ERS and Radarsat data for surface roughness monitoring over bare agricultural fields: application to catchments in Northern France. Remore Sens. **23**, 3427–3442 (2002)
17. Baghdadi, N., Cerdan, O., Zribi, M., Auzet, V., Darboux, F., El Hajj, M., Kheir, R.B.: Operational performance of current synthetic aperture radar sensors in mapping soil surface characteristics in agricultural environments: application to hydrological and erosion modelling. Hydrol. Process. **22**, 9–20 (2008)
18. Schuler, D.L., Lee, J.-S., Kasilingam, D.: Surface roughness and slope measurements using polarimetric SAR data. IEEE Trans. Geosci. Remote Sens. **40**, 687–698 (2002)
19. Genisab, A., Vulfson, L., Blumberga, D.G., Sprinstinad, M., Kotlyarc, A., Freilikherc, V., Ben-Asherabd, J.: Retrieving parameters of bare soil surface roughness and soil water content under arid environment from ERS-1, -2 SAR data. Int. J. Remote Sens. **34**, 6202–6215 (2013)
20. Collingwood, A., Treitz, P., Charbonneau, F.: Surface roughness estimation from RADARSAT-2 data in a high arctic environment. Int. J. Appl. Earth Obs. Geoinf. **27**, 70–80 (2014)
21. Deroin, J.-P., Djemai, S., Bendaoud, A., Brahmi, B., Ouzegane, K., Kienast, J.-R.: Integrating geologic and satellite radar data for mapping dome-and-basin patterns in the In Ouzzal Terrane, Western Hoggar. Algeria. J. African Earth Sci. **99**, 652–665 (2014)
22. Deroin, J.-P.: Combining ALOS and ERS-2 SAR data for the characterization of tidal flats. Case study from the Baie des Veys, Normandy, France. Int. J. Appl. Earth Obs. Geoinf. **18**, 183–194 (2012)
23. Ulaby, F.T., Moore, R.K., Fung, A.K.: Microwave remote sensing active and passive: from theory to applications. Artech House Inc., US (1986)
24. Gade, M., Alpers, W., Melsheimer, C., Tanck, G.: Classification of sediments on exposed tidal flats in the german bight using multi-frequency radar data. Remote Sens. Environ. **112**, 1603–1613 (2008)
25. Kim, D.-J., Choe, B.-H., Moon, W.M.: Remote sensing of oyster reefs and groundwater discharge in coastal area using synthetic aperture radar. IGARSS **13**, 2435–2438 (2013)
26. Reineck, H.E., Singh, I.B.: Depositional Sedimentary Environments. Springer, Berlin Heidelberg (1980)
27. Hoa, M.H.: Morphological dynamics estuary of the delta in north Vietnam serves rational use of natural resources and environment in estuary area. Faculty of Geography, vol. Doctor, pp. 147. Ha Noi University of Science, Vietnam National University, Ha Noi (2001)
28. Oh, Y., Sarabandi, K., Ulaby, F.T.: Semi-empirical model of the ensemble-averaged differential mueller matrix for microwave backscattering from bare soil surfaces. Trans. Geosci. Remote Sens. **40**, 1348–1355 (2002)
29. Fung, A.K., Chen, K.S.: An update on the IEM surface backscattering model. IEEE Geosci. Remote Sens. Lett. **1**, 75–77 (2004)

30. Mattia, F., Davidson, M.W.J., Toan, T.L., D'Haese, C.M.F., Verhoest, N.E.C., Gatti, A.M., Borgeaud, M.: A comparison between soil roughness statistics used in surface scattering models derived from mechanical and laser profilers. IEEE Trans. Geosci. Remote Sens. **41**, 1659–1671 (2003)
31. Verhoest, N.E.C., Lievens, H., Wagner, W., Álvarez-Mozos, J., Moran, M.S., Mattia, F.: On the soil roughness parameterization problem in soil moisture retrieval of bare surfaces from synthetic aperture radar. Sensors **8**, 4213–4248 (2008)
32. Zhixiong, L., Nan, C., Perdok, U.D., Hoogmoed, W.B.: Characterisation of soil profile roughness. Biosys. Eng. **91**, 369–377 (2005)
33. Wang, J.R., Hsu, A., Shi, J.C., O'Neill, P.E., Engman, E.T.: A comparison of soil moisture retrieval models using SIR-C measurements over the Little Washita River watershed. Remote Sens. Environ. **59**, 308–320 (1997)
34. Panciera, R., Mihai, A.T., Kim, L., Jeffrey, P.W.: Evaluation of IEM, dubois, and oh radar backscatter models using airborne L-band SAR. IEEE Trans. Geosci. Remote Sens. **52**, 4966–4979 (2014)
35. Topp, G.C., Davis, J.L., Annan, A.P.: Electromagnetic determination of soil water content: measurements in coaxial transmission lines. Water Resour. **16**, 574–582 (1980)
36. Holah, N., Baghdadi, N., Zribi, M., Bruand, A., King, C.: Potential of ASAR/ENVISAT for the characterization of soil surface parameters over bare agricultural fields. Remote Sens. Environ. **96**, 78–86 (2005)
37. Ulaby, F.T., Moore, R.K., Fung, A.K.: Microwave remote sensing: active and passive. In: Radar Remote Sensing and Surface Scattering and Emission Theory, vol. 2, pp. 624. NASA (1982)
38. Nguyen, V.C.: Tidal flats in the northern coast of Vietnam. Vietnam Academy of Science and Technology (2006)
39. White, K.H., Hesham, M.E.-A.: Monitoring changing position of coastlines using Thematic Mapper imagery, an example from the Nile Delta. Geomorphology **29**, 93–105 (1999)
40. Tong, S.S.: Mapping tidal flats in Vietnam using Remote sensing techniques. Doctoral School in Science, Technology, Health (547), vol. Doctor, pp. 295. University of Reim Champagne Ardenne, Reims, France (2016)

Reconstruction of Missing Imagery Data Caused by Cloudcover Based on Beyesian Neural Network and Multitemporal Images

Hien Phu La(✉) and Minh Quang Nguyen

Faculty of Geomatics and Land Administration,
Hanoi University of Mining and Geology, Hanoi, Vietnam
hien.phu.la@gmail.com

Abstract. One of passive sensor's limitations is its high sensitivity to weather condition during image acquiring process. Consequently, the image is often affected by cloud cover. This phenomenon severely influences the completeness of land use/cover obtained from optical satellite imagery and make image processing more complicatedly. However, the pattern of pixel values based on the season and weather changes determined from substantial remote sensing data within a region can help to reconstruct the imagery data which was missed due to the presence of clouds. Taking advantage of datasets containing a substantial amount of multitemporal images, this study proposed a method to reconstruct missed imagery data caused by cloud cover based on relationship between air temperature, humidity, visibility, rainfall, normalized difference vegetation index, direct solar radiation, diffuse solar radiation, reflected radiation and spectral radiance of each pixel obtained by Beyesian Neural Network. The proposed method was applied to generate a cloud-free Landsat image. The results showed that pixels generated by the proposed algorithm are very similar to the actual pixels, especially in non-change area with percentage of correlation coefficients (R) over 0.99 is approximate to 91%. However, the similarity reduced in areas which changed significantly over time period, with the percentages of R over 0.99 are about 78%.

Keywords: Beyesian neural network · Cloud-free image generation · Landsat image

1 Introduction

One disadvantage of a passive remote-sensing and optical sensor is its high sensitivity to weather conditions during data acquiring process. That means the weather events such as cloud cover and fog are big problems and compromise the usability of optical remote sensing and make the image processing more complicated [1]. To overcome those problems, the pattern of pixel values determined from substantial remote sensing data within a region can aid the reconstruction of data that is contaminated on account of the presence of clouds [2, 3].

Scientific research has been done on the detection and removal of clouds and their shadows from remote sensing images acquired by various sensors [4–8]. One of

© Springer International Publishing AG 2018
D. Tien Bui et al. (eds.), *Advances and Applications in Geospatial Technology and Earth Resources*, https://doi.org/10.1007/978-3-319-68240-2_6

common approaches for cloud removal is to generate composite image by selecting non-cloud pixels from satellite image time series [4, 6, 7, 9]. However, a drawback of multi-temporal image composition is residual in cloud-contaminated regions, since some types of landcover may rapidly change over time period [10]. Other method was based on regression trees to predict pixel values underneath clouds and cloud shadows in reference scenes from other scene dates [11]. However, in [11] the regression tree model only considers DN value of image, other parameters such as weather parameters, solar radiation which affect spectral radiance measured by satellite sensor are not taken into account.

In recent years, the US Geological Survey (USGS) provides a huge number of free satellite imagery online. As a result, many studies have shown the interest of utilizing multi-temporal satellite images [12–14]. [2] used multitemporal Landsat images to reconstruct imagery data covered by cloud based on local spectro-temporal relationships between considered image and reference images based on contextual prediction process. This contextual prediction process was implemented by linear predictors or by single non-linear prediction based on the support vector machines (SVM) [2]. [13] also took advantages of Landsat image time series to remove cloudy portions of an image and then reconstructed missing imagery data by cloning information from a set of reference images based on temporal correlation [13]. To obtain the temporal correlation, both of these methods used information in the neighborhood of the cloudy area, which may not always represent the information covered by cloud, especially in rapid change areas or heterogeneous regions [2, 13]. [3] used a large number of Landsat images to simulate an image acquired on a certain date by apply multi-linear regression between spectral radiance and eight parameters including air temperature, humidity, visibility, rainfall, Normalized Difference Vegetation Index (NDVI), direct solar radiation, diffuse solar radiation, reflected radiation. This prediction model does not depend on information around the predicted pixels [3]. However, this multi-linear regression may not fit the pattern well, a non-linear function could be considered to improve the prediction [3]. Unfortunately, estimating parameters of a non-linear model is not a trivial task. One solution for this problem is to replace the non-linear function by an Artificial Neural Network (ANN), which has been proved to be an efficient technique to approximate a non-linear function [15–17], but has been rarely used in reconstructing imagery data covered by cloud. Among the learning functions of neural networks, back-propagation algorithm has been used very popularly. However, Bayesian learning can provide more optimal and robust approximations [18].

Therefore, this study attempted to investigate potential application of Bayesian Neural Network (BNN) in retrieving pixel values underneath clouds by taking advantage of available dataset containing large amount of multi-date Landsat images to reconstruct missed data covered by cloud. To achieve this, BNN was used to model the relationship between eight variables including: air temperature, humidity, visibility, rainfall, NDVI, direct solar radiation, diffuse solar radiation, reflected radiation and spectral radiance of each pixel. The fitted model was used to predict values of the pixels covered by cloud. The cloud-free composite image was compared to actual image for quality assessment.

2 Study Site and Data

A 18 km × 18 km area partly covering Iksan and Gimje in the Republic of Korea, which is approximately 180 km south of Seoul (see Fig. 1), was chosen to test the proposed method. Agricultural fields occupy most of the study area; however, it additionally includes a few high-rise residential areas and some public and commercial buildings, and is partly covered by forest areas. This area was selected because of the availability of quality Landsat images covering the area and the available meteorological data. There are two meteorological ground stations (indicated by red triangles in Fig. 1) close to the area, from which we can obtain details meteorological data. Furthermore, it is a developing region covered by various landcover types, which means that the landcover can changes significantly, so that the ability of the proposed method can be explored.

Korea has four very distinct seasons: spring, which is from March to the end of May; summer, which is from June through August; autumn, which is from September through November; and winter, which is from December to the end of February [19]. Spring begins with the sprouting of various species of trees and the first crops of strawberries. Summer is relatively hot and humid and may feature clouds and frequent rainfall for one to three weeks. In autumn, as the season progresses, the leaves change

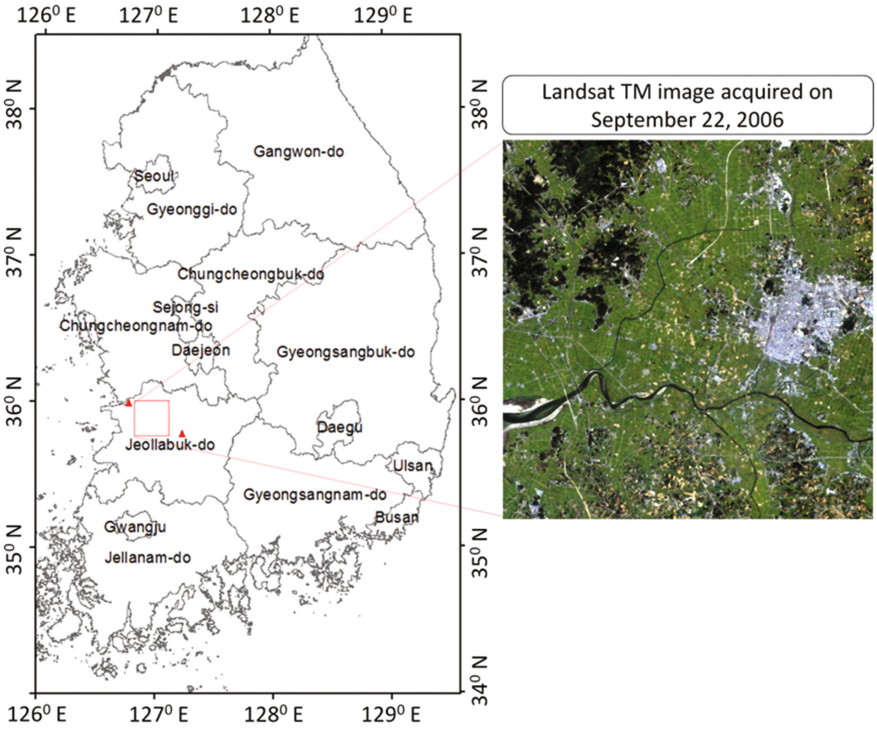

Fig. 1. Study area and Landsat image acquired on September 22, 2006.

colors and harvesting begins. Winter is generally cold and dry, and snow typically occurs in December and January. Therefore, to reconstruct missing data on a sub-Landsat image acquired on September 22, 2006, a dataset of 25 Landsat images acquired from May to November of 1994 to 2016 was used. Nineteen Landsat 5 Thematic Mapper (TM) images, three Landsat 7 Enhanced Thematic Mapper Plus (ETM+) images, three Landsat 8 images, and ASTER Global DEM (GDEM) were freely obtained from the USGS (http://earthexplorer.usgs.gov/). All of these images have spatial resolution of 30 m. Along with this dataset, meteorological data (i.e., air temperature, humidity, rainfall, and visibility) at two ground stations near the study area were collected from the Korean Meteorological Administration (KMA) (http://www.kma.go.kr). For each parameter, value measured by the two stations on acquisition time was averaged.

3 Methodology

3.1 Background of Bayesian Neural Network

A BNN is a kind of ANN with a prior distribution in its weights [20]. An ANN is a computational model based on the structure and functions of human brain. It is able to learn from information that flows through the network, then generalization and prediction can be performed [17]. After "learning" the ANN can provide the unknown relation f between the input vectors $X = [X_{i1}, X_{i2}, \ldots, X_{ip}]$ and the output vector $Y = [Y_{i1}, Y_{i2}, \ldots, Y_{iq}]$ as Eq. (1) [17]:

$$Y = f(X). \tag{1}$$

BNN was developed based on Bayes' theorem [20]. Generally, the training step is aimed at reducing the sum squared error of the model output and target value [18]. Hyper-parameter values can be automatically estimated, and the uncertainty ones can be marginalized based on the posterior distribution [21]. The posterior probability for the parameter α can be written according to Bayes' rules as Eq. (2) [22].

$$p(\alpha|D, M) = \frac{p(D|\alpha, M)p(\alpha|M)}{p(D|M)}. \tag{2}$$

where D is the data of the training set; M is the neural network model; $p(\alpha|\mathrm{D}, M)$ is the likelihood of the parameters; and $p(\alpha|M)$ is the prior probability of α; $p(D|M)$ is normalizing factor, which is also called evidence for the model M and can be expressed by Eq. (3) [22].

$$p(D|M) = \int_{\alpha} p(D|\alpha, M)p(\alpha|M)d\alpha. \tag{3}$$

Bayesian regularization generates a sequence of weights in the network parameter space in relation to the given data set and the network model. Then unnecessary linkage

weights are effectively reduced to zero. The network will calculate and train on the nontrivial weights, also known as the effective number of parameters, which will converge to a constant as the network grows [23]. Consequently, it can be optimized and can provide more optimal solution [18, 22].

3.2 Data Preprocessing

Several preprocessing steps were carried out before the data reconstruction takes place. USGS provides the Landsat imagery with digital number (DN). Therefore, radiometric calibration was conducted by using Eq. (4) to convert the DNs into spectral radiance [24].

$$L = Gain \times DN + Bias. \tag{4}$$

where L is the radiance of the pixel; DN is the digital number of the pixel; *Gain* is the gain for a specific band; *Bias* is the bias for a specific band; *Gain* and *Bias* can be obtained from the metadata file.

After the conversion, subset containing 600 pixel × 600 pixel images was then clipped. To increase the number of satellite images, some Landsat images with a small amount of cloud cover were also included (maximum cloud coverage of selected images is 10%). Therefore, it was necessary to mask cloud pixels before the analysis. To do this, algorithm described by [25] was applied to generate cloud mask of used images. In addition, the dataset contained images acquired at different times; therefore, a shadow cast by high features, such as high buildings and mountains, was also different. To reduce this effect, a shadow mask for each image was additionally created based on ASTER GDEM with spatial resolution of 30 m using the method described in [26]. To reconstruct missing data, solar radiation including direct solar radiation, diffuse solar radiation, reflected radiation were used as predictor variables. The Solar radiation is estimated by Eq. (5) to (7) based on method described in [27].

$$I_{dir} = I_0 \tau_b cos\, i. \tag{5}$$

$$I_{diff} = I_0(0.271 - 0.294\tau_b)cos^2 \frac{\beta}{2} sin\, \alpha. \tag{6}$$

$$I_r = rI_0(0.271 + 0.706\tau_b)sin^2 \frac{\beta}{2} sin\alpha. \tag{7}$$

where I_{dir} is direct solar radiation; I_{diff} is diffuse solar radiation; I_r reflected solar radiation; I_0 is extraterrestrial radiation; τ_b is atmospheric transmittance for beam radiation; r is ground reflectance coefficient; i is angle between the normal to the surface and the direction to the Sun; β is slope of the surface, and α is solar elevation angle.

3.3 Reconstruction of Contaminated Pixels by BNN

The spectral radiance measured by a sensor is affected by many components [28, 29]. Therefore, the correlation between the at-sensor radiance and the impact factors is very

complex. In brief, the complex relationship of measured radiance and impact factors can be expressed as a nonlinear or linear function. Due to the simplicity, the linear model is usually preferred. [3] used multi-linear regression to simulate Landsat image based on temporal correlation between the pixel values and eight important factors including air temperature (T), humidity (H), visibility (V), and rainfall (R), NDVI for every input image was computed by Eq. (8) [30], direct solar (DR), diffuse solar (DFR), and reflected radiation (RR). Here, the temperature, humidity, rainfall, and visibility are single values; NDVI, direct solar radiation, diffuse solar radiation, and reflected radiation are spatially distributed parameters. NDVI is used as a solution to reduce the effects of landcover changes. The equation obtained from the multilinear regression can be expressed as Eq. (9) [3].

$$NDVI = \frac{L_{NIR} - L_{Red}}{L_{NIR} + L_{Red}}. \tag{8}$$

where L_{NIR} and L_{Red} is spectral radiance of NIR and Red band of the Landsat images.

$$\begin{aligned} L^t_{(i,j,b)} &= a_{1(i,j,b)}T^t + a_{2(i,j,b)}H^t + a_{3(i,j,b)}V^t + a_{4(i,j,b)}R^t + a_{5(i,j,b)}NDVI^t_{(i,j)} \\ &+ a_{6(i,j,b)}RR^t_{(i,j)} + a_{7(i,j,b)}DR^t_{(i,j)} + a_{8(i,j,b)}DFR^t_{(i,j)} + a_{9(i,j,b)}. \end{aligned} \tag{9}$$

where L is spectral radiance; t is acquisition time.

i, j, and b are the row, column, and band indices, respectively.

a_1 through a9 are the regression coefficients.

However, as mentioned above, there are many factors affecting the radiance measured by a satellite sensor. The fact that it can be expressed by non-linear equations [28, 29]. Therefore, a linear model may not provide a suitable approximation. Whereas, a complex nonlinear function can provide a more accurate prediction [3]. Consequently, more complex mixing models need to be considered. However, estimating non-linear model requires complex analysis with multiple-step algorithms. One of optimal solutions is to replace the non-linear function by an ANN, which can handle the nonlinear correlation well [15–17]. There are various types of neural networks, such as feed-forward neural network, BNN, stochastic neural network, recurrent neural network [17]. However, BNN can provide more optimal and robust approximations [18, 23].

In this study, BNN was used to model complex relationships between spectral radiance measured by satellite sensor and eight variables including air temperature (T), humidity (H), visibility (V), and rainfall (R), NDVI, direct solar (DR), diffuse solar (DFR), and reflected radiation (RR). Generally, it can be expressed by Eq. (10). NDVI for every input image was computed from Red and NIR band of the Landsat images by Eq. (8) [30], NDVI on target date requiring the reconstruction of missing imagery data can be interpolated from images obtained during the same season.

$$L^t_{(i,j,b)} = \mathrm{f}\left[T^t, H^t, V^t, R^t, NDVI^t_{(i,j)}, DR^t_{(i,j)}, DFR^t_{(i,j)}, RR^t_{(i,j)}\right]. \tag{10}$$

where L is spectral radiance; t is acquisition time.

i, j, and b are the row, column, and band indices, respectively.

a_1 through a_9 are the regression coefficients.

Before training the networks, the selection of the number of hidden layer and hidden neurons is very important [31]. This depends on the complexity of the relation f to be modeled and the fact that there is no standard for choosing them [32]. In this study, after many trials, the network was designed to use 1 hidden layer with 4 hidden neurons as illustrated in Fig. 2. To train the network, various training algorithms are available [33, 34]. In this study, after many trials the network was trained using Bayesian Regularization function with 500 epochs, which showed the best performance in this case study.

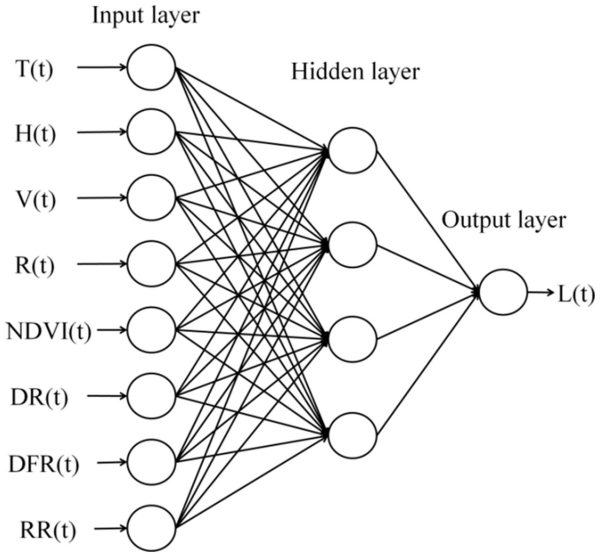

Fig. 2. Architecture of BNN used in this study.

3.4 Quality Assessment

In order to verify the retrieved imagery data, both visual comparison and quantitative analysis were used. Visually, the cloud-free image generated by the proposed method was compared to the actual image. For quantitative analysis, Spectral Correlation Mapper (SCM) [35] was used to assess the difference between a retrieved pixel compared with the corresponding actual pixel. The SCM method employs Pearson's correlation coefficient (R) computed by Eq. (11) to detect changes [35]. R values range from −1 to +1. Large values indicate that two spectra are similar. The value of 1 indicates that there is no difference between the two spectra.

$$R = \frac{\sum_{i=1}^{nb} \left(T1_i - \overline{T1}\right)\left(T2_i - \overline{T2}\right)}{\sqrt{\sum_{i=1}^{nb} \left(T1_i - \overline{T1}\right)^2 \sum_{i=1}^{nb} \left(T2_i - \overline{T2}\right)^2}}. \quad (11)$$

where $T1$ and $T2$ $\overline{T1}$ *and* $\overline{T2}$ are the spectra of a certain pixel in each band in the first and the second images, respectively; $\overline{T1}$ and $\overline{T2}$ are the mean values of $T1$ and $T2$ of each pixel; *nb* is the number of bands in an image.

4 Methodological Flowchart

A cloud-free sub-Landsat image acquired on September 22, 2006 (see Fig. 4(a)) was selected as a target image which was required missing imagery data reconstruction. This date was selected because it is in the middle of the acquisition period of the dataset; additionally, the image on this date was clear, so that it is good for quality assessment. Three portions of this image were masked in assumption that they were covered by cloud (see Fig. 4(b), where white zones denote cloud regions, which means pixels' value within those areas need to be reconstructed): area #1 was almost covered by forest; area #2 was an urban region; area #3 was a mixed area almost covered by agricultural fields and small amount of man-made structures. To test the proposed model, the experiment was carried out by five main steps as shown in Fig. 3: 1. Preprocessing; 2. BNN training; 3. Reconstructing missing imagery data; 4. Histogram

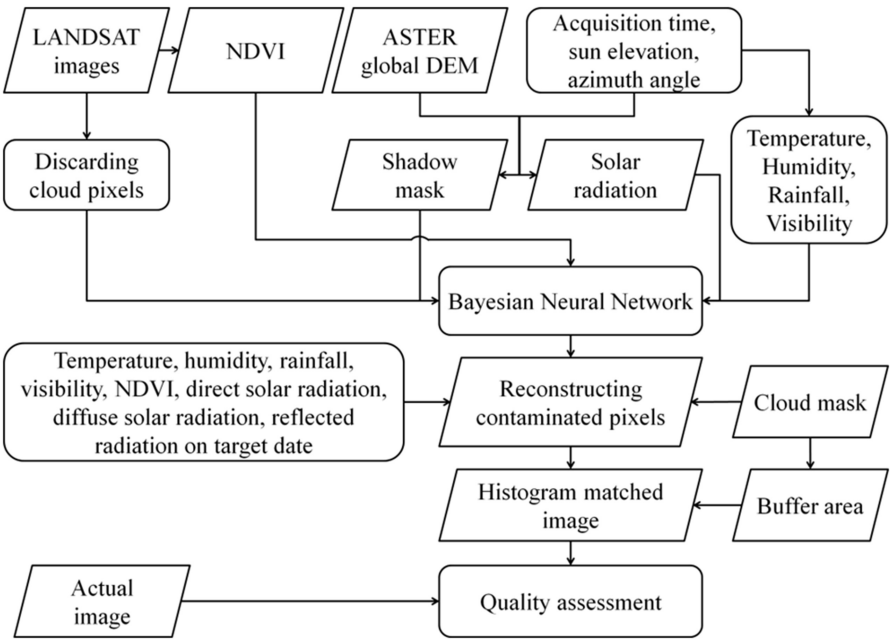

Fig. 3. Methodological flowchart.

matching; 5. Quality assessment. After aforementioned preprocessing steps, cloud masks, shadow masks as well as solar radiations were obtained. After that, BNN illustrated by Fig. 2 was trained for every contaminated pixel. In this step the shadow pixels and cloudy pixels in the input images were excluded based on the masks generated in the preprocessing phase. Subsequently, the obtained model expressing the relationship between measured radiance and the eight predictor variables (i.e. air temperature, humidity, rainfall, visibility, NDVI, direct solar radiation, diffuse solar radiation and reflected radiation) was used to reconstruct pixels' value covered by cloud on September 22, 2006. Finally, the reconstructed image was compared to the actual image for quality assessment. In order to reduce color difference between reconstructed pixels and the surrounding actual pixels, histogram matching was conducted base on a 10-pixel buffer around the masking areas.

5 Results and Discussions

The experiment was implemented by using MATLAB programming language. After many attempts, the network with 1 hidden layer and 4 hidden neurons was trained using Bayesian Regularization function, number of epochs was set to 500, the transfer function for the hidden layer and the output layer was tan-sigmoid and linear function, respectively. The processing was implemented by using MATLAB Neural Network Toolbox. The trained network was used to generate new pixels' value within the three cloud regions of the cloud mask described in Fig. 4(b). Then the old pixels were replaced with the new pixels to generate a cloud free image on September 22, 2006 as shown in Fig. 4(d). In this study, NDVI on September 22, 2006 was linearly interpolated from the NDVIs on August 31, 2004 and October 24, 2006. In order to reduce the color difference between the reconstructed area and the surrounding area, histogram matching was performed solely on each cloud cover region based on adjacent pixels of 10-pixel buffer around each masking area. The result after histogram matching was illustrated in Fig. 4(e).

Visual comparison between the actual image (Fig. 4(a)) and the reconstructed image (Fig. 4(d)) showed that the reconstructed pixels and the actual pixels are very similar in man-made area (Area #2). However, the color similarity is declined slightly in forest area (Area #1), and the most color difference appears in mixed area (Area #3). This could be due to the vegetation changed much over time. However this difference was almost overcome after conducting histogram matching based on the buffer areas (see Fig. 4(e)). For quantitative assessment, the SCM was carried out on non-corrected images. The results of SCM were shown in Fig. 5 and Table 1.

Figure 5 and Table 1 proved that the pixels generated by the proposed algorithm are very similar to the actual pixels, especially in urban area, where can be considered as non-change area. The similarity is illustrated by the high average of R in all three areas, and the large amount of pixel has R over 0.99, which can be considered as no difference between the two pixels. Actually, the highest percentage of R over 0.99 is approximate to 91% in urban area. In the other two areas, the percentages of R over 0.99 are also quite high, about 78%. If considering the pixel with R over 0.98 is almost similar, the percentages of these pixels were much greater: the lowest value is 92.8%

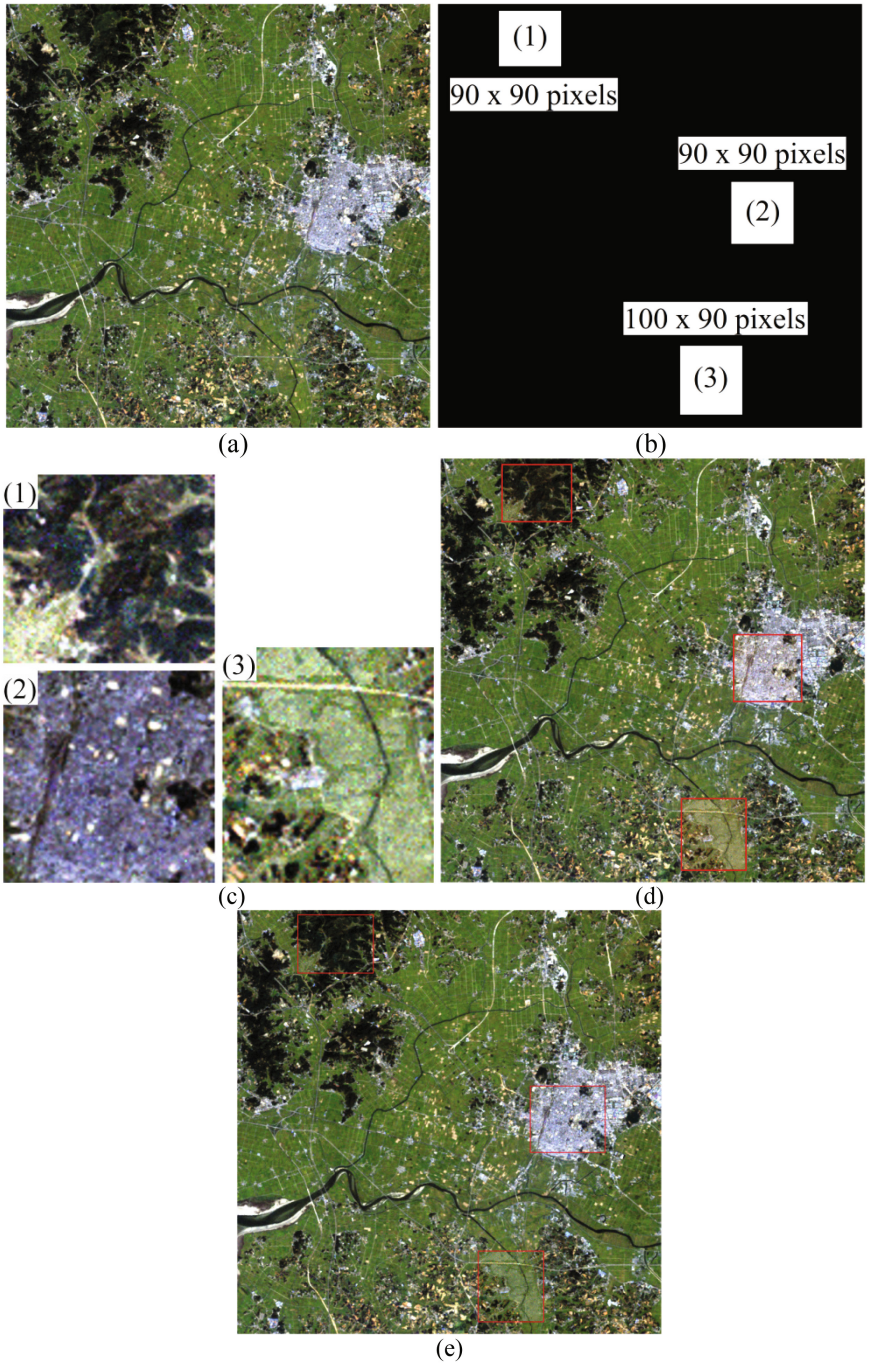

Fig. 4. (a) Original image; (b) cloud mask; (c) three reconstructed areas; (d) reconstructed image; (e) histogram matched image; Red rectangles denote the reconstructed areas.

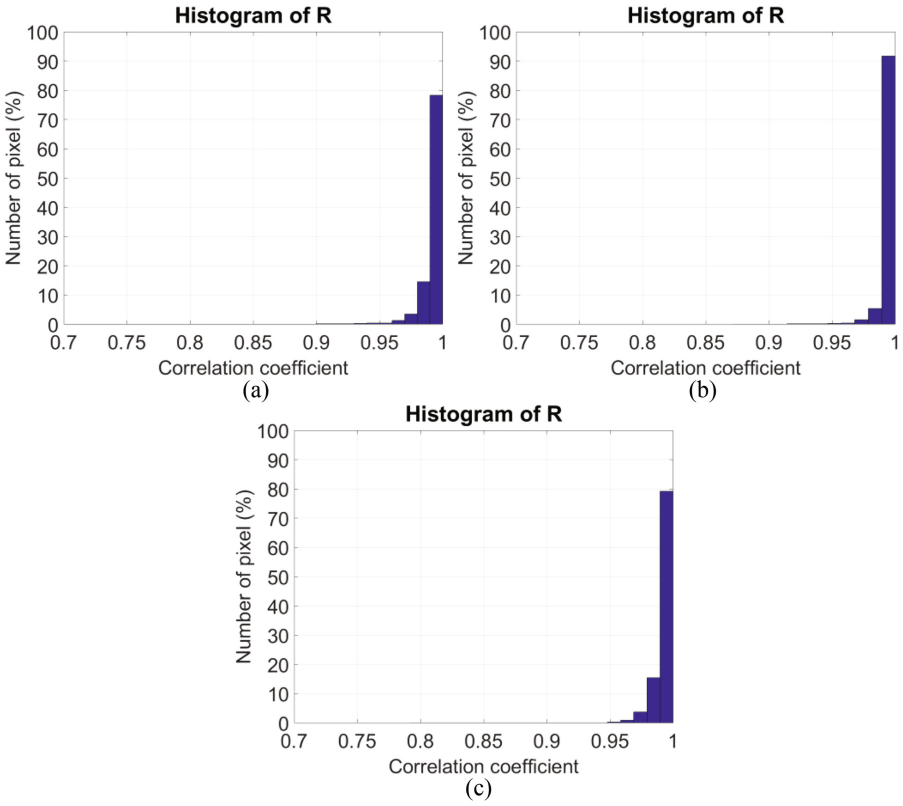

Fig. 5. Correlation coefficients between reconstructed image and actual image on September 22, 2006: (a) area #1; (b) area #2; (c) area #3.

Table 1. Summary of Correlation coefficients.

	Area 1	Area 2	Area 3
Mean	0.993	0.995	0.992
Max	1.000	1.000	1.000
Min	0.792	0.871	0.629
Percentage of pixel (%)			
R > 0.99	78.0	90.9	78.1
R > 0.98	94.1	96.6	92.8
R < 0.95	0.4	0.7	1.9

for mixed area, and the greatest value is 96.1% for man-made area. Meanwhile, percentage of pixels with $R < 0.95$ are close to zero in area #1 and #2, and it is just 1.9% in area #3.

Visually and quantitatively, the results generated by the proposed method are very similar to those in the actual image. This seems to be better than image composite

based methods such as [6, 7, 9]. Additionally, owing to its flexibility, the proposed method can be used to reconstruct pixels' value contaminated by cloud on any date within the period of acquisition time of input images. However, similar to other multitemporal-based method such as [13, 36], missing imagery data reconstructed by the proposed method was mainly affected by landcover changes. As a result, the percentage of pixels, whose R greater than 0.99, which can represent a state of no difference, is highest in urban area, where change slowly over time. This was reduced dramatically in the other two areas, where were mostly covered by vegetation, which changes seasonally. Noticeably, unlike method of [13, 36], the pixels' value predicted by the proposed method did not depend on information around them, the buffer areas were only used to improve visualization. Furthermore, by taking advantage of BNN, the proposed approach can obtain appropriate temporal correlation to reconstruct missing information, and thus, it can potentially yield better results in terms of radiometric accuracy. However, more quantitative analysis and comparison are needed to make widespread use of the proposed method.

Unlike simple linear model, the non-linear model requires multiple-step solutions. As a result, it takes more time to train the BNN. However, reconstructing pixels' value covered by cloud is usually carried out on small portions of images. Therefore, the time requirement for training the model is not a big problem. Additionally, the modern computer systems are more and more powerful that can minimize the difficulty in training the BNN.

6 Conclusion

This paper proposed an approach to reconstruct pixels' value contaminated by cloud in a remote sensing image by taking advantage of a dataset containing a large amount of image time series and BNN. The proposed method was used to generate new pixels' value where covered by cloud of a Landsat image acquired on September 22, 2006. The result showed that reconstructed pixels' value were similar to the actual value in non-change area with the percentage of R over 0.99 is about 91%. However, the similarity reduced in areas which changed significantly over time period. The color difference between reconstructed areas and the rest of image was almost overcome after running histogram matching based on the buffer of 10-pixel surrounding the cloud masks.

The similarity of the retrieved imagery data and the actual ones indicates that the BNN can be an effective technique for recovering the original pixels' value where were covered by cloud. However, more quantitative comparisons with other related techniques are necessary to bring BNN into more widespread use in this field. Additionally, like other multitemporal-based methods, limitation of the proposed method is its sensitivity to changes in land cover during the period in which the input satellite images were acquired. Nevertheless, given its flexibility, the proposed method can be reconstruct pixels' value covered by cloud on any date within the period of acquisition time of input images. Although, the results of SCM can prove the reliability of the proposed method, further study is still needed to reduce the effect of landcover changes on predicting new pixels' value.

Acknowledgement. This work was supported by Vietnam National Foundation of Science and Technology Development under the project 105.99-2014.15.

References

1. Ju, J., Roy, D.P.: The availability of cloud-free Landsat ETM + data over the conterminous United States and globally. Remote Sens. Environ. **112**, 1196–1211 (2008)
2. Melgani, F.: Contextual reconstruction of cloud-contaminated multitemporal multispectral images. IEEE Trans. Geosci. Remote Sens. **44**, 442–455 (2006)
3. La, H.P., Eo, Y.D., Lee, S., Park, W.Y., Koo, J.H.: Image simulation from multitemporal landsat images. GISci. Remote Sens. **52**, 586–608 (2015)
4. Liew, S.C., Li, M., Kwoh, L.K., Chen, P., Lim, H.: Cloud-free multi-scene mosaics of SPOT images. In: International Geoscience and Remote Sensing Symposium 2, pp. 1083–1085. IEEE Press, Seattle (1998)
5. Abd-Elrahman, A., Shaker, I.F., Abdel-Gawad, A.K., Abdel-Wahab, A.: Enhancement of cloud-associated shadow areas in satellite images using wavelet image fusion. World Appl. Sci. **4**, 363–370 (2008)
6. Tseng, D.C., Tseng, H.T., Chien, C.L.: Automatic cloud removal from multi-temporal SPOT images. Appl. Math. Comput. **205**, 584–600 (2008)
7. Gui, Z., Chen, F., Yang, J., Li, X., Li, F., Zhao, J.: Automatic cloud and cloud shadow removal method for landsat TM images. In: 10th International Conference on Electronic Measurement & Instruments (ICEMI), pp. 80–84. IEEE Press, Chengdu (2011)
8. Jin, S., Homer, C., Yang, L., Xian, G., Fry, J., Danielson, P., Townsend, P.A.: Automated cloud and shadow detection and filling using two-date Landsat imagery in the USA. Int. J. Remote Sens. **34**, 1540–1560 (2013)
9. Li, M., Liew, S., Kwoh, L.: Automated production of cloudfree and cloud shadow-free image mosaics from cloudy satellite imagery. In: 20th Congress of the International Society of Photogrammetry and Remote Sensing, pp. 15–23 (2004)
10. Gui, Z., Liu, J., Chen, F.: Automatic local phenology simulation for landsat TM image. In: 2012 IEEE International Conference on Information Science and Technology, Wuhan, Hubei, China (2012)
11. Helmer, E.H., Ruefenacht, B.: Cloud-free satellite image mosaics with regression trees and histogram matching. Photogram. Eng. Remote Sens. **9**, 1079–1089 (2005)
12. Hwang, T., Song, C., Bolstad, P.V., Band, L.E.: Downscaling real-time vegetation dynamics by fusing multi-temporal MODIS and Landsat NDVI in topographically complex terrain. Remote Sens. Environ. **115**, 2499–2512 (2011)
13. Lin, C.-H., Tsai, P.-H., Lai, K.-H., Chen, J.-Y.: Cloud removal from multitemporal satellite images using information cloning. IEEE Trans. Geosci. Remote Sens. **51**, 232–241 (2013)
14. Guyet, T., Nicolas, H.: Long term analysis of time series of satellite images. Pattern Recogn. Lett. **70**, 17–23 (2016)
15. Harter, F.P., de Campos Velho, H.F.: New approach to applying neural network in nonlinear dynamic model. Appl. Math. Model. **32**, 2621–2633 (2008)
16. Xiong, C., Li, T.: Application of artificial neural networks to prediction of deformation in deep foundation pit. In: 2011 International Conference on Multimedia Technology (ICMT), pp. 1448–1453. IEEE Press, Hangzhou (2011)
17. Amato, F., Havel, J., Gad, A.-A., El-Zeiny, A.M.: Remotely sensed soil data analysis using artificial neural networks: a case study of el-fayoum depression, Egypt. ISPRS Int. J. Geo-Inf. **4**, 677–696 (2015)

18. Ticknor, J.L.: A Bayesian regularized artificial neural network for stock market forecasting. Expert Syst. Appl. **40**, 5501–5506 (2013)
19. KMA. http://web.kma.go.kr/eng/biz/climate_01.jsp
20. MacKay, D.J.C.: Bayesian interpolation. Neural Comput. **4**, 415–447 (1992)
21. Hernández-Lobato, J.M., Adams, R.P.: Probabilistic backpropagation for scalable learning of Bayesian neural networks. In: 32nd International Conference on Machine Learning, vol. 37, pp. 1861–1869. JMLR, Lille (2015)
22. Lampinen, J., Vehtari, A.: Bayesian approach for neural networks – review and case studies. Neural Netw. **14**, 7–24 (2001)
23. Burden, F., Winkler, D.: Bayesian regularization of neural networks. Methods Mol. Biol. **458**, 25–44 (2008)
24. Chander, G., Markham, B.: Revised Landsat-5 TM radiometric calibration procedures and postcalibration dynamic ranges. IEEE Trans. Geosci. Remote Sens. **41**, 2674–2677 (2003)
25. Ouaidrari, H., Vermote, E.F.: Operational atmospheric correction of landsat TM data. Remote Sens. Environ. **70**, 4–15 (1999)
26. Ratti, C., Richens, P.: Raster analysis of urban form. Environ. Plan. **31**, 297–309 (2004)
27. Kumar, L., Skidmore, A.K., Knowles, E.: Modelling topographic variation in solar radiation in a GIS environment. Int. J. Geogr. Inf. Sci. **11**, 475–497 (1997)
28. Photon Research Associates: GCI Toolkit Manual. Photon Research Associates, San Diego, CA (1998)
29. Schott, J.R.: Remote Sensing: The Image Chain Approach, 2nd edn. Oxford University Press, New York (2007)
30. Rouse, J.W., Haas, R.H., Schell, J.A., Deering, D.W.: Monitoring vegetation systems in the great plains with ERTS. In: 3rd ERTS Symposium, pp. 309–317. NASA SP-351, NASA, Washington, DC (1974)
31. Pham, B.T., Bui, D.T., Prakash, I., Dholakia, M.B.: Hybrid integration of Multilayer Perceptron Neural Networks and machine learning ensembles for landslide susceptibility assessment at Himalayan area (India) using GIS. CATENA **149**, 52–63 (2017)
32. Maduako, I.D., Yun, Z., Patrick, B.: Simulation and prediction of land surface temperature (LST) dynamics within Ikom City in Nigeria using artificial neural network (ANN). J. Remote Sens. GIS **5**, 1–7 (2016)
33. Zupan, J.G.J.: Neural Networks in Chemistry and Drug Design, 2nd edn. Wiley VCH, Weinheim (1999)
34. Ahmed, F.E.: Artificial neural networks for diagnosis and survival prediction in colon cancer. Mol. Cancer **4** (2005)
35. Carvalho Júnior, O.A., Guimarães, R.F., Gillespie, A.R., Silva, N.C., Gomes, R.A.T.: A new approach to change vector analysis using distance and similarity measures. Remote Sens. **3**, 2473–2493 (2011)
36. Benabdelkader, S., Melgani, F., Boulemden, M.: Cloud-contaminated image reconstruction with contextual spatio-spectral information. In: IEEE International Geoscience and Remote Sensing Symposium, pp. 373–376, IEEE Press, Barcelona (2007)

Monitoring Mangrove Forest Changes in Cat Ba Biosphere Reserve Using ALOS PALSAR Imagery and a GIS-Based Support Vector Machine Algorithm

Tien Dat Pham[1,2(✉)], Kunihiko Yoshino[3], and Naoko Kaida[4]

[1] Graduate School of Systems and Information Engineering,
The University of Tsukuba,
1-1-1 Tennodai, Tsukuba 305-8573, Ibaraki Prefecture, Japan
dat6784@gmail.com
[2] Center for Agricultural Research and Ecological Studies (CARES),
Vietnam National University of Agriculture (VNUA),
Trau Quy, Gia Lam, Hanoi, Vietnam
tiendat@cares.org.vn
[3] Department of Biological and Environmental Engineering,
Faculty of Agriculture, The University of Tokyo,
1-1-1 Yayoi, Bunkyo-Ku, Tokyo 113-8657, Japan
asky@mail.ecc.u-tokyo.ac.jp
[4] Faculty of Engineering, Information, and Systems, The University of Tsukuba,
1-1-1 Tennodai, Tsukuba 305-8573, Ibaraki Prefecture, Japan
naoko.kaida@sk.tsukuba.ac.jp

Abstract. Cat Ba is one of the most well-known islands located in North Vietnam, which has been recognized as a biosphere reserve by United Nations Educational, Scientific and Cultural Organization (UNESCO) since 2004. Despite the large potential carbon stocks in mangrove forests of Cat Ba, the mangrove ecosystem of this island has suffered severe deforestation and forest degradation due to the conversion to shrimp aquaculture. Monitoring mangrove forest changes plays an important role for effective mangrove conservation and management. The objectives of this study were to map the spatial distribution of mangrove forest and to assess their changes between 2010 and 2015 in Cat Ba Biosphere Reserve, Hai Phong city of Vietnam using ALOS PALSAR data and a GIS-based support vector machine algorithm. For this purpose, ALOS PALSAR imagery for the above period and GIS data were collected. Then, spatial distributions of mangroves were derived using the support vector machine classifier. The results showed that the ALOS-2 PALSAR for 2015 achieves the overall accuracy of 85% and the kappa coefficient of 0.81, compared with those of 81% and 0.77, respectively from the ALOS PALSAR for 2010. The mangrove forest areas in the Cat Ba Biosphere Reserve, Vietnam decreased by 15% from 2010 to 2015. This research shows the potential use of ALOS PALSAR data combined with machine learning techniques in monitoring mangrove forest changes in tropical and semi-tropical climates.

Keywords: ALOS PALSAR · Cat Ba biosphere reserve · Hai Phong city · Mangrove changes · Support vector machines

© Springer International Publishing AG 2018
D. Tien Bui et al. (eds.), *Advances and Applications in Geospatial Technology and Earth Resources*, https://doi.org/10.1007/978-3-319-68240-2_7

1 Introduction

Mangroves are found in most tropical and semi-tropical regions along the sheltered coastlines such as river estuaries or tidal marshes [1]. They are considered to be the most important ecosystems on earth [2] as they play a vital role in mitigating the impact of climate change in tropical climates [3] by sequestering carbon in both above and below-ground biomass as well as their sediment [4].

Despite their significant roles in providing habitats for marine species and serving the local communities with ecological and economic services, mangroves have been lost in the past 50 years worldwide due to high population growth, rapid urbanization, aquaculture expansion and other human activities [5]. Among regions of the world, Asia has suffered the greatest loss of 1.9 million hectares [6]. Like many other countries in Southeast Asia, the mangroves in Vietnam have cleared for coastal development, aquaculture expansion, and fuel production in the early 20th century [7]. Thus, mapping the spatial distribution of mangrove forests is important in order to support coastal zone management and planning programs.

Satellite remotely sensed data and various techniques have been applied for mapping mangrove forests including optical data [8, 9] and synthetic aperture radar (SAR) data [10, 11]. Pixel-based classification methods are most frequently used for mapping mangrove forests in Vietnam [12–14]. Béland et al. [15] used Landsat imagery to investigate the land-cover changes from mangrove to aquaculture in the Red River Delta using Tasselled Cap Transformation. Pixel-based approaches were employed by previous studies conducted in the Mekong Delta by Tong et al. [12] and Thu and Populus [13]. Recent studies reported that object-based classification approaches have been successfully applied in mapping mangrove forests and assessing their changes based on optical sensors such as Landsat images [16] and SPOT-5 data [17]. These studies have been conducted in specific regions, such as Ca Mau Peninsula in South Vietnam [14, 16, 18]. However, only a few studies in Vietnam have been used SAR data to map the spatial distribution of mangrove forests and assess their changes despite the fact that SAR can penetrate clouds, which occur constantly in the tropical area and acquire data throughout the year [19]. As a result, the spatial distribution of the mangroves in Vietnam is still limited and not well documented. Thus, there is a need to map and assess their spatial distribution in Vietnam using SAR data and suitable methodology.

Recently, machine learning techniques have been shown as an effective tool for mapping Land-use and Land-cover (LULC) [20–23], mapping mangrove forests and their distribution using remotely sensed data [24, 25]. Recent studies have demonstrated that support vector machines (SVM) classifier is one of the most popular machine learning algorithms in LULC classification [26, 27] as it can provide high accuracy and require a small number of the training data [28]. We selected a support vector machine algorithm for mapping mangroves and assessing their changes because, among numerous number of machine learning techniques, the support vector machine (SVM) has been widely used for nonlinear mapping and complex classification problems such as land cover change detection [26]. However, the SVM classifier has rarely been used for monitoring mangroves changes using SAR data in the tropics.

The overall goal of this study was to map the spatial distribution of mangrove forests in the Cat Ba Biosphere Reserve, Vietnam and to evaluate their changes using ALOS PALSAR data and a GIS-based support vector machine classifier. Such studies are crucial for monitoring mangroves changes at a regional scale and play an important role in conserving mangrove resources in Vietnam. This study has demonstrated the potential use of ALOS PALSAR data combined with machine learning algorithms for mapping the spatial distribution mangrove forests and assessing their changes in the tropical area.

2 Study Area and Spatial Data

2.1 Study Area

Cat Ba is the largest island in the Cat Ba Archipelago in Hai Phong City, located in the north of Vietnam. The Cat Ba Biosphere Reserve consists of six communes and one town (Fig. 1). The core ecosystem of the island is tropical forest including tropical evergreen forest in the lowlands, limestone forest in the mountains, and mangrove forests along the coast. Cat Ba Island has been recognized by United Nations Educational, Scientific and Cultural Organization (UNESCO) as a biosphere reserve since 2004. The total area of the Cat Ba Biosphere Reserve is about 26,241 hectares. The biosphere is a well-known destination for tourists from not only all parts of Vietnam, but also from around the world. The number of tourists has significantly increased over the last decade [29], and now is around 500,000 annually [30].

The Cat Ba Biosphere Reserve is under serious threat from deforestation and forest degradation. The tropical forest of the reserve decreased by around 660 hectares while the mangrove forest decreased by almost 50% from 1990 to 2001 [31]. The mangrove forest area in the reserve declined largely due to over-expansion of shrimp aquaculture [32].

2.2 SAR Data Used

The Advanced Land Observing Satellite (ALOS) Phased Arrayed L-band SAR (PALSAR) images acquired in 2010 and 2015 were used to map the spatial distribution of mangrove forests and assess their changes. The images used were acquired by ALOS PALSAR and ALOS-2 PALSAR sensors (Table 1).

ALOS and ALOS-2 PALSAR data level 1.5 were acquired from the Remote Sensing Technology Centre (RESTEC) of Japan. The ALOS PALSAR data was acquired in the same period during summer time for the years 2010 and 2015 to avoid seasonal and tidal effects. Since terrain can significantly influence backscatters and

Table 1. Acquired SAR remote sensing data in the study area.

Satellite sensor	Date of acquisition	Pixel spacing	Processing level	Polarizations
ALOS PALSAR	2010/8/25	12.50 m	1.5	HH, HV
ALOS-2 PALSAR	2015/7/31	6.25 m	1.5	HH. HV

Source: JAXA, Japan.

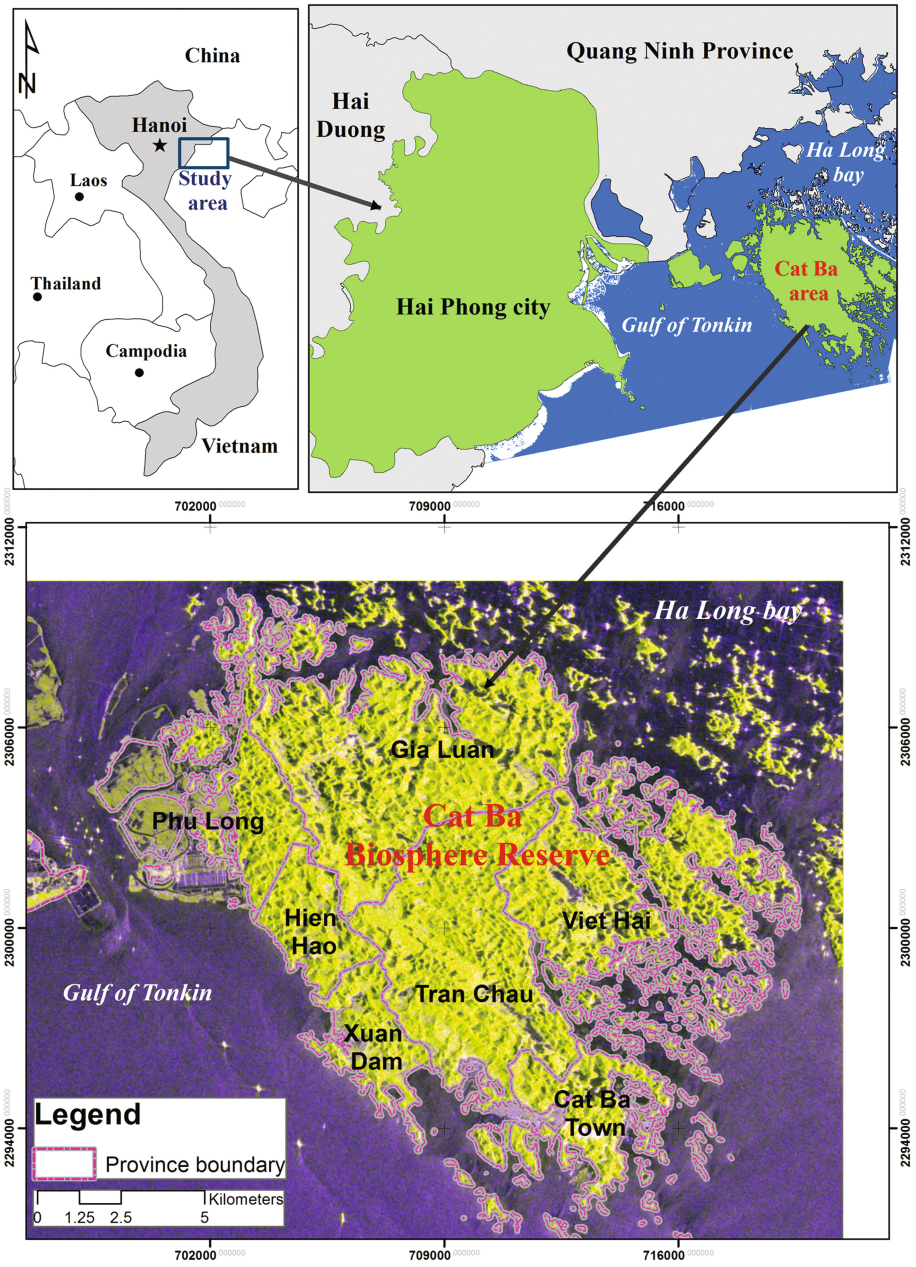

Fig. 1. Map of the study area in the Cat Ba Biosphere Reserve, Vietnam.

image projection, the ALOS PALSAR data were orthorectified using the Advanced Spaceborne Thermal Emission and Reflection Radiometer (ASTER), Global Digital Elevation Model (GDEM) [33]. Two images then were geocoded and projected into the Universal Transverse Mercator (UTM) coordinate system, Zone 48 North based on the World Geodetic System datum (WGS84). The DN (Digital Number) was converted to normalized radar sigma-zero using Eq. 1

$$\sigma^0[\mathrm{dB}] = 10.\log_{10}(\mathrm{DN})^2 + \mathrm{CF} \tag{1}$$

where σ^0 is backscattering coefficient, DN is a digital number of the amplitude image, and CF is the Calibration Factor and CF = −83 dB for both HH and HV polarizations [34]. The CF used to process ALOS-2 PALSAR is similar to ALOS PALSAR [35]. The DN of each pixel was transformed into backscattering sigma naught (σ^0) in decibel (dB).

The ALOS PALSAR images were moderately despeckled using the Frost filter with a 5 × 5 moving window kernel to retain textural information [36]. To minimize the blurring effect on filtered images, image pixels were then averaged to 30-meter resolution, allowing the detection of small-area forest disturbances and comparability to Landsat-based datasets [37] as suggested by Neha, Edward, Natalia, Jorge, Julian, Andrea, Murray, Martin and Rasmus [38].

Since surface moisture and tidal height can affect radar backscatters, we also carefully took the time to conduct field work into consideration to minimize effects of surface moisture and tidal height [39–42].

2.3 Field Data Collection

The field data at the Cat Ba Biosphere Reserve was conducted several times in July, August 2010 and July 2015 with the help and permission from local authorities. The former dataset was used for mapping mangroves for 2010 and the latter dataset was used to generate a mangroves cover map for 2015. During the field survey, we collected ground-truth points (GTP) using Global Positioning Systems (GPS) to create training data for supervised classification and assess the accuracy of the post classification of the mangrove cover maps in 2010 and 2015. All GTPs data were transformed into a GIS format to select the training and validation datasets for SAR images classification. We also took photos for different land-cover types and mangrove species during the field survey for two periods. A total of five land-cover types (forest, mangrove, settlement, aquaculture, and water bodies) and two dominant mangrove species such as *Rhizophora stylosa* and *Avicennia marina* are found in the Cat Ba Biosphere Reserve were recorded during the survey (Fig. 2).

Rhizophora stylosa *Avicennia marina*

Fig. 2. Mangrove communities in the Cat Ba Biosphere Reserve (Source: Field survey, 2015).

3 Method Used

3.1 Support Vector Machine Classifier

Support vector machine (SVM) is a supervised non-parametric statistical learning method and has been widely used in numerous applications in remote sensing. SVMs have been successfully utilized in classifying LULC [25], mapping LULC [22], mapping mangrove forests [43], and monitoring mangrove change detection [44]. The SVMs consist of a large number of vectors that have functions in separating different objects. However, selecting an optimal SVM algorithms for classifying these objects is not an easy task [28]. To overcome this problem, different kernel functions such as polynomial, sigmoid, and radial basis function (RBF) are used in the SVM-based classification algorithms. The accuracy of the SVM-based methods is relatively influenced by the selecting the kernel functions [27, 28]. We chose the RBF kernel in this study because it may be the most commonly used in satellite image classification and it generally requires a few parameters as well as can produce good results [45, 46]. Additionally, suggestions provided in the ENVI User' Guide [47] were also taken into consideration in choosing the RBF kernel function parameters. As a result, the γ parameter was set to a value equal to the inverse of the number of the polarizations used of the ALOS imagery (i.e., 0.166). The penalty parameter was set to its maximum value (i.e., 100), showing no misclassification during the training process while the pyramid parameter was set to a value of zero, showing the ALOS imagery to be processed at full resolution. It is noted that a classification probability threshold of zero was used, reflecting that all image pixels had to be classified into one class.

In order to produce better accuracy, the support vector machine supervised classification generally requires a large number of input data for the classification. In this study, we selected multi-polarizations generated from dual-polarization such as HH, HV, HH/HV, HV/HH, HH-HV, and ½(HH + HV) as suggested by Pham, Yoshino and

Bui [48] as input bands for classifying ALOS PALSAR imagery using ENVI. The ALOS PALSAR imagery was classified using a supervised training method by applying pixel-based support vector machines algorithms. The ENVI 5.2 software was employed for SAR imagery processing.

3.2 Mangrove Forest Change Detection

A pixel-based supervised classification using the SVM classifier was carried out on the ALOS PALSAR imagery using ENVI 5.2. Figure 3 shows the flowchart used for mapping mangrove species and monitoring their changes in the Cat Ba Biosphere Reserve, Hai Phong. Classification results for two periods were overlaid in ArcGIS 10.3 environment to detect mangrove forests changes.

It is noted that the GIS data and the statistical results were conducted in ArcGIS environment. The classification results were transformed into a GIS format for analyzing the mangrove forest changes in ArcGIS 10.3. Additionally, ancillary GIS data such as commune boundary were overlaid in the final classification results to analyze mangrove area statistics changes from 2010 to 2015 (Fig. 3).

3.3 Accuracy Assessment

We used the confusion matrix to assess the performance of the SVMs for mapping mangrove forests. The confusion matrix table was generated by comparing error value for each class that is classified with its value in ground truth data (reference data). The confusion matrix table contains the same number of column and row and equals to the number of classes [49, 50].

The reliability of the mangrove forests classification using SVM algorithm was measured using Kappa coefficient (K) [11, 16, 50, 51]. The kappa coefficient was calculated using Eq. 2.

$$\hat{k} = \frac{N\sum_{i=1}^{r} X_{ii} - \sum_{i=1}^{r} X_{i+}X_{+i}}{N^2 - \sum_{i=1}^{r} X_{i+}X_{+i}} \tag{2}$$

where r is the number of row in confusion matrix; X_{ii} is the number of rows i and column i; X_{i+} and X_{+i} are the totals of row i and column i, and N is the number of observations.

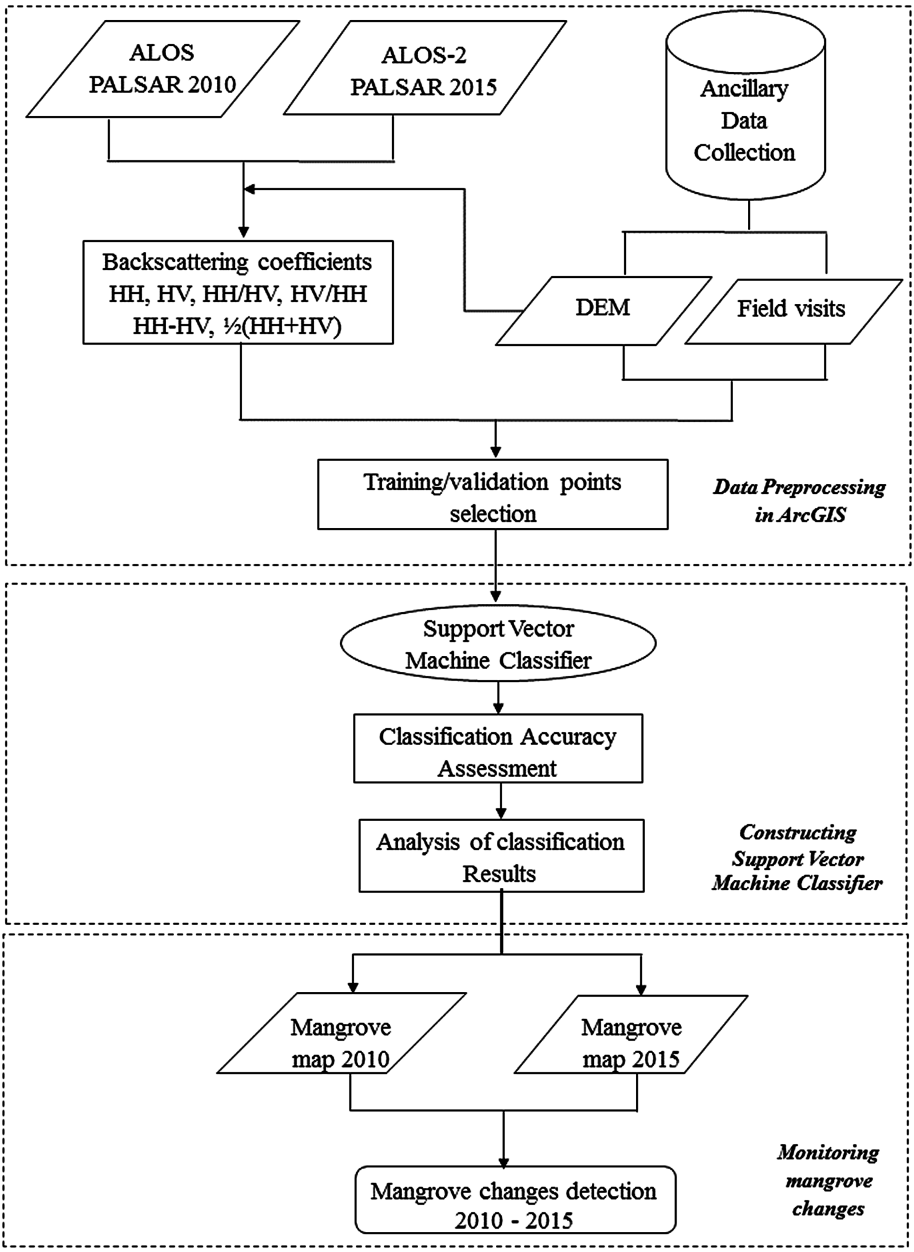

Fig. 3. Flowchart used for mapping mangroves and monitoring their changes.

4 Results and Discussion

4.1 Mangrove Forests Mapping

The classification results using the SVM algorithm with radial functions were converted to a GIS format for use in ArcGIS 10.3. The land-cover maps for 2010 and 2015 visualized five classes including forest, mangrove, settlement, aquaculture, and water bodies. Figures 4 and 5 show the spatial distribution of mangroves in the Cat Ba Biosphere Reserve, Hai Phong for 2010 and 2015, respectively. Mangroves are found mostly in the coast and the river mouths of Phu Long commune, accounting for the vast majority of the total mangrove area of the Cat Ba Biosphere Reserve. Additionally, a small grove of mangroves on the shore is found in Gia Luan and Xuan Dam communes.

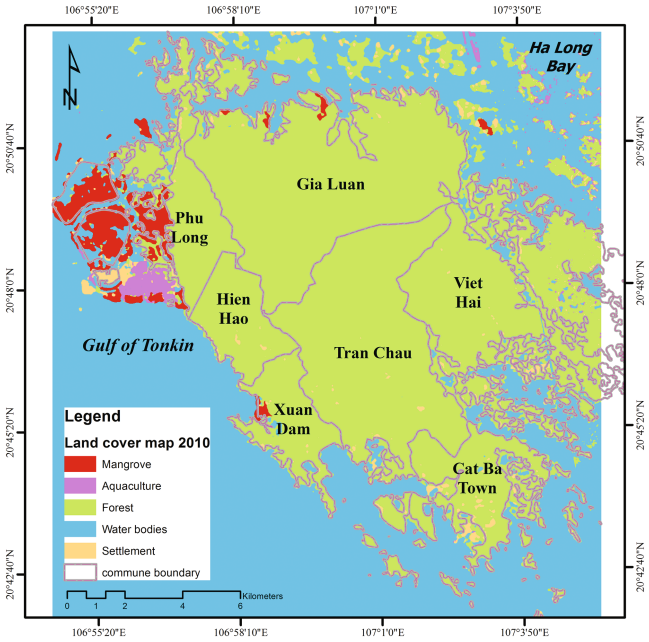

Fig. 4. Mangrove forests mapping of the Cat Ba Biosphere Reserve in 2010.

The classification accuracy (Producer, User, and Overall accuracies) and the Kappa coefficients of the SAR image processing are shown in Table 2. The overall accuracy of SAR data processing for the years 2010 and 2015 are 81%, 85%, and the Kappa indexes are 0.77 and 0.81, respectively. Mangroves, forest and water bodies produced higher user and producer accuracies among the five land cover classes. Settlement class also produced higher user and producer accuracies except for producer accuracy for the year 2010 (62%). Meanwhile, aquaculture class produced lowest user and producer accuracies for both two years 2010 and 2015. The low accuracies observed for the aquaculture class may be attributed to the backscattering coefficients similarity at HH

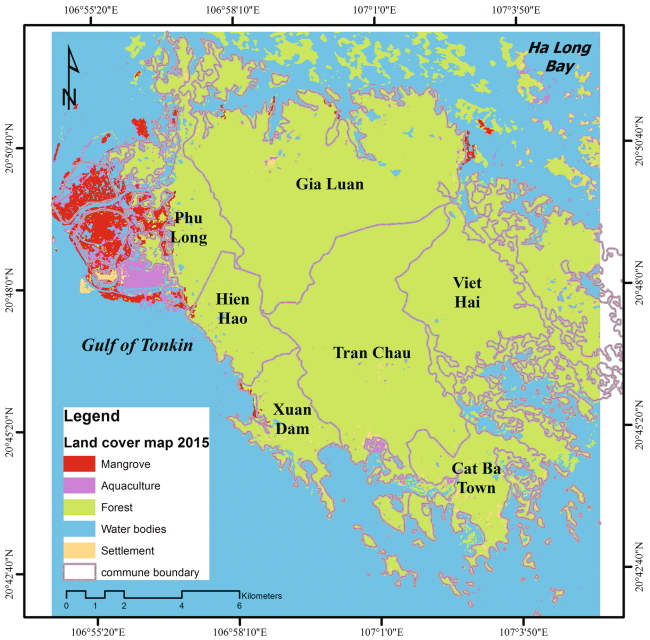

Fig. 5. Mangrove forests mapping of the Cat Ba Biosphere Reserve in 2015.

Table 2. Accuracy assessment of the SAR images classification for the years 2010 and 2015

Land cover type	2010		2015	
	Producer's accuracy (%)	User's accuracy (%)	Producer's accuracy (%)	User's accuracy (%)
Mangrove	84.6	91.7	76.9	83.3
Aquaculture	70.0	77.8	60.0	85.7
Forest	94.4	73.9	88.9	84.2
Settlement	61.5	88.9	92.3	100
Water bodies	90.9	83.3	100	73.3
Overall accuracy	81.5		84.6	
Kappa coefficient	0.77		0.81	

and HV polarizations of aquaculture with water bodies which was reported by Tien Dat and Kunihiko [52]. These may be due to the presence of speckles in ALOS PALSAR images. Speckle is a common problem for SAR sensors, influencing the accuracy of SAR images classification. SAR image despeckling is expected to remove speckle and retain image features. The main limitation of the current work is that we applied the Frost filter for the despeckling of SAR images may cause the blurring effect on filtered images, resulting in the changes information on the smoothed images. Thus, a nonlocal

filter for SAR images such as the probabilistic patch-based filter, the Bayesian nonlocal mean filter, and the SAR block-matching 3D filter [53–55] should be cautiously performed to solve the limitations of speckles in future studies. More research is, therefore, needed to investigate the usability of the nonlocal filters for the preservation of image features for the change detection of SAR data.

It can be seen from Table 2 that the overall accuracy and Kappa coefficient of 2015 are higher than those of 2010. It is likely due to the fact that ALOS-2 PALSAR imagery acquired for 2015 with high sensitivity mode has better spatial resolution than ALOS PALSAR imagery for 2010. The performance of the final images classification using the SVM algorithm with radial functions for both two periods 2010 and 2015 show satisfactory results, compared to previous studies [25, 43, 44].

4.2 Mangrove Forests Changes from 2010 to 2015

Figure 6 shows a mangrove forests change map in the Cat Ba Biosphere Reserve from 2010 to 2015. By overlaying the land-cover maps for two periods within the ArcGIS environment, it can be possibly detected what land cover is currently converted into mangroves. Thus, we also can determine that the past mangrove forest cover has been converted into aquaculture, which a common trend throughout South East Asia [56, 57] and in the Mekong Delta [13, 16, 17] and in the Red River Delta of Vietnam [32, 58–60].

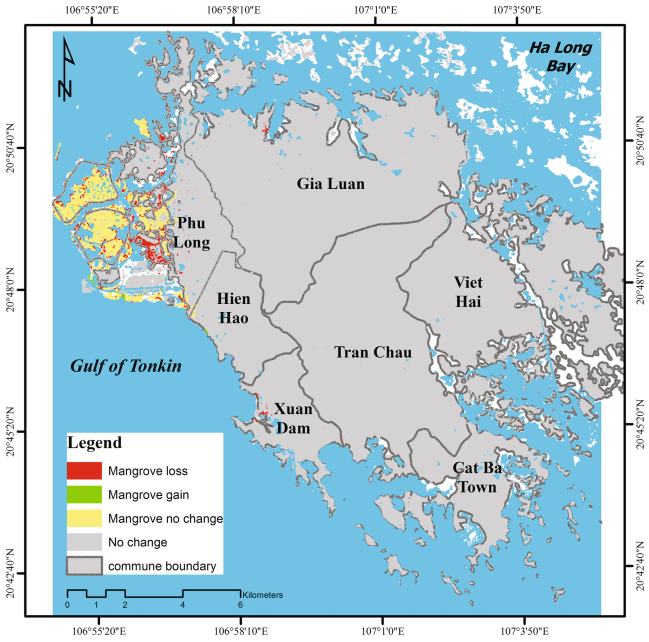

Fig. 6. Mangrove forests change map in the Cat Ba Biosphere Reserve from 2010 to 2015.

Mangrove forests in the Cat Ba Biosphere Reserve decreased by 14.6% from 2010 to 2015 (Table 3). It is likely due to over-shrimp aquaculture in the coastal area of Hai Phong. Mangrove forest areas converted to shrimp aquaculture from mangroves by local people in several communes of Cat Hai districts including the Cat Ba Biosphere Reserve [61].

Table 3. Mangroves changes in the Cat Ba Biosphere Reserve from 2010 to 2015.

Period	Onset of period (ha)	End of period (ha)	Change (ha)	% change
2010-2015	856 ± 32	731 ± 21	−125	−14.6

The analysis of mangrove changes from 2010 to 2015 using ALOS PALSAR data shows that the mangrove forests area in the Cat Ba Biosphere Reserve, Hai Phong has decreased slightly. However, mangrove area statistics showed significant differences among the three coastal communes of the Cat Ba Biosphere Reserve, Hai Phong (Table 4).

Table 4. Mangroves changes per commune in the Cat Ba Biosphere Reserve from 2010–2015.

Period	2010 (ha)	2015 (ha)	Change (ha)	Annual rate loss /gain rate (ha/year)
Phu Long	781.5	632.3	−149.2	−29.8
Gia Luan	45.9	79.0	33.1	6.6
Xuan Dam	28.6	19.7	−8.9	−1.8

Among the three coastal communes, mangrove forests area in Phu Long declined gradually. The annual rate of this loss was about 30 hectares. On the other hand, in Gia Luan, mangroves increased slightly. The annual rate of the gain was just 6.5 hectares. The statistic shows the potential use of ALOS PALSAR imagery in mapping spatial distribution of mangroves and providing a synoptic view of mangrove changes that can be used for prioritizing mangrove restoration and rehabilitation in the Cat Ba Biosphere Reserve. The findings of this study also update the statistical status of the mangroves ecosystem in one of the most well-known islands located on the Northern coast of Vietnam. Our research illustrates that ALOS PALSAR sensor together with a GIS-based SVM classifier provides the promising tool for mapping mangrove forest species and analyzing mangroves changes on a regional scale. This work is essential to support monitoring, reporting, and verification (MRV) work as part of United Nations' Reducing Emission from Deforestation and Forest Degradation (REDD+) program in the developing countries.

5 Conclusions

Overall, mangroves areas in the Cat Ba Biosphere Reserve, Vietnam have decreased at a low rate (15%) from 2010 to 2015. The statistical results of this research are important as a valuable reference to understand the current situation of mangrove forests in the Cat Ba Biosphere Reserve, Hai Phong city of Vietnam. As mangroves can significantly contribute to mitigating climate change impacts and their ecosystem can serve the local communities with ecological and economic services, the local government of Hai Phong city should plan necessary regulations and policies to monitor and conserve mangroves of the Biosphere Reserve.

The results of this study show that ALOS PALSAR data and SVM classifier technique can be used to map and assess mangroves changes along the coast of the Cat Ba Biosphere Reserve, Hai Phong, while a GIS can be employed to integrate ancillary information and spatial data of the mangrove forests in order to effectively monitor mangroves in the Cat Ba Biosphere Reserve, Vietnam.

The ALOS-2 PALSAR sensor used for 2015 provides higher overall accuracy and Kappa coefficient in mapping land-cover and mangrove forest than the ALOS PALSAR for 2010. The ALOS-2 produced the overall accuracy of 85% and the kappa coefficient of 0.81, compared with those of 81% and 0.77, respectively from the ALOS. Therefore, ALOS-2 PALSAR with high sensitive mode should be used for mapping and monitoring mangroves on national and regional scales. This research demonstrates the potential use of ALOS PALSAR data together with a GIS-based SVM algorithm for mapping mangroves and assessing their changes in coastal zones.

Acknowledgements. The authors would like to thank CARES (Centre for Agricultural Researches and Ecological Studies) of Vietnam National University of Agriculture (VNUA), Vietnam for providing spatial data for this research and logistical support during the fieldwork of this research. We are highly thankful to MEXT (Ministry of Education, Culture, Sports, Science, and Technology) of the Japanese Government for financial support to this study.

References

1. Giri, C., Ochieng, E., Tieszen, L.L., Zhu, Z., Shingh, A., Loveland, T.: Status and distribution of mangrove forests of the world using earth observation satellite data. Glob. Ecol. Biogeogr. **20**, 154–159 (2011)
2. Barbier, E.B., Cox, M.: An economic analysis of shrimp farm expansion and mangrove conversion in Thailand. Land Econ. **80**, 391–407 (2004)
3. Donato, D.C., Kauffman, J.B., Murdiyarso, D., Kurnianto, S., Stidham, M., Kanninen, M.: Mangroves among the most carbon-rich forests in the tropics. Nature Geosci. **4**, 293–297 (2011)
4. Kauffman, J.B., Heider, C., Norfolk, J., Payton, F.: Carbon stocks of intact mangroves and carbon emissions arising from their conversion in the Dominican Republic. Ecol. Appl. **24**, 518–527 (2013)
5. Alongi, D.M.: Present state and future of the world's mangrove forests. Environ. Conserv. **29**, 331–349 (2002)

6. FAO: The World's mangroves 1980–2005. A thematic study prepared in the framework of the Global Forest Resources Assessment 2005. Food and Agriculture Organization of the United Nations (2007)
7. Tuan, L.X., Munekage, Y., Dao, Q.T.Q., Tho, N.H., Dao, P.T.A.: Environmental management in mangrove areas. Environ. Inform. Arch. **1**, 38–52 (2003)
8. Conchedda, G., Durieux, L., Mayaux, P.: An object-based method for mapping and change analysis in mangrove ecosystems. ISPRS J. Photogramm. Remote Sens. **63**, 578–589 (2008)
9. Long, J.B., Giri, C.: Mapping the philippines' mangrove forests using landsat imagery. Sensors **11**, 2972–2981 (2011)
10. Lucas, R.M., Mitchell, A.L., Rosenqvist, A., Proisy, C., Melius, A., Ticehurst, C.: The potential of L-band SAR for quantifying mangrove characteristics and change: case studies from the tropics. Aquat. Conserv. Mar. Freshw. Ecosyst. **17**, 245–264 (2007)
11. Tien Dat, P., Yoshino, K.: Mangrove analysis using ALOS imagery in Hai Phong City, Vietnam, pp. 85250U-1–85250U-8 (2012)
12. Tong, P.H.S., Auda, Y., Populus, J., Aizpuru, M., Habshi, A.A., Blasco, F.: Assessment from space of mangroves evolution in the Mekong Delta, in relation to extensive shrimp farming. Int. J. Remote Sens. **25**, 4795–4812 (2004)
13. Thu, P.M., Populus, J.: Status and changes of mangrove forest in Mekong Delta: Case study in Tra Vinh Vietnam. Estuar. Coast. Shelf Sci. **71**, 98–109 (2007)
14. Tran, L.X., Fischer, A.: Spatiotemporal changes and fragmentation of mangroves and its effects on fish diversity in Ca Mau Province (Vietnam). J. Coast. Conserv., 1–14 (2017)
15. Béland, M., Goïta, K., Bonn, F., Pham, T.T.H.: Assessment of land-cover changes related to shrimp aquaculture using remote sensing data: a case study in the Giao Thuy District, Vietnam. Int. J. Remote Sens. **27**, 1491–1510 (2006)
16. Nguyen-Thanh, S., Chi-Farn, C., Ni-Bin, C., Cheng-Ru, C., Ly-Yu, C., Bui-Xuan, T.: Mangrove mapping and change detection in Ca Mau Peninsula, Vietnam, using landsat data and object-based image analysis. IEEE J. Sel. Top. Appl. Earth Obs. Remote Sens. **8**, 503–510 (2015)
17. Vo, Q., Oppelt, N., Leinenkugel, P., Kuenzer, C.: Remote Sensing in mapping mangrove ecosystems—an object-based approach. Remote Sens. **5**, 183 (2013)
18. Binh, T.N.K.D., Vromant, N., Hung, N.T., Hens, L., Boon, E.K.: Land cover changes between 1968 and 2003 in Cai Nuoc, Ca Mau Peninsula, Vietnam. Environ. Dev. Sustain. **7**, 519–536 (2005)
19. Lu, D.: The potential and challenge of remote sensing-based biomass estimation. Int. J. Remote Sens. **27**, 1297–1328 (2006)
20. Mas, J.F.: Mapping land use/cover in a tropical coastal area using satellite sensor data, GIS and artificial neural networks. Estuar. Coast. Shelf Sci. **59**, 219–230 (2004)
21. Rogan, J., Franklin, J., Stow, D., Miller, J., Woodcock, C., Roberts, D.: Mapping land-cover modifications over large areas: a comparison of machine learning algorithms. Remote Sens. Environ. **112**, 2272–2283 (2008)
22. Petropoulos, G.P., Arvanitis, K., Sigrimis, N.: Hyperion hyperspectral imagery analysis combined with machine learning classifiers for land use/cover mapping. Expert Syst. Appl. **39**, 3800–3809 (2011)
23. Kamusoko, C., Gamba, J., Murakami, H.: Mapping woodland cover in the miombo ecosystem: a comparison of machine learning classifiers. Land **3**, 524 (2014)
24. Wang, L., Silván-Cárdenas, J.L., Sousa, W.P.: Neural network classification of mangrove species from multi-seasonal ikonos imagery. Photogramm. Eng. Remote Sens. **74**, 921–927 (2008)

25. Petropoulos, G.P., Kalaitzidis, C., Prasad Vadrevu, K.: Support vector machines and object-based classification for obtaining land-use/cover cartography from Hyperion hyperspectral imagery. Comput. Geosci. **41**, 99–107 (2012)
26. Nemmour, H., Chibani, Y.: Multiple support vector machines for land cover change detection: an application for mapping urban extensions. ISPRS J. Photogramm. Remote Sens. **61**, 125–133 (2006)
27. Ustuner, M., Sanli, F.B., Dixon, B.: Application of support vector machines for landuse classification using high-resolution rapideye images: a sensitivity analysis. Eur. J. Remote Sens. **48**, 403–422 (2015)
28. Mountrakis, G., Im, J., Ogole, C.: Support vector machines in remote sensing: a review. ISPRS J. Photogramm. Remote Sens. **66**, 247–259 (2011)
29. Mai, T., Smith, C.: Addressing the threats to tourism sustainability using systems thinking: a case study of Cat Ba Island, Vietnam. J. Sustain. Tour. **23**, 1504–1528 (2015)
30. Le Viet, T., Choisy, M., Bryant, J.E., Vu Trong, D., Pham Quang, T., Horby, P., Nguyen Tran, H., Tran Thi Kieu, H., Nguyen Vu, T., Nguyen Van, K., Le Quynh, M., Wertheim, H. F.: A dengue outbreak on a floating village at Cat Ba Island in Vietnam. BMC Pub. Health **15**, 1–8 (2015)
31. Hoang, V., Lin, C.K.: Cat Ba National Park. Asian Institute of Technology, Bangkok (2001)
32. Pham, T.D., Yoshino, K.: Impacts of mangrove management systems on mangrove changes in the Northern Coast of Vietnam. Tropics **24**, 141–151 (2016)
33. Tachikawa, T., Kaku, M., Iwasaki, A., Gesch, D.B., Oimoen, M.J., Zhang, Z., Danielson, J. J., Krieger, T., Curtis, B., Haase, J.: ASTER global digital elevation model version 2-summary of validation results. NASA (2011)
34. JAXA: ALOS-2/PALSAR-2 Level 1.1/1.5/2.1/3.1 CEOS SAR Product Japan Aerospace Exploration Agency (2014)
35. Shimada, M., Isoguchi, O., Tadono, T., Isono, K.: PALSAR radiometric and geometric calibration. IEEE Trans. Geosci. Remote Sens. **47**, 3915–3932 (2009)
36. de Leeuw, M.R., de Carvalho, L.M.T.: Performance evaluation of several adaptive speckle filters for SAR imaging. Anais XIV Simpósio Brasileiro de Sensoriamento Remoto, pp. 7299–7305 (2009)
37. Hansen, M.C., Potapov, P.V., Moore, R., Hancher, M., Turubanova, S.A., Tyukavina, A., Thau, D., Stehman, S.V., Goetz, S.J., Loveland, T.R., Kommareddy, A., Egorov, A., Chini, L., Justice, C.O., Townshend, J.R.G.: High-resolution global maps of 21st-century forest cover change. Science **342**, 850 (2013)
38. Neha, J., Edward, T.A.M., Natalia, W., Jorge, T., Julian, M.-R., Andrea, E., Murray, C., Martin, R.J., Rasmus, F.: Mapping dynamics of deforestation and forest degradation in tropical forests using radar satellite data. Environ. Res. Lett. **10**, 034014 (2015)
39. Darmawan, S., Takeuchi, W., Vetrita, Y., Wikantika, K., Sari, D.K.: Impact of topography and tidal height on ALOS PALSAR polarimetric measurements to estimate aboveground biomass of mangrove forest in Indonesia. J. Sens. **2015**, 13 (2015)
40. Lucas, R., Armston, J., Fairfax, R., Fensham, R., Accad, A., Carreiras, J., Kelley, J., Bunting, P., Clewley, D., Bray, S., Metcalfe, D., Dwyer, J., Bowen, M., Eyre, T., Laidlaw, M., Shimada, M.: An evaluation of the ALOS PALSAR L-Band backscatter - above ground biomass relationship queensland, australia: impacts of surface moisture condition and vegetation structure. IEEE J. Sel. Top. Appl. Earth Obs. Remote Sens. **3**, 576–593 (2010)
41. Wang, Y., Hess, L.L., Filoso, S., Melack, J.M.: Understanding the radar backscattering from flooded and nonflooded Amazonian forests: results from canopy backscatter modeling. Remote Sens. Environ. **54**, 324–332 (1995)

42. Kasischke, E.S., Tanase, M.A., Bourgeau-Chavez, L.L., Borr, M.: Soil moisture limitations on monitoring boreal forest regrowth using spaceborne L-band SAR data. Remote Sens. Environ. **115**, 227–232 (2011)
43. Heumann, B.W.: An object-based classification of mangroves using a hybrid decision tree—support vector machine approach. Remote Sens. **3**, 2440–2460 (2011)
44. Kanniah, K., Sheikhi, A., Cracknell, A., Goh, H., Tan, K., Ho, C., Rasli, F.: Satellite images for monitoring mangrove cover changes in a fast growing economic region in Southern Peninsular Malaysia. Remote Sens. **7**, 14360 (2015)
45. Nong, D., Fox, J., Miura, T., Saksena, S.: Built-up area change analysis in hanoi using support vector machine classification of landsat multi-temporal image stacks and population data. Land **4**, 1213 (2015)
46. Huang, C., Song, K., Kim, S., Townshend, J.R.G., Davis, P., Masek, J.G., Goward, S.N.: Use of a dark object concept and support vector machines to automate forest cover change analysis. Remote Sens. Environ. **112**, 970–985 (2008)
47. EX User's: ENVI on-line software user's manual. ITT Visual Information Solutions (2008)
48. Pham, T.D., Yoshino, K., Bui, D.T.: Biomass estimation of Sonneratia caseolaris (l.) Engler at a coastal area of Hai Phong city (Vietnam) using ALOS-2 PALSAR imagery and GIS-based multi-layer perceptron neural networks. GISci. Remote Sens. **54**, 329–353 (2017)
49. Stehman, S.V.: Selecting and interpreting measures of thematic classification accuracy. Remote Sens. Environ. **62**, 77–89 (1997)
50. Jensen, J.R.: Introductory Digital Image Processing: A Remote Sensing Perspective. Prentice-Hall Inc., Upper Saddle River (1996)
51. Congalton, R.G., Green, K.: Assessing the accuracy of remotely sensed data - Principles and Practices. Lewis Publishers, New York (1999)
52. Tien Dat, P., Kunihiko, Y.: Characterization of mangrove species using ALOS-2 PALSAR in Hai Phong city, Vietnam. IOP Conf. Ser. Earth Environ. Sci. **37**, 012036 (2016)
53. Qiu, F., Berglund, J., Jensen, J.R., Thakkar, P., Ren, D.: Speckle noise reduction in SAR imagery using a local adaptive median filter. GISci. Remote Sens. **41**, 244–266 (2004)
54. Zhong, H., Li, Y., Jiao, L.: SAR image despeckling using bayesian nonlocal means filter with sigma preselection. IEEE Geosci. Remote Sens. Lett. **8**, 809–813 (2011)
55. Zhu, H.M., Zhong, W.Q., Jiao, L.C.: Combination of target detection and block-matching 3D filter for despeckling SAR images. Electron. Lett. **49**, 495–497 (2013)
56. Giri, C., Long, J., Abbas, S., Murali, R.M., Qamer, F.M., Pengra, B., Thau, D.: Distribution and dynamics of mangrove forests of South Asia. J. Environ. Manage. **148**, 101–111 (2015)
57. Richards, D.R., Friess, D.A.: Rates and drivers of mangrove deforestation in Southeast Asia, 2000–2012. Proc. Natl. Acad. Sci. **113**, 344–349 (2016)
58. Dat, P.T., Yoshino, K.: Monitoring mangrove forest using multi-temporal satellite data in the northern coast of Vietnam. In: The 32nd Asian Conference on Remote Sensing (2011)
59. Pham, T.D., Yoshino, K.: Mangrove mapping and change detection using multi-temporal landsat imagery in Hai Phong city, Vietnam. In: International Symposium on Cartography in Internet and Ubiquitous Environments 2015 (2015)
60. Seto, K.C., Fragkias, M.: Mangrove conversion and aquaculture development in Vietnam: a remote sensing-based approach for evaluating the Ramsar Convention on Wetlands. Glob. Environ. Change **17**, 486–500 (2007)
61. Dat, P.T., Yoshino, K.: Comparing mangrove forest management in Hai Phong City, Vietnam towards sustainable aquaculture. Proc. Environ. Sci. **17**, 109–118 (2013)

Detection and Prediction of Urban Expansion of Hanoi Area (Vietnam) Using SPOT-5 Satellite Imagery and Markov Chain Model

Trung Van Nguyen[1(✉)], Nam Van Nguyen[2,3], Ha Thu Thi Le[1], Hien Phu La[1], and Dieu Tien Bui[4]

[1] Faculty of Geomatics and Land Administration, Hanoi University of Mining and Geology, 18 Vien Street, Duc Thang Ward, Bac Tu Liem District, Hanoi City, Vietnam
nguyenvantrung@humg.edu.vn
[2] Faculty of Surveying and Mapping, Hanoi University of Natural Resources and Environment, 41A Phu Dien Street, Cau Dien Ward, Tu Liem District, Hanoi City, Vietnam
[3] Moscow State University of Geodesy and Cartography, MIIGAiK #4, Gorokhovsky Pereulok, 105064 Moscow, Russia
[4] GIS Group, Department of Business and IT, University College of Southeast Norway, Gullbringvegen 36, 3800 Bø i Telemark, Norway

Abstract. The main objective of this study is to detect and predict the urban area expansion at Hanoi, a typical urbanization city in Vietnam. For this purpose, firstly, temporal SPOT-5 images for years 2003, 2007, and 2011 were used to classify four land cover classes, open water, vegetation, barren, and residential area. Secondly, Impervious Surface Index (ISI) computed from the spectral bands of the above imagery. This index was then used to extract impervious surface information of the study area from residential area. Using the three derived land use/land cover maps, the area of land use/land cover types in the Hanoi area for years 2019 and 2027 were simulated and predicted using a Markov chain model. There results showed that the impervious surfaces of the Hanoi will increase 8.27% and 14.09% of total study area in 2019 and 2027, respectively. The results from this study provide valuable information to the local city planners in their urban planning and development.

Keywords: Hanoi city · Impervious surfaces · SPOT · Markov chain model · Urban

1 Introduction

Vietnam is considered as one of the countries that has the highest rate of urbanization in Southeast Asia due to the rapid development of economy [1]. The rate of urbanization is especially high for Hanoi and Ho Chi Minh cities where the population accounts for 16.8% (15 million people) of total population of the country [2]. For the case of Hanoi, the population increased from 3.2 million in 2003 to 6.3 million in 2007

© Springer International Publishing AG 2018
D. Tien Bui et al. (eds.), *Advances and Applications in Geospatial Technology and Earth Resources*, https://doi.org/10.1007/978-3-319-68240-2_8

[3] and to 7.216 million in 2015 with the urbanization rate is 49.1% [2]. The high rate of urbanization has resulted in complex problems such as reduced open space, environmental pollution, traffic overflows, and high pressure on the infrastructures [4]. Therefore, prediction of urban expansion for different future scenarios is highly necessary that helps the local planers useful information for their urban planning and development.

The aim of this study is to detect and predict the urban expansion in Hanoi area. For this purpose, SPOT-5 data for years 2003, 2007, and 2011 were used to derive four land cover classes, open water, vegetation, barren, and residential area. Since the sprawl of impervious surfaces may provide valuable information for planning urban in the future, therefore conversion from other LULC types to impervious surfaces was estimated. Accordingly, Impervious Surface Index (ISI) was also computed from the spectral bands of the above imagery, and then, the multi-temporal LULC maps, which include impervious surfaces, vegetation, open water, barren, and garden, were used for predicting LULC area types in future time.

In order to predict urban expansion, various method and techniques have been proposed such as knowledge experts, landscape metrics, agent based modelling, cellular automata, and machine learning [5]. However, Markov chain, a stochastic process system for predicting one status being changed to another known status [6]. has proven a powerful and effective for prediction of urban changes [7], and therefore, this model was selected for this study. The main advantage of this method is that it has ability to summarize and analyze the change in urban land-use where changes of transition are estimated intern of probabilities. These probabilities are employed to predict and discover possible situations of future urban land use changes and urban expansion patterns.

2 Study Area and Data

Hanoi city is the capital of Vietnam that lines between latitudes 20°30′30″N and 21°20′30′N, and longitudes 105°20′30″E and 106°05′30″E (Fig. 1). The city covers an area of about 3324.5 km^2 with the population of 7.216 million people in 2015 [2, 3]. The strong economic development has spurred expansions of industrial parks, urban construction and traffic system, and infrastructure for living people [8]. These are main causes of impervious surface expansion in this study area.

In this research, SPOT-5 images of Hanoi area in 2003, 2007 and 2011 (Table 1) were used. Acquisition dates of three SPOT-5 data were chosen with time step of 4 years for satisfying date requirement of Markov chain model. In addition, a land use map for the study area produced in 2010 at scale of 1:10,000 was provided by Center of Surveying and Map Data (COSAMD) was used. This map was used for evaluating the LULC maps derived from the aforementioned SPOT-5 images.

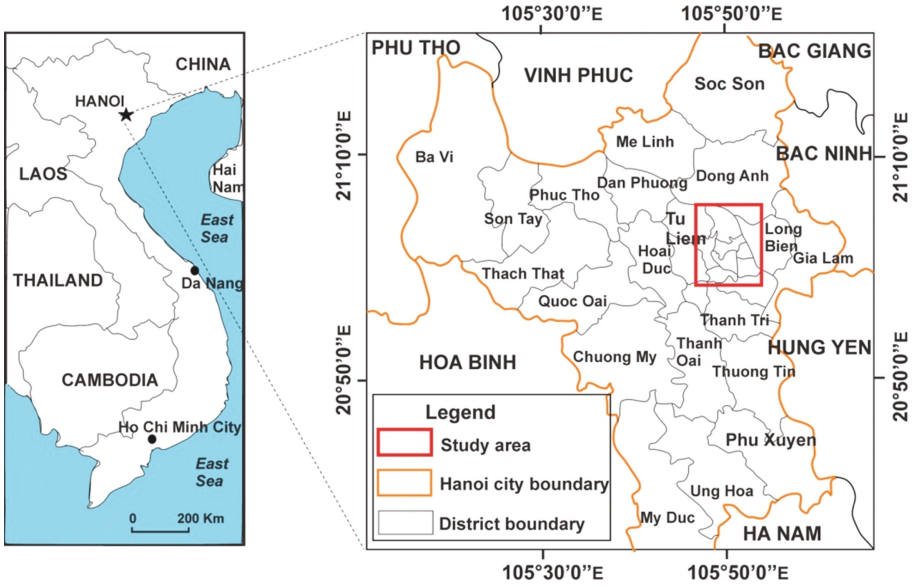

Fig. 1. Location of the study area, Hanoi city

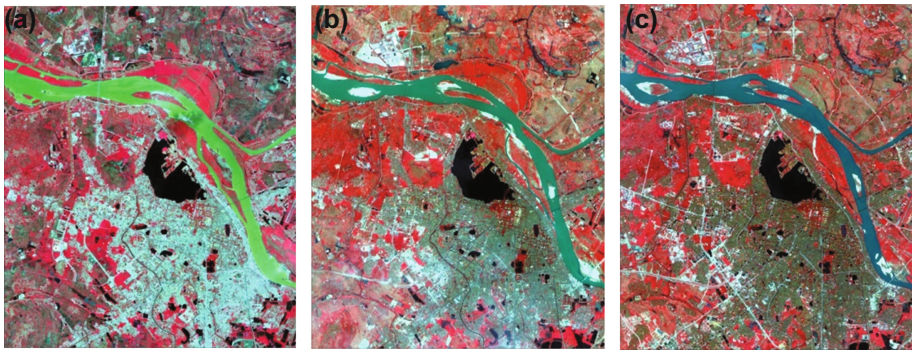

Fig. 2. SPOT-5 subset images of the study area: (a) 24/06/2003 (b) 21/08/2007 (c) 12/12/2011

Table 1. SPOT-5 satellite imagery used in this study

No.	Satellite	Sensor	Parth/Row	Date (dd/mm/yyyy)	Resolution (m)
1	SPOT-5	HRG	269/307	24/06/2003	10
2	SPOT-5	HRG	270/308	21/08/2007	10
3	SPOT-5	HRG	270/308	12/12/2011	10

3 Methodology

Methodological flowchart for this research consists of three main steps: (i) Object-oriented classification; (ii) Extraction of impervious surface; and (iii) Prediction of land use change based on Markov model (Fig. 3).

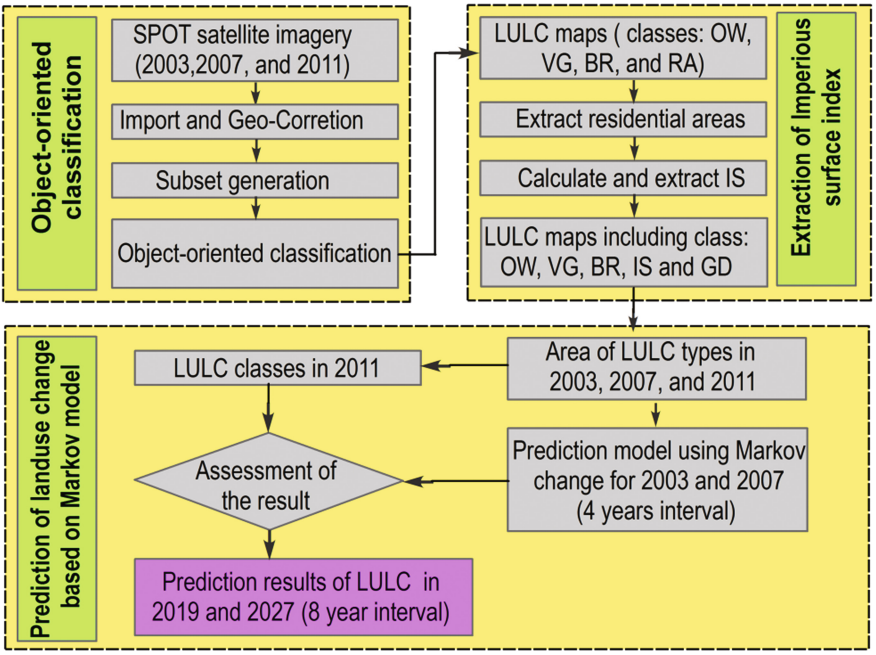

Fig. 3. Methodological flowchart for this research, OW: open water; VG: vegetation; BR: Barren; and RA: residential area.

3.1 Object-Oriented Classification

This step aims to derive four land cover classes, open water, vegetation, barren, and residential area for the three years 2003, 2007, and 2011 from the SPOT-5 data. Before the classification is conducted, a preprocessing process for these images was carried out. Because SPOT-5 images were acquired at level 1A, the SPOT-5 orbital Push-broom Model was used for geo-correcting SPOT-5 data with Ground Control Points (GCPs) derived from land use map at scale of 1:10,000. It should be noted that a digital elevation model for Hanoi was not used because this area is a quite flat. Then, these obtained images were projected to the UTM projection (VN2000) (Fig. 2). To solve the effects due to the different times of acquisition, the haze reduction and atmospheric correction for these images were also carried out. In the next step, the combination of homomorphic filter and the matching mean reflectance in both hazy/clear regions method was used for removing the haze of the SPOT-5 bands. As result, the surface reflectance images were retrieved by removing atmospheric effect by means of the retrieved aerosol

optical depth using MOTRAN 4.0 [9]. Finally, the contrast stretching and spatial filtering were used to enhance the quality of these images.

Once the preprocessing process has been completed, the object-oriented classification was carried out that includes multi-scale segmentation and classification steps. In the first step, the multi-scale segmentation was conducted for these SPOT-5 images using eCognition Developer 8.7 software [10]. The segmentation of the images into objects is based on three parameters: scale, shape, and compactness [11]. The scale directly affects the size of the segmentation objects, whereas, the shape value refers to the form and the structure of the individual objects and characterizes the spectral or spatial homogeneity of the resulting segmentation. Meanwhile, the compactness value is the ratio of an object's perimeter to the square root of the number of pixels within that image objects. This segmentation method is the most appropriate for the purpose of our work. For this research, the segmentations were conducted at a scale of 20, shape value of 0.3, and smoothness value of 0.5 and these values were found the best for the images data at hand.

Once the multi-scale segmentation has been completed, the classification of these image objects was carried out using hierarchical structures that describes the object's neighbor, its parent object, and its child objects. Features inherited from the parent object can transfer to the child objects. The user interacts with the procedure and based on statistics, texture, form and mutual relations among objects defines training areas. The classification of an object can then follow nearest neighbor method [12], and accordingly, each class of a classification scheme contains a class description. Each class description consists of a set of rule expressions allowing the evaluation of specific features and their logical operation. A rule can have one single condition or can consist of a combination of several conditions that have to be fulfilled for an object to be assigned to a class [13].

For this research, a total of four land cover classes including open water, vegetation, barren and residential area were identified based on the structural formation of the urban. Class rules for the objects were then developed using spectral signatures, shape, location and the contextual relationships of the objects. Samples for each class were selected from the image objects to act as training areas for the classification. Objects were assigned class rules using spectral signatures, shape and contextual relationships. The rules were then used as a basis for the classification of the data with the most probable/likely class being assigned to each object.

3.2 Extraction of Impervious Surface

In this section, four indicators including Soil Index (SI), Soil Adjusted Vegetation Index (SAVI), Normalized Difference Water Index (NDWI), Impervious Surface Index (ISI) were calculated as following [14]. To classify the four land cover classes, open water, vegetation, barren and residential area, the three indicators, SI, SAVI, and NDWI that computed from the spectral bands of the SPOT-5 imagery (Eqs. 1, 2, and 3) were then used to assign classes based on the rules. The Impervious Surface Index (ISI) derived from the spectral bands of the SPOT-5 imagery and NDVI (Eq. 5) was then used to extract impervious surface information of the study area from residential

area. Remaining part of residential area after extracting impervious surface was the garden area.

$$\mathrm{SI} = (\mathrm{GREEN} - \mathrm{BLUE})/(\mathrm{GREEN} + \mathrm{BUE}) \tag{1}$$

where GREEN is spectral value of green band and BLUE is spectral value of blue band.

The soil adjusted vegetation index (SAVI) was used in this research because it could remove contamination associated with bare soil [15].

$$\mathrm{SAVI} = [(\mathrm{NIR} - \mathrm{RED})(1 + l)]/(\mathrm{NIR} + \mathrm{RED} + l) \tag{2}$$

where l = soil adjusted factor ranging from 0 and 1, however, in this research, we chose 0.5 to eliminate the impact of different background; RED is spectral value of red band; NIR is spectral value of near-infrared band.

Normalized difference water index (NDWI) was used because the SPOT data include both GREEN and NIR band. NDWI is calculated using equation as follows [16].

$$\mathrm{NDWI} = (\mathrm{GREEN} - \mathrm{NIR})/(\mathrm{GREEN} + \mathrm{NIR}) \tag{3}$$

where GREEN is spectral value of green band; NIR is spectral value of near-infrared band.

Impervious Surface Index (ISI) was introduced by [14] using four bands for each SPOT image (B1, B2, B3, and B4), and the offset Ij (I1, I2, and I3) available at the acquired SPOT images:

$$\mathrm{ISI} = a_0 + I_j + a_1 \cdot PC_1 + a_2 \cdot PC_2 + a_3 \cdot PC_3 + a_5 \cdot PC_5 \tag{4}$$

where a_i (i = 1, 2, .., 5) are the coefficients of principal components calculated from the four bands (B_1, B_2, B_3, and B_4) of the SPOT data and Normalized Different Vegetation Index (NDVI) in Eq. 5 [14].

$$\mathrm{NDVI} = (\mathrm{B3} - \mathrm{B2})/(\mathrm{B3} + \mathrm{B2}) \tag{5}$$

In order to extract impervious surfaces areas, a threshold of ISI was chosen to extract impervious surface area within residential area. The remained area of the residential area was used as a garden class. Finally, land cover maps for 2003, 2007 and 2011 consisting of open water, vegetation, barren, impervious surfaces, and garden classes were constructed.

3.3 Markov Chain Model for Predicting Land Use Change

Markov chain model is a popular method used to predict temporal land use change [17]. In the Markov chain model, a stochastic process could be used to generate sequences of random variables [18] by probabilistic laws. The process is considered discrete in time, such as T = 0, 4, 8 … years, which is considered a reasonable time interval for studying LULC change phenomenon. If the stochastic process follows a

Markov process then the sequence of random variables could be generated using the Markov property as in Eq. 6 below:

$$P[X_{n+1} = a_{in+1} | X_0 = a_{i0}, \ldots, X_{in} = a_{in}] = P[X_{in+1} = a_{in+1} | X_{in} = a_{in}] \quad (6)$$

where the double index (*in*) means, and in this study, for n ∈T with T = 0, 4, 8,… years; i = 5, a_i is the LULC class.

When the range of possible values for a_i is either finite or infinite denumerable, as in this study, the Markov process may be referred as a Markov chain. Therefore, one must prove that there is a statistical dependence between X_{n+1} and X_n (Eq. 7); and that statistical dependence is a first-order Markov process (Eq. 8).

$$P(X_n = a_n | \ X_{n-1} = a_{n-1}) \neq P(X_n = a_n) * P(X_{n-1} = a_{n-1}) \quad (7)$$

$$P[X_n = a_n | X_{n-1} = a_{n-1}] = P[X_n = a_n, X_{n-1} = a_{n-1}] / P[X_{n-1} = a_{n-1}] \quad (8)$$

A first-order Markov process is a Markov process where the transition from a class to any other does not require intermediate transitions to other states. The statistical dependence can be tested as in any contingency table [18] displaying the LULC change between X_n and X_{n-1}. In our study, this test was performed for the LULC change between 2007 and 2011. To infer from the association or independence between the LULC classes in different years from the contingency table, the random variable, with the chi-square distribution will be defined by Eq. 9:

$$\chi^2 = \sum_i \sum_j \frac{(O_{ij} - E_{ij})^2}{E_{ij}} \quad (9)$$

where *O* is the contingency matrix displaying the LULC change between 2007 and 2011, and *E* the contingency matrix with the expected values of change assuming the independence hypotheses [19]. χ^2 measures the distance between the observed values of LULC change and the expected ones assuming independence and must be high enough to prove Eq. 9, for 5° of freedom.

4 Results and Discussion

4.1 Landuse/Landcover Classification and Accuracy Assessment

For accuracy assessment of LULC map classified from the SPOT-5 images, the Land use map at scale of 1/10000 provided by COSAMD was used. 187, 276, 274 and 307 random pixels were chosen for four land cover classes consisting of open water, vegetation, barren and residential area, respectively. The summary of the accuracy assessment for LULC map in 2003, 2007 and 2011 was shown in Tables 2, 3, and 4, respectively. It was found that the accuracy of the open water class was the highest among the four land cover classes (both Producer's and User's accuracy were approximately 90%) because open water is very hemogeneous. However, the accuracy of residential area was lowest, this

Table 2. Accuracy assessment report of LULC map on 24/06/2003

Samples		Reference				Row total	Producer's accuracy
		Open water	Vegetation	Residential area	Barren		
Generated	Open water	171	9	0	7	187	0.91
	Vegetation	11	231	16	18	276	0.84
	Residential area	6	32	208	28	274	0.76
	Barren	2	8	45	252	307	0.82
Column total		190	280	269	305	1044	
User's accuracy		0.90	0.83	0.77	0.83		
Overall accuracy		0.83					
Kappa index		0.77					

Table 3. Accuracy assessment report of LULC map on 21/08/2007

Samples		Reference				Row total	Producer's accuracy
		Open water	Vegetation	Residential area	Barren		
Generated	Open water	172	8	0	7	187	0.92
	Vegetation	12	229	16	19	276	0.83
	Residential area	6	31	210	27	274	0.77
	Barren	2	9	46	250	307	0.81
Column total		192	277	272	303	1044	
User's accuracy		0.90	0.83	0.77	0.83		
Overall accuracy		0.82					
Kappa Index		0.76					

could be due to mixing between vegetation, barren and impervious surfaces (both Producer's and User's accuracy were approximately 76%).

Although, it is difficult to classify land cover classes of the urban area because of the mixing between vegetation, barren and impervious surfaces, and the conversion between land use depending on the time during the development period of city. The Kappa index of all land cover maps assessed was from 0.76 to 0.77. Meanwhile, the overall accuracy ranged from 0.82 to 0.83. These demonstrated the reliability of the classified maps.

Based on the LULC maps derived from object-oriented classification and ISI computed from SPOT-5 data of Hanoi area, final LULC maps for 2003, 2007 and 2011

Table 4. Accuracy assessment report of LULC map on 12/12/2011

Samples		Reference				Row total	Producer's accuracy
		Open water	Vegetation	Residential area	Barren		
Generated	Open water	173	8	0	6	187	0.93
	Vegetation	10	232	15	19	276	0.84
	Residential area	7	30	207	30	274	0.76
	Barren	3	8	43	253	307	0.82
Column total		193	278	265	308	1044	
User's accuracy		0.90	0.83	0.78	0.82		
Overall accuracy		0.83					
Kappa Index		0.77					

were established as shown in Fig. 4. Then the area of open water, vegetation, barren, impervious surfaces and garden were calculated and shown in Table 5. The changes of area by LULC classes were illustrated Fig. 5. It can be seen that the area of impervious surfaces increased dramatically from 6125.10 ha (21.30% of total area) in 2003 to 8426.88 ha (29.30% of total area) in 2007, and to 10525.21 ha (36.60% of total area) in 2011. Whereas, the area of vegetation decreased gradually from 10658.67 ha (37.07% of total area) to 9301.15 ha (32.34% of total area) in time period of 2003 to 2011. The same pattern can be seen for the area of garden reducing from 4760.47 ha in 2003 to 1964.33 ha in 2011. Meanwhile, area of barren and open water was almost steady. This indicated that vegetation and garden was mainly converted to impervious surface in the period of 2003 and 2011.

To generate map of change from four LULC classes (i.e. open water, vegetation, barren, and garden) to impervious surface, the LULC maps in 2003 and 2011 were superimposed by using ArcGIS software. The change of each class was represented by one different color for distinguishing one class among others classes as shown in Fig. 6.

Besides the visualization, the determination of land cover area changes from the land cover classes and impervious surfaces area between 2003 and 2011 was computed and shown in Table 6. From 2003 to 2011, the main changed area is from garden to impervious surfaces, which was changed about 3142.207 ha. This changed area was represented by red color area in Fig. 6. Besides, the vegetation and barren area transferred to vegetation area were about 882.47 ha and 340.19 ha, respectively.

According to Table 6 and Fig. 7, there was a lot changes among land cover classes from 2003 to 2011, but we only considered the increased area of impervious surfaces caused by changing from vegetation, open water, barren, and garden area. The percentage of change of vegetation, barren, open water, and garden area corresponding to the increased area of impervious surfaces was about 8.28% of total vegetation area, 10.27% of total barren area, 1.91% of total open water, and 66.01% of total garden area, respectively. This means that the change from garden area to impervious surfaces

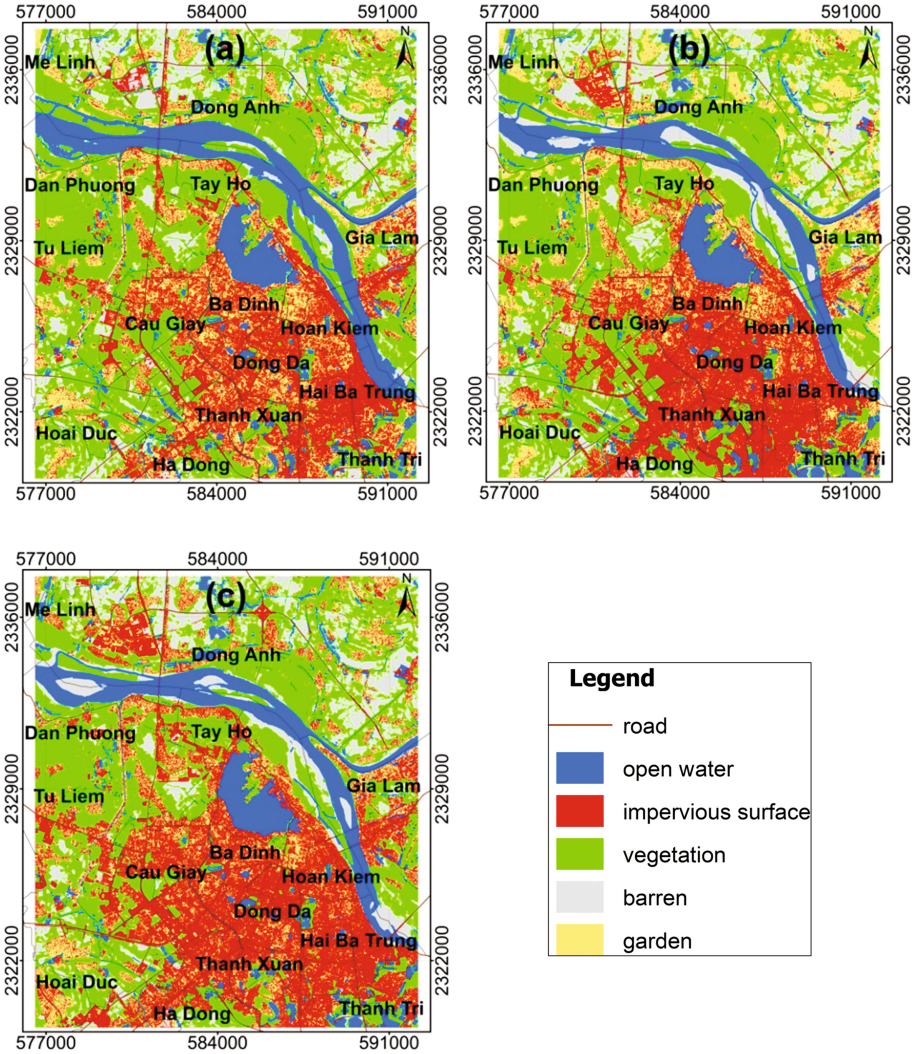

Fig. 4. LULC and impervious surfaces maps for different year: (a) year of 2003, (b) year of 2007, and (c) year of 2011

was dominant change for urbanization in Hanoi area. It may be explained that the policy of land use planing for urban in this period was the conversion of agricultural land to other land use classes.

4.2 Prediction Based on Markov Chain Model

4.2.1 Modelling Results and Validation

In this study, the Markov model was performed using IDRISI Selva® software, version 17.0. To validate the model, the simulated LULC types need to be compared with

Table 5. LULC types and impervious surfaces area extracted from the SPOT data for the study area

Land cover	2003		2007		2011	
	ha	%	ha	%	ha	%
Open water	3899.77	13.56	3529.06	12.27	3465.95	12.05
Impervious surfaces	6125.10	21.30	8426.88	29.30	10525.21	36.60
Vegetation	10658.67	37.07	10157.38	35.32	9301.15	32.34
Barren	3312.35	11.52	3762.43	13.08	3499.72	12,17
Garden	4760.47	16.55	2880.61	10.02	1964,33	6.83
Total	**28756.36**	**100**	**28756.36**	**100**	**28756.36**	**100**

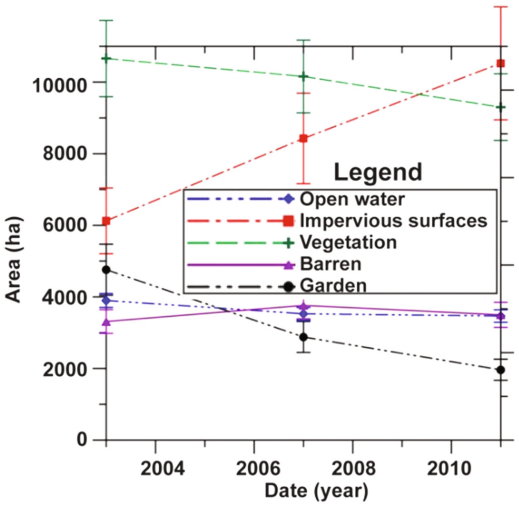

Fig. 5. LULC and impervious surfaces changes

actual area. Therefore, the simulated LULC types of 2011 generated from LULC maps in 2003 and 2007 with time step of 4 years was compared with the land use in 2011 classified from SPOT-5 image acquired in 2011. For this purpose, χ^2 test expressed as Eq. 10 was used in order to ensure suitability of the model. The test results were as follows (see Table 7):

$$\chi^2 = \sum \frac{(O-E)^2}{E} = 1.88 \tag{10}$$

According to Table 7, there was no significant difference between simulated value and actual value (1.88 is much smaller than 11.01). Therefore, Markov chain model can be used for predicting LULC types in Hanoi area.

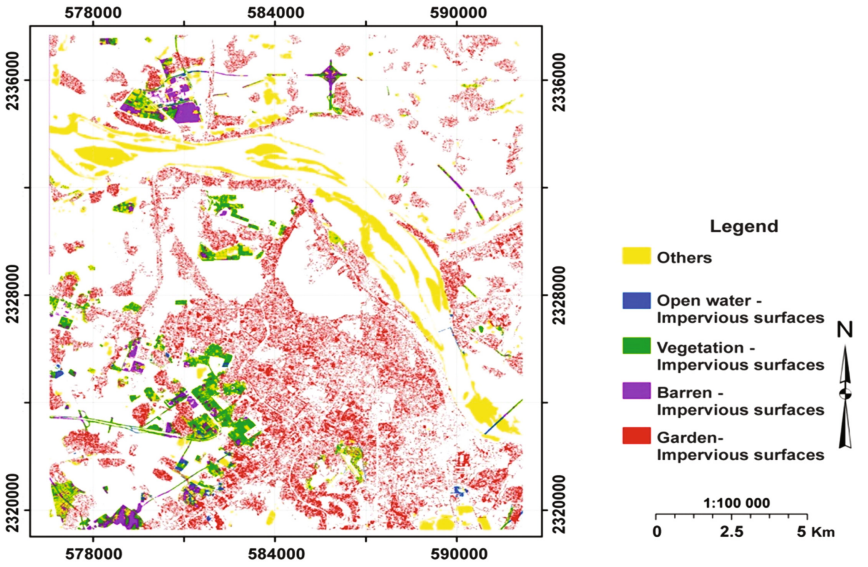

Fig. 6. Map of change from LULC to impervious surfaces between 2003 and 2011

Table 6. Change of LULC types to impervious surfaces between 2003 and 2011

2011	2003					
	Open water (ha)	Impervious surfaces (ha)	Vegetation (ha)	Barren (ha)	Garden (ha)	Total of 2003 (ha)
Open water	**3180.82**	74.59	49.39	583.02	11.95	**3899.77**
Impervious surfaces	15.96	**6085.76**	10.53	10.53	2.32	**6125.10**
Vegetation	171.07	882.47	**9221.28**	92.36	291.49	**10658.67**
Barren	91.07	340.19	7.97	**2807.94**	65.18	**3312.35**
Garden	7.03	3142.20	11.98	5.87	**1593.39**	**4760.47**
Total of 2011	**3465,95**	**10525.21**	**9301.15**	**3499.72**	**1964.33**	**28756.36**

4.2.2 Prediction of LULC Types in 2019 and 2027

Based on LULC maps in 2003 and 2011, the Markov chain model with time step of 8 years were used for predicting LULC types in 2019 and 2027. The results were shown in Table 8. According to Table 8, the increased area of impervious surfaces in 2019 and 2027 were about 8.27% and 14.09% of total study area, respectively due to the conversion from vegetation (4.09% and 7.64% of total study area, respectively) and open water (1.26% and 2.33% of total study area, respectively) and garden (3.22% and 4.46% of total study area, respectively). Besides, there was a little increase in area of barren could be due to loss of vegetation and open water caused by changing the

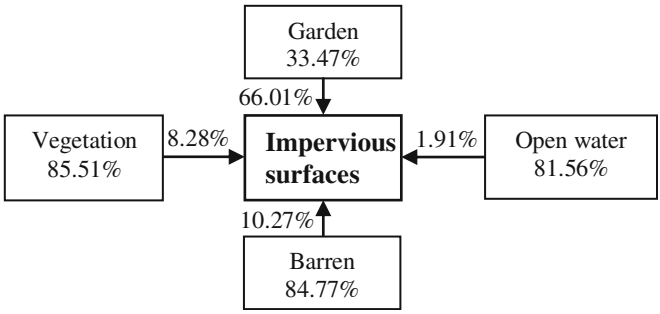

Fig. 7. Percentages of LULC transforming into impervious surfaces between 2003 and 2011

Table 7. Validation of LULC change forecast based on Markov chain model

LULC types	Chi-square test				
	Simulate value (O)	Actual value (E)	(O-E)	$(O-E)^2$	$(O-E)^2/E$
Open water	32.23	34.65	−2.42	5.87	0.17
Impervious surfaces	99.32	105.25	−5.93	35.18	0.33
Vegetation	96.82	93.01	3.81	14.56	0.15
Barren	41.16	34.99	6.17	38.08	1.09
Garden	18.01	19.64	−1.63	2.66	0.13
Total	**287.56**	**287.56**	**0**	**96.37**	**1.88**

Note: 5 degrees of freedom, χ^2 0.05 (5) = 11.01

Table 8. Trend of LULC changes simulated by Markov chain model in 2019 and 2027.

Year	LULC types					
	Open water (ha)	Impervious surfaces (ha)	Vegetation (ha)	Barren (ha)	Garden (ha)	Total (ha)
2003	3899.77	6125.10	10658.67	3312.35	4760.47	28756.36
2011	3465.95	10525.21	9301.15	3499.72	1964.33	28756.36
2019	3102.92	12902.69	8124.79	3586.95	1038.98	28756.36
2027	2795.15	14576.65	7103.02	3600.14	681.34	28756.36

purpose of land use. Those conversions among LULC types can be valuable information for the urban planning in Hanoi area.

5 Conclusion

In this study, the three SPOT images acquired in 2003, 2007 and 2011 were used to classify and extract the land cover classes consisting of vegetation, barren, open water, garden and impervious surfaces. The overall accuracy and Kappa index of all land

cover maps assessed were ranged from 0.76 to 0.77. Meanwhile, the overall accuracy ranged from 0.82 to 0.83. The impervious surfaces area has increased about 15.30% of total study area from 2003 to 2011 due to urban development. The main conversion was from garden to impervious surfaces area with the converted area was about 10.93% of total study area. The validation of the Markov chain model used to simulate LULC types in 2011 showed that Chi-square test was about 1.88 satisfied requirement of 5 degrees (χ^2 0.05 (5) = 11.01). Therefore, land cover maps in 2003 and 2011 were used to predict LULC types in 2019 and 2027 with time step of 8 years. The prediction indicated that there could be a significant expansion of impervious surfaces area in 2019 and 2027 with the expandable area of 8.27% and 14.09% of total study area, respectively. Those changes of LULC types revealed the trend of land use conversion, which may be caused by the policy of city administration.

References

1. Gregg, H., Angeles, L.: Globalization, industrialization and urbanization in pre-world War II Southeast Asia. Explor. Econ. Hist. **48**, 20–36 (2011)
2. Vu, M.H., Kawashima, H.: Effects of urban expansion on suburban farmers' livelihood in Vietnam: a comparative analysis of Ho Chi Minh City and Hanoi. Habitat Int. **65**, 49–58 (2017)
3. Hanoi Statistical Office: Hanoi Statistical Yearbook. Statistics Publishing House (2003, 2007 and 2011)
4. Park, S., Jeon, S., Kim, S., Choi, C.: Prediction and comparison of urban growth by land suitability index mapping using GIS and RS in South Korea. Landscape Urban Plan. **99**, 104–114 (2011)
5. Jat, M.K., Choudhary, M., Saxena, A.: Urban growth assessment and prediction using RS, GIS and SLEUTH model for a heterogeneous urban fringe. Egypt. J. Remote Sens. Space Sci. (2017). In Press, Corrected Proof
6. Muller, M.R., Middleton, J.: A Markov model of land-use change dynamics in the Niagara Region, Ontario. Can. Landscape Ecol. **9**, 151–157 (1994)
7. Yang, X., Zheng, X.Q., Lv, L.N.: A spatiotemporal model of land use change based on ant colony optimization, Markov chain and cellular automata. Ecol. Model. **233**, 11–19 (2012)
8. Hanoi Statistical Office: General inventory results of the census, economic, administrative and professional establishments (2007)
9. Chen, W.T., Zhang, Z., Wang, Y.X., Wen, X.P.: Atmospheric Correction of SPOT5 land surface imagery. In: 2nd International Congress on Image and Signal Processing. IEEE, Tianjin (2009)
10. Trimble: eCognition Developer 8.7: User Guide. Trimble Germany GmbH, Trappentreustr. 1, D-80339 München, Germany (2011)
11. Willhauck, G., Schneider, T., De Kok, R., Ammer, U.: Comparison of object-oriented classification techniques and standard image analysis for the use of change detection betweeen SPOT multispectral satellite images and aerial photos. In: XIX ISPRS Congress (2000)
12. Manakos, I.: eCognition and Precision Farming. eCognition Application Notes 2, (2001)

13. Mitri, G.H., Gitas, I.Z.: The development of an object-oriented classification model for operational burned area mapping on the Mediterranean island of Thasos using LANDSAT TM images. In: Viegas, D.X. (ed.) Forest Fire Research & Wildland Fire Safety. Millpres, Rotterdam (2002)
14. Pairman, D., McNeill, S., Belliss, S.: Impervious surface mapping for the auckland region. Prepared by Landcare Research for Auckland Regional Council (2010)
15. Huete, A., Justice, C., Liu, H.: Development of vegetation and soil indexes for MODIS-EOS. Remote Sens. Environ. **49**, 224–234 (1994)
16. Hanqiu, X.: Modification of normalized difference water index(NDWI) to enhance open water feature in remotely sensed imagery. Int. J. Remote Sens. **27**, 3025–3033 (2006)
17. Zheng, H.W., Shen, G.Q., Wang, H., Hong, J.: Simulating land use change in urban renewal areas: A case study in Hong Kong. Habitat Int. **46**, 23–34 (2015)
18. Murteira, B.: Probabilidades e estatística. McGraw-Hill Portugal (1990)
19. Cabral, P., Zamyatin, A.: Markov processes in modeling land use and land cover changes in Sintra-Cascais, Portugal. DYNA **76**, 191–198 (2009)

Analysis of Land Cover Changes in Northern Vietnam Using High Resolution Remote Sensing Data

Thanh Tung Hoang[1(✉)], Kenlo Nishida Nasahara[2], and Jin Katagi[2]

[1] Viet Nam Institute of Meteorology, Hydrology and Climate Change, Hanoi, Vietnam
hoangthanhtung.kttv@gmail.com
[2] University of Tsukuba, Tsukuba, Japan

Abstract. This study attempts to produce 15-meter resolution land cover maps over Northern Vietnam in 2007 and 2015 using multi-temporal and multi-sensor data including ASTER, Landsat, and PALSAR mosaic based on a kernel-based probabilistic classification method. Other ancillary such as SuomiNPP nightlight image, OpenStreetMap road network and SRTM30 were applied for additional information supplement. A number of about 60,000 reference data was built by field GPS photos as well as visual interpretation using Google Earth for training and validation. Results showed that the overall accuracy of the land cover maps is 81% and 89% in 2007, 2015 respectively. The results indicated many changes in areas of land cover types between 2007 and 2015 in Son La hydropower dam area and in selected sites for forest gain detection. The analysis showed that water area demonstrated an increasing trend while cropland area presented a decreasing trend in Son La hydropower dam area; and forest area experienced a rising trend whereas grassland area indicated a declining trend in the other selected sites. The results introduced a new high-resolution regional land cover data in Northern Vietnam for environmental modeling or other regional studies.

Keywords: Land cover · Kernel density estimation · Multi-temporal · High resolution · High accuracy · Northern Vietnam

1 Introduction

As a vital component of Earth ecosystem, land cover plays an important role in various ranges including climate and hydrological modelling, biogeochemical cycling studies, environmental protection, biodiversity conservation, resource management and the complex interactions between human activities and global changes [1–3, 37]. Land cover products, therefore, have become an indispensable input in Earth sciences' applications such as climate modelling [4–6], greenhouse gases emissions [7], carbon cycle [8–10], biomass modelling [11–13], hydrological modelling [14], land erosion [15], biodiversity [16], and disaster [17].

Changing in land cover is one of the most important factors of environmental variability. From the time of industrial revolution, natural resources exploitation for

© Springer International Publishing AG 2018
D. Tien Bui et al. (eds.), *Advances and Applications in Geospatial Technology and Earth Resources*, https://doi.org/10.1007/978-3-319-68240-2_9

development caused enormous changes in the Earth surface and its environment [18]. Consequently, anthropogenic modifications of land cover had feedback impacts on our ecosystems, especially in biodiversity loss, carbon emission increase, surface albedo change and their implications such as climate change. Newbold (2015) [16] found out that 8.1% species richness on average globally has been reduced because of land use change and the richness is projected to fall by a further 3.4% globally by 2100. On the other hand, Houghton (2010) [9] and Shevliakova et al. (2009) [10] revealed that the land use and land cover change caused a gradually increasing trend in carbon emissions, from $\sim$0.6 PgC yr^{-1} in 1850 to $\sim$1.3 PgC yr^{-1} in the period 1950–2005. The fifth report of Intergovernmental Panel on Climate Change [19] showed that surface albedo variability caused by land cover, land use change contributed a negative radiative forcing of -0.15 Wm^{-2}. Likewise, change in albedo could lead to change in surface energy, moisture budget, atmospheric circulation and temperature.

Global land cover map production is presently facing two main challenges which are coarse spatial resolution and disagreement between the products. Validation works demonstrated that among the original global land cover data set, MODIS show highest accuracy at 78.3% [1], then the accuracy of GLC2000, GlobCover and IGBP-DISCover were 68.6% [20], 67.5% [21], 66.9% [22] respectively. The highest resolution (30 m) land cover map named FROM-GLC reached only 64.9% of accuracy [3].

Northern Vietnam has experienced large modification in land use/land cover over the last decade due to forest plantation, transformation of land use purposes, building infrastructure and urbanization. Vietnam's Country report on Forest Resources Assessment of Food and Agriculture Organization of the United Nations (FAO) (2015) [23] documented that forest are in Vietnam increased 1.696 million hectares (from 13.077 mil hectares in 2005 to 14.773 mil hectares in 2015). Other researches gave the proofs that the main cause of the forest gain was forest and rubber plantation in the North and the Central of Vietnam [24, 25]. On the other hand, the construction of the largest hydropower plant in Southeast Asia caused 7670 ha agricultural land and 3170 ha forest to be under water level in the basin [26].

Previous researches on land cover mapping in the study area mainly used multi-temporal medium resolution data from MODIS [27] or ADEOS II – GLI [28]. However, it is difficult to analyze the changes of land use/land cover in such highly heterogeneous Northern Vietnam with 250 m resolution data like MODIS or ADEOS II – GLI. It is thus of an essential need to produce land cover maps with higher accuracy and resolution.

The purpose of this study is to produce 15-meter resolution and high accuracy land cover maps in over Northern Vietnam in 2007 and 2015 using multi-temporal and multi-sensor data. The change between the two years was then analyzed to see the land cover dynamics in the recent decade, focusing on forest gain and the land cover changes in the Son La hydropower reservoir area.

2 Methods

2.1 Study Area

The study area is Northern Vietnam, located in the range from $102^0 8'41''$E to $108^0 4'12''$E of longitude and from $19^0 17'15''$N to $23^0 23'35''$N of latitude (Fig. 1a). The study area covers about 127,200 km^2 with a variety of landscapes such as delta, hill lands, mountainous area, mountainous highland, coastal zone. Topography is characterized by the Red River Delta and other small coastal deltas in the south-eastern and high mountain ranges in the north and north-western. According to Köppen climate classification, the entire territory of Northern Vietnam belongs to humid subtropical climate strata with hot and humid summers and cold winters. Such seasonal variation of climate performs essential control to agricultural calendar over the region. The Red River Delta is the second largest delta in Vietnam, which covers about 15,000 km^2, in which about 11,000 km^2 is recorded as paddy (https://www.gso.gov.vn). This region also includes remarkable orchard areas in intensively cultivated land allocating mainly in hill lands in the north of Red River Delta and within Red River Delta. The dominant forest type in terms of biophysical aspect is evergreen broadleaf forest while bamboo, deciduous and needleleaf vegetation were recorded in a small percentage.

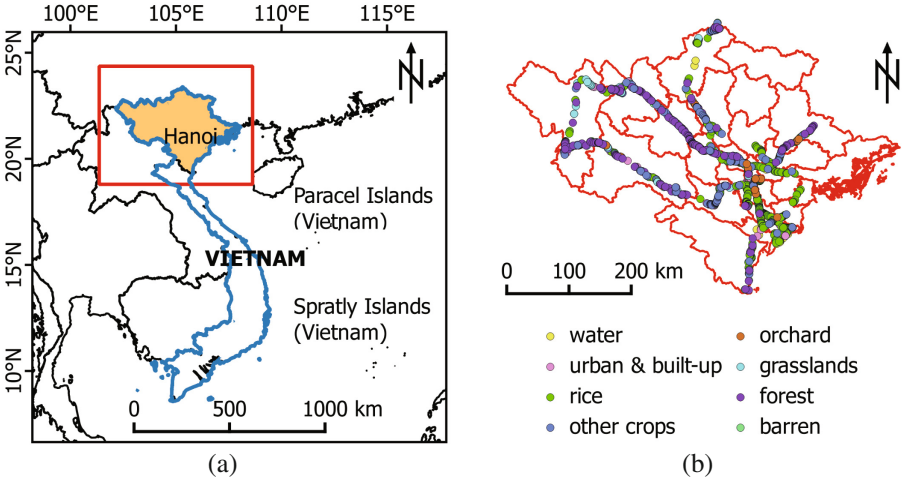

Fig. 1. **(a)** Study area **(b)** Distribution of field survey reference data

2.2 Data Used

The input data includes multi-temporal and multi-sensor satellite imagery (Table 1). All multi-temporal data were selected within one-year period which is either during 2007 or during 2015. We used Surface Reflectance products of 140 Landsat-5 TM scenes in 2007 and 199 Landsat-8 OLI scenes in 2015 available at United States Geological Survey (USGS) EarthExplorer. Since basic atmospheric corrections and

geometric corrections are already included in this high level product, the Landsat images are ready to use after cloud removal. ASTER data including 55 images in 2007 and 68 images in 2015 were retrieved freely at MADAS system from the National Institute of Advanced Industrial Science and Technology (AIST), Japan. The source provides ASTER-VA product which already included ortho-rectification processing. PALSAR mosaic (2007) and PALSAR-2 mosaic (2015) were obtained from JAXA Earth Observation Research Center (EORC). Synthetic Aperture Radar (SAR) imagery's characteristics such as cloud-free, sensitive to moisture of surface and multi-backscattering mechanisms facilitate to exploit more information, which can hardly be observed in optical data. After estimating the backscattering coefficient from original data, slope effect areas were masked using the mask files included in downloaded data. Then the gaps created from the masking process were filled using the nearest neighbor technique.

Table 1. Characteristics of data used

Data	Provider	Quantity (scene)	Time (year)	Band	Resolution (m)	Advantage
Landsat-8 OLI	USGS	199	2015	2,3,4,5 (VNIR)	30	High temporal resolution
Landsat-5 TM	USGS	140	2007	1,2,3,4 (VNIR)	30	High temporal resolution
ASTER-VA version	AIST	68	2015	1,2,3n (VNIR)	15	High spatial resolution
		55	2007			
PALSAR mosaic	JAXA	1	2015	HH,HV	25	Cloud-free
PALSAR-2 mosaic		1	2007			
SRTM30	NASA	1	–	–	30	Information on topography
Suomi NPP	NOAA	1 (averaged)	2015		500	Urban detecting
Open street map	OSMF	1	–	–	30	Human activity

For ancillary data, we used SRTM30 data to calculate slope in order to making use of topography information. Other ancillary data such as 500 m night-time light SuomiNPP and OpenStreetMap were employed to enhance the detection capability by using presence of human activities' information derived from night-time light and road network. SuomiNPP images acquired from National Oceanic and Atmospheric Administration (NOAA) were averaged to make a representative composite image and reduce cloud contamination. OpenStreetMap (OSM) road network were used to create a rasterized distance map to road network using gdal_proximity.py function in GDAL library. Pixel value of the distance map presents the shortest distance to road network. For geometric system consistency purpose, all the input data was converted to the Geographic Coordinates System with WGS84 datum (EPSG 4236). The preprocessing

was carried out using Geographic Resources Analysis Support System (GRASS) GIS version 7.0 and QGIS version 2.14 and Geospatial Data Abstraction Library (GDAL).

2.3 Training and Validation Data

Reference data for training and validation was collected through field survey as well as visual interpretation using Google Earth. Field survey was implemented in February 2015 and February 2016 over Northern Vietnam. We used high accuracy GPS integrated cameras Casio H20G to collect photographs of land cover objects including barren, water, forest, grasslands, orchard, other crop, rice and urban (Fig. 2). The homogenous area of those objects must be more than 15 m in diameter. Total length of field route reached about 2000 km and a total of 1801 GPS photos was collected (Fig. 1b). Each GPS photo was then extracted all needed information about the field observation including geolocation, land cover category, observation time, homogenous degree of targeted objects and the photo itself. This process was carried out using a web-based reference dataset named "Site-based dataset for Assessment of Changing Land cover by JAXA (SACLAJ)".

Regional scale of study area requires larger number and denser spatial distribution of reference data. Therefore, we conducted an image-based visual interpretation using Google Earth in combination with ASTER in 2007, Landsat-5 images for 2007 and ASTER in 2015, Landsat-8 for 2015. A number of 60,000 reference data was created in addition. We used 66% of the total number 62000 samples for training data and 34% of those for validation.

2.4 Classification Method

This study employed a kernel-based probabilistic classification which is based on Bayesian inference. We adopted this classification method from Hashimoto et al.'s research and the mathematics details were clearly described in [29–31]. Hashimoto et al. (2013) indicated that kernel-based probabilistic classification showed the highest overall accuracy in comparison to maximum likelihood classification and support vector machines when conducting land cover classification in Japan territory [30]. The core of this method is that using a probabilistic model to simulate a distribution of observable data, given some hidden parameters, like a generative model. Specifically, this method builds a generative model based on training data using kernel density estimation in order to calculate probability for each feature vector. The joint probability is then calculated by multiplying multi-temporal and multi-sensor posterior probability of each land cover class. After that, joint probability distribution is normalized so that the sum of joint probabilities of all classes is equal to 1. In the end, the land cover class having highest joint probability will be defined as the classification result.

Multi-temporal aspect was functioned by two time variables demonstrated in Eq. (1). Time information was extracted from imagery acquisition date (DOY: date of year) and was demonstrated by the coordinates in the trigonometric circle. The two time variables were then added to feature vectors. Therefore, feature vectors were comprised by spectral information and temporal information. The kernel-based probabilistic classification was then conducted for the feature space.

Fig. 2. Land cover types' photos from the field

$$[t_1, t_2] = \left[\cos\left(2\pi \frac{DOY}{DOY_{max}}\right), \sin\left(2\pi \frac{DOY}{DOY_{max}}\right)\right] \quad (1)$$

Imagery data were managed in 14 square tiles in order to avoid large volume data processing. Each tile has size of 1° × 1° (Fig. 3). The classification was conducted separately for each tile and each dataset including Landsat, ASTER, SAR and ancillary data. Training data were prepared for each tile. In order to avoid edge mismatching effect, the spatial extent of training data of its corresponding tile was expanded toward outside of its tile 0.5°. The classification process was supported by the Saclass software version 1.2 developed by University of Tsukuba and JAXA, and a computer having General-Purpose computing on Graphics Processing Units (GPGPU).

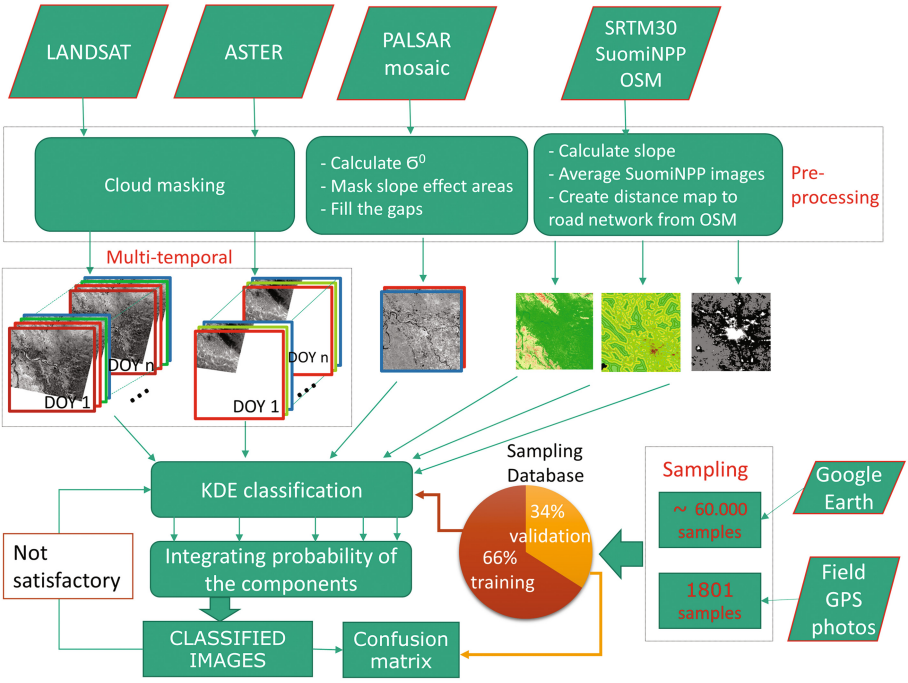

Fig. 3. Schematic diagram of the classification process

We categorized 9 land cover types (Table 2) based on knowledge of geography in the study area. This region includes remarkable orchard areas in intensively cultivated land allocating mainly in hill lands in the North of Red River Delta and in the plain. Forest is dominated by evergreen broadleaf forest whereas bamboo, deciduous and needleleaf vegetation occupied small percentages. Therefore, we used only a forest category for all the forest types. In order to support convertibility between land cover category systems for comparative studies or further applications, we used LCCS classification system recommended by FAO [32] to set up our category system with standard definitions and standard hierarchical classification schemes (Table 2).

Table 2. Land cover categories description in this study

Order	Class name	LCCS label	Description
1	Water	B27A1 B28A1	The land cover consists of artificial water bodies. A further specification can be made in flowing or standing water. The land cover consists of natural water bodies. A further specification can be made in flowing or standing water
2	Urban and built-up	B15A1	The land cover consists of built up area(s)
3	Rice	A11A4XXXXC1D3-S0308	Field(s) are covered by a single irrigated graminoid crop. The crop covers the land during the cropping period of a fallow system. The irrigation systems commonly used are surface, sprinkler and drip irrigation. Crop type is Rice (Oryza spp.)
4	Other crops	A11A2 A11A3	A defined area is covered by herbaceous crops. Shrub crops cover a defined area. The leaf type and leaf phenology can be further specified optionally
5	Grasslands	A12A2A20B4	The main layer consists of closed to open herbaceous vegetation. The crown cover is between 100 and 15% (a further sub range can be defined – Closed to Open 100–40%). The height is in the range of 3 - 0.03 m but may be further defined into a smaller range
6	Orchards	A11A1-W8	Tree crops cover a defined area. The leaf type and leaf phenology can be further specified optionally. Crop Cover: Orchard(s)
7	Barren	B16	Primarily non-vegetated areas containing less than four percent vegetation during at least 10 months a year. The environment is influenced by the edaphic substratum. The cover is natural. Included are areas like bare rock and sands

(*continued*)

Table 2. (*continued*)

Order	Class name	LCCS label	Description
8	Forest	A12A3A20B2	The main layer consists of closed to open trees. The crown cover is between 100 and 15% (a further sub range can be defined – Closed to Open 100–40%). The height is in the range of 30-3 m and is not further defined
9	Mangrove	A24A1A20B1C3	The main layer consists of closed to open woody vegetation on waterlogged soil. The crown cover is between 100 and 15% (a further sub range can be defined – Closed to Open 100–40%). The height is in the range of 7 – 2 m and is not further defined

3 Results and Discussion

Figure 4 shows the resulting land cover map in 2015 (Fig. 4a) and the resulting land cover map in 2007 (Fig. 4b). The land cover categories are described in Table 2. The overall accuracies of the land cover maps in 2015 and 2007 are 89.0% and 81.3%, respectively and the kappa coefficients are 0.8723 and 0.7815 respectively (Table 3). The classes with lowest accuracies in both land cover maps are grasslands and other crops. In terms of land cover map 2015, grasslands showed 73.6% and 81.3% in user's accuracy and producer's accuracy respectively, while these number of other crops showed 76.5% and 82.9%. The other land cover types with low accuracies is barren. The land cover types which have highest accuracies include water, urban, urban and built-up and forest with accuracies ranging from 88% to 97% in land cover map 2015. The reason of this uncertainty of grasslands and other crops may come from the similarity of spectral characteristic of other crops and grasslands, while barren exerts high possibility to mixed with dry terrace paddy, grasslands and urban areas.

During the last decade, research works, government's information and media documented that there are significant changes in land use/land cover in Northern Vietnam due to forest plantation [24, 25], transformation of land use purposes [33, 34], construction of large hydropower dams [26] and urbanization. In this paper, we focused on the most outstanding changes which are forest gain and land cover changes in Son La hydropower plant's reservoir area before and after the activation of the plant in 2010. In order to analyze those changes, we selected some focusing areas which those changes occurred: site A is the Son La hydropower reservoir area; site B and site C are places which were considered forest gain [25] (Fig. 4). Figure 5 show the magnitude figures of the selected sites in 2007 and 2015.

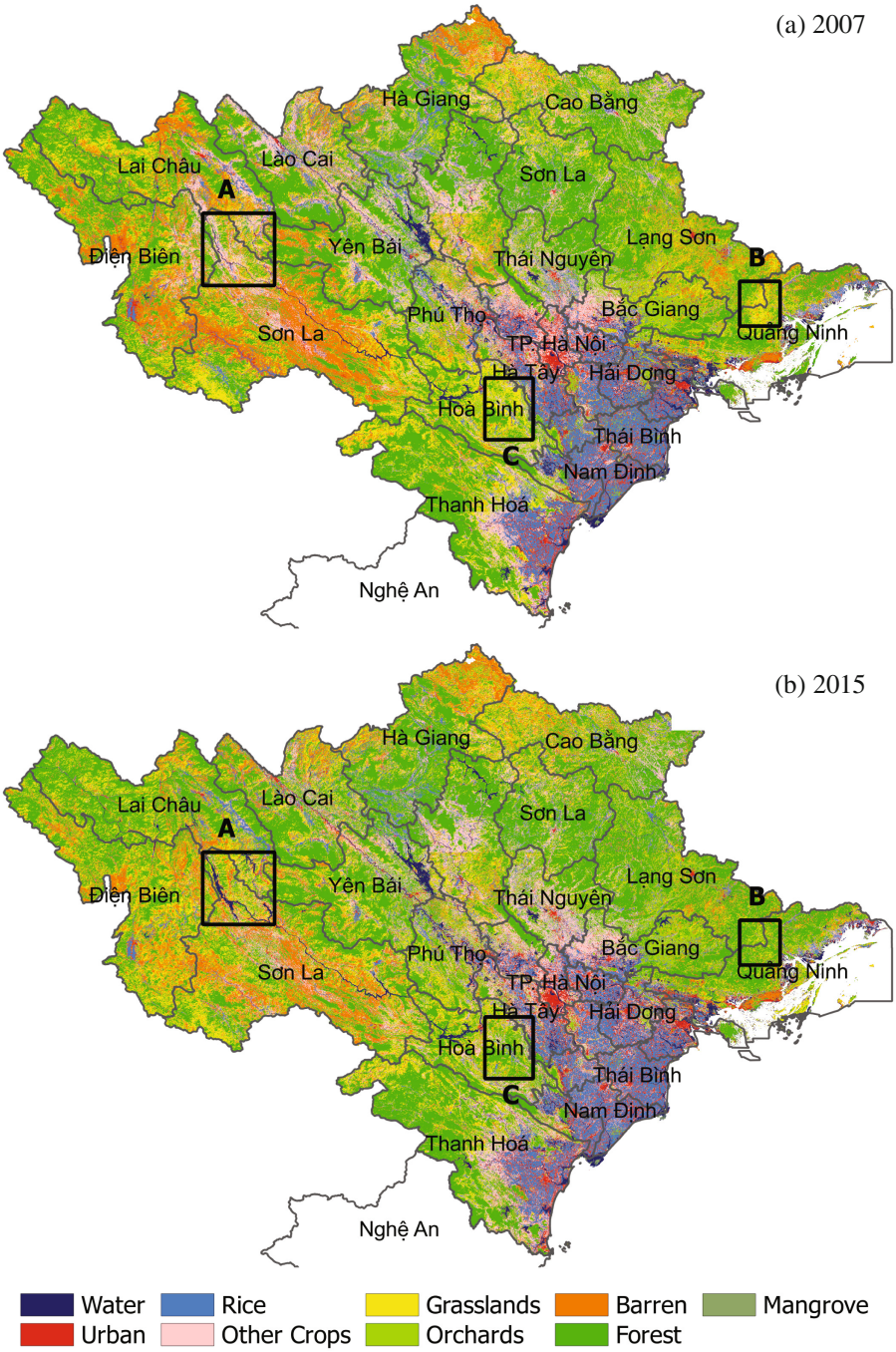

Fig. 4. (. a) Land cover map in 2007 and (**b**) Land cover map in 2015. A, B, C are the selected sites for analyzing land cover change

Table 3. Confusion matrix of the land cover map in 2015 (a) and the land cover map in 2007 (b)

	Validation											
		Water	Urban – builtup	Rice	Other crops	Orchard	Man-grove	Grass-lands	Barren	Forest	Total	Producer's accuracy (%)
(a) Land cover map in 2015												
Results	Water	1096	3	22	6	0	2	0	6	1	1136	96.5
	Urban – builtup	13	2429	49	55	9	1	1	40	4	2601	93.4
	Rice	31	23	4066	98	8	0	9	30	6	4271	95.2
	Other crops	12	66	283	1712	42	0	29	29	65	2238	76.5
	Orchard	11	25	34	108	1650	2	16	19	50	1915	86.2
	Mangrove	2	2	6	0	14	300	5	13	25	367	81.7
	Grasslands	1	0	9	48	6	2	1246	106	275	1693	73.6
	Barren	3	5	99	11	4	1	75	1738	35	1971	88.2
	Forest	2	0	2	28	32	1	146	24	3603	3838	93.9
	Total	1171	2553	4570	2066	1765	309	1527	2005	4064	20030	–
	User's accuracy (%)	93.6	95.1	89.0	82.9	93.5	97.1	81.6	86.7	88.7	–	89.0
	Kappa coefficient: 0.8723											

(*continued*)

Table 3. (*continued*)

	Validation											
		Water	Urban – builtup	Rice	Other crops	Orchard	Man-grove	Grass-lands	Barren	Forest	Total	Producer's accuracy (%)
(b) Land cover map in 2007												
Results	Water	1029	6	48	5	0	0	6	0	16	1110	92.7
	Urban – builtup	17	2410	69	70	3	20	43	7	1	2640	91.3
	Rice	60	18	3746	237	20	24	26	10	2	4143	90.4
	Other crops	18	35	404	1336	30	41	73	42	1	1980	67.5
	Orchard	9	2	16	106	1082	44	296	351	1	1907	56.7
	Mangrove	13	72	137	215	19	1569	31	69	1	2126	73.8
	Grasslands	13	5	128	65	163	34	1331	81	0	1820	73.1
	Barren	2	0	5	31	206	9	193	3490	0	3936	88.7
	Forest	10	5	17	1	4	24	6	14	287	368	78.0
	Total	1171	2553	4570	2066	1527	1765	2005	4064	309	20030	–
	User's accuracy (%)	87.9	94.4	82.0	64.7	70.9	88.9	66.4	85.9	92.9	–	81.3
	Kappa coefficient: 0.7815											

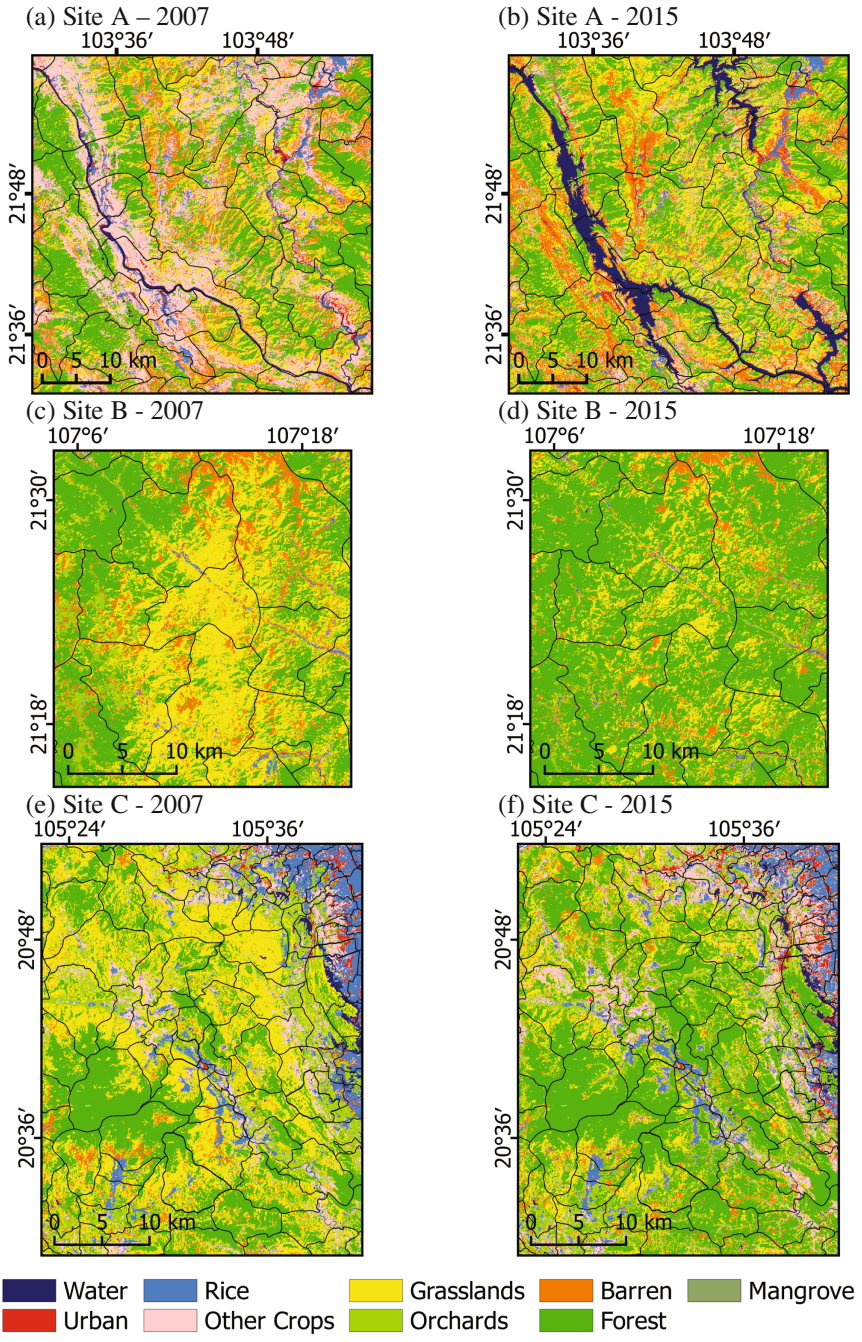

Fig. 5. The selected sites for analyzing land cover change between 2007 and 2015. The solid gray line shows the administrative boundaries of communes.

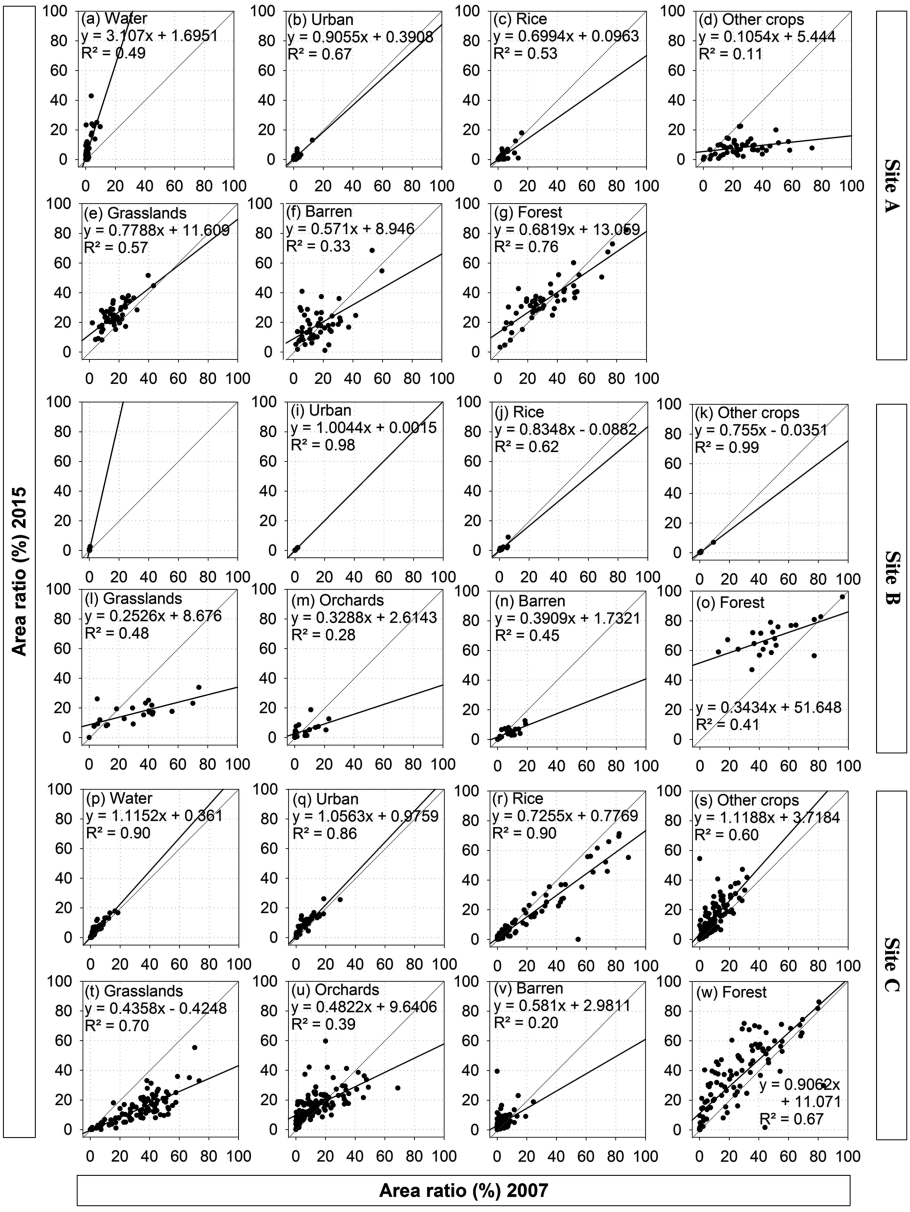

Fig. 6. The comparison of area ratio of the land cover categories for each commune in 2015 and 2007. In each single graph, the Y axis shows the ratio (in percentage) of a land cover type's area in a commune to the total area of the commune in 2015; the X axis shows the ratio in 2007. The solid gray line shows the 1:1 relationship. The solid black line shows the linear regression line.

To analyze the changes, we used area ratio to compare the dynamics of each land cover type in commune level. The administrative boundaries of communes were demonstrated by solid gray lines in Fig. 6. The area ratio was calculated by dividing area of each land cover type in a commune by the total area of the commune.

Figure 6a to g show the ratio area comparison of water, urban and built-up, rice, other crops, grasslands, barren and forest respectively in site A. In water category, the area ratio showed a greatly increasing trend (Fig. 6a) whereas in other crops category, the area ratio indicated an obviously decreasing trend (Fig. 6d). This change was also depicted visually in Fig. 5a and b through the replacing cropland in 2007 with water body in 2015 over the Son La hydropower reservoir area. In mountainous area of Northern Vietnam, people tend to live near rivers and use the narrow plain along the rivers for agriculture. Therefore, cropland area around the river was eliminated by water in the reservoir area [35]. The area ratio in the urban and rice categories showed virtually no change between 2007 and 2015 (Fig. 6b and c). In grasslands category, the area ratio showed slight increase between the periods (Fig. 6e). It may due to abandoned cropland following the evacuation of a great number of people from the reservoir area [26]. The area ratio in the barren and forest categories showed mixed behavior pattern (Fig. 6f and g).

Forest gain between 2007 and 2015 in site B (Fig. 5c and d) and in site C (Fig. 5e and f) were visually illustrated through replacing grasslands and barren in 2007 with forest in 2015. Along with the increasing area ratio in the forest category (Fig. 6o and w), the area ratio in the grasslands category (Fig. 6l and t) and the area ratio in the barren category (Fig. 6n and v) showed decreasing trend over the two years.

In site B, the area ratio in other land cover categories including water (Fig. 6h), urban (Fig. 6i) and rice (Fig. 6j) showed no significant change. Almost all the data in the plots were close to the 1:1 relationship line. In site C, the area ratio in the water category (Fig. 6p) and urban category (Fig. 6q) showed no significant change. In the rice category of site C, however, the area ratio shows slightly decreasing trend with $R^2 = 0.9$ between the two years (Fig. 6r). As site C locates in suburban area, the decline of rice paddy areas may be caused by urbanization in which paddy areas are commonly transferred to urban and built-up or infrastructure [36].

4 Conclusion

The land cover maps in 2007 and 2015 of Northern Vietnam produced by kernel-based probabilistic classification using multi-temporal and multi-sensor data achieved the accuracies of 81% and 89% respectively. These results introduced high-resolution regional land cover data in Northern Vietnam for environmental modeling or other regional studies. Moreover, in comparison to other land cover dataset such as MODIS, CCI or FROM-GLC, the innovation of our land cover data is that rice paddy, which is very important land cover type in South East Asia, was separated from cropland. The most outstanding land use/land cover dynamics between the two years which are forest gain and land cover changes induced by Son La reservoir's presence were well captured by the results. The analysis showed that there was a large increase in water are and there was a great decrease in cropland area in the Son La hydropower dam are

between 2007 and 2015. In the selected sites for forest gain detection, obvious increase in forest area and noticeable decrease in grassland area were also revealed by the analysis.

Northern Vietnam has been considered to have large changes in land use/land cover in near future because of (1) human activities including urbanization, resources exploitation and changing land use purposes and (2) vulnerability to environmental changes including climate change, sea level rise and disasters. Therefore, it is of importance to continually monitor changes in land cover using satellite data and using land cover data in environmental modeling. That leads to an essential need for improving land cover data products in terms of accuracy, resolution and classification schemes.

For further applications or other interests, readers can download the land cover map results in this study on the JAXA/EORC website:

http://www.eorc.jaxa.jp/ALOS/en/lulc/lulc_vnm.htm

Acknowledgements. The authors thank the USGS, AIST, JAXA, NASA, NOAA and OpenStreetMap Foundation for the distribution of the data used. We would like to thank Dr. Takeo Tadono for providing necessary hardware for classification running. We thank members of ecosystem group in JAXA/EORC for technical support.

References

1. Friedl, M.A., McIver, D.K., Hodges, J.C.F., Zhang, X.Y., Muchoney, D., Strahler, A.H.: Global land cover mapping from MODIS: algorithms and early results. Remote Sens. Environ. **83**, 287–302 (2002)
2. Yu, L., Liang, L., Wang, J., Zhao, Y., Cheng, Q., Hu, L., Liu, S., Yu, L., Wang, X., Zhu, P., Li, X., Xu, Y., Li, C., Fu, W., Li, X., Li, W., Liu, C., Cong, N., Zhang, H., Sun, F., Bi, X., Xin, Q., Li, D., Yan, D., Zhu, Z., Goodchild, M.F., Gong, P.: Meta-discoveries from a synthesis of satellite-based land-cover mapping research. Int. J. Remote Sens. **35**, 4573–4588 (2014)
3. Gong, P., Wang, J., Yu, L.L., Zhao, Y.Y.Y.Y., Liang, L., Niu, Z., Huang, X., Fu, H., Liu, S., Li, C., Li, X., Fu, W., Liu, C., Xu, Y., Wang, X., Cheng, Q., Hu, L., Yao, W., Zhang, H.H., Zhu, P., Zhao, Z., Zheng, Y., Ji, L., Zhang, Y., Chen, H., Yan, A., Guo, J., Wang, L., Liu, X., Shi, T., Zhu, M., Chen, Y., Yang, G., Tang, P., Xu, B., Giri, C., Clinton, N., Zhu, Z., Chen, J.J.: Finer resolution observation and monitoring of global land cover: first mapping results with Landsat TM and ETM+ data. Int. J. Remote Sens. **34**, 2607–2654 (2013)
4. Running, S.W.: Climate change. Ecosystem disturbance, carbon, and climate. Science **321**, 652–653 (2008)
5. Bontemps, S., Herold, M., Kooistra, L., Van Groenestijn, A., Hartley, A., Arino, O., Moreau, I., Defourny, P.: Revisiting land cover observation to address the needs of the climate modeling community. Biogeosciences **9**, 2145–2157 (2012)
6. Pielke, R.A., Pitman, A., Niyogi, D., Mahmood, R., McAlpine, C., Hossain, F., Goldewijk, K.K., Nair, U., Betts, R., Fall, S., Reichstein, M., Kabat, P., de Noblet, N.: Land use/land cover changes and climate: modeling analysis and observational evidence. Wiley Interdiscip. Rev. Clim. Change **2**, 828–850 (2011)

7. Streets, D.G., Canty, T., Carmichael, G.R., de Foy, B., Dickerson, R.R., Duncan, B.N., Edwards, D.P., Haynes, J.A., Henze, D.K., Houyoux, M.R., Jacob, D.J., Krotkov, N.A., Lamsal, L.N., Liu, Y., Lu, Z., Martin, R.V., Pfister, G.G., Pinder, R.W., Salawitch, R.J., Wecht, K.J.: Emissions estimation from satellite retrievals: a review of current capability. Atmos. Environ. **77**, 1011–1042 (2013)
8. Jung, M., Henkel, K., Herold, M., Churkina, G.: Exploiting synergies of global land cover products for carbon cycle modeling. Remote Sens. Environ. **101**, 534–553 (2006)
9. Houghton, R.A.: How well do we know the flux of CO2 from land-use change? Tellus Ser. B Chem. Phys. Meteorol. **62**, 337–351 (2010)
10. Shevliakova, E., Pacala, S.W., Malyshev, S., Hurtt, G.C., Milly, P.C.D., Caspersen, J.P., Sentman, L.T., Fisk, J.P., Wirth, C., Crevoisier, C.: Carbon cycling under 300 years of land use change: importance of the secondary vegetation sink. Global Biogeochem. Cycles **23**, 1–16 (2009)
11. Van Tuyl, S., Law, B.E., Turner, D.P.: Gitelman, a.I.: Variability in net primary production and carbon storage in biomass across Oregon forests—an assessment integrating data from forest inventories, intensive sites, and remote sensing. For. Ecol. Manage. **209**, 273–291 (2005)
12. Avitabile, V., Herold, M., Henry, M., Schmullius, C.: Mapping biomass with remote sensing: a comparison of methods for the case study of Uganda. Carbon Balance Manage. **6**, 7 (2011)
13. Pham, T.D., Yoshino, K.: Aboveground biomass estimation of mangrove species using ALOS-2 PALSAR imagery in Hai Phong City, Vietnam. J. Appl. Remote Sens. **11**, 026010 (2017)
14. Miller, S.N., Guertin, D.P., Goodrich, D.C.: Hydrologic Modeling Uncertainty Resulting, 43 (2008)
15. Shi, Z.H., Ai, L., Li, X., Huang, X.D., Wu, G.L., Liao, W.: Partial least-squares regression for linking land-cover patterns to soil erosion and sediment yield in watersheds. J. Hydrol. **498**, 165–176 (2013)
16. Newbold, T., Hudson, L.N., Hill, S.L., Contu, S., Lysenko, I., Senior, R.A., Borger, L., Bennett, D.J., Choimes, A., Collen, B., Day, J., De Palma, A., Diaz, S., Echeverria-Londono, S., Edgar, M.J., Feldman, A., Garon, M., Harrison, M.L., Alhusseini, T., Ingram, D.J., Itescu, Y., Kattge, J., Kemp, V., Kirkpatrick, L., Kleyer, M., Correia, D.L., Martin, C.D., Meiri, S., Novosolov, M., Pan, Y., Phillips, H.R., Purves, D.W., Robinson, A., Simpson, J., Tuck, S.L., Weiher, E., White, H.J., Ewers, R.M., Mace, G.M., Scharlemann, J.P., Purvis, A.: Global effects of land use on local terrestrial biodiversity. Nature **520**, 45–50 (2015)
17. Ishihara, M., Tadono, T.: Land cover changes induced by the great east Japan earthquake in 2011. Sci. Rep. **7**, 45769 (2017)
18. Foley, J.A., Defries, R., Asner, G.P., Barford, C., Bonan, G., Carpenter, S.R., Chapin, F.S., Coe, M.T., Daily, G.C., Gibbs, H.K., Helkowski, J.H., Holloway, T., Howard, E.A., Kucharik, C.J., Monfreda, C., Patz, J.A., Prentice, I.C., Ramankutty, N., Snyder, P.K.: Global consequences of land use. Science **309**, 570–574 (2005)
19. IPCC: Climate Change 2013 The Physical Science Basis - Summary for Policymakers, Contribution of Working Group I to the Fifth Assessment Report of the Intergovernmental Panel on Climate Change. Cambridge University Press, Cambridge (2013)
20. Mayaux, P., Eva, H., Gallego, J., Strahler, A.H., Herold, M., Agrawal, S., Naumov, S., De Miranda, E.E., Di Bella, C.M., Ordoyne, C., Kopin, Y., Roy, P.S.: Validation of the global land cover 2000 map. IEEE Trans. Geosci. Remote Sens. **44**, 1728–1737 (2006)
21. Bontemps, S., Defourny, P., Bogaert, E.V., Kalogirou, V., Perez, J.R.: GLOBCOVER 2009 Products Description and Validation Report, p. 53 (2011)

22. Scepan, J., Estes, J.E.: Thematic validation of global land cover data sets-procedures and interpretation methods. In: IEEE 2001 International Geoscience and Remote Sensing Symposium, IGARSS 2001, vol. 1113, pp. 1119–1121 (2001)
23. FAO: Global Forest Resources Assessment 2015 – Country Report - Vietnam. Food and Agriculture Organization of the United Nations (2015)
24. Stibig, H.J., Achard, F., Carboni, S., Raši, R., Miettinen, J.: Change in tropical forest cover of Southeast Asia from 1990 to 2010. Biogeosciences **11**, 247–258 (2014)
25. Hansen, M.C., Potapov, P.V., Moore, R., Hancher, M., Turubanova, S.A., Tyukavina, A., Thau, D., Stehman, S.V., Goetz, S.J., Loveland, T.R., Kommareddy, A., Egorov, A., Chini, L., Justice, C.O., Townshend, J.R.: High-resolution global maps of 21st-century forest cover change. Science **342**, 850–853 (2013)
26. Decision No.196/2004/QD-TTg: Decision of the Prime Minister of Vietnam on regulations of compensation, displacement and resettlement of the Son La Hydropower Project (in Vietnamese). The Government of Viet Nam (2004)
27. Duong, N.D.: Land cover mapping of Vietnam using modis 500M 32-Day. In: International Symposium on Geoinformatics for Spatial Infrastructure Development in Earth and Allied Sciences 2004, pp. 1–6 (2004)
28. Hoan, N.T., Duong, N.D., Tateishi, R.: Combination of ADEOS II - GLI and MODIS 250m data for land cover mapping of indochina Peninsula. In: Asian Association on Remote Sensing - 26th Asian Conference on Remote Sensing and 2nd Asian Space Conference, ACRS 2005, pp. 417–424 (2005)
29. Hashimoto, S., Tadono, T., Onosato, M., Hori, M., Moriyama, T.: Probabilistic land cover classification approach toward knowledge-based satellite data interpretations. In: 2012 IEEE International Geoscience and Remote Sensing Symposium (IGARSS), pp. 1513–1516 (2012)
30. Hashimoto, S., Tadono, T., Onosato, M., Hori, M.: Land use and land cover inference in large areas using multi-temporal optical satellite images. In: 2013 IEEE International Geoscience and Remote Sensing Symposium (IGARSS), pp. 3333–3336. IEEE (2013)
31. Hashimoto, S., Tadono, T., Onosato, M., Hori, M., Shiomi, K.: A New method to derive precise land-use and land-cover maps using multi-temporal optical data. J. Remote Sens. Jpn. **34**, 102–112 (2014)
32. Gregorio, A.D.: Land Cover Classification System (LCCS), version 2: Classification concepts and user manual. FAO (2005)
33. Decision No.272/QD-TTg: Decision by The Prime Minister on Ratifying The Results of The 2005 General Land Inventory (in Vietnamese). The Government of Viet Nam (2007)
34. National Land Use Status Quo Classified by Geographical and Economic Regions in 2014. http://thongke.monre.gov.vn
35. Bui, T.M.H., Schreinemachers, P., Berger, T.: Hydropower development in Vietnam: involuntary resettlement and factors enabling rehabilitation. Land Use Policy **31**, 536–544 (2013)
36. Rutten, M., van Dijk, M., van Rooij, W., Hilderink, H.: Land use dynamics, climate change, and food security in Vietnam: a global-to-local modeling approach. World Dev. **59**, 29–46 (2014)
37. Van, T.T., Wilson, N., Thanh-Tung, H., Quisthoudt, K., Quang-Minh, V., Xuan-Tuan, L., Dahdouh-Guebas, F., Koedam, N.: Changes in mangrove vegetation area and character in a war and land use change affected region of Vietnam (Mui Ca Mau) over six decades. Acta Oecologica **63**, 71–81 (2015)

Change Detection in Multitemporal SAR Images Using a Strategy of Multistage Analysis

Thu Trang Lê(✉), Van Anh Tran, Ha Thai Pham, and Xuan Truong Tran

Photogrammetry and Remote Sensing Department,
Hanoi University of Mining and Geology,
18 Vien Street, Duc Thang Ward, Bac Tu Liem District, Hanoi, Vietnam
lethutrang@humg.edu.vn

Abstract. This paper presents a change detection framework for Synthetic Aperture Radar (SAR) Image Time Series (ITS) based on Change Detection Matrix (CDM) approach. This framework allows the identification of changes on the ground in multiple scales. First, the Patch-based Change Detection Matrix (P-CDM) is proposed for the detection of changes in patch scale. Then changed regions and images acquired on dates related to the change occurrence are selected from P-CDMs. Finally, changes between selected images are defined with more details for each changed region in pixel scale by using Kullback-Leibler divergence between two Log-normal distributions. The proposed approach was illustrated by a time series including 11 ascending ALOS PALSAR images with resolution of 33.2 m × 28.4 m (range × azimuth) and polarization HH over Bat Xat district, Lao Cai province, and a part of Phong Tho district, Lai Chau province, Vietnam. There are different kinds of surface change in this test-site, such as: abrupt changes caused by flash floods and landslides, progressive changes due to plant evolution of rice terrace fields and forests. The experimental results have proven the effectiveness of the proposed framework.

Keywords: Change detection · SAR image time series · Multistage analysis · Kullback-Leibler divergence · Patch-based CDM

1 Introduction

The Earth's surface has been altered by human activities and natural processes, such as: deforestations, forest fires, erosions, floods, landslides, volcanic eruptions, tsunamis, earthquakes. These phenomena often impact natural environment as well as human life. With the development of sensor technology, a large number of satellite images can be available in days, even hours before and after such events [1]. These data provide an interesting tool for damage assessment and disaster monitoring. In particular, multitemporal Synthetic Aperture Radar (SAR) images acquired over the same area at different times have shown the effectiveness in monitoring tasks [2–6].

The exploitation of an Image Time Series (ITS) for analyzing the temporal evolution of regions of interest can make use of redundant information of these data to

© Springer International Publishing AG 2018
D. Tien Bui et al. (eds.), *Advances and Applications in Geospatial Technology and Earth Resources*, https://doi.org/10.1007/978-3-319-68240-2_10

increase the change detection accuracy. New generation satellites (e.g. Sentinel 1-2, ALOS2/PALSAR2, RADARSAT constellation) allow the acquisition of SAR images with high resolution, large coverage (large size images) in short repeat cycles (large number of images). Therefore, the use of these data relates to deal with processing big data that often requires robust algorithms, but even so, it may still be time consuming.

Recent approaches on change detection and analysis with SAR ITS have been focused on both spatial and temporal localization of changes. The Multi-Date Divergence Matrix (MDDM) framework [7] uses a matrix of cross-dissimilarity computed upon wavelet and curvelet features to identify acquisitions of interest, then these acquisitions are compared to detect spatial changes. In the case that images cover over a large area, this method may not be appropriate since it uses distribution parameters representing each entire image of the ITS to determine changes. The Method for generalIzed Means Ordered Series Analysis (MIMOSA) [8] was proposed to compare two different temporal means between amplitude images (geometric mean with harmonic or arithmetic or quadratic mean), the joint-use of the two temporal means can identify spatial changes, but it cannot point out dates when changes occurred. To overcome this, the Change Detection Matrix (CDM) framework was introduced in [4] that is based on a matrix constructed by similarity cross-tests, change information derived from this matrix can be exploited for different applications, multitemporal change detection, analysis of change dynamics, and non-local temporal mean SAR image filtering. In another approach, the NORmalized Cut on chAnge criterion Matrix (NORCAMA) method in [9] proposed to use likelihood ratio test to detect changes, change classification is then performed by a normalized cut based clustering and recognizing method on change criterion matrix. Although both CDM and NORCAMA methods can provide spatio-temporal change information, however they may be time consuming when processing long SAR ITS with large size images as they are pixel-wise based approaches. Therefore, new change detection framework that tackles this issue is highly necessary.

In this paper, we address the above issue by proposing a new change detection framework using a strategy including two stages of analysis which can overcome limitations of these previous approaches. This strategy can determine changes on the ground in multiple scales, i.e., (i) patch scale for the rapid detection of changed regions and acquisition dates before and after these changes, and (ii) pixel scale for detailed change detection in determined regions.

2 Strategy of Multistage Analysis

Change information of an ITS can be extracted by a strategy including two stages (see Fig. 1):

(i) Multitemporal stage: In this stage, changes are detected between each two dates using Change Detection Matrix (CDM) approach [10] with patch-wise analysis instead of pixel-wise analysis as in the original approach. The P-CDMs obtained in this stage contain spatio-temporal change information of the ITS, and

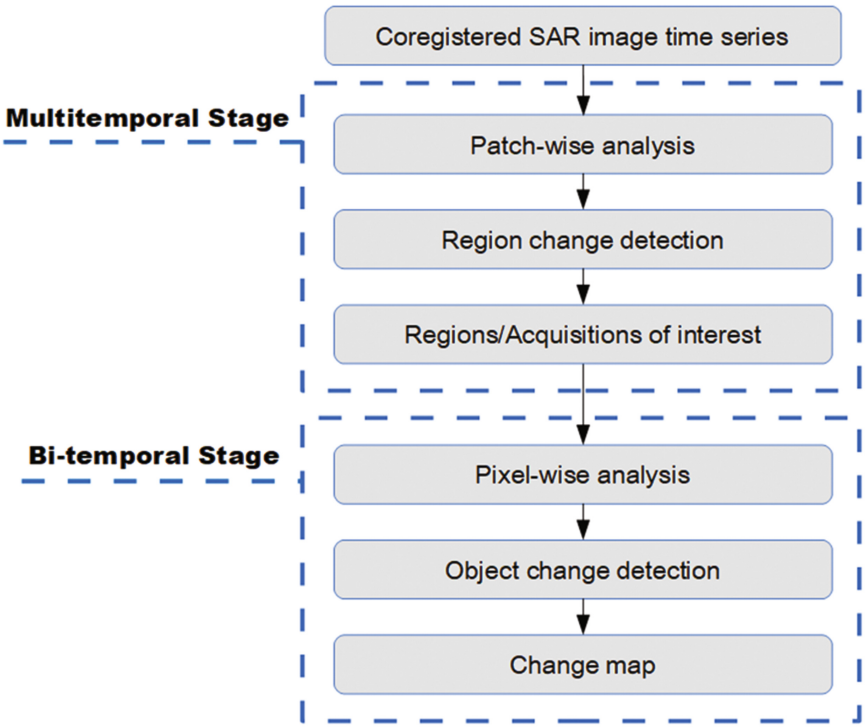

Fig. 1. Strategy of multistage analysis for change detection of SAR ITS

(ii) Bi-temporal stage: Based on the results of the first stage, one can select regions and acquisitions of interest, i.e., changed regions and images acquired on date related to the change occurrence (dates of pre-, during- and post-event). Then, detailed changes between acquisitions of interest are detected for selected regions by using Kullback-Leibler (KL) divergence of two Log-normal distributions in pixel scale.

2.1 Multitemporal Stage

Let us consider a coregistered SAR ITS including N images of size $(m \times n)$ over the same area at N different times, denoted as $I = \{I_t\}_{1 \leq t \leq N}$.

In this first stage, CDM approach is used to determine changed regions in the observed area. CDM framework can be applied to different tasks: change analysis, nonlocal temporal mean filtering of SAR ITS. In order to reduce computational cost when using CDM approach to perform the change analysis for long SAR ITS with large size of each image, a patch-wise based version of this approach, called *Patch-based CDM (P-CDM),* is presented, hereafter.

Indeed, each image I_t of size $(m \times n)$ of the ITS is divided into patches:

$$\{W_t(i,j)\}_{1 \le i \le \frac{m}{p}; 1 \le j \le \frac{n}{q}} = I_t([(i-1)p+1;\ (i-1)p+p],\ [(j-1)q+1;\ (j-1)q+q]) \quad (1)$$

with $(p \times q)$, size of each patch, $p|m$ and $q|n$.

For each position (i,j), we have a stack of patches of N images $\{W_t(i,j)\}_{1 \le t \le N}$.

- **First step of P-CDM:** changed and unchanged patches in each stack are identified by similarity cross-tests between each two different dates (t,k). Each element of the similarity matrix of the stack (i,j) is denoted as:

$$S_{(t,k)}(i,j) = \Delta(W_t(i,j), W_k(i,j))_{1 \le t,k \le N} \quad (2)$$

with Δ, a similarity measure.

Giving a threshold value T in order to assign the considering patch into changed or unchanged class, we obtain the first step patch-based change detection matrix (P-CDM1) as follows:

$$M_{(t,k)}(i,j) = \begin{cases} 0 & if\ S_{(t,k)}(i,j) < T \\ 1 & if\ S_{(t,k)}(i,j) \ge T \end{cases} \quad (3)$$

M is a symmetric matrix containing 0 and 1 values representing unchanged and changed patches in each patch stack, respectively.

- **Second step of P-CDM:** Change information provided by P-CDM1 is refined in this step to derive more accurate change detection results. By taking into account all unchanged patches determined in P-CDM1, temporal neighborhoods corresponding to each date t are defined as:

$$\Phi(W_t(i,j)) = \left\{ W_k(i,j) | M_{(t,k)}(i,j) = 0;\ 1 \le k \le N \right\} \quad (4)$$

These temporal neighborhoods are then used to recalculate similarity cross-tests between each two dates (t,k) to obtain the second step patch-based change detection matrix (P-CDM2).

$$\hat{S}_{(t,k)}(i,j) = \Delta(\Phi(W_t(i,j)), \Phi(W_k(i,j)))_{1 \le t,k \le N} \quad (5)$$

$$\hat{M}_{(t,k)}(i,j) = \begin{cases} 0 & if\ \hat{S}_{(t,k)}(i,j) < T \\ 1 & if\ \hat{S}_{(t,k)}(i,j) \ge T \end{cases} \quad (6)$$

- **Index of change dynamics:** This index gives the level of change dynamics of each patch stack. For a given patch stack $\{W_t(i,j)\}_{1 \le t \le N}$, index of change dynamics ε is calculated by the proportion of "1" representing the probability of "changed" responses of similarity tests in P-CDM2.

$$\varepsilon(i,j) = \frac{2}{N(N-1)} \sum_{t=1}^{N} \sum_{k=t+1}^{N} \hat{M}_{(t,k)}(i,j) \tag{7}$$

This index has values in [0, 1], where 0 means that the patch stack at (*i, j*) is absolutely stable, on the other hand, 1 means that it is extremely unstable.

2.2 Bi-Temporal Stage

P-CDMs obtained in the first stage provide spatio-temporal change information of the SAR ITS. From the map of change dynamics, we can define regions of interest where changes regularly occurred over the whole ITS (with index ε of high values) or changes associated with a specific event. P-CDM of these defined regions indicates acquisitions of interest. In this stage, pixel-wise analysis is performed for each changed regions between two dates (*t, k*) in order to obtain detailed change map $CM_{(t,k)}$.

$$H_{(t,k)} = D\left(I_t^W, I_k^W\right)_{t \neq k} \tag{8}$$

$$CM_{(t,k)} = \begin{cases} 0 & if\ H_{(t,k)} < \lambda \\ 1 & if\ H_{(t,k)} \geq \lambda \end{cases} \tag{9}$$

where H is the similarity degree of the similarity measurement D between regions I_t^W, I_k^W of images I_t, I_k acquired on dates t and k.

It is worth noting that the similarity measurement D and the threshold value λ in this stage, and the respective Δ and T in the previous stage can be the same or different.

3 Case Study

3.1 Description of Study Area and Data Used

To illustrate the relevancy of the proposed framework, we exploited a time series of 11 ALOS PALSAR images over Bat Xat district, Lao Cai province, and a part of Phong Tho district, Lai Chau province, Vietnam (Fig. 2). Located in the Northwest of Vietnam, this test-site is a heterogeneous area with high mountains, rivers, and narrow valleys. This area has a tropical climate influenced by monsoon, which usually brings heat, humidity and rain in the summer (from April to September), and dry, cold/cool in the winter (from October to March) [11].

Two main reasons for surface changes in this area [12] are:

(i) most part of this mountainous area is covered by rice terrace fields and forests, therefore the surface changes seasonally in consequence of plant evolution;
(ii) under the influence of heavy rains brought by tropical storms, flash floods and landslides often occur, resulting in abrupt changes on the surface and causing great damage to human life, infrastructure, crops, transport.

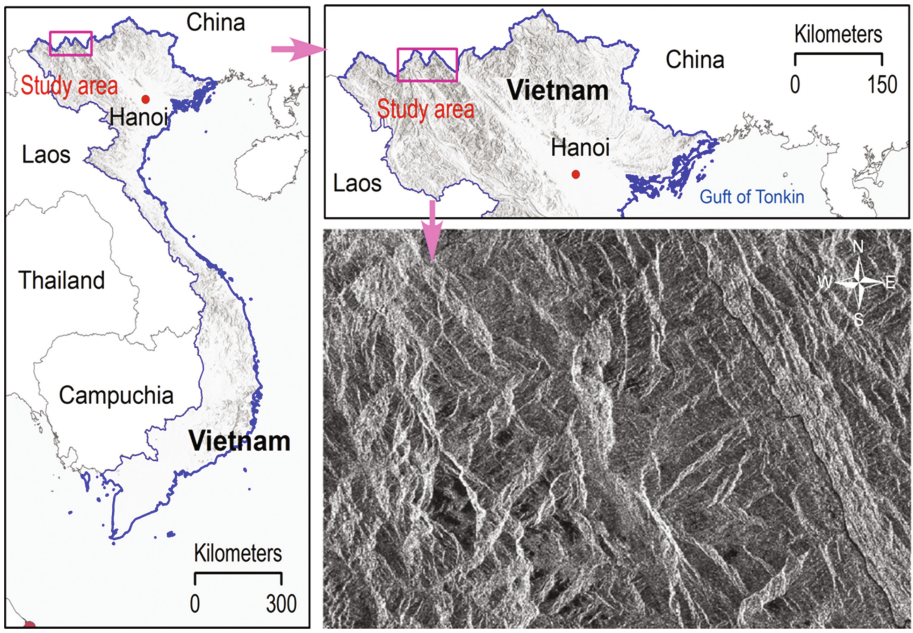

Fig. 2. Location of the study area and the amplitude ALOS PALSAR image (acquired on November 18, 2010) used in this study

The collected time series includes 11 ascending ALOS PALSAR images with resolution of 33.2 m × 28.4 m (range × azimuth) and HH polarization. Table 1 shows main characteristics of this dataset.

For the quantitative evaluation of change detection results, the ground truth samples were used. These samples were manually extracted based on visual interpretation of optical data, and by referring to field-based data and landslide susceptibility map

Table 1. Characteristics of the ALOS PALSAR data used in this study

Specifications	ALOS PALSAR data
Manufacturer	JAXA
Satellite orbit	Ascending
Repeat cycle	46 days
Imaging frequency	L-band at 1.27 GHz
Beam mode	High resolution Double Polarization
Data product	Single look complex (Level 1.1)
Spatial resolution	33.2 m × 28.4 m (range × azimuth)
Polarization	HH
Test-site	Bat Xat, Lao Cai & Phong Tho, Lai Chau, Vietnam
Acquisition dates (YYYY/MM/DD)	2007/09/25; 2007/11/10; 2008/06/27; 2008/08/12; 2009/06/30; 2009/08/15; 2009/09/30; 2010/07/03; 2010/08/18; 2010/10/03; 2010/11/18.

provided by Vietnam Institute of Geosciences and Mineral Resources (from the state-funded landslide project: "Investigation, assessment and warning zonation for landslides in the mountainous regions of Vietnam").

3.2 Methodology

In this study, the proposed framework was carried out by the following steps:

Step 1: Data preparation and preprocessing: After collecting SAR ITS and ancillary data, single look complex (SLC) ALOS PALSAR images were read and coregistered by ENVI SARscape modules. It should be noted that in this research, ENVI SARscape modules were only used for reading and coregistering SAR ITS, other computation processes were conducted using MATLAB 8.0.0.783. Then SLC data were converted into amplitude data and multilooked in azimuth direction.

Step 2: Similarity measure and thresholding method selection:
The critical factors for the effectiveness of the proposed framework are: a similarity measure to calculate the difference between each two images, and a threshold value to discriminate changed elements from unchanged ones. The proposed P-CDM operates with patch-wise sliding windows, number of samples in each patch is thus quite large. In this paper, we adopted statistical similarity measure derived from the information theory called Kullback-Leibler (KL) divergence [13] to calculate the similarity between two patches.
KL divergence is a way of measuring the differences (distances) between probability distributions, however, it is not a true metric. For discrete probability distributions P_X and P_Y of random variables X and Y, the KL divergence from P_Y and P_X is defined:

$$K(X\|Y) = \int P_X(x) \log\left(\frac{P_{X(x)}}{P_{X(x)}}\right) dx \tag{10}$$

$K(X\|Y) \neq K(Y\|X)$, therefore the KL distance (KLD) can be defined as:

$$d_{KL}(X,Y) = d_{KL}(Y,X) = \frac{1}{2}(K(X\|Y) + K(Y\|X)) \tag{11}$$

KLD is used to identify the difference of shapes of the local probability density functions (PDF). This difference is due to the temporal evolution of the local statistics of images.
For amplitude ALOS PALSAR time series over a non-homogeneous area like this mountainous test-site, the data present non-Rayleigh distribution, and empirical distributions are appropriate to describe these data. Applying the analysis of statistical model fit for SAR data in [14], we chose the KLD between Log-normal distributions to measure the differences of images in SAR ITS.

The KLD between two Log-normal distributions is given in [7] as:

$$d_{KL-Logn}(\alpha_X, \beta_X; \alpha_Y, \beta_Y) = \frac{1}{2}(\alpha_X - \alpha_Y)^2 \left(\frac{1}{\beta_X^2} + \frac{1}{\beta_Y^2}\right) + \frac{1}{2}\left(\frac{\beta_X^2}{\beta_y^2} + \frac{\beta_Y^2}{\beta_X^2}\right) \quad (12)$$

where α and β are the log-scale and shape parameters, respectively.
The minimum error thresholding method [15] was then applied to select the threshold value used for the separation of changed elements from unchanged ones.
In this paper, the same similarity measurement and thresholding method were employed for both stage 1 and 2 of the proposed multistage strategy.

Step 3: SAR ITS dividing: The whole SAR ITS was divided into patch stacks as described in Eq. (1). Change information in each stack was then extracted by the proposed P-CDM method.

Step 4: P-CDM 1 construction: The first step P-CDM was constructed using Eqs. (2) and (3), this is the preliminary change detection results.

Step 5: P-CDM 2 construction: Change information in P-CDM1 was refined using mutitemporal neighborhood defined in Eq. (4), and P-CDM2 containing more accurate change information was derived using Eqs. (5) and (6).

Step 6: Map of change dynamics: This map was obtained by calculating index of change dynamics from P-CDM2 of each patch stack, using Eq. (7).

Step 7: Analysis of P-CDM and map of change dynamics: Changed regions and images acquired on dates when changes occurred were identified by analyzing obtained P-CDM and map of change dynamics.

Step 8: Change detection in pixel scale: Changed regions were detected in patch scale in previous steps. In this step, change detection was performed in pixel scale to derive change map for each changed regions between acquisitions of interest, using Eqs. (8) and (9).

Step 9: Accuracy assessment: By comparing change map to ground truth samples, confusion matrix was calculated to evaluate the accuracy of change detection results. Limited errors (i.e., false alarms, missed alarms, and overall error) were also computed from this matrix.

3.3 Results and Discussion

Figure 3(a) shows divided patches on each image of the time series. Each initial large image was divided into 12 × 18 patches, so that, 12 × 18 patch stacks were made for the ITS. Figure 3(b) provides the map of change dynamics over the time series which presents temporal evolution of each patch stack. This map is sensitive to all types of changes detected between each two images of the time series. Therefore, changes in regions affected by regular evolution of vegetation in the whole ITS, and regions impacted by abrupt events (e.g. landslides, flash floods) in a short period as well as transient alterations are all appeared on this map with different levels of change dynamics.

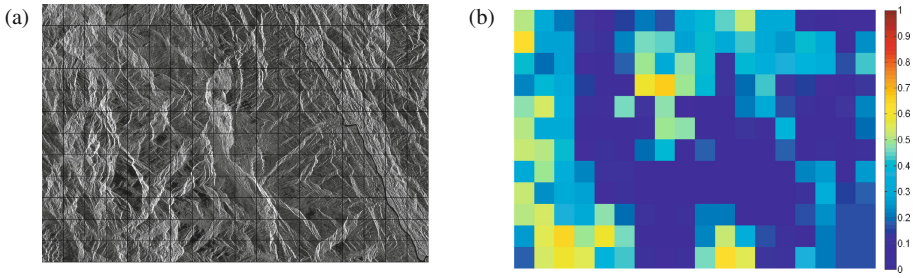

Fig. 3. Divided patches and change dynamics of patch stacks: (a) Divided patches on large size image; (b) Map of change dynamics

The map of change dynamics in Fig. 3(b) reveals some dynamic zones of the test-site with quite high index ε (0.4 to 0.6 in this map). In these regions, changes occurred more frequently than those in other regions of the test-site during the acquisition period. We were interested in four changed regions detected by P-CDM which were marked on Fig. 4.

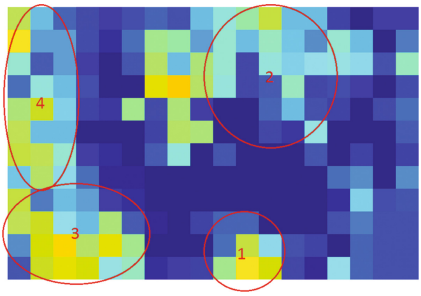

Fig. 4. Regions of interest detected by P-CDM approach

Images acquired on dates when significant changes were detected in the ITS (acquisitions of interest) were determined thanks to P-CDMs of each selected region (see Fig. 5). In this SAR ITS, images were acquired from September 2007 to November 2010, most of acquisitions of the ITS were taken from June to September of each year. This is the period when flash floods and landslides often occur in a year in regions 1 and 2. In regions 3 and 4 (rice terrace fields and forest), seasonal changes can be observed. Therefore, we can detect in this SAR ITS almost periodic changes. For all selected regions, we can see on the P-CDMs that these matrices contain black blocks representing stable periods of the time series, i.e., blocks of dates 4, 5, 6; dates 7, 8 and dates 10, 11 for region 1; blocks of dates 1 to 6, dates 7, 8 and dates 9, 10 for region 2; blocks of dates 3, 4 and dates 6 to 10 for region 3; and blocks of dates 1 to 4, dates 6, 7 and dates 9 to 11 for region 4. After the analysis of P-CDMs, one can select pairs of acquisition dates of interest for each region. We chose dates 9 and 10 for regions 1; date 6 and 7 for region 2; dates 5 and 6 for regions 3 and 4.

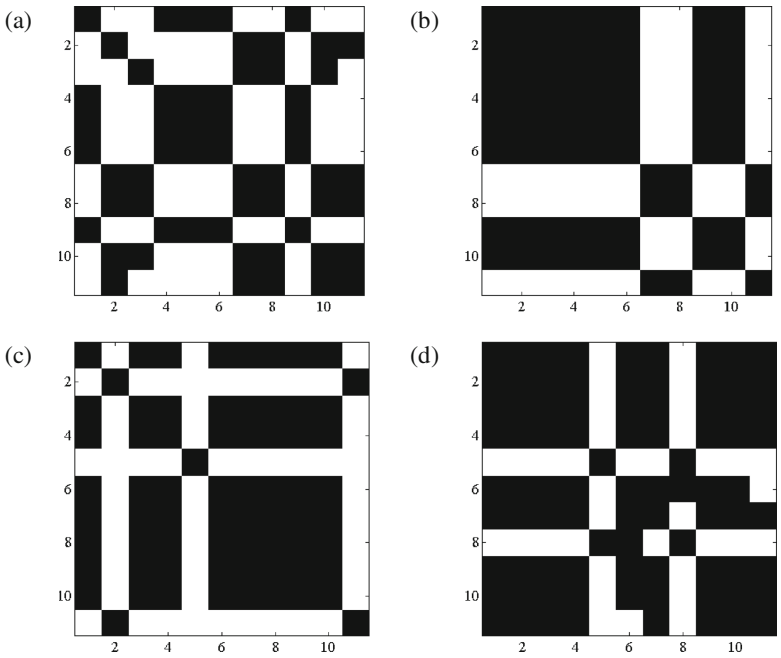

Fig. 5. P-CDMs at regions of interest: (a) P-CDM at region 1; (b) P-CDM at region 2; (c) P-CDM at region 3; (d) P-CDM at region 4

Changes were then detected with more details for each region between selected acquisitions (see Figs. 6, 7, 8 and 9).

It could be seen that on the change map of each region of interest, the proportion of changed pixels is high. It means that P-CDM method detected changed areas and acquisition dates before and after these changes correctly. The proposed framework can detect all types of change in this test-site, i.e., abrupt change due to occurrences of landslide and flash flood (regions 1 and 2) and progressive change like seasonal changes caused by plant evolution of forest and rice terrace areas (regions 3 and 4). These change maps also contain changed pixels in several zones affected by foldover effect of SAR data. This effect also leads to radiometric changes on different acquisitions of SAR ITS.

3.4 Accuracy Assessment

For the quantitative evaluation of change detection results, we used the ground truth samples of region 1 where landslide occurrence caused the surface changes.

Table 2 shows the confusion matrix of change detection results when comparing change map to 4892 ground truth samples of both changed and unchanged classes. The proposed approach detected 2199 correct and 116 false changed pixels, while it missed 608 changed pixels which were assigned as unchanged pixels. The limited errors are 5.0% false alarms, 21.7% missed alarms, and 14.8% overall error.

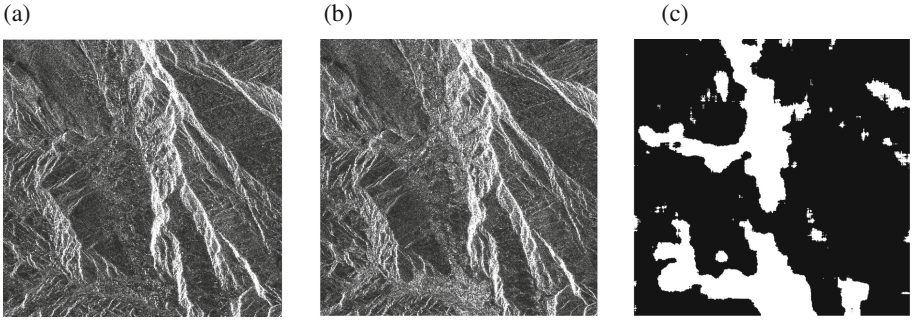

Fig. 6. Change detection result at region 1: (a) Region 1 on date 9; (b) Region 1 on date 10; (c) Change map

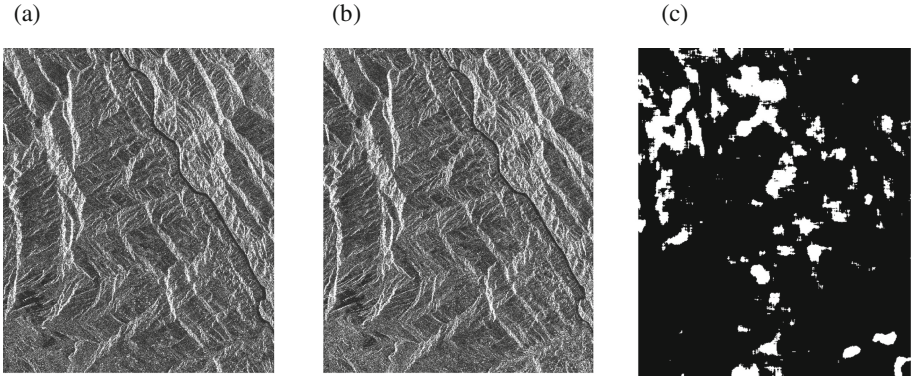

Fig. 7. Change detection result at region 2: (a) Region 2 on date 6; (b) Region 2 on date 7; (c) Change map

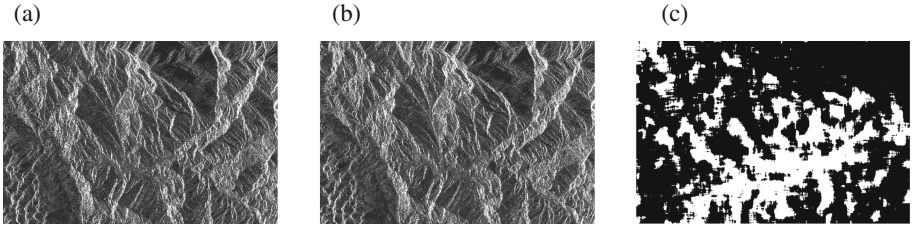

Fig. 8. Change detection result at region 3: (a) Region 3 on date 5; (b) Region 3 on date 6; (c) Change map

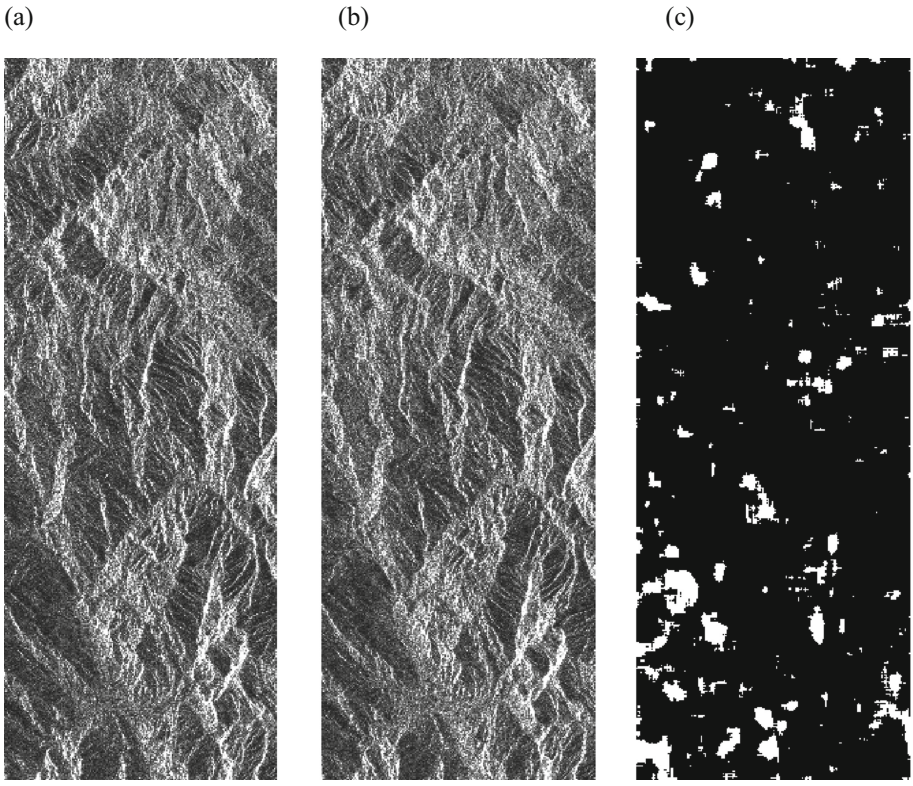

Fig. 9. Change detection result at region 4: (a) Region 4 on date 5; (b) Region 4 on date 6; (c) Change map

Table 2. Confusion matrix of change detection results

Class		Ground truth (pixels)		Total
		Changed	Unchanged	
Change map (pixels)	Changed	2199	116	2315
	Unchanged	608	1969	2577
Total		2807	2085	4892

4 Conclusions

In this paper, a new methodological framework for the detection of changes in long SAR ITS with large size images has been proposed. In the first stage of the framework, the P-CDM approach was introduced to detect changes in region scale. SAR ITS was divided into patch stacks, then change information of each stack was extracted by P-CDM in order to detect changed regions and acquisition dates related to change occurrences. In the second stage of the proposed framework, changes were detected

between acquisitions of interest for each selected region with more details in pixel scale, using Log-normal KLD.

The relevancy of the proposed approach was illustrated by a time series including 11 ascending ALOS PALSAR over Bat Xat District, Lao Cai Province, and a part of Phong Tho District, Lai Chau Province, Vietnam. The proposed approach can fast and correctly detect different kinds of change occurred in this large test-site. The obtained change maps are with overall accuracy of 85.2%, and low false alarm rate (5%). This research demonstrate the effectiveness of the proposed framework when processing long SAR ITS with large size images for change detection purpose.

In future works of this approach, higher spatial resolution (e.g. Sentinel-1, Radarsat-2, TerraSAR-X) SAR ITS should be exploited to detect changes of small objects on the ground. Furthermore, the development of an automatic thresholding according to expected false alarm rates is also taken into our consideration.

Acknowledgements. The authors would like to thank the Japan Aerospace Exploration Agency (JAXA) for providing the SAR ITS, and Dr Q.P. Nguyen (HUMG) for the ground truth information used in this work.

References

1. Baylis, P., Kroll, G., Madon, T.: Micro-satellite Data: Measuring Impact from Space. Creative Commons Attribution-NonCommercial-NoDerivatives 4.0 International License (2014) https://www.poverty-action.org/sites/default/files/publications/Goldilocks-Deep-Dive-Micro-satellite-Data-Measuring-Impact-from-Space_4.pdf
2. Waske, B., Braun, M.: Classifier ensembles for land cover mapping using multitemporal. ISPRS J. Photogramm. Remote Sens. **64**, 450–457 (2009)
3. Marin, C., Bovolo, F., Bruzzone, L.: Building change detection in multitemporal very high resolution SAR images. IEEE Trans. Geosci. Remote Sens. **53**(5), 2664–2682 (2015)
4. Le, T.T., Atto, A.M., Trouve, E., Solikhin, A., Pinel, V.: Change detection matrix for multitemporal filtering and change analysis of SAR and PolSAR image time series. ISPRS J. Photogramm. Remote Sens. **107**, 64–76 (2015)
5. Dellepiane, S.G., Angiati, E.: A new method for cross-normalization and multitemporal visualization of SAR images for the detection of flooded areas. IEEE Trans. Geosci. Remote Sens. **50**(7), 2765–2779 (2012)
6. Jiao, X., Kovacs, J.M., Shang, J., McNairn, H., Walters, D., Ma, B., Geng, X.: Object-oriented crop mapping and monitoring using multitemporal polarimetric RADARSAT-2 data. ISPRS J. Photogramm. Remote Sens. **96**, 38–46 (2014)
7. Atto, A.M., Trouve, E., Berthoumieu, Y., Mercier, G.: Multidate divergence matrices for the analysis of SAR image time series. IEEE Trans. Geosci. Remote Sens. **51**(4), 1922–1938 (2013)
8. Quin, G., Pinel-Puyssegur, B., Nicolas, J.-M., Loreaux, P.: MIMOSA: an automatic change detection method for SAR time series. IEEE Trans. Geosci. Remote Sens. **52**(9), 5349–5363 (2014)
9. Su, X., Deledalle, C.-A., FlorenceTupin, F., Sun, H.: NORCAMA: change analysis in SAR time series by likelihood ratio change matrix clustering. ISPRS J. Photogramm. Remote Sens. **101**, 247–261 (2015)

10. Le, T.T., Atto, A.M., Trouve, E., Nicolas, J.-M.: Adaptive multitemporal SAR image filtering based on the change detection matrix. IEEE Geosci. Remote Sens. Lett. **11**(10), 1826–1830 (2014)
11. Do, T., Nguyen, C., Phung, T.: Assessment of Natural Disasters in Vietnam's Northern Mountains. MPRA Paper No. 54209 (2014). http://mpra.ub.uni-muenchen.de/54209/
12. Vu, K.C., Van Rompaey, A., Govers, G., Vanacker, V., Schmook, B., Nguyen, H.: Land transitions in Northwest Vietnam: an integrated analysis of biophysical and socio-cultural factors. Hum. Ecol. **41**(1), 37–50 (2013)
13. Kullback, S., Leibler, R.A.: On information and sufficiency. Ann. Math. Stat. **22**(1), 79–86 (1951)
14. Le, T.T.: Change information extraction from synthetic aperture radar image time series. Ph.D. dissertation, Grenoble Alpes University (2015)
15. Kittler, J., Illingworth, J.: Minimum error thresholding. Pattern Recogn. **19**(1), 41–47 (1986)

Understanding Factors Affecting the Outbreak of Malaria Using Locally-Compensated Ridge Geographically Weighted Regression: Case Study in DakNong, Vietnam

Tuan-Anh Hoang(✉), Le Hoang Son, Quang-Thanh Bui, and Quoc-Huy Nguyen

VNU University of Science, Vietnam National University, Hanoi, Vietnam
{hoangtuananh88, sonlh, thanhbq}@vnu.edu.vn,
huyquoc23ll@gmail.com

Abstract. In this paper, we propose a new scheme to analyze factors that affect outbreak of malaria using the Locally-Compensated Ridge Geographically Weighted Regression (LCR-GWR). Since malaria prevalence is location dependence, the relationships between natural and social-economic factors to the development and concentration of malaria hotspots have been investigated. The proposed method is applied to DakNong province, one of the most vulnerable areas to malaria risk in Vietnam due to the lack of social infrastructure and the limited accessibility to health services. Even though mitigation campaigns were launched in the last several years, the number of new cases was found increasingly and several hotspots are still remained. The result is compared to those of several local analyses of spatial collinearity. It has been shown that LCR-GWR considerably improves the model fit and is useful to determine several factors including NDVI, DEM, distance to residential areas, distance to road that are highly associated with malaria risks. The results of this study help measuring the incidence of malaria in the context of climate change and under the impact of change in people's livelihoods.

Keywords: Malaria · Locally-compensated ridge · Geographically weighted regression · Hotspots

1 Introduction

Malaria is one of the most widespread parasitic diseases worldwide and is considered as one of the most dangerous endemic in 91 countries with 212 million cases and 429, 000 deaths [33]. Vietnam is one of those malaria - endemic countries which has 74% of the population having malaria risk mainly in the Central Coastal and Central Highland region [33]. There were several activities aim to reduce the morbidity and mortality of malaria in Vietnam, typical of which is National Malaria Control and Elimination Program launched officially by Vietnamese Government in 2011 [32]. The program achieved some successes with confirming cases in 2016 was 9331 and 3 deaths compared to 18387 cases and 8 deaths in 2012 [32, 33]. However, there are still challenges

© Springer International Publishing AG 2018
D. Tien Bui et al. (eds.), *Advances and Applications in Geospatial Technology and Earth Resources*, https://doi.org/10.1007/978-3-319-68240-2_11

especially in the context of climate change where climate factors affect the distribution of malaria [3].

Several methods have been proposed to this problem including epidemiological expert methods [15], Remote Sensing and GIS [1, 24] and the hybrid GIS with soft computing [6, 25, 31]. Lubetzky-Vilnai et al. [19] and Mosha *et al.* [21] used statistics and spatial analysis based on time series [4]. However, the statistical approach is not sufficient to handle complex structures and nonlinearity of malaria risk datasets. Incorporating artificial intelligence, remote sensing and GIS is an alternative way to overcome this drawback [18, 24]. Specifically, Ch *et al*. [7] integrated a support vector model and Firefly algorithms to evaluate the risk of malaria. Buczak *et al.* [6] applied fuzzy logic to study malaria in Korea. Zacarias *et al.* [34] compared the support deployment models and random forest in Mozambique. Recently, Geographically Weighted Regression (GWR) and its variants have been used in the study of the relationship between malaria and geographical factors [5, 12, 25–29].

Unlike conventional regression methods that assume the relationship between malaria and geographic factors is the same across regions in a study area, GWR creates separate regressions for each set of observed data (local regression) using adjacent objects in a defined "bandwidth" distance [2]. Although GWR is important to explore spatial non-stationary data relationship, a problem found in many regression models is collinearity which affects the precision of the model. Locally-compensated ridge GWR aims to reduce the influence of the collinearity to the regression model; thus improving its accuracy [8].

Taking advantage of regression in epidemiological studies, in this paper, we propose a new scheme to analyze factors that affect outbreak of malaria using the Locally-Compensated Ridge Geographically Weighted Regression (LCR-GWR). The new method is used to ascertain the relationship between factors such as land use, distance to residence, distance to road, elevation, NDVI and the development of malaria. For variables related to geography, collinearity is used to verify two variables if they have linear relationship or highly correlated [8]. For example, the higher the elevation, the lower the temperature and contrary the higher the humidity (at the troposphere), or the age group will have a relationship with the employment. It is indeed obvious that the LCR-GWR can reduce the effects of local collinearity so as to improve the models' efficiency.

The proposed method is applied to Dak Nong province, located in the Central Highland region of Vietnam- an inhabited area for the minority community who has lacks condition and infrastructure with limited access to health services [23]. Dak Nong is determined within the geographical coordinate: $11^{\circ}45'$ to $12^{\circ}50'$ north latitude, $107^{\circ}13'$ to $108^{\circ}10'$ east longitude. Dak Nong shares border with Dak Lak province to the North and Northeast, border with Lam Dong province to the East and Southeast, border with Binh Phuoc province, "the cradle" of malaria in Vietnam [9], to the Southern and Southwestern and border with Cambodia to the West [10]. With its geographical conditions, Dak Nong has been one of the malaria hotspots. In the first 4 months of 2015, 176 cases of malaria and 175 patients were detected, with an increase of 68 cases and 72 patients compared to the same period in 2014. Although in 2016, the province set up impact mitigation campaigns for malaria and got some achievements.

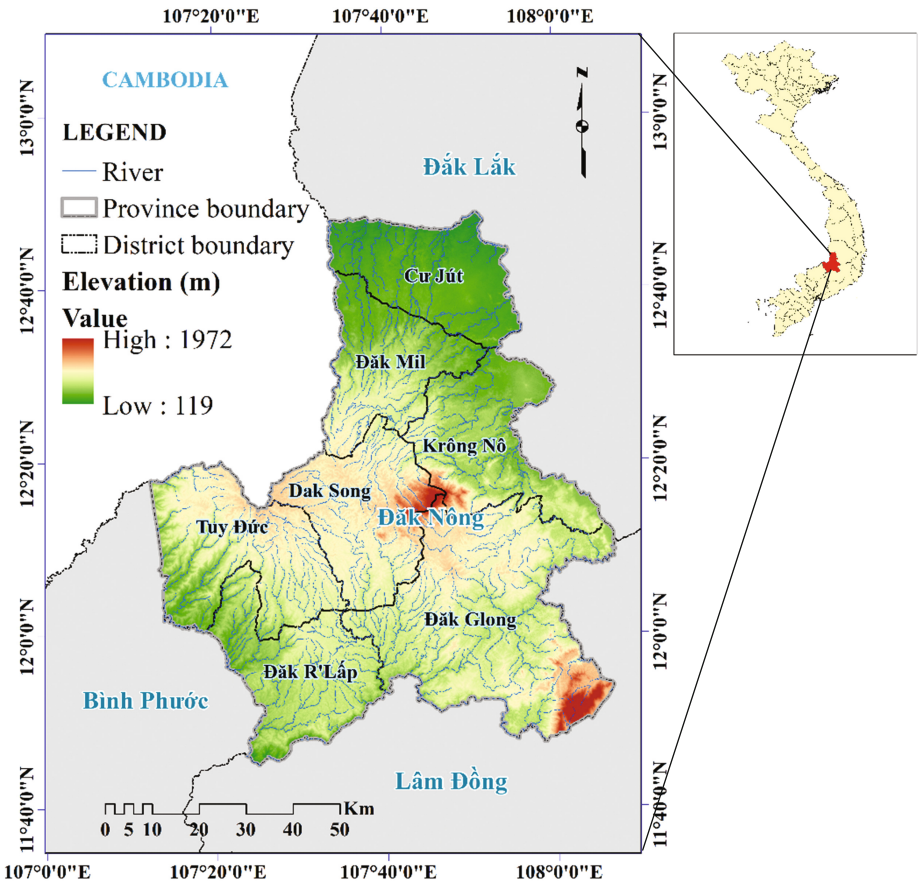

Fig. 1. Location of Dak Nong province, Vietnam

However, this region is still considered as hotspots of malaria from the past to present (Fig. 1).

The remainder of this paper is organized as follows: Sect. 2 introduces the datasets and LCR-GWR method. Section 3 presents the experimental results. Section 4 highlights some conclusions and further works of the paper.

2 Materials and Methods

2.1 Datasets

The vector for transmission of malaria is from infected mosquitoes' bite. In hot and humid climate territories, such as Vietnam, mosquitoes thrive as a favorable condition for malaria outbreaks [15]. According to WHO, the malaria parasites commonly found in Vietnam are P. vivax and P. falciparum through Anopheles mosquitoes [33]. In this

study, we do not focus on the epidemiology of malaria but would like to point out the conditions that affect the development of malaria through the collected survey data. The malaria data were collected from the Provincial Center for Preventive Medicine through a survey and inspection of more than 50,000 people from DakNong province in which 198 people were infected by malaria parasites in 2016. To assure and enhance the data quality, we have also visited the field to check and investigate more in prevalence malaria cases with a total of 209 observations which is expressed through Fig. 2a. From the data, we conduct a malaria hotspot map using Kriging algorithm. The result turns out that the malaria area is close to the border of Cambodia and Binh Phuoc province (Fig. 2b).

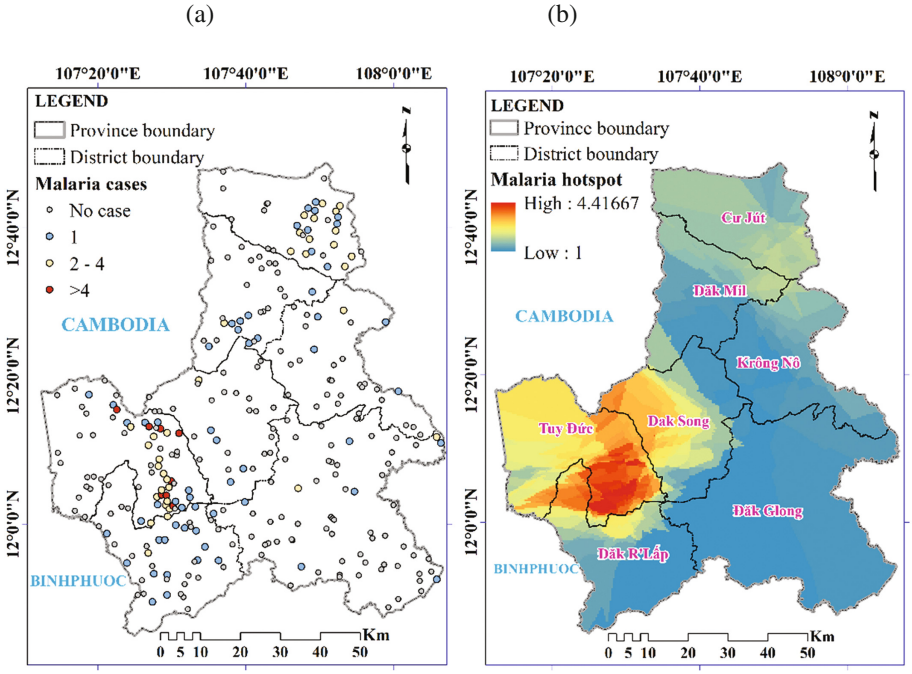

Fig. 2. (a) Distribution map of malaria; (b) Hotspot map of malaria in DakNong

2.2 Methods

In each regression model, the results indicate the level of predictor variable influence on the dependent variable. In this study, the dependent variable is the 209 malaria cases in 2016 for the whole province. The probable predictor variables were chosen based on the relation to malaria and through previous research and source of data. Several researches can provide these variables, such as vegetation, which plays a very important role in transmitting malaria. There are few indicators to express the properties vegetation but NDVI is the most widely used index. Temperature, rainfall,

humidity are the meteorological variables that are often used in predicting malaria transmission [17]. In addition, age group, gender are the social variables that are highly associated with malaria [32]. To take advantage of data collected, we selected 40 predictor variables as follows: the variables were divided into 2 groups which are natural conditions and social - economic conditions.

Natural condition variables

A DEM was provided globally from Aster Global DEM data (available at https://earthexplorer.usgs.gov/). The DEM is then used to generate Aspect and Slope using ArcGIS 10.4.1. Daily climatic data during 2016 were collected from 18 national meteorological stations and then averaged. Then we used Kriging in ArcGIS 10.4.1 to interpolate for the whole study area. NDVI, NDBI, and NDMI are calculated using bands from Landsat 8 OLI captured in Fed 12 2017 in which NDVI is Normalized Difference Vegetation Index, NDBI is Normalized Difference Built-up Index and NDMI is Normalized Difference Moisture Index. NDVI, NDMI and NDBI are defined as follow:

$$\begin{aligned} \mathrm{NDVI} &= (\mathrm{NIR}-\mathrm{R})/(\mathrm{NIR}+\mathrm{R}) \\ \mathrm{NDMI} &= (\mathrm{NIR}-\mathrm{IR})/(\mathrm{NIR}+\mathrm{IR}) \\ \mathrm{NDBI} &= (\mathrm{SWIR2}-\mathrm{NIR})/(\mathrm{SWIR2}+\mathrm{IR}) \end{aligned} \tag{1}$$

where NIR is the Near Infrared band, R is the Red band and SWIR is the Short-Wave Infrared band. The last variables are determined using Dak Nong land use map 2015 which was collected at the Dak Nong Department of Natural Resources and Environment at the scale of 1:50000. The land use map is categorized into 16 types name TTN (Religious land), SMN (Water surface), RSX (Production forest land), RPH (Protective forest land), RMP (Protective planted forest land), RDD (special forest land), OTC (Residential land), NTS (Aquaculture land), NHK (Upland land cultivate another annual crop), NKH (Other agricultural land), CSK (Productive land, non-agricultural business), CSD (Unused land), CLN (Perennial crops), CHN (Annual crop land), CDG (Specialized land), CCC (Public land) and few other point and line layers (river, road, hospital, school). Variable as forest is extracted in a combination of RSX, RPH, RPM and RDD. Agriculture land is extracted using CHN, CLN, NHK, NKH. Aquaculture land and residential land are NTS and OTC. The point and line objects as hospitals, rivers and roads were also extracted from land use map. For distance to hospital, we also selected few others which are inside 10 km distance from Dak Nong. These objects are respectively used to calculate distance using Euclidean Distance tool from ArcGIS software [13] (Table 1).

Social – economic condition variables

Data about population including population, density, gender, age group and building structure are collected from Dak Nong Statistic Yearbook 2015 at commune level. The data are then divided into sub-groups as shown in Table 2:

Due to the reason that the statistic is at commune level while the spatial malaria data are points, the statistic was calculated as the average of the whole commune. In addition, natural condition variables are also at Raster format and were added to the malaria table base on the location of the malaria point.

Table 1. Natural condition variables

Variable name	Code	Resolution/Unit/Method	Source
Aspect	Aspect	30 m	Extracted from Aster global DEM data
Elevation	DEM	30 m	Extracted from Aster global DEM data
Slope	Slope	30 m	Extracted from Aster global DEM data
Normalized Difference Built-up Index	NDBI	30 m	Calculated using SWIR 2 and NIR bands of Landsat 8 OLI Feb 12, 2017
Normalized Difference Vegetation Index	NDVI	30 m	Calculated using NIR and Red Bands of Landsat 8 OLI Feb 12, 2017
Normalized Difference Moisture Index	NDMI	30 m	Calculated using NIR and IR Bands of Landsat 8 OLI Feb 12, 2017
Distance to residence	DRe	Calculated using Euclidean Distance in ArcGIS, resolution 30 m	Resident area extracted from Landuse map 2015
Distance to road	DRo	Calculated using Euclidean Distance in ArcGIS, resolution 30 m	Roads extracted from Landuse map 2015
Distance to river	DRi	Calculated using Euclidean Distance in ArcGIS resolution 30 m	Rivers extracted from Landuse map 2015
Distance to hospital	DHo	Calculated using Euclidean Distance in ArcGIS, resolution 30 m	Hospital extracted from Landuse map 2015
Distance to aquaculture land	DAqL	Calculated using Euclidean Distance in ArcGIS, resolution 30 m	Aquaculture land extracted from Landuse map 2015
Distance to agriculture land	DAgL	Calculated using Euclidean Distance in ArcGIS, resolution 30 m	Agriculture land extracted from Landuse map 2015
Distance to wetland	DWe	Calculated using Euclidean Distance in ArcGIS, resolution 30 m	Agriculture land extracted from Landuse map 2015
Distance to forest	DFo	Calculated using Euclidean Distance in ArcGIS, resolution 30 m	Resident area extracted from Topography map 2015
Rainfall	Rain	Kriging (ArcGIS) average of daily rainfall during the year 2016 (mm)	Rainfall collected from 18 national stations

(*continued*)

Table 1. (*continued*)

Variable name	Code	Resolution/Unit/Method	Source
Temperature	Temp	Kriging (ArcGIS) average of daily temperature during the year 2016 (^{o}C)	Temperature collected from 18 national stations
Humidity	Humid	Kriging (ArcGIS) average of daily humidity during the year 2016 (%)	Humidity collected from 18 national stations

Table 2. Social – economic variables

Variable name	Code	Resolution/Unit	Source
Population	Pop	Population group includes 4 variables as Sum_pop, Urban_pop, Rural_pop, Pop_dens	DakNong Statistic yearbook 2015
Age	Age	Age is divided into 10 subs – group as 0–5 years old, 5–9 years old 10–19 years old, 20–29 years old, 30–39 years old, 40–49 years old, 50–59 years old, 60–69 years old, 70–79 years old, >80 years old (10 variables)	DakNong Statistic Yearbook 2015
Sex	Sex	Sex is divided into 2 subs – group as Pop_male, Pop_femal. (2 variables)	DakNong Statistic Yearbook 2015
Building structure	Build_struct	Building structure group includes 7 variables as Sum_build, Solid_build, Semi_sol_bui,un_so_bui,Simp_build, undef_build and Area_per_cap.	DakNong Statistic Yearbook 2015

We presume that the non-stationary relationship exists between malaria occurrences and influential factors. Therefore, the following scheme is proposed to analyze factors that affect outbreak of malaria using LCR-GWR (Fig. 3).

Step 1 is to determine the correlation coefficient between variables to eliminate those which are highly correlated. For instance, one of these variables as NDVI, NDBI, and NDMI can be eliminated if the correlation coefficient is higher than 0.7 (the correlation ranges from -1 to 1, with 0 value means there is no correlation between variables, we will give a table pairing all variables in the next section), we decide to keep those having high impact in the model. Then, in step 2, we run an OLS model to test the explanatory variables and determine how many percents of the data that potentially explain the malaria disease. However, spatial data, as variables in this research has unique characteristics. Firstly, the geographical factors are spatial auto-correlation which means the two locations that are close together should have similar characteristics compared to locations that are far away from each other. Secondly, geographic related factors for instance elevation, NDVI, population density are spatial

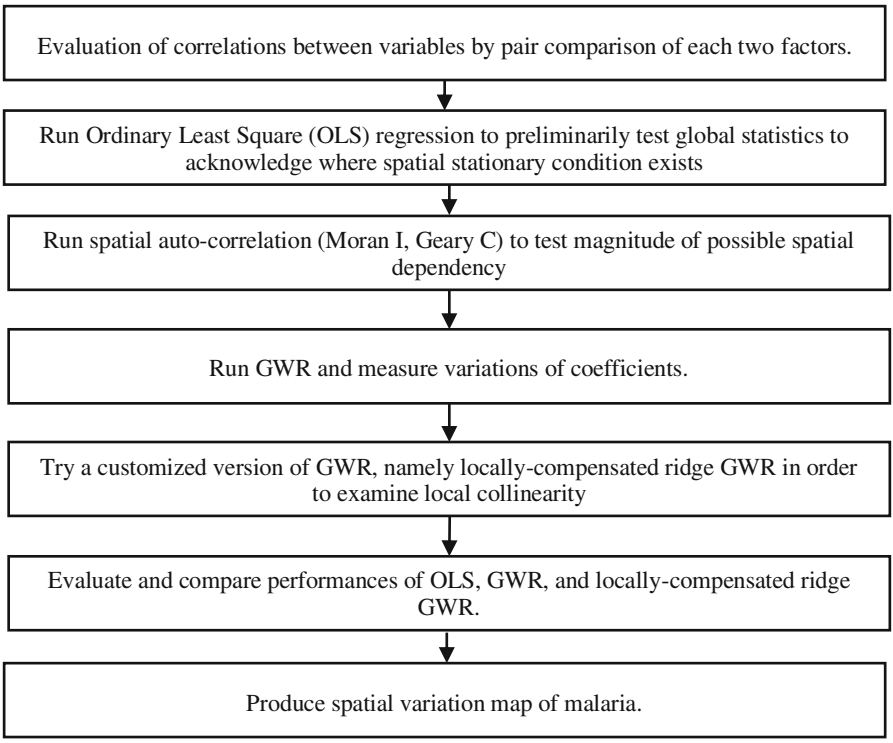

Fig. 3. Schematic overview of using LCR-GWR in prediction of malaria incidences

non-stationary. These factors value vary differently across the research area. Therefore, in step 3, spatial autocorrelation statistics as Moran I and Geary C are calculated to estimate the degree of spatial autocorrelation in a dataset [12, 22]. The Moran I runs with the residual of OLS regression. If Moran I approximately equals to 0 or less than 0, that means the data are randomly distributed or dispersed and an OLS model is fit. But if Moran Index is greater than 0, then the data are clustered and an OLS model is not appropriate. Step 4 in hence provides a GWR model will be run with the significant variables extracted from OLS model. The basic GWR model is:

$$y_i = \beta_{i0} + \sum_{k=1}^{m} \beta_{ik} x_{ik} + \epsilon_i \tag{2}$$

where y_i is the dependent variable at location i, x_{ik} is the value of the k_{th} independent variable at location i, m is the number of independent variables, β_{i0} is the intercept term at location i, β_{ik} is the local regression coefficient for the k^{th} independent variable at location i and ε_i is the random error at location i. In this step, we need to consider the variable collinearity, which can be measured as condition number (CN) and variance inflation factors (VIFs). The condition number is used to assess the whole model while VIFs consider each variable in turn [8]. Therefore, the local condition number

(CN) was tested in this model to check if it is greater than 30, as proved in literature, means that there are local collinearities between variables [8, 16]. Step 5 is to provide a better GWR model in which AICc, R^2 and R^2 adjusted will be observed. Step 6 is to compare between OLS, GWR and LCR.GWR. In the final step, the coefficients of variables from LCR.GWR are used to calculate and provide a spatial variation map of malaria.

3 Results and Discussion

3.1 Evaluation of Correlation

Correlation coefficient (r) is a statistical indicator that measures the correlation between two variables. In this research, Pearson correlation coefficient is used to indicate the relationship of variables globally using *cor(x,y)* function in R [14]. The definition of the correlation coefficient is defined as follow:

$$r(x,y) = \frac{\sum_{i=1}^{n}(x_i - \bar{x})(y_i - \bar{y})}{\sqrt{\sum_{i=1}^{n}(x_i - \bar{x})^2 \sum_{i=1}^{n}(y_i - \bar{y})^2}} \quad (3)$$

where $\bar{x}$ and $\bar{y}$ is the mean value of variables x and y. Some variables were eliminated due to the correlation coefficient absolute value is higher than 0.7 (age structure group, gender group, NDBI, NDMI, Temperature). Strong correlations amongst the predictor variables indicate prominent level of collinearity. Therefore, this step is to filter the significant variables for OLS model (Table 3).

Table 3. Correlation between variables

	DEM	DAgL	DAqL	DFo	DHo	DRe	DRi	DRo	NDVI	Rain	Slope	Aspect	DWe
DEM	1	0.043	0.12	−0.32	−0.34	0.13	−0.25	0.03	0.06	0.46	0.17	0.006	0.16
DAgL	–	1	0.36	−0.19	0.02	0.68	−0.07	0.5	0.11	−0.03	0.048	0.04	0.30
DAqL	–	–	1	−0.28	0.23	0.58	0.008	0.43	0.11	−0.006	−0.000	0.001	0.25
DFo	–	–	–	1	0.06	−0.39	0.17	−0.3	−0.05	−0.28	−0.10	0.02	−0.11
DHo	–	–	–	–	1	0.04	0.14	0.09	0.08	−0.34	−0.06	−0.05	−0.13
DRe	–	–	–	–	–	1	−0.09	0.66	0.25	0.020	0.09	0.05	0.39
DRi	–	–	–	–	–	–	1	−0.03	−0.09	−0.24	−0.16	0.19	0.24
DRo	–	–	–	–	–	–	–	1	0.22	0.06	0.041	0.06	0.18
NDVI	–	–	–	–	–	–	–	–	1	0.08	0.23	0.04	−0.06
Rain	–	–	–	–	–	–	–	–	–	1	0.23	−0.006	−0.01
Slope	–	–	–	–	–	–	–	–	–	–	1	−0.08	0.05
Aspect	–	–	–	–	–	–	–	–	–	–	–	1	0.06
DWe	–	–	–	–	–	–	–	–	–	–	–	–	1

After calculating correlation between 40 preliminary input variables, only 13 variables are selected to use for regression models. They are elevation, distance to agriculture land, distance to aquaculture land, distance to forest, distance to hospital,

distance to residence, distance to river, distance to road, distance to wetland, NDVI, rainfall, slope, and aspect. These variables seem to be appropriated to explain the malaria incidence in this study area. However, we need to indicate which are the most significant variables.

3.2 Ordinary Least Square Regression (OLS) and Spatial Autocorrelation

Predictor variables listed in Table 3 were used as inputs to construct a model to predict malaria incident. ArcGIS 10.4.1 is used for generating and visualizing the OLS model. The global coefficient estimates together with their significance and VIFs for each predictor variable are shown in Table 4. Table 4 indicates significant variables to predict malaria which has p-value < 0.05 and none of VIFs are greater than 10 which mean that globally there is evidence of variable collinearity [8].

Table 4. Estimated regression coefficient for OLS model

Variables	Coefficient	Standard error	t-value	p-value	VIF [c]
Intercept	1.604376	1.239738	1.294125	0.197158	—
DEM	0.001541	0.000597	2.578767	**0.010645***	1.543405
DRe	0.000178	0.000124	2.032316	**0.049665***	3.781569
DRo	−0.000294	0.000146	−2.01361	**0.045420***	1.918792
NDVI	−1.736418	0.658739	−2.635972	**0.009060***	1.194432

Table 5. OLS summary

Number of observations	209
Akaike's Information Criterion (AICc) [d]:	714.086802
Multiple R-Squared [d]:	0.127098
Adjusted R-Squared [d]:	0.068905

Overall, summary of the OLS model in Table 5 shows that malaria is dependent on elevation, distance to residence, distance to road, and NDVI. This is reasonable because elevation influences many other variables as precipitation, temperature, slope and aspect, therefore it directly or indirectly influences the widespread of malaria. Meanwhile, NDVI represents factors such as forests and crops. For epidemiology, forestland is a good place for the development of malaria [32]. Distance to residential area and distance to roads are also explained by the activities of Central Highland people of the central highlands who have the custom to go into forests for cultivation or cutting wood, they move back and forth between regions, provinces, even across Cambodia borders for months and sometimes sleep in the forest. These people are at higher risk of malaria infection than the others [15]. Therefore, we can see that the area outside the residence, away from the main roads and close to the border have a higher incidence of malaria than normal.

There are several different measures: The R^2 is 0.127098 and the adjusted R^2 is 0.068905. The R^2 measures the proportion of the variation in the dependent variable which is accounted for by the variation in the model which has possible values range from 0 to 1. The adjusted R^2 is a preferable measure since it contains some adjustment for the number of variables in the model. In our OLS model, the value of R^2 adjusted is 0.068905 indicates that it accounts for about 6% of the variation in the dependent variable. This means this model has a substandard performance. There is a need to consider another model.

Another measure for evaluating model fit is provided by the Akaike Information Criterion (AIC) [16, 20]. Unlike the R^2 the AIC measure the 'relative distance' between the model that has been fitted and the unknown 'true' model [20]. Models with smaller values of the AIC is better fit than other with higher AIC value. The AIC in this case is 714.086802.

3.3 Moran Index of Residual

Global Moran I is used to determine autocorrelation of input variables for OLS model through interpretation of the residual.

$$I = \frac{\sum_{i=1}^{n}\sum_{j=1}^{n} w_{ij}(x_i - \bar{x})(x_j - \bar{x})}{(\sum_{i=1}^{n}\sum_{j=1}^{n} w_{ij})\sum_{i=1}^{n}(x_i - \bar{x})} \tag{4}$$

where N is the number of observation, $\bar{x}$ is the mean of variable x, x_i is the variable value at location i, x_j is the variable value at location j, w_{ij} is the spatial weight. Moran I ranges from −1 (negative correlation) to +1 (positive correlation) (Table 6).

Table 6. Global Moran Index summary

Moran's Index:	**0.376422**
Expected Index:	−0.004808
Variance:	0.001222
z-score:	10.906042
p-value:	0.000000

In this research, the Moran I value is 0.376422 indicating that the variables are positively correlated. After the Moran I is computed, the Expected Index value will also be generated using the following formula:

$$E(I) = \frac{-1}{(n-1)} \tag{5}$$

where n is the number of observation. The Expected Index will also help to measure the variance. The Expected Index is then used in comparison with the Observed Index. The

z-score (standard deviation) and p-value (probability) are calculated using this comparison, which will indicate whether this data is statistically significant or not. Z-score is defined as follow:

$$z(I) = \frac{I - E(I)}{\sqrt{V(I)}} \tag{6}$$

where

$$V(I) = E(I^2) - E(I)^2 \tag{7}$$

V(I) is the variance. The value of z-score and p-value will also show whether or not to reject the null hypothesis. For this tool, the null hypothesis states that the values associated with features are randomly distributed [11]. The z-score and p-value in this situation mean that the null hypothesis will be rejected, the data is highly clustered with approximately 0% percent of being randomly distributed.

3.4 GWR and Variations of Coefficients

The results of Moran I OLS' residual indicate the consideration of using GWR while OLS can only explain 6% malaria collected data (R^2 adjusted = 0.068905). There are two main parameters required for GWR including bandwidth and kernel type. In this research, we used a corrected version of AICc to automatically specify the bandwidth. For the kernel, there are two possible choices for the Kernel type, FIXED and ADAPTIVE. FIXED kernel type is used for observations which are regularly distributed across the research area while ADAPTIVE kernel is for clustered observation [16, 20]. The Moran I have already indicated that data are clustered. Therefore, for better fit and accuracy, and also an ADAPTIVE kernel will cover most applications [20], an ADAPTIVE kernel was used. GWR function in ArcGIS (spatial statistic toolbox) was used to generate GW model.

The results from GWR model are express in Table 7 and Fig. 4.

Table 7. GWR summary

	Standard GWR	Compare to OLS model
Kernel type	Adaptive	
AICc	**679.41602964841491**	714.086802
R2	**0.36841843019175602**	0.127098
R2Adjusted	**0.23326644249726569**	0.068905

The results show a significant improvement of GWR compare to OLS: AICc decreased from 714.09 to 689.42. The lower the AICc, the better performance the model. R^2 and R^2 adjusted are highly improved indicate that GWR explained more in malaria collected data than OLS (23.32%). However, the condition number is higher than 30 in some locations which is considered to have collinearity between variables

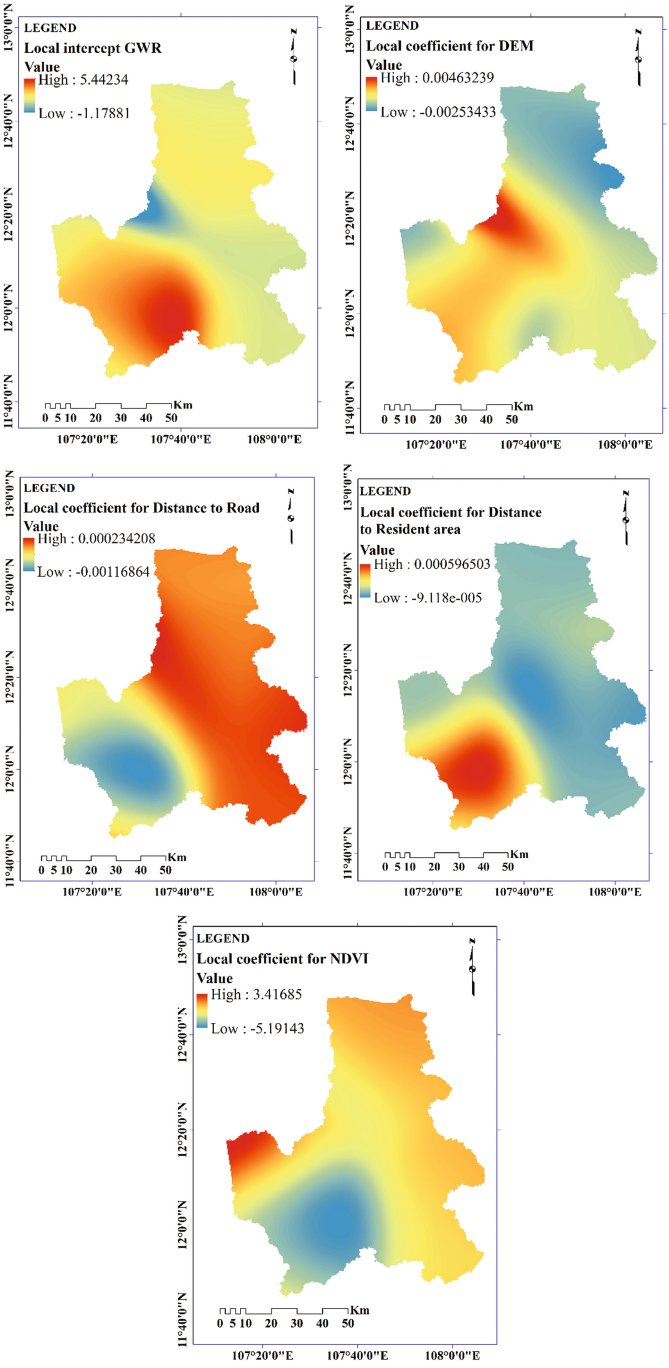

Fig. 4. Local parameters for GWR

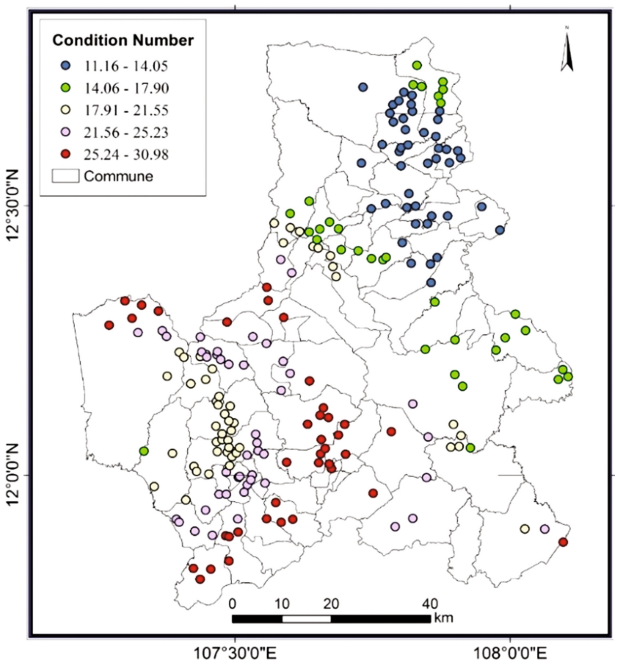

Fig. 5. Spatial variations in condition number (CN) of coefficients

[16]. The CN values shown in Fig. 5 demonstrate that the collinearity appeared near the malaria hotspots.

3.5 Locally-Compensated Ridge GWR

One of the methods to reduce collinearity in the explanatory variables of a linear model is ridge regression. The estimator of a ridge regression is altered to include a small change to values of diagonal of the cross-product matrix known as ridge shown as λ in the following equation:

$$\beta = \left(x^T x + \lambda I\right)^{-1} x^T y. \tag{8}$$

The relationship between condition number and ridge parameter is shown as follow:

$$\lambda = \{(\epsilon_1 - \epsilon_P) \,/\, (\kappa - 1)\} - \epsilon_P, \tag{9}$$

where $\epsilon_1, \epsilon_2 \ldots \epsilon_P$ are the eigenvalues of the matrix $(x^T x)$, κ is the condition number. In locally-compensate ridge, the estimator for GW regression model is:

$$\beta(u_i, v_i) = \left(x^T W(u_i, v_i)x + \lambda I(u_i, v_i)\right)^{-1} x^T W(u_i, v_i)y. \quad (10)$$

$\lambda I(u_i, v_i)$ is locally-compensated value of λ at location (u_i, v_i). The weight $W(u_i, v_j)$ (weight at location i with coordinate value (u,v)) is calculated based on its distance to the center of the kernel as follows:

$$W(u_i, v_i) = 1 - \left(d(u_i, v_i))^2 / b^2\right), \quad (11)$$

where $d(u_i, v_i)$is the distance in meters from the center of the kernel to the data point and b is the bandwidth [16, 30]. The same bandwidth of GWR can be applied to LCR-GWR model. LCR-GWR bandwidth was run in R environment *(bw.gwr.lcr* in GWmodel) then put into ArcGIS for generating intercept and coefficients. From the results, the bandwidth 51 which has the smallest CV score was chosen for GWR model with the CN threshold less than 30 (Table 8 and Fig. 6).

Table 8. Locally compensated ridge GWR summary

	Locally-compensated ridge GWR (LCR-GWR)	Compare to standard GWR model
Kernel type	Adaptive	Adaptive
AICc	**220.50814901236132**	679.41602964841491
R2	**0.63565935117477057**	0.36841843019175602
R2Adjusted	**0.50627226519768787**	0.23326644249726569

Variations maps of malaria occurrences

The results of LCR-GWR is improved in comparison with basic GWR with R^2 adjusted = 0.506. The intercept and coefficient will then be used in ArcGIS along with the DEM, distance to road, distance to residence, NDVI value run in the previous steps to generate the spatial variation of malaria occurrence (Fig. 7). The malaria prevalence map seems to be appropriate with the malaria occurrence near the border of Cambodia and Binh Duong at the low terrain area.

The results of this study indicated that it is necessary to focus on the collinearity among variables, especially variables that varied spatially. The regression models also show that the influence of variables on the incidence of malaria is reasonable, especially with high mountainous areas with most people being ethnic minorities who have different customs. OLS or standard GWR may explain some cases of malaria. However, when collinearity occurs between variables, the model becomes less precise and predictive. LCR-GWR was used to reduce the local collinearity by using the locally-compensated value of ridge with condition number less than 30. The results showed a significant improvement within which the established model capable of

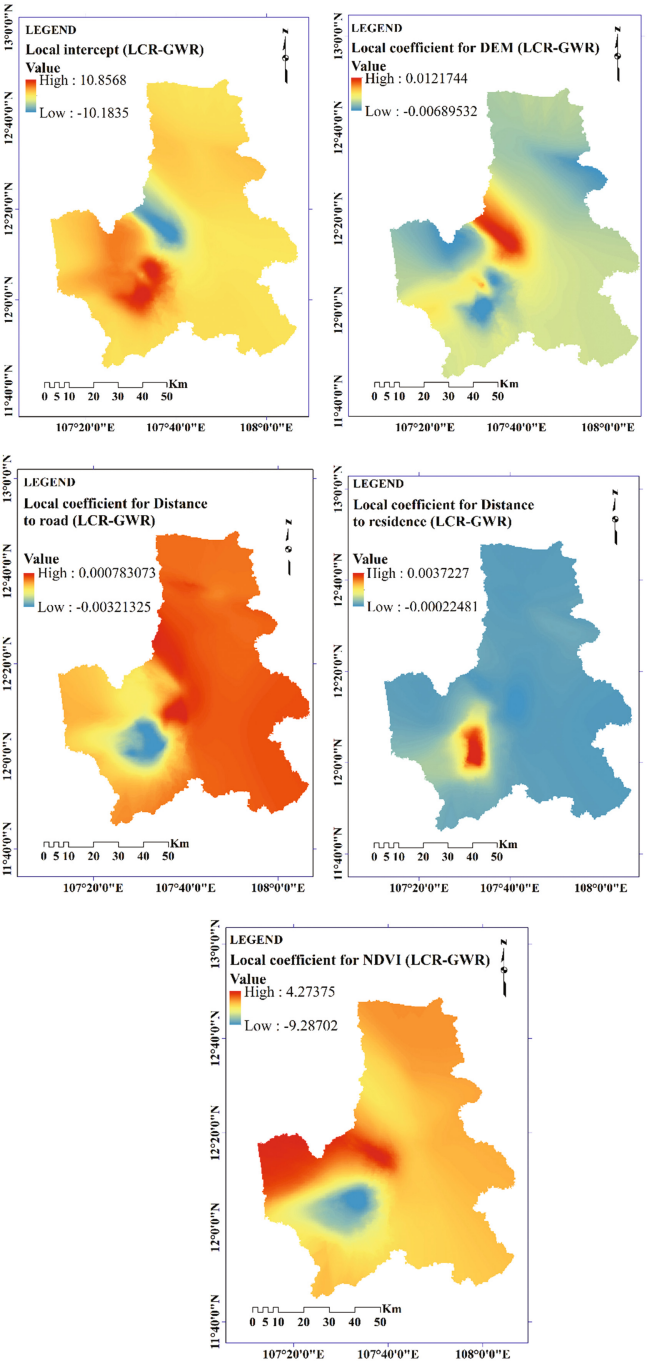

Fig. 6. Spatial variations of coefficients by locally-compensated ridge GWR

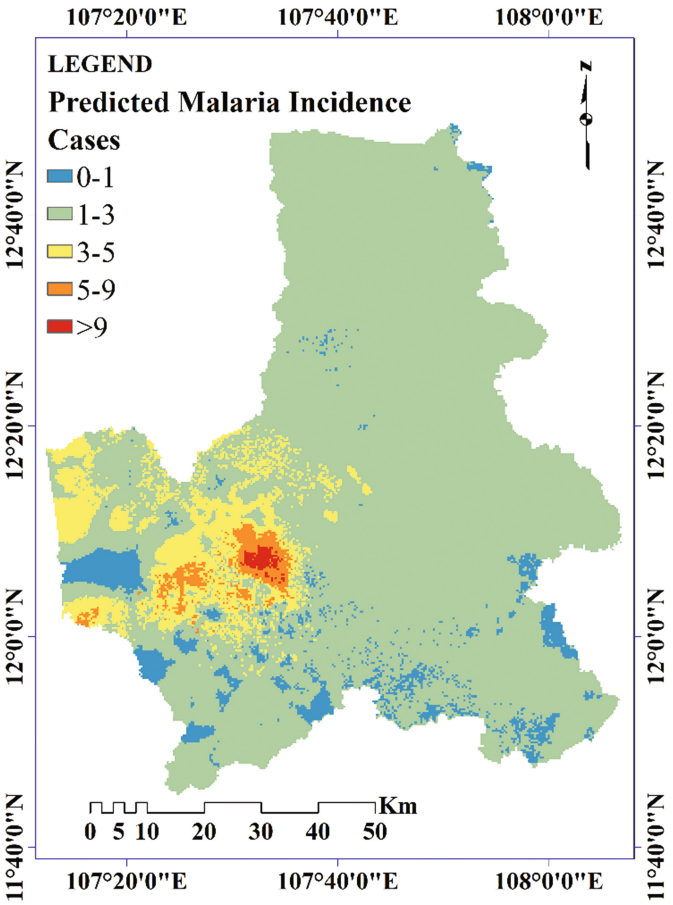

Fig. 7. Spatial variation of malaria occurrence

explaining more than 50% of cases of malaria in the study area by considering factors such as elevation, distance to roads, distance to residential areas and NDVI.

4 Conclusions

Variation of malaria hotspot is subject to change across the study area depending on local physical and environmental conditions. In this paper, we proposed a new scheme to analyze factors that affect outbreak of malaria using the LCR-GWR. Forty variables that were likely to influence the distribution of malaria occurrences were selected and filtered out by correlation to keep the most predictive power ones for modeling. The remaining variables were analyzed by the ordinary least square, GWR and GWR analysis with LCR term to result in the final variation map of malaria incidences in Dak Nong province, Viet Nam. The results showed a significant improvement from OLS to

GWR, and from GWR to LCR-GWR, where local collinearity was taken into consideration. The local collinearity between variables significantly reduced the results of GWR analysis with about twenty three percent of the malaria cases were explained compare to nearly fifty percent of LCR-GWR. However, LCR-GWR can only be necessary when local condition number was found to be greater than 30 that indicate the collinearity between variables. In addition, the results also support the fact that NDVI, DEM, Distance to residence and Distance to road are the most controlling factors to detect malaria hotspot in the study area. The local combination of the four significant variables determined magnitudes in local community that exposures to the diseases.

From the view of statistics, it shows that malaria occurrences in Dak Nong mainly distribute in the low terrain and near the border of "malaria cradle" Binh Duong and Cambodia. The application of statistics and regression model feature the advantage of eliminating the human's subjective thought but requires accurate statistical and large enough sample size data. For malaria, the factors that affect the incidence of malaria are very complex and vary in different areas. However, the regression model in this research, especially LCR-GWR accounts for approximately half of the cases in the study area. In this way to show, this tool is useful for the study of malaria in the future in Vietnam and across the world in general.

As its name, GWR is much depended on the variation of local physical and social condition. This method should be used in different geographical regions to validate its predictive capability. On the other hand, since this study employed point locations of malaria occurrences (because of data limitation), all aggregated social factors were removed from the analysis that might reduce accuracies of prediction map. There is a possibility to divide the study area into small sub parts to take explanatory capability of social statistics factors such as occupation or livelihood behaviors. The spatial variation in scale selection between point and polygons might produce new insight into malaria hotspot study.

Acknowledgment. This research is funded by the Vietnam National University, Hanoi (VNU) under project number QG.17.20

References

1. Adimi, F., Soebiyanto, R.P., Safi, N., Kiang, R.: Towards malaria risk prediction in Afghanistan using remote sensing. Malar. J. **9**, 125 (2010)
2. Comber, A., Harris, P., Quan, N., Chi, K., Hung, T., Phe, H.H.: Local variation in hedonic house price, Hanoi: a spatial analysis of SQTO theory. In: GIScience 2016
3. Beguin, A., Louis, V.R., Hales, S., Rocklov, J., Astrom, C., Sauerborn, R.: The opposing effects of climate change and socio-economic development on the global distribution of malaria. Glob. Environ. Change **21**, 1209–1214 (2011)
4. Aregawi, M., Lynch, M., Bekele, W., Kebede, H., Jima, D., Taffese, H.S., Yenehun, M.A., Lilay, A., Williams, R., Thomson, M., Nafo-Traore, F., Admasu, K., Gebreyesus, T.A., Coosemans, M.: Time series analysis of trends in malaria cases and deaths at hospitals and the effect of antimalarial interventions, 2001–2011 Ethiopia. PLoS ONE **9**, e106359 (2014)

5. Wijayanto, A.W., Purwarianti, A., Son, L.H.: Fuzzy geographically weighted clustering using artificial bee colony: an efficient geo-demographic analysis algorithm and applications to the analysis of crime behavior in population. Appl. Intell. **44**, 377–398 (2016)
6. Buczak, A.L., Baugher, B., Guven, E., Ramac-Thomas, L.C., Elbert, Y., Babin, S.M., Lewis, S.H.: Fuzzy association rule mining and classification for the prediction of malaria in South Korea. BMC Med. Inform. Decis. Mak. **15**, 1–17 (2015)
7. Ch, S., Sohani, S.K., Kumar, D., Malik, A., Chahar, B.R., Nema, A.K., Panigrahi, B.K., Dhiman, R.C.: A support vector machine-firefly algorithm based forecasting model to determine malaria transmission. Neurocomputing **129**, 279–288 (2014)
8. Brunsdon, C., Charlton, M., Harris, P.: Living with collinearity in local regression model. In: Proceedings of the 10th International Symposium on Spatial Accuracy Assessment in Natural Resources and Environmental Sciences
9. http://www.impehcm.org.vn/noi-dung/sot-ret/binh-phuoc-cai-noi-sot-ret-va-sot-ret-khang-thuoc-cua-viet-nam.html
10. http://daknong.gov.vn/web/dak-nong-english/daknong-introduction
11. http://resources.esri.com/help/9.3/arcgisengine/java/gp_toolref/spatial_statistics_tools/how_spatial_autocorrelation_colon_moran_s_i_spatial_statistics_works.htm
12. Ge, Y., Song, Y., Wang, J., Liu, W., Ren, Z., Peng, J., Lu, B.: Geographically weighted regression-based determinants of malaria incidences in northern China. Trans. GIS (2016)
13. Gonçalves, D.N.S., de Morais Gonçalves, C., de Assis, T.F., da Silva, M.A.: Analysis of the difference between the euclidean distance and the actual road distance in Brazil. Transp. Res. Procedia **3**, 876–885 (2014)
14. Zhou, H., Deng, Z., Xia, Y., Fu, M.: A new sampling method in particle filter based on Pearson correlation coefficient. Neurocomput. J. **69**, 2138–2141 (2016)
15. Hoang, H.: Nghiên cứu thực trạng sốt rét và đánh giá kết quả can thiệp phòng chống sốt rét tại một số xã biên giới của huyện Hưzng Hóa, tỉnh Quảng Trị (Malaria situation and evaluation of malaria control interventions in several border communes of Huong Hoa district, Quang Tri province). Ph.D. in Community Medicine, vol. PhD. Hue College of Medicine and Pharmacy, Hue, Viet Nam (2014)
16. Gollini, I., Lu, B., Charlton, M., Brunsdon, C., Harris, P.: GW model: an R package for exploring spatial heterogeneity using geographically weighted models. J. Stat. Softw. **63**, 1–49 (2015)
17. Kiang, R., Adimi, F., Soika, V., Nigro, J., Singhasivanon, P., Sirichaisinthop, J., Leemingsawat, S., Apiwathnasorn, C., Looareesuwan, S.: Meteorological, environmental remote sensing and neural network analysis of the epidemiology of malaria transmission in Thailand. Geospat. Health **1**(1), 71–84 (2006)
18. Krefis, A.C., Schwarz, N.G., Nkrumah, B., Acquah, S., Loag, W., Oldeland, J., Sarpong, N., Adu-Sarkodie, Y., Ranft, U., May, J.: Spatial analysis of land cover determinants of malaria incidence in the ashanti region Ghana. PLoS ONE **6**, e17905 (2011)
19. Lubetzky-Vilnai, A., Ciol, M., McCoy, S.W.: Statistical analysis of clinical prediction rules for rehabilitation interventions: current state of the literature. Arch. Phys. Med. Rehabil. **95**, 188–196 (2013)
20. Charlton, M., Fotheringham, A.S.: Geographically Weighted Regression - A tutorial on using GWR in ArcGIS 9.3 (2007)
21. Mosha, J.F., Sturrock, H.J.W., Greenwood, B., Sutherland, C.J., Gadalla, N.B., Atwal, S., Hemelaar, S., Brown, J.M., Drakeley, C., Kibiki, G., Bousema, T., Chandramohan, D., Gosling, R.D.: Hot spot or not: a comparison of spatial statistical methods to predict prospective malaria infections. Malar. J. **13**, 1–12 (2014)

22. Ndiath, M.M., Cisse, B., Ndiaye, J.L., Gomis, J.F., Bathiery, O., Dia, A.T., Gaye, O., Faye, B.: Application of geographically-weighted regression analysis to assess risk factors for malaria hotspots in Keur Soce health and demographic surveillance site. Malar. J. **14**, 463 (2015)
23. General Statistical Office: Statistical Yearbook of Dak lak. Dak Lak statistical office, Dak Lak (2016)
24. Masimalai, P.: Remote sensing and Geographic Information Systems (GIS) as the applied public health & environmental epidemiology. Int. J. Med. Sci. Pub. Health **3**, 1430–1438 (2014)
25. Rusk, A., Highfield, L., Wilkerson, J.M., Harrell, M., Obala, A., Amick, B.: Geographically-weighted regression of knowledge and behaviour determinants to anti-malarial recommending and dispensing practice among medicine retailers in western Kenya: capacitating targeted interventions. Malar. J. **15**, 562 (2016)
26. Son, L.H.: Enhancing clustering quality of geo-demographic analysis using context fuzzy clustering type-2 and particle swarm optimization. Appl. Soft Comput. **22**, 566–584 (2014)
27. Son, L.H.: A novel kernel fuzzy clustering algorithm for Geo-Demographic Analysis. Inf. Sci. **317**, 202–223 (2015)
28. Son, L.H., Cuong, B.C., Lanzi, P.L., Thong, N.T.: A novel intuitionistic fuzzy clustering method for geo-demographic analysis. Expert Syst. Appl. **39**, 9848–9859 (2012)
29. Son, L.H., Cuong, B.C., Long, H.V.: Spatial interaction – modification model and applications to geo-demographic analysis. Knowl. Based Syst. **49**, 152–170 (2013)
30. Son, L.H., Lanzi, P.L., Cuong, B.C., Hung, H.A.: Data mining in GIS: a novel context-based fuzzy geographically weighted clustering algorithm. Int. J. Mach. Learn. Comput. (IJMLC) **3**, 235–238 (2012)
31. Stensgaard, A.-S., Vounatsou, P., Onapa, A.W., Simonsen, P.E., Pedersen, E.M., Rahbek, C., Kristensen, T.K.: Bayesian geostatistical modelling of malaria and lymphatic filariasis infections in Uganda: predictors of risk and geographical patterns of co-endemicity. Malar. J. **10**, 298 (2011)
32. Thanh, P.V., Van Hong, N., Van Van, N., Van Malderen, C., Obsomer, V., Rosanas-Urgell, A., Grietens, K.P., Xa, N.X., Bancone, G., Chowwiwat, N., Duong, T.T., D'Alessandro, U., Speybroeck, N., Erhart, A.: Epidemiology of forest malaria in Central Vietnam: the hidden parasite reservoir. Malar. J. **14**, 86 (2015)
33. WHO: World Malaria Report 2016 (2016)
34. Zacarias, O.P., Boström, H.: Comparing support vector regression and random forests for predicting malaria incidence in Mozambique. In: 2013 International Conference on Advances in ICT for Emerging Regions (ICTer), pp. 217–221 (2013)

A Novel Hybrid Model of Rotation Forest Based Functional Trees for Landslide Susceptibility Mapping: A Case Study at Kon Tum Province, Vietnam

Binh Thai Pham[1(✉)], Viet-Tien Nguyen[2], Van-Liem Ngo[3], Phan Trong Trinh[2], Huong Thanh Thi Ngo[4], and Dieu Tien Bui[5]

[1] Department of Geotechnical Engineering, University of Transport Technology, 54 Trieu Khuc, Thanh Xuan, Hanoi, Viet Nam
binhpt@utt.edu.vn

[2] Institute of Geological Sciences, Vietnam Academy of Sciences and Technology, 84 Chua Lang Street, Dong da, Hanoi, Viet Nam

[3] Faculty of Geography, VNU University of Science, 334 Nguyen Trai, Thanh Xuan, Hanoi, Vietnam

[4] University of Transport Technology, 54 Trieu Khuc, Thanh Xuan, Hanoi, Vietnam

[5] Geographic Information System Group, Department of Business and IT, University College of Southeast Norway, Gulbringvegen 36, 3800 Bø i Telemark, Norway
buitiendieu@gmail.com

Abstract. In this study, we proposed a novel hybrid model namely Rotation Forest based Functional Trees (RFFT), which is a hybrid intelligent approach of two state of the art machine learning techniques of Functional Trees (FT) classifier and Rotation Forest (RF) ensemble, for landslide susceptibility mapping at the Kon Tum Province, Viet Nam. Landslide affecting factors (slope angle, slope aspect, elevation, valley depth, land use, NDVI, soil type, lithology, distance to geology boundaries, and distance to faults), and 1404 past and current landslide locations have been first collected from the study area for generating training and testing datasets. Secondly, the hybrid model RFFT has been constructed for landslide susceptibility assessment using training dataset. Performance of the proposed RFFT model has been validated by analysis of the Receiver Operating Characteristic (ROC) curve and statistical indexes, and compared with a well-known landslide models namely Support Vector Machines (SVM) and the single FT. Results show that the proposed RFFT model has good performance for landslide susceptibility assessment. It has better predictive capability compared with well-known SVM model and single FT model. Therefore, it can be concluded that the proposed RFFT model should be used as a great alternative method for better landslide susceptibility assessment in landslide prone area.

Keywords: Landslide susceptibility assessment · Ensemble techniques · Rotation Forest · Functional Trees · Viet Nam

© Springer International Publishing AG 2018
D. Tien Bui et al. (eds.), *Advances and Applications in Geospatial Technology and Earth Resources*, https://doi.org/10.1007/978-3-319-68240-2_12

1 Introduction

Landslide susceptibility mapping is known as a first step in landslide hazard mitigation [1]. It helps in identifying the high and very high prone areas so that the suitable land use planning strategies and decisions can be made in advance to protect the stability of the slopes and prevent the occurrences of future landslides. Landslide susceptibility mapping is carried out on the basis of the analysis of spatial relationship between past and current landslides and a set of influencing factors [2, 3]. Geographic Information Systems (GIS), which has been used widely as a basic tool for data manipulation and spatial management [4], is also a helpful tool for producing the landslide susceptibility map.

In recent years, many literatures have shown landslide susceptibility mapping studies using GIS. Many of these studies have applied machine learning methods such as artificial neural networks [5, 6], decision trees [7, 8], support vector machines [9, 10], logistic regression [11, 12]. More recently, new hybrid techniques have been developed and used for landslide susceptibility mapping. Bui et al. [13] developed a novel hybrid model of least-squares support vector machines and differential evolution optimization for landslide spatial prediction. Pham et al. [14] proposed a novel hybrid machine learning model of rotation forest ensemble and fuzzy unordered rules induction algorithm classifier for landslide prediction. In general, the hybrid models often outperform the single models for landslide susceptibility mapping [15, 16].

In this paper, we proposed a novel hybrid model namely Rotation Forest based Functional Trees (RFFT), which is a hybrid intelligent approach of two state of the art machine learning techniques of Functional Trees (FT) classifier and Rotation Forest (RF) ensemble, for landslide susceptibility mapping at the Kon Tum Province, Viet Nam. Another objective of this study is to compare the novel hybrid RFFT model with another well-known landslide model namely Support Vector Machines (SVM), and the single FT model. To validate and compare the models, the Receiver Operating Characteristic (ROC) curve and statistical indexes analysis have been applied in both training and testing datasets.

2 Methods Used

2.1 Rotation Forest

Rotation Forest (RF), which is one of the popular ensemble techniques, was proposed by Rodriguez et al. [17]. It is known as an efficient technique to improve the weaker classifiers [18]. The RF uses Principal Component Analysis (PCA), which is a multivariate technique to analyze the large multivariate datasets for reducing their dimensionality [19], and to separate the original training datasets into subsets which are then used to train the classifiers [20]. Even though the RF is a relatively new ensemble technique, its application has been in many different fields such as medical [21, 22], remote sensing data classification [23, 24]. In landslide susceptibility modeling, the RF has also been applied in few cases [14, 25, 26].

2.2 Functional Trees

Functional Trees (FT), which was proposed by Gama [27], is a combination of a discriminant function and a multivariate decision trees by means of constructive induction [28]. It is considered as a generalization of multivariate trees. The FT combines attributes at leaf nodes, decision nodes, or both nodes and leaves for learning classification trees [28] in which decision nodes are constructed as the tree is growing whereas functional leaves are constructed as the tree is pruning [27]. In prediction, the FT can be used to predict the value of the target variables for unclassified samples. Firstly, the sample traverses the tree from the root node to a leaf in which the set of attributes of the sample is extended at each decision node using the constructor function constructed at the node. Thereafter, the decision test of the node is applied to define the path on which the sample will follow. Finally, the sample is classified as a leaf is reached using either the constructor function constructed at the leaf or the constant related with the leaf [28].

2.3 Proposed Rotation Forest Based Functional Trees

Rotation Forest Based Functional Trees (RFFT) is a hybrid approach of the RF ensemble and the FT classifier. In landslide modeling, the RFFT is constructed in three main steps as follows:

Step 1, Optimization: In this step, the RF ensemble was used to optimize the input data for modeling. Original training dataset was divided into different sub-training datasets which were then used for classification. Optimal sub-training datasets were determined as the best performance of the RFFT model was obtained. Iterations were applied in this step in which the number of iteration was determined as "16" based on a trial-and-error test to give the best for training the RF ensemble.
Step 2, Classification: In this step, the FT classifier was used to classify the classes (landslide and non-landslide) for predicting spatially landslides. Different FT classifiers were generated using different sub-training datasets which were generated by the RF ensemble. To train the FT classifier, the parameters of the algorithm were selected using trial-error process such as the minimum number of instances at which a node is considered for splitting is "15", and the number of iterations for the RF is "15".
Step 3, Combination: In the final step of modeling, the RF ensemble was used to combine the FT classifiers generated to construct the final RFFT model.

2.4 Validation Methods

Receiver Operating Characteristic (ROC) curve which is a useful tool to represent the quality of models [29, 30], and the area under the ROC curve (AUC) were selected to validate the overall performance of the hybrid RFFT model in this study. On the ROC curve graph, the "sensitivity" is shown on the y-axis whereas the "100-specificity" is shown on the x-axis. The highest AUC value of "1" indicates the best or perfect performance of the model whereas higher AUC value shows a better model [31–33].

In addition, statistical indexes namely negative predictive value (NPV), positive predictive value (PPV), specificity (SPF), sensitivity (SST), accuracy (ACC), Kappa (K), and Root Mean Squared Error (RMSE), which shows more detail performance of models, were also selected to validate the predictive capability of the proposed hybrid model in the present study. Detail description of these statistical indexes were presented in Bennett et al. [34] and Pham et al. [35].

3 General Characteristics of the Study Area

The study area is Kon Tum province located in Central Highland plateau where many geo-hazards (i.e. landslides and human induced earthquakes) occurred as the result of the interaction between natural hazards and human activities [36–40]. Geographically, the study area is located on the western part of Truong Son mountain range, between longitudes 107° 20′ E to 108° 32′ E and latitudes 13° 55′ N to 15° 26′ N (Fig. 1). It covers an area of approximately 9689.6 km^2, and has nine administrative units namely Kon Tum city, Dak Glei, Dak To, Kon Ray, Kon Plong, TuMoRong, Sa Thay, Ngoc Hoi, and Dak Ha districts. The study area belongs to the highly precipitation zone of the Central Highland where total annually rainfall varies from 1700 mm to above 3000 mm in which rainfall (90.9%) concentrates strongly in rainy season (April to November). The Kon Tum area has three main large drainages such as the Dak Bla River, the KrongPoKo River, and the Sa Thay River. The drainage density in the study area is measured around 0.45 km/km^2.

In the study area, the topography feature is aligned in the N - S direction. The elevation varies from 800–1200 m in the north part whereas it ranges from 500–530 m in the southern part, and the highest point of 2598 m is at the Ngoc Linh peak in the southern part of Vietnam.

The geology is complex with 33 geologic formations and complexes from Archean to Cenozoic of ages. Metamorphic rocks are mostly dominated, followed by intrusive

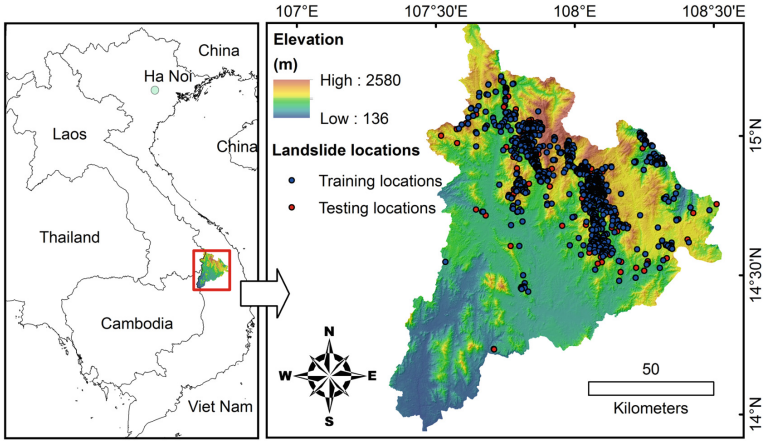

Fig. 1. Landslide inventory map and location map of study region

igneous rocks, extrusive igneous rocks, and sedimentary. The study area belongs to the Kon Tum block which is one of the main uplift blocks in the Central Highland affected strongly by the tectonic activities. Fault zones in the Kon Tum province follow the sub-meridian and northwest-southeast directions. Major faults traverse area including Ngoc Linh - Dak To, Po Co River, Xe Ca Man, Dak Sa, and Sa Thay.

4 GIS Database

4.1 Landslide Inventory Map

Landslide inventory map of this area was constructed from 1404 landslides occurred during the years from 2004 to 2015, data for the inventory has been collected from various sources such as interpretation of Google Earth images and field investigation.

Landslides in this area can be classified into 3 main types in size such as large landslides (above 10000 m^2), medium landslides (1000–10,000 m^2), and small landslides (less than 1000 m^2). Among these landslides, the largest landslide covers an area of approximately 361485 m^2 whereas the smallest one is about 118.4 m^2.

Landslides, in the study area, have been identified as polygons. However, due to the number of landslides are of big size, thus the center representative landslide pixels converted from polygons have been used for landslide susceptibility analysis. Out of these, a total of 983 landslide pixels have been used for generating training dataset whereas 420 remaining pixels have been utilized for creating testing dataset.

4.2 Landslide Affecting Parameters

In the present study, a total of ten parameters (Table 1) namely slope, aspect, elevation, land use, lithology, Normalized Difference Vegetation Index (NDVI), soil type, distance to faults, distance to geology boundaries, and valley depth were selected and used for landslide susceptibility modeling as they are known as landslide influencing factors for landslide spatial prediction [13, 41].

A Digital Elevation Model (DEM) with the spatial resolution of 30 × 30 m was generated from national topographic maps (1:50,000), and then the DEM was used to generate slope map (Fig. 2), aspect map, elevation map, and valley depth map (Fig. 3) using GIS application and SAGA software.

Soil type map (Fig. 4) at a scale of 1:100000 was collected from the Agricultural Planning and Projection of Vietnam in 2000. Geological and mineral resource maps at the scale of 1:200.000 collected from Ministry of Natural Resources and Environment of Vietnam were used to construct lithology map (Fig. 5). These maps have been also used to extract the faults which were then used to generate distance to faults map using the buffering function in ArcGIS application. Landsat 8 OLI (30 m resolution, with three paths/rows 124-50, 125-50 and 125-49) that was acquired on 14 April 2015 was used to generate NDVI map. Land use map at scale of 1:50000 was provided by the local authority of the study area. In addition, distance to geology boundaries was used for landslide susceptibility modeling. Distance to geology boundaries map was constructed using the geology boundaries extracted from geological and mineral resource

Table 1. Landside affecting parameters and their classes

No	Landslide affecting parameters	Classes
1	Slope (degrees)	(1) 0–3.69, (2) 3.69–9.95, (3) 9.95–15.92, (4) 15.92–21.32, (5) 21.32–26.44, (6) 26.44–31.55, (7) 31.55–38.09, and (8) 38.09–72.49
2	Aspect	(1) flat; (2) south; (3) southeast; (4) southwest; (5) east; (6) west; (7) north; (8) northeast; and (9) northwest
3	Elevation	(1) 136.85–433.86, (2) 433.86–673.38, (3) 673.38–855.42, (4) 855.42–1037.46, (5) 1037.46–1200.34, (6) 1200.34–1372.8, (7) 1372.9–1583.58, (8) 1583.58–1880.59, and (9) 1880.59–2580
4	Valley depth (m)	(1) 0–5; (2) 5–30; (3) 30–60; (4) 60–100; (5) 100–150; and (6) >150
5	Lithology	(1) quaternary sediments; (2) sedimentary classic rocks; (3) extrusive mafic - ultramafic igneous rocks; (4) intrusive mafic - ultramafic igneous rocks; (5) extrusive acid - neutral igneous rocks; (6) intrusive acid - neutral igneous rocks; and (7) metamorphic rock with rich quartz components
6	Soil type	(1) water: (lakes and rivers); (2) Fluvisols: Humi-Gleyic Fluvisols, Dystri-Arenic-Fluvisols; (3) Gleysols: Hapli-Umbric Gleysols; (4) Cambisols: Anthraqui-Fluvic Cambisols; (5) Haplic Acrisols; (6) Chromi-Hyperdystri Acrisols, Chromi-Arenic Acrisols, Hapli-Hyperdystric Acrisols; (7) Hapli-Chromic Acrisols; (8) Alumi-Humic Acrisols; (9) Ferralsols: Humi-Acric Ferralsols, Verti-Acric Ferralsols; (10) Humi-Endoleptic Acrisols; (11) Leptosols: Dystri-lithic Leptosols; and (12) Anthraqui-Plinthic Acrisols
7	Land use	(1) wet rice land; (2) upland rice; (3) grass land; (4) annual crop land; (5) perennial crops; (6) productive forest land; (7) protective forest land; (8) Specialized use forest land; (9) rivers, lakes; (10) non-agricultural land; and (11) unused land
8	Distance to faults (m)	(1) 0–200; (2) 200–400 m; (3) 400–600; (4) 600–800; (5) 800–1000; (6) 1000–1200; and (7) >1200
9	Distance to geology boundaries (m)	(1) 0–200; (2) 200–400 m; (3) 400–600; (4) 600–800; (5) 800–1000; (6) 1000–1200; and (7) >1200
10	NDVI	(1) [(−0.23)–(0.02)]; (2) 0.02–0.12; (3) 0.12–0.19; (4) 0.19–0.25; (5) 0.25–0.3; (6) 0.3–0.35; (7) 0.35–0.4; (8) 0.4–0.45; and (9) 0.45–0.63

maps, and buffered into the study area. For landslide susceptibility assessment, different classes of these factors have been classified on the basis of the study of literatures [13, 42] and the analysis of the characteristics of the study area in relation with landslide occurrences.

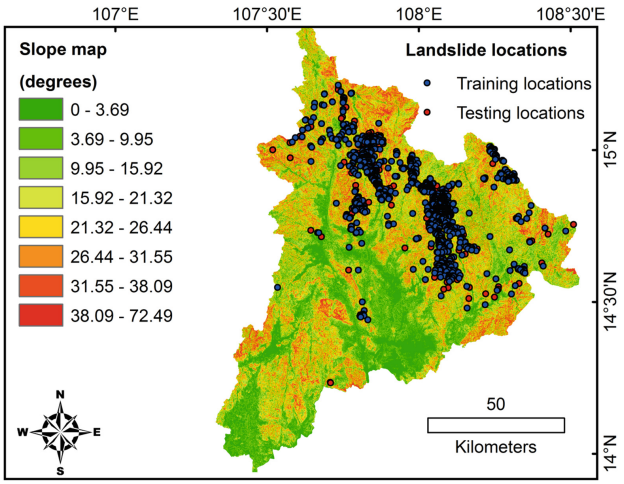

Fig. 2. Slope map of the study area

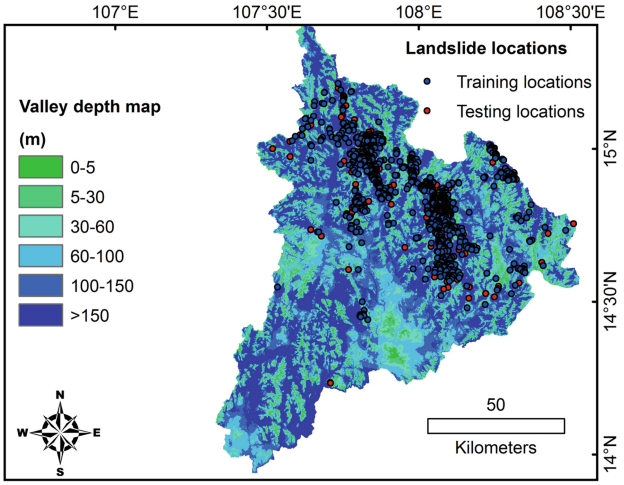

Fig. 3. Valley depth map of the study area

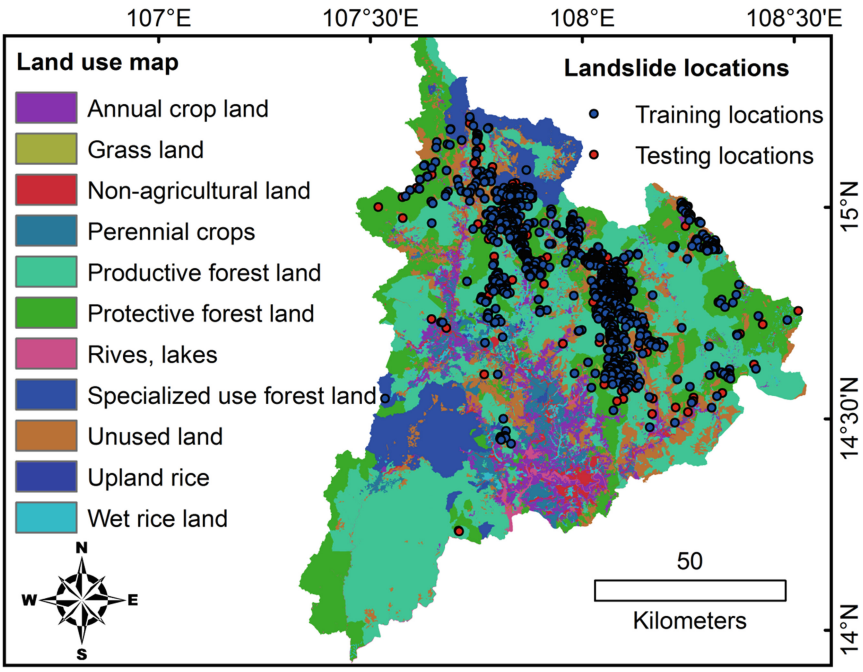

Fig. 4. Land use map of the study sarea

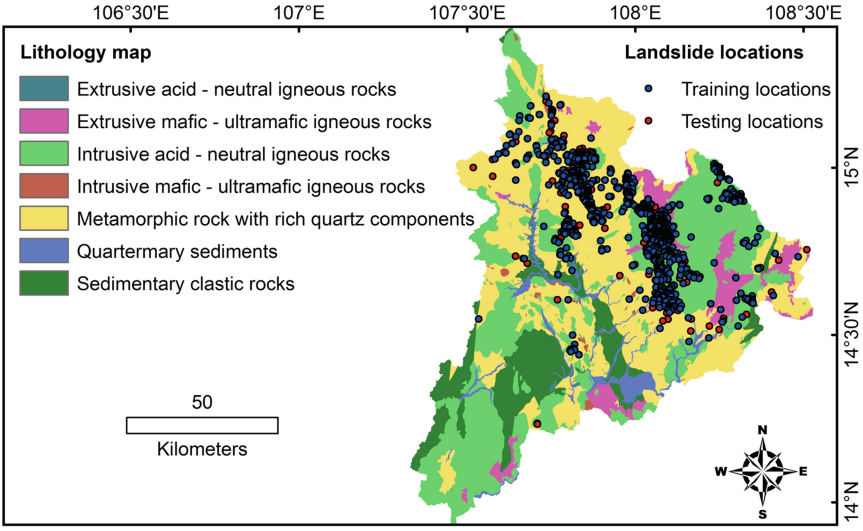

Fig. 5. Land use/ land cover map of the study area

5 Results and Discussion

Landslide susceptibility model using the novel hybrid RFFT model has been constructed and validated using training and testing datasets, respectively, and the results are shown in Figs. 6, 7, 8, and 9. According to the ROC curve analysis (Figs. 6 and 7), it can be observed that the RFFT model has high AUC values for training (0.926), and testing (0.811) datasets. These values are higher than those of the SVM model (0.904 for training dataset and 0.806 for testing dataset), and the single FT model (0.892 for training dataset and 0.761 for testing dataset).

Likewise, according to the statistical indexes analysis (Figs. 8 and 9), the RFFT model has the highest values of PPV (80.57% for training dataset and 70.31% for testing dataset), NPV (90.05% for training dataset and 78.15% for testing dataset), SST (90.00% for training dataset and 76.29% for testing dataset), SPF (82.41% for training dataset and 72.47% for testing dataset), ACC (85.81% for training dataset and 74.23% for testing dataset), and K (0.716 for training dataset and 0.485 for testing dataset), followed by the SVM model with PPV (80.16% for training dataset and 70.30% for testing dataset), NPV (90.74% for training dataset and 77.67% for testing dataset), SST (89.65% for training dataset and 75.90% for testing dataset), SPF (82.06% for training dataset and 72.35% for testing dataset), ACC (85.45% for training dataset and 73.99% for testing dataset), and K (0.710 for training dataset and 0.480 for testing dataset), and the single FT model with PPV (79.86% for training dataset and 68.65% for testing dataset), NPV (90.54% for training dataset and 76.96% for testing dataset), SST

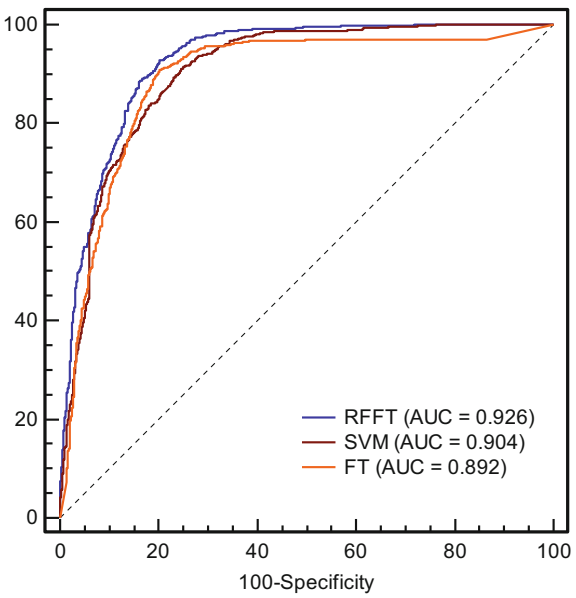

Fig. 6. The ROC curve analysis of landslide models using training dataset

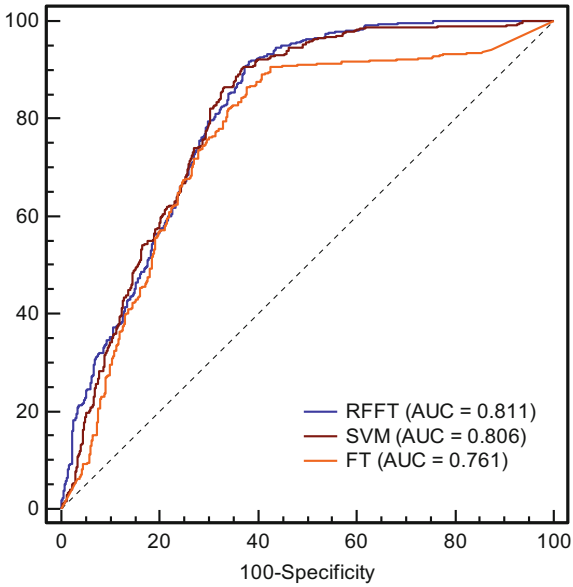

Fig. 7. The ROC curve analysis of landslide models using testing dataset

(89.41% for training dataset and 74.87% for testing dataset), SPF (81.80% for training dataset and 71.05% for testing dataset), ACC (85.20% for training dataset and 72.80% for testing dataset), and K (0.704 for training dataset and 0.456 for testing dataset), respectively. In contrast, the RFFT model has the lowest value of RMSE (0.322 for training dataset and 0.412 for testing dataset), followed by the SVM model (0.349 for training dataset and 0.419 for testing dataset), and the single FT model (0.395 for training dataset and 0.454 for testing dataset), respectively.

In landslide susceptibility modeling, the hybrid model is known as a great alternative tool [16]. In this study, the RFFT model, which is a hybrid approach of the RF ensemble and the FT classifier, also performed very well for landslide susceptibility modeling based on the analysis of above results as it outperforms both the well-known SVM model and single FT model. It can be reasonably explained that the RFFT model takes advantage of machine learning ensemble method of the RF ensemble for improving the prediction ability of FT classifier [17]. In the RF, the diversity is guaranteed by the rotation strategy, thus the classification accuracy of the RFFT model is better than single FT classifier [43]. In addition, the PCA used in the RF is a good filter method which will help in reducing the learning errors [17].

Landslide susceptibility map has been constructed at the Kontum province, Viet Nam using the novel hybrid model RFFT in this study. For this, a total of 24021009 pixels of the study area has been assigned the susceptibility indexes which have been generated during training the RFFT model. Thereafter, susceptibility classes namely

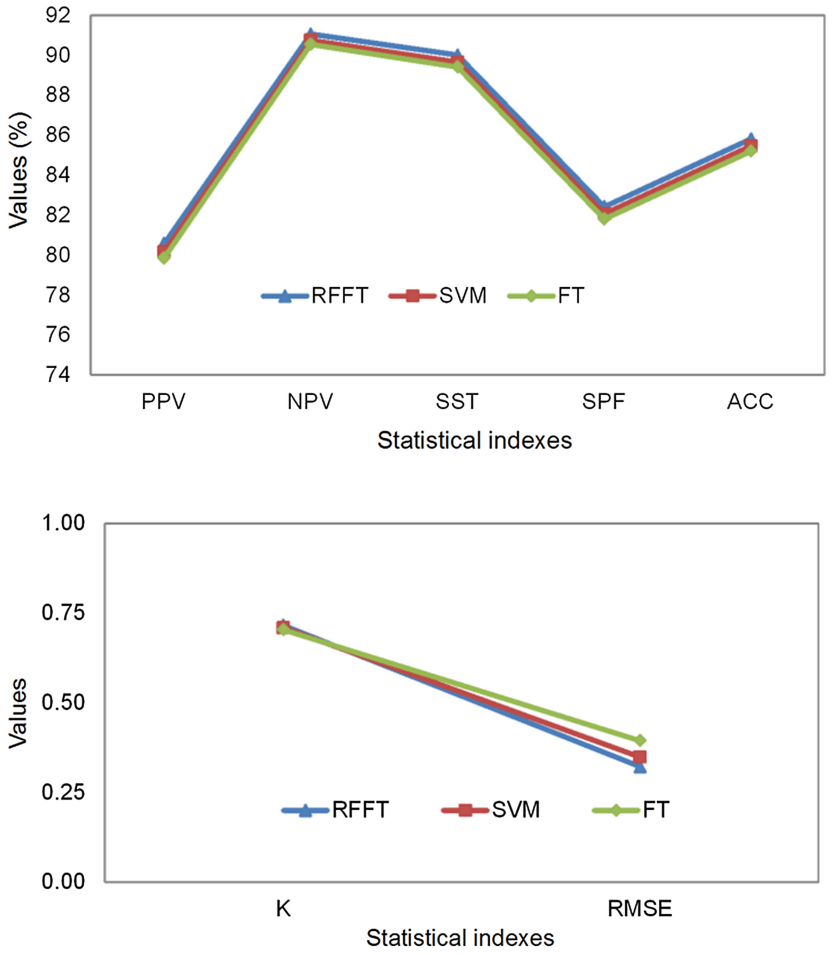

Fig. 8. Model performance using training dataset

very low, low, moderate, high, and very high were determined to construct the landslide susceptibility map (Fig. 10) based on the classification of the generated susceptibility indexes using the natural breaks method [44] in ArcGIS environment. Furthermore, landslide pixels frequency analysis on the map has been carried out to validate the reliability of the landslide susceptibility map, and the results are shown in Fig. 11. It can be observed that the highest frequency of landslides is on the very high class (69.82%), followed by the high class (15.63%), the moderate class (9.47%), the low class (3.71), and the very low class (1.37%), respectively. Based on the frequency analysis results, it is reasonably to state that the produced landslide susceptibility map is much reliable for landslide hazard management in the study area.

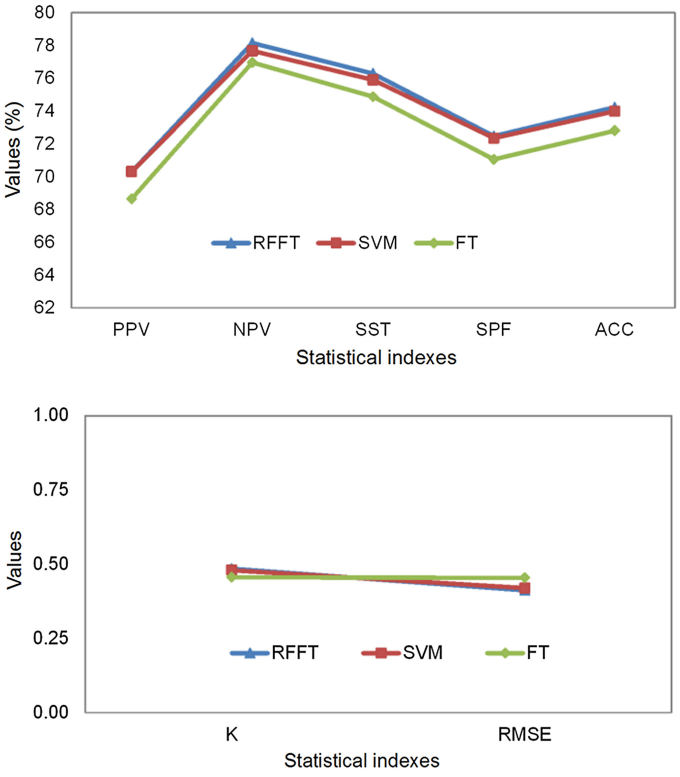

Fig. 9. Model performance using testing dataset

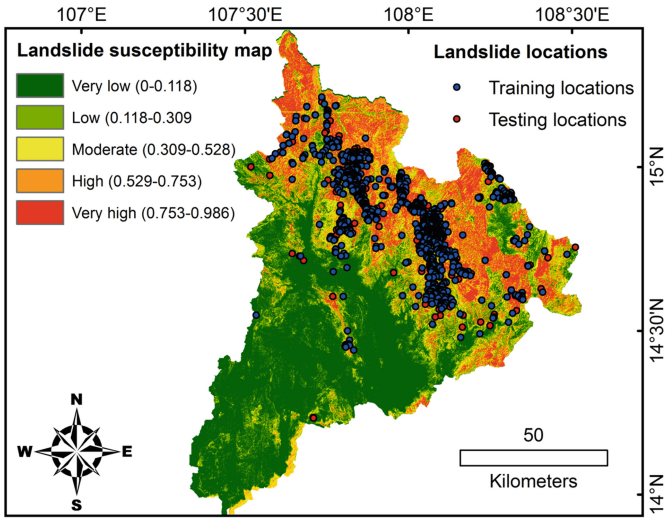

Fig. 10. Landslide susceptibility map using the proposed hybrid model RFFT

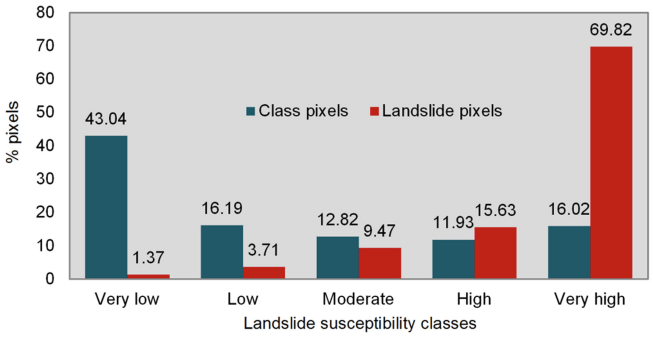

Fig. 11. Pixels distribution analysis on landslide susceptibility map

6 Concluding Remarks

Landslide susceptibility mapping has been conducted at the Kontum province, Viet Nam using the novel hybrid model named RFFT which is a combination of two state of the art machine learning methods of the RF ensemble and the FT classifier. Performance of the proposed RFFT model has been validated by analysis of the ROC curve and statistical indexes, and compared with a well-known landslide model namely Support Vector Machines (SVM), and the single FT model.

Results show that the proposed RFFT model has very good performance for landslide susceptibility assessment. It has better predictive capability compared with well-known SVM model and single FT model. Therefore, it can be concluded that the proposed RFFT model should be used as a great alternative method for better landslide susceptibility assessment in landslide prone areas. Results of this study also reconfirmed that the hybrid model using ensemble techniques such as the RF is a promising approach for landslide susceptibility modeling.

Acknowledgement. Authors are thankful to the Director, Bhaskarcharya Institute for Space Applications and Geo-Informatics (BISAG), Department of Science & Technology, Government of Gujarat, Gandhinagar, Gujarat, India for providing facilities to carry out this research work.

References

1. Ercanoglu, M., Gokceoglu, C., Van Asch, T.W.: Landslide susceptibility zoning north of Yenice (NW Turkey) by multivariate statistical techniques. Nat. Hazards **32**, 1–23 (2004)
2. Guzzetti, F., Carrara, A., Cardinali, M., Reichenbach, P.: Landslide hazard evaluation: a review of current techniques and their application in a multi-scale study, Central Italy. Geomorphology **31**, 181–216 (1999)
3. Pourghasemi, H.R., Pradhan, B., Gokceoglu, C.: Application of fuzzy logic and analytical hierarchy process (AHP) to landslide susceptibility mapping at Haraz watershed, Iran. Nat. Hazards **63**, 965–996 (2012)
4. Oh, H.-J., Pradhan, B.: Application of a neuro-fuzzy model to landslide-susceptibility mapping for shallow landslides in a tropical hilly area. Comput. Geosci. **37**, 1264–1276 (2011)

5. Ermini, L., Catani, F., Casagli, N.: Artificial neural networks applied to landslide susceptibility assessment. Geomorphology **66**, 327–343 (2005)
6. Pham, B.T., Tien Bui, D., Pourghasemi, H.R., Indra, P., Dholakia, M.B.: Landslide susceptibility assessment in the Uttarakhand area (India) using GIS: a comparison study of prediction capability of naïve Bayes, multilayer perceptron neural networks, and functional trees methods. Theor. Appl. Climatol. **122**, 1–19 (2015)
7. Tsangaratos, P., Ilia, I.: Landslide susceptibility mapping using a modified decision tree classifier in the Xanthi Perfection, Greece. Landslides **13**, 305–320 (2016)
8. Nefeslioglu, H., Sezer, E., Gokceoglu, C., Bozkir, A., Duman, T.: Assessment of landslide susceptibility by decision trees in the metropolitan area of Istanbul, Turkey. Math. Probl. Eng. **2010**, 0–15 (2010)
9. Kavzoglu, T., Sahin, E.K., Colkesen, I.: Landslide susceptibility mapping using GIS-based multi-criteria decision analysis, support vector machines, and logistic regression. Landslides **11**, 425–439 (2014)
10. Pham, B.T., Bui, D.T., Prakash, I., Dholakia, M.: Evaluation of predictive ability of support vector machines and naive Bayes trees methods for spatial prediction of landslides in Uttarakhand state (India) using GIS. J. Geomat. **10**, 71–79 (2016)
11. Pham, B.T., Bui, D.T., Prakash, I.: Landslide susceptibility assessment using bagging ensemble based alternating decision trees, logistic regression and J48 decision trees methods: a comparative study. Geotech. Geol. Eng. **31**, 1–15 (2017)
12. Ohlmacher, G.C., Davis, J.C.: Using multiple logistic regression and GIS technology to predict landslide hazard in northeast Kansas, USA. Eng. Geol. **69**, 331–343 (2003)
13. Tien Bui, D., Pham, B.T., Nguyen, Q.P., Hoang, N.-D.: Spatial prediction of rainfall-induced shallow landslides using hybrid integration approach of Least-Squares Support Vector Machines and differential evolution optimization: a case study in Central Vietnam. Int. J. Digit. Earth **9**, 1–21 (2016)
14. Pham, B.T., Tien Bui, D., Prakash, I., Dholakia, M.B.: Rotation forest fuzzy rule-based classifier ensemble for spatial prediction of landslides using GIS. Nat. Hazards **83**, 1–31 (2016)
15. Tien Bui, D., Tuan, T.A., Hoang, N.-D., Thanh, N.Q., Nguyen, D.B., Van Liem, N., Pradhan, B.: Spatial prediction of rainfall-induced landslides for the Lao Cai area (Vietnam) using a hybrid intelligent approach of least squares support vector machines inference model and artificial bee colony optimization. Landslides **14**, 447–458 (2017)
16. Dehnavi, A., Aghdam, I.N., Pradhan, B., Varzandeh, M.H.M.: A new hybrid model using step-wise weight assessment ratio analysis (SWARA) technique and adaptive neuro-fuzzy inference system (ANFIS) for regional landslide hazard assessment in Iran. CATENA **135**, 122–148 (2015)
17. Rodriguez, J.J., Kuncheva, L.I., Alonso, C.J.: Rotation forest: a new classifier ensemble method. IEEE Trans. Pattern Anal. Mach. Intell. **28**, 1619–1630 (2006)
18. Ozcift, A.: SVM feature selection based rotation forest ensemble classifiers to improve computer-aided diagnosis of Parkinson disease. J. Med. Syst. **36**, 2141–2147 (2012)
19. Jolliffe, I.: Principal component analysis. Wiley Online Library (2002)
20. Kuncheva, L.I., Rodríguez, J.J.: An experimental study on rotation forest ensembles. In: International Workshop on Multiple Classifier Systems, pp. 459–468. Springer (2007)
21. Ozcift, A., Gulten, A.: A robust multi-class feature selection strategy based on rotation forest ensemble algorithm for diagnosis of Erythemato-Squamous diseases. J. Med. Syst. **36**, 941–949 (2012)
22. Ozcift, A., Gulten, A.: Classifier ensemble construction with rotation forest to improve medical diagnosis performance of machine learning algorithms. Comput. Methods Programs Biomed. **104**, 443–451 (2011)

23. Xia, J., Du, P., He, X., Chanussot, J.: Hyperspectral remote sensing image classification based on rotation forest. IEEE Geosci. Remote Sens. Lett. **11**, 239–243 (2014)
24. Kavzoglu, T., Colkesen, I.: An assessment of the effectiveness of a rotation forest ensemble for land-use and land-cover mapping. Int. J. Remote Sens. **34**, 4224–4241 (2013)
25. Pham, B.T., Bui, D.T., Dholakia, M.B., Prakash, I., Pham, H.V., Mehmood, K., Le, H.Q.: A novel ensemble classifier of rotation forest and Naïve Bayer for landslide susceptibility assessment at the Luc Yen district, Yen Bai Province (Viet Nam) using GIS. Geomat. Nat. Hazards Risk, 1–23 (2016)
26. Pham, B.T., Tien Bui, D., Prakash, I., Dholakia, M.B.: Hybrid integration of Multilayer Perceptron Neural Networks and machine learning ensembles for landslide susceptibility assessment at Himalayan area (India) using GIS. CATENA **149**(Part 1), 52–63 (2017)
27. Gama, J.: Functional trees for classification. In: Proceedings IEEE International Conference on Data Mining, 2001, ICDM 2001, pp. 147–154. IEEE (2001)
28. Gama, J.: Functional trees. Mach. Learn. **55**, 219–250 (2004)
29. Shirzadi, A., Bui, D.T., Pham, B.T., Solaimani, K., Chapi, K., Kavian, A., Shahabi, H., Revhaug, I.: Shallow landslide susceptibility assessment using a novel hybrid intelligence approach. Environ. Earth Sci. **76**, 60 (2017)
30. Tien Bui, D., Ho, T.-C., Pradhan, B., Pham, B.-T., Nhu, V.-H., Revhaug, I.: GIS-based modeling of rainfall-induced landslides using data mining-based functional trees classifier with AdaBoost, Bagging, and MultiBoost ensemble frameworks. Environ. Earth Sci. **75**, 1–22 (2016)
31. Pham, B.T., Tien Bui, D., Dholakia, M.B., Prakash, I., Pham, H.V.: A comparative study of least square support vector machines and multiclass alternating decision trees for spatial prediction of rainfall-induced landslides in a tropical cyclones area. Geotech. Geol. Eng. **34**, 1–18 (2016)
32. Pham, B.T., Tien Bui, D., Pham, H.V., Le, H.Q., Prakash, I., Dholakia, M.B.: Landslide hazard assessment using random subspace fuzzy rules based classifier ensemble and probability analysis of rainfall data: a case study at Mu Cang Chai District, Yen Bai Province (Viet Nam). J. Indian Soc. Remote Sens. **45**, 1–11 (2016)
33. Dou, J., Bui, D.T., Yunus, A.P., Jia, K., Song, X., Revhaug, I., Xia, H., Zhu, Z.: Optimization of causative factors for landslide susceptibility evaluation using remote sensing and GIS data in parts of Niigata, Japan. PLoS ONE **10**, e0133262 (2015)
34. Bennett, N.D., Croke, B.F., Guariso, G., Guillaume, J.H., Hamilton, S.H., Jakeman, A.J., Marsili-Libelli, S., Newham, L.T., Norton, J.P., Perrin, C.: Characterising performance of environmental models. Environ. Model Softw. **40**, 1–20 (2013)
35. Pham, B.T., Pradhan, B., Tien Bui, D., Prakash, I., Dholakia, M.B.: A comparative study of different machine learning methods for landslide susceptibility assessment: a case study of Uttarakhand area (India). Environ. Model Softw. **84**, 240–250 (2016)
36. Thanh, T.T.M., Vung, V.V., Miyake, H., Irikura, K.: Simulated ground motion of the earthquake on October 22nd, 2012, M4. 6 at Song Tranh 2 dam area. J. Earth Sci. **37**, 241–251 (2016)
37. Thanh, T.T.M., Minh, N.L., Vung, V.V., Irikura, K.: Values for peak ground acceleration and peak ground velocity using in seismic hazard assessment for Song Tranh 2 hydropower region. Vietnam J. Earth Sci. **36**, 462–469 (2014)
38. Nam, N.T.: Probabilistic seismic hazard assessment for the Tranh river hydropower plant No2 site, Quang Nam Province. Vietnam J. Earth Sci. **38**, 188–201 (2016)
39. Toan, D.V., Phong, L.H., Vu, T.A., Quang, N.T.H.: Study of the Earth's crustal structure in the Area of Song Tranh and it's adjacents. Vietnam J. Earth Sci. **37**, 127–138 (2015)

40. Duan, B.V., Giang, H.T., Duong, N.A., Nguyen, P.D.: About factors related to the occurrence of earthquakes in the Song Tranh 2 hydropower area in period 2011–2014. Vietnam J. Earth Sci. **37**, 228–240 (2016)
41. Pham, B.T., Khosravi, K., Prakash, I.: Application and comparison of decision tree-based machine learning methods in landside susceptibility assessment at Pauri Garhwal Area, Uttarakhand, India. Environ. Processes **4**, 1–20 (2017)
42. Pham, B.T., Tien Bui, D., Pham, H.V.: Spatial prediction of rainfall induced landslides using Bayesian network at Luc Yen District, Yen Bai Province (Viet Nam). In: International Conference on Environmental Issues in Mining and Natural Resources Development (EMNR 2016), pp. 1–10 (2016)
43. Liu, K.-H., Huang, D.-S.: Cancer classification using rotation forest. Comput. Biol. Med. **38**, 601–610 (2008)
44. Ayalew, L., Yamagishi, H., Ugawa, N.: Landslide susceptibility mapping using GIS-based weighted linear combination, the case in Tsugawa area of Agano River, Niigata Prefecture, Japan. Landslides **1**, 73–81 (2004)

Effects of Residual Soil Characteristics on Rainfall-Induced Shallow Landslides Along Transport Arteries in Bac Kan Province, Vietnam

Do Minh Duc[1(✉)], Dao Minh Duc[2], and Do Minh Ngoc[3]

[1] Department of Geotechnics, Faculty of Geology, Hanoi University of Science, 334 Nguyen Trai, Thanh Xuan, Hanoi, Vietnam
ducdm@vnu.edu.vn
[2] Department of Geotechnics, Institute of Geology, Chua Lang, Hanoi, Vietnam
daominhduc_dkt@yahoo.com
[3] Institute of Geotechnology and Environment, 26/82 Tran Cung, Cau Giay, Hanoi, Vietnam
ngocdm2l3@gmail.com

Abstract. Slope failures depend strongly on the geotechnical properties of soils and rocks. Therefore, thresholds of rainfall-induced landslides vary according to changes in soil properties. This study assesses the effects of residual soil characteristics on 73 rainfall-induced shallow landslides along three main routes in Bac Kan province, Northeast Vietnam. All of these landslides occurred during or after torrential rains. Of the total number of landslides, 71 were shallow rotational and translational slides. They occurred in residual soils of silty sand (SM), silt with sand (ML), and elastic silt (MH), among which SM was the most dominant. Rain infiltration modeling and deterministic and probabilistic analyses of slope stability were used to assess the effects of soil permeability, strength, thickness of residual soils and slope excavation on rainfall-induced shallow landslides. The slopes constituted by the SM soil type were more vulnerable to rainfall-induced shallow landslides than the ML and MH types due to its higher mean saturated hydraulic conductivity. Shallow translational and rotational earth slides were dominant on cut slopes when the thickness of the residual soils was less than 1.5 m and greater than 2.5 m, respectively. Slope excavation in the study area decreased the factor of safety by 20%. Three thresholds of rain intensity-duration (ID) were defined for deterministic stability analysis (ranging between extremely high and low landslide hazard levels): $I = 204.47\ D^{-1.073}$, $I = 174.91\ D^{-1.039}$ and $I = 133.34\ D^{-0.981}$.

Keywords: Shallow landslide · Residual soil · Slope stability analysis · Rainfall threshold · Vietnam

1 Introduction

Landslides cause major disasters on a global scale every year. They rank 7th with respect to the number of people killed during the period of 1992–2001 [1]. During 2000–2009, 212 large landslide events were recorded worldwide (The International

© Springer International Publishing AG 2018
D. Tien Bui et al. (eds.), *Advances and Applications in Geospatial Technology and Earth Resources*, https://doi.org/10.1007/978-3-319-68240-2_13

Disaster Database: http://www.emdat.be/) [2]. More than 95% of the landslide events were triggered by rain. Approximately 10,508 people were killed and more than 4 million were affected by landslides. Currently, the number of disastrous landslides appears to be increasing. As a result of population growth, socio-economic activities on hillsides in urban areas are developing at an accelerated rate. This development increases the risk of urban landslides that are triggered by rainfall or earthquake activity [3]. The potential for more extreme weather conditions may also contribute to landslides in the future [1]. Landslides and flooding are the most severe geohazards in Vietnam [4–6]. Landslides induced by rainfall are extremely dominant in the mountainous areas [7]. Among all of the landslides, more than 60% were shallow.

Rainfall thresholds for landslides are defined physically (process-based conceptual thresholds) or empirically (historical, statistical thresholds) [8]. Various rainfall thresholds are defined from the statistical analysis of rain gauges, which report several climate variables, such as intensity-duration (ID) and accumulative rainfall [8–13]. Satellite-based rainfall can also be used where there is a lack of data from rain gauges [14, 15]. Due to uncertainties, the thresholds in one area may greatly vary [16, 17]. Slope stability analysis was used to assess the effects of rain intensity and duration on hillsides in Hong Kong [18, 19]. An automatic recording system connected to various sensors was installed, which provided correlations between rainfall, groundwater level and displacement as recorded by extensometric and inclinometric devices [20]. Another approach combines field monitoring and numerical analysis. In situ rainfall infiltration was monitored, which provided important information for designing slopes, such as those in the Three Gorges Dam, China [21] and a clay slope in the Apennines [22]. A review of monitoring systems, techniques and real-time warning systems of landslides [3] emphasised the rainfall intensity-duration thresholds. An assessment of the rainfall-induced slope instability was performed by considering the soil properties, rain infiltration and spatial and temporal variability of pore water pressure (PWP) [23–25]. The thresholds were numerically determined and calibrated by the actual time of the landslide occurrence. The material properties were proven to have a close relationship to shallow landslide size [26] and failure mode [27]. The effects of the soil properties on safety were represented by the variability of soil friction and cohesion [28, 29], soil thickness [30], modeled wetting front in infinite slope with SEEP/W and SLOPE/W [31] or strength reduction factor [32].

The effects of variations in the geotechnical soil properties on rainfall-induced shallow landslides are still not completely understood. Therefore, this study aims to define numerical thresholds of rain intensity-duration by considering the variation of soil properties, such as soil type, hydraulic conductivity, initial soil moisture, wet density, shear strength parameters, soil thickness, and excavation. The study area is Bac Kan province in north-eastern mountain of Vietnam. Herein, landslides have caused serious loss of life and property in the area. In this study, the landslide investigation was performed along national route No. 3 and provincial routes No. 256 and 257 (Fig. 1).

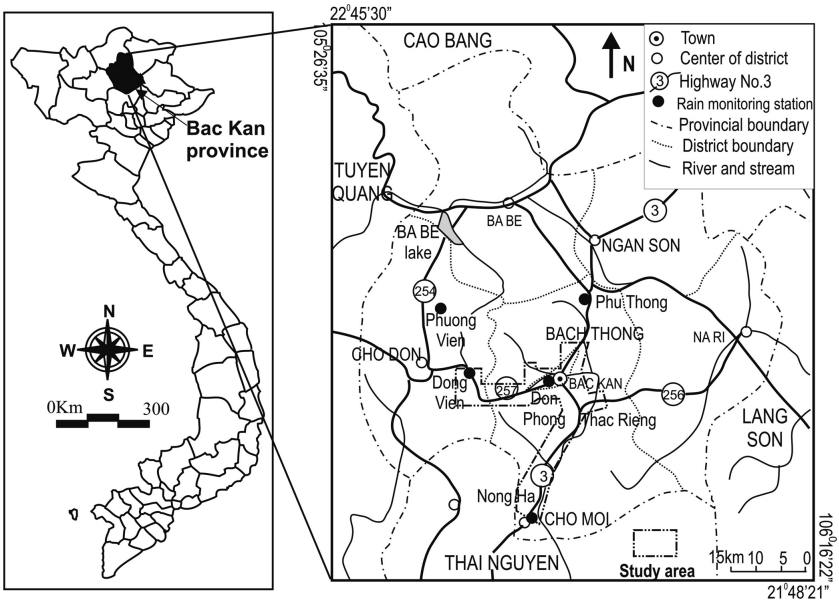

Fig. 1. Location of study area

2 Materials and Methods

2.1 Field Investigation

Field investigations were conducted in 2001, 2002, 2006, and 2008. The first field trip (2001) was conducted in the winter (i.e., December) during the dry season. The other trips were conducted immediately following periods of heavy rainfall in summer: July 2002, June 2006 and June 2008. The areas of interest were along national route No. 3 (the town of Cho Moi - Bac Kan), provincial road No. 257 (the town of Bac Kan – Cho Don), the town of Bac Kan, and some segments of road No. 256 (the town of Bac Kan – Na Ri) (Fig. 1). The following data were obtained at each investigation point.

a. The geographical location of investigation points were identified by GPS with an accuracy of 5–10 m.
b. Slope angle and height. The description of a shallow landslide includes further information, such as slope angles of adjacent areas, the upper and lower lengths of the shallow landslide, the thickness of the sliding mass, and characteristics of the slip surface. The data are used to estimate the volume of the shallow landslide. The date of occurrence was identified by conversations with transportation managers and local residents.
c. Geological description: Lithological composition, colour and initial classification of rocks, bedding surface, dip angle, measurement of fractures, and identification of rock strength grades according to the International Society of Rock Mechanics [33].

d. Residual soil description: Thickness, distribution and description (composition, colour, moisture, and consistency) of residual soil layers.
e. Surface and groundwater: Gullies, streams at the slope, existence and discharge of groundwater at the slope (if any). The groundwater level was measured in the adjacent wells of local residents. Local land owners also provided information on seasonal discharge and water level changes.
f. Vegetable coverage: Types of trees and brush, density of coverage, and comparisons to adjacent areas.
g. Available structures: Description of structures on and/or nearby the slope (if any).

The number of occurrences of shallow landslides and damage were recorded (via conversations with local authority and residents). All of these parameters were collected for 73 landslides. During the investigations, 40 undisturbed and 32 disturbed samples of residual soils were obtained for further laboratory analysis.

2.2 Laboratory Testing

All of the samples were analysed in the laboratory to determine the geotechnical properties of the soils and bedrock (Table 1). Tests were performed according to the specifications of ASTM (American Society for Testing and Materials, 2001). The number of tests and specifications are listed in Table 2. A modification was made for the grain-size distribution in which all steps followed D422 except for the sieve diameters (i.e., 20, 10, 4.75, 2, 1.0, 0.5, 0.25, and 0.075 mm). Soils were classified by the Unified Soil Classification System (USCS-ASTM D 2487).

Table 1. Specifications and quantity of soil testing

Property	Specification (ASTM)	Number of tests
Specific gravity of the soil grains	D854 [35]	26
Grain-size distribution	D422 [36]	30
Natural water content	D2216 [37]	26
Natural unit weight	Brass ring	26
Liquid, plastic limits	D4318 [38]	26
Classification of soils	D2487 [39]	30
Direct shear test	D3080 [40]	20
Hydraulic conductivity	D5084 [41]	12
Soil-water characteristic curve	Tempe cell	2

Because residual soils at slopes are often unsaturated, two samples were taken to determine the soil-water characteristics curve using the tempe cell method (e.g., following the method of Fredlund and Rahardjo [34]). The samples were first saturated and then tested for drying and wetting curves using applied air pressures of 5, 10, 20, 40, 80, 200, and 400 kPa.

Table 2. Geotechnical properties of residual soils

Properties	Soil type											
	Silty sand (SM)				Silt with sand (ML)				Elastic silt (MH)			
	Mean	Min	Max	σ	Mean	Min	Max	σ	Mean	Min	Max	σ
W (%)	33.1	24.3	37.8	3.4	30.2	26.7	33.0	3.2	35.1	30.2	38.9	3.6
γ (kN/m^3)	17.0	15.6	17.7	0.05	16.3	15.8	17.0	0.08	16.8	16.4	17.0	0.3
Void ratio (e)	1.123	0.986	1.302	0.084	1.147	1.091	1.230	0.073	1.185	1.093	1.304	0.089
Plastic limit (%)	28.0	24.0	30.8	2.6	32.1	30.3	35.1	2.6	37.9	36.1	41.4	2.4
Liquid limit (%)	38.2	31.5	43.1	2.5	46.9	43.4	49.5	3.1	55.9	63.0	50.1	5.4
S (%)	80	91	67	6.1	71	82	61	9.8	80	83	75	3.6
K_s (10^{-6} m/s)	20	5	32	10.9	15	11	20	4.7	12			
ϕ (deg.)	28.2	27.3	29.5	1.0	25.3	22.0	28.0	3.1	23.3	21.0	24.5	1.6
C (kPa)	9	5	14	3.2	13	5.5	21	7.8	16	12	20.5	3.7
ϕ^b (deg.)	15.8				7.9				12.4			
Number of test	Direct shear: 13; Hydraulic conductivity: 5; Others: 19				3				Hydraulic conductivity: 01, Others: 4			

W – Water content, γ – Natural density, S – Saturated degree, K_s – Saturated hydraulic conductivity, σ – Standard deviation, ϕ – Effective internal friction, C – Effective cohesion, ϕ^b – Influence of suction on strength

2.3 Rainfall Data

Bac Kan has one distinct season in which rainfall occurs from May to October. These months experience 85–90% of the total annual rainfall. The remaining months (November to April) are considered the dry season. The average annual rainfall in Bac Kan province is 1400–1800 mm, which decreases from the west to the east and from high to low elevations [42]. Long-term monitoring indicates that rainfall is most concentrated from June to August, which accounts for 75% of the total annual rainfall (Fig. 2). The amount of rainfall is mainly contributed to a few distinct large rainstorm events in which the rainfall can total hundreds of millimetres per day [43].

Rainfall data were collected from 5 monitoring stations for the period of 2000–2010. The stations were Cho Moi, Bac Kan (town), Phu Thong, Dong Vien, and Phuong Vien (Fig. 1). As mentioned in other studies [9, 16], hourly data are necessary for analysing rainfall-induced shallow landslides. However, the rainfall data in Bac Kan province was only retrieved every 6 h. Due to this limitation, the paper focuses on the numerical analysis of slope stability in various rainfall intensity scenarios. When the actual hourly rainfall was required, it was assumed to be constant over 6 h.

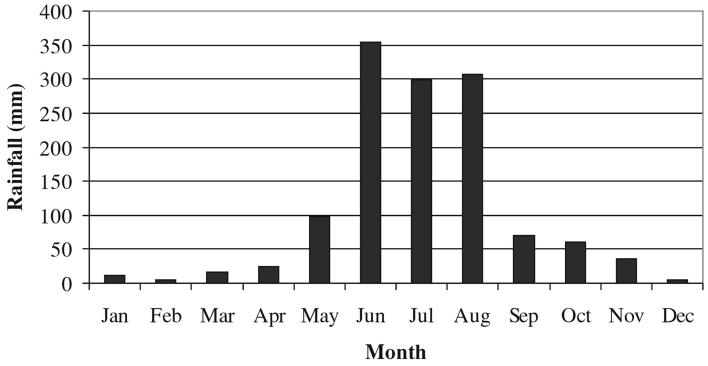

Fig. 2. Monthly rainfall in Bac Kan province

2.4 Slope Stability Analysis

Slope stability was assessed by using the limit equilibrium method and SLOPE/W (GEO-SLOPE) [44]. The slope stability analysis was conducted by using the general limit equilibrium method (GLE). A safety factor (Fs) smaller than 1.0 is considered an indicator of slope instability. PWP distributions in various rainfall scenarios were analysed with the SEEP/W module (GEO-SLOPE) [45]. Rain infiltration was modeled in SEEP/W as a transient process with an unstructured mesh of finite elements. The results were imported to SLOPE/W to analyse the slope stability. Probabilistic analysis was used to assess the variability of soil properties on slope stability. SLOPE/W uses the Monte Carlo method to perform this analysis. First, one or more critical slip surfaces are determined using the average soil properties (deterministic analysis).

Probabilistic analysis is then performed on these surfaces while considering the variability of the input parameters (GEO-SLOPE, 2004).

3 Results

3.1 Geological Settings

Bedrock in the study area is characterised by five formations: Phu Ngu (O_3-S_1pn), Mia Le (D_1ml), Song Hien (T_1-$_2sh$), Quaternary sediments and Phia Bioc complex (γaT_3npb). These formations were defined during geological mapping at the 1:200,000 scale over the region (Vietnam Department of Geology and Mineral Resources [46]). Among the formations, shallow landslides only occur in the weathered crust and highly fractured Phu Ngu and Mia Le formations and the Phia Bioc complex (Fig. 3).

The Phu Ngu formation is approximately 80 km^2 (Fig. 3), which occupies 75% of the entire study area. It has two sub-formations. The lower $(O_3 - S_1pn_2^1)$ sub-formation, which comprises one third of the study area, is distributed along national route 3 from Cho Moi to Bach Thong, and a small portion is located east of the Dong Vien commune. The sub-formation includes layers of sandstone, shale, and quartzite sandstone in the lower section and shale, siltstone, and shale containing black coal in the upper section. Each area is 350–450 m thick. The upper sub-formation $(O_3 - S_1pn_2^2)$ uniformly covers $O_3 - S_1pn_2^1$. It is distributed as two small lenses with three sections. The lower section contains layers of shale with lenses of limestone, fine sand-silt stone mixed with tuff sandstone, and quartz sandstone. The middle section has layers of quartzite sandstone, chlorite-sericite schist, siliceous schist, and quartz sandstone. The upper section includes layers of shale mixed with thin layers of siltstone, quartzite sandstone, and shale. The thickness of the upper sub-formation is 700–1000 m.

Rocks in the Phu Ngu formation are monotonically inclined. The strike and dip angle of the bedding planes are 30–50°/30–40°W. In term of bedding planes, the excavated slopes that face the west, northwest, and north are more vulnerable to shallow landslides. The dip direction of a slope is a factor that leads to translational shallow landslides along the road from the town of Bac Kan to Dong Vien (Fig. 3).

Shale and sericite schist layers in the formation are easily weathered. Residual soils from these rocks are mainly ML and MH, which have brownish red and yellowish red colours, respectively. The thickness of the residual soils is 1–10 m. The soils lie directly on the bedding planes of lower weathered rocks, such as siltstone, sandstone, and quartzite. Siltstone is intensively weathered. The strength of weathered siltstone at slopes is normally R0-R2. The residual soils from siltstone are ML and SM with a thickness of 0.5–2 m; they lie directly on the bedding planes of weathered siltstone, sandstone, and quartzite. Sandstone and quartzite are slightly weathered. The rock strengths are R3-R5. The residual soils from these rocks are breccias of rocks with a thickness less than 0.5 m. Limestone undergoes chemical weathering in which the calcium carbonate is changed to dissolved bicarbonate and is transported away. The limestone remains as separate blocks with various shapes and sizes within the weathered crust. The strength of the limestone is R4-R5.

The Mia Le formation *(D_1ml)* is arranged as stripes along national route No. 3 in the town of Cho Moi, Thac Rieng, and south of the town of Bac Kan. Mia Le has two sub-formations. The lower sub-formation (400 m thick) contains layers of shale and

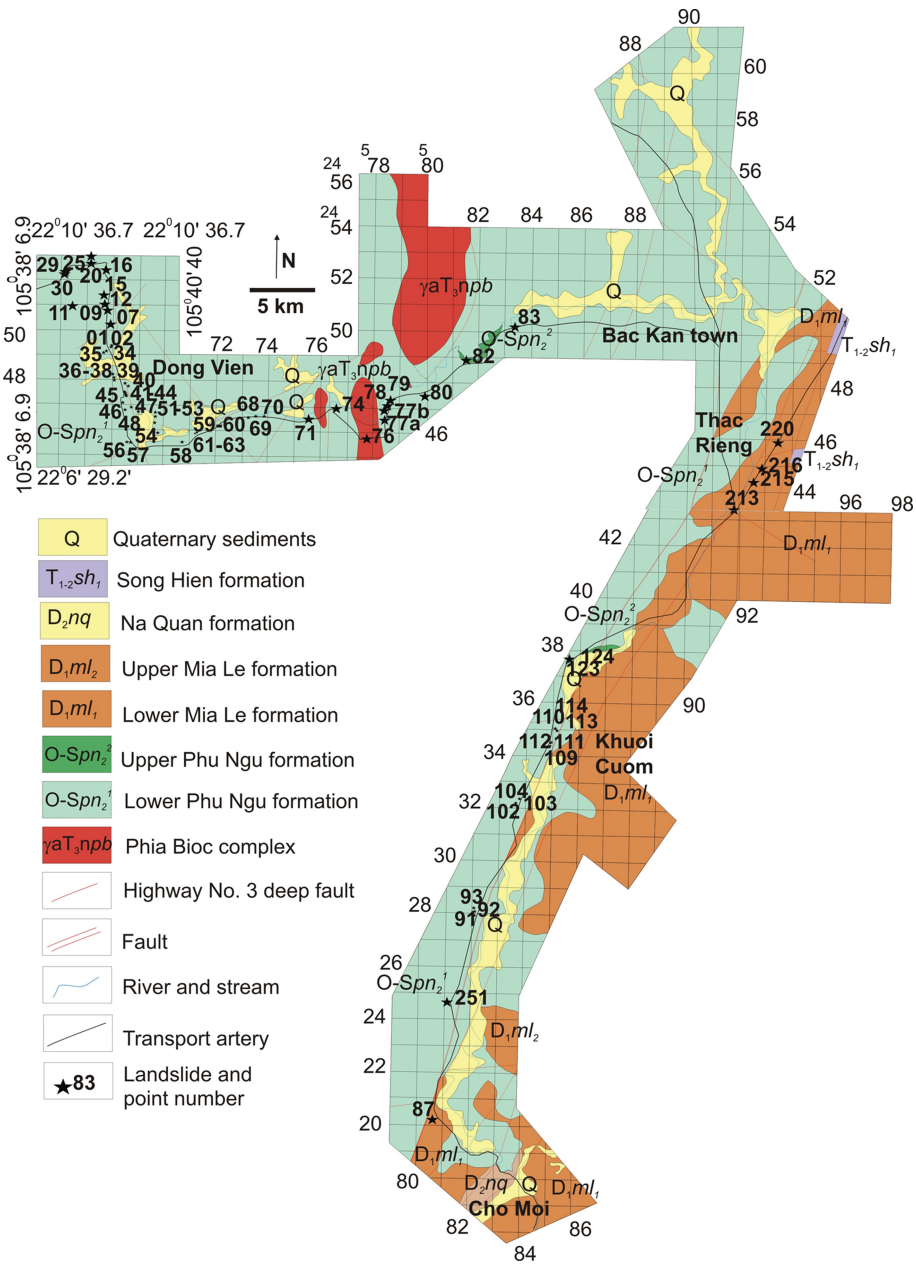

Fig. 3. Geological settings and landslide distribution

sand-siltstone with lenses of limestone. The upper sub-formation (300 m thick) contains layers of carbonate shale, siliceous shale, and lenses of limestone. The residual soils formed from the disintegration of shale and siltstone are mainly ML, MH and SM. The weathered crust is composed of limestone blocks with various round shapes. A shallow landslide will develop rock falls of limestone blocks that can significantly affect the down slope area.

3.2 Geotechnical Properties of Residual Soils

Three different types of residual soils were identified at shallow landslide sites based on laboratory tests of 26 undisturbed samples, including SM (silty sand), ML (silt with sand) and MH (elastic silt). Among those, SM is dominant. Four samples of tectonic breccias were obtained for grain-size analysis. The soil type was then classified as GW.

The geotechnical properties of the soils are shown in Table 2. The natural unit weights of the residual soils range from 15.6 to 17.7 kN/m^3. The degree of saturation is 61–83%; this large range can have a significant effect on the slope stability (see Sect. 3.4.1). The soils in landslides are mainly SM and ML, which have low plasticity. Few landslides occur where the residual soils are MH. All 3 of the soil types have high void ratios (ranging from 0.986 to 1.304). The hydraulic conductivity is significant large: 5×10^{-6} to 32×10^{-6} m/s for SM and 11×10^{-6} to 20×10^{-6} m/s for ML. The effective angle of internal friction for each soil type slightly varies (i.e., the coefficient of variation (V) ranges from 3.5 to 12%). In contrast, the effective cohesion greatly varies (from 5.5 to 31 kPa). The values of V are 35.6%, 60.0% and 23.2% for SM, ML and MH, respectively. The soil-water characteristic curves (SWCC) of the residual soils were defined at two shallow landslides (BK01 and BK54) (Fig. 4). The residual soils are ML and SM, respectively.

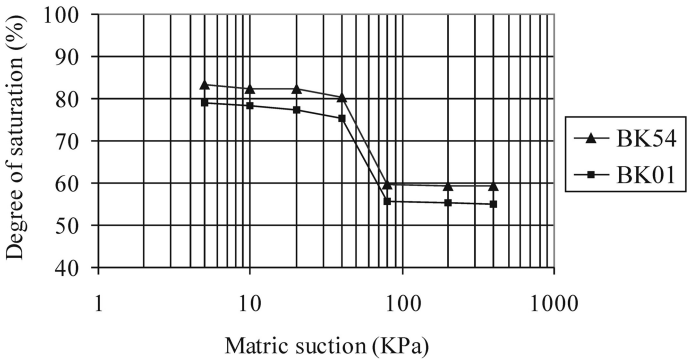

Fig. 4. Soil water characteristic curves of residual soils (wetting curve)

3.3 Characteristics of Shallow Landslides

Shallow landslides occurred intensively at the excavated slopes of national routes, provincial roads, and areas of local settlements. Seventy-three landslides were recorded

(Table 3 and Fig. 3) without any natural slope failure. Among those, 71 were shallow landslides. These landsides are most common the in Dong Vien commune, west and south of the town of Bac Kan, and the Khuoi Cuom commune (Fig. 3). Shallow landslides only took place during or after periods of heavy rain. They dominantly occurred in residual soils (66/71) and, to a lesser extent, in tectonic breccias and bedrock (5/71).

All of the recorded shallow landslides occurred at the excavated slopes of routes where the slope angles were 50–60°. The landslide dimensions ranged from 5 to hundreds of meters in length and 4 to 20 m in height. The volumes of shallow landslides range from a few cubic meters to approximately 2,000 m^3; the most common volumes are 100–500 m^3. Shallow landslides are categorised into 3 main types: translational earth slide, rotational earth slide and debris fall (according to the classification of Varnes [47] and Cruden and Varnes [48]). Among these types, rotational and translational earth slides are dominant. Rotational earth slides occurred in residual soils. The volumes are often small, ranging from 3 to 250 m^3. The thicknesses of the translational slides varied from 0.5 to 4 m. The volumes greatly varied from 44 to 1,935 m^3 (the average volume was 386 m^3). Debris falls occurred in tectonic breccias four times in the record. Shallow landslides of this type occurred on slopes as a mixture of soils and breccias of bedrock. The volumes ranged from 168 to 1,163 m^3, with an average value of 602 m^3.

Additionally, a translational rock slide in siltstone was also recorded. Two deep landslides occurred in the Dong Vien commune (BK37) and in the town of Bac Kan (BK54); the thicknesses of the slides were more than 15 m and 5 m, respectively. The residual soils are SM. BK37 is a chronic landslide that includes a series of slip surfaces; it has occurred and buried portions of road No. 257 several times since the end of the 1990s (based on conversations with the local people).

3.4 Effects of Soil Properties on Slope Stability

In this study, only shallow earth slides were analysed in detail. Geometry was obtained from slopes where landslides commonly occurred in the study area. The tilting angle of the natural slope is 28°, the excavated slope angle is 60°, the height is 4 m, and the dip angle of the bedrock is 32° (Fig. 5). Three common soils of SM, ML and ML were taken into account. The initial negative pore water pressure (PWP) was set to −50 kPa, which is equivalent to saturation of approximately 70%. The bedrock was set as an impermeable boundary. The slope surface was set to the unit discharge condition (the rainfall rate). The boundary was also set to the potential seepage face review to avoid surface water ponding on the slope. The upper and lower sections of the slope were set to a “no flow” boundary condition. One point on the trough of the slope was set to a constant head to ensure convergence of the numerical calculation [49].

Slope stability analysis was conducted for 6 scenarios of rainfall intensity: one light rain scenario of 2.5 mm/h, two moderate scenarios of 5.0 mm/h and 7.5 mm/h, two heavy scenarios of 15 mm/h and 30 mm/h and one violent scenario of 60 mm/h (based on the classification of the MetOffice, 2012 [50]). To assess the effects of geotechnical properties, the rainfall intensity of 15 mm/h was used. The other scenarios were used to investigate the rainfall intensity-duration thresholds.

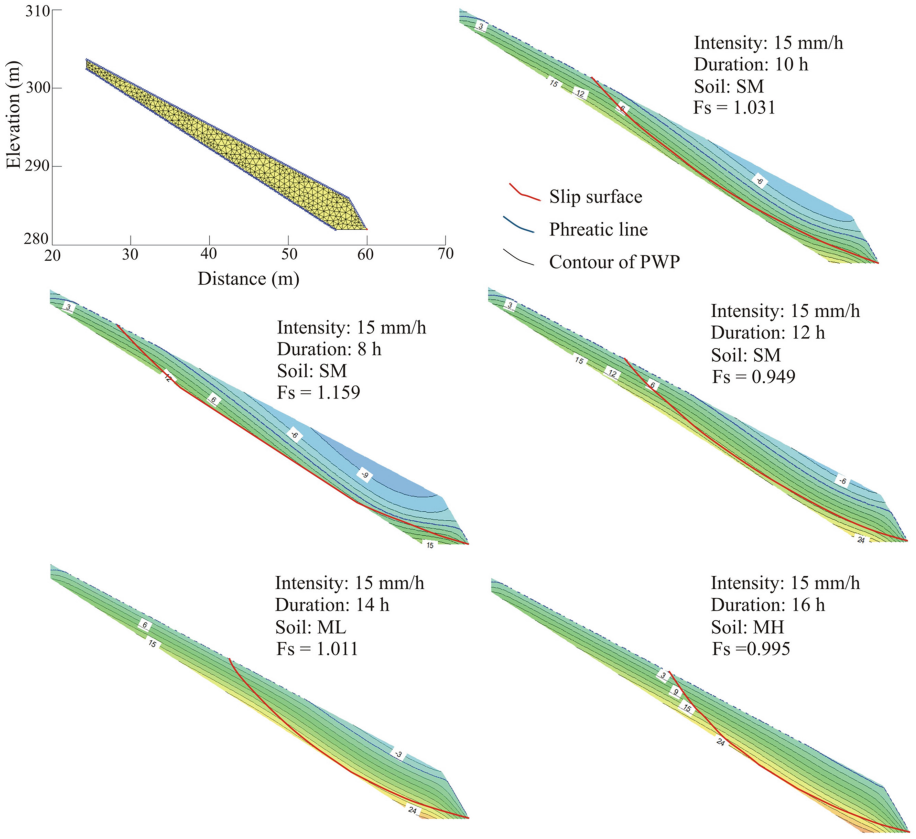

Fig. 5. Geometry of slope, FEM mesh, PWP distribution and slip surfaces

The soil property that reflects the influence of suction ($u_w - u_a$) on strength ϕ^b was estimated by [51]:

$$\tan \phi^b = (S - S_r)/(100 - S_r) \tan \phi' \quad (1)$$

where S is the current saturation (%), S_r is the residual saturation (%), and ϕ' is the effective angle of friction.

3.4.1 Effects of Hydraulic Conductivity and Initial Soil Moisture

Rain infiltration plays the most important role in moisture conditions and the shear strength of the residual soils [52]. As a consequence, hydraulic conductivity (K) and initial soil moisture have a strong influence on rainfall-induced landslides. The K of SM varies widely and covers the variability of the K for ML and MH. Therefore, the analysis was conducted with 3 values of K at saturation: 5×10^{-6}, 9.1×10^{-6} and 2×10^{-5} m/s, which were equivalent to the minimum, mean (σ) and average values of

Table 3. Landslides in the study area (from NW to SE)

Slide	Volume (m^3)	Date of occurrence	Type	Material
BK01	1,210	4 Jul. 2001	T	ML
BK02	449	4 Jul. 2001	T	SM
BK07	103	4 Jul. 2001	T	SM
BK09	28	4 Jul. 2001	R	MH
BK11	30	Before 2001	R	ML
BK12	20	4 Jul. 2001	R	ML
BK15	136	4 Jul. 2001	R	SM
BK16	283	4 Jul. 2001	T	ML
BK20	89	4 Jul. 2001	T	Siltstone
BK25	48	4 Jul. 2001	R	MH
BK29	78	16 Jul. 2002	R	ML
BK30	134	16 Jul. 2002	R	ML
BK34	85	4 Jul. 2001	R	ML
BK35	370	4 Jul. 2001	T	SM
BK36	887	4 Jul. 2001	T	SM
BK37	5,080	4 Jul. 2001	R	SM
BK38	820	4 Jul. 2001	D	GW
BK39	189	16 Jul. 2002	T	SM
BK40	1,163	4 Jul. 2001	D	GM
BK41	675	4 Jul. 2001	T	SM
BK42	187	16 Jul. 2002	T	ML
BK43	711	16 Jul. 2002	T	ML
BK44	26	4 Jul. 2001	R	SM
BK45	14	16 Jul. 2002	R	SM
BK46	125	16 Jul. 2002	R	SM
BK47	66	16 Jul. 2002	R	SM
BK48	1,024	4 Jul. 2001	T	SM
BK50	1,935	4 Jul. 2001	T	SM
BK51	168	4 Jul. 2001	D	GW
BK52	636	4 Jul. 2001	T	SM
BK53	153	4 Jul. 2001	T	SM
BK54	228	4 Jul. 2001	R	SM
BK56	106	4 Jul. 2001	R	ML
BK57	36	4 Jul. 2001	R	ML
BK58	31	4 Jul. 2001	R	ML
BK59	3	4 Jul. 2001	R	MH
BK60	44	4 Jul. 2001	T	MH
BK61	37	4 Jul. 2001	R	ML
BK62	39	4 Jul. 2001	R	ML
BK63	17	4 Jul. 2001	R	ML

(*continued*)

Table 3. (*continued*)

Slide	Volume (m^3)	Date of occurrence	Type	Material
BK68	155	4 Jul. 2001	T	ML
BK69	36	4 Jul. 2001	R	MH
BK70	90	4 Jul. 2001	R	SM
BK71	256	4 Jul. 2001	D	GW
BK74	116	4 Jul. 2001	T	SM
BK76	250	4 Jul. 2001	R	SM
BK77a	76	4 Jul. 2001	T	SM
BK77b	85	4 Jul. 2001	T	SM
BK78	288	4 Jul. 2001	T	SM
BK79	74	4 Jul. 2001	T	SM
BK80	318	4 Jul. 2001	T	SM
BK82	207	16 Jun. 2006	T	SM
BK83	588	16 Jun. 2006	T	SM
BK87	29	4 Jul. 2001	R	SM
BK91	48	4 Jul. 2001	R	SM
BK92	39	4 Jul. 2001	R	SM
BK93	45	4 Jul. 2001	R	SM
BK102	19	4 Jul. 2001	R	SM
BK103	18	4 Jul. 2001	R	SM
BK104	210	4 Jul. 2001	T	SM
BK109	46	4 Jul. 2001	T	SM
BK110	13	4 Jul. 2001	R	SM
BK111	134	4 Jul. 2001	T	SM
BK112	40	4 Jul. 2001	R	SM
BK113	4	4 Jul. 2001	R	SM
BK114	49	4 Jul. 2001	T	SM
BK123	88	4 Jul. 2001	T	SM
BK124	101	4 Jul. 2001	T	SM
BK251	563	Before 2001	T	ML
BK213	4	4 Jul. 2001	R	SM
BK215	70	4 Jul. 2001	R	SM
BK216	48	4 Jul. 2001	R	SM
BK220	70	4 Jul. 2001	R	SM

T – Translational earth slide, R – Rotational earth slide, D – Debris fall

K for the SM soil. The initial moisture was set to 70% saturation (i.e., a matric suction of 50 kPa). The suction and the initial K of the residual soils were assessed at S values of 60% and 80%. The unsaturated K of soils were estimated by the method of Fredlund and Xing [53]. It shows that S is 60% (suction = 70 kPa) and 80% (suction = 5 kPa), the initial K are 2×10^{-7} and 8×10^{-5} m/s, respectively.

The results in Fig. 6 indicate that when K varies from 5 to 20 $\times$ 10^{-6} m/s, the duration of rainfall-induced slope failure decreases from 13.5 h to 10.5 h (approximately a 30% difference). A change of S from 60 to 80% yields a completely different slope stability outcome. The duration of rainfall-induced slope failures were 4 h and 13.5 h when the initial S was 80% and 70%, respectively. When S was 60%, only two days of consecutive rainfall (15 mm/h) triggered a landslide; however, these conditions have not occurred in the study area. The results verified the importance of the moisture flux boundary conditions at the ground surface for slope stability. Further studies must focus on several components to determine the net moisture flux entering the soil at the ground surface, such as precipitation, runoff, actual evaporation, and transpiration [54].

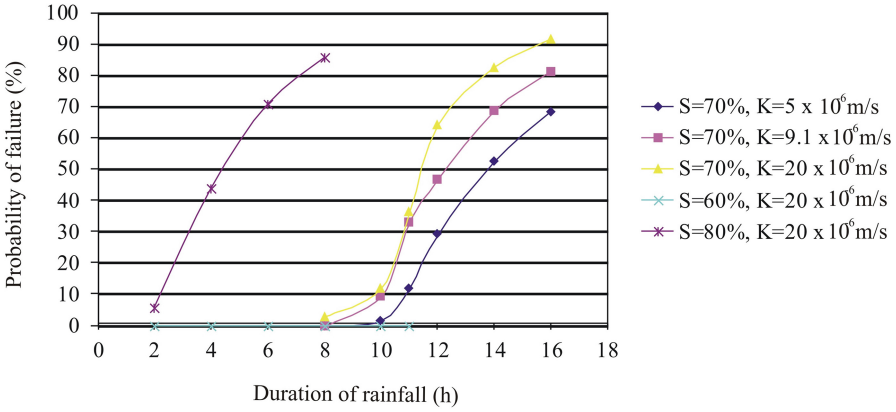

Fig. 6. Effects of hydraulic conductivity and degree of saturation on Fs

3.4.2 Effects of Soil Types

The results of the slope stability analysis for the residuals of SM, ML and MH are presented in Fig. 7. At a density of 15 mm/h, the durations of rainfall-induced slides from the deterministic analysis were approximately 10.2 h, 14 h and 16 h for SM, ML and MH, respectively; soil cohesion increases from SM to ML and MH, while permeability decreases in that order. The slip surfaces were almost rotational and similar for all 3 types. However, the slips also have partial planar surfaces in ML and MH. The Fs in the probability analysis exhibit strong dependence on the variability of the soil parameters, especially cohesion. The maximum Fs of ML for any rainfall duration were almost double the minimum values. The difference was 30–40% for the cases of SM and MH. The mean Fs was lower than the deterministic Fs. As the soil strength parameters become more variable, mean and deterministic Fs become more similar. Therefore, a slope design with a deterministic Fs is safer compared to a statistical mean value.

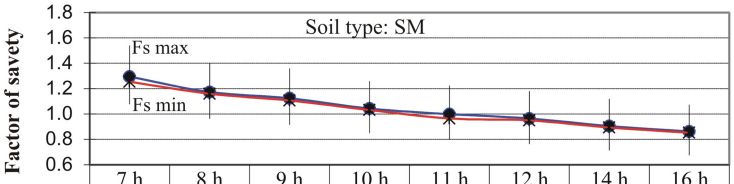

	7 h	8 h	9 h	10 h	11 h	12 h	14 h	16 h
Fs max	1.54	1.40	1.36	1.26	1.22	1.18	1.12	1.07
Fs min	1.08	0.96	0.92	0.85	0.80	0.76	0.71	0.68
Mean	1.29	1.17	1.12	1.04	1.00	0.96	0.90	0.86
Fs	1.25	1.16	1.11	1.03	0.96	0.95	0.89	0.85

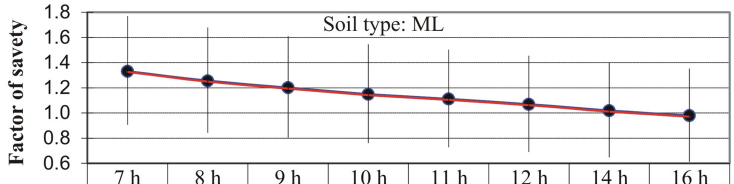

	7 h	8 h	9 h	10 h	11 h	12 h	14 h	16 h
Fs max	1.77	1.68	1.61	1.55	1.50	1.46	1.40	1.35
Fs min	0.91	0.84	0.80	0.76	0.73	0.69	0.65	0.61
Mean	1.33	1.26	1.20	1.15	1.11	1.07	1.02	0.98
Fs	1.33	1.25	1.19	1.14	1.10	1.06	1.01	0.97

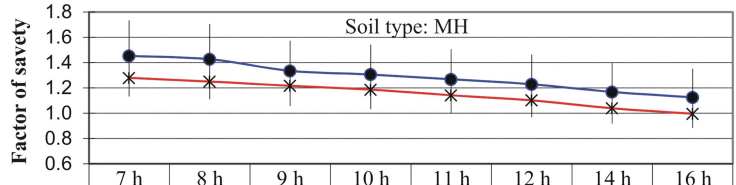

	7 h	8 h	9 h	10 h	11 h	12 h	14 h	16 h
Fs max	1.73	1.70	1.57	1.54	1.51	1.46	1.40	1.35
Fs min	1.13	1.11	1.06	1.03	1.00	0.97	0.92	0.88
Mean	1.45	1.43	1.33	1.31	1.27	1.23	1.17	1.12
Fs	1.28	1.25	1.22	1.19	1.14	1.10	1.04	1.00

Duration of rainfall (with 15mm/h intensity)

Fig. 7. Effects of soil types on Fs and probability of failure. Vertical bars show maximum and minimum of Fs. Asterisks and dots indicate Fs of deterministic analysis and statistical mean, respectively

3.4.3 Effects of Soil Thickness

The only SM soil was used for additional analyses due to its dominance in the study area. Slope stability was considered in 3 cases with average thicknesses of 1.5 m, 2.5 m and 8 m. A slope of thin residual soils failed after 6 h of rainfall (15 mm/h); the rainfall durations were 10.2 h and 27 h for slopes with 2.5 and 8 m of soil, respectively. Translation earth slides formed where the slopes had a soil thickness of 1.5 m. Rotational slides formed where the slopes had a soil thickness of 2.5 m. The volumes

of translational earth slides are often much larger than those of rotational slides. However, the planar slip surfaces in translational slides were either tectonically discontinued or the bedding surfaces of bedrock, which can continue over a long distance. Therefore, translational slides have much longer lengths. Deep rotational slides were potentially formed in residual soils of 8 m. However, the rainfall duration with an intensity of 15 mm/h reached 27 h at failure, which was not recorded in the study area. Deep slides, which are not comprehensively considered in this paper, are related rainfall and other factors, such as tension cracks and the creep behaviour of soils.

3.4.4 Effects of Excavation

The results indicate that a natural slope has a deterministic Fs that is approximately 20% higher than that of a cut slope. A rainfall-induced landslide occurred after a duration of 16 h (15 mm/h), which is 50% longer than that of a cut slope. Thus, even a small-scale excavation to a height of 4 m on a natural slope led to a significant change in stability. However, natural slopes experienced a probability of failure after a short rain duration of 11 h because of their rather high slope angle of 28°. Using the same numerical analysis, a natural slope of 25° only failed after 16 h of similar rain conditions.

4 Discussion

4.1 Other Affecting Factors

Tectonic activity has highly fractured the bedding planes of the bedrock. Slopes in the study area are very vulnerable to slides when they are excavated near the fault zone in Dong Vien [55]. The study area was affected by at least 3 major tectonic phases. The oldest tectonic phase, which was oriented NW-SE, was responsible for the folding and thrusting activities [56, 57]. The second phase was responsible for the reactivation of the fault or fracture system in the NW-SE, E-W and NE-SW directions. The most recent phase was characterised by extensional to trans-tensional tectonics with an extensional axis oriented NE-SW. The third phase played an important role in forming the factures, joints and axial cleavage, which already existed during earlier tectonic activity [58]. These activities created two typical materials at the slopes in the shear zones. Gouge was formed where the original bedrock was shale and breccias were formed from sandstone and quartzite. Shallow landslides often occur very close to faults (Fig. 3). Bedrock in the Dong Vien commune is strongly impacted by the tectonic activities of 4 faults. Thus, the greatest density of shallow landslides is observed in this area.

Shallow landslides were more likely to occur near faults and/or where the inclined direction of a slope coincides with the direction of the bedding planes. Streams and gullies were not affected by landslides, but were nearby in some cases. The groundwater level is far from the troughs of the slopes, even in the rainy season. Groundwater discharge appears in some outcrops of limestone, but it has no impact on the recorded shallow landslides. The role of vegetable cover on slope instability was not significant. High density vegetable coverage was observed at most shallow landslides [43].

4.2 Rainfall Intensity-Duration Thresholds

In this study, rainfall thresholds were investigated by numerically analysing the slope stability in various rainfall path scenarios. The residual soil considered was SM. The results indicate that a light rain (2.5 mm/h) cannot trigger landslides in deterministic analysis. However, in probability analysis, failure can occur after a duration of 60 h of consecutive light rain (cumulative rainfall of 150 mm). A moderate rainfall of 7.5 mm/h and heavy rainfall of 15 mm/h, with similar amounts of cumulative rainfall as the light rain case, led to a lower Fs and higher probabilities of failure. A moderate rainfall of 5 mm/h and a heavy rainfall of 30 mm/h have almost the same effects. Violent rainfall of 60 mm/h resulted in Fs values that were 8–10% and 3–6% higher than those of rain intensities of 15 mm/h and 30 mm/h, respectively.

The relationships between rainfall intensity, duration, Fs and probability of failure (Pf) are described in Table 4. As mentioned, the Fs from the probabilistic analysis is very stable. Therefore, it was used to assess the relationships between the landslide hazard level and rainfall paths. Two hazard levels were considered: low (5% probability of failure) and extremely high (30% probability of failure) [59, 60]. The rainfall intensities and durations at slope failures with various hazard levels are summarized in Table 4. The rainfall thresholds of intensity-duration (ID) were derived as follows (Fig. 8):

$$I = 204.47\,D^{-1.073} (R^2 = 0.995) \text{ for deterministic slope stability analysis} \quad (2)$$

$$I = 174.91\,D^{-1.039} (R^2 = 0.992) \text{ for the extremely high landslide hazard level} \quad (3)$$

$$I = 133.34\,D^{-0.981} (R^2 = 0.988) \text{ for the low landslide hazard level} \quad (4)$$

In the case of 5 mm/h rain intensity, the duration of the rain-induced landslides of deterministic Fs was slightly lower than that of the extremely high hazard level. However, the durations were 7–9% higher for the remaining intensity scenarios (Table 4). As a result of this study, deterministic stability analysis leads to late warning in terms of the landslide hazard level. The duration of an extremely high hazard level was approximately 25% higher than that of a low hazard level during a 5 mm/h rainfall intensity; in the other intensity scenarios, the extremely high hazard levels were 15–20% higher.

Table 4. Rainfall intensity and duration at slope failures

Intensity (mm/h)	Duration (h)		
	Fs = 1.00 (deterministic)	Pf = 5%	Pf = 30%
2.5	–	68.0	–
5.0	33.2	27.0	34.0
7.5	20.8	16.0	19.2
15	10.53	8.33	9.80
30	5.90	4.67	5.37
60	3.33	2.60	3.02

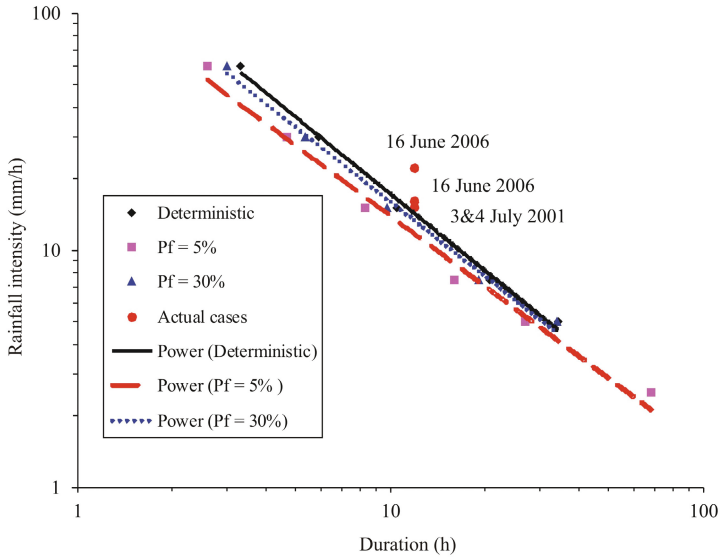

Fig. 8. Rainfall intensity-duration thresholds

Three rain-induced landslides were recorded during the period of 2000–2010 by rain data at 5 monitoring stations (i.e., Cho Moi, Bac Kan, Phu Thong, Dong Vien, and Phuong Vien). The first event occurred during 3–4 July 2001 when storm No. 2 appeared. The rainfall intensity was 90 mm/6 h and the duration was 12 h. The storm induced many large, shallow landslides with a total volume of approximately 16,000 m^3. National route No. 3 and many other provincial roads were interrupted for a few days [55]. The second (16 July 2002) and third (16 June 2006) events had rain intensities of 96 mm/6 h and 132 mm/6 h, respectively, and durations of 12 h. The three actual cases of rainfall-induced landslides are above all of the thresholds (Fig. 8). The worst case, 4 July 2001, is near the line of deterministic analysis.

The results prove that hourly data (and even shorter time intervals) are important to provide early warnings for rainfall-induced shallow landslides in the study area. The historical monitoring practice of 6-hourly measurements does not meet this requirement. However, the monitoring system has gradually shifted to automatically record hourly data (per communication with local authorities).

5 Conclusions

The excavated slopes along routes in Bac Kan province, Vietnam are very vulnerable to landslides. Along three routes, 71 shallow landslides were recorded. The landslides mainly occurred in residual soils and, to a lesser extent, in tectonic breccias. The landslides were classified into 4 types: translational, rotational earth slide, debris fall and translational rock slide. The volumes of shallow landslides varied from a few cubic

meters to approximately 2,000 m^3. Approximately 93% of the shallow landslides were rotational and translational earth slides.

The effects of residual soil characteristics on rainfall-induced shallow landslides were assessed by modeling rain infiltration with SEEP/W and using deterministic and probabilistic analyses of slope stability with SLOPE/W. The slopes constituted by soil type SM were more vulnerable to rainfall-induced shallow landslides than ML and MH. The mean value of saturated hydraulic conductivity (K_s) of SM soil led to a 30% lower Fs compared to the minimum K_s. The slope excavation in the study area decreased the Fs by 20%.

Shallow translational earth slides are dominant on cut slopes where the thickness of residual soils are less than 1.5 m. Shallow rotational earth slides occurred in residual soils with thicknesses greater than 2.5 m. Deep rotational earth slides occurred on slopes with residual soils that were approximately 8 m thick.

Based on the results of the slope stability analyses for various rainfall path scenarios, three thresholds of rainfall intensity-duration were identified for the deterministic stability analysis of extremely high and low landslide hazard levels: $I = 204.47\ D^{-1.073}$, $I = 174.91\ D^{-1.039}$ and $I = 133.34\ D^{-0.981}$.

Acknowledgment. The data analysis and numerical calculation of the paper was supported by the project of Ministry of Science and Technology, coded ĐTĐLCN. 23/17.

References

1. Nadim, F., Kjekstad, O., Peduzzi, P., Herold, C., Jaedicke, C.: Global shallow landslide and avalanche hotspots. Shallow Fail. **3**, 159–173 (2006)
2. The International Disaster Database. http://www.emdat.be/
3. Schuster, R., Highland, L.: The Third Hans Cloos Lecture. Urban shallow landslides: socioeconomic impacts and overview of mitigative strategies. Bull. Eng. Geol. Env. **66**, 1–27 (2007)
4. Hung, L.Q., Nguyen, T.H.V., Do, M.D., Le, T.C.H., Pham, V.S., Nguyen, H.K., Luu, T.B.: Landslide susceptibility mapping by combining the analytical hierarchy process and weighted linear combination methods: a case study in the upper Lo River catchment (Vietnam). Landslides **13**, 1285–1301 (2015)
5. Bui, D.T., Binh, T.P., Phi, Q.N., Nhat, D.H.: Spatial prediction of rainfall-induced shallow landslides using hybrid integration approach of Least-Squares Support Vector Machines and differential evolution optimization: a case study in Central Vietnam. Int. J. Digit. Earth **9**(11), 1077–1097 (2016)
6. Tran, V.T., Duc, D.M., Nguyen, M.T., Van, D.C.: Preliminary assessments of debris flow hazard in relation to geological environment changes in mountainous regions, North Vietnam. Vietnam J. Earth Sci. **38**, 277–286 (2016)
7. Duc, D.M.: Rainfall-triggered large landslides on 15 December 2005 in Van Canh District, Binh Dinh Province, Vietnam. Landslides **10**, 219–230 (2012)
8. Guzzetti, F., Peruccacci, S., Rossi, M., Stark, C.: The rainfall intensity-duration control of shallow landslides and debris flows: an update. Landslides **5**, 3–17 (2008)
9. Caine, N.: The rainfall intensity-duration control of shallow landslides and debris flows. Geogr. Ann. **62A**, 23–27 (1980)

10. Aleotti, P.: A warning system for rainfall-induced shallow landslides. Eng. Geol. **73**, 247–265 (2004)
11. Brunetti, M., Peruccacci, S., Rossi, M., Luciani, S., Valigi, D., Guzzetti, F.: Rainfall thresholds for the possible occurrence of landslides in Italy. Nat. Hazards Earth Syst. Sci. **10**, 447–458 (2010)
12. Martelloni, G., Segoni, S., Fanti, R., Catani, F.: Rainfall thresholds for the forecasting of landslide occurrence at regional scale. Landslides **9**, 485–495 (2012)
13. Sengupta, A., Gupta, S., Anbarasu, K.: Rainfall thresholds for the initiation of shallow landslide at Lanta Khola in north Sikkim. India. Nat. Hazards **52**, 31–42 (2010)
14. Hong, Y., Adler, R., Negri, A., Huffman, G.: Flood and landslide applications of near real-time satellite rainfall products. Nat. Hazards Earth Syst. Sci. **43**, 285–294 (2007)
15. Apip, Takara, K., Yamashiki, Y., Sassa, K., Ibrahim, A., Fukuoka, H.: A distributed hydrological–geotechnical model using satellite-derived rainfall estimates for shallow landslide prediction system at a catchment scale. Landslides **7**, 237–258 (2010)
16. Chleborad, A., Baum, R., Godt, J.: Rainfall thresholds for forecasting shallow landslides in the Seattle, Washington, area - Exceedance and probability (2006)
17. Baum, R., Godt, J.: Early warning of rainfall-induced shallow landslides and debris flows in the USA. Landslides **7**, 259–272 (2010)
18. Ng, C., Shi, Q.: Influence of rainfall intensity and duration on slope stability in unsaturated soils. Q. J. Eng. Geol. **31**, 105–113 (1998)
19. Chen, H., Lee, C.: Geohazards of slope mass movement and its prevention in Hong Kong. Eng. Geol. **76**, 3–25 (2004)
20. Angeli, M., Pasuto, A., Silvano, S.: A critical review of shallow landslide monitoring experiences. Eng. Geol. **55**, 133–147 (2000)
21. Zhang, J., Jiao, J., Yang, J.: In situ rainfall infiltration studies at a hillside in Hubei Province. China. Eng. Geol. **57**, 31–38 (2000)
22. Simoni, A., Berti, M., Generali, M., Elmi, C., Ghirotti, M.: Preliminary result from pore pressure monitoring on an unstable clay slope. Eng. Geol. **73**, 117–128 (2004)
23. Rahardjo, H., Leong, E., Rezaur, R.: Studies of rainfall-induced slope failures. In: Proceedings of the National Seminar, Slope 2002, pp. 15–29 (2002)
24. Tofani, V., Dapporto, S., Vannocci, P., Casagli, N.: Infiltration, seepage and slope instability mechanisms during the 20–21 November 2000 rainstorm in Tuscany, central Italy. Nat. Hazards Earth Syst. Sci. **6**, 1025–1033 (2006)
25. Rahardjo, H., Aung, K., Leong, E., Rezaur, R.: Characteristics of residual soils in Singapore as formed by weathering. Eng. Geol. **73**, 157–169 (2004)
26. Frattini, P., Crosta, G.: The role of material properties and landscape morphology on landslide size distributions. Earth Planet. Sci. Lett. **361**, 310–319 (2013)
27. McKenna, J., Santi, P., Amblard, X., Negri, J.: Effects of soil-engineering properties on the failure mode of shallow landslides. Landslides **9**, 215–228 (2011)
28. Shakoor, A., Smithmyer, A.: An analysis of storm-induced shallow landslides in colluvial soils overlying mudrock sequences, southeastern Ohio, USA. Eng. Geol. **78**, 257–274 (2005)
29. Arnone, E., Noto, L., Lepore, C., Bras, R.: Physically-based and distributed approach to analyze rainfall-triggered landslides at watershed scale. Geomorphology **133**, 121–131 (2011)
30. Ho, J., Lee, K., Chang, T., Wang, Z., Liao, Y.: Influences of spatial distribution of soil thickness on shallow landslide prediction. Eng. Geol. **124**, 38–46 (2012)
31. Kim, J., Jeong, S., Park, S., Sharma, J.: Influence of rainfall-induced wetting on the stability of slopes in weathered soils. Eng. Geol. **75**, 251–262 (2004)

32. Fowze, J., Bergado, D., Soralump, S., Voottipreux, P., Dechasakulsom, M.: Rain-triggered landslide hazards and mitigation measures in Thailand: from research to practice. Geotext. Geomembr. **30**, 50–64 (2012)
33. International Society of Rock Mechanics: Rock Characterization, Testing and Monitoring: ISRM Suggested Method. Pergamon Press, Oxford (1981)
34. Fredlund, D., Rahardjo, H.: Soil Mechanics for Unsaturated Soils. Wiley, New York (1993)
35. ASTM: D 854 Test methods for specific gravity of soil solids by water pycnometer. ASTM Standards on Disc CD 1, vol. 04.08, Soil and Rock (I): D420–D5779 (2001)
36. ASTM: D 422 Test method for particle size analysis of soils. ASTM Standards on Disc CD 1, vol. 04.08, Soil and Rock (I): D420–D5779 (2001)
37. ASTM: D 2216 Test method for laboratory determination of water (moisture) content of soil and rock by mass. ASTM Standards on Disc CD 1, vol. 04.08, Soil and Rock (I): D420–D5779 (2001)
38. ASTM: D 4318 Standard test methods for liquid limit, plastic limit, and plasticity index of soils. ASTM Standards on Disc CD 1, vol. 04.08, Soil and Rock (I): D420–D5779 (2001)
39. ASTM: D 2487 Practice for classification of soils for engineering purposes. ASTM Standards on Disc CD 1, vol. 04.08, Soil and Rock (I): D420–D5779 (2001)
40. ASTM: D 3080 Test method for direct shear test of soils under consolidated drained conditions. ASTM Standards on Disc CD 1, vol. 04.08, Soil and Rock (I): D420–D5779 (2001)
41. ASTM: D 5084 Standard test method for measurement of hydraulic conductivity of saturated porous materials using a flexible wall permeameter. ASTM Standards on Disc CD 1, vol. 04.08, Soil and Rock (I): D420–D5779 (2001)
42. Bien, M.T.: Geography of Bac Kan Province (2000)
43. Duc, D.M.: Rainfall-induced shallow landslides in Bac Kan and Binh Dinh provinces. VNU J. Sci. Earth Sci. **26**, 1–10 (2010)
44. Geo-Slope International Ltd.: Stability Modeling with SLOPE/W – An Engineering Methodology (2004)
45. Geo-Slope International Ltd.: Seepage Modeling with SEEP/W – An Engineering Methodology (2004)
46. Department of Geology and Mineral Resources: The Geological map of Bac Kan and adjacent areas, scale 1: 200,000 (1984)
47. Varnes, D.: Slope movement types and processes. In: Schuster, R., Krizek, R. (eds.) Landslides, Analysis and Control, pp. 11–33. Transportation Research Board Special Report No. 176, National Academy of Sciences (1978)
48. Cruden, D., Varnes, D.: Landslide types and processes. In: Turner, A., Shuster, R. (eds.) Landslides: Investigation and Mitigation. Transportation Research Board, Special Report 247, pp. 36–75 (1996)
49. Rahardjo, H., Leong, E., Rezaur, R.: Rainfall-induced slope failures: mechanism and assessment. In: International Workshop on "Saving Our Water and Protecting Our Land", 20–22 October 2001, Hanoi (2001)
50. http://www.metoffice.gov.uk/media/pdf/f/c/Fact_sheet_No._3.pdf
51. Vanapalli, S., Fredlund, D., Pufahl, D., Clifton, A.: Model for prediction of shear strength with respect to matric suction. Can. Geotech. J. **33**, 379–392 (1996)
52. Blatz, J., Ferreira, N., Graham, J.: Effects of near-surface environmental conditions on instability of an unsaturated soil slope. Can. Geotech. J. **41**, 1111–1126 (2004)
53. Fredlund, D., Xing, A.: Equations for the soil–water characteristic curve. Can. Geotech. J. **31**, 521–532 (1994)
54. Fredlund, D., Vu, H., Stianson, J.: Engineering protocols for the assessment of the net moisture flux at the ground surface. Geotech. Eng. J. SEAGS AGSSEA **41**, 1–11 (2010)

55. Duc, D.: Numerical simulation for slope stability analysis and shallow landslide prediction in Bac Kan province, Northeast Vietnam. In: International Symposium on GeoInformatics for Spatial-Infrastructure Development in Earth and Allied Sciences, Hanoi, Vietnam (2004)
56. Lepvrier, C., Faure, M., Vuong, N., Tich, V., Wei, L., Thang, T., Phuong, T.: North-directed Triassic nappes in Northeastern Vietnam (East Bac Bo). J. Asian Earth Sci. **41**, 56–68 (2011)
57. Bui, V.D., Nguyen, A.D.: The relation between fault movement potential and seismic activity of major faults in Northwestern Vietnam. Vietnam J. Earth Sci. **39**, 240–255 (2017)
58. Vuong, N.V., Anh, N.N., Hoai, L.T.T., Dong, B.V., Duan, B.V., Nguyen, N.D., Thanh, H. Q., Hai, B.X.: Investigation of the influences of tectonic activities on landslides in Bac Kan town (2011)
59. Fell, R.: Landslide risk assessment and acceptable risk. Can. Geotech. J. **31**, 261–272 (1996)
60. Chacon, J., Irigaray, C., Fernandez, T., El Hamdouni, R.: Engineering geology maps: landslides and geographical information systems. Bull. Eng. Geol. Env. **65**, 341–411 (2006)

Spatial Prediction of Rainfall Induced Shallow Landslides Using Adaptive-Network-Based Fuzzy Inference System and Particle Swarm Optimization: A Case Study at the Uttarakhand Area, India

Binh Thai Pham[1(✉)] and Indra Prakash[2]

[1] Department of Geotechnical Engineering, University of Transport Technology, 54 Trieu Khuc, Thanh Xuan, Ha Noi, Viet Nam
binhpt@utt.edu.vn

[2] Department of Science and Technology, Bhaskarcharya Institute for Space Applications and Geo-Informatics (BISAG), Government of Gujarat, Gandhinagar, India
indra52prakash@gmail.com

Abstract. Landslides generally occur during rainy season in Himalayas. Most of the landslides observed in the Uttarakhand part of Himalaya, India are of shallow nature. In the present study, we proposed a hybrid model Particle Swarm Optimization based Adaptive-Network-Based Fuzzy Inference System (PSOANFIS), which is a hybrid intelligent approach of Adaptive-Network-Based Fuzzy Inference System (ANFIS) and Particle Swarm Optimization (PSO), for spatial prediction of shallow landslides in part of Uttarakhand State. Firstly, a total of 1295 historical landslide events occurred in the area were identified and mapped from satellite images in conjunction with available historical data from reports to construct a landslide inventory map. In addition, 16 affecting factors (slope angle, slope aspect, elevation, curvature, plan curvature, profile curvature, lithology, soil, distance to lineaments, lineament density, land cover, rainfall, road networks, distance to roads, road density, river networks, distance to river, and river density) were taken into account for landslide spatial modeling. Datasets (training and testing) were then generated from the analysis of the collected data using GIS application. Thereafter, landslide model PSOANFIS was constructed using training dataset for spatial prediction of landslides. Performance of the proposed hybrid model has been compared with another benchmark landslide model namely Support Vector Machines (SVM). Lastly, the predictive capability of the hybrid model was validated using Receiver Operating Characteristic (ROC) curve and Root Mean Square Error (RMSE) and Mean Absolute Error (MAE) indexes. The results of the present study show that the PSOANFIS model performed well for spatial prediction of rainfall induced shallow landslides, thus the PSOANFIS method can also be applied for the development of better landslide predictive models in other landslide prone areas of the world.

Keywords: Landslide susceptibility mapping · Adaptive-Network-Based Fuzzy Inference System · Particle Swarm Optimization · GIS · India

© Springer International Publishing AG 2018
D. Tien Bui et al. (eds.), *Advances and Applications in Geospatial Technology and Earth Resources*, https://doi.org/10.1007/978-3-319-68240-2_14

1 Introduction

Major part of Himalaya is prone to landslides especially during rainy season. Landslides in Himalayan ranges have caused the damages of about 1 billion USD besides the deaths of approximately 200 people every year [1, 2]. In the present study, Uttarakhand part of the Himalaya, India has been selected where most of the landslides are of shallow nature. This area is highly susceptible to landslides due to prolong and heavy rainfall, complex geological structures integrated with contemporary crustal movements, and increasing interferences of human in the ecosystem [2]. Landslide spatial prediction is considered as a useful task to construct landslide susceptibility map on the basis of the analysis of degrees of actual or potential landslides in relation with a set of affecting factors [3, 4]. Landslide susceptibility map can help planners and decision makers to choose favorable sites for developing habitant areas, road constructions, dams, and to take suitable precautionary measures in advance to avoid future landslides [2]. Machine learning techniques are being applied popularly and efficiently for the prediction of shallow landslides [5–7]. Logistic regression [8, 9], support vector machines [5, 10, 11], artificial neural networks [12, 13] are the most popular machine learning methods for landslide spatial prediction. In modeling, the optimization techniques such as particle swarm optimization can be used to improve the performance of single machine learning methods [14].

In this study, Particle Swarm Optimization based Adaptive-Network-Based Fuzzy Inference System (PSOANFIS), which is a hybrid intelligent approach of two state of the art machine learning methods of Adaptive-Network-Based Fuzzy Inference System (ANFIS) classifier and Particle Swarm Optimization (PSO) technique, has been proposed for landslide spatial prediction at part of the Pauri Garhwal district in Uttarakhand State (India). In addition, performance of the proposed hybrid model has been compared with another benchmark landslide model namely Support Vector Machines (SVM). For validation and comparison of models, the Receiver Operating Characteristic (ROC) curve and Root Mean Square Error (RMSE) and Mean Absolute Error (MAE) indexes have been selected and used. For this study, the programming language of MATLAB 2014 has been used to design the hybrid model whereas ArcMap version 10.2 has been used for data processing and development of maps.

2 General Characteristics of the Study Area

The study area is located in the Pauri Garhwal district of Uttarakhand State, India between longitudes 78°37′22″ to 78°52′55″ and latitudes 30°4′37″ to 29°52′22″, covering an area of about 560.986 km^2 (Fig. 1). The area is situated in tropical monsoon region with average annual rainfall of about 1500 mm, and temperature varying from sub-zero to 45 °C. Humidity in the area varies from 54% to 63%. The area receives adequate rainfall generally from mid-June to mid-September. Occasional rainfall also occurs during winter.

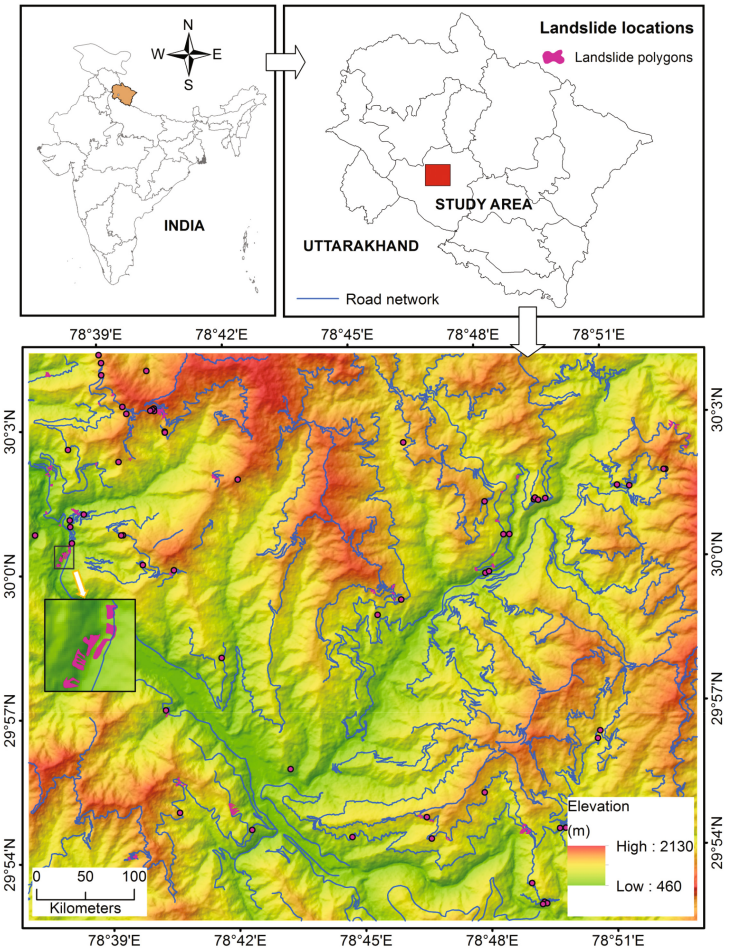

Fig. 1. Landslide inventory and location map of the study area

Topography of the area is hilly with high mountains and deep valleys. Elevation in the area ranges from 460 m to 2130 m. Slopes of the hills are generally moderate to steep having slope angles up to 70°.

Geologically, the study area is occupied by metamorphic, sedimentary rocks, and alluvium ranging from palaeozoic age to Quaternary. Amri group (quartzite, phyllite); Blaini and Krol groups (boulder bed and limestone); Bijni group (quartzite, phyllite); Tal group (sandstone, shale, quartzite, phyllite, and limestone) rocks are exposed in the area [15, 16]. Tectonically, the area is highly folded, faulted, and thrusted. Krol thrust has brought Blainis over Krol group of rocks. These rocks are highly folded and faulted due to tectonic activity. Part of the area is covered by silt and loamy soil.

3 Methods and Materials

3.1 Particle Swarm Optimization Based Adaptive-Network-Based Fuzzy Inference System

Particle Swarm Optimization based Adaptive-Network-Based Fuzzy Inference System (PSOANFIS), is proposed in this study for landslide spatial prediction modeling. This is a hybrid model of the ANFIS and PSO methods. In this model the ANFIS is used as a classifier for classifying the classes (landslide and non-landslide) for prediction, and the PSO is used to optimize the parameters of the ANFIS to get the best performance of the proposed hybrid model.

3.1.1 Adaptive-Network-Based Fuzzy Inference System

Adaptive-Network-Based Fuzzy Inference System (ANFIS was proposed by Jang [17]. It is a fuzzy inference systems (fuzzy models, fuzzy-rule-based systems, and fuzzy associative memories) carried out in the framework of adaptive networks (nodes connected by directional links). The ANFIS is known as a hybrid learning approach which can be trained on the basis of both stipulated input-output data pairs and human knowledge [17]. However, the ANFIS is more systematic and less reliant on expert knowledge by using the framework of adaptive systems [18]. The ANFIS is considered as a promising for the generation of information processing systems. It is having good performance in the task of classification and prediction [18]. This method has been applied popularly and efficiently in various fields such as medical [19, 20], water resource management [21, 22]. In landslide spatial prediction, so far, the ANFIS has been applied in very few cases [23–25].

3.1.2 Particle Swarm Optimization

Particle Swarm Optimization (PSO) proposed by Eberhart and Kennedy [26] is known as a powerful and realistic solution to get the global optimums in optimization problems. The main idea of the PSO is based on the swarming behavior of a school of fish and a flock of birds [26]. In the PSO, individuals called particles fly around in a multidimensional search space, and then a population-based search procedure is provided to change the position of particles with time [27]. Each particle flying in the space is adjusted by the experience of itself and neighbors to find the best position, and the direction of a particle is defined by its history experience and the set of neighboring particles [28]. The PSO, as a optimization tool, has been used to solve many real-world problems such as power systems [29, 30], medical [31, 32]. However, its application has been considered earlier very limited in landslide spatial prediction. In the present study, the PSO has been used to optimize the parameters of the ANFIS classifier to create the novel hybrid model PSOANFIS for landslide spatial prediction.

3.2 Validation Criteria

In the validation of models, various statistical indexes can be used as suggested by Bennett et al. [33]. In the present study, two popular statistical indexes namely Root Mean Square Error (RMSE) and Mean Absolute Error (MAE) have been selected to

validate the performance of the proposed hybrid model for landslide spatial prediction. The RMSE is known as one of the most widely error measures whereas the MAE is considered as a natural measure of average error [34]. Good performance of Model is indicated when RMSE and MAE values are close to zero, and model is perfect when these values are equal to zero. The RMSE and MAE indexes can be calculated through following equations:

$$\mathrm{RMSE} = \sqrt{\frac{1}{n}\sum_{i=1}^{n}\left(V_{predicted} - V_{actual}\right)^2} \tag{1}$$

$$\mathrm{MAE} = \sqrt{\frac{1}{n}\sum_{i=1}^{n}\left(V_{predicted} - V_{actual}\right)} \tag{2}$$

where n is the number of samples in a dataset, $V_{predicted}$ is the value predicted from model, and V_{actual} is the actual value in dataset [33].

In addition, validation of model can be done by using Receiver Operating Characteristic (ROC) curve [35]. It is a well-known quantitative method proposed by DeLeo [36] for validating models. In the graph of the ROC curve, the x-axis and y-axis show the sensitivity and 100-specificity values, respectively [37, 38]. Using the area under the ROC curve (AUC), the performance of models can be validated quantitatively [39]. More specifically, the AUC value equals "1" indicating the perfection of model, and the AUC value is closer to "1" indicating better performance of model.

3.3 Data Used

3.3.1 Landslide Inventory Map

Landslide inventory map, which shows the spatial distribution of current and past landslide locations, was constructed from 1295 rainfall induced shallow landslide locations which were identified from Google Earth images (2016) using the tools in Google Earth pro 7.0 software. Validation of these landslide locations was carried out by field investigation, and compared with landslide reports. Size of the landslides varies from 750 m^2 to 60989 m^2. Landslides observed in the area are mainly three types: translational landslides (750 locations); rotational landslides (120 locations); and debris flows (425 locations).

Landslide inventory has been used to generate training and testing datasets for training and validating models. More specifically, 906 landslide locations (70% of landslide inventory) were used for generating training dataset whereas 389 landslide locations (30% of landslide inventory) were utilized for creating testing dataset.

3.3.2 Landslide Influencing Parameters

In this study, landslide influencing parameters namely slope, elevation, curvature, plan curvature, profile curvature, aspect, lithology, land cover, soil type, rainfall, distance to roads, distance to lineaments, distance to rivers, road density, lineament density, and rive density (Table 1) have been selected for landslide susceptibility modeling based on the evaluation of geo-environmental characteristics of the study area over landslide

Table 1. Landside influencing parameters and their classes

No.	Landslide influencing parameters	Classes
1	Slope angle (degree)	(1) [0,10); (2) [10,20); (3) [20,30); (4) [30,40); (5) [40,50); (6) [50, 60); (7) [60,72]
2	Slope aspect	(1) flat; (2) north; (3) northeast; (4) east; (5) southeast; (6) south; (7) southwest; (8) west; (9) northwest
3	Elevation (m)	(1) [0,700); (2) [700,900); (3) [900,1100); (4) [1100,1300); (5) [1300,1500); (6) [1500,1700); (7) [1700,1900); (8) [1900,2130]
4	Curvature	(1) concave (<−0.05); (2) flat [−0.05,0.05]; (3) convex (>0.05)
5	Plan curvature	(1) [−10.134,−1.042); (2) [−1.042,−0.331); (3) [−0.331,0.223); (4) [0.223,0.934); (5) [0.934,10.026]
6	Profile curvature	(1) [−14.22,−1.33); (2) [−1.33,−0.44); (3) [−0.44,0.26); (4) [0.26,1.25); (5) [1.25,11.07]
7	Lithology	(1) Amri group (quartzite, phyllite); (2) Blaini and Krol groups (boulder bed and limestone); (3) Bijni group (quartzite, phyllite); (4) Tal group (sandstone, shale, quartzite, phyllite, and limestone)
8	Soil	(1) course loamy; (2) skeletal loamy; (3) fine loamy; (4) mixed loamy; (5) fine silt
9	Land cover	(1) dense forest; (2) open forest; (3) scrub land; (4) non forest
10	Rainfall (mm)	(1) [455,700); (2) [700,900); (3) [900,1100); (4) [1100,1300); (5) [1300,1500); (6) [1500,1700); (7) [1700,1900); (8) [1900,2100); (9) [2100,2300); (10) [2300,2552]
11	Distance to lineaments (m)	(1) [0,50); (2) [50,100); (3) [100,150); (4) [150,200); (5) [200,250); (6) [250,300); (7) [300,350); (8) [350,400); (9) [400,450); (10) [450,500); (11) ≥ 500
12	Distance to roads (m)	(1) [0,50); (2) [50,100); (3) [100,150); (4) [150,200); (5) [200,250); (6) ≥ 250
13	Distance to rivers (m)	(1) [0,50); (2) 50–100; (3) 100–150; (4) 150–200; (5) 200–250; (6) ≥ 250
14	Lineament density (km/km^2)	(1) very low [0,0.224); (2) low [0.224,0.579); (3) moderate [0.579,0.916); (4) high [0.9156,1.308); (5) very high [1.308,2.382]
15	Road density (km/km^2)	(1) very low [0,0.633); (2) low [0.633,1.542); (3) moderate [1.542,2.534); (4) high [2.534,3.773); (5) very high [3.773,7.023]
16	River density (km/km^2)	(1) very low [0,0.05); (2) low [0.05,0.154); (3) moderate [0.154,0.268); (4) high [0.268,0.423); (5) very high [0.423,1.268]

occurrences [16]. In detail, aster global Digital Elevation Model (DEM) (Available at https://earthexplorer.usgs.gov) has been used to generate geomorphological factors such as slope (Fig. 2a), elevation, curvature, plan curvature, profile curvature, aspect. Land cover (Fig. 2b), soil (Fig. 2c), lithology (Fig. 2d) maps were generated from state thematic maps (Available at http://www.ahec.org.in/wfw/maps.htm). Rainfall map (Fig. 2e) was generated using the meteorological data collected from National Centers for Environmental Prediction [40] for 30 years (1984–2014). LANDSAT-8 satellite images have been used to extract lineaments. Distance to lineaments and lineament density maps were generated by creating buffer and using density functions. Similarly, distance to roads (Fig. 2f) and road density maps were constructed from the road network created from Google Earth images. Distance to river and river density maps were also built by using buffer and density functions on the river network generated from DEM using hydrological functions of ArcGIS application.

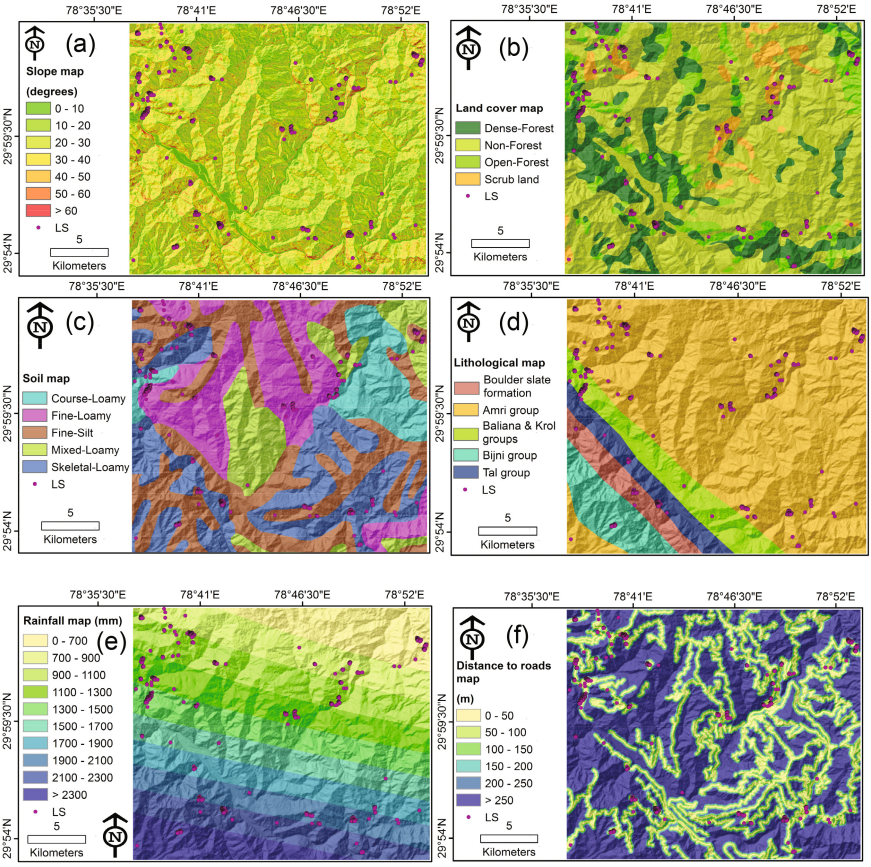

Fig. 2. Thematic maps of the study area: (a) slope map, (b) land cover map, (c) soil map, (d) lithological map, (e) rainfall map, and (f) distance to roads map

4 Results and Discussion

Landslide spatial model construction has been done using the proposed hybrid PSOANFIS method (Figs. 3, 4, 5, and 6). In this study, the PSOANFIS model has been trained using the Gaussian membership function, the population of 25 particles, and the stopping criterion of 1000 iterations for giving the best performance of the model. Results indicate that the predicted values (outputs) are mostly closer to the actual values (targets) for both training and testing dataset (Fig. 3). The MSE values of the hybrid model for training and testing datasets are 0.0693 and 0.0933, respectively whereas the RMSE values of the hybrid model for training and testing datasets are 0.263 and 0.306, respectively (Fig. 4). Analysis of frequency errors of samples shows that the error mean values are 0.0096 and 0.0087 for training and testing datasets, respectively, whereas the error standard deviation values (Error St.D.) are 0.2632 and 0.3056 for training and testing datasets, respectively (Fig. 5). In general, error analysis results of the hybrid model are relatively low which means that performance of the PSOANFIS model for landslide spatial prediction is good. In addition, the training iterations versus RMSE values of the proposed PSOANFIS model shows that the RMSE value is reducing from iteration 67 until iteration 999, and then it is stable afterward (Fig. 6). It suggests that performance of the PSOANFIS model has been improved significantly by using the PSO technique.

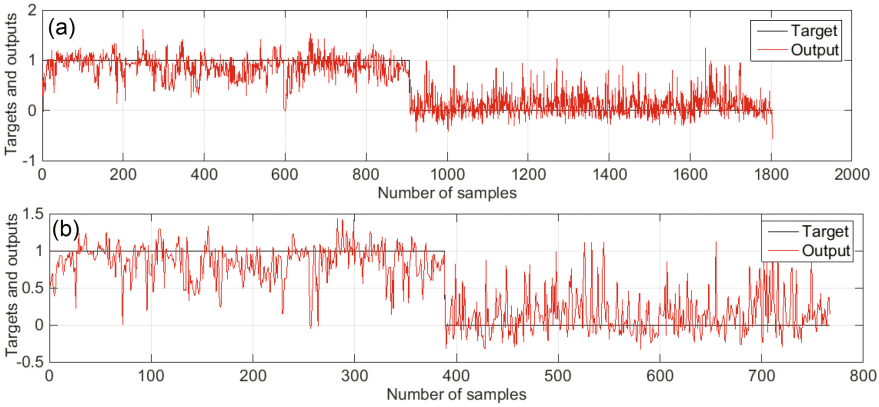

Fig. 3. Target and output values of samples: (a) training dataset, and (b) testing dataset

The performance of the PSOANFIS model, which is relatively new for landslide spatial prediction, has been compared with other benchmark landslide model namely Support Vector Machines (SVM) [6, 41]. Radial basic function (RBF) kernel is used to train the SVM in which kernel parameters such as the regularization (C) and the kernel width (γ) were set as 0.25 and 1, respectively based on a trial-and-error test to obtain best performance of the SVM.

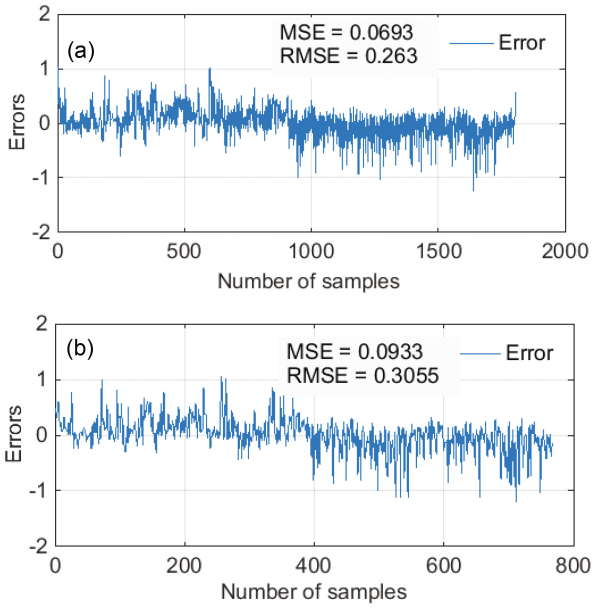

Fig. 4. MSE and RMSE values of samples: (a) training dataset, and (b) testing dataset

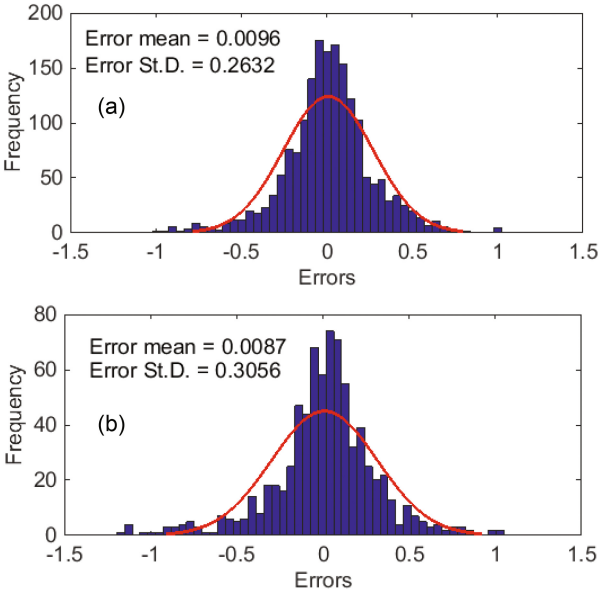

Fig. 5. Frequency errors of samples: (a) training dataset, and (b) testing dataset

For comparison of two applied methods, the ROC curves have been used for both training and testing datasets (Figs. 7 and 8). Results of the ROC curve analysis show that the proposed hybrid model PSOANFIS has higher values of the AUC compared with the SVM model which means that the PSOANFIS model outperforms the SVM model for landslide spatial prediction in this study. This may be due to fact that hybrid model takes advantage of both the state of art machine learning methods namely the ANFIS and the PSO. More specifically, the ANFIS technique has the learning capability of artificial neural networks and also expert knowledge of fuzzy interference systems [42] whereas the PSO is known as a robust technique in solving continuous nonlinear optimization problems, and can generate high-quality solutions with stable convergence characteristics [27].

Landslide susceptibility map has been generated for the study area using the proposed hybrid model PSOANFIS (Fig. 9). This map is considered as a helpful tool for the demarcation and visualization of high and very high susceptibility areas for better land use planning and management [43, 44]. Landslide susceptibility indexes of a total of 1402128 pixels covering study area have been generated during the learning process of the PSOANFIS model. Accordingly, five susceptibility classes namely very low, low, moderate, high, and very high have been classified to construct the landslide susceptibility map. In the classification of landslide susceptibility indexes, natural breaks classification method, which is based on big jumps in the continuous data for classification [45], has been used.

Landslide density analysis has been carried out to validate the reliability of the landslide susceptibility map produced by the hybrid PSOANFIS model. Landslide inventory has been used to combine it with the landslide susceptibility map to determine the number of landslide pixels on each susceptibility class, and then the landslide density values of each class has been calculated (Fig. 10). It can be clearly seen that the highest landslide density value (13.03) is on very high class, followed by high class (1.68), moderate class (0.1), and low class (0.02), respectively. No landslide pixel has been observed in very low class. Results of landslide density analysis show that the landslide susceptibility map produced by the hybrid model PSOANFIS in this study is much reliable, and it can be used for proper landslide hazard management.

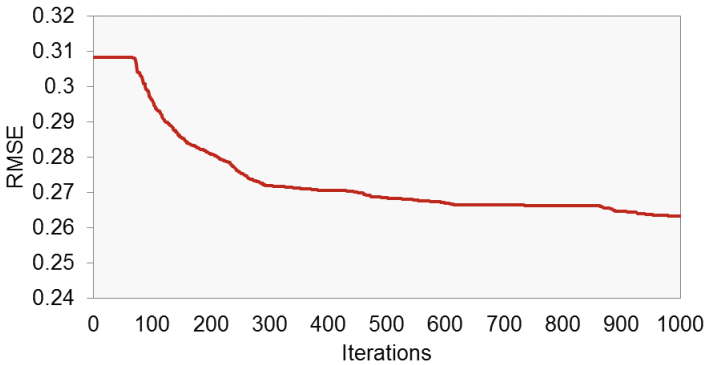

Fig. 6. Training iterations versus RMSE of the proposed PSOANFIS model

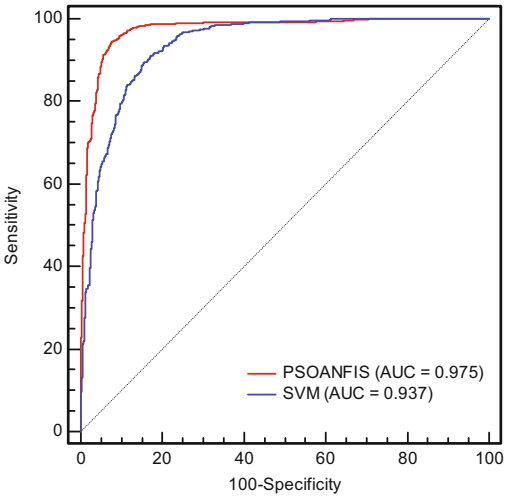

Fig. 7. Model performance using the ROC curve for training dataset

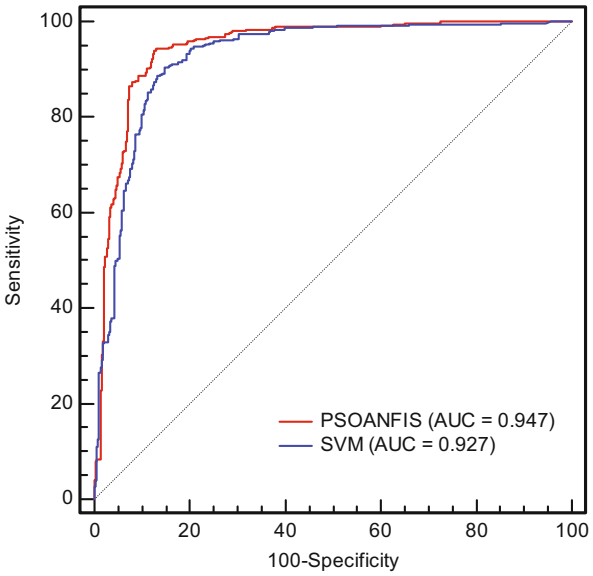

Fig. 8. Model performance using the ROC curve for testing dataset

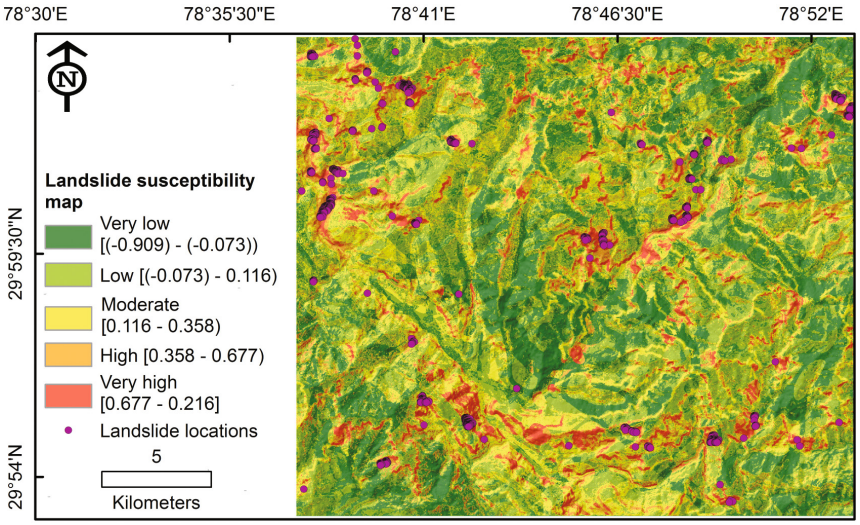

Fig. 9. Landslide susceptibility map using the PSOANFIS model

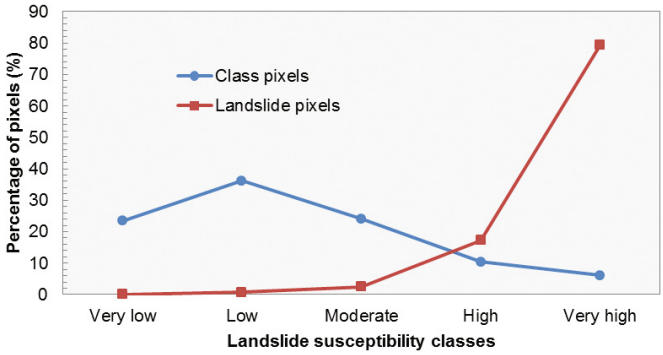

Fig. 10. Landslide frequency analysis on landslide susceptibility map

5 Conclusions

Landslide spatial modeling is a non-linear problem and a typical complex process which is not easy to assess and predict in the regional scale. In this study, spatial prediction of rainfall induced shallow landslides has been done at part of the Pauri Garhwal district of Uttarakhand State, India using a hybrid model namely PSOANFIS which is a hybrid intelligent approach of the ANFIS classifier and the PSO technique. Predictive capability of the proposed hybrid model was validated using the ROC curve, and the RMSE and MAE indexes, and compared with well-known landslide model SVM.

From the results of this study, it can be clearly seen that the proposed hybrid model PSOANFIS has a good predictive capability of landslide spatial prediction, its performance is even better than a well-known landslide model SVM. Thus, it is reasonably concluded that the PSOANFIS is a promising method for modeling of landslide spatial prediction. This model can be used as an better alternative tool for landslide susceptibility mapping and hazard management in landslide prone areas.

Acknowledgement. Authors are thankful to the Director, Bhaskarcharya Institute for Space Applications and Geo-Informatics, Gujarat, India for providing facilities to carry out this research work.

References

1. Naithani, A.: The Himalayan landslides. Employ. News **23**, 20–26 (1999)
2. Saha, A., Gupta, R., Arora, M.: GIS-based landslide hazard zonation in the Bhagirathi (Ganga) valley, Himalayas. Int. J. Remote Sens. **23**, 357–369 (2002)
3. Kanungo, D., Sarkar, S., Sharma, S.: Combining neural network with fuzzy, certainty factor and likelihood ratio concepts for spatial prediction of landslides. Nat. Hazards **59**, 1491–1512 (2011)
4. Pham, B.T., Tien Bui, D., Dholakia, M.B., Prakash, I., Pham, H.V.: A comparative study of least square support vector machines and multiclass alternating decision trees for spatial prediction of rainfall-induced landslides in a tropical cyclones area. Geotech. Geol. Eng. **34**, 1–18 (2016)
5. Pham, B.T., Bui, D.T., Prakash, I., Dholakia, M.: Evaluation of predictive ability of support vector machines and naive Bayes trees methods for spatial prediction of landslides in Uttarakhand state (India) using GIS. J. Geomat. **10**, 71–79 (2016)
6. Tien Bui, D., Pham, B.T., Nguyen, Q.P., Hoang, N.-D.: Spatial prediction of rainfall-induced shallow landslides using hybrid integration approach of least-squares support vector machines and differential evolution optimization: a case study in Central Vietnam. Int. J. Digit. Earth **9**, 1–21 (2016)
7. Tsangaratos, P., Ilia, I.: Landslide susceptibility mapping using a modified decision tree classifier in the Xanthi Perfection, Greece. Landslides **13**, 305–320 (2016)
8. Yesilnacar, E., Topal, T.: Landslide susceptibility mapping: a comparison of logistic regression and neural networks methods in a medium scale study, Hendek region (Turkey). Eng. Geol. **79**, 251–266 (2005)
9. Bai, S.-B., Wang, J., Lü, G.-N., Zhou, P.-G., Hou, S.-S., Xu, S.-N.: GIS-based logistic regression for landslide susceptibility mapping of the Zhongxian segment in the three Gorges area, China. Geomorphology **115**, 23–31 (2010)
10. Kavzoglu, T., Sahin, E.K., Colkesen, I.: Landslide susceptibility mapping using GIS-based multi-criteria decision analysis, support vector machines, and logistic regression. Landslides **11**, 425–439 (2014)
11. Pham, B.T., Pradhan, B., Tien Bui, D., Prakash, I., Dholakia, M.B.: A comparative study of different machine learning methods for landslide susceptibility assessment: a case study of Uttarakhand area (India). Environ. Model Softw. **84**, 240–250 (2016)
12. Melchiorre, C., Matteucci, M., Azzoni, A., Zanchi, A.: Artificial neural networks and cluster analysis in landslide susceptibility zonation. Geomorphology **94**, 379–400 (2008)

13. Pham, B.T., Tien Bui, D., Prakash, I., Dholakia, M.B.: Hybrid integration of multilayer perceptron neural networks and machine learning ensembles for landslide susceptibility assessment at Himalayan area (India) using GIS. CATENA **149**(Part 1), 52–63 (2017)
14. Gordan, B., Armaghani, D.J., Hajihassani, M., Monjezi, M.: Prediction of seismic slope stability through combination of particle swarm optimization and neural network. Eng. Comput. **32**, 85–97 (2016)
15. Bartarya, S., Virdi, N., Sah, M.: Landslide hazards: some case studies from the Satluj Valley, Himachal Pradesh. Himalayan Geol. **17**, 193–207 (1996)
16. Pham, B.T., Khosravi, K., Prakash, I.: Application and comparison of decision tree-based machine learning methods in landside susceptibility assessment at Pauri Garhwal area, Uttarakhand, India. Environ. Process. **4**, 1–20 (2017)
17. Jang, J.-S.: ANFIS: adaptive-network-based fuzzy inference system. IEEE Trans. Syst. Man Cybern. **23**, 665–685 (1993)
18. Güler, I., Übeyli, E.D.: Adaptive neuro-fuzzy inference system for classification of EEG signals using wavelet coefficients. J. Neurosci. Methods **148**, 113–121 (2005)
19. Dogantekin, E., Dogantekin, A., Avci, D.: Automatic hepatitis diagnosis system based on linear discriminant analysis and adaptive network based on fuzzy inference system. Expert Syst. Appl. **36**, 11282–11286 (2009)
20. Dogantekin, E., Dogantekin, A., Avci, D., Avci, L.: An intelligent diagnosis system for diabetes on linear discriminant analysis and adaptive network based fuzzy inference system: LDA-ANFIS. Digit. Signal Proc. **20**, 1248–1255 (2010)
21. Chang, F.-J., Chang, Y.-T.: Adaptive neuro-fuzzy inference system for prediction of water level in reservoir. Adv. Water Resour. **29**, 1–10 (2006)
22. Talei, A., Chua, L.H.C., Wong, T.S.: Evaluation of rainfall and discharge inputs used by Adaptive Network-based Fuzzy Inference Systems (ANFIS) in rainfall–runoff modeling. J. Hydrol. **391**, 248–262 (2010)
23. Tien Bui, D., Pradhan, B., Lofman, O., Revhaug, I., Dick, O.B.: Landslide susceptibility mapping at Hoa Binh province (Vietnam) using an adaptive neuro-fuzzy inference system and GIS. Comput. Geosci. **45**, 199–211 (2012)
24. Sezer, E.A., Pradhan, B., Gokceoglu, C.: Manifestation of an adaptive neuro-fuzzy model on landslide susceptibility mapping: Klang valley, Malaysia. Expert Syst. Appl. **38**, 8208–8219 (2011)
25. Dehnavi, A., Aghdam, I.N., Pradhan, B., Varzandeh, M.H.M.: A new hybrid model using step-wise weight assessment ratio analysis (SWARA) technique and adaptive neuro-fuzzy inference system (ANFIS) for regional landslide hazard assessment in Iran. CATENA **135**, 122–148 (2015)
26. Eberhart, R., Kennedy, J.: A new optimizer using particle swarm theory. In: Proceedings of the Sixth International Symposium on Micro Machine and Human Science, MHS 1995, pp. 39–43. IEEE (1995)
27. Gaing, Z.-L.: Particle swarm optimization to solving the economic dispatch considering the generator constraints. IEEE Trans. Power Syst. **18**, 1187–1195 (2003)
28. Park, J.-B., Lee, K.-S., Shin, J.-R., Lee, K.Y.: A particle swarm optimization for economic dispatch with nonsmooth cost functions. IEEE Trans. Power Syst. **20**, 34–42 (2005)
29. Del Valle, Y., Venayagamoorthy, G.K., Mohagheghi, S., Hernandez, J.-C., Harley, R.G.: Particle swarm optimization: basic concepts, variants and applications in power systems. IEEE Trans. Evol. Comput. **12**, 171–195 (2008)
30. Abido, M.: Optimal design of power-system stabilizers using particle swarm optimization. IEEE Trans. Energy Convers. **17**, 406–413 (2002)

31. Eberhart, R.C., Hu, X.: Human tremor analysis using particle swarm optimization. In: Proceedings of the 1999 Congress on Evolutionary Computation, CEC 1999, pp. 1927–1930. IEEE (1999)
32. Chakraborty, S., Samanta, S., Biswas, D., Dey, N., Chaudhuri, S.S.: Particle swarm optimization based parameter optimization technique in medical information hiding. In: 2013 IEEE International Conference on Computational Intelligence and Computing Research (ICCIC), pp. 1–6. IEEE (2013)
33. Bennett, N.D., Croke, B.F., Guariso, G., Guillaume, J.H., Hamilton, S.H., Jakeman, A.J., Marsili-Libelli, S., Newham, L.T., Norton, J.P., Perrin, C.: Characterising performance of environmental models. Environ. Model Softw. **40**, 1–20 (2013)
34. Willmott, C.J., Matsuura, K.: Advantages of the mean absolute error (MAE) over the root mean square error (RMSE) in assessing average model performance. Climate Res. **30**, 79–82 (2005)
35. Pham, B.T., Tien Bui, D., Pham, H.V., Le, H.Q., Prakash, I., Dholakia, M.B.: Landslide hazard assessment using random subspace fuzzy rules based classifier ensemble and probability analysis of rainfall data: a case study at Mu Cang Chai District, Yen Bai Province (Viet Nam). J. Indian Soc. Remote Sens., 1–11 (2016)
36. DeLeo, J.M.: Receiver operating characteristic laboratory (ROCLAB): software for developing decision strategies that account for uncertainty. In: 1993 Proceedings of the Second International Symposium on Uncertainty Modeling and Analysis, pp. 318–325. IEEE (1993)
37. Shirzadi, A., Shahabi, H., Chapi, K., Bui, D.T., Pham, B.T., Shahedi, K., Ahmad, B.B.: A comparative study between popular statistical and machine learning methods for simulating volume of landslides. CATENA **157**, 213–226 (2017)
38. Tien Bui, D., Ho, T.-C., Pradhan, B., Pham, B.-T., Nhu, V.-H., Revhaug, I.: GIS-based modeling of rainfall-induced landslides using data mining-based functional trees classifier with AdaBoost, Bagging, and MultiBoost ensemble frameworks. Environ. Earth Sci. **75**, 1–22 (2016)
39. Pham, B.T., Tien Bui, D., Prakash, I., Dholakia, M.B.: Rotation forest fuzzy rule-based classifier ensemble for spatial prediction of landslides using GIS. Nat. Hazards **83**, 1–31 (2016)
40. NCEP: Global weather data for SWAT (2014). http://globalweather.tamu.edu/home
41. Pham, B.T., Bui, D.T., Dholakia, M.B., Prakash, I., Pham, H.V., Mehmood, K., Le, H.Q.: A novel ensemble classifier of rotation forest and Naïve Bayer for landslide susceptibility assessment at the Luc Yen district, Yen Bai Province (Viet Nam) using GIS. Geomat. Nat. Hazards Risk, 1–23 (2016)
42. Akkoç, S.: An empirical comparison of conventional techniques, neural networks and the three stage hybrid adaptive neuro fuzzy inference system (ANFIS) model for credit scoring analysis: the case of Turkish credit card data. Eur. J. Oper. Res. **222**, 168–178 (2012)
43. Pham, B.T., Bui, D.T., Prakash, I.: Landslide susceptibility assessment using bagging ensemble based alternating decision trees, logistic regression and J48 decision trees methods: a comparative study. Geotech. Geol. Eng., 1–15 (2017)
44. Pham, B.T., Tien Bui, D., Prakash, I., Nguyen, L.H., Dholakia, M.B.: A comparative study of sequential minimal optimization-based support vector machines, vote feature intervals, and logistic regression in landslide susceptibility assessment using GIS. Environ. Earth Sci. **76**, 371 (2017)
45. Pourghasemi, H.R., Pradhan, B., Gokceoglu, C.: Application of fuzzy logic and analytical hierarchy process (AHP) to landslide susceptibility mapping at Haraz watershed, Iran. Nat. Hazards **63**, 965–996 (2012)

GIS-Based Landslide Spatial Modeling Using Batch-Training Back-propagation Artificial Neural Network: A Study of Model Parameters

Nhat-Duc Hoang[1(✉)] and Dieu Tien Bui[2]

[1] Faculty of Civil Engineering, Institute of Research and Development, Duy Tan University, P809 - K7/25 Quang Trung, Danang, Vietnam
hoangnhatduc@dtu.edu.vn

[2] Geographic Information System Group, Department of Business and IT, School of Business, University College of Southeast Norway, Gullbringvegen 36, 3800 Bø, Norway
dieu.t.bui@usn.no

Abstract. The ability of delivering accurate appraisal on landslide occurrences is of practical need for establishing land-use plans in regional scales. Back-propagation Artificial Neural Network (BpANN) has been demonstrated to be an effective tool for landslide spatial prediction. In this study, Batch-Training Back-Propagation Artificial Neural Network which is an integration of BpANN, batch-training strategy, and early stopping criteria is proposed for landslide spatial modeling. The employed early stopping criteria include the Generalization Loss (GL) criterion and the Quotient of Generalization Loss and Progress (QGP) criterion. In addition, BpANN training performance has been known to be highly dependent on various tuning parameters. This paper focuses on the parameter setting of BpANN regarding the investigated early stopping criteria. A Geographic Information System (GIS) database, collected from the mountainous regions in Northern Vietnam, is utilized as a case study. Experimental results show that GL criterion may result in an underfitted BpANN; meanwhile, QGP criterion can help to avoid overfitting. Based on experimental outcomes, several recommendations are put forward for future studies on landslide spatial modeling with batch-training BpANN.

Keywords: Landslide spatial prediction · Backpropagation Artificial Neural Network · Geographic Information System · Batch-training · Model parameter · Early stopping

1 Introduction

Landslide is a recurrent natural hazard in the mountainous areas around the world and it has brought about various types of damage that affect people lives, the national infrastructure, and the environment [1–5]. Along mountain roads in Northern Vietnam, this hazard has frequently occurred on cut slopes, especially along national highways [6]. Therefore, it is immensely useful for government agencies to be equipped with better tools for analyzing its occurrence [7, 8]. Based on recent literature, statistical based and

© Springer International Publishing AG 2018
D. Tien Bui et al. (eds.), *Advances and Applications in Geospatial Technology and Earth Resources*, https://doi.org/10.1007/978-3-319-68240-2_15

machine learning based approaches for landslide spatial modeling have gained an increasing attention within the research community [9].

To construct spatial prediction models, an appropriate set of data samples in the landslide-prone areas must be collected. By using Geographic Information Systems (GIS), the capability for collecting data of large regions has been significantly improved [10, 11]. The availability of geostatistic operators within the GIS allows the extraction of morphometrical and hydrological parameters from Digital Elevation Models (DEM) [12]. Information regarding terrain features, lithology, and rainfall can be conveniently incorporated into a single database for landslide analysis.

Based on the constructed GIS database, landslide occurrences are then analyzed by means of statistical analysis and machine learning techniques [13–15]. Recently, machine learning algorithms have extensively employed by the research community for tackling the problem of interest [16]. Among those machine learning methods, Back-propagation Artificial Neural Network (BpANN) models have been extensively utilized to construct landslide spatial prediction models [17–19]. Nevertheless, previous studies on BpANN with the application on landslide prediction rarely addressed crucial issues such as overfitting prevention, early stopping criteria, and the tuning of parameters regarding early stopping strategies. Thus, this study attempts enrich the body of knowledge by investigating such issues for spatial predicting rainfall-induced landslide occurrences using BpANN models with batch-training strategy. The batch-training strategy is selected to be investigated due to its advantage in network training speed.

In addition, a GIS-based dataset, which features ten landslide conditioning factors and 7580 data samples, has been collected along the national road No. 32 in the northern region of Vietnam is employed as a case study. Furthermore, an experiment to reveal the relative importance of each landslide conditioning factor has also been carried out. The rest of this study is organized as follows. The second section of this paper reviews the research methodology. Experimental result and comparison are provided in the next section. Conclusions and recommendations of this study are stated in the final part.

2 Material and Method

2.1 The Study Area and GIS Database

The study area (see Fig. 1) covers an area of approximately 3,164 km^2; the topographical elevation varies from 120 to 3,140 m with average value of 1,078 m and standard deviation of 556 m. The location of the study area is between the longitude 103°33′23″E and 104°52′58″E, and between the latitude 22°20′18″N and 21°19′53″N. Within the landslide inventory, 262 landslide incidences have been recorded in the study region.

In this study, a landslide inventory map, which records information regarding historical landslide incidences along the National Road 32 (Vietnam), were collected during the field works and interpreted from aerial photographs in a national project carried [20]. The National Road 32 is around 250 km long and locates in the northern region of Vietnam.

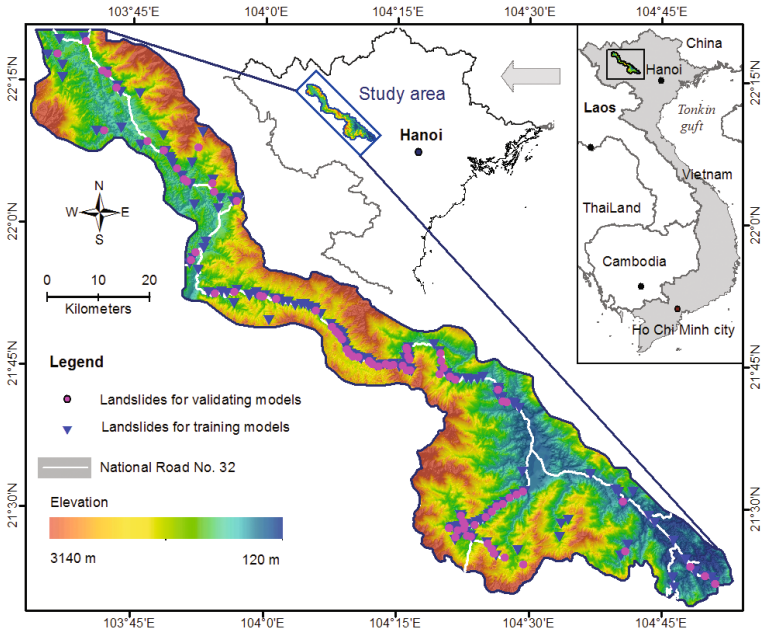

Fig. 1. Historical landslide records and location of the study area (Source: [20])

Based on previous investigations in the study area [21] and findings in landslide literature [22], this research takes into account ten landslide conditioning factors including slope (IF_1), aspect (IF_2), relief amplitude (IF_3), topographic wetness index (TWI) (IF_4) toposhape (IF_5), lithology (IF_6), distance to faults (IF_7), distance to roads (IF_8), distance to rivers (IF_9), and rainfall (IF_{10}). The information of the aforementioned landslide conditioning factors are summarized in Table 1.

To construct a landslide prediction model, information regarding 3790 landslide pixels has been collected. Moreover, since the spatial prediction of landslides is formulated as a binary classification problem with two distinctive class labels ("landslide" and "non-landslide"), 3790 non-landslide pixels have been randomly sampled from the non-landslide areas. Accordingly, the GIS-dataset includes a total of 7580 data samples. It is noted that for the purpose of modeling, the label $C_1 = 1$ is assigned for landslide pixels and the label $C_2 = 0$ is for non-landslide pixels. Within the dataset, 70% of the samples are employed to construct the prediction model, the rest of the dataset is reserved for the phase of model verification. For more details of the data set under investigation, readers are guided to the previous work of Tien Bui, Ho and Revhaug [20].

Table 1. Landslide conditioning factors and their classes

Factors		Factor classes
Slope (°)	IF_1	(**1**) 0–8; (**2**) 8–15; (**3**) 15–25; (**4**) 25–35; (**5**) 35–45; (**6**) >45
Aspect	IF_2	(**1**) Flat; (**2**) North; (**3**) Northeast; (**4**) East; (**5**) Southeast; (**6**) South; (**7**) Southwest; (**8**) West; (**9**) Northwest
Relief amplitude	IF_3	(**1**) 0–50; (**2**) 50–200; (**3**) 200–350; (**4**) 350–500; (**5**) >500
TWI	IF_4	(**1**) <5; (**2**) 5–10; (**3**) 10–15; (**4**) 15–20; (**5**) >20
Toposhape	IF_5	(**1**) Flat; (**2**) Ridge; (**3**) Saddle; (**4**) Ravine; (**5**) Convex hillside; (**6**) Saddle hillside; (**7**) Slope hillside; (**8**) Concave hillside; (**9**) Inflection hillside; (**10**) Unknown hillside
Lithology	IF_6	(**1**) Aluvium; (**2**) Conglomerate; (**3**) Dyke; (**4**) Intermediate; (**5**) K-Pluton; (**6**) K-Volcanic; (**7**) Limestone; (**8**) P-Volcanic; (**9**) Sandstone; (**10**) Schist; (**11**) Shale; (**12**) Tuff
Distance to faults (m)	IF_7	(**1**) 0–200; (**2**) 200–400; (**3**) 400–600; (**4**) >600
Distance to roads (m)	IF_8	(**1**) 0–40; (**2**) 40–80; (**3**) 80–120; (**4**) >120
Distance to rivers (m)	IF_9	(**1**) 0–40; (**2**) 40–80; (**3**) 80–120; (**4**) >120
Rainfall (mm)	IF_{10}	(**1**) <1500; (**2**) 1500–1700; (**3**) 1700–1900; (**4**) 1900–2200; (**5**) >2200

2.2 Batch-Training Back-propagation Artificial Neural Network (BpANN)

2.2.1 BpANN Model Structure

Batch-Training Back-Propagation Artificial Neural Network (BpANN) is a back-propagation artificial neural network trained with batch mode. This algorithm attempts to mimic the knowledge acquisition and reasoning processes occurring the biological brain [23]. The advantages of the BpANN are its flexibility, learning efficiency, and universal approximation capability [24, 25]. This section describes a BpANN model used for 2-class recognition problems.

Given the learning task is to establish a mapping function $f : X \in R^D \rightarrow Y \in R^2$ where D represents the number of input attributes, a BpANN model, which includes the input, hidden, and output layers, is demonstrated in Fig. 2. In Fig. 2, W_1 and W_2 denotes weight matrices of the hidden layer and the output layer, respectively; N denotes the number of neurons in the hidden layer; $b_1 = [b_{11}, b_{12,}\ldots, b_{1N}]$ is a bias vector of the hidden layer; b_2 denotes a bias vector of the output layer; f_A represents an activation function (e.g. log-sigmoid function or hyperbolic tangent). It is worth

noticing that to convert the real values of output layer into probability of class, a softmax function is often employed [25]. The BpANN structure is expressed as follows:

$$f(X) = b_2 + W_2 \times (f_A(b_1 + W_1 \times X)) \tag{1}$$

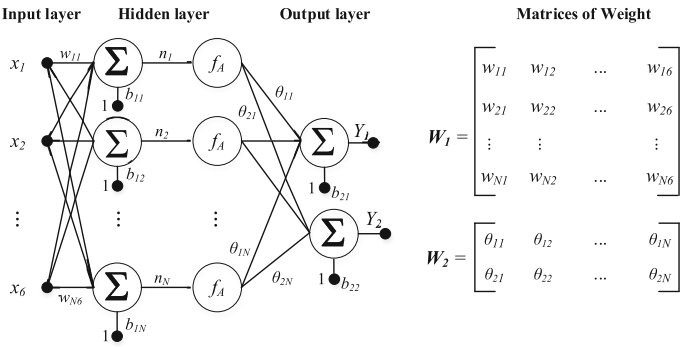

Fig. 2. Structure of a BpANN used for pattern classification

The weight matrices and the bias vectors of a BpANN can be trained by error backpropagation. The general step of the BpANN training with batch mode is briefly described in Fig. 3; for more details of the training algorithm, readers are recommended to study the previous work of Freeman and Skapura [26]. The typical formula used for updating a network's parameters is illustrated as follows:

$$W_{new} = W_{old} - Lr \times \frac{dE}{dW_{old}} + Mt \times W_{old} \tag{2}$$

where W_{old} and W_{new} denote a current and an updated network parameter. E is the objective function (model error). Lr and Mt represent the learning rate and the momentum term, respectively.

Randomly initialize W_1 and W_2
For Epoch = 1 : MaxEpoch
    For data point in the training set
        Compute updates of weights and bias
        Accumulate the updates
    End For
    Adjust W_1 and W_2 using the accumulated updates
End For

Fig. 3. BpANN with batch training mode

Moreover, the Mean Square Error (MSE) is employed as the objective function (E) for training an BpANN structure:

$$E = \min_{W_1, W_2, b_1, b_2} \frac{1}{M} \left(\sum_{i=1}^{M} e_{i,1}^2 + \sum_{i=1}^{M} e_{i,2}^2 \right) \tag{3}$$

where M represents the number of data samples; $e_{i,1}$ and $e_{i,2}$ denote deviations of the first and second outputs, respectively.

2.2.2 Overfitting Prevention with the Generalization Loss and the Quotient of Generalization Loss and Progress Criteria

It is noted that the purpose of network training is to obtain a model structure with good generalization. Nevertheless, all machine learning models including BpANN are susceptible to overfitting. As the training phase progresses, the network performance seems to get better; this is reflected in a decreasing trend of error performance on the training data set. In fact, the data pattern in training set can be perfectly learnt by the machine. Nevertheless, the error of the model when used for predicting unseen data samples can be immensely high. This fact indicates that overfitting has occurred. The BpANN simply memorizes the training instances instead of discovering the underlying nature hidden in the data set.

To detect and prevent overfitting, a validation measure is usually employed in the training progress of an BpANN. The general idea is to halt the model training before convergence to fence off the overfitting occurrence. This method of early stopping has been proved to deliver better training outcomes than other methods such as regularization [27, 28]. In this study, we employ two stategies of early stopping [28]: the Generalization Loss (GL) criterion and the Quotient of Generalization Loss and Progress (QGP) criterion. These two strategies are described in the following section of the paper.

The GL is defined as follows:

$$GL(ep) = 100 * \left(\frac{E_{va}(ep)}{E_{\min}(ep)} - 1 \right) \tag{4}$$

where ep denotes the current epoch. E_{va} and E_{min} represent the current validating error and the minimum-so-far, respectively.

Intuitively, a high value of GL is a signal for stopping the training process. It is because it clearly exhibits overfitting. Therefore, it is beneficial to halt the training phase at the epoch ep when the GL is greater than a pre-specified value. This criterion can be stated as a following rule:

"Stop the network training phase at ep when GL(ep) > α."

In addition, it may be beneficial to continue the training process as long as the training error is decreasing very quickly. The idea behind this strategy is that when the training error falls rapidly, the validating error can have higher change to be meliorated and probably reach a better minimum. Moreover, it is often observed that overfitting

does not arise until the training error is reduced at a slow rate [28]. This leads to the QGP as the second early stopping criterion. This quotient is defined as follows:

$$QGP = \frac{GL(ep)}{P_k} \tag{5}$$

where GL(ep) is explained in Eq. 4. P_k denotes the training performance during a training strip of k epochs. LeCun, Bottou, Orr and Müller [28] assume $k = 5$ and the validation error is appraised at the end of each strip.

P_k generally expresses the speed of training error diminishment in k successive epochs and it is computed in the following manner:

$$P_k = 1000\left(\frac{\sum_{ep-k+1}^{ep} E_{tr}(ep-k+1)}{k \min_{ep-k+1}^{ep} E_{tr}(ep-k+1)} - 1\right) \tag{6}$$

Based on the definition of QGP, GL, and P_k, we define the second rule of early stopping as follows: "Stop the network training phase when QGP(ep) > β."

2.3 Performance Measurement

Since the landslide prediction problem in this study is formulated as a binary classification task, the Classification Accuracy Rate (CAR), which measures the percentage of correctly classified cases, is commonly employed. Besides the CAR, the true positive rate (the fraction of 'landslide' instances correctly classified 'landslide' instances), the false positive rate (the fraction of 'non-landslide' instances incorrectly classified as 'landslide' instances), the true negative rate (the fraction of 'non-landslide' instances correctly classified 'non-landslide' instances), the false negative rate (the fraction of 'landslide' instances wrongly classified as 'non-landslide' instances) can be calculated to evaluate the landslide prediction results [29]. Furthermore, these four metrics can be summarized by a confusion matrix.

A good way to combine all of these four metrics and to exhibit an integrated performance measurement is to use the Receiver Operating Characteristic (ROC) curve; the Area Under the ROC Curve (AUC) provides a single index to for quantifying a model's [30, 31]. It is noticed that a desirable classifier should accompany with a high value of the AUC. In general, the AUC = 1 exhibits a classifier with a perfect classification capability; the AUC $\geq$ 0.9 indicates a classifier with an outstanding performance; the AUC varying between 0.8 and 0.9 exhibits an excellent classification result; if 0.7 $\leq$ AUC $\leq$ 0.8, the classification is acceptable; a poor classification with random predictions has an AUC of 0.5.

3 Experimental Result and Comparison

3.1 Experimental Setting

For the purpose of model construction and verification, the originally described data set is randomly separated into two exclusive sets: the model construction set (80%) and the model testing set (20%). In order to detect overfitting, the model construction set is further divided into two exclusive subsets: the training set and the validating set; these two subsets occupy 80% and 20% of the model construction set, respectively.

In this section, the BpANN with batch training method is employed to establish a classification model used for spatial landslide prediction. Generally, prior to the model training and predicting phases, several common parameters of a neural network, including the number of hidden layers, the number of neurons, type of activation function, the learning rate (*Lr*), the momentum term (*Mt*) parameter, must be configured. Furthermore, since this study investigates the Generalization Loss (GL) criterion and the Quotient of Generalization Loss and Progress (QGP) criterion used for overfitting prevention, the free parameters of these two criterion should be analyzed.

In the literature, there are several useful guidance for configuring a network's parameters. Generally, a network with one hidden layer sufficiently possess the capability of universal approximation. Additionally, using too few neurons in the hidden layer leads to underfitting and employing too many neurons results in overfitting and lengthening the training process.

Heaton [32] suggested that the number of neurons (*Nr*) should be 2/3 the size of the input layer, plus the size of the output layer. The learning rate controls the convergence rate of the backpropagation-based weight tuning process; the usual candidates for setting such parameters range from 0.0001 to 1. On the other hand, the momentum parameter is often selected within the range of 0.1 to 0.9. In practice, the learning rate and momentum term can be identified via several trial-and-error runs. In this study, to ease the investigation of the parameters of the GL and QGP criteria, based on several preliminary model runs, *Nr*, *Lr*, and *Mt* are fixed to be 9, 0.0001, and 0.1, respectively. Furthermore, the parabolic tangent is employed as the nonlinear activation function. The maximum number of training epochs is set to be 1000. Relied on such setting, the influences of the free parameters of the GL and QGP criteria (α, β, and k) on the BpANN based landslide prediction model are investigated.

3.2 Experimental Results

In this section, the performance of BpANN with the employments of the GL and QGP criteria for overfitting prevention is investigated. As mentioned earlier, these two methods require the specification of three parameters: α, β, and k. The parameter k used by both methods and it is the number of epochs used to inspect the trend the training performance. Overfitting is detected when the GL and QGP exceed certain threshold values; they are α for the case of GL criterion and β for the case of QGP criterion.

At first, based on the suggestion of LeCun, Bottou, Orr and Müller [28], k is fixed to be 5. The model performance is studied with different values of threshold parameters α and β. Figures 4 and 5 graphically summarize the experimental outcomes. In the case

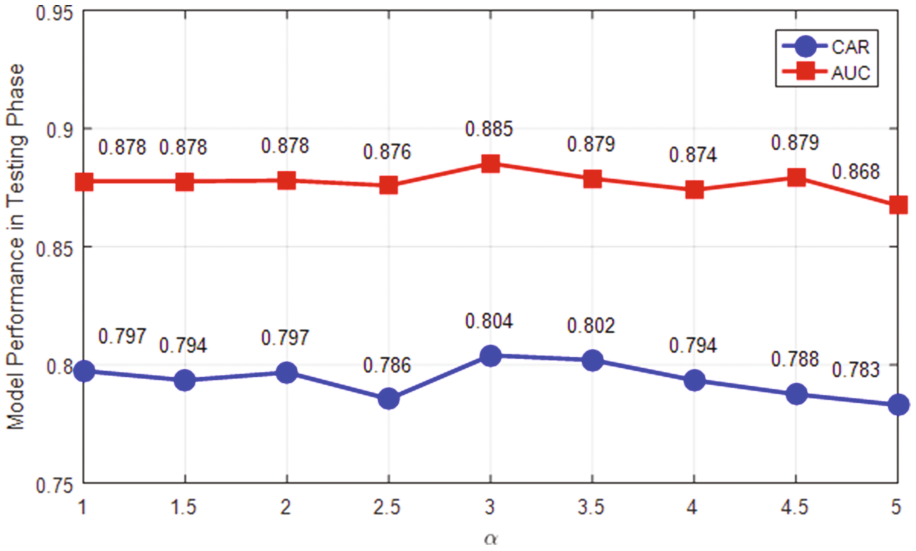

Fig. 4. Prediction result of BpANN with GL criterion (k = 5)

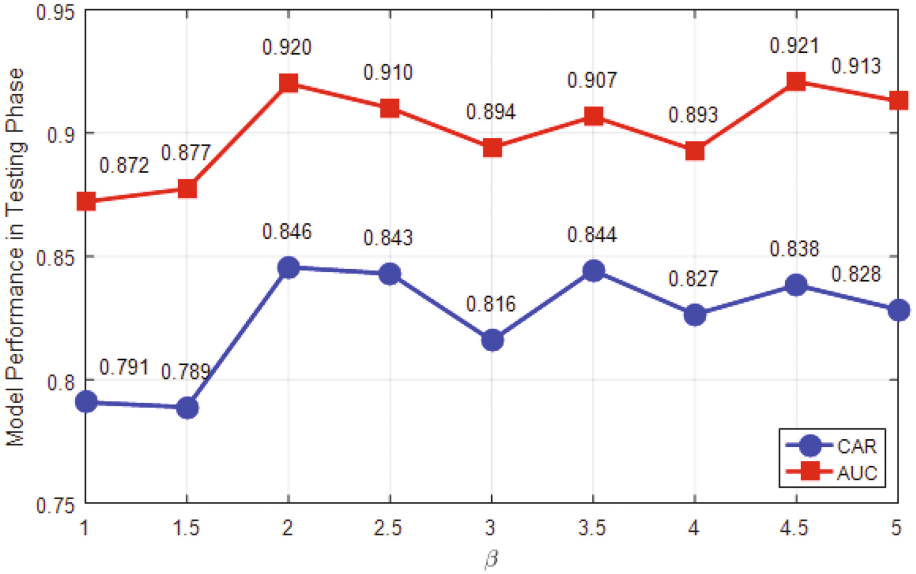

Fig. 5. Prediction result of BpANN with QGP criterion (k = 5)

of GL criterion, the BpANN model achieves the best testing results of AUC = 0.89 and CAR = 80% with $\alpha = 3$. Meanwhile, the BpANN model equipped with the QGP criterion demonstrates a clearly better performance of AUC = 0.92 and CAR = 85% with $\alpha = 2$. Furthermore, an experiment of BpANN without the use of the two early stopping criteria has also been performance. The result comparison of the BpANN model without early stopping criteria, the BpANN model with GL criterion (BpANN-GL), and the BpANN model with QGP criterion (BpANN-QGP) are summarized in Table 2.

Table 2. Result comparison

	BpANN-GL	BpANN-QGP	BpANN
Training phase			
AUC	0.90	0.94	0.93
CAR (%)	82.40	86.42	87.10
Testing phase			
AUC	0.89	0.92	0.90
CAR (%)	80.41	84.56	82.92

Observably, BpANN (trained in 1000 epochs) is better than BpANN-GL (only trained in 45 epochs). However, the performance of BpANN without early stopping methods (AUC = 0.90 and CAR = 82.92%) is worse than that of BpANN-QGP

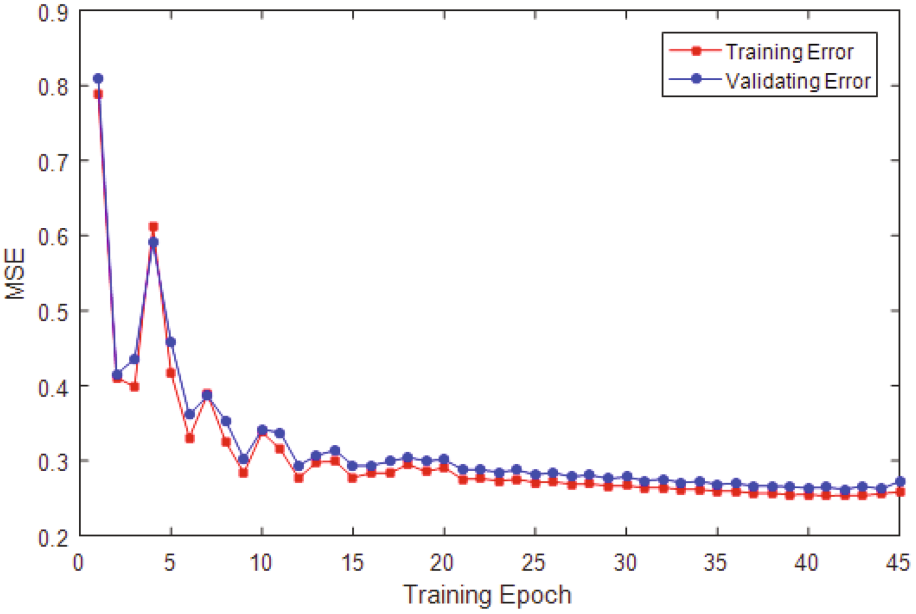

Fig. 6. Convergence record of model using GL criterion ($\alpha = 3$, $k = 5$)

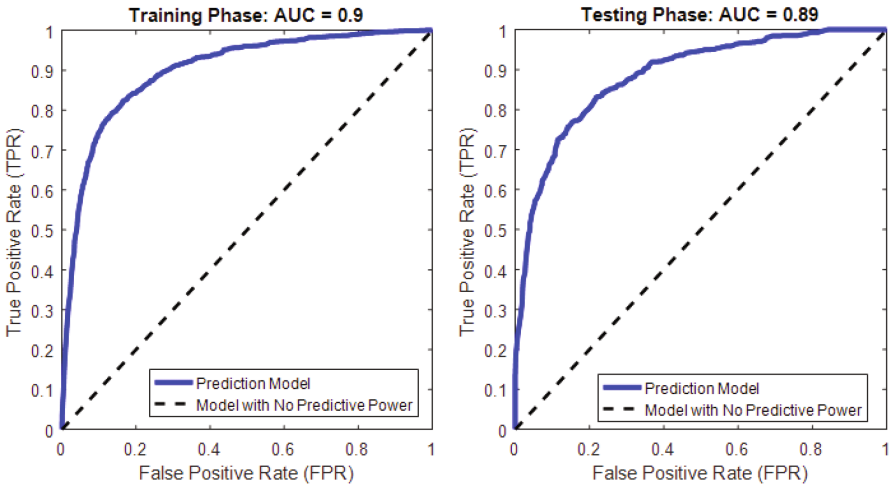

Fig. 7. ROC plots of model using GL criterion ($\alpha = 3$, $k = 5$)

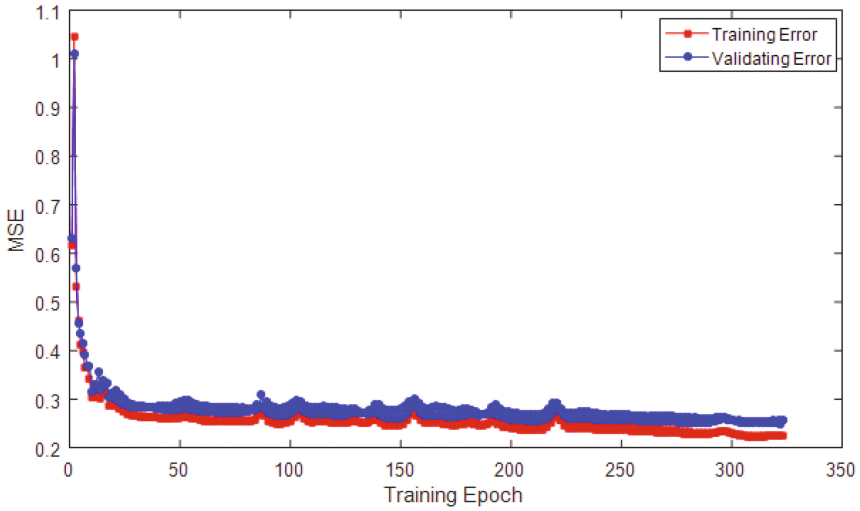

Fig. 8. Convergence record of model using QGP criterion ($\beta = 2$, $k = 5$)

(AUC = 0.92 and CAR = 85%). Therefore, it can be confirmed that the employment of the QGP early stopping strategy can help to improve the prediction result of BpANN used for landslide spatial prediction. In addition, the outcome of the BpANN-QGP (CAR = 85%) is shown to be better than those of Logistic Regression (CAR = 82%) and competitive with that of Relevant Vector Machines (CAR = 84%) [6].

In addition, the training results and performances of BpANN with the two early stopping methods are presented in Figs. 6, 7, 8, and 9. From the convergence rates of BpANN coupled with two criteria (Figs. 6 and 8), it can be seen that GL criterion cause

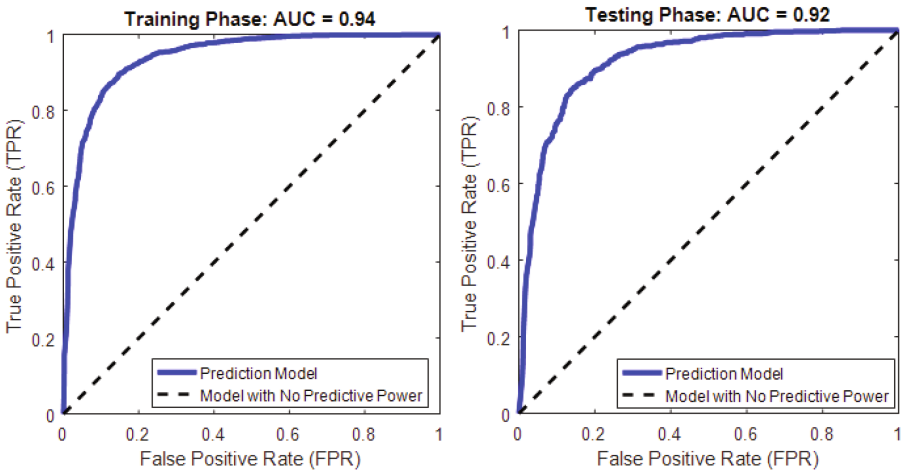

Fig. 9. ROC plots of model using QGP criterion ($\beta = 2$, $k = 5$)

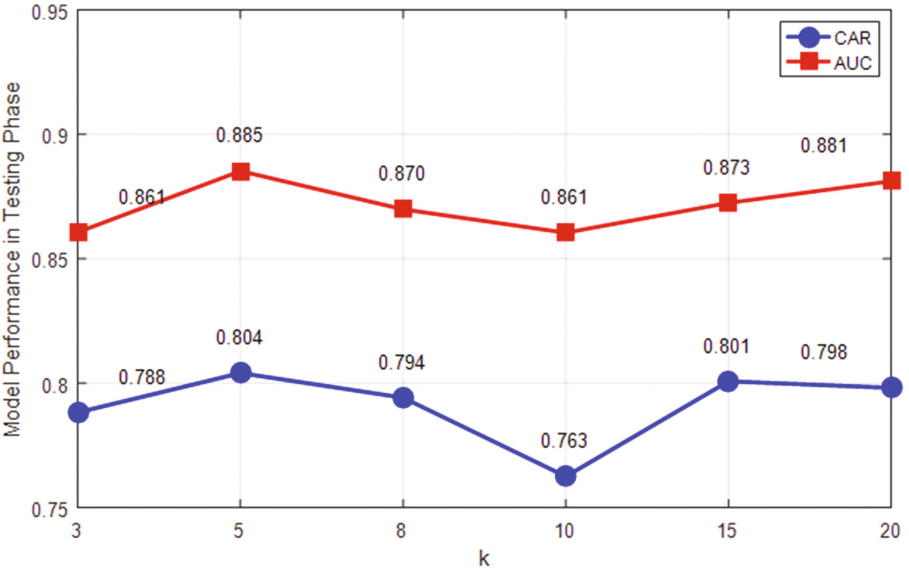

Fig. 10. Model performance using GL criterion ($\alpha = 3$) with different strip length (k)

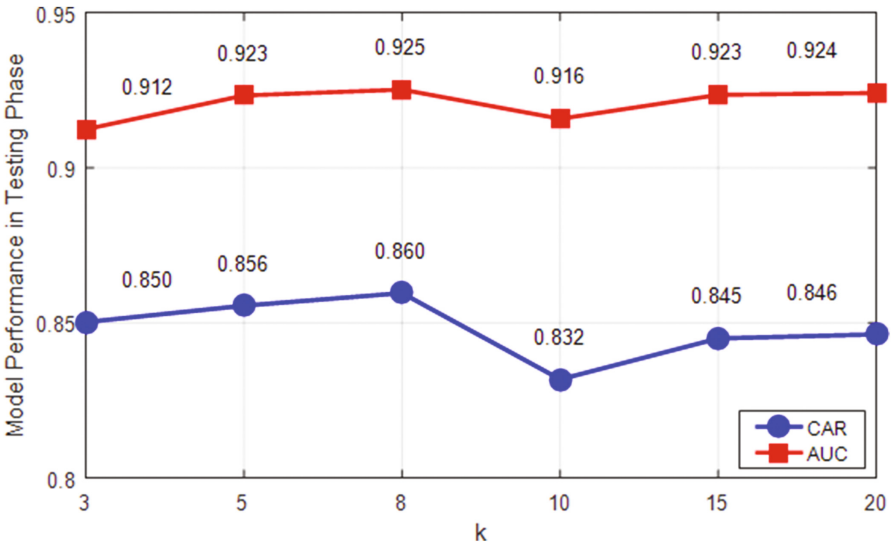

Fig. 11. Model performance using QGP criterion ($\beta = 2$) with different strip length (k)

a premature stop during the training process; meanwhile, QGP criterion has not suffered from such problem, it has provided a decent adjustment on the network's weight and successfully halted the training due to the detection of overfitting.

Based on the previous experiments, it can be seen that $\alpha = 3$ and $\beta = 2$ can lead to better prediction outcomes in testing phase. Thus, in the next experiments, the model performance is studied according to different value of the parameter k. Figures 10 and 11 report the predictive capability of the BpANN based landslide prediction model when the strip length of epochs varies. In the case of GL criterion, $k = 5$ as suggested by [28] is a good choice (as shown in Fig. 10); increased or decreased values of k cannot lead to better performances. In the case of QGP criterion (see Fig. 11), the model with $k = 8$ can lead to a slightly better predictive outcome (AUC = 0.925 and CAR = 86.00%). Therefore, values k ranging from 5 to 8 are recommended for BpAnn model with QGP criterion. Larger values of k cannot enhance the BpANN performance.

4 Conclusion

This paper carries out an investigative study on the performance of BpANN based landslide prediction models equipped with early stopping criteria. The two criteria including the GL and QGP methods are employed for detecting overfitting and terminating the training process before the standard stopping condition of maximum number of epochs is met. Experimental results with the case study have shown that the GL criterion lead to premature training halt and therefore, the model performance on testing is deteriorated compared with a model that consumes the maximum number of

training epochs. On the other hand, the QGP strategy successfully lead to a better predictive outcome. The model equipped with QGP criterion has not suffered from a premature stop.

Analyses with different stopping thresholds for the two criteria elucidate that for this particular data set under study, the appropriate values of α and β are 3 and 2, respectively. In addition, a strip length (k) smaller than 5 clearly deteriorate the model capability for both early stopping strategies. It is noted in the case of QGP criterion, $k = 8$ leads to a slightly better performance. Therefore, based on these experimental outcomes, the BpANN model with QGP criterion is recommended for application in landslide spatial prediction. $\beta = 2$ (based on this study) and $k = 5$ (according to suggestion in [28]) can be a good parameter setting. In addition, a larger value of k can be tried to seek for a better refinement of the model parameter. The future extension of the current study may include the application of BpANN-QGP with other training schemes (e.g. online, mini-batch, metaheuristic) for landslide spatial modeling.

References

1. Tien Bui, D., Tuan, T.A., Hoang, N.-D., Thanh, N.Q., Nguyen, D.B., Van Liem, N., Pradhan, B.: Spatial prediction of rainfall-induced landslides for the Lao Cai area (Vietnam) using a hybrid intelligent approach of least squares support vector machines inference model and artificial bee colony optimization. Landslides, 1–12 (2016)
2. Ahlheim, M., Fror, O., Heinke, A., Keil, A., Duc, N.M., Dinh, P.V., Saint-Macary, C., Zeller, M.: Landslides in mountainous regions of northern Vietnam: causes, protection strategies and the assessment of economic losses. Int. J. Ecol. Econ. Stat. **15**, 108–130 (2009)
3. Tien Bui, D., Ho, T.-C., Pradhan, B., Pham, B.-T., Nhu, V.-H., Revhaug, I.: GIS-based modeling of rainfall-induced landslides using data mining-based functional trees classifier with AdaBoost, Bagging, and MultiBoost ensemble frameworks. Environ. Earth Sci. **75**, 1101 (2016)
4. Pham, B.T., Tien Bui, D., Prakash, I.: Landslide susceptibility assessment using bagging ensemble based alternating decision trees, logistic regression and J48 decision trees methods: a comparative study. Geotech. Geol. Eng., 1–15 (2017)
5. Nguyen, Q.-K., Tien Bui, D., Hoang, N.-D., Trinh, P., Nguyen, V.-H., Yilmaz, I.: A novel hybrid approach based on instance based learning classifier and rotation forest ensemble for spatial prediction of rainfall-induced shallow landslides using GIS. Sustainability **9**, 813 (2017)
6. Hoang, N.-D., Tien-Bui, D.: A novel relevance vector machine classifier with cuckoo search optimization for spatial prediction of landslides. J. Comput. Civ. Eng. **30**, 04016001 (2016)
7. Meinhardt, M., Fink, M., Tünschel, H.: Landslide susceptibility analysis in central Vietnam based on an incomplete landslide inventory: Comparison of a new method to calculate weighting factors by means of bivariate statistics. Geomorphology **234**, 80–97 (2015)
8. Pham, B.T., Tien Bui, D., Pham, H.V., Le, H.Q., Prakash, I., Dholakia, M.B.: Landslide hazard assessment using random SubSpace fuzzy rules based classifier ensemble and probability analysis of rainfall data: a case study at Mu Cang Chai District, Yen Bai Province (Viet Nam). J. Indian Soc. Remote Sens. **45**, 673–683 (2017)

9. Pham, B.T., Tien Bui, D., Prakash, I., Nguyen, L.H., Dholakia, M.B.: A comparative study of sequential minimal optimization-based support vector machines, vote feature intervals, and logistic regression in landslide susceptibility assessment using GIS. Environ. Earth Sci. **76**, 371 (2017)
10. Shahabi, H., Hashim, M.: Landslide susceptibility mapping using GIS-based statistical models and Remote sensing data in tropical environment. Sci. Rep. **5**, 9899 (2015)
11. Pham, B.T., Khosravi, K., Prakash, I.: Application and comparison of decision tree-based machine learning methods in landside susceptibility assessment at Pauri Garhwal Area, Uttarakhand, India. Environ. Process. **4**, 711–730 (2017)
12. Cheng, M.-Y., Hoang, N.-D.: A swarm-optimized fuzzy instance-based learning approach for predicting slope collapses in mountain roads. Knowl. Based Syst. **76**, 256–263 (2015)
13. Goetz, J.N., Brenning, A., Petschko, H., Leopold, P.: Evaluating machine learning and statistical prediction techniques for landslide susceptibility modeling. Comput. Geosci. **81**, 1–11 (2015)
14. Feizizadeh, B., Blaschke, T., Nazmfar, H.: GIS-based ordered weighted averaging and Dempster-Shafer methods for landslide susceptibility mapping in the Urmia Lake Basin. Iran. Int. J. Digit. Earth **7**, 688–708 (2014)
15. Tien Bui, D., Tran, A.T., Klempe, H., Pradhan, B., Revhaug, I.: Spatial prediction models for shallow landslide hazards: a comparative assessment of the efficacy of support vector machines, artificial neural networks, kernel logistic regression, and logistic model tree. Landslides, 1–18 (2015)
16. Shirzadi, A., Bui, D.T., Pham, B.T., Solaimani, K., Chapi, K., Kavian, A., Shahabi, H., Revhaug, I.: Shallow landslide susceptibility assessment using a novel hybrid intelligence approach. Environ. Earth Sci. **76**, 60 (2017)
17. Tsangaratos, P., Benardos, A.: Estimating landslide susceptibility through a artificial neural network classifier. Nat. Hazards, 1–28 (2014)
18. Chauhan, S., Sharma, M., Arora, M.K., Gupta, N.K.: Landslide susceptibility zonation through ratings derived from artificial neural network. Int. J. Appl. Earth Obs. **12**, 340–350 (2010)
19. Pham, B.T., Tien Bui, D., Pourghasemi, H., Indra, P., Dholakia, M.B.: Landslide susceptibility assessment in the Uttarakhand area (India) using GIS: a comparison study of prediction capability of Naïve Bayes, multilayer perceptron neural networks, and functional trees methods. Theor. Appl. Climatol., 1–19 (2015)
20. Tien Bui, D., Ho, C.T., Revhaug, I.: GIS-based landslide susceptibility assessment along the National road 32 (Vietnam) using logistic regression and index of entropy models. In: Proceedings of the International Symposium on Geoinformatics for Spatial Infrastructure Development in Earth and Allied Sciences, 16–20 October 2012, Ho Chi Minh City, Vietnam (2012)
21. Ho, T.C.: Application of structural geology methods, remote sensing, and GIS for the assessment and prediction of landslide and flood along the National Road 32 in the Yen Bai and Lai Chau provinces of Vietnam. Technical report, Vietnam Institute of Geosciences and Mineral Resources (2008)
22. Glade, T., Anderson, M., Crozier, M.J.: Landslide Hazard and Risk. Wiley, West Sussex (2005)
23. Hoang, N.-D., Vu, D.-T., Tran, X.-L., Tran, V.-D.: Modeling punching shear capacity of fiber-reinforced polymer concrete slabs: a comparative study of instance-based and neural network learning. Appl. Comput. Intell. Soft Comput. **2017**, 11 (2017)
24. Sadowski, Ł., Hoła, J.: ANN modeling of pull-off adhesion of concrete layers. Adv. Eng. Softw. **89**, 17–27 (2015)

25. Heaton, J.: Artificial Intelligence for Humans. Deep Learning and Neural Networks, vol. 3. Heaton Research Inc., St. Louis (2015)
26. Freeman, J.A., Skapura, D.M.: Neural Networks - Algorithms, Applications, and Programming Techniques. Addison-Wesley Publishing Company, Inc., Paris (1991)
27. Bishop, C.: Neural Networks for Pattern Recognition. Clarendon Press, Oxford (1995)
28. LeCun, Y.A., Bottou, L., Orr, G.B., Müller, K.-R.: Efficient BackProp. In: Montavon, G., Orr, G.B., Müller, K.R. (eds.) Neural Networks Tricks of the Trade. Lecture Notes in Computer Science, vol. 7700. Springer, Heidelberg (2012)
29. López, V., Fernández, A., García, S., Palade, V., Herrera, F.: An insight into classification with imbalanced data: Empirical results and current trends on using data intrinsic characteristics. Inf. Sci. **250**, 113–141 (2013)
30. van Erkel, A.R., Pattynama, P.M.T.: Receiver operating characteristic (ROC) analysis: basic principles and applications in radiology. Eur. J. Radiol. **27**, 88–94 (1998)
31. Fawcett, T.: An introduction to ROC analysis. Pattern Recogn. Lett. **27**, 861–874 (2006)
32. Heaton, J.: Introduction to Neural Networks for C#. Heaton Research, Inc., St. Louis (2008)

A Novel Hybrid Intelligent Approach of Random Subspace Ensemble and Reduced Error Pruning Trees for Landslide Susceptibility Modeling: A Case Study at Mu Cang Chai District, Yen Bai Province, Viet Nam

Binh Thai Pham[1(✉)] and Indra Prakash[2]

[1] Department of Geotechnical Engineering, University of Transport Technology, 54 Trieu Khuc, Thanh Xuan, Ha Noi, Viet Nam
binhpt@utt.edu.vn

[2] Department of Science and Technology, Bhaskarcharya Institute for Space Applications and Geo-Informatics (BISAG), Government of Gujarat, Gandhinagar, India
indra52prakash@gmail.com

Abstract. In the present study, a hybrid approach of Random Subspace Ensemble (RSS) and Reduced Error Pruning Trees (REPT) has been proposed to create a novel hybrid model namely RSS-REPT for landslide susceptibility modeling of the Mu Cang Chai district, Yen Bai province of Vietnam where is affected by a number of landslides every year. For the development of model, a spatial database consisting of 248 historic landslide events and 15 affecting factors (slope, aspect, curvature, plan curvature, profile curvature, elevation, lithology, land use, distance to faults, fault density, distance to roads, road density, distance to rivers, river density, and rainfall), was constructed to generate training and testing datasets. The novel hybrid model was then constructed using training dataset for landslide susceptibility assessment, and its predictive capability was validated using Receiver Operating Characteristic (ROC) curve and Statistical Indexes (SI) analysis. Performance of this novel model has been compared with another popular model namely Support Vector Machines (SVM). Results indicate that its performance (AUC = 0.835) is higher in comparison to the SVM model (AUC = 0.804). Thus the RSS-REPT can be considered as one of the promising methods for better landslide susceptibility assessment of landslide prone areas.

Keywords: Landslide susceptibility modeling · Random subspace ensemble · Reduced error pruning trees · Viet Nam

1 Introduction

Landslides frequently occur in hilly region of Viet Nam causing loss of life and damage to property every year [1–3]. Most of these landslides are triggered by heavy rains during monsoon (from May to October) [4]. It is well known that rainfall-induced

© Springer International Publishing AG 2018
D. Tien Bui et al. (eds.), *Advances and Applications in Geospatial Technology and Earth Resources*, https://doi.org/10.1007/978-3-319-68240-2_16

landslides cannot be prevented but can be predicted in regional scale by identifying high susceptible areas using GIS technology to minimize damages caused by future landslides [5].

In recent decades, many algorithms have been developed and applied to predict landslides which can be grouped broadly into three categories namely qualitative, semi-quantitative, and quantitative methods [6, 7]. Qualitative methods, which are based on expert's perspective, often use landside inventories to predict locations having identical geomorphological and geological characteristics [8]. Semi-quantitative methods use the expert's perspective in conjunction with the idea of weighting and ranking for predicting potential landslides [9]. Quantitative methods are based on the numerical analysis of the spatial relationship between affecting factors and historical landslides [10]. Out of these, quantitative methods are more objective and popular for landslide susceptibility modeling [11].

In literature, Support Vector Machines [12], Artificial Neural Networks [13], Decision Trees [14] are some of the most popular quantitative methods for landslide susceptibility modeling. However, in recent years, the hybrid models, which are a combination of ensemble techniques and individual classifiers, are considered more efficient than single models such SVM [15]. Therefore, in this study, we have proposed a novel hybrid model namely RSS-REPT which is a combination of two machine learning methods of Random Subspace (RSS) ensemble and Reduced Error Pruning Trees (REPT) classifier for landslide susceptibility modeling at the Mu Cang Chai district, Yen Bai province (Viet Nam). Predictive capability of this hybrid model has been validated using the Receiver Operating Characteristic (ROC) curve and Statistical Indexes (SI) analysis and its performance has been compared with SVM.

2 Methods Used

2.1 Random Subspace

Random Subspace (RSS) was proposed by Ho [16] to generate multiple feature spaces for constructing multiple decision trees in classification. Main objective of the RSS is to sample a feature set from the original high dimensional feature space into low dimensional subspaces on which classifiers are then constructed for classifying the classes, and, finally, the final decision is obtained by applying a majority voting rule for combining the generated classifiers [17].

More specifically, let each training sample set $X = (X_1, X_2, \ldots, X_m)$ is an n-dimensional vector $X_i = (x_{i1}, x_{i2}, \ldots, x_{in})\,(i = 1, 2, \ldots, n)$, described by n features (landslide affecting factors). In the RSS, we randomly select $r < n$ features from the n-dimensional dataset of the original p-dimensional feature space X to obtain the r-dimensional random subspace. Thus, the modified training dataset $X^e = \left(X_1^e, X_2^e, \ldots, X_m^e\right)$ includes r-dimensional training objects $X_i^e = \left(x_{i1}^e, x_{i2}^e, \ldots, x_{ir}^e\right)$.

Thereafter, the classifiers are constructed in the random subspace X^e, and combined by applying simple majority voting in the final decision rule as following [18]:

$$\alpha(x) = \arg\max_{y \in \{0,1\}} \sum_{a} \delta_{\mathrm{sgn}}(C^a(x)), y \tag{1}$$

where $y \in (0, 1)$ is a decision of the classifier, δ_{ij} is the Kronecker symbol, $C^a(x)$ are the generated classifiers $(a = 1, 2, \ldots, A)$ [18].

2.2 Reduced Error Pruning Trees

Reduced Error Pruning Trees (REPT) introduced by Quinlan [19] is a combination of Decision Trees (DT) method and Reduced Error Pruning (REP) technique. The DT is one of the most popular classification tree methods for solving a lot of real world problems including landslide prediction [20]. However, it has a problem of producing the outcome of a large decision tree in classification. The REP is an effective machine learning technique in reducing the size of decision trees so that it can reduce the complexity of the final classifier [21]. It can also improve the predictive accuracy of the classifier by reducing the over-fitting and removing the tree sections which might cause the noisy or erroneous data [21]. Thus, the hybrid REPT method can give the desirable outcomes for classification problems. In this study, the hybrid REPT method has been used as a base classifier in ensemble framework for landslide spatial prediction.

2.3 Evaluation and Comparison Methods

In this study, the Receiver Operating Characteristic (ROC) curve and several statistical indexes have been selected for validating the performance of the novel hybrid model. Out of these methods, the ROC curve is one of the most popular quantitative evaluation methods in landslide susceptibility modeling. It is based on the graph which is plotted using two statistical values ("sensitivity" and "100-specificity") [11, 22]. To validate quantitatively the predictive capability of the model, the area under the ROC curve called AUC has been used. Model has better performance as the AUC values closer to "1" [10, 23]. Models with high AUC values are better than those with lower AUC values. In landslide modeling studies, statistical indexes namely positive and negative predictive values, sensitivity, specificity, accuracy, kappa, and root mean squared error have been widely used for validating the performance of models [24]. These statistical indexes are calculated on the basis of calculation of the probability of pixels (landslide pixels and non-landslide pixels) in the relation with variable classes (landslide and non-landslide). Models with higher values of positive and negative predictive values, sensitivity, specificity, accuracy, and kappa have better performance than those with lower values. In contrast, models with low root mean squared error values have better predictive capability than those with high values. Models are perfect when the root mean squared error values are equal to zero.

In addition, the SVM, which is known as a benchmark single landslide model [12], has been selected to compare with the proposed hybrid RSS-REPT model. The SVM is a binary classifier which is based on the statistical algorithm to separate two classes

(landslide and non-landslide) by hyper-plane in the original space [25]. This method has already been applied widely and efficiently in many landslide studies [26, 27].

3 Description of the Study Area

The Mu Cang Chai district (long. 103°56′00″E to 104°23′00″E and lat. of 21°39′00″N to 21°50′00″N), the study area, is located in Yen Bai province in the northern part of Viet Nam (Fig. 1). It covers an area approximately 1196.47 km^2. The study area falls into the humid subtropical climate region having annual average humidity of 81% and annual average temperature of 25°C. There are two separate seasons in a year namely dry season (November to April) and rainy season (May to October). Heavy rainfall usually happens in the rainy season generally during August and September. The total annual rainfall varies from 3700 mm to 5490 mm. Excessive rains is the main triggering factor causing many landslides in this area.

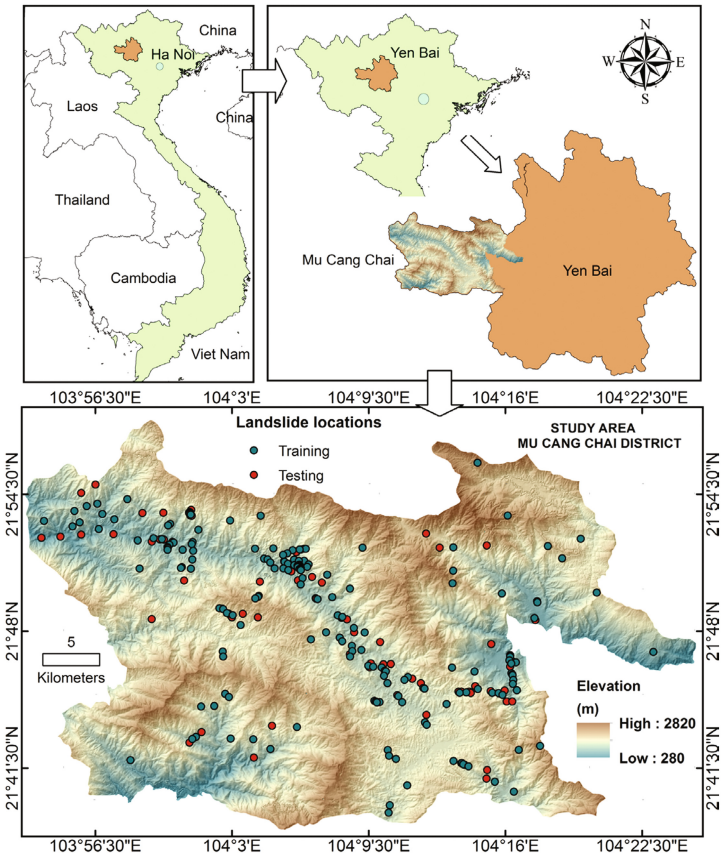

Fig. 1. Landslide inventory and location map of the study area

Topography of the study area is adulatory. The study area is occupied by high mountain ranges and deep intervening valleys. Elevation varies in this area from 280 m to 2820 m. About eighty percent of the ground slope in the area varies from 10 to 40 degrees. Some of the hills are having very steep slopes up to 88 degrees.

The study area is occupied mainly by extrusive volcanic rocks of Ngoi Thia and Tu Le complexes. The intrusive magmatic rocks of Tram Tau formation and Phu Sa Phin complex occupy the smaller part of the study area. Terrigenous sedimentary rocks and Quaternary sediments are also present in the area (Fig. 3). Tectonically, the area is disturbed and dissected by various faults namely Nghia Lo, Nam Co- Minh An, and Phong Tho- Van Yen.

4 Preparation of GIS Database

4.1 Landslide Inventory Map

Landslide inventory map has been constructed with 248 historical landslide locations which have been identified using Remote Sensing techniques based on the interpretation of 1:30000 scale air photos (Year 2013) and Google Earth images. Field investigation has been carried out to check and validate these landslide locations under the national project of Viet Nam named "Survey, assessment and zoning of landslide warning in the mountainous region of Vietnam" at Vietnam Institute of Geosciences and Mineral Resources. In the study area, the largest size of landslides observed is of 100000 m^3 volume at the Che Cu Na commune (2011).

4.2 Landslide Affecting Factors

In the study area, fifteen landslide affecting factors namely slope, aspect, profile curvature, curvature, plan curvature, elevation, distance to rivers, distance to faults, distance to roads, river density, fault density, road density, lithology, land use, and rainfall have been selected for landslide susceptibility modeling (Table 1). Thematic data has been obtained from the Vietnam Institute of Geosciences and Mineral Resources for the development of raster maps of 20 $\times$ 20 m size for the GIS analysis in conjunction with Digital Elevation Model (DEM).

Lithology and faults have been extracted from the available geological and mineral resources maps of the study area (1:50,000 scale) (Fig. 2). Distance to faults and fault density maps have been generated by using buffer and density functions in ArcGIS application. Similarly, distance to roads, road density, distance to rivers, and river density maps have been generated for the analysis.

Land use map (Fig. 4) has been generated from the interpretation of 1:30000 scale air photos (Year 2013) and updated from Google images. Rainfall data has been extracted from the Global Weather data for SWAT [28] of 30 years (1984 to 2014), and used to generated rainfall map of the study.

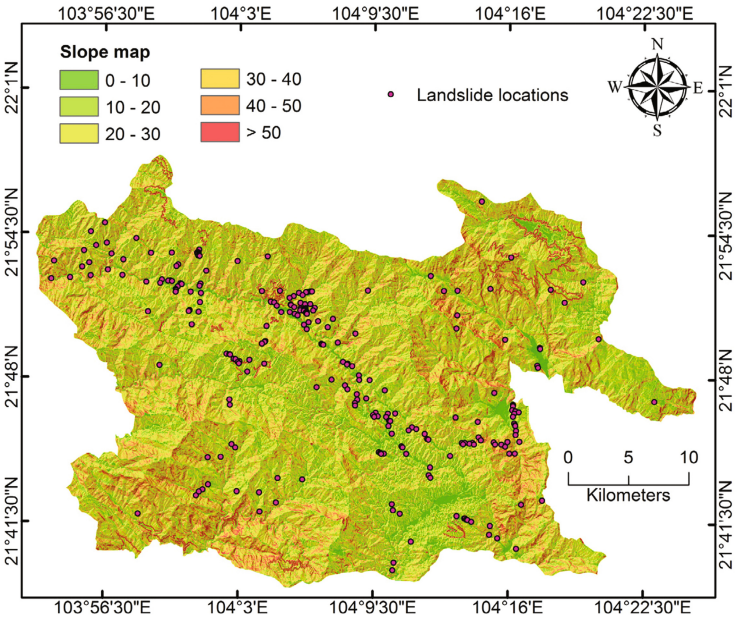

Fig. 2. Slope map of the study area

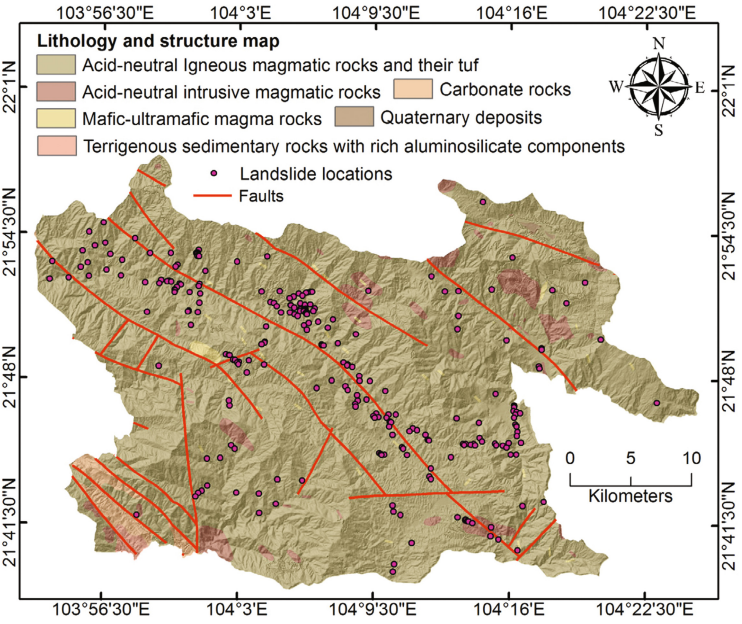

Fig. 3. Lithology and structure map of the study area

Table 1. Landslide affecting geo-environmental factors and their classes

No	Geo-environmental factors	Classes
1	Slope (degrees)	(1) 0–10, (2) 10–20, (3) 20–30, (4) 30–40, (5) 40–50, and (6) >50
2	Elevation (m)	(1) 280–700, (2) 700–900, (3) 900–1100, (4) 1100–1300, (5) 1300–1500, (6) 1500–1700, (7) 1700–1900, (8) 1900–2100, (9) 2100–2300, and (10) >2300
3	Aspect	(1) flat, (2) north, (3) northeast, (4) east, (5) southeast, (6) south, (7) southwest, (8) west, and (9) northwest
4	Plan curvature	(1) [(−334.189)–(−69.843)], (2) [(−69.843)–(−13.507)], (3) [(−13.507)–(−2.673)], (4) 4 [(−2.673)–3.827], and (5) [3.827–218.338]
5	Curvature	(1) concave (<−0.05), (2) flat (−0.05–0.05), and (3) convex (>0.05)
6	Profile curvature	(1) [(−255.398)–(−52.003)], (2) [(−52.003)–(−9.183)], (3) [(−9.183)–5.804], (4) [5.804–48.624], and (5) [48.624–290.557]
7	Land use	(1) barren land, (2) cultivated land, (3) forest land, (4) residential area, (5) scrub land, and (6) water bodies
8	Lithology	(1) acid-neutral igneous magmatic rocks and their tuff, (2) acid-neutral intrusive magmatic rocks, (3) terrigenous sedimentary rocks with rich aluminosilicate components, (4) mafic-ultramafic magma rocks, (5) carbonate rocks, and (6) quaternary deposits
9	Distance to faults (m)	(1) 0–100, (2) 100–200, (3) 200–300, (4) 300–400, (5) 400–500, (6) 500–600, (7) 600–700, and (8) >700
10	Fault density (km/km^2)	(1) very low (0–0.319), (2) low (0.319–0.861), (3) moderate (0.861–1.436), (4) high (1.436–2.169), and (5)very high (2.169–4.068)
11	Distance to roads (m)	(1) 0–50, (2) 50–100, (3) 100–150, (4) 150–200, (5) 200–250, and (6) > 250
12	Road density (km/km^2)	(1) very low (0–0.319), (2) low (0.319–0.861), (3) moderate (0.861–1.435), (4) high (1.435–2.169), and (5) very high (2.169–4.0676)
13	Distance to rivers (m)	(1) 0–50, (2) 50–100, (3) 100–150, (4) 150–200, (5) 200–250, and (6) >250
14	River density (km/km^2)	(1) very low (0–0.186), (2) low (0.186–0.428), (3) moderate (0.428- 0.703), (4) high (0.703–1.164), and (5) very high (1.1642–2.061)
15	Rainfall (mm)	(1) < 4000, (2) 4000–4250, (3) 4250–4500, (4) 4500–4750, (4) 4750–5000, (6) 5000–5250, and (7) >5250

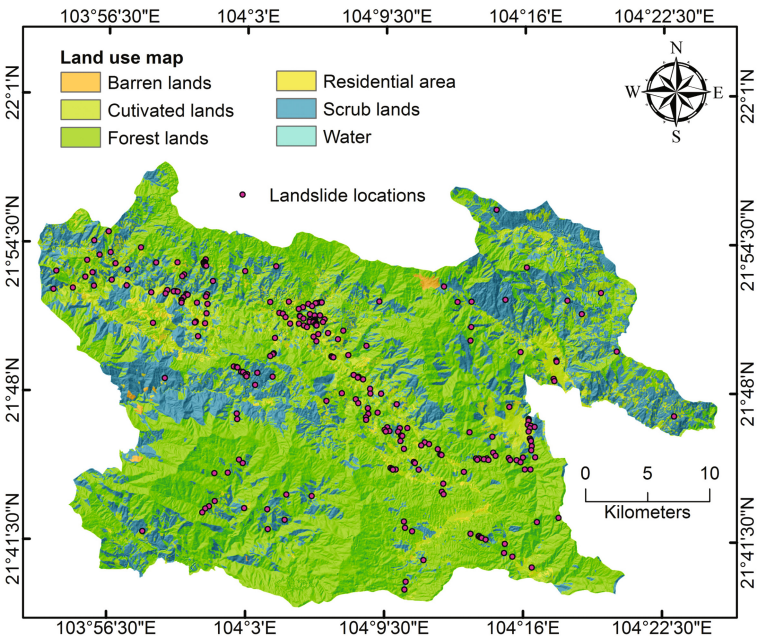

Fig. 4. Land use/ land cover map of the study area

5 Landslide Susceptibility Assessment Using a Novel Hybrid RSS-REPT Model

Landslide susceptibility assessment at the Mu Cang Chai district using a novel hybrid model RSS-REPT has been carried out in four main steps: (1) generating training and testing datasets, (2) constructing landslide model, (3) validating landslide model, (4) constructing landslide susceptibility map.

(1) Generating training and testing datasets: Data collected from the study area has been processed to generate the training dataset and testing dataset. Training data set has been used to construct landslide models, and the testing dataset for validating models. For generating the training dataset, 70% of landslide locations (174 locations) have been selected randomly and remaining 30% landslide locations (74 locations) have been used to generate the testing dataset. These landslide locations have also been used to sample with landslide affecting factors for generating the final datasets for machine learning models.

(2) Constructing landslide model: In this step, the training dataset has been used. The RSS ensemble has been applied to divide the training datasets into different sub-training datasets in different ways with different iterations. Simultaneously, the REPT classifiers have been applied using the generated sub-training datasets for classification. Finally, the RSS ensemble has been used to combine all generated REPT classifiers to construct the RSS-REPT model. For constructing the

hybrid model RSS-REPT, the parameters of algorithms have been set using trial-and-error process as follows: the number of iterations to be performed is 24; the amount of data used for pruning (folds) is 10; the minimum total weight of the instances in a leaf is 2; and tree pruning is applied.

(3) Validating landslide model: In this step, the testing dataset has been used. Predictive capability of the proposed model RSS-REPT has been validated using different evaluation criteria such as the ROC curve and SI analysis. In addition, the performance of the RSS-REPT has been validated by comparing with another well-known landslide model namely SVM.

(4) Constructing landslide susceptibility map: Landslide susceptibility map has been constructed by generating and classifying landslide susceptibility indexes using the results of proposed RSS-REPT model.

6 Results and Discussions

6.1 Training and Validating the RSS-REPT Model

Results of training of the proposed RSS-REPT model are shown in Table 2 and Fig. 5. The results show that the values of statistical indexes and the ROC curve analysis using training dataset are high. More specifically, the positive predictive value is 79.89% indicating that the probability of classification of pixels to landslide class is high; the negative predictive value is 75.86% indicating that probability of classification of pixels to non-landslide class is high; the sensitivity value is 76.80% indicating that the probability of classification of landside pixels to landside class is high; the specificity value is 79.04% indicating that the probability of classification of non-landside pixels to non-landside class is high; the accuracy value is 77.87% indicating that the classification accuracy of the model is high; the Kappa value is 0.558 indicating that the results of the proposed model is reliable; the RMSE value is 0.384 indicating that the error of training model is relative low; and the AUC value is 0.896 indicating that the general performance of the model is very good.

Table 2. Model performance using training dataset

No	Statistical indexes	RSS-REPT	SVM
1	Positive predictive value (%)	79.89	79.31
2	Negative predictive value (%)	75.86	75.29
3	Sensitivity (%)	76.80	76.24
4	Specificity (%)	79.04	78.44
5	Accuracy (%)	77.87	77.30
6	Kappa (k)	0.558	0.546
7	Root Mean Squared Error (RMSE)	0.384	0.395

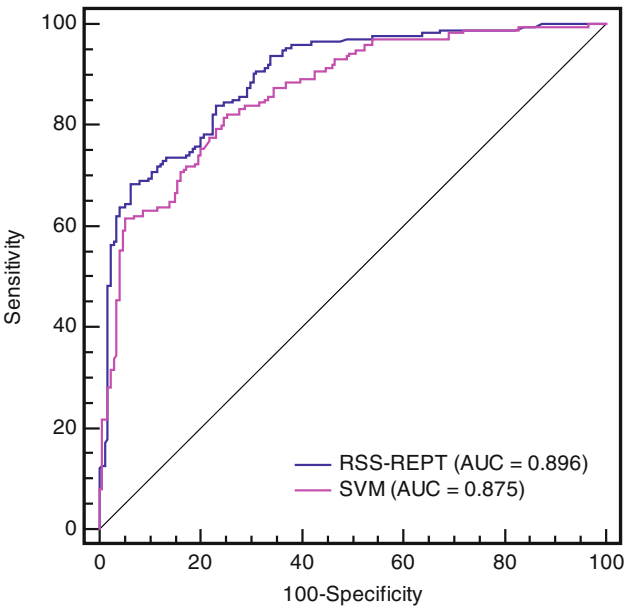

Fig. 5. The ROC curve analysis of landslide models using training dataset

Results of validating the proposed RSS-REPT model are shown in Table 3 and Fig. 6. The results show that the values of statistical indexes and the ROC curve analysis using testing dataset are high. More specifically, the positive predictive value is 79.73% indicating that the probability of classification of pixels to landslide class is high; the negative predictive value is 72.97% indicating that probability of classification of pixels to non-landslide class is high; the sensitivity value is 74.68% indicating that the probability of classification of landside pixels to landside class is high; the specificity value is 78.26% indicating that the probability of classification of non-landside pixels to non-landside class is high; the accuracy value is 76.35% indicating that the classification accuracy of the model is high; the Kappa value is 0.527 indicating that the results of the proposed model is reliable; the RMSE value is 0.419

Table 3. Model performance using testing dataset

No	Statistical indexes	RSS-REPT	SVM
1	Positive predictive value (%)	79.73	73.68
2	Negative predictive value (%)	72.97	70.83
3	Sensitivity (%)	74.68	72.73
4	Specificity (%)	78.26	71.83
5	Accuracy (%)	76.35	72.30
6	Kappa (k)	0.527	0.473
7	Root mean squared error (RMSE)	0.419	0.424

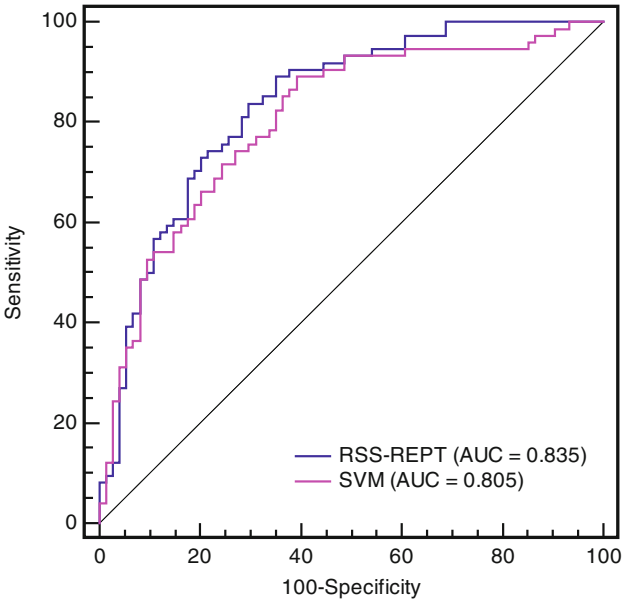

Fig. 6. The ROC curve analysis of landslide models using testing dataset

indicating that the error of training model is relative low; and the AUC value is 0.835 indicating that the general performance of the model is good.

Based on the analysis of the results, it is clearly observed that the proposed hybrid model RSS-REPT has a good performance for landslide susceptibility modeling in the present study, even better than the benchmark model SVM. Outperformance of good hybrid model in comparison to single model has also been observed by other workers [3]. In the present case, the hybrid RSS-REPT model takes advantages of both state of the art machine learning methods of the RSS and REPT. More specifically, the RSS ensemble used in the hybrid model RSS-REPT is known as one of the efficient ensemble techniques which can help in improving the performance of the single models [7, 29]. It has been observed that the RSS ensemble might get the benefits by using random subspaces for building and aggregating the classifiers, especially in the case of datasets with many redundant features [18]. Moreover, the classifiers combined by the RSS in random subspaces might be superior to a single classifier built in the original feature space [18]. In addition, the REPT classifier used in the hybrid model RSS-REPT also has many advantages, which can enhance the predictive capability of the hybrid model, such as (i) the REPT is also a hybrid tree model of the DT and REP which can be utilized efficiently for complex classification problems including landslide prediction, (ii) the sub-trees constructed in the REPT can be adapted to characteristics specific to different subsets of the data; and thus producing more accurate results [19, 30], and (iii) it uses the REP technique which can help in minimizing the error from the variance [31].

6.2 Cartographic Generation of Landslide Susceptibility Map

Landslide susceptibility map is a great tool for land use planners and decision makers in landslide hazard management [32, 33]. In the present study, the landslide susceptibility map has been constructed using the proposed hybrid model RSS-REPT through two main steps. Firstly, landslide susceptibility indexes have been generated for all pixels of the study area. Secondly, these susceptibility indexes have been classified to construct the landslide susceptibility map (Fig. 7) with different susceptibility classes (very low, low, moderate, high, and very high) using geometrical interval method [34, 35].

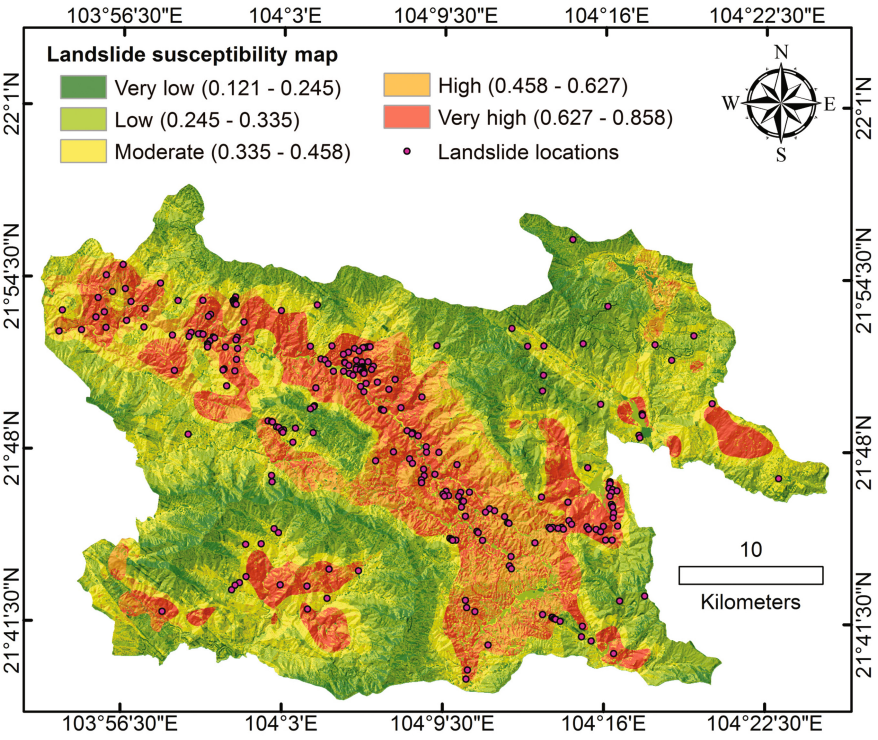

Fig. 7. Landslide susceptibility map of the study area using the RSS-REPT model

To validate the reliability of the landslide susceptibility map produced in this study, the landslide density analysis has been carried out on the basis of the analysis of the distribution of historial landslide pixels on susceptibility classes of the map. The results of landslide density analysis are shown in Table 4. It can be observed that the highest density of landslide pixels is on the very high susceptibility class (4.08), followed by the high susceptibility class (0.98), the moderate susceptibility class (0.62), the low susceptibility class (0.17), and very low susceptibility class (0.07), respectively. These results indicate the reliability of the landslide susceptibility map.

Table 4. Landslide density analysis on landslide susceptibility map

No	Classes	Class pixels	Landslide pixels	% Class pixels	% Landslide pixels	Landslide density
1	Very low	365259	2	12.21	0.81	0.07
2	Low	1107124	16	37.01	6.45	0.17
3	Moderate	660522	34	22.08	13.71	0.62
4	High	367999	30	12.30	12.1	0.98
5	Very high	490283	166	16.39	66.94	4.08

7 Concluding Remarks

Landslide susceptibility modeling has been done at the Mu Cang Chai district, Yen Bai province (Viet Nam) using a novel hybrid model namely RSS-REPT which is a combination of two state of the art machine learning methods of the RSS ensemble and the REPT classifier. For validation, the ROC curve and several statistical indexes have been used. In addition, performance of the proposed hybrid model has been compared with another benchmark single landslide model SVM.

Result analysis shows that the proposed hybrid model RSS-REPT performed well for landslide susceptibility modeling. Its predictive capability outperforms the well-known landslide model SVM. Therefore, it can be reasonably concluded that the proposed hybrid model RSS-REPT is a promising tool for landslide susceptibility modeling which can be considered as a better alternative method for landslide hazard management also in other landslide prone areas.

Acknowledgement. Authors are thankful to the Vietnam Institute of Geosciences and Mineral Resources for sharing the data. Authors are also thankful to the Director, Bhaskarcharya Institute for Space Applications and Geo-Informatics, Gujarat, India for providing facilities to carry out this research work.

References

1. Pham, B.T., Bui, D.T., Dholakia, M.B., Prakash, I., Pham, H.V., Mehmood, K., Le, H.Q.: A novel ensemble classifier of rotation forest and Naïve Bayer for landslide susceptibility assessment at the Luc Yen district, Yen Bai Province (Viet Nam) using GIS. Geomatics, Natural Hazards and Risk, pp. 1–23 (2016)
2. Tien Bui, D., Ho, T.-C., Pradhan, B., Pham, B.-T., Nhu, V.-H., Revhaug, I.: GIS-based modeling of rainfall-induced landslides using data mining-based functional trees classifier with AdaBoost, Bagging, and MultiBoost ensemble frameworks. Environ. Earth Sci. **75**, 1–22 (2016)
3. Tien Bui, D., Pham, B.T., Nguyen, Q.P., Hoang, N.-D.: Spatial prediction of rainfall-induced shallow landslides using hybrid integration approach of least-squares support vector machines and differential evolution optimization: a case study in Central Vietnam. Int. J. Digital Earth **9**, 1–21 (2016)

4. Pham, B.T., Tien Bui, D., Dholakia, M.B., Prakash, I., Pham, H.V.: A comparative study of least square support vector machines and multiclass alternating decision trees for spatial prediction of rainfall-induced landslides in a tropical cyclones area. Geotech. Geol. Eng. **34**, 1–18 (2016)
5. Tsangaratos, P., Ilia, I.: Landslide susceptibility mapping using a modified decision tree classifier in the Xanthi Perfection. Greece Landslides **13**, 305–320 (2016)
6. Abella, E.A.C., Van Westen, C.J.: Qualitative landslide susceptibility assessment by multicriteria analysis: a case study from San Antonio del Sur, Guantánamo. Cuba. Geomorphol. **94**, 453–466 (2008)
7. Shirzadi, A., Bui, D.T., Pham, B.T., Solaimani, K., Chapi, K., Kavian, A., Shahabi, H., Revhaug, I.: Shallow landslide susceptibility assessment using a novel hybrid intelligence approach. Environ. Earth Sci. **76**, 60 (2017)
8. Saha, A.K., Gupta, R.P., Sarkar, I., Arora, M.K., Csaplovics, E.: An approach for GIS-based statistical landslide susceptibility zonation—with a case study in the Himalayas. Landslides **2**, 61–69 (2005)
9. Mathew, J., Jha, V., Rawat, G.: Application of binary logistic regression analysis and its validation for landslide susceptibility mapping in part of Garhwal Himalaya, India. Int. J. Remote Sens. **28**, 2257–2275 (2007)
10. Pham, B.T., Tien Bui, D., Pourghasemi, H.R., Indra, P., Dholakia, M.B.: Landslide susceptibility assesssment in the Uttarakhand area (India) using GIS: a comparison study of prediction capability of naïve bayes, multilayer perceptron neural networks, and functional trees methods. Theor. Appl. Climatol. **122**, 1–19 (2015)
11. Mathew, J., Jha, V., Rawat, G.: Landslide susceptibility zonation mapping and its validation in part of Garhwal Lesser Himalaya, India, using binary logistic regression analysis and receiver operating characteristic curve method. Landslides **6**, 17–26 (2009)
12. Pham, B.T., Pradhan, B., Tien Bui, D., Prakash, I., Dholakia, M.B.: A comparative study of different machine learning methods for landslide susceptibility assessment: a case study of Uttarakhand area (India). Environ. Model Softw. **84**, 240–250 (2016)
13. Tsangaratos, P., Benardos, A.: Estimating landslide susceptibility through a artificial neural network classifier. Nat. Hazards **74**, 1489–1516 (2014)
14. Pham, B.T., Bui, D.T., Prakash, I., Dholakia, M.: Evaluation of predictive ability of support vector machines and naive Bayes trees methods for spatial prediction of landslides in Uttarakhand state (India) using GIS. J. Geomatics **10**, 71–79 (2016)
15. Pham, B.T., Tien Bui, D., Prakash, I., Dholakia, M.B.: Rotation forest fuzzy rule-based classifier ensemble for spatial prediction of landslides using GIS. Nat. Hazards **83**, 1–31 (2016)
16. Ho, T.K.: The random subspace method for constructing decision forests. IEEE Trans. Pattern Anal. Mach. Intell. **20**, 832–844 (1998)
17. Xia, J., Dalla Mura, M., Chanussot, J., Du, P., He, X.: Random subspace ensembles for hyperspectral image classification with extended morphological attribute profiles. IEEE Trans. Geosci. Remote Sens. **53**, 4768–4786 (2015)
18. Skurichina, M., Duin, R.P.: Bagging, boosting and the random subspace method for linear classifiers. Pattern Anal. Appl. **5**, 121–135 (2002)
19. Quinlan, J.R.: Simplifying decision trees. Int. J. Man Mach. Stud. **27**, 221–234 (1987)
20. Nefeslioglu, H., Sezer, E., Gokceoglu, C., Bozkir, A., Duman, T.: Assessment of landslide susceptibility by decision trees in the metropolitan area of Istanbul, Turkey. Mathe. Probl. Eng. **2010** (2010)
21. Galathiya, A., Ganatra, A., Bhensdadia, C.: Improved decision tree induction algorithm with feature selection, cross validation, model complexity and reduced error pruning. Int. J. Comput. Sci. Inf. Technol. **3**, 3427–3431 (2012)

22. Pham, B.T., Tien Bui, D., Indra, P., Dholakia, M.: Landslide susceptibility assessment at a part of Uttarakhand Himalaya, India using GIS–based statistical approach of frequency ratio method. Int. J. Eng. Res. Technol. **4**, 338–344 (2015)
23. Gorsevski, P.V., Gessler, P.E., Foltz, R.B., Elliot, W.J.: Spatial prediction of landslide hazard using logistic regression and ROC analysis. Trans. GIS **10**, 395–415 (2006)
24. Bennett, N.D., Croke, B.F., Guariso, G., Guillaume, J.H., Hamilton, S.H., Jakeman, A.J., Marsili-Libelli, S., Newham, L.T., Norton, J.P., Perrin, C.: Characterising performance of environmental models. Environ. Model Softw. **40**, 1–20 (2013)
25. Marjanović, M., Kovačević, M., Bajat, B., Voženílek, V.: Landslide susceptibility assessment using SVM machine learning algorithm. Eng. Geol. **123**, 225–234 (2011)
26. Kavzoglu, T., Sahin, E.K., Colkesen, I.: Landslide susceptibility mapping using GIS-based multi-criteria decision analysis, support vector machines, and logistic regression. Landslides **11**, 425–439 (2014)
27. Wu, Y., Li, W.: GIS-based landslide susceptibility analysis using support vector machine model at a regional scale. Electron. J. Geotech. Eng. **21**, 6938–6945 (2016)
28. NCEP: Global weather data for SWAT (2014). http://globalweather.tamu.edu/home
29. Pham, B.T., Bui, D.T., Prakash, I.: Landslide susceptibility assessment using bagging ensemble based alternating decision trees, logistic regression and j48 decision trees methods: a comparative study. Geotech. Geol. Eng., 1–15 (2017)
30. Brodley, C.E., Utgoff, P.E.: Multivariate decision trees. Mach. Learn. **19**, 45–77 (1995)
31. Tama, B.A., Rhee, K.-H.: Tree-based classifier ensembles for early detection method of diabetes: an exploratory study. Artif. Intell. Rev., 1–16 (2017)
32. Pham, B.T., Tien Bui, D., Pham, H.V., Le, H.Q., Prakash, I., Dholakia, M.B.: Landslide hazard assessment using random subspace fuzzy rules based classifier ensemble and probability analysis of rainfall data: a case study at Mu Cang Chai District, Yen Bai Province (Viet Nam). J. Indian Soc. Remote Sens., 1–11 (2016)
33. Pham, B.T., Tien Bui, D., Prakash, I., Nguyen, L.H., Dholakia, M.B.: A comparative study of sequential minimal optimization-based support vector machines, vote feature intervals, and logistic regression in landslide susceptibility assessment using GIS. Environ. Earth Sci. **76**, 371 (2017)
34. Frye, C.: About the geometrical interval classification method (2007). http://blogs.esri.com/esri/arcgis
35. Pham, B.T., Tien Bui, D., Prakash, I., Dholakia, M.B.: Hybrid integration of multilayer perceptron neural networks and machine learning ensembles for landslide susceptibility assessment at Himalayan area (India) using GIS. CATENA **149**(Part 1), 52–63 (2017)

Recent Tectonic Movements Along the Coastal Zone of Tuy Hoa Area (Central Vietnam) and Its Significance for Coastal Hazards in the Case of Sea Level Rise

Hai Thanh Tran(✉)

Department of Geology, Hanoi University of Mining and Geology, North Tu Liem, Hanoi, Vietnam
tranthanhhai@humg.edu.vn

Abstract. The Tuy Hoa area is part of central coastal zone of Vietnam, which is commonly exposed to natural calamity including several types of geological hazards. The area is underlain by dominantly magmatic rocks and subordinated sedimentary units, which were formed during the Paleozoic to Early Cenozoic. These were variably covered by thin Cenozoic sedimentary cover including subordinate Quaternary volcanics and predominant fluvial, marine and aeolian deposits, which overlying most part of the area. All of the crystalized rocks and unconsolidated sedimentary units are variably affected by regional tectonic deformation, including extensive fracturing, faulting, subsidence and uplift, which were resulted from multiphase paleotectonic and neotectonic activities. Recent recorded earthquake also indicates active ground movement in the area. Local structural elements can be documented on the basis of numerous geological and morphological evidences and qualitative dating of the displaced Quaternary materials, which revealed significant local uplift, subsidence or displacement during recent time in the study area. The northern part of the area has been uplifted at the rate of at least 0.17 mm per year. In contrast, some areas such as Ban Thach River basin and Hao Son Lake are subsided significantly, in which Hao Son Lake area has subsided at the rate of ca. 0.96 mm per year. Incorporating the local uplift and subsidence with the predicted regional sea level rise scenario during next 100 years, most of the coastal area in the north of Tuy Hoa area will be slightly flooded under maximum 0.60 m of sea level rise compared with the prediction of regional ca. 0.77 m of sea level rise. In contrast, the tectonic subsidence will lead to serve flooding by sea water in which Hao Son Lake area will be submerged at least to the depth of 0.9 m and Ban Thach River basin will be also flooded deeply under the sea level during next 100 years. Other hazards including landslides, beach erosion are locally developed along the coastal zone and are controlled by bedrock inhomogeneity, zones of structural weakness, and active tectonic movement. Thus, basement architecture and bedrock fracturing within an area of active tectonic regime are major factors to influence landscape morphology and geological hazards in the coastal zone. Therefore, accurate identification and proper documentation of regional and

© Springer International Publishing AG 2018
D. Tien Bui et al. (eds.), *Advances and Applications in Geospatial Technology and Earth Resources*, https://doi.org/10.1007/978-3-319-68240-2_17

local structural elements must be properly addressed in order to predict natural hazards, especially in the context of a predicted global sea level change.

Keywords: Coastal zone · Structural control · Subsidence · Uplift · Central Vietnam

1 Introduction

The Tuy Hoa area is located in the central portion of the coastal zone of Vietnam, which is openly faced to the East Sea (Fig. 1). Previous geological works [1–6] show that the area is underlain by a numerous rock types of varying composition, ages and environments, which are covered by Tertiary-Quaternary volcanics and sedimentary units of either fluvial-deltaic or marine aeolian environments. The basement rocks have undergone numerous phases of tectonic deformation that extended from at least Mesozoic to present, which have led to strong fracturing and local dismemberment of the basement units. The tectonic activities in the area are remained active [6, 7] indicated by a number of indicators such as the presence of neotectonic and active faults, deformation of Quaternary sedimentary deposits, local terrane uplift and/or subsidence, abrupt change of topographic features such as water flow direction. The coastal morphology in the area is complicated, which is derived from the interaction of many factors such as variation in basement rock composition, tectonic fracturing that couple with the effect of surface process such as weathering, water flow, wave and sea action.

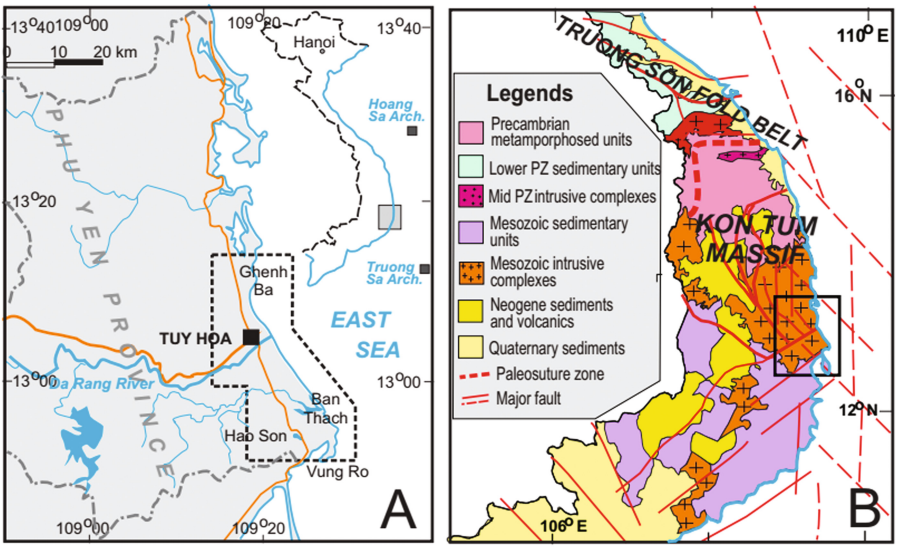

Fig. 1. A. Geographic location of the Tuy Hoa coastal zone in Phu Yen Province, central Vietnam. B. Generalized geological setting of central Vietnam showing the relative location of Tuy Hoa area (black box) and its underlying basement. Modified from [5].

The coastal zone is commonly affected by natural calamity such as flooding, storm, sea invasion, coastal erosion, landslide, land subsidence or uplift [6, 8] or man-made causes [9].

The development of the coastal geological hazards such as landslide coastal erosion has widely considered to result from a combination of endogenic factors such as lithological composition spatial distribution of differing geological units and tectonic deformation couple with exogenic processes under heavy influence of tropical monsoon climate [10–12]. Among them, the endogenic processes are important factors that govern the movement or deformation of the rock units and the exogenic activities produces addition parameters for the hazards to take place. In addition, the effects of relative sea level rise or fall will also create addition factor that enhance the coastal hazards [11]. However, the importance of geological structures within the coastal zone that govern the formation and/or development of coastal morphology, and particular their role as controlling factors for geological hazards in Tuy Hoa area as well as other areas along the coastal zone of Vietnam to date have not been adequately addressed.

In order to fully understand the nature of the neotectonic geological structures and their association with geological hazards in Tuy Hoa area and use them as the basis for assessment of other areas along the coastal zone of Vietnam, a comprehensive approach must be carried out. This paper reviews the general structural features of the area with a special emphasis on recent tectonic movements and evaluates their significance as regional controlling factors in the formation and occurrence of coastal morphological features and geological hazards using the combination of field mapping, structural interpretation and radiocarbon dating of Quaternary materials. These new geological data can be used as a basis for the assessment, prediction and mitigation of future hazards in coastal zone areas, especially on the case of a predicted global sea level rise cause by climate change during 21st Century.

2 Geological Feature of the Tuy Hoa Area

2.1 Stratigraphy and Magmatism

The Tuy Hoa area locates along the southeastern margin of Kon Tum Massif, a tectonically complex terrane comprising predominant Precambrian high-grade metamorphosed para- and ortho-gneissic basement, remnants of Paleozoic sedimentary units, which are either covered by late Mesozoic sedimentary sequences or intruded variably by numerous types of plutonic rocks [1–5]. These in turn are covered by Cenozoic sedimentary deposits and subordinate volcanic rocks, which range in age from Neogene to Quaternary that dominantly overlays and shape the coastal topography of the area (Fig. 2). The general characteristics of lithological units can be summarized as follow.

Sedimentary and volcanic rocks

The oldest exposed units in the Tuy Hoa area are of middle Mesozoic sedimentary rocks, which exposed as scattered units in the southwest and central of the area (Fig. 2). These comprise the Early Jurassic terrigenous deposits (Dray Linh Formation-J_1dl), which exposed in a small area in southwestern of the area.

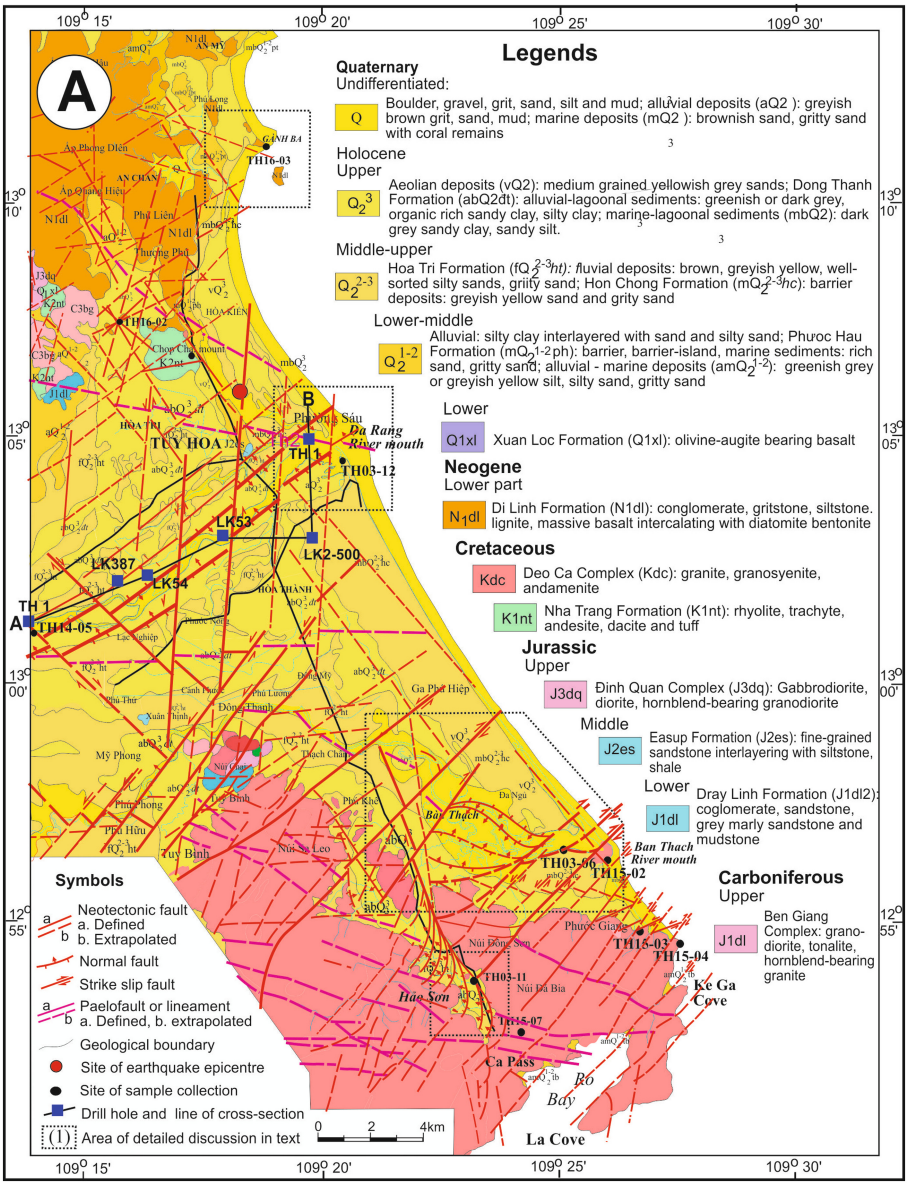

Fig. 2. A. General geological map of the Tuy Hoa area (geological background modified from [3] with additional geological data of this work). B. Generalized geological cross-section along line AB in Fig. 2A. Data used for construction is adapted from [13]. Note the opposing movement direction along the faults extrapolated from the identification of the offset of Quaternary sedimentary units and unconformities, which indicates a complicated movement history and basin forming process during the Quaternary.

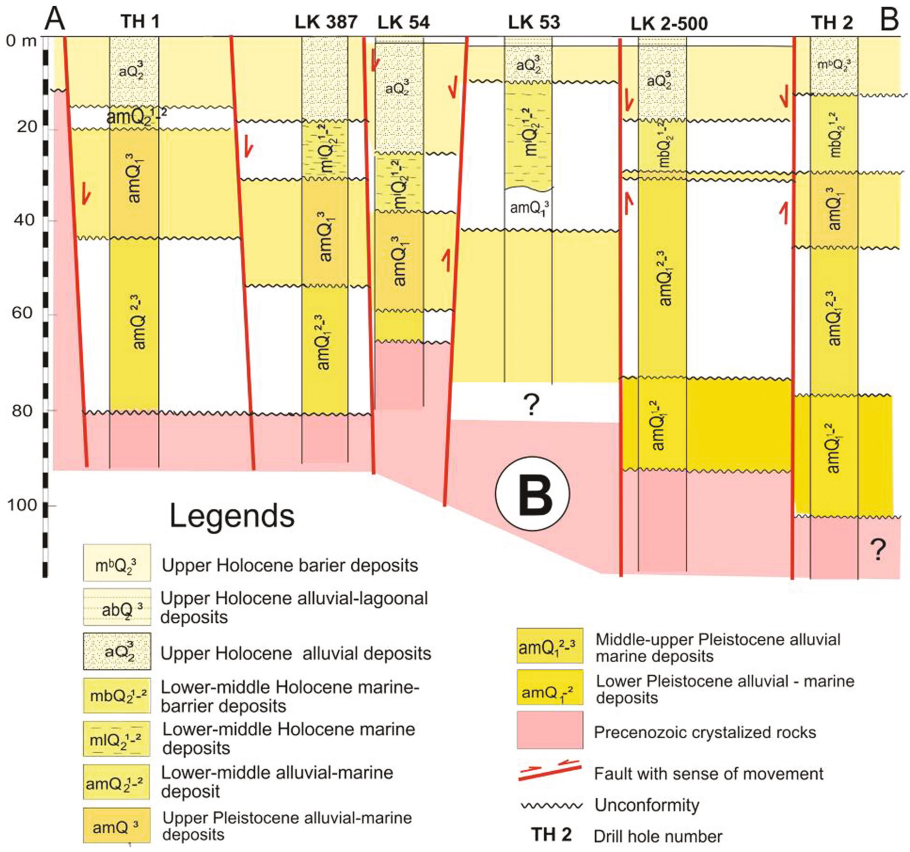

Fig. 2. (*continued*)

Late Jurassic rocks crop put as small unit in the central of Tuy Hoa City, comprising fine-grained terrigenous deposits (Easup Formation-J_2es). Cretaceous rocks comprise mostly felsic volcanic rocks and their tuffs forming parts of the Nha Trang Formation (Knt) that expose in the north of the Tuy Hoa City (Fig. 2).

Within the Tuy Hoa area, Cenozoic sedimentary and subordinate volcanic units occupy large part of the lowland terrane in the central portion and along the coastal zone of the study area (Fig. 2). These comprise two major associations including Neogene to Early Quaternary volcanic and sedimentary units and Quaternary sedimentary sequences (Fig. 2). Neogene units comprise alluvial and/or diatomite-bearing lacustrine deposits that interlayer with basalt and its associated tuffs. They are exposed extensively in the north and northeast portions of the area and have been assigned as parts of the Di Linh Formation (N_1dl) (Fig. 2; [3]). The Quaternary cover comprises subordinate volcanic rocks and predominantly variable unconsolidated sediments and can be classified on the basis of their age and origin (Fig. 2, [3]). Pleistocene deposits comprise basalt, marine-fluvial deposits that form the terraces adjacent to the foot-hill areas in the west, aeolian-marine deposits occur as remnants of sand dunes that scatter

locally along the coastal zone in the north and south-central part of the area. Holocene deposits comprise lacustrine/lagoon, marine, aeolian and fluvial sediments, which occur within the coastal area (Fig. 2).

Intrusive rocks

The area was intruded by large volume of plutonic rocks of varying composition, which are exposed extensively in the southern part of the area (Fig. 2) and have been assigned to several complexes [3, 5]. Oldest intrusive rocks are weakly foliated granitoid of the Carboniferous Ben Giang Complex, which expose as small bodies in the northwest of the area (Fig. 2). Late Jurassic intrusives, which comprise intermediate to felsic rocks, are part of Dinh Quan Complex. They expose as small bodies that scattered in the southern and western parts of the area. Late Cretaceous Deo Ca Complex, which is dominated by coarse-grained granitoid, exposes as batholith bodies in the southern part of the area (Fig. 2). The Paleogene Cu Mong Complex comprises small felsic bodies, dikes and veins that locally cross cut the above complexes.

2.2 Structural Features

All the rocks and Quaternary materials in the area are variable fractured and partly dismembered, which caused by numerous stages of regional deformation. On the basis of field mapping and structural interpretation, a number of tectonic structures can be identified. The major structures include fracture zones and faults of different orientation and ages (Figs. 2 and 3; [14]); some of them are multiple reactivated and remain active during the Quaternary. The faults can be subdivided into paleotectonic and neotectonic systems [15–17]. The paleotectonic faults and fracture systems are those considered to be predated 5 Ma in age whereas those postdated 5 Ma are considered to be neotectonics [17].

Paleotectonic faults and fractures

The Paleotectonic faults and fractures are widely developed within pre-Quaternary rock units and form numerous systems, including northwest-southeast, longitudinally, and northeast-southwest trending (Figs. 2 and 3). This type of structure can be distinguished by a number of direct evidences including large fracture zones, tectonic breccia, slickensides, and fault scarps (Fig. 4). Kinematic indicators within the fault zones show that the relative movements along the faults are complicated: some are reverse whereas the others are strike-slip or oblique slip (Figs. 2 and 3). Many faults are reactivated at least several times, indicated by the presence of overprinting and cross-cutting fault products (Figs. 2, 3, 4, and 5).

Asides major fault zones, fracture systems are also occurred extensively, which commonly led to the dismemberment of the rock units (Figs. 2 and 3).

Neotectonic faults and fractures

Neotectonic faults and fractures are common in the Tuy Hoa area, which are indicated by both direct and indirect evidences. Field observation have found many indicators pointing towards the presence of the neotectonic and active faults including the occurrence of unconsolidated brittle fault gouge zones, brittle slickensides, and open-spaced brittle fractures that cross-cut and/or deformation of Quaternary sediments

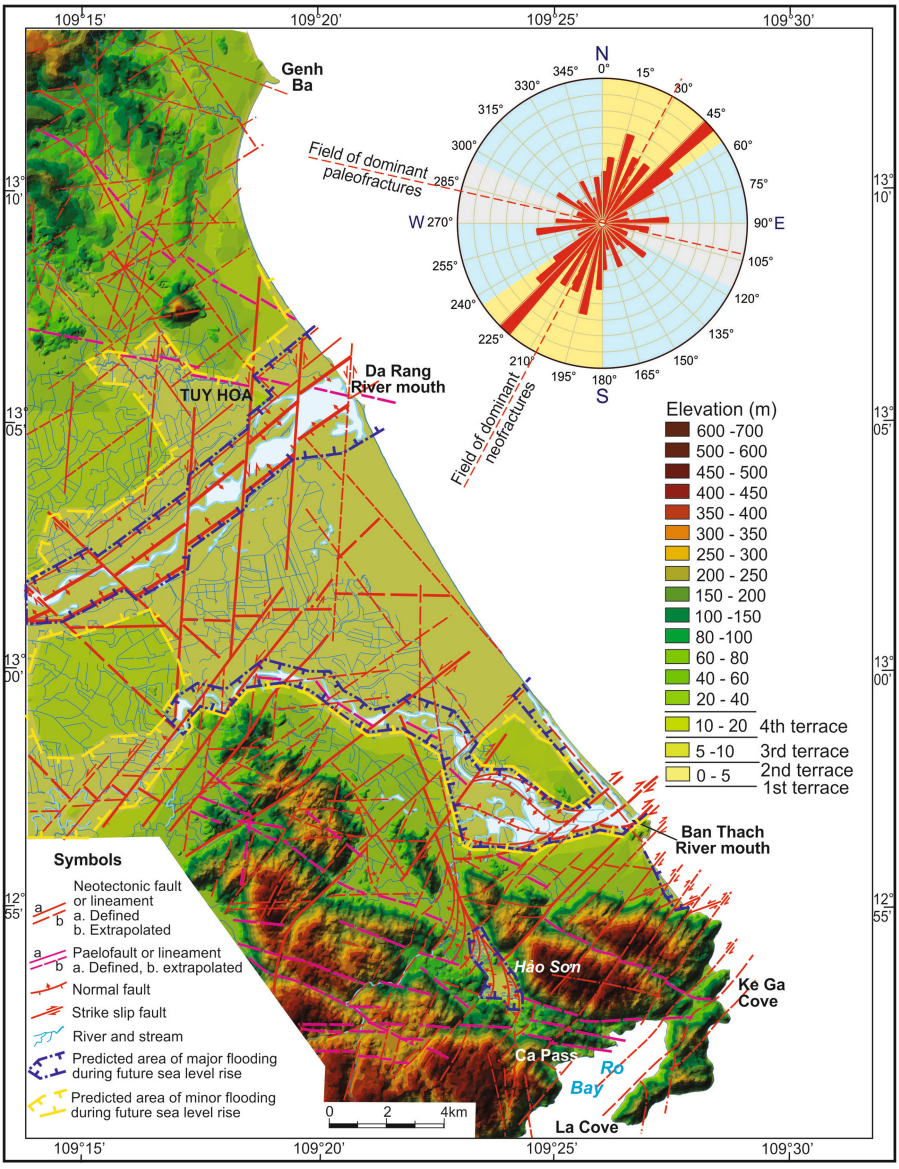

Fig. 3. Digital elevation model map of the Tuy Hoa area showing interpretive faults and fractures combined with results of field observation. Insert shows trends of major faults and fractures systems. The distribution and cross-cutting relationship between the fault and fracture systems indicate the domination of northeast-trending, neotectonic systems that commonly over print older, northwest-southeast trending systems, transect Quaternary deposits, and modify the geomorphological features of the area. The areas of possible effected by flooding due to relative sea level rise in the future are also predicited.

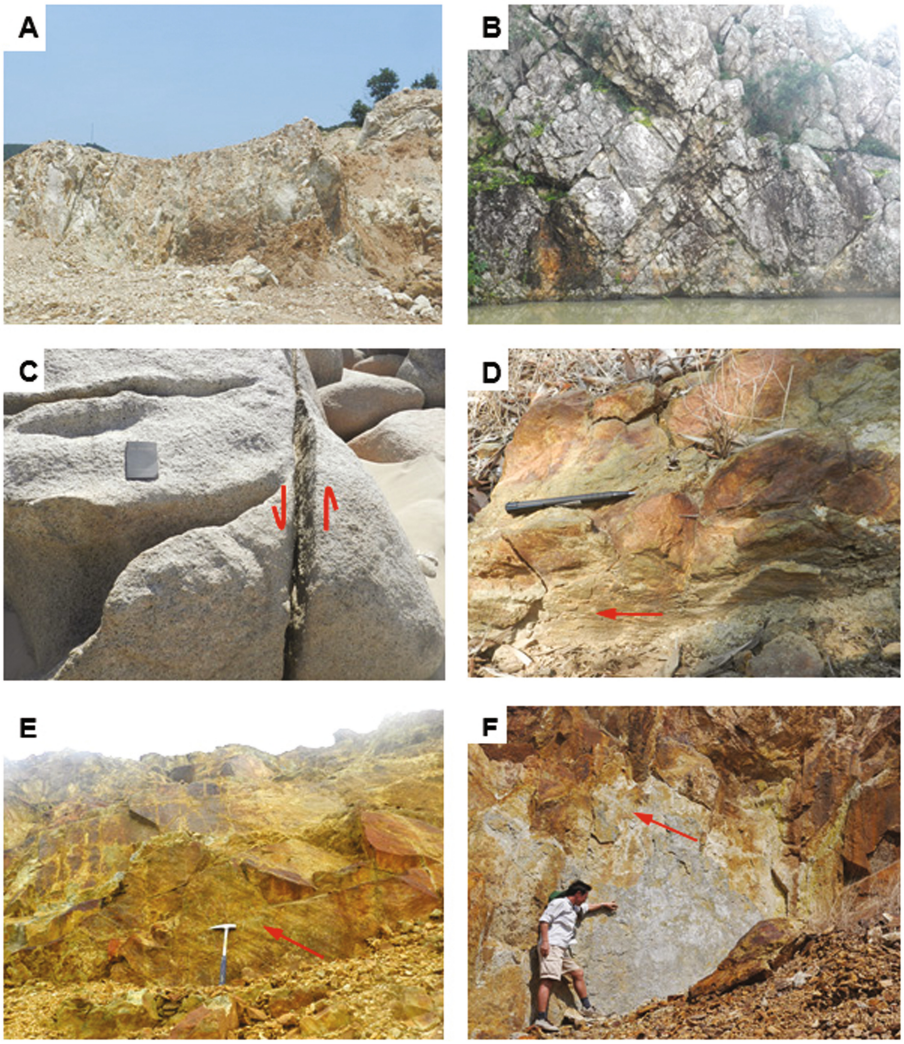

Fig. 4. Outcrop appearance of paleotectonic faults in Tuy Hoa area: A. Large breccia zone developed in granite of Deo Ca Complex crop out in the west of Ke Ga Cove, south of the area (TH15-05). The zone is formed by multiple reactivated faults, which produced large fracture zone; B. A conjugate fracture system cut a large pegmatite dike seen in the southwest of the Tuy Hoa City; C. A single fault zone with related fractures developed in granite of Deo Ca Complex exposed in southeast of the area (TH15-02); D: Part of a mineralized fault zone with slickensides seen in the east of Chop Chai Mount, northwest of Tuy Hoa City. E. Part of a heavily mineralized fault zone exposed in the northwest of Tuy Hoa (TH16-02); F. A mineralized slickenside seen in E. Note the fault surface is cut by younger fault and fractures. Red arrows in figures indicate sense of displacement of the fault walls

and/or weathering profiles (Figs. 2, 3, and 5). In addition, many tectono-geomorphological features related to fault movement such as tectonic lineaments, triangle facets, uneven development and distribution of drainage systems, sudden change of flow direction of drainage systems, abrupt uplift or subsidence of the terranes that governed by faults and fractures [16, 18] are also common in the area (Figs. 2 and 3). In many cases, the neotectonic faults and fractures also reactivated the paleotectonic fault zones were reactivated at least several times during the Quaternary. The opposing slip directions along the faults can be observed or extrapolated (eg., Fig. 2B), which indicates unstable tectonic regime during the Quaternary that have greatly affected configuration of neotectonic sedimentary basins and the spatial distribution of Quaternary deposits within the study area (Figs. 2 and 3).

2.3 Morphological Variation in Tuy Hoa Area

The geomorphology of the Tuy Hoa area comprises several types of landform that formed by a comprehensive processes [19–21]. The current landscapes are resulted from the effects of many geological phenomena including the presence and variability of geologic structures, lithofacies and their physical property, seismicity and tectonic activities, surface and underground water flows, sediment transport and deposition, sea/wave and wind actions, weathering and erosion. On the basis of analysis of overall relationship between morphological appearance with the underlying geological architecture, exogenic processes, and landform associations, several genetic types of morphology are identified in the area, including erosional, fluvial, marine, wind and composite landforms.

Erosional landform is developed on the high-relief area above exposed basement rock units, which are mostly in the south and west of the Tuy Hoa area (Fig. 3). The fluvial-related landform comprises valleys, flood plains and terraces that formed by subsidence, deposition and uplift of the drainage systems (Fig. 3). In many places, the shape and flow patterns of the drainage systems are controlled by the underlying fracture and fault zones (Figs. 2 and 3). Marine related landforms including erosional terraces, low relief plains and shoreline occur along the eastern part of the area (Figs. 2, 3, and 6). Wind-related landform comprises sand dunes that occur as elongated sand hills adjacent to the shoreline in the north and south central portions of the area (Fig. 2).

Composite topography, formed by combination of fluvial-sea-wind actions and tectonic subsidence or uplift processes, is common along the coastal zone and produced some types of composite morphology such as marine-aeolian or fluvial-marine depositional and terrace systems (Figs. 2 and 3).

Local neotectonic movement, including uplift and subsidence or lateral displacement along the neotectonic faults have greatly influenced the formation of current morphology, especially the drainage systems, valleys, and plains ([18, 20, 22–24]; Figs. 2 and 3). Many rivers and streams in the study area either flow along the neotectonic fault and/or fracture zones, or are being offset and diverted their flow due to the movement of the active faults or local uplift/subsidence (Figs. 3 and 4; [18, 24]). The shape and distribution of drainage systems in the study area could also indicate recent tectonism [18, 24] where tectonic uplift commonly lead to the rise of base level and

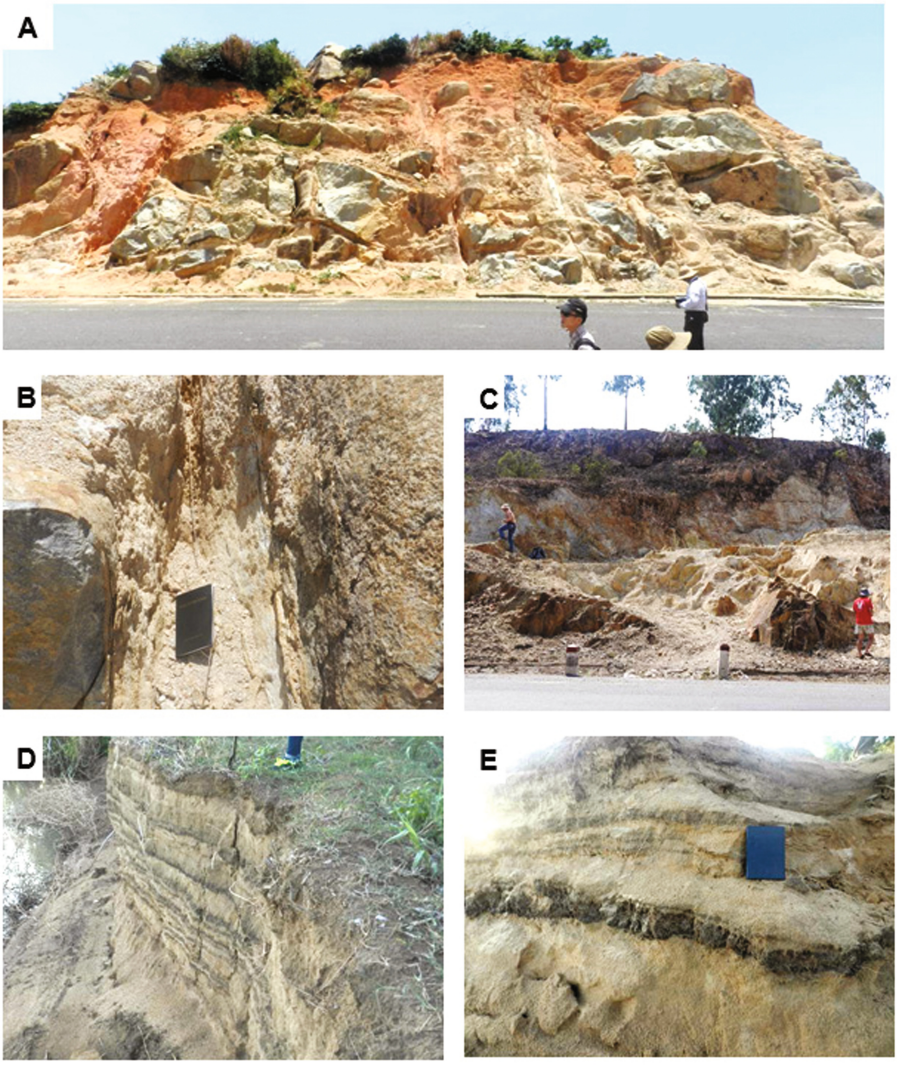

Fig. 5. Examples of outcrop appearance of the Neotectonic faults in Tuy Hoa area: A. Panoramic view of a large fault zone cross-cut the weathering profile in the south of the study area (TH15-06); B. Unconsolidated fault gouge zone as part of A; C. A fault gouge zone developed in highly altered granite of the Ben Giang Complex northwest of Tuy Hoa City (TH16-02); D. Vertical fracture system cross cut Quaternary sediments seen on the left bank of Da Rang River (TH 03-05); E. Tilted and slightly folded Quaternary deposits seen along the Da Rang River bank, which is part of outcrop TH 03-05. Black dots are positions of sample collection for C14 dating (see text for discussion)

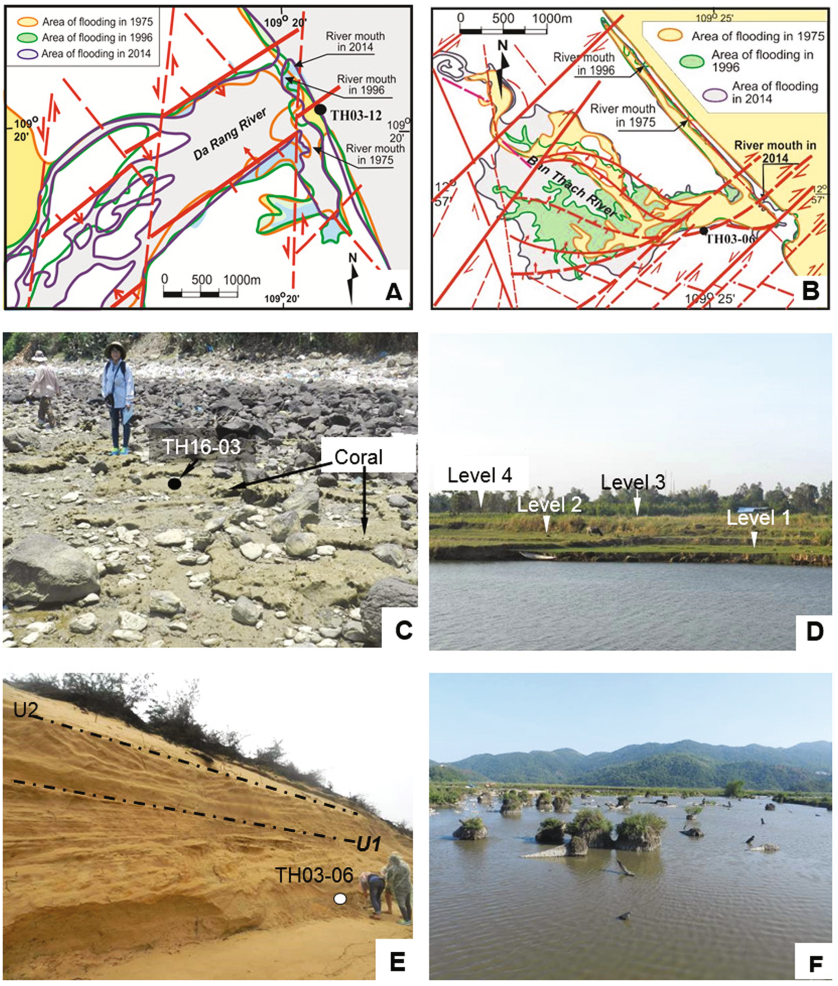

Fig. 6. Examples of morphological features related to tectonic movement along Tuy Hoa coastal zone: A. Lateral shifting of river mouth from south to north and variation of levees of the Da Rang River estuary through time; B. Lateral shifting of Ban Thach River mouth from north to south and the expansion of Ban Thach River basin through time. A and B were constructed based on the interpretation of Landsat and Spot satellite images taken in 1975, 1996, 2014 and modified after [14]. Red lines are faults extracted from Fig. 2. Note the systematic migration of Da Rang River mouth from south to north and Ban Thach River mouth generally from north to south possibly caused by active fault zones (see text for discussion); C. Exposure of uplifted coral remains along the shoreline in Ganh Ba area; D. River terraces developed successively as consequent of uplift of the river basin seen on the north bank of the upstream part of Ban Thach River (TH15-09); E. Exposure of sedimentary units in the right bank of Ban Thach River (TH03-06) showing the unconformable relationship between sedimentary units. The lower unit is well layered marine-lagoon deposits that had been tilted, eroded and unconformably overlain by a sequence of marine-fluvial deposits, which are in turn overlain by aeolian sand. U1 and U2 are angular unconformities between the subunits; E. Part of the Hao Son Lake showing remnants of the ancient plants buried by tectonic-controlled subsidence of the ground that formed an active basin (Area 4 in Fig. 2).

vertical incision, which consequently led to the straightening of the river, development of V-shape valleys, angular and antecedent drainage systems, expansion of deltaic basins through time [20, 24, 25].

In the study area, the general northwards migration of the lower Da Rang River and southwards migration of Ban Thach River mouth during last 40 years (Figs. 2, 7A, and B) indicate differential terrane displacement, uplift or subsidence in different portions of the area, which could be driven by active fault movement. The northwards shifting of the lower course portion of Da Rang River, including its mouth is coincidence with the area of occurrence of major regional cross-cutting fracture and fault systems that currently active (Figs. 2, 3, and 7A) and as such could be controlled by the difference in subsident rate of active faults that run along or cross-cut the river (Figs. 2 and 7A). Similarly, the general southwards migration of Ban Thach River mouth, together with the generation of a pull-apart style basin in the area (Figs. 2 and 7B) could also be controlled by active subsidence along the faults in this area. In addition, the abandonment of stream or rivers, the periodically formation of fluvial and marine terraces as well as exposure of coral reefs or tide marks (Fig. 6), and angular unconformities within the Quaternary deposits in the area are also clear indicators of the terrane uplift. Tectonic subsidence, on the other hand, is also locally observed indicated by the formation of fault-controlled, graben-style valleys such as Hao Son Lake (Fig. 2) and local river basin expansion such as Ban Thach River basin (Figs. 2 and 6B).

2.4 Geological Hazards

In the Tuy Hoa area, geological hazards are common, mostly in the form of landslides and coastal erosion. Landslides, including creep, flow, slide, fall of fragmented rocks, weathered products and debris that take place locally along the Da Rang River banks, hill slopes, roads, and shorelines (Fig. 7). Field observation shows that the landslides are strictly occurred in the areas underlain by fault or fracture zones where the basement rocks are strongly fractured and dismembered, which produced deeply weathered zones (Fig. 7A). Landslides also occur along the river banks (Fig. 7B); many are taken place within the zones of active faulting/fracturing or locally abrupt uplift and/or subsidence, which commonly lead to sudden change of flow pattern of the river systems.

Shoreline erosion is unevenly occurred within the area and mostly takes place in the Da Rang and Ban Thach river mouths areas (Figs. 2, 6A, B, 7C, and D). As discussed earlier, the Da Rang River mouth has migrated northwards (Fig. 6A), whereas the Ban Thach River mouth generally moves southwards (Fig. 6B) during last few decades. Consequently, the shoreline on both sides of the river mouths has also either retreated landwards or expands seawards hundreds of metre (Figs. 6A and B). In addition, the dip-slip movement along the faults also creates local subsidence that leads to local relative sea level rise and landwards invasion of the sea water. The movements along the faults also create zones of local weakness, which in turn exaggerate the chemical and physical weathering and mass wasting and therefore increase the chance for landslide hazards. This process is currently in active, which have led to great damage to infrastructures of the local community (Fig. 7). The major cause of river mouth and shoreline erosion in the area will be discussed in the following session.

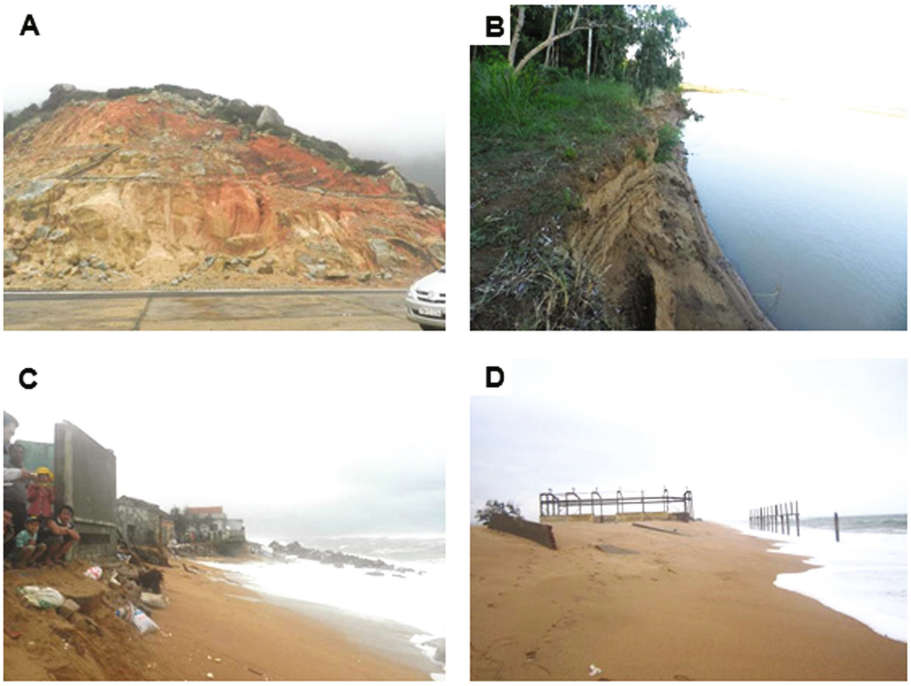

Fig. 7. A. A large landslide occurs above the heavily fractured and weathered granitic basement in southern part of Tuy Hoa area (TH15-03); B. Part of the Da Rang River bank being eroded and collapsed; C and D. Shoreline erosion and beach loose caused by northward migration of Da Rang River mouth together with the subsidence and unstability on both side of the Da Rang River mouth. Note the destruction of village along the coastline in the south side of the mouth (C) and remnant of a ship yard now destroyed and submerged on the north side of the mouth (D).

The study area is considered as a seismic active zone and is part of and seismic generation source zone of Vietnam [27]. Earthquake activity also presents in the study area. Current available data shows that at least a minor earthquake has been recorded recently in Tuy Hoa area in which the quake epicentre locates along some active fault zones in the north of Tuy Hoa city (Fig. 2) with the intensity (Mmax) of up to scale of 5 [26, 27]. The presence of seismic epicentre within the study area, which coincides with the location of neotectonic faults (Fig. 2) strongly demonstrates the active movement of the faults in this area. The occurence of earthquake also signal to a seismic active zone of the study area.

3 Significance of Neotectonic Movement in the Tuy Hoa Area

As mentioned above, the neotectonic movement in the Tuy Hoa area is common, which causes irregular variation in uplift or subsidence along the coastal zone as well as influenced landslide or coastal erosion in the study area. In order to qualitatively

evaluate the nature of recent tectonic movement, 6 samples were collected from organic-rich Quaternary sedimentary units in different locations have been collected for radiocarbon dating (Table 1).

Table 1. Radiocarbon (C14) dating results for organic materials collected from Quaternary sediments in Tuy Hoa area.

No	Sample number	Sample location	Type of dating materials	Age (years BC)
1	TH 16-03/2	Genh Ba	Coral remains	3 000 ± 300
2a	TH14-05/a	Phong Nien Village, Hoa Thang Commune	Upper layer, organic-rich sediments	2 390 ± 215
2b	TH 14-05/b		Lower layer, organic-rich sediments	2 740 ± 220
4	TH03-06	Ban Thach River	Organic-rich sandy sediments	2 210 ± 220
5a	TH 03-11/b	Hao Son Lake, Hoa Xuan South Commune	Pith part of a tree remnant in a peat-bearing layer	2 090 ± 215
5b	TH 03/11/c		Outer part of a tree remnant in peat-bearing layer	1 870 ± 215

3.1 Sample Collection and Analysis for Radiocarbon Dating

A sample (TH 16-03/2) was collected from uplifted and exposed of the basal part of a coral reef at the Genh Ba Commune, north of the study area (Figs. 2, 7C, and 8A). Dating of the exposed coral could be useful for the determination of the minimum uplift rate in this area. Two samples (TH14-05a and TH14-05b) were collected from 2 layers of organic-rich sediments that are separated by a sequence of 0.8 m thick sandy and silty beds (Fig. 5E) that exposes in the west of the study area (Fig. 2). Samples TH03-11b and TH03-11c (Table 1) were collected from root parts of a tree remain, one from the pith (TH03-11c) and the other from the wood (TH03-11b) that occurs uprising at a depth of ca. 1.8 m underneath the Hao Son Lake south of the area (Figs. 2, 6F, and 8B). Sample H03-06 was collected from the top part of a marine-lagoon sedimentary unit under an angular unconformity that exposed along the foot wall of an extrapolated oblique normal fault along the southern margin of the Ban Thach River basin (Figs. 2, 6B, and D).

The radiocarbon dating samples were prepared and analysed for C14 age by the determination of the annual beta dose (Dβ) based on measuring gross beta activity using a Tri-carb 2770TR/SL Liquid Scintillation Analyzer at the Institute of Archaeology of Vietnam. The preparation and analytical procedures and standards were described by [28]. Analytical results are presented in Table 1.

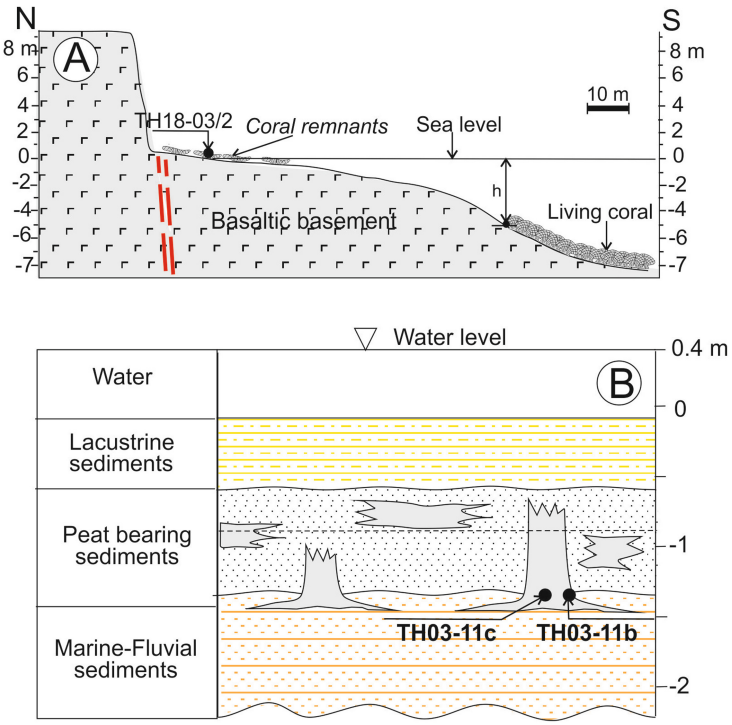

Fig. 8. A. Generalized cross section at Genh Ba area in the north of the Tuy Hoa area showing relationship between uplifted coral and living coral in this area as well as the location of sampling for radiocarbon (C14) dating; B. Generalized stratigraphic column of the peat bearing sediments along the east side of the Hao Son Lake (TH03-11) and location of sampling for radiocarbon (C14) dating. Absolute elevation in the areas was measured by geodetic surveying.

3.2 Interpretation of Analytical Results

Sample TH 16-03/2 yielded an age of 3000 ± 300 BC. The samples were collected from the bottom part of the corals that currently exposed at elevation level of 0 m. Field investigation shows that living corals are resided on the sea bed at a depth range from 5 m to 25 m below the sea level in the area, where samples were collected. Therefore, it is can be assumed that the degree of uplifting of the sea bed and coastal zone in the area is at a minimum of 5 m during last 3000 years, or in other case, the sea level has dropped relatively at a minimum of 5 m since 3000 years ago. If take this minimum uplifted amount into consideration, the rate of the uplift in the area is approximately 1.7 mm per year or 0.17 m per 100 years.

Sample TH14-05a yielded ca. 2390 ± 215 years BC for the upper layer and sample TH14-05b yielded ca. 2740 ± 220 years BC for the lower layer (Table 1). As both layers are tilled, folded and locally uplifted due to active fault movement, the age of the fault movement should be younger than the youngest sedimentary units and therefore should be younger than ca. 2390 years ago.

Sample TH 03/11/b collected from the pith part of the tree remain yielded an age of 2090 ± 215 BC whereas its outer part (TH 03/11/c) is 1870 ± 215 years BC (Table 1). This means that the tree has been grown and then buried at least since 1870 years ago. The vertical subsidence of the ground in the area and the deposition of the sediments has gradually buried the plants, and led to the formation of a basin that filled by surface water forming a swampy Hao Son Lake area (Figs. 2 and 6F). Given the absolute elevation of the sampling locations based on current available geodesic data of 0.4 m and the depth to the sample location of 1.8 m (Fig. 8), the minimum local subsidence rate since the plants were buried can be calculated with the assumption that the present base level (lake surface) remain unchanged since 1870 years ago. The resultant calculated subsidence rate is then equivalent to at least 0.96 mm per year (or ca. 0.1 m per 100 years).

Sample H03-06, collected from the top part of a tilted marine-lagoon sedimentary unit (Fig. 6E), yields an age of 2210 ± 220 years BC. This indicates that the dated sedimentary unit was deposited at least at 2210 year BC before it uplifted, tilted and unconformably covered by younger sedimentary strata (Fig. 6E). Field observation shows that the block in the south of Ban Thach River (Fig. 6B) has been uplifted so that the marine-lagoon sedimentary unit is exposed, whereas the terrane in the north, including the Ban Thach River basin has been subsided relatively (Fig. 6B). The post-ca. 2200 years BC uplifting and tilting of the dated sediments strongly indicates that the faulting and localized ground uplift and subsidence have been active after ca. 2200 years BC.

4 Impacts of Neotectonic Movement to Geohazards in the Study Area

In general, geological hazards in an area can be the combined results of many natural and man-made phenomena including the geological conditions, tectonic activities, climate condition or man-made activities [11, 29–32]. In the case of the study area, the relationship between the geohazards including landslide, riverbank and coastal erosion, beach loss and neotectonic movement including faulting, subsidence and uplift are clearly evident (see above). Field observation and data analysis show that these hazards are closely related to local active tectonic conditions and movement of parts of the study area. These relationships are discussed here after.

4.1 Subsidence and Uplift

The predominant conditions that lead to land subsidence or uplift include the nature of underlying soil and rock types, active tectonic movements, natural and human impacts on ground water level, or other man-made actions such as underground mining [33–36]. These factors must be considered comprehensively while evaluating the cause of land subsidence and uplift.

Land subsidence

Land subsidence may be the result of a number of factors. Compaction of soft sedimentary units or peat may act as a primary cause for land subsidence in many places [34, 36]. However, in the Tuy Hoa area, the overlaying unconsolidated sedimentary units are generally thin and deposited directly on crystalized basement rocks (Fig. 2) and it is unlikely to be a major cause for subsidence. Man-made activities such as underground mining and/or groundwater exploitation may be another cause for land subsidence. This, however, is not be the case for the subsided areas in Tuy Hoa as all subsided areas discussed are located in remote locations with little or no influence of groundwater exploitation or underground mining activities. Instead, the subsided areas appear to be tectonically driven where these areas are controlled by complex networks of neotectonic fault zones (Figs. 2, 7A, and B). In this case, the active movement along the fault systems plays a major role that led to the formation of varied types structural controlled basins or valley [37, 38]. The subsidence of the ground inland would eventually lead to the formation of intracratonal valley or basin, whereas the subsidence along the coastal zone would lead to local relative sea level rise and the landwards invasion of the sea, which eventually result in shoreline erosion and beach loss [16, 31, 32]. This couples with the rate of relative sea level rise caused by global climate change [31, 32, 39]; the local ground subsidence will be exaggerated by the amount of active tectonic subsidence.

In the case of the Tuy Hoa area, a recent calculation of relative sea level rise with intermediate CO_2 emission scenario during the next 100 years has predicted an amount of sea level rise of 0.62 to 0.77 m by the year of 2100 [39]. Given the rate of subsidence calculated from radiocarbon dating for some areas within the Tuy Hoa area discussed above, the prediction of total subsident amount can be calculated.

In this case, if take the amount of maximum 0.77 m of sea level rise due to climate change [39] coupled with the rate of tectonic subsidence calculated above into account,

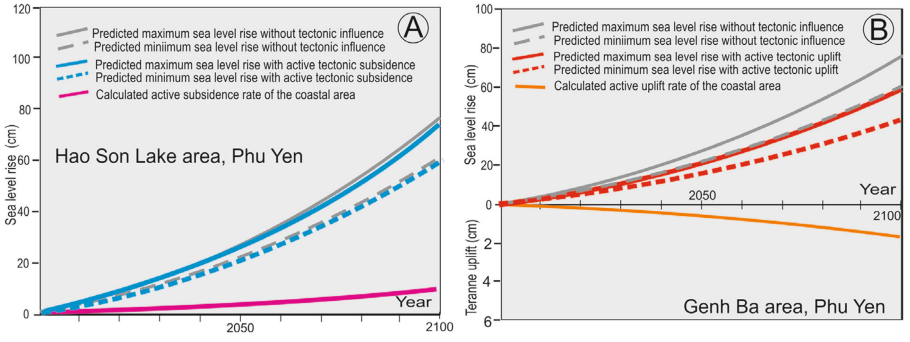

Fig. 9. Generalized diagrams show the relationship between local subsidence or uplift rate and predicted sea level rise scenario [39] in Tuy Hoa area. A. The calculated amount of sea level rise in Hao Son Lake area compared to the predicted sea level curves; B. Calculated amount of sea level rise accounting for the amount of tectonic uplift in the Genh Ba area. Total amount of sea level rise will be the amount of predicted sea level rise minor the amount of tectonic uplift. The sea level rise curves are for the intermediate Carbon emission scenery by [39].

the total amount of sea level rise in the Hao Son Lake area during next 100 years would be at ca. 0.9 m. Given the current high of local base level (lake water surface level) of 0.4 m based on geodesic data obtained by this study (Fig. 9), the sea level would be equivalent to the high of lake surface and therefore the area would be at least submerged under 0.5 m of the sea water by the year of 2100 (Figs. 3 and 9A). Similarly, in the Ban Thach River basin area, rapid local subsidence and basin expansion have been identified (Fig. 6B). As this area is currently submerged under the sea level, in the case of sea level rise, the Ban Thach River basin will be seriously flooded (Fig. 3).

Land uplift

The uplifting of the ground are common along the coastal zone of the Tuy Hoa area, indicated by both morphologic indicators as well as dating of the uplifted materials (see above). The uplifting rate for the Genh Ba area has been calculated at an average of ca. 1.7 mm per year (see above). If relative sea level rise of maximum 0.77 m for the next 100 years [39], the total amount of flooding will be minimized by the amount of tectonic uplift. In this case, it can be predicted that the Genh Ba coastal zone along the north part of the area will be affected by an amount of the sea level rise equivalent to 0.60 m, lower than that predicted without tectonic movement by nearly 0.2 m (Fig. 9B).

4.2 Landslide and Shoreline Erosion

In addition to subsidence and uplift, other types of geological hazards are also commonly found in the Tuy Hoa area in the form of shoreline erosion, and landslide, which

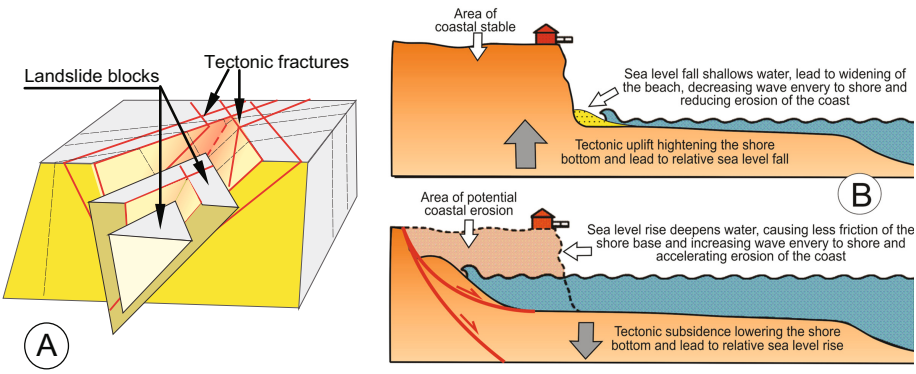

Fig. 10. A. Cartoon model demonstrating the relationship between neotectonic fracturing and the landslide that commonly takes place in Tuy Hoa area. The intersection of many fractures and faults with differing trend and dip leads to dismemberment of the rocks and potentially produce the loose blocks that slide down slop along the fractures and/or faults surfaces (adapted from [6]). B. The impacts of tectonic uplift (upper) and subsidence (lower) to the construction and destruction of the coast. The uplifting leads to relative sea level fall, widening the beach and lowering the wave energy to shore and reducing erosion of the coast. In contrast, the subsidence lead to relative sea level rise deepens water, causing less friction of the shore base and increasing wave energy to shore and therefore accelerating erosion of the coast.

are localized in some areas such as along Da Rang River and the Ban Thach River mouth. Field observation shows that these hazards are commonly related to the sites of structurally weakness or being tectonically active.

Landslide

Landslide commonly occurs in area of strong tectonic deformation, lead to faulting and fracturing of the rocks. While being deformed, the near surface part of the Earth crust commonly takes place in brittle condition, which produces pervasive fracturing. Moreover, large fault zones commonly comprise many branches of smaller faults and fractures, which are occurred not parallel to one another but commonly intersected and lead to the dismemberment of the rock bodies. Thus, the upper crust in tectonically active regions commonly fragmented into blocks down to the scale of boulders or smaller [39]. This not only provide avenue for meteoric water to flow downwards and thus promote chemical weathering and further disintegration of rock but also fragmentate the bedrock into debris that is readily extracted and transported by surface processes ([39]; Fig. 10A).

It also has been demonstrated that the depth of bedrock fracturing influences the magnitude and frequency of landslide response to tectonic uplift [40]. In many places, the local uplift of the upper crust, which result in the variation of relative base-level, cause rapid incision of valleys or erosion of hill slope. The relative motions of fault zones also create differentiation on the topography such as sudden change in elevation along the dip-slip faults or horizontal displacement along the strike-slip faults. As a corollary, the brittle and recently-deformed and dismembered rocks should be more susceptible to detachment and subsequent transport by surface processes [41]. These dismembered parts of the crust are easily to be transported away if the additional parameters such as slope instability, rain fall or other surface processes and man-made activities result in larger and deeper landslides ([40]; Fig. 10A).

Coastal erosion

The destruction of the river levees or coastal erosion constantly takes place along the lower portion of Da Rang River and its mouth (Figs. 2, 3, 6A, 7C, and D) that has led to significant retreat of the shoreline hundreds of metres landwards (Figs. 6A, 7C, and D). In addition, the river mouth have constantly moved northwards during last few decades (Fig. 6A). The causes for coastal erosion have been discussed to comprise numerous factors such as the natural (geological conditions, relative sea level rise, sea current and wave actions, storm) or human effects [42].

Some regional effects such as the global sea level rise, climate, sea current or wave action are region-wide and equally distributed along the coast and can be considered as constant parameters in the study area. Therefore, the localization of hazards within an area of generally coastal stability such as the study area requires additional factors, among which the most important are local subsidence, which lead to local relative sea level rise, instability of the shoreline by active tectonic movement, zones of structural weakness, loss of sediment supply or man-made factors such as construction of dam, dike or ground water exploitation. As in the case of the study area, results of investigation show that most of the eroded coastal areas are relatively underdeveloped with a small population where the exploitation of groundwater is minimized and it is therefore not the case for ground subsidence. Sediment compaction is not a significant cause for

subsidence as unconsolidated sediments commonly form very thin layers along the coastal zone (Fig. 2B; see above). The damping of upstream part of the Da Rang river system for hydropower generation during the last decade may result in the reduction of material supply to the downstream or river mouth and can contribute to shoreline erosion and beach loss recently. In addition, the construction of seawalls, revetments, jetties and detached breakwaters along the eroded area may also cause a negative effect on beaches because these could increase the wave energy when approaching the shore and further carry sand off shore, promoting beach loss. All of above mentioned structures, however have just constructed during last ten years long after the erosion had seriously occurred. In contrast, the coastal erosion and river mouth migration has been constantly taken place for long period of time, far before the man-made structures were constructed. As such, the man-made and surface activities may contribute but cannot be the main cause for shoreline erosion. Instead, the problem of shore erosion and beach loss shall be exaggerated if the area is affected by modern tectonic activities [43–45]. Therefore, the strongly fragmented and unstable basement and active tectonic motions within the Tuy Hoa area, which have been discussed above, are main factors for coastal erosion in the Da Rang River mouth. In this case, the subsidence and recent movements along the neotectonic faults (Figs. 2 and 3) are the governing factors that lead to the localized unstability of the coastal zone, migration of the river mouths subsidence, and resultant relative sea level fall, which consequently result in the coastal erosion in the Da Rang River and Ban Thack River mouth areas (Fig. 10).

5 Conclusions

Field observation and analysis of the geological structural pattern and its relationship to the active tectonic activities and geological hazards in Tuy Hoa area reveals a complex regional structural framework produced by a multiphase deformational history that is still in active in Central Vietnam. Modern tectonic activities have played an important role in the shaping of present-day geomorphology and coastal landscapes of the area. The overprinting neotectonic activities, in the form of non-penetrative, highly fractured zones on older structures resulted in localized vertical movements and horizontal displacements, which led to the local uplift, subsidence, tilting, fracturing, or dismemberment of both basement and Quaternary sedimentary cover. The qualitative documentation of volume of tectonic uplift and/or subsidence have led to more accurate estimation and prediction of the degree of local subsidence and uplift in the context of sea-level rise scenario.

The combination of all structural elements with the exogenic processes have resulted several types of geological hazards within the area. Neotectonic movements have led to local subsidence and uplift, which led to the formation of tectonic-controlled subsided basins within area of generally regional uplift. Whereas the cross-cutting structures lead to bedrock fragmentation that enhance significantly the exogenic processes including weathering, hill slope and drainage activities that caused the development of geological hazards such as landslide, riverbank and coastal erosion in the area.

Thus, neotectonic activities and their related tectonic structures, especially active ground movements are important controlling factors in the shaping of modern morphology, landscape, as well as geological hazards of the Tuy Hoa area and probably other parts of the central coastal zone of Vietnam. Proper identification of all types of structures, especially those produced by or related to neotectonic activities are therefore important and must be properly addressed in any geological study of the coastal areas, especially in assessment and prediction of natural hazards in the context of global sea level rise caused by global warming and climate change.

Acknowledgement. This work is funded by the National Project BDKH 13/16-20 to the author under the Science and Technology Program for the National Focus Program on Climate Change Responses No. KHCN-BDKH/16-20 led by the Ministry of Natural Resources and Environment of Vietnam.

References

1. Tran, D.L., Nguyen, X.B.: Geological Map of Vietnam scale 1:500 000 (Vietnamese). Department of Geology, Hanoi (1982)
2. Tran, T.: Geology and Mineral Resources Map of Vietnam scale 1:200,000, Tuy Hoa Sheet. Department of Geology and Minerals of Vietnam, Hanoi (1997)
3. Truong, K.V.: Report on the results of geological mapping and mineral resources prospecting, Tuy Hoa map sheets, scale 1:50000. Department of Geology and Minerals of Vietnam Achieves (1997)
4. Tong, D.T., Vu, K.: Stratigraphic Units of Viet Nam. Vietnam National University Publisher, Hanoi (2006)
5. Tran, V.T., Vu, K.: Geology and Natural Resources of Vietnam. Natural Sciences and Technology Publishing House, Hanoi (2011)
6. Tran, T.H. (ed.): Research and evaluation of active tectonics in central Vietnam coastal area and its role for the natural hazards for predicting and mitigation of natural hazards in the climate change condition (Vietnamese). Final Report of National Project BĐKH.42 (2015)
7. Pham, V.H.: Characteristics of neotectonic faults in South Central Vietnam. Geological Institute, Ph.D. Thesis. Academy of Science and Technology of Vietnam, Hanoi (2002)
8. Dao, M.T. (ed.): Report on investigation of geology, mineral resources, geological environment and geohazards in the South Central Sea area from 0 to 30 metres depth and some focus areas at 1:50.000 (2004)
9. Phan, M.N., Nguyen, T.T.H.: Studying the impacts of dredging on changes in erosion and deposition in da dien estuary area, Phu Yen Province. In: 9th Scientific Conference, Abstract. Ho Chi Minh City (2014)
10. Bell, F.G.: Geological Hazards: Their Assessment, Avoidance and Mitigation. Taylor & Francis, New York (2003)
11. McGuire, B., Maslin, M.A.: Climate Forcing of Geological Hazards. Wiley-Blackwell, Oxford (2013)
12. Bubeck, A., Wilkinson, M., Roberts, G.P., Cowie, P., McCaffrey, K., Phillips, R., Sammonds, P.: The tectonic geomorphology of bedrock scarps on active normal faults in the Italian Apennines mapped using combined ground penetrating radar and terrestrial laser scanning. Geomorphology **237**, 38–51 (2015)

13. Pha, P.D., Yen, T.H.: Development History of Quaternary Sediment formations in Tuy Hoa Plain. J. Mar. Sci. Technol. **12**, 136–143 (2012)
14. Bui, T.M., Nguyen, T.V., Mai, V.C.: Neotectonic deformation in the Tuy Hòa area, Phú Yên Province and its significance for geological hazards. J. Geol. **355**, 22–33 (2016)
15. Pirazzoli, P.A.: Tectonics and neotectonics. In: Schwartz, M.L. (ed.) Encyclopedia of Coastal Science, pp. 941–948. Springer, Amsterdam (2005)
16. National Research Council (NRC): Active Tectonics: Impact on Society. Study in Geophysics (1986)
17. Moores, E.D., Twiss, R.J.: Tectonics. Freeman and Company, New York (1995)
18. Burbank, D.W., Anderson, R.S.: Tectonic Geomorphology. Wiley, Hoboken (2011)
19. Ritter, D.F., Kockel, R.C., Miller, J.R.: Process Geomorphology. Waveland Press Inc., Long Grove (2002)
20. Ritter, M.E.: The Physical Environment: An Introduction to Physical Geography (2006). http://www.earthonlinemedia.com/ebooks/tpe_3e/title_page.html
21. Huggett, R.J.: Fundamentals of Geomorphology. Taylor & Francis E-library (2007)
22. Easterbrook, D.J.: Principles of Geomorphology. McGraw-Hill Book Company, New York (1969)
23. Pidwirny, M.: The drainage basin concept. In: Fundamentals of Physical Geography. Physical Geography.net (2006)
24. Schumm, S.A., Dumont, J.F., Holbrook, J.M.: Active Tectonics and Alluvial Rivers. Cambridge University Press, Cambridge (2000)
25. Hurtrez, J.E., Lucazeau, F., Lavé, J., Avouac, J.P.: Investigation of the relationships between basin morphology, tectonic uplift, and denudation from the study of an active fold belt in the Siwalik Hills, central Nepal. J. Geophys. Res. Solid Earth **104**, 12779–12796 (1999)
26. Nguyen, H.P., Pham, T.T.: Probabilistic seismic hazard maps of Vietnam and the East Vietnam Sea. J. Mar. Sci. Technol. **15**, 77–90 (2015)
27. Nguyen, H.P., Pham, T.T., Nguyen, T.N.: Probabilistic seismic hazard assessment for the Tranh River hydropower plant No2 site, Quang Nam province. Vietnam J. Earth Sci. **38**, 181–203 (2016)
28. Nguyen, Q.M., Bui, V.L.: Determination of the annual beta dose by meaming beta activity using the liquid scintillation technique. VNU J. Sci. Math. Phys. **24**, 36–41 (2008)
29. Montgomery, C.W.: Environmental Geology, vol. Engineering. McGraw-Hill Science, New York (2010)
30. Keller, E.A., Pinter, N.: Active Tectonics: Earthquakes, Uplift, and Landscape. Prentice Hall, Upper Saddle River (2001)
31. N.O.A.A.: Incorporating sea level change scenarios at the local level (2012). http://www.csc.noaa.gov/digitalcoast//pdf/slcscenarios.pdf
32. N.O.A.A.: Technical considerations for use of geospatial data in sea level change mapping and assessment. NOAA Technical report NOS 2010-01 (2010)
33. Bloch, E.A.: Effects of subsidence, sea-level rise, and erosion. In: GIS & GPS Applications in Earth Sciences, pp. 1–24 (2009)
34. Kooi, H.: Land subsidence due to compaction in the coastal area of The Netherlands: the role of lateral fluid flow and constraints from well-log data. Global Planet. Change **27**, 207–222 (2000)
35. Holzer, T.L., Galloway, D.L.: Impacts of land subsidence caused by withdrawal of underground fluids in the United States. Rev. Eng. Geol. **16**, 87–99 (2005)
36. González, J.L., Tornqvist, T.E.: Coastal Louisiana in crisis: subsidence or sea level rise. EOS Trans. Am. Geophys. Union **87**, 493–498 (2006)
37. Frisch, W., Meschede, M., Blakey, R.C.: Plate Tectonics: Continental Drift and Mountain Building. Springer, Heidelberg (2011)

38. Wu, J.E., McClay, K., Whitehouse, P., Dooley, T.: 4D analogue modelling of transtensional pull-apart basins. Mar. Pet. Geol. **26**, 1608–1623 (2009)
39. Ministry of Natural Resources and Environment (MONRE): Climate Change, Sea Level Rise Scenario for Vietnam Resources. Environment and Maps Publisher, Vietnam (2012)
40. Clarke, B.A., Burbank, D.W.: Bedrock fracturing, threshold hillslopes, and limits to the magnitude of bedrock landslides. Earth Planet. Sci. Lett. **297**, 577–586 (2010)
41. Molnar, P., Anderson, R.S., Anderson, S.P.: Tectonics, fracturing of rock, and erosion. J. Geophys. Res. **112**, 2156–2202 (2007)
42. http://www.coastal.wiki.org
43. Schwartz, M.L.: Beaches and Coastal Geology. Springer, Heidelberg (1982)
44. Genter, A., Duperret, A., Martinez, A., Mortimore, R.N., Vila, J.-L.: Multiscale fracture analysis along the French chalk coastline for investigating erosion by cliff collapse. Geol. Soc. London Eng. Geol. Special Publ. **20**, 57–74 (2004)
45. Kennedy, D.M., Stephenson, W.J., Naylor, L.A.: Rock Coast Geomorphology: A Global Synthesis. Geol. Soc. Mem. **40**, 304 (2014)

Isotopic and Hydrogeochemical Signatures in Evaluating Groundwater Quality in the Coastal Area of the Mekong Delta, Vietnam

Tran Dang An[1,2(✉)], Maki Tsujimura[1], Vo Le Phu[3], Doan Thu Ha[4], and Nguyen Van Hai[2]

[1] School of Life and Environmental Sciences, University of Tsukuba, Tsukuba, Japan
anctn2014@gmail.com
[2] Department of Water Resources Engineering and Environment, Thuyloi University, Ho Chi Minh City, Vietnam
[3] Faculty of Environment and Natural Resources, Ho Chi Minh City University of Technology (HCMUT) – VNU HCM, Ho Chi Minh City, Vietnam
[4] Department of Water Supply and Drainage System, Thuyloi University, Hanoi, Vietnam

Abstract. In the 21st century, fresh water scarcity is perhaps one of the biggest challenges in many coastal regions worldwide due to the rapid population growth, fast urbanization and unpredictable impacts of global climate change. Given this context, the identification of groundwater status is a crucial task for sustainable groundwater use and management practices in coastal areas around the world. This work, conducted in coastal areas of Soc Trang province, is an effort to assess groundwater quality and its controlling factors in a coastal area of the Mekong Delta, Vietnam. In this study, we investigate groundwater quality based on chemical parameters, stable isotopes ($\delta^{18}O$, $\delta^{2}H$) and saturation indices (SI). The study showed that groundwater in the study area is mainly classified into four groups: Na-Cl, Na-Mg-Ca-HCO3, Na-Mg-Ca-HCO3-SO4 and Na-HCO3-Cl. Groundwater quality might be substantially controlled by the rock-water interaction, particularly by mineral dissolution and ion-exchange process. Further, the stable isotopes and saturation indices depict the origin of salt water presenting in the aquifers because of three factors, including paleo-saline water dissolution at deeper aquifers, seawater intrusion into shallow aquifers and saline water diffusion at middle aquifers. This result suggests that the characteristics of hydrogeology, inappropriate groundwater pumping activities and change of hydrological regimes might be the main driving forces of disturbance groundwater flow systems and expansion of saline boundary in the coastal areas of the Vietnamese Mekong Delta.

Keywords: Stable isotopes · Hydrogeochemistry · Groundwater quality · Soc Trang · Mekong Delta

© Springer International Publishing AG 2018
D. Tien Bui et al. (eds.), *Advances and Applications in Geospatial Technology and Earth Resources*, https://doi.org/10.1007/978-3-319-68240-2_18

1 Introduction

It is widely recognized that fresh water shortage is becoming the most challenge for satisfying domestic, industrial and agricultural water demands in many countries around the world in the 21st century [1, 2]. As groundwater is a largely invisible resource, its dynamic change of quantity and quality is difficult to grasp even for experts [3]. Understanding the groundwater quality and its controlling factors, therefore, is the critical task for groundwater planning and management, ensuring sustainability of safe water use for national and global socio-economic development [4].

In natural conditions, groundwater moves slowly through the aquifer system under controlling by geological characteristics, hydrological and geological processes [5–8]. However, the human development might disturb this process, resulting in the serious changes of groundwater quality. The groundwater depletion due to excessive extraction and significant land-use changes, for instance, results in many groundwater quality-related problems, especially arsenic release from soils and sediments into groundwater [9–13], heavy metals and nitrate contamination [14–19], as well as the adverse seawater intrusion into coastal aquifers worldwide [20–25]. Additionally, the unpredictable impacts of climate change and sea level rise in the coastal regions might potentially accelerate the degradation of groundwater quality and put this resource be likely high crisis [3, 26, 27]. This fact, thus, poses the biggest issue to sustainable water management in coastal regions around the world in this century [26, 28].

Over the last several decades, hydrochemistry and stable isotopes have been widely applied to understand hydrological processes and groundwater evolution such as mixing different water sources, mineral weathering and evaporating [29–33]. Recently, by employing hydrochemistry and stable isotopes techniques, many studies [23, 34–37] has been proven that the deterioration of groundwater quality in many coastal regions is a result of excessive groundwater extraction and significant land-use changes coupled with unpredictable impacts of climate change, and sea level rise. As the intensive human development and natural dynamic might cause the changes of hydrogeological characteristics and groundwater quality, the combination of chemical and stable isotopes signatures, therefore, is a unique tool for investigating groundwater characteristics and suitable groundwater quality for drinking and irrigation [38].

Groundwater is a key resource for socio-economic development in the Vietnamese Mekong Delta region. The long-term exploitation and inappropriate management of groundwater, however, has resulted in many severe issues in the Mekong Delta, especially land subsidence [39] and arsenic contamination related to serious public health problems [40–42]. Some previous studies such as Ho et al. [43], Khoi et al. [44] and An et al. [45] employed the stable isotopes and hydrochemistry to understand the groundwater quality in term of salinization in the Mekong Delta. Yet the contribution of geological features and groundwater exploitation activities to hydrochemical characteristics and groundwater quality in the coastal area of the Mekong Delta has remained unknown. Meanwhile, towards sustainability of groundwater use and management in the context of rapid socio-economic development and natural variation requires an in-depth understanding not only groundwater characteristics but also the

main driver. The study, therefore, is the first effort to investigate groundwater quality and its controlling factors based on hydrogeochemical and stable isotopes signatures in a coastal area of the Vietnamese Mekong Delta.

2 Study Area

2.1 Location and Climatic Background

The study area – Soc Trang province is located at a low-lying part of the Mekong River Basin, reaching directly to the East Sea of Vietnam. It covers approximately 2311.76 km^2 and accounts for around 0.7% and 5.9% areas of Vietnam and Mekong Delta, respectively with an average population of 1,310,700 people (General Statistics Office of Vietnam 2015). The study site falls in a strong tropical monsoon region with two distinguish seasons, the dry and rainy seasons. In the rainy season, climate condition is strongly affected by the Southwest Monsoon, which brings more than 85% amount of annual rainfall, having a high temperatures and humidity. Meanwhile, the Northeast Monsoon dominates in the dry season from November until April, contributing to 15% of the annual rainfall with a relative low temperature and humidity. The average annual air temperature is 26.8 °C with over 36 °C in the warmest months (April and May) and the lowest mean monthly temperature in January is around 24 °C; average annual relative humidity of 84%; and annual precipitation of 1,772 mm with low rainfall from January to April. As relative low lying inland (0.5–2.5 m above mean sea level) and reaching directly with East Sea, the hydrological regime in the Delta, therefore is strongly controlled upstream discharge, local rainfall and river-marine dynamic interactions. These factors remarkably affect water quality of both surface water and groundwater sources in this region.

2.2 Hydrogeology

The geology and geomorphology of Soc Trang province were formed by the glaci-eustatic sea-level change and the ongoing tectonic subsidence of the Mekong River Basin, therefore, its hydrogeology is somewhat complex [46]. In general, hydrogeology consists of seven distinct aquifers namely, Holocene (qh), Upper Pleistocene (qp_3), Upper-Middle Pleistocene (qp_{23}), Lower Pleistocene (qp_1), Middle Pliocene (n_{22}), Lower Pliocene (n_{21}), Upper Miocene (n_{13}) aquifer layers. Generally, the lithology of each aquifer consists of fine to coarse sand, gravel, and pebbles (Fig. 2).

The Holocene layer (qh) was formed from the coarse-grained rocks sedimentary rocks originating from mainly three types of sediments, including: Lower to Middle Holocene sediments (qh_{1-2}) of alluvial and marine origin composed dominantly of clayey silt and fine sand and are rich organic compositions. Alluvial, marine and eolian sediments (qh_{2-3}) include 1.0–12.0 m below ground level (mbgl) thick remnants of sand dunes from paleo-sea shores which can be found in Long Phu, Vinh Chau, Soc Trang and My Tu districts. These sand dunes are often shaped arc extends parallel with the coast of the northeast - southwest or northwest – southeast, extending from 3.0 to

4.0 km along the coast and distributing around 200–300 m from the shoreline to inland. Upper Holocene sediments (qh_3), accumulated in the river valleys and flood plains, consists of clayey silt, silt-mud, and fine sand. Slug tests results of wells in this area point out that groundwater flow rate (Q) ranges approximately 0.20–0.50 L/s (aveg. 0.30 L/), drawdown (S) is 0.30–0.70 m (aveg. 0.53 m) (Fig. 1).

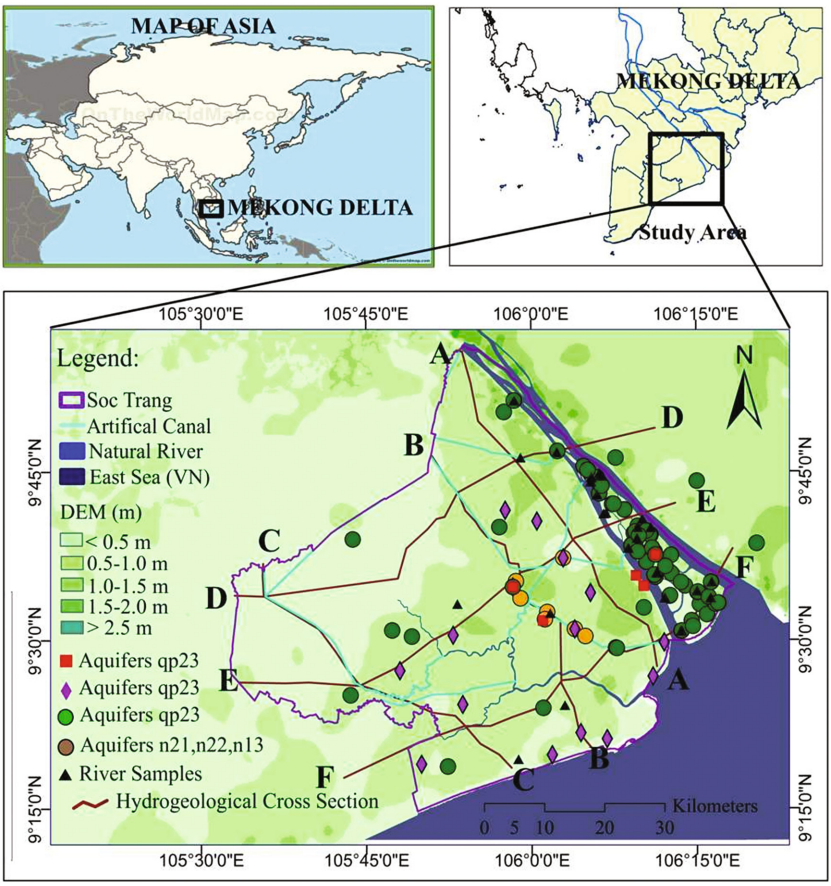

Fig. 1. Sampling locations in Soc Trang Province, Vietnam

The Upper Pleistocene unit (qp_3) is widely distributed over the whole Soc Trang province, mainly overlaying by Holocene sediments. This aquifer was formed by coarse-grained sedimentary rock formations of Long My (mQ13 lm), composed mainly of fine sand, fine gravel and medium and small gray-green shells, gray and white sand with thickness changing 3.0–50.9 m (aveg. 20.50 m). Hydro-geologically, qp3 strata could be divided into two parts: The Lower part of the high permeable aquifer is covered by an upper part of low permeable aquitards, generally consisting of silt to a clay-size fraction. The top of qp3 aquifer distributes heterogeneously with a depth of

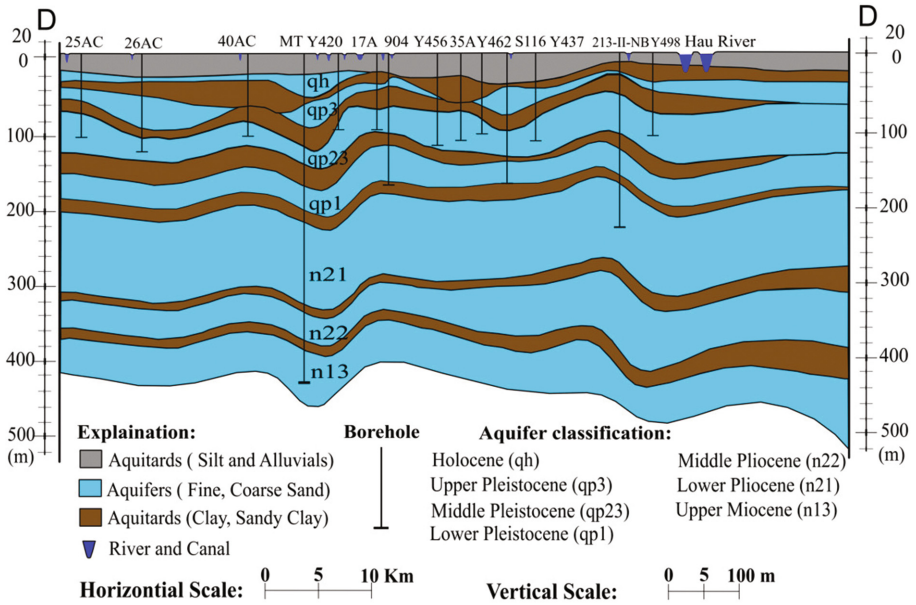

Fig. 2. Hydrogeological cross section D-D of Soc Trang Province, Vietnam

24.0 m–95.0 mbgl (aveg. 50.39 mbgl) and its bottom ranges around 30.0–125.0 mbgl (aveg. 70.74 mbgl). There is limited slug test result of the qp3 aquifer, however, based on analyzing the thickness and grain size suggests that groundwater flow rate of this aquifer is 0.185 L/s–0.195 L/s.

Middle Pleistocene aquifer (qp_{23}) was overplayed by Upper Pleistocene (qp_3). The lithology is dominantly composed of alluvial sediments, marine alluvial and marine origins from Long Toan formations system. The aquifer covers and distributes widely throughout the province. This aquifer is also divided into a low permeable part, composing silt and clay, which can be encountered in depth from 54.0 mbgl to 137.0 mbgl (aveg. 83.63 mbgl). A confined aquifer represents the low part, consisting of well stored and high permeable fine to coarse sand mixing with gravel sand and thin lenses of clay powder in the depth of 92.0–175.0 mbgl (aveg. 131.47 mbgl). The thickness of this part ranges from 7.0 m to 81.0 m (aveg. 49.75 m). The composition is mainly coarse sand in various sizes containing water. The result of pumping test showed that water absorption is very high in aquifers with groundwater flow rate from 9.05 to 19.10 L/s (aveg. 14.57 l L/s), drawdown (S) is 2.51–18.81 m (aveg. 10.31 m).

Lower Pleistocene aquifer (qp_1) is generally formed from the coarse-grained rock under the bottom part of the Binh Minh formation system (m, amQ11bm). Lithology consists of dominate fine to coarse sand and less gravel. The qp_1 aquifer is widely distributed over the whole Soc Trang province. The depth of the top part of the qp1 aquifer varies from 110.50 mbgl to 192.0 mbgl (aveg. 145.29 mbgl) while that of bottom part ranges from 146.00 m to 250.0 m (aveg. 187.40 m). The thickness of the aquifer varies from 6.0 m to 79.50 m (aveg. 40.29 m depth). The static groundwater

level of this aquifer varies from −0.50 m to −8.78 m above sea level (masl) with an aveg. of −1.78 masl. The slug test result shows that this aquifer has very high groundwater flow rate (Q) distributing from 12.26 to 33.90 L/s (aveg. 17.92 L/s), drawdown (S) ranges 2.571–13.55 m (aveg. 8.48 m).

Since the last several decades, the Middle Pleistocene (qp_{23}), Lower Pleistocene (qp_1) have become the most attractive aquifer for groundwater pumping practices as they have high potential groundwater capacity and also good quality compared to remaining aquifers [45]. Recently, however, groundwater degradation has occurred in many parts of these aquifers due to intensive groundwater withdrawal with approximately 200 wells/km^2. Consequently, the residents have to access groundwater at deeper aquifers (n_{21}, n_{22} and n_{13} aquifers). This fact coupled with the changes of recharge pattern into aquifer system, seawater intrusion obviously poses a big challenge to the sustainable use and effective management practices of water resources in the study area.

3 Materials and Method

3.1 Data Collection and Analysis

During 2013 and 2014, a hundred and forty-two groundwater and surface samples were collected and stored into 100 ml plastic bottles. The water samples drive from households' wells, municipal groundwater treatment plants and monitoring boreholes both shallow (qh - Holocene, qp_3 - Upper Pleistocene), and deep aquifers (qp_{23} - Middle Pleistocene, qp_1 - Lower Pleistocene, n_{22} - Middle Pliocene, n_{21} - Lower Pliocene and n_{13} - Miocene) with an average depth of wells ranges from 4.5 m to 480 m below ground level (m.bgl). The water chemistry characteristics were on-site measured using HANNA portable instruments, including: pH, Dissolved Oxygen (DO), Electrical Conductivity (EC), and Total dissolved solids (TDS).

All water samples were filtered with a 0.02 μm cellulose ester filter before analyzing chemical and stable isotopes compositions. The bicarbonate (HCO_3^-) was deduced by using the titration method with sulfuric acid (0.05 M H_2SO_4). Major anions (Cl^-, SO_4^{2-}, and NO_3^-) were analyzed using ion liquid chromatography (Shimadzu Co. Ltd., HIC-SP/VP Super) at the Hydrological sciences laboratory in the University of Tsukuba. The main cations (Na^+, K^+, Ca^{2+} and Mg^{2+}) were analyzed using inductively coupled plasma optical emission spectrometer (ICP-OES, PERKIN ELMER, Optima 7300) at the Center of Chemical Analysis, University of Tsukuba, Japan. The stable isotopes of water samples were analyzed with a Finnigan MAT 252. Results were expressed relative to the international standards (V-SMOW for $\delta^{18}O$ and δ^2H) represented in ‰ the uncertainties were ±0.1‰ for $\delta^{18}O$ and ±1‰ for δ^2H.

3.2 Graphical and Geochemical Techniques

The Piper diagram was employed to classify water types in the study area, and the geochemical process was analyzed by using inverse-geochemical model. Geochemical modeling is a useful tool to determine the thermodynamic processes, which control

groundwater quality [8, 31]. It simulates the mass balance with responses to chemical reactions and geochemical processes such as mineralization, gasses dissolution and precipitation throughout different hydrogeological settings. In this study, the Saturation Indices (SI) of minerals were calculated by using PHREE QC version 3 model [47]. The SI of a mineral is defined as Eq. (1) as followed:

$$SI = \log(IAP/Ks) \quad (1)$$

where IAP is the ion activity product of the mineral-water reaction, and Ks is the thermodynamic equilibrium constant adjusted to the temperature of the given sample. The SI values depict three states of saturation including saturation (SI = 0), undersaturation (SI < 0), and supersaturation (SI > 0). The result of SI is useful information to understand the different hydrogeochemical processes that have been occurring in the specific aquifers. In this study, five major saturation indices were calculated to understand hydro-geochemical processes of groundwater in coastal aquifers including saturation index of calcite (S_{Cal}), dolomite (S_{Dol}), anhydrite (S_{An}), gypsum (S_{Gyp}) and halite (S_{Ha}).

4 Results and Discussion

4.1 General Hydrogeochemistry

Table 1 shows the statistical analysis of water chemistry in Soc Trang province. Obviously, the groundwater temperature in all aquifers in study site is relatively different between shallow and deep aquifers ranging from 25.0 °C to 40.3 °C, respectively. The pH values of shallow (qh, qp_3), middle (qp_{23}, qp_1) and deep aquifers (n_{21}, n_{22}, n_{13}) range from 6.52 to 7.05 and 6.53 to 8.68 with an average of 7.05 and 7.99, respectively. The changes of alkalization processes among these aquifers with high pH values suggest the interaction between soil, rain water and groundwater along flow path [8], while low pH value may be attributed to dilution and reaction between acid sulfate soils and groundwater [48, 49].

The DO varies widely among aquifers, ranging from (1.16–2.37) mg/L to (2.36–3.62) mg/L for shallow and deep groundwater, respectively. The EC values of groundwater samples were significant difference among aquifers with 906–21,200 µS/cm; 116.7–4,760 µS/cm and 204–13,720 µS/cm for (qh, qp_3), (qp_{23}, qp_1) and (n_{21}, n_{22}, n_{13}) aquifers, respectively. For a century, groundwater from middle aquifers (qp_{23}, qp_1) and deeper aquifers (n_{21}, n_{22}, n_{13}) has become an important fresh water source for the Mekong Delta, especially along coastal areas because this is the only freshwater sources with high yields, good quality and cost-effective extraction. Conversely, shallow groundwater has very high salinity (TDS > 1000 mg/L) and is unsuitable for drinking and irrigation purposes. The wide variation of ionic composition reflects the complexity of groundwater evolution processes in different aquifers. Although groundwater samples of the (qh, qp_3) and the (n_{21}, n_{22}, n_{13}) aquifers were dominantly occupied by sodium (Na^+) and chloride (Cl^-), these aquifers showed different trends of salinity concentration. For instance, the salinity concentration in

Table 1. Statistical summary of hydrogeochemical constituents and stable isotopes

Type	T (°C)	pH	DO (mg/L)	EC (us/cm)	Na (mg/L)	K (mg/L)	Ca (mg/L)	Mg (mg/L)	CL (mg/L)	NO3 (mg/L)	SO4 (mg/L)	HCO3 (mg/L)	d2H (‰)	d18O (‰)
Rainy Season														
Aquifer qp23														
Min	27.30	6.85	1.14	514.00	45.11	4.03	25.28	20.32	2.85	0.80	12.47	295.34	−46.58	−6.58
Max	29.60	7.51	3.18	1023.00	90.32	28.63	90.25	68.60	135.57	10.99	96.48	453.38	−31.97	−4.51
Mean	28.48	7.12	1.74	653.82	58.23	8.46	39.91	34.00	17.54	3.54	45.99	360.93	−37.99	−5.24
SD	0.51	0.17	0.47	119.25	10.53	4.85	14.48	10.33	27.61	3.04	22.16	39.53	3.13	0.49
Dry Season														
Aquifer qh, qp3														
Min	26.80	6.52	1.16	906.00	266.85	22.80	60.21	37.67	345.71	12.38	26.82	195.87	−49.74	−7.10
Max	28.40	7.05	2.37	21200.00	8535.80	278.81	970.48	1290.06	16970.45	264.18	2511.29	502.19	−8.66	−1.73
Mean	27.97	6.75	1.50	12034.33	4331.75	102.74	510.54	554.92	8876.39	153.26	1143.56	341.20	−29.26	−4.43
SD	0.55	0.16	0.43	7355.73	3177.66	85.50	441.99	423.97	6459.40	105.30	905.84	117.46	13.63	1.81
Aquifer qp23														
Min	27.10	7.02	0.59	390.00	38.56	4.78	24.54	21.06	5.27	0.81	13.19	244.00	−49.49	−7.04
Max	31.20	7.48	3.18	896.00	67.72	13.75	80.89	62.96	37.13	7.27	111.04	532.09	−32.92	−4.38
Mean	28.71	7.26	1.92	616.81	53.61	8.56	41.09	33.67	12.91	3.49	42.41	318.73	−38.00	−5.10
SD	0.99	0.13	0.64	105.87	7.00	1.95	10.97	8.87	8.69	1.73	23.67	52.55	3.44	0.57

(*continued*)

Table 1. (*continued*)

Type	T (°C)	pH	DO (mg/L)	EC (us/cm)	Na (mg/L)	K (mg/L)	Ca (mg/L)	Mg (mg/L)	CL (mg/L)	NO3 (mg/L)	SO4 (mg/L)	HCO3 (mg/L)	d2H (‰)	d18O (‰)
Aquifer qp1														
Min	27.10	6.53	0.88	116.70	16.88	1.95	4.00	4.53	5.00	0.11	0.02	70.17	−53.53	−7.92
Max	32.40	7.68	5.13	4760.00	1881.13	75.91	77.40	147.58	3191.94	128.73	425.91	472.53	−9.57	−2.24
Mean	30.08	7.19	2.18	979.27	172.56	11.62	34.98	33.72	157.26	10.10	115.14	324.29	−40.32	−5.50
SD	1.64	0.31	0.87	743.44	314.61	12.54	15.94	23.83	553.75	22.68	111.62	109.89	7.80	1.29
Aquifers n21, n22, n13														
Min	25.00	7.66	1.21	204.00	320.51	7.93	1.05	3.15	84.66	3.87	75.28	37.83	−49.88	−7.25
Max	40.30	8.68	3.13	13720.00	3512.51	131.33	187.52	394.71	7286.02	257.29	779.33	779.23	−32.19	−4.89
Mean	35.31	7.99	1.74	3246.30	976.42	30.73	37.35	78.60	1436.83	44.17	208.51	545.21	−44.53	−6.48
SD	6.17	0.33	0.55	3687.99	1095.88	40.59	65.61	144.84	2494.14	79.37	207.69	258.30	6.35	0.79

shallow groundwater samples were very high Na^+ (266.85–8,535.80 mg/L) and Cl^- (345.71–16,970.45 mg/L) compared to deep groundwater samples with concentration of Na^+ (320.51–3,512.51 mg/L) and Cl^- (84.66–7,286.02 mg/L). Conversely, middle groundwater samples presented relatively low of (Na^+) and chloride (Cl^-) concentration, ranging from 16.88–51.25 mg/L and 2.85–69.74 mg/L, respectively. Solutes concentration (K^+, Ca^{2+}, $Mg^{2+,}$ HCO_3^- and NO_3^-) varies widely from shallow to deep aquifers, especially deep groundwater samples displayed very high HCO_3^- concentration varying from 561.38 to 779.33 mg/L, reflecting the strong influence of mineral calcite dissolution in this aquifer. More noticeably, a high concentration of NO_3^- (113.33–264.18 mg/L) was detected in some locations surrounding shrimp farms close to the coastline (Fig. 3a). This fact might be attributed to moving pollutant sources into shallow and deep aquifers via leaking aquitards and unprotected wells as a result of excessive groundwater [50].

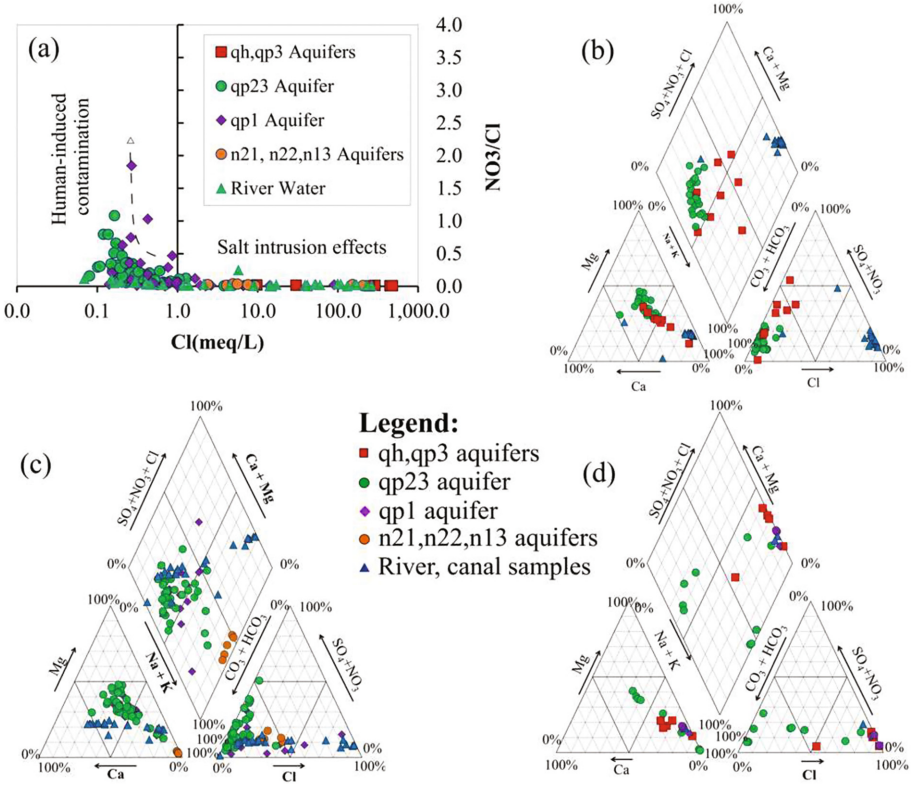

Fig. 3. (a) CL plotted NO3/CL ratio; (b) Trilinear diagram of water samples in Soc Trang province, in the dry season, 2013; (c) Trilinear diagram of water samples from Soc Trang province, in the rainy season, 2013; (d) Trilinear diagram of water samples from Soc Trang province, in the dry season, 2014

4.2 Hydrogeochemical Facies

In this study, Piper diagram [51] was employed to classify the characteristics of groundwater and surface between 2013 and 2014. As can be seen in Figs. 3b, c and d, groundwater quality shows a distinguish trend from aquifers. Although groundwater chemistry of most groundwater samples at qp_{23} and qp_1 aquifers was stable in both season, it represented relatively a different trend with other aquifers (qh,qh_3, n_{21}, n_{22} and n_{13}). Groundwater samples from these aquifers were characterized by fresh water (Ca-Mg-HCO3) and were suitable for water supply system. Shallow groundwater aquifers (qh, qh_3), however, was classified into saline water (Na-Cl) type, ranging from moderate to very heavy salinity and were unusable for drinking and irrigation purposes. The remaining groundwater samples of deeper aquifers (n_{21}, n_{22}, n_{13}) were grouped into brackish water (Na-Cl, Ca-Mg-Cl) type and mixed water type (Na-HCO3-Cl) which limited to fresh water demands.

The quality of surface water showed a seasonal variation, indicating the impacts of changing water flow between dry and rainy season as well as seawater intrusion on the surface water system of the Mekong Delta. Although almost all groundwater samples from qp_{23} and qp_1 aquifers show seasonal stability in chemistry and stable isotopes, some of these aquifers closing to estuary have a relative high chloride and isotopic concentration, indicating effects of heterogeneous stratigraphy, salinization and freshening processes on groundwater quality. Similarly, groundwater samples from deeper aquifers were classified by Na-HCO3-Cl type with high salinity (around 750 mg/L), compared with other aquifers, demonstrating the different magnitudes of calcite and dolomite minerals dissolution processes. The difference of groundwater quality between shallow and deep aquifers reflects the complexity of stratigraphic formation processes of the Delta as a result of marine transgression and regression processes [52, 53], and the possibility human-induced activities resulting in modern seawater intrusion [54].

The spatial distribution of stiff diagrams and isotopic concentration of oxygen-18 was shown in the Figs. 4, 5 and 6. The chemical and isotopic compositions of middle and deep aquifers show a stable trend while those of shallow groundwater presented a similar trend to river water closed to river estuary, indicating the possibility of mixing between shallow groundwater and river water in this area. The spatial and seasonal variation of chemical and isotopic concentration of river water reveals effects of seawater intrusion in coastal river system with very high salinity along the coast in the dry season. The stability of groundwater chemistry and stable isotopes of (qp_1, qp_{23}) and (n_{21}, n_{22}, n_{13}) aquifers might indicate a low-hydraulic connection between these aquifers and river water in this area.

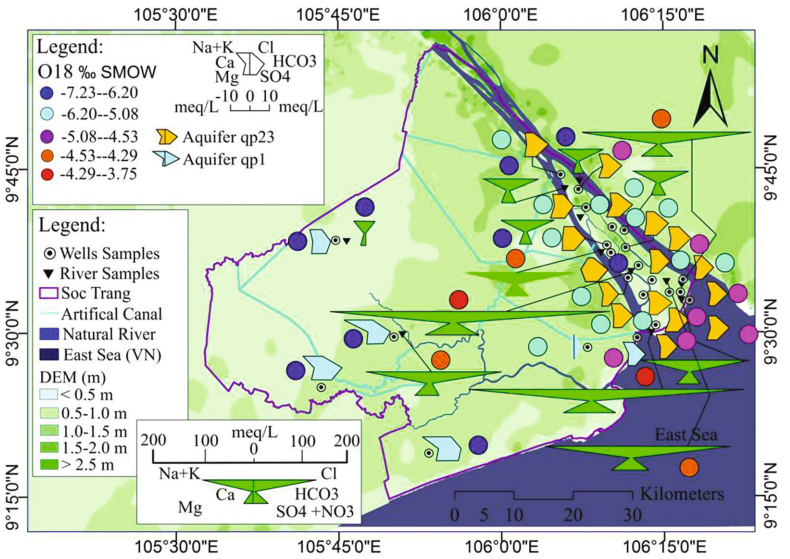

Fig. 4. Spatial distribution of hexa diagram and stable isotope δ18O in the dry season(March, 2013).

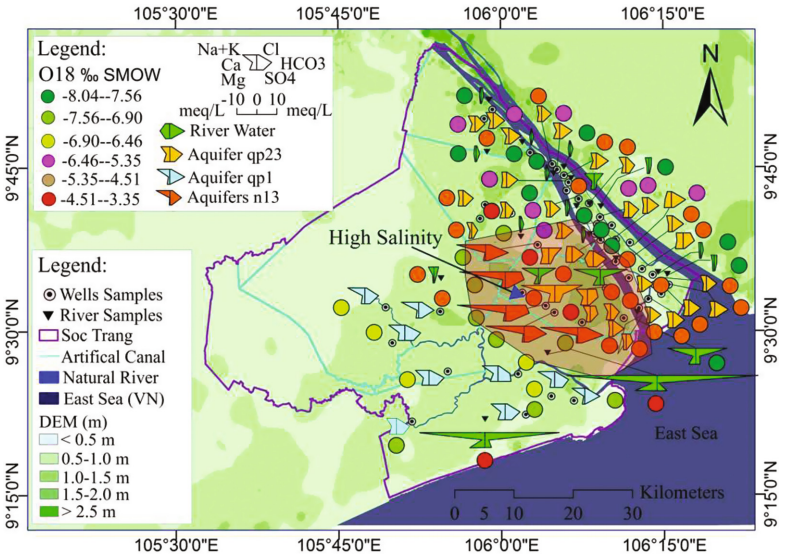

Fig. 5. Spatial distribution of hexa diagram and stable isotope δ18O in the rainy season(August, 2013).

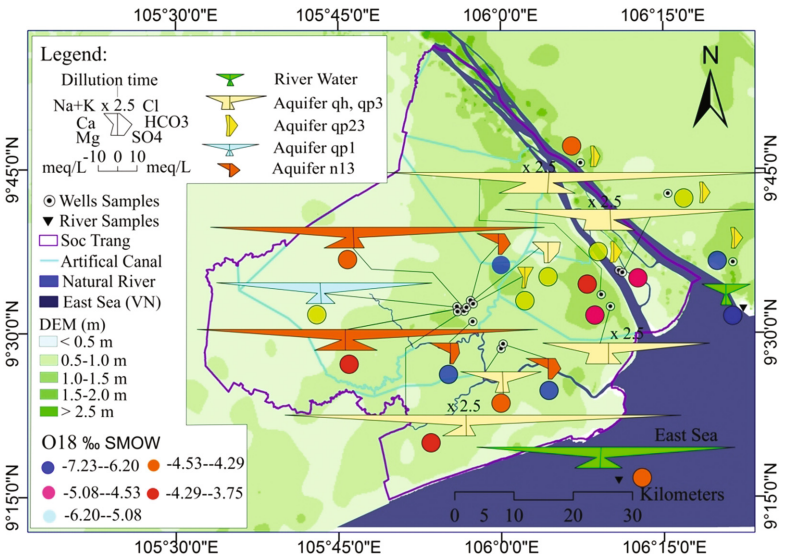

Fig. 6. Spatial distribution of hexa diagram and stable isotope $\delta^{18}O$ in dry season 2014

4.3 Stable Isotopes Signatures

Stable isotopes of $\delta^{18}O$ and δD have been widely used as useful signatures to understand hydrogeological processes such recharge, evaporation and mixing with different water sources that might significantly control groundwater quality [31, 55]. The $\delta^{18}O$, δD values of groundwater and surface samples were plotted in the conventional diagram (Fig. 7) with respect to the Meteoric Global Water Line [56] and the Local Meteoric Water Lines(LMWLs) of Cambodia [57] and An Long, Dong Thap province in the Mekong Delta. The isotopic values of groundwater samples among aquifers vary widely, ranging −7.92‰–−1.73‰ for $\delta^{18}O$, and −53.53‰–−8.66‰ for δD, which can be divided into three groups (G1, G2 and G3). Most of the groundwater samples from deep aquifers classifying into group G1 that is depleted in stable isotopes of oxygen-18 and detium, closing to river water in rainy season. The depletion of isotopic values in these deep aquifers can be explained by effects of ultrafiltration process on groundwater during passage via compacted clayey sediment layers [58] for a long period of time. This also suggests the complex processes of mixing between paleo-groundwater with different water sources during the period of aquifer formation. The variation in $\delta^{18}O$ and δD values of surface water was larger than that of groundwater, indicating effects of seasonal variation on surface water than groundwater in this area with relatively light isotopic values of surface water (aveg. $\delta^{18}O = -7.06‰$, $\delta D = -50.20‰$) in the rainy season and high isotopic enrichments (aveg.$\delta^{18}O = -5.40‰$, $\delta D = -40.15‰$) in the dry season.

More surprisingly, most of the groundwater samples (group G1, G2 and G3) distributed consistently under the Local Meteoric Water Line of Cambodia, illustrating groundwater resource in the study might originate from Cambodia or upstream parts of

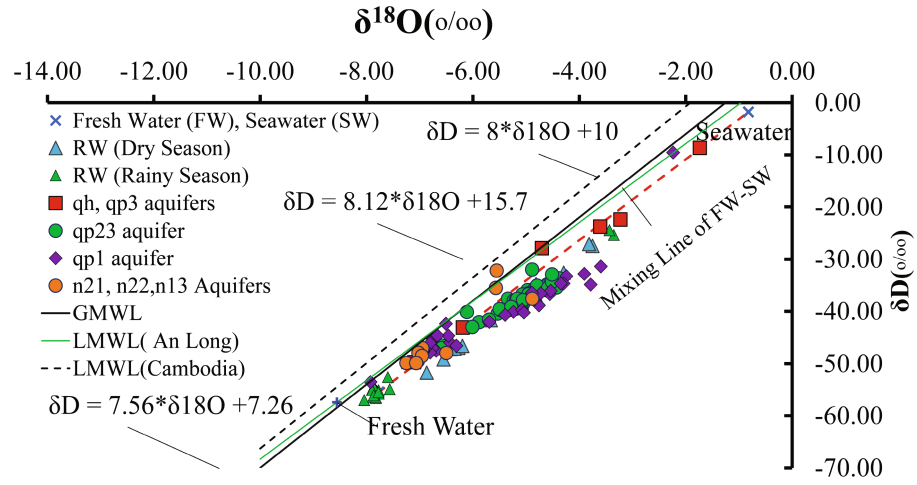

Fig. 7. $\delta^{18}O$ v.s δD in the groundwater, surface water and annual volume weighted mean precipitation. qh, qp_3, qp_{23}, qp_1, n_{22}, n_{21} and n_{13} denote the groundwater samples of Holocene, upper Pleistocene, Middle Pleistocene, Lower Pleistocene, Middle Pliocene, Lower Pliocene and Miocene aquifers, respectively.

the Mekong River Basin. This also suggests that local recharge may less contribute to these aquifers. These results were supported by recent research [45, 59].

Effect of evaporation on the physico-chemical characteristics of groundwater water is also confirmed by decreasing d-excess [60]. In general, groundwater has experienced to evaporation process but in different magnitudes. As shown in Fig. 8, groundwater at qp_{23} and qp_1 aquifers show a strong impact of evaporation process while the shallow groundwater (qh, qp_3 aquifers) presents a wide variation trend and have high isotopic

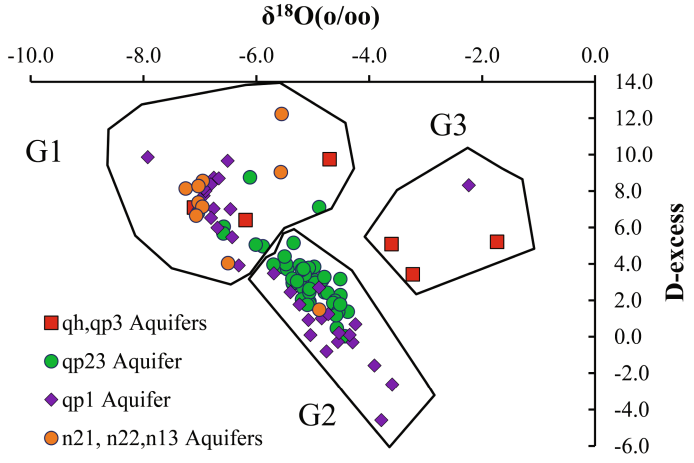

Fig. 8. The $\delta^{18}O$ versus d-excess values of groundwater in 2013–2014.

values, suggesting the effects of both evaporation and seawater intrusion. The groundwater samples from deeper aquifers (n_{22}, n_{21}, n_{13}) have low isotopic values but show a wide variation indicating different states of evaporation affecting on these aquifers.

4.4 Hydrogeochemical Processes

Mineral Dissolution Processes

In the coastal aquifers, the mineral dissolution processes are frequently controlled groundwater quality [8, 61], therefore the PHREEQC version 3 model was used to calculate the Saturation Indices (SI). As shown in the Fig. 9a, most of the groundwater samples showed the trend of sub-saturation to oversaturation of calcite, dominating Ca^{2+} concentration, while some deep groundwater samples were only under saturated by dolomite dissolution. An increasing Ca^{2+} concentration, however, might result in calcite precipitation these aquifers. Additionally, groundwater quality in coastal aquifer could be strongly affected by gypsum and anhydrite dissolution due to the undersaturated status of gypsum and anhydrite dissolution (Fig. 9b). Deep groundwater samples show only undersaturation of gypsum dissolution, which suggests the fact that groundwater quality of these aquifers is also influenced by gypsum mineral dissolution. These processes might increasingly accelerate in the context of intensive groundwater extraction from these aquifers.

Seawater Intrusion

Groundwater salinization is perhaps one of the most concern issues in many coastal regions in the world since it causes degradation of groundwater quality and threat to sustainability of groundwater use and management [62, 63]. In fact, the origin of salinity in coastal aquifers may be driven from different sources such as paleo-saline [64], seawater intrusion due to over pumping [65], wastewater and irrigation return flow [66]. In the Mekong delta, salt intrusion into aquifers is being major concerned due to excessive practices of groundwater extraction for drinking and irrigation. The earliest study on seawater intrusion in the Mekong Delta aquifers was conducted by Ho et al. [43]. They argue that shallow groundwater (qh, qp_3 aquifers) was directly recharged by surface water and local precipitation and were intruded by seawater while deep aquifers had isolated each other and recharged by meteoric water from different altitudes. This was also confirmed by the recent research conducting in Dong Thap Province – a flooded plain of the Mekong Delta [59], in which canals and river water contributes dominantly to shallow groundwater but widely spatial variation while deep groundwater might be recharged by water driving from upstream of the Mekong River Basin. Until recently, however saline water in the Mekong Delta's aquifer system is still poorly known [45].

In Soc Trang province, groundwater at shallow (qh, qp_3) and some parts of deep aquifers (n_{22}, n_{21}, n_{13}) has very high salinity (TDS > 1500 mg/L) that is unsuitable for both drinking and irrigation purposes. Meanwhile, groundwater samples from qp_{23} and qp_1 aquifers are relatively high yield and low salinity concentration (TDS < 1000 mg/L), becoming the only freshwater choice for water supply system along the coast. However, some parts of these fresh aquifers close to the estuarial and coastal

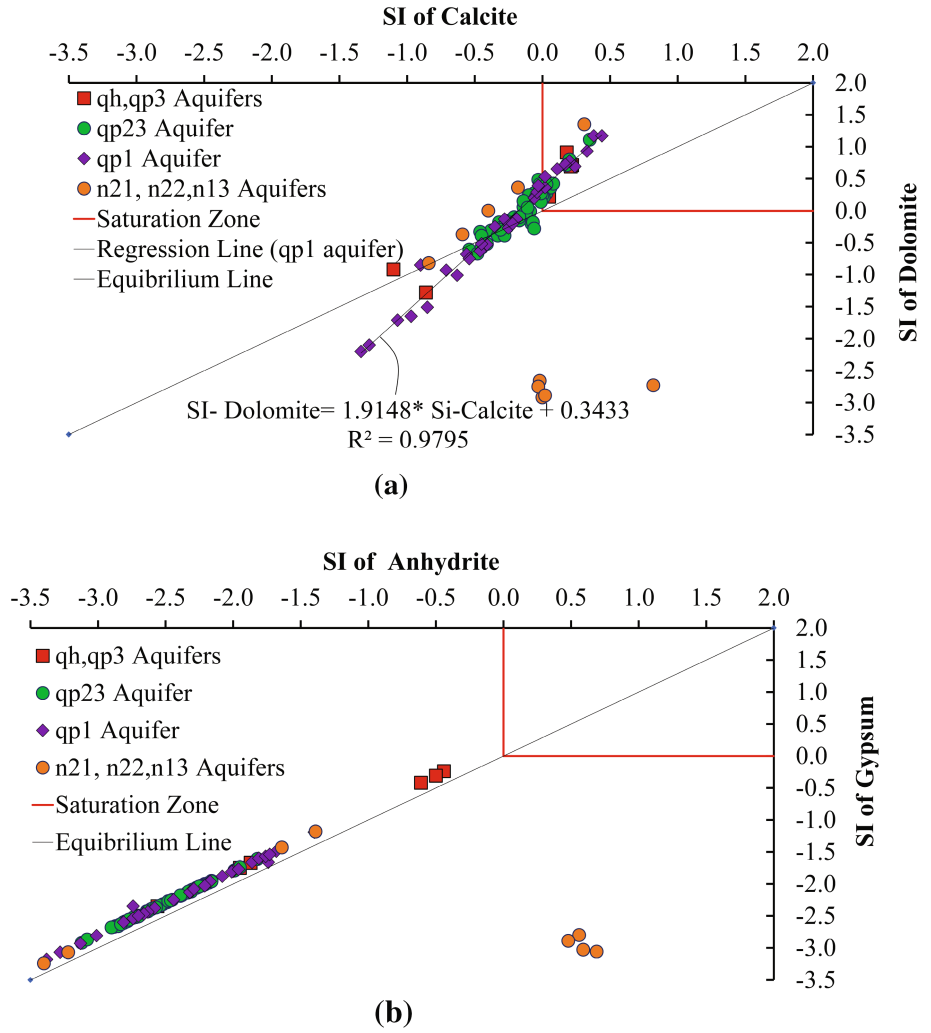

Fig. 9. **a.** The saturation state of groundwater in Soc Trang province with respect to calcite and dolomite. **b.** The saturation state of groundwater in Soc Trang province with respect to gypsum and anhydrite.

areas have relatively high salinity such as in the locations of T9 N, T10, T12, T14 samples, indicating the possibility of salt intrusion (see Fig. 10). An increase of salinity in these locations exhibits the impacts of saline diffusion from saline layers into fresh groundwater aquifers and/or an increase of halite dissolution due to over groundwater extraction for a long time. To classify groundwater salinization processes in coastal aquifers of the study area, a plot of stable isotopes and chlorite concentration was created shown in Fig. 10. It is obvious that groundwater samples from different aquifers represent variable hydrogeological processes. Most of the shallow

groundwater and some deep groundwater samples, for example, distributes around mixing fresh-seawater line might indicate the influence of seawater intrusion, while the remaining groundwater samples from deeper aquifers (n_{21}, n_{22}, n_{13}) display stably in the stable isotopes and relative increase of the Cl^- values, exhibiting effects of paleo-saline water intrusion and halite rocks dissolution. More specifically, groundwater samples at qp_{23} and qp_1 aquifers reveal two main tendencies. On the one hand, an increase of stable isotopes composition associated with a stability of Cl^- values in almost all the groundwater samples might suggest the impacts of evaporation process during the paleo-recharge period or/and during groundwater flow paths. On the other hand, an increase of both stable isotopic oxygen-18 and Cl^- concentration might attribute to saline water diffusion and halite-dissolution. These processes might be the main factors controlling the quality of groundwater responding to salinity.

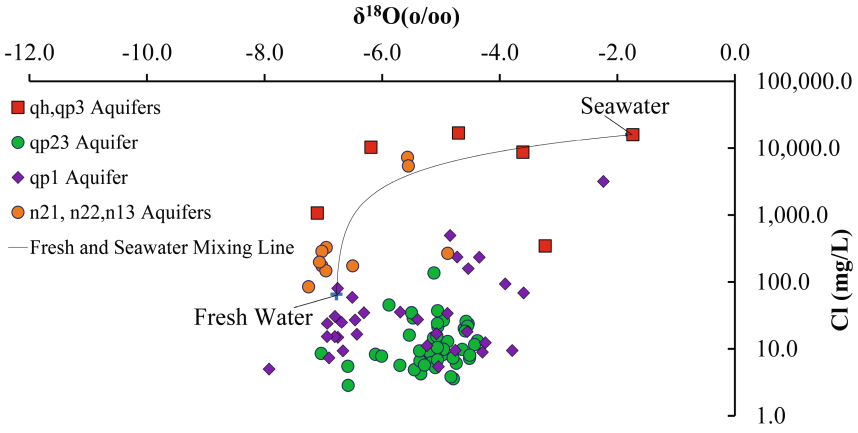

Fig. 10. The $\delta^{18}O$ vs. Cl^- concentration of groundwater in 2013–2014.

5 Conclusion

The combination of chemical parameters, stable isotopes and geochemical reaction modeling was successfully applied to assess groundwater quality and its controlling factors in the coastal area of the Vietnamese Mekong Delta. The major finding of this study can be summarized as follows:

(1) Groundwater in the study area is mainly classified into four groups: Na-Cl, Na-Mg-Ca-HCO3, Na-Mg-Ca-HCO3-SO4 and Na-HCO3-Cl.
(2) Groundwater quality was strongly influenced by the rock-water interaction, particularly by calcite, dolomite, and gypsum and anhydrite dissolution.
(3) The stable isotopes and saturation indices depict the origin of salt water presenting in the aquifers because of paleo-saline water dissolution at deeper aquifers, seawater intrusion into shallow aquifers and saltwater diffusion at Middle aquifers;

(4) Groundwater in the study area might be mainly originated from upstream parts of the Mekong River Basin and experienced effects of evaporation before recharging into coastal aquifer system of the Mekong Delta;
(5) An increase of salinity in some locations close to the coast might indicate the fact of modern seawater intrusion into coastal aquifers of the study site.

These findings suggest that its hydrogeological features might mainly control groundwater quality in the coastal aquifer system of the Mekong Delta. Additionally, the intensive groundwater extraction, uncontrolled drilling and unprotected unusable wells coupled with the severe seawater intrusion might potentially accelerate the deterioration of groundwater quality in the coastal aquifers of the Mekong Delta. Further study, therefore is needed to understand impacts of human activities and natural dynamic on the coastal aquifers of the Mekong Delta in both quality and quantity.

Acknowledgments. The authors would like to express their gratefulness to University of Tsukuba, Japan for providing necessary facilities for this research. We also would like to thank the Thuyloi University, Department of Natural Resources and Environment of Soc Trang Province, Vietnam for their support during the field surveys between 2013 and 2014. Our thankfulness also is extended to Dr. Bui Tran Vuong, Vice Director of the Division for Water Resources and Planning for South Vietnam, and Mr. Nguyen Van Chanh, Mr. Thach Hoang Linh the hydro-geological specialists in Soc Trang province for their kind supports. Particularly, we would like to address special thanks to Japanese Grant Aid for Human Resources Development Scholarship (JDS program) and MEXT scholarship for supporting successful completion of this study.

References

1. Wichelns, D.: Volumetric water footprints, applied in a global context, do not provide insight regarding water scarcity or water quality degradation. Ecol. Ind. **74**, 420–426 (2017)
2. Liu, J., Liu, Q., Yang, H.: Assessing water scarcity by simultaneously considering environmental flow requirements, water quantity, and water quality. Ecol. Ind. **60**, 434–441 (2016)
3. Aeschbach-Hertig, W., Gleeson, T.: Regional strategies for the accelerating global problem of groundwater depletion. Nat. Geosci. **5**, 853–861 (2012)
4. Alaya, M.B., Saidi, S., Zemni, T., Zargouni, F.: Suitability assessment of deep groundwater for drinking and irrigation use in the Djeffara aquifers (Northern Gabes, south-eastern Tunisia). Environ. Earth Sci. **71**, 3387–3421 (2014)
5. Zhang, R., Hu, S., Zhang, X., Yu, W.: Dissolution kinetics of dolomite in water at elevated temperatures. Aquat. Geochem. **13**, 309–338 (2007)
6. Rosenthal, E., Zilberbrand, M., Livshitz, Y.: The hydrochemical evolution of brackish groundwater in central and northern Sinai (Egypt) and in the western Negev (Israel). J. Hydrol. **337**, 294–314 (2007)
7. Wen, X., Diao, M., Wang, D., Gao, M.: Hydrochemical characteristics and salinization processes of groundwater in the shallow aquifer of Eastern Laizhou Bay, China. Hydrol. Process. **26**, 2322–2332 (2012)
8. Singh, C.K., Kumar, A., Shashtri, S., Kumar, A., Kumar, P., Mallick, J.: Multivariate statistical analysis and geochemical modeling for geochemical assessment of groundwater of Delhi, India. J. Geochem. Explor. **175**, 59–71 (2017)

9. Kaltreider, R.C., Davis, A.M., Lariviere, J.P., Hamilton, J.W.: Arsenic alters the function of the glucocorticoid receptor as a transcription factor. Environ. Health Perspect. **109**, 245–251 (2001)
10. Mandal, B.K., Suzuki, K.T.: Arsenic round the world: a review. Talanta **58**, 201–235 (2002)
11. Bui Huy, T., Tuyet-Hanh, T.T., Johnston, R., Nguyen-Viet, H.: Assessing health risk due to exposure to arsenic in drinking water in Hanam Province, Vietnam. Int. J. Environ. Res. Public Health **11**, 7575–7591 (2014)
12. Shankar, S., Shanker, U., Shikha: Arsenic contamination of groundwater: a review of sources, prevalence, health risks, and strategies for mitigation. Sci. World J. **2014**, 18 (2014)
13. Jiang, J.-Q., Ashekuzzaman, S.M., Jiang, A., Sharifuzzaman, S.M., Chowdhury, S.R.: Arsenic contaminated groundwater and its treatment options in Bangladesh. Int. J. Environ. Res. Public Health **10**, 18–46 (2013)
14. Singh, B., Sekhon, G.S.: Nitrate pollution of groundwater from nitrogen fertilizers and animal wastes in the Punjab, India. Agric. Environ. **3**, 57–67 (1976)
15. Zhang, W.L., Tian, Z.X., Zhang, N., Li, X.Q.: Nitrate pollution of groundwater in northern China. Agr. Ecosyst. Environ. **59**, 223–231 (1996)
16. Almasri, M.N.: Nitrate contamination of groundwater: a conceptual management framework. Environ. Impact Assess. Rev. **27**, 220–242 (2007)
17. Vithanage, M., Mikunthan, T., Pathmarajah, S., Arasalingam, S., Manthrithilake, H.: Assessment of nitrate-N contamination in the Chunnakam aquifer system, Jaffna Peninsula, Sri Lanka. SpringerPlus **3**, 271 (2014)
18. Zhang, Q., Sun, J., Liu, J., Huang, G., Lu, C., Zhang, Y.: Driving mechanism and sources of groundwater nitrate contamination in the rapidly urbanized region of south China. J. Contam. Hydrol. **182**, 221–230 (2015)
19. Zhai, Y., Zhao, X., Teng, Y., Li, X., Zhang, J., Wu, J., Zuo, R.: Groundwater nitrate pollution and human health risk assessment by using HHRA model in an agricultural area, NE China. Ecotoxicol. Environ. Saf. **137**, 130–142 (2017)
20. Vengosh, A.: 9.09 - Salinization and Saline Environments A2 - Holland, Heinrich D. In: Turekian, K.K. (ed.) Treatise on Geochemistry, pp. 1–35. Pergamon, Oxford (2003)
21. Abd-Elhamid, H.F., Javadi, A.A.: Impact of sea level rise and over-pumping on seawater intrusion in coastal aquifers. J. Water Clim. Chang. **2**, 19–28 (2011)
22. Park, H.-Y., Jang, K., Ju, J.W., Yeo, I.W.: Hydrogeological characterization of seawater intrusion in tidally-forced coastal fractured bedrock aquifer. J. Hydrol. **446–447**, 77–89 (2012)
23. Werner, A.D., Bakker, M., Post, V.E.A., Vandenbohede, A., Lu, C., Ataie-Ashtiani, B., Simmons, C.T., Barry, D.A.: Seawater intrusion processes, investigation and management: recent advances and future challenges. Adv. Water Resour. **51**, 3–26 (2013)
24. De Filippis, G., Foglia, L., Giudici, M., Mehl, S., Margiotta, S., Negri, S.L.: Seawater intrusion in karstic, coastal aquifers: Current challenges and future scenarios in the Taranto area (southern Italy). Sci. Total Environ. **573**, 1340–1351 (2016)
25. Mahlknecht, J., Merchán, D., Rosner, M., Meixner, A., Ledesma-Ruiz, R.: Assessing seawater intrusion in an arid coastal aquifer under high anthropogenic influence using major constituents, Sr and B isotopes in groundwater. Sci. Total Environ. **587–588**, 282–295 (2017)
26. Ferguson, G., Gleeson, T.: Vulnerability of coastal aquifers to groundwater use and climate change. Nature Clim. Change **2**, 342–345 (2012)
27. Russo, T.A., Lall, U.: Depletion and response of deep groundwater to climate-induced pumping variability. Nature Geosci **10**, 105–108 (2017)
28. Gleeson, T., Wada, Y., Bierkens, M.F.P., van Beek, L.P.H.: Water balance of global aquifers revealed by groundwater footprint. Nature **488**, 197–200 (2012)

29. Chae, G.-T., Yun, S.-T., Kim, K., Mayer, B.: Hydrogeochemistry of sodium-bicarbonate type bedrock groundwater in the Pocheon spa area, South Korea: water–rock interaction and hydrologic mixing. J. Hydrol. **321**, 326–343 (2006)
30. Lorenzen, G., Sprenger, C., Baudron, P., Gupta, D., Pekdeger, A.: Origin and dynamics of groundwater salinity in the alluvial plains of western Delhi and adjacent territories of Haryana State, India. Hydrol. Process. **26**, 2333–2345 (2012)
31. Slimani, R., Guendouz, A., Trolard, F., Moulla, A.S., Hamdi-Aïssa, B., Bourrié, G.: Identification of dominant hydrogeochemical processes for groundwaters in the Algerian Sahara supported by inverse modeling of chemical and isotopic data. Hydrol. Earth Syst. Sci. **21**, 1669–1691 (2017)
32. Ben Moussa, A., Mzali, H., Zouari, K., Hezzi, H.: Hydrochemical and isotopic assessment of groundwater quality in the Quaternary shallow aquifer, Tazoghrane region, north-eastern Tunisia. Quatern. Int. **338**, 51–58 (2014)
33. Mohammed, N., Celle-Jeanton, H., Huneau, F., Le Coustumer, P., Lavastre, V., Bertrand, G., Charrier, G., Clauzet, M.L.: Isotopic and geochemical identification of main groundwater supply sources to an alluvial aquifer, the Allier River valley (France). J. Hydrol. **508**, 181–196 (2014)
34. Boschetti, T., González-Hernández, P., Hernández-Díaz, R., Naclerio, G., Celico, F.: Seawater intrusion in the Guanahacabibes Peninsula (Pinar del Rio Province, western Cuba): effects on karst development and water isotope composition. Environ. Earth Sci. **73**, 5703–5719 (2015)
35. Lu, C., Xin, P., Li, L., Luo, J.: Seawater intrusion in response to sea-level rise in a coastal aquifer with a general-head inland boundary. J. Hydrol. **522**, 135–140 (2015)
36. Arfib, B., Charlier, J.-B.: Insights into saline intrusion and freshwater resources in coastal karstic aquifers using a lumped Rainfall–Discharge–Salinity model (the Port-Miou brackish spring, SE France). J. Hydrol. **540**, 148–161 (2016)
37. Mehdizadeh, S.S., Karamalipour, S.E., Asoodeh, R.: Sea level rise effect on seawater intrusion into layered coastal aquifers (simulation using dispersive and sharp-interface approaches). Ocean Coast. Manag. **138**, 11–18 (2017)
38. Hornero, J., Manzano, M., Ortega, L., Custodio, E.: Integrating soil water and tracer balances, numerical modelling and GIS tools to estimate regional groundwater recharge: application to the Alcadozo aquifer system (SE Spain). Sci. Total Environ. **568**, 415–432 (2016)
39. Minderhoud, P.S.J., Erkens, G., Pham, V.H., Bui, V.T., Erban, L., Kooi, H., Stouthamer, E.: Impacts of 25 years of groundwater extraction on subsidence in the Mekong Delta, Vietnam. Environ. Res. Lett. **12**, 064006 (2017)
40. Benner, S.G., Polizzotto, M.L., Kocar, B.D., Ganguly, S., Phan, K., Ouch, K., Sampson, M., Fendorf, S.: Groundwater flow in an arsenic-contaminated aquifer, Mekong Delta, Cambodia. Appl. Geochem. **23**, 3072–3087 (2008)
41. Merola, R.B., Hien, T.T., Quyen, D.T.T., Vengosh, A.: Arsenic exposure to drinking water in the Mekong Delta. Sci. Total Environ. **511**, 544–552 (2015)
42. Stuckey, J.W., Schaefer, M.V., Kocar, B.D., Benner, S.G., Fendorf, S.: Arsenic release metabolically limited to permanently water-saturated soil in Mekong Delta. Nat. Geosci. **9**, 70–76 (2016)
43. Ho, H.D., Aramyossy, J.F., Louvat, D., Huu, M.Q., Nguyen, T.V., Nguyen, K.C.: Environmental isotopes study related to the origin, salinization and movement of groundwater in the Mekong Delta (Vietnam). IAEA, UNESCO (1991)
44. Khoi, L.V., Chinh, N.K., Hung, D.T.: Groundwater salinity study in the Mekong Delta using isotope techniques. Commun. Phys. **1**, 30–35 (2002)

45. An, T.D., Tsujimura, M., Le Phu, V., Kawachi, A., Ha, D.T.: Chemical characteristics of surface water and groundwater in coastal watershed, Mekong Delta, Vietnam. Procedia Environ. Sci. **20**, 712–721 (2014)
46. Wagner, F., Tran, V.B., Renaud, F.G.: Groundwater resources in the Mekong Delta: availability, utilization and risks. In: Renaud, F., Kuenzer, C. (eds.) The Mekong Delta System: Interdisciplinary Analyses of a River Delta. Springer, Dordrecht (2010). Chap. 7
47. Slimani, R., Guendouz, A., Trolard, F., Moulla, A.S., Hamdi-Aissa, B., Bourrié, G.: Geochemical inverse modeling of chemical and isotopic data from groundwaters in Sahara (Ouargla Basin, Algeria). Hydrol. Earth Syst. Sci. Discuss. **2016**, 1–49 (2016)
48. Indraratna, B., Sullivan, J., Nethery, A.: Effect of groundwater table on the formation of acid sulphate soils. Mine Water Environ. **14**, 71–83 (1995)
49. Vahedian, A., Aghdaei, S.A., Mahini, S.: Acid sulphate soil interaction with groundwater: a remediation case study in East Trinity. APCBEE Procedia **9**, 274–279 (2014)
50. Erban, L.E., Gorelick, S.M., Zebker, H.A., Fendorf, S.: Release of arsenic to deep groundwater in the Mekong Delta, Vietnam, linked to pumping-induced land subsidence. Proc. Natl. Acad. Sci. **110**, 13751–13756 (2013)
51. Piper, A.M.: A graphic procedure in the geochemical interpretation of water-analyses. EOS Trans. Am. Geophys. Union **25**, 914–928 (1944)
52. Hoang, T.M., van Lap, N., Oanh, T.T.K., Jiro, T.: The influence of delta formation mechanism on geotechnical property sequence of the late Pleistocene-Holocene sediments in the Mekong River Delta. Heliyon **2**, e00165 (2016)
53. Delsman, J.R., Hu-a-ng, K.R.M., Vos, P.C., de Louw, P.G.B., Oude Essink, G.H.P., Stuyfzand, P.J., Bierkens, M.F.P.: Paleo-modeling of coastal saltwater intrusion during the Holocene: an application to the Netherlands. Hydrol. Earth Syst. Sci. **18**, 3891–3905 (2014)
54. Robinson, G., Ahmed, A.A., Hamill, G.A.: Experimental saltwater intrusion in coastal aquifers using automated image analysis: Applications to homogeneous aquifers. J. Hydrol. **538**, 304–313 (2016)
55. West, A.G., February, E.C., Bowen, G.J.: Spatial analysis of hydrogen and oxygen stable isotopes ("isoscapes") in ground water and tap water across South Africa. J. Geochem. Explor. **145**, 213–222 (2014)
56. Craig, H.: Isotopic variations in meteoric waters. Science **133**, 1702–1703 (1961)
57. Kabeya, N., Shimizu, A., Chann, S., Tsuboyama, Y., Nobuhiro, T., Keth, N., Tamai, K.: Stable isotope studies of rainfall and stream water in forest watersheds in Kampong Thom, Cambodia. In: Sawada, H., Araki, M., Chappell, N.A., LaFrankie, J.V., Shimizu, A. (eds.) Forest Environments in the Mekong River Basin, pp. 125–134. Springer, Tokyo (2007)
58. Coplen, T.B., Hanshaw, B.B.: Ultrafiltration by a compacted clay membrane—I. Oxygen and hydrogen isotopic fractionation. Geochim. Cosmochim. Acta **37**, 2295–2310 (1973)
59. Thu, N.T.: Groundwater and surface water cycle system in Mekong Delta, Vietnam. Life and Environmental Sciences, p. 171. University of Tsukuba, Tsukuba (2017)
60. Tsujimura, M., Abe, Y., Tanaka, T., Shimada, J., Higuchi, S., Yamanaka, T., Davaa, G., Oyunbaatar, D.: Stable isotopic and geochemical characteristics of groundwater in Kherlen River Basin, a semi-arid region in eastern Mongolia. J. Hydrol. **333**, 47–57 (2007)
61. Senthilkumar, S., Balasubramanian, N., Gowtham, B., Lawrence, J.F.: Geochemical signatures of groundwater in the coastal aquifers of Thiruvallur district, south India. Appl. Water Sci. **7**, 263–274 (2017)
62. Wang, Y., Jiao, J.J.: Origin of groundwater salinity and hydrogeochemical processes in the confined Quaternary aquifer of the Pearl River Delta, China. J. Hydrol. **438–439**, 112–124 (2012)

63. Li, C., Liu, T., Xu, S., Gao, X., Wang, Y.: Groundwater salinization in shallow aquifers adjacent to a low-altitude inland salt lake: a case study at Yuncheng Basin, northern China. Environ. Earth Sci. **75**, 370 (2016)
64. Tijani, M.N.: Evolution of saline waters and brines in the Benue-Trough, Nigeria. Appl. Geochem. **19**, 1355–1365 (2004)
65. Kim, Y., Lee, K.-S., Koh, D.-C., Lee, D.-H., Lee, S.-G., Park, W.-B., Koh, G.-W., Woo, N.-C.: Hydrogeochemical and isotopic evidence of groundwater salinization in a coastal aquifer: a case study in Jeju volcanic island, Korea. J. Hydrol. **270**, 282–294 (2003)
66. Ghabayen, S.M.S., McKee, M., Kemblowski, M.: Ionic and isotopic ratios for identification of salinity sources and missing data in the Gaza aquifer. J. Hydrol. **318**, 360–373 (2006)

Research Progress on Stabilization/Solidification Technique for Remediation of Heavy Metals Contaminated Soil

Yu Zhang[1], Cong Lu[2], Mengyi Xu[1], Lingling Pan[1], Nguyen Chau Lan[3], and Qiang Tang[1(✉)]

[1] School of Urban Rail Transportation, Soochow University, Suzhou, China
tangqiang@suda.edu.cn
[2] School of Civil Engineering, Suzhou University of Science and Technology, Suzhou, China
[3] Geotechnical Engineering Lab, Civil Engineering Faculty, University of Transport and Communications, Hanoi, Vietnam

Abstract. The soil contamination by heavy metals significantly damages the environment, human health, plants and animals, which has become a burning issue recently. Several types of technology have long been in use to remedy the heavy metal contaminated soil. Among of them, solidification/stabilization was widely adopted to manage metal-contaminated soils due to its relatively low cost, easy use, comprehensive strength, and high resistance to biodegradation. In this paper, common binders and the mechanisms of heavy metal-soil-binder interaction were introduced based on literature studies. In general, the effectiveness of S/S process was studied by strength and leaching characteristics. Firstly, the unconfined compressive strength of solidified metal-contaminated soils was evaluated in terms of heavy metal content, curing time, metal type, binder content, soil property, binder type and nature condition. Furthermore, some strength prediction formulas of cement solidified heavy metal contaminated soils were summarized. Subsequently, the performance of the leaching test for S/S products was presented and the influence factors were the same as those of unconfined compressive strength, except for one more factor—soil-solution contact time. Finally, the cases of large-scale contaminated site restoration in China were introduced, and the restorative effects of which achieved the expected objectives.

Keywords: Heavy metal · Contaminated soil · Stabilization/Solidification · Strength · Leaching

1 Introduction

Increasingly affluent lifestyles as well as continued industrial and commercial growth around the world has led to a large number of abandoned industrial parks, most of which have large quantities of heavy metal (Cd, Zn, Pb, Hg, etc.) contaminated soils without proper treatment, especially in developing countries [1–3]. The leachability of

© Springer International Publishing AG 2018
D. Tien Bui et al. (eds.), *Advances and Applications in Geospatial Technology and Earth Resources*, https://doi.org/10.1007/978-3-319-68240-2_19

heavy metal from contaminated sites has caused serious contamination of soil and groundwater [4–7]. Unlike organic pollutants which are susceptible to biological degradation, heavy metal ions do not degrade into any harmless end products. Through soil and water, heavy metals enter the food chain, finally cause harm to humans [8]. In China, a government report published in 2014 estimated that 19.4% of the agricultural land may be contaminated, among which over 1.3 million hectares may be seriously contaminated [9]. Table 1 lists some contaminated events by heavy metal in China in recent years.

Table 1. Information regarding harmful effects and some contamination events of heavy metals

Heavy metal	Harmful effects	Events
Cd	Carcinogenic, mutagenic, hypercalciuria resulting in bone damage and kidney stone and failure [10]	In April 2016, the waste water from Yichun Zhong'an Industrial Co., Ltd. cause excessive cadmium in the surrounding soil and river water
Pb	Renal failure, cardiovascular disease, reduced intelligence, short term memory loss, coordination problem, decreased learning ability in children [11]	In 2014, 300 children in Hunan, Hengyang, had excessive blood lead levels
Hg	damage human nervous system, brain, heart, kidneys, and immune system [12]	In 2005, a survey report issued by the Guizhou Institute of Environmental Sciences shows that there are 117.4 hectares of Hg contaminated soil in Guizhou Wanshan
As	Interferes with cellular processes such as oxidative phosphorylation and ATP synthesis [13]	In 2009, Pizhou suffered two arsenic pollutions within six months

Soil is a precious natural resource that is nonrenewable on human time scale [14]. In 2016, the State Council issued the Action Plan for Soil Pollution Prevention and Control (the "Soil Ten Measures") to prevent and control pollution nationwide, which established the basic institutional framework for soil pollution control. The promulgation of the Soil Ten Measures has received wide attention from local governments, some of which have also issued the local Soil Ten Measures, for instance, "Scheme of soil pollution prevention and control in Liaoning", "Implementation scheme of action plan for soil pollution prevention and control in Fujian" and so on. In 2017, the Ministry of environmental protection of China has made public for the first time the specifics of a key project – "Air, water and soil pollution prevention action plan implementation management project", the budget of which is about 18448 million. The remediation of the heavy metal contaminated land represents a huge challenge to environmental professionals in the coming decades. In order to address this challenge, an effective soil method which could feasibly and efficiently remediate heavy metal contaminated soils should be deployed imperatively.

2 Remediation Technology of Contaminated Soil

According to current researches, the treatment of heavy metal contaminated soil starts from the following three ideas: (1) increase the mobility of heavy metals in the soil so as to separate them from the soil; (2) change the existing form of heavy metals in soil, and fix the heavy metal in the soil to reduce its mobility; (3) isolate heavy metals from the environment and prevent them from spreading and polluting the surroundings [15].

In terms of the above mentioned three ideas, the common technical method of soil management can be divided into three groups: monitored natural attenuation, shield and insulation, and soil remediation. Compared with the first two methods, soil remediation is of high efficiency and good operability.

There are two main types of remediation for metal-contaminated soils: (1) technologies that leave the metal in the soil, and (2) technologies that remove the heavy metals from the soil [16]. Technologies such as solidification/stabilization and vitrification can immobilize contaminants so as to minimizing their migration. Techniques such as soil washing and in situ soil flushing can transfer the contaminants to a liquid phase by desorption and solubilization [17]. Table 2 shows the commonly restoration technology.

Table 2. Classified comparison of commonly used restoration technology

Restoration technology	Advantages	Disadvantages
Soil washing	Easy operation, high practicality	Relative high requirements on extraction fluid
Phytoremediation	Good effect, low cost, no secondary pollution	Limited repair capacity, long repairing cycle, limited treatment depth
Electrokinetic remediation	Short repair time, low energy consumption, complete repair	Limited treatment depth, long processing time
Thermal desorption	Environment friendly, high efficiency	Big power loss, high cost, easy damage soil structure
Stabilization/solidification	Good performance on long-term stability, good engineering applicability	Limited treatment depth
Vitrification	Strong adaptability, wide application range	Big power loss, high cost, not suitable for large-area repair

According to the version 12 of the remediation technology annual status report, during the period of 1982–2005, the United States super fund has repaired 977 contaminated sites, 22% of which, i.e., 217 sites, were repaired by solidification/stabilization techniques [18]. The US Environmental Protection Agency also recognizes cementitious solidification as the best demonstrated available technology for land disposal of most toxic elements [19].

3 Solidification/Stabilization

Solidification/stabilization, also referred to as waste fixation, reduces the mobility of hazardous substances and contaminants in the environment through both physical and chemical means [20, 21]. In terminology, stabilization is a process of converting a toxic waste to a physically and chemically more stable form, that is, alters hazardous waste chemically to produce a less toxic or less mobile form. It involves chemical interactions between waste and the binding agent [22]. Solidification refers to the process that encapsulates the waste materials in a monolithic solid of high structural integrity [21, 23]. The objectives of solidification/stabilization are to achieve and maintain the desired physical properties and to chemically stabilize or permanently bind contaminants [24]. Hence, a good binder plays a decisive role in the effect of solidification/stabilization.

The choice of binders is mainly about of three aspects. First of all, it requires that the curing agent itself be free of contamination or very low in pollution so as to not bring secondary pollution. Secondly, the binders need to have high performance price ratio and reasonable construction cost. Finally, the selected curing agent can be combined with the heavy metal to be repaired, and the solidified product is stable.

4 Engineering Characteristics of Solidified Heavy Metal Contaminated Soil

4.1 Strength Characteristic

Heavy metals are not only hazardous to the environment and public health, but they also lead to the degradation of mechanical properties of soils, which results in unfavorable conditions for the redevelopment of contaminated sites [25]. The strength of those contaminated soil would improve obviously after treatment of binders. It is well-documented that the strength characteristics of the solidified soil can be mainly evaluated by unconfined compressive strength [25, 26].

Cement chemistry is complex and is made more so by the addition of metals. It was previously reported that the presence of heavy metals had a negative effect on the curing reaction, delayed the setting time and reduced the strength of the solidified soil. Zinc is of special interest because it is known to retard hydration significantly [27, 28]. It has been proposed that zinc retards the hydration and setting of cement by the surface precipitation of an amorphous layer of zinc hydroxide on the anhydrous clinker grains, and that calcium hydroxide reacts with the zinc hydroxide to form $CaZn_2(OH)_6 \cdot 2H_2O$ [29, 30]. The two waters of hydration indicate that water can be physically involved in the amorphous surface coating [31]. A similar amorphous water containing iron oxide material that resists material transport has been found to be important in the passivation layer on iron [32]. This amorphous Zn compound can function in a similar fashion preventing material (water and ion) transport necessary for the hydration of the cement clinker so as to retarded the formation of the silicate polymer, and eventually lead to the reduction of soil strength [31]. Similar results were also found by Zhao, who showed that the setting time is prolonged with the increase in Zn^{2+} concentration, and only

when the amount of cement is higher than 7.5% can a good curing effect be achieved [33]. According to Etris et al., both copper and lead retard hydration through the formation of insoluble precipitates that coat cement grains [34]. Yin et al. found that the final setting times were directly correlated with the lead concentration [35]. Figure 1 presents the effect of lead concentration on initial and final setting time of stabilized soils with various lead concentrations. As shown in Fig. 1, significantly lengthened final setting times (>19 h) were recorded for 25000 and 50000 mg/kg lead concentration. Meanwhile, an increase in initial setting time of the mixture was also caused. These findings confirmed the notion that the increases of these setting times were caused by the presence of these contaminants.

Some scholars mainly have made a bunch of exploration to study the influence of soil property on the solidification effect. Wang et al. used cement or lime as a binder to solidify the sludge to study the effects of initial water content on strength of solidified sludge [36]. The results are shown in Fig. 2, the strength of cement or lime solidified sludge decreases with the increase of initial water content, increases with cement or lime content, and increases with curing period. The compaction degree of soil also has a significant influence on the engineering properties of solidification/stabilization samples. According to Li et al., cement stabilized/solidified lead-contaminated soils with low compaction degrees are more likely to be damaged by freeze-thaw cycles and the strength of them reduced obviously [37].

Different external environment, such as acid rain, carbonization, freeze-thaw cycle, salinization and other conditions, will have different influences on the curing effect. According to He et al., the compressive strength of cemented soil decreases with alternative cycles [38]. Liu considered that NaCl solution will affect the pore structure, compressive strength and compressibility of cement solidified heavy metal contaminated soil [39]. Figure 3 presents the variation of unconfined compressive strength of stabilized lead contaminated soil with the concentration of NaCl. As shown in Fig. 4, along with the increase of NaCl concentration, the strength of cement solidified specimens reduces.

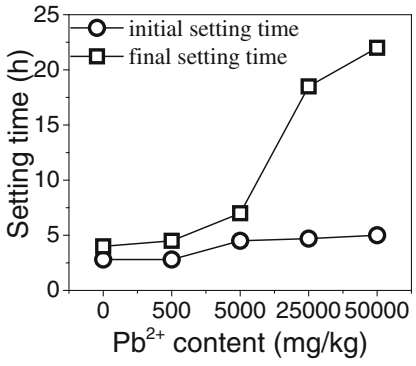

Fig. 1. Effect of lead concentration on initial and final setting time of stabilized soils

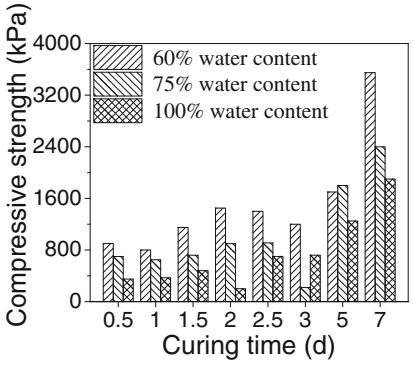

Fig. 2. Variation of unconfined compressive strength of stabilized sludge with 10% cement content

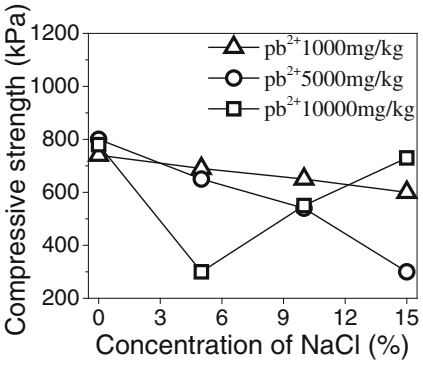

Fig. 3. The variation of unconfined compressive strength of stabilized lead contaminated soil with the concentration of NaCl

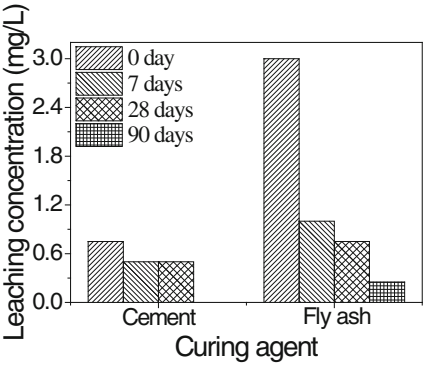

Fig. 4. Effect of solidifying addition type on the leachability of solidified chromium contaminated soil

4.2 Leaching Characteristic

New regulations have already been established for heavy metals in several countries [40, 41]. The environmental concern that is associated to heavy metal contaminated soil includes the subsequent risk of leaching which may release harmful substances such as inorganic salts and metal elements unto the environment [42]. Thus, the toxicity characteristic leaching procedure (TCLP) from US Environmental Protection Agency (EPA) was conducted to investigate the leaching behavior of heavy metals and the corresponding criteria. In view of the remediation technology for contaminated soils in China is still in the growth stage, remediation standards have not yet been promulgated. Based on opinions of specialists, "Identification standard for hazardous wastes—Identification for extraction toxicity" (GB5085.3-1996) is used as the acceptance criteria for soil remediation [43]. Table 4 shows the standard value for identification of leaching toxicity.

Generally, leaching characteristics are related to binder type, binder content and the curing time. According to Hao, two binder mixtures were used for the solidification/stabilization process, cement/soil and fly ash/soil [44]. The effect of these two binders on the leachability of solidified chromium contaminated soil was presented

Table 4. Standard value for identification of leaching toxicity (mg/L)

Heavy metal	Maximum allowable concentration of leaching solution	Heavy metal	Maximum allowable concentration of leaching solution
Pb	3	Be	0.1
Cd	0.3	Ba	100
Cr	10	Ni	10
Cu	50	As	1.5
Zn	50		

in Fig. 4. As it can be seen, compared with fly ash, cement can better prevent heavy metal leaching from solidified body. Du et al. considered that the higher the binder contents, the lower the leached concentrations. The hydration products of the binders absorb and enclose the heavy metal ions, more binders mixed will absorb and enclose more heavy metal ions, thereupon, less heavy metal ions can be leached [24]. According to Tang et al., the leaching concentration gradually decreases with the increasing curing time. This is because the sustained hydration reaction of cement provides a high alkaline environment, in which the low solubility of hydroxide precipitation ($Pb(OH)_2$, $Cd(OH)_2$, $Cr(OH)_3$) can be formed [45].

The contents and types of heavy metals can also influence the leaching characteristics [46–48]. According to Wang, it found that with the increase of pollutant content, the concentration of heavy metal in the leaching solution increases continuously [49]. Zha et al. consider that the leaching characteristics of solidified soils with different metals are also different [50]. As it can be seen, Fig. 5 shows the variation of leaching concentration of stabilized soil with different metals. It is found that the leached heavy metal concentrations increased with pollutant content. Comparatively speaking, when the amount of pollutants is low, the solidified soil that had lead in it exhibited the best solidification effectiveness, with the minimum leached heavy metal concentration. When the amount of pollutants is high, the curing effect of binder on Zn^{2+} is better than that on Pb^{2+}.

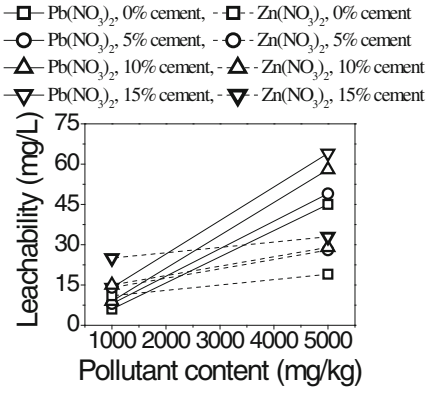

Fig. 5. Effect of pollutant content on concentrations of lead and zinc in leaching solution

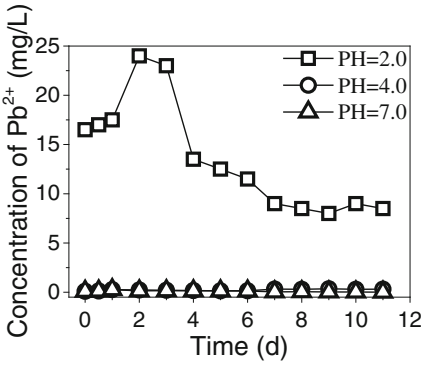

Fig. 6. Variation of leached Pb concentration with different pH

Similarly, complex environmental conditions also affect the leaching characteristics of solidified heavy metal contaminated soil. Du et al. studied the effect of acid rain with various pH on leaching and hydraulic characteristics of cement-based solidified/stabilized lead contaminated clay through infiltration and soaking tests, obtaining the results that the leached concentration was significantly influenced by pH of acid rain and the sulfate ions in it [24]. Figure 6 presents the variations of the leached Pb concentration with pH for different erosion time. As the pH values

decreased, the leached Pb concentration grew on the whole. According to Li et al., it was found that the freeze-thaw cycle will destroy the integrity of the solidified body and increase the leaching concentration of lead [51].

5 Repair Cases of Heavy Metals Contaminated Sites

Soil is a precious natural resource that is nonrenewable on human time scale. The scarcity of land resources has made people pay more attention to the heavy metal pollution. With regard to the remediation of contaminated sites, China is later than the developed countries. But in recent years, many large-scale pollution site restoration projects came into being, such as, Chenzhou waste residue yard rehabilitation project, Shanghai World Expo planning site and Shougang two pass Park restoration project. It takes Chenzhou waste residue yard rehabilitation project for example to discuss the effectiveness of solidification/stabilization technology. The residue deposit covered 3.3 acres and soil was contaminated with heavy metals, including Cr, Pb and As. Approximately 3492 cy of soil were excavated and mixed with cement, stabilization agent and water (proportions not provided) and pumped back into the excavation. After the restoration, the leaching concentrations of Cd, Pb, As are 0.1 mg/L, 1 mg/L, and 0.5 mg/L respectively, which are lower than the standard value for identification of leaching toxicity (GB5085.3-1996) that showed in Table 4. It is obvious that S/S technique managed to control over contaminants quite well, which has a good demonstration and reference significance for the follow-up of such technology.

6 Conclusions

Solidification/stabilization technology can not only improve the strength of contaminated soil, but also reduce the leached heavy metal concentrations. Different working conditions will have various effects on the strength, leached heavy metal concentrations of the solidified soil. In order to achieve better solidification effect, solidified materials should be adopted purposefully and selectively. Along with the development of solidification/stabilization and the research being unceasingly thorough, some large repair cases have appeared in China, and good repair effects have been achieved. It can be seen that the application prospect of solidification/stabilization technology is broad.

Acknowledgments. The research presented herein is supported by the National Nature Science Foundation of China (50879023, 41630633), China Postdoctoral Science Foundation funded project (2016M591756), Jiangsu Planned Projects for Postdoctoral Research Funds (1601175C), and project from Jiangsu Provincial Department of Housing and Urban-Rural Development (2016ZD18). The research is also supported by Jiangsu Provincial Transport Bureau (2016T05), Six Talent Peaks Project in Jiangsu Province, China (2015-JNHB-018), and Bureau of Housing and Urban-Rural Development of Suzhou.

References

1. Tang, Q., Wang, H.Y., Tang, X.W., Wang, Y.: Removal of aqueous Ni(II) with carbonized leaf powder: kinetic and equilibrium studies. J. Centr. South Univ. **23**, 778–786 (2016)
2. Tang, Q., Kim, H.J., Endo, K., Katsumi, T., Inui, T.: Size effect on lysimeter test evaluating the properties of construction and demolition waste leachate. Soils Found. (JGS) **55**(4), 720–736 (2015)
3. Tang, Q., Tang, X.W., Li, Z.Z., Wang, Y., Hu, M.M., Zhang, X.J., Chen, Y.M.: Zn(II) removal with activated Firmiana Simplex Leaf: kinetics and equilibrium studies. J. Environ. Eng. (ASCE) **138**(2), 190–199 (2012)
4. Tang, Q., Tang, X.W., Hu, M.M., Li, Z.Z., Chen, Y.M., Lou, P.: Removal of Cd(II) from aqueous solution with activated Firmiana Simplex Leaf: behaviors and affecting factors. J. Hazard. Mater. **179**, 95–103 (2010)
5. Tang, Q., Tang, X.W., Li, Z.Z., Chen, Y.M., Kou, N.Y., Sun, Z.F.: Adsorption and desorption behaviour of Pb(II) on a natural kaolin: equilibrium, kinetic and thermodynamic studies. J. Chem. Technol. Biotechnol. **84**, 1371–1380 (2009)
6. Tang, Q., Liu, Y., Gu, F., Zhou, T.: Solidification/stabilization of fly ash from a municipal solid waste incineration facility using Portland cement. In: Advances in Materials Science and Engineering **2016**, Article ID 7101243, 10p. (2016). doi:10.1155/2016/7101243
7. Tang, Q., Katsumi, T., Inui, T., Li, Z.Z.: Membrane behavior of bentonite amended compacted clay. Soils Found. (JGS) **54**(3), 329–344 (2014)
8. Tang, Q., Chu, J.M., Wang, Y., Zhou, T., Liu, Y.: Characteristics and factors influencing Pb (II) desorption from a Chinese clay by citric acid. Sep. Sci. Technol. **51**(17), 2734–2743 (2016)
9. MEP. National Soil Contamination Survey Report. Ministry of Environmental Protection, Beijing, China (2014)
10. Hou, D., Gu, Q., Ma, F.: Life cycle assessment comparison of thermal desorption and stabilization/solidification of mercury contaminated soil on agricultural land. J. Clean. Prod. **139**, 949–956 (2016)
11. Salem, H.M., Eweida, E.A., Farag, A.: Heavy Metals in Drinking Water and Their Environmental Impact on Human Health, pp. 542–556. ICEHM. Cairo University, Egypt (2000)
12. Awofolu, O.: A survey of trace metals in vegetation, soil and lower animal along some selected major roads in metropolitan city of Lagos. Environ. Monit. Assess. **105**, 431–447 (2005)
13. Tripathi, R.D., Srivastava, S., Mishra, S., Singh, N., Tuli, R., Gupta, D.K., Maathuis, F.J.M.: Arsenic hazards: strategies for tolerance and remediation by plants. Trends Biotech. **25**, 158–165 (2007)
14. Jenny, H.: The Soil Resource: Origin and Behavior. Springer Science and Business Media, New York (1980)
15. Xie, Y.F., Cao, Y.Z., Zhang, D.D., Liu, X.J., Li, F.S.: Engineering control technologies and its application in the risk management for contaminated sites. J. Environ. Eng. Technol. **2**(1), 51–59 (2012)
16. Rampley, C.G., Ogden, K.L.: Preliminary studies for removal of lead from surrogate and real soils using a water soluble chelator: adsorption and batch extraction. Environ. Sci. Technol. **32**(7), 987–993 (1998)
17. Reed, B.E., Carriere, P.C., Moore, R.: Flushing of a Pb II contaminated soil using HCl, EDTA, and $CaCl_2$. J. Environ. Chem. Eng. **122**(1), 48–50 (1996)
18. EPA. Treatment technologies for site cleanup: Annual status report (2007)

19. Gougar, M.L.D., Scheetz, B.E., Roy, D.M.: Ettringite and C S H Portland cement phases for waste ion immobilization: a review. Waste Manag. **16**(4), 295–303 (1996)
20. Sherwood, L.J., Qualls, R.G.: Stability of phosphorus within a wetland soil following ferric chloride treatment to control eutrophication. Environ. Sci. Technol. **35**(20), 4126–4131 (2001)
21. Khan, F.I., Husain, T., Hejazi, R.: An overview and analysis of site remediation technologies. J. Environ. Manage. **71**(2), 95–122 (2004)
22. Chen, Q.Y., Tyrer, M., Hills, C.D.: Immobilisation of heavy metal in cement-based solidification/stabilisation: a review. Waste Manag. **29**(1), 390–403 (2009)
23. Anderson, A., Mitchell, P.: Treatment of mercury-contaminated soil, mine waste and sludge using silica micro-encapsulation. In: TMS Annual Meeting, Extraction and Processing Division, March 2–6 2003, San Diego, CA, pp. 265–274 (2003)
24. Du, Y.J., Wei, M.L., Reddy, K.R.: Effect of acid rain pH on leaching behavior of cement stabilized lead-contaminated soil. J. Hazard. Mater. **271**(4), 131 (2014)
25. Gu, F., Sahin, H., Luo, X., Luo, R., Lytton, R.L.: Estimation of resilient modulus of unbound aggregates using performance-related base course properties. J. Mater. Civ. Eng. **27**(6), 04014188 (2015)
26. Gu, F., Zhang, Y., Droddy, C.V., Luo, R., Lytton, R.L.: Development of a new mechanistic empirical rutting model for unbound granular material. J. Mater. Civ. Eng. **28**(8), 04016051 (2016)
27. Tashiro, C., Takahashi, H., Kanaya, M., Hirakida, I., Yoshida, R.: Hardening properties of cement mortar adding heavy metal compounds and solubility of heavy metal hardened mortar. Cem. Concr. Res. **7**, 283–290 (1977)
28. Tashiro, C., Oba, J.: The effect of Cr_2O_3, $Cu(OH)_2$, ZnO and PbO on the compressive strength and the hydrates of hardened C3A paste. Cem. Concr. Res. **9**, 253–258 (1979)
29. Arliguie, G., Ollivier, J.P., Grandet, J.: Etude de l'effet retardateur du zinc sur l'hydration de la pate de ciment Portland. Cem. Concr. Res. **12**, 79–86 (1982)
30. Arliguie, G., Grandet, J.: Influence de la composition d'un ciment portland sur son hydratation en presence de zinc. Cem. Concr. Res. **20**, 517–524 (1990)
31. Yousuf, M., Mollah, A., Parga, J.R.: An infrared spectroscopic examination of cement-based solidification/stabilization systems–Portland types V and IP with zinc. J. Environ. Sci. Health. Part A **27**(6), 1503–1519 (1992)
32. Murphy, O.J., Bockris, J.O.M., Pou, T.E., Cocke, D.L., Sparrow, G.: SIMS evidence concerning water in passive layers. J. Electrochem. Soc. **129**, 2149–2151 (1982)
33. Zhao, Z.J.: Strength and deformation characteristics of cement stabilized contaminated soi. Water Res. Power **2**, 120–123 (2016)
34. Etris, S.F., Fiorini, Y.R., Lieb, K.C., Moore, I.C., Batik, A.L., Kantro, D.L.: Tricalcium silicate hydration in the presence of various salts. J. Test. Eval. **3**(4), 312–321 (1975)
35. Yin, C.Y., Mahmud, H.B., Shaaban, M.G.: Stabilization/solidification of lead-contaminated soil using cement and rice husk ash. J. Hazard. Mater. **137**(3), 1758–1764 (2006)
36. Wang, Z., Si, F.X., Guo, C.W.: Study of early strength and shrinkage properties of cement or lime solidified soil. Energy Procedia **16**, 302–306 (2012)
37. Li, J.S., Wang, P., Zhang, T., Li, Z.Z., Xue, Q.: Effect of freeze-thaw cycle on engineering properties and microstructure of stabilized/solidified lead contaminated soil treated by cement. Chin. J. Geotechn. Eng. **38**(11), 2043–2050 (2016)
38. He, Z., Tang, S.W., Zhao, G.S., Chen, E.: Comparison of three and one dimensional attacks of freeze-thaw and carbonation for concrete samples. Constr. Build. Mater. **127**, 596–606 (2016)
39. Liu, J.J.: The stability of solidified/stabilized heavy metal contaminated soils under corrosive environment. Hefei University of Technology (2014)

40. Nagajyoti, P.C., Lee, K.D., Sreekanth, T.V.M.: Heavy metals, occurrence and toxicity for plants: a review. Environ. Chem. Lett. **8**(3), 199–216 (2010)
41. Duruibe, J.O., Ogwuegbu, M.O.C.: Heavy metal pollution and human biotoxic effects. Int. J. Phys. Sci. **2**(5), 112–118 (2007)
42. Son, J.H., Baek, J.W., Choi, A.E.S., Park, H.S.: Thiomer solidification of an ASR bottom ash: optimization based on compressive strength and the characterization of heavy metal leaching. J. Clean. Prod. **166**, 12–20 (2017)
43. Chen, Y.T.: Remediation of heavy metal contaminated soil by combined technology of chemical washing and solidification/stabilization. J. Anhui Agric. Sci. **1**, 156–158 (2016)
44. Hao, A.L.: Study on engineering properties and mechanism of heavy metal contaminated soil. Hefei Polytechnic University (2015)
45. Tang, Q., Zhang, Y., Gao, Y.F., Gu, F.: Use of cement-chelated solidified MSWI fly ash for pavement material: mechanical and environmental evaluations. Can. Geotechn. J. (2017)
46. Tang, Q., Liu, W., Wang, H.Y., Cheng, R., Qian, Y.F.: Membrane behavior of bentonite-amended Fukakusa clay under K, Na and Ca solutions. J. Cent. South Univ. **23**, 3122–3131 (2016)
47. Tang, Q., Katsumi, T., Inui, T., Li, Z.Z.: Influence of pH on the membrane behavior of bentonite amended Fukakusa clay. Sep. Purif. Technol. **141**, 132–142 (2015)
48. Tang, Q., Katsumi, T., Inui, T., Li, Z.Z.: Membrane behavior of bentonite-amended compacted clay towards Zn(II) and Pb(II). Membr. Water Treat. **6**(5), 393–409 (2015)
49. Wang, L.B.: Experimental study on engineering properties of heavy metal contaminated soil treated with alkali residue. Hefei Polytechnic University (2016)
50. Zha, F.S., Hao, A.L., Xu, L.: Experiment study of leaching characteristics of cement solidified and stabilized heavy metal contaminated soils. Ind. Constr. **1**, 65–70 (2014)
51. Li, J.S., Xue, Q., Wang, P., Li, Z.Z., Liu, L.: Effect of drying-wetting cycles on leaching behavior of cement solidified lead-contaminated soil. Chemosphere **117**, 10–13 (2014)

Distribution and Reserve Potential of Titanium-Zirconium Heavy Minerals in Quang an Area, Thua Thien Hue Province, Vietnam

Nguyen Tien Dung, Bui Hoang Bac(✉), Do Manh An, and Tran Thi Van Anh

Faculty of Geosciences and Geoengineering,
Hanoi University of Mining and Geology, Hanoi, Vietnam
{nguyentiendung, buihoangbac}@humg.edu.vn,
manhan.humg@gmail.com, vananhtranhumg@gmail.com

Abstract. Quang An, Thua Thien Hue province, Vietnam, is one of the areas with great heavy-mineral potential. The heavy-mineral ore body distributes along the beach with the width of 300–800 m and the length of about 6,100 m. A total of 4,398 samples were collected vertically in a grid pattern from 585 bore holes covering an area of 2.882 km^2. The results indicate that the ore body is in marine-eolian sediments at Late Holocene (mvQ_2^{2-3}). Useful heavy minerals were ilmenite, rutile, leucoxene, anatase, zircon and monazite which could be found in the intrusive and other rocks in the region. The total heavy minerals (THM) content in the bulk samples is not so high with average of 1.172%. The heavy mineral grains are small with the size of 0.05–0.25 mm and they are well liberated, rounded to sub-rounded. The average thickness of ore body is about 8.3 m, however, its variation is relatively stable with the coefficient of 39.28%. The average content of TiO_2 in ilmenites of 58.02% and ZiO_2 in zircons of 60.89% indicate that titanium-zirconium heavy minerals in Quang An area have relatively good quality. The proven reserves of total heavy minerals in study area were determined reliably with about 406.595 thousand tons, of which the measured mineral reserve is 68.177 thousand tons and the indicated mineral reserve is 338.418 thousand tons. This paper deals with the distribution and potential of heavy minerals in the study area in order to promote efficient mineral exploitation and mineral processing.

Keywords: Heavy minerals · Ilmenite · Zircon · Distribution · Reserve potential

1 Introduction

Beach-placer deposits are accumulations of heavy, resistant minerals with high specific gravity that form on upper regions of beaches or in long-shore bars in a marginal-marine environment. They form by mechanical concentration of heavy minerals by the action of waves, currents, and winds [6]. They typically consist of titanite, zircon, magnetite, ilmenite, monazite, apatite, rutile, xenotime, garnet, and

© Springer International Publishing AG 2018
D. Tien Bui et al. (eds.), *Advances and Applications in Geospatial Technology and Earth Resources*, https://doi.org/10.1007/978-3-319-68240-2_20

allanite, among other minerals. Titanium-zirconium placer deposits have been exploited and served in various industries in many countries around the world like USA, Canada, Africa, Brazil, India, China [2–8, 12, 16]. Many studies on distribution, characteristics of heavy minerals in beach placer deposits around the world have been published [2–8, 12, 16]. Tyler and Minnitt pointed out the importance of the titanium-zircon heavy minerals and new business opportunities in the exploitation of these minerals in in South Africa [16]. Distribution, mineralogy and chemistry of heavy minerals in some placer deposits in India had been studied by Acharya et al. [2–5]. Based on detailed mapping and exploration drilling of some Late Cretaceous heavy mineral deposits in San Juan Basin, New Mexico, USA, McLemore fully evaluated resource and economic potential for these deposits in current changing economic market [12]. Recent years, many studies related to marine environmental geochemistry, marine sedimentary as well as heavy mineral placer deposits in Vietnam have been interested by scientist and investing companies [9–11, 13–15]. Existing survey reports indicate that there is great potential for total heavy mineral deposits along the coast of the country with high potential of titanium - zirconium heavy minerals. In the surveying report on potential of heavy minerals along coastal line from Thanh Hoa to Thua Thien Hue, it indicated that this region has a significant potential of heavy minerals and it should be studied systematically [9].

Quang An, Thua Thien Hue province, is one of the areas with great heavy-mineral potential in Vietnam (Fig. 1A). However, studies on heavy minerals in detailed for providing important data to investors are still limited. The aim of this paper is to discuss about the quality, spatial distribution characteristics of ore placer minerals and clarifies titanium-zirconium heavy minerals potential in Quang An area, in order to providing the necessary information for efficient exploration, exploitation, use of the resource.

2 Geological Features of the Study Area and Surrounding Region

2.1 Stratigraphy

Middle Cambrian - early Ocdovician A Vuong Formation ($\in_2$-O_1 av) is the oldest metamorphic unit in the region. It is exposed in the west of the study area as a range following a northwest - southeast orientation. Younger metamorphic unit is Late Ocdovician - Early Silurian Long Dai Formation (O_3-S_1 ld) which is exposed as a large area in the central region. The metamorphosed rocks comprise mostly shale, chert, tuffaceous sandstone, sandstone (Long Dai Formation) and quartz-feldspathic schist, quart-mica schist (A Vuong Formation). In the region, sedimentary rocks include Tan Lam (D_1 tl), A Lin (P_2 al), A Ngo (J_1 an) Formations which are exposed as scattered units in the region and alternated with other rocks (Fig. 1B). Compositions of these formations are mainly sandstone, musdstone, limestone [9].

The exploration results indicate that the study area presents two types of unconsolidated sediments with different origins (Fig. 2). Marine-eolian sediments at Late Holocene (mvQ_2^{2-3}) cover the whole study area with sand strips and dunes. The sediments

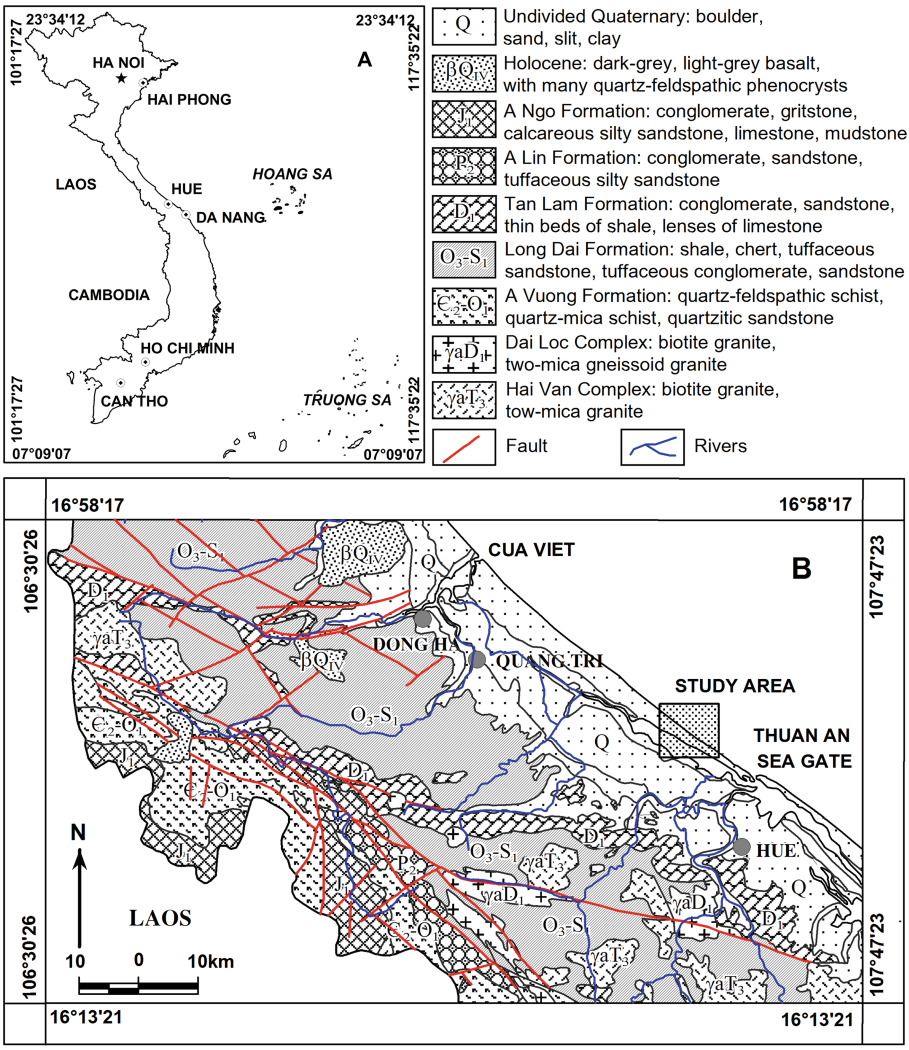

Fig. 1. Location of the study area in Vietnam (A); regional geological map (B)

comprise of small to medium-sized dark yellow, brownish-yellow quartz sand showing yellowish-gray color in the surface, containing many black heavy minerals. The average thickness of this layer is 8.3 m. Late Holocene fluvio-marine sediments (amQ_2^3) distribute along the western coast and are usually affected by sea waves, tides and river from the Tam Giang lagoon. The fluvio-marine sediments comprise of clay, clayey sand, sand containing less titanium-zircon minerals with thickness of 3–10 m.

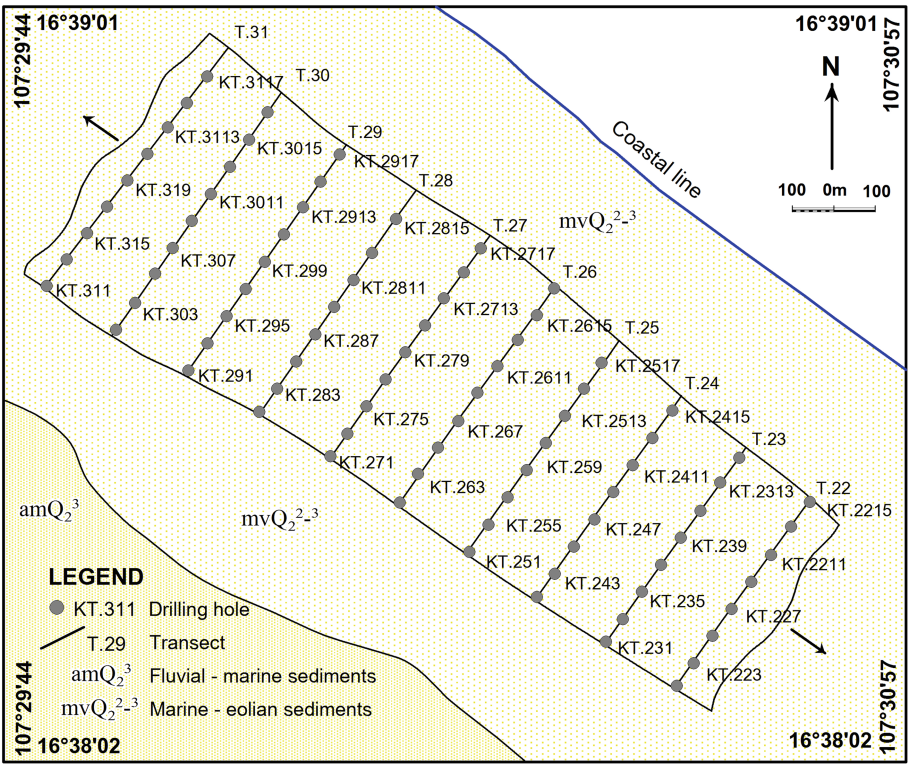

Fig. 2. Representive grid pattern of sampling in the study area

2.2 Magmatism

There is no intrusive rocks exposed in the Quang An study area. However, Dai Loc and Hai Van Complexes can be found in the surrounding areas (Fig. 1B). The rocks expose as small to medium bodies scattering in the western and southern parts of the region. These complexes consist mainly of biotite granite and two-mica granite. Containing a significant content of heavy minerals, these rocks were referred as important sources of the heavy minerals to the study area.

3 Methodology

3.1 Grid Pattern of Sampling

Samples were collected according to the regulations for the classification of reserves and resources of solid minerals of Minister of Natural Resources and Environment of Vietnam. Drilling grid patterns were defined with grids of 100 m × 20 m and 100 m × 40 m for the measured mineral reserve (121) and the indicated mineral reserve (122), respectively (Fig. 2) [1]. Fifty exploration transects with striking N35°E

were set up to be perpendicular to the coast line in the study area. The 585 boreholes were drilled by hand augur drilling method. The bore depths were from 3.0 m to 16.0 m depending on the specific positions and ensure to cut through the thickness of the ore body. Each drilling interval of 0.5–1.0 m was taken one sample and the total number of collected sample is 4398. Drilling and sampling methods were described in detailed by Nguyen et al., 2011 [15].

3.2 Sample Preparation and Analysis

All samples were brought to the laboratory, dried and thoroughly mixed. The samples were then sieved with ASTM sieve numbering 16 (Size of 1.18 mm). Each sample was reduced to 20–30 g by coning and quartering processes. The samples were treated with water to remove the ultra fine clays. The dried sample was put in a heavy liquid Bromoform to separate to heavy and light minerals and the total heavy mineral concentration was calculated. Three groups of magnetic, electromagnetic and non-electromagnetic minerals were separated by using handling magnets. The heavy mineral fractions were taken to prepare the slides for the study under the microscope. The number percent of each of the heavy minerals was multiplied with their respective specific gravity values and the wt% of the individual member was calculated.

The heavy minerals were characterized using various techniques. The distribution of heavy minerals was determined by manual grain counting using an optical microscope (Leica-Wild M8). The morphological properties and mineral chemistry of heavy minerals were examined by using the scanning electron microscope (SEM - Quanta 450) with energy dispersive X-ray spectroscopy (EDS). X-ray powder diffraction patterns of the heavy mineral samples with different conditions were also measured using a D5005 S model powder diffractometer with Cu-Kα radiation at 40 kV and 30 mA, scanned from 3 to 70° at a goniometer rate of $2\theta = 2°\text{min}^{-1}$. The chemical composition of the samples was determined using X-ray fluorescence (XRF, Philips X Unique2).

3.3 Statistical Analysis

The content of heavy minerals are presented by descriptive statistics (mean, standard deviation (SD), minimum and maximum concentrations, skewness, variation coefficient etc.) using the SPSS Statistics software for Windows (SPSS Inc., Chicago, IL, USA, 2007). Together with standard deviation, coefficient of variation (CV), which is SD/mean, was used to reflect the degree of discrete distribution of different metal element concentrations and to indicate indirectly the activeness of selected element in examined environment.

The Spearman's rank correlation was used to examine the correlation between minerals. The correlation coefficient matrix measures how well the variance of each constituent can be explained by relationship with each other.

3.4 Reserve Calculation

The reserve of total heavy minerals in the study area is calculated by the geological block method. The equation is as follow: Q = S. M.C.D. Where: Q: Reserves of total

heavy minerals (ilmenite + rutile + anatase + leucoxene + monazite + zircon, thousand tons. S: Square, thousand m^2. M: Average thickness of the ore body in the block, m. C: Content of THM, %. D: Weight of ore sand (ton/m^3).

4 Results

4.1 Mineralogy

Analysis results of heavy mineral samples indicate that there is almost no presence of magnetic minerals. Electromagnetic group includes mainly ilmenite, tourmaline, amphibole, sphene limonite, granate, epidote, monazite and so on. Heavy non-electromagnetic group consists of mainly zircon, less rutile, sillimanite, anatase, leucoxene. Among the above-mentioned minerals, useful ones in ore placers are ilmenite, zircon, rutile, anatase, leucoxene and monazite. SEM images indicate that the main heavy mineral grains are well liberated, rounded to sub-rounded (Fig. 3).

Statistic results show that the contents of total heavy minerals in deposits of the study area vary considerably with the average of 1.172%. The variation of ore mineral contents are uneven with a coefficient of variation of 49.0–87.4%. Useful heavy minerals correlate quite closely with a coefficient of correlation from 0.27 to 0.91 (Table 1).

Table 1. Pearson's correlation matrix for the useful heavy minerals in study area [16]

Minerals	Ilmenite	Anatase	Rutile	Leucoxene	Zircon	Monazite
Ilmenite	1.0					
Anatase	0.78	1.0				
Rutile	0.76	0.91	1.0			
Leucoxene	0.51	0.27	0.29	1.0		
Zircon	0.79	0.80	0.75	0.52	1.0	
Monazite	0.86	0.77	0.74	0.34	0.70	1.0

4.2 Grain Size Distribution

The heavy mineral distribution in different size fractions in bulk sample and after processing is given in Table 2 and Fig. 4.

Table 2. Grain size distribution of heavy minerals in the study area

Size fractions (mm)	Bulk (%)	Heavy minerals distribution after processing (%)			
		Ilimenite	Zircon	Rutile	Monazite
>0.5	0.33	0.0	0.0	0.0	0.0
0.50 ÷ 0.25	77.33	0.67	0.0	0.70	0.0
0.25 ÷ 0.10	20.18	48.07	4.05	63.30	1.15
<0.10	2.16	51.27	95.50	36.00	98.85

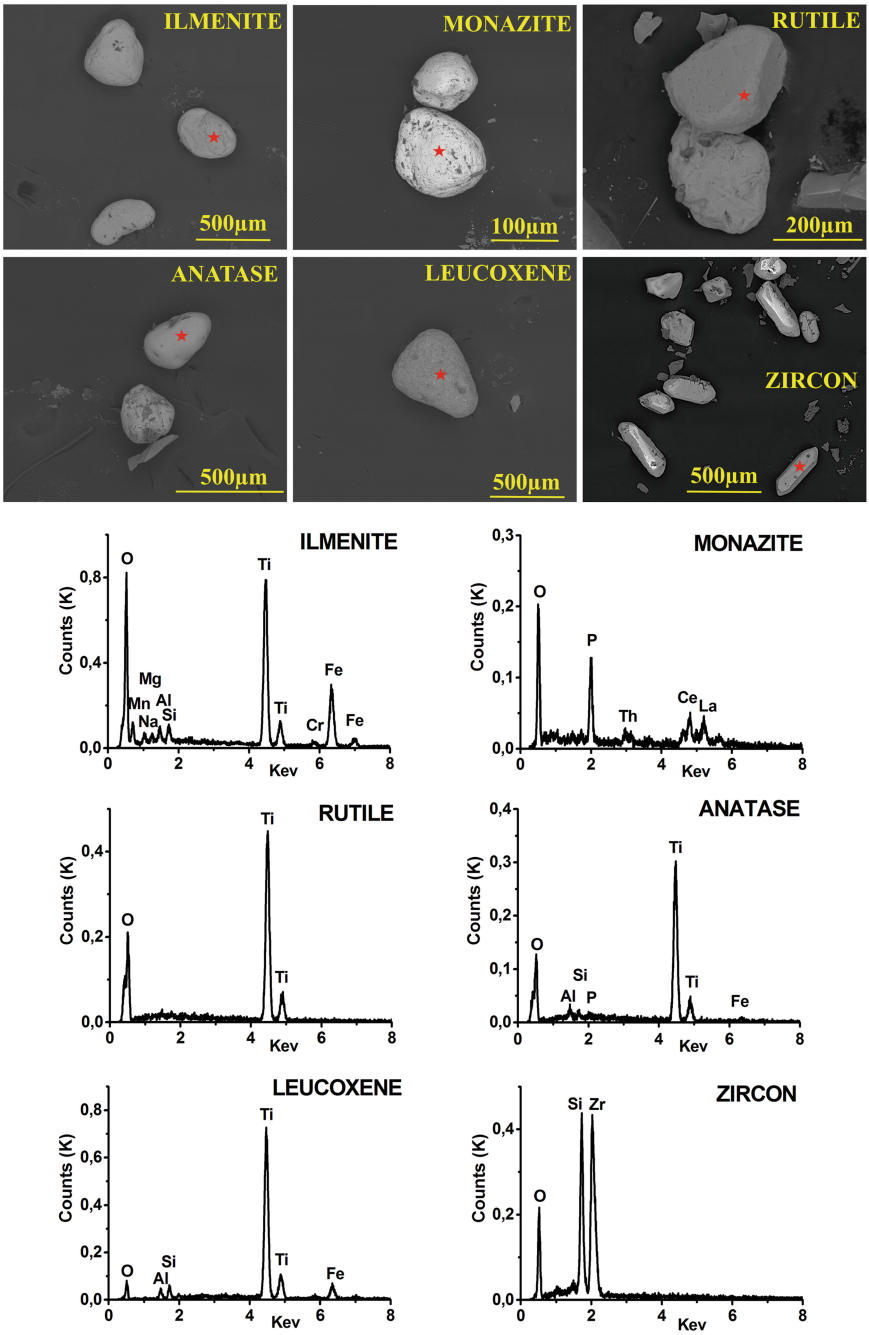

Fig. 3. SEM-EDS images of main heavy minerals in the study area

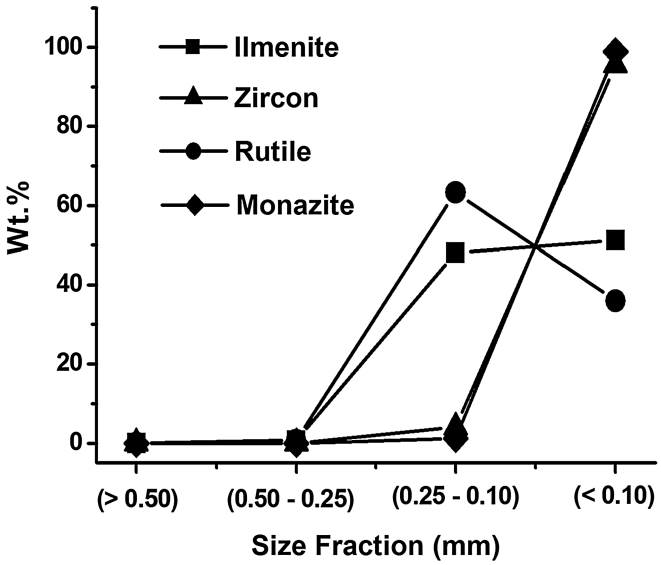

Fig. 4. Heavy mineral distribution after processing in different sieve fractions

Grain-size analysis shows that the bulk samples contain mainly small to medium and fairly uniform grains. Sand particles in the range of 0.1–0.5 mm account for about 97.51%. Minerals with size fraction above 0.5 mm are negligible with an average of 0.33%. Those with size fraction of less than 0.1 mm has a low percentage with an average of 2.16%. However, analysis results of concentrating ore indicate that concentrating ores of ilmenite, rutile, zircon and monazite contain small-sized particles mainly in the range of 0.25–0.05 mm. Ilmenite and rutile in the size of 0.5–0.25 mm are insignificant. Monazite and zircon grains are finer in size. The presence of heavy minerals above 0.25 mm is negligible.

4.3 Mineral Chemistry

Chemical analysis of bulk samples indicates that TiO_2 content ranges from 0.40% to 1.33%, average of 0.88%. ZrO_2 content ranges from 0.09% to 0.29%, average of 0.18% (Table 3).

SEM-EDS was used to determine the semi-quantitative contents of the oxides in the major heavy minerals in the study area (Fig. 3, Table 4). *Ilmenite* grains contain 58.02% TiO_2, 37.33% FeO, 1.97% MnO, 0.08% MgO, 0.07% Al_2O_3, 0.43% SiO_2, 0.51% Cr_2O_3, 0.22% Cao, 0.21% Na_2O, 0.23% K_2O and 0.30% P_2O_5 in average. Ilmenite in the studied mine has higher titanium dioxide and smaller ferrous iron than ilmenite in other places [2–8, 12, 16]. The existence of Mn^{+2} and Mg^{+2} may be due to their replacement for Fe^{+2} in the ilmenite structure. *Rutile* contains 95.12% TiO_2, 0.81% FeO, 0.87% Al_2O_3, 0.55% SiO_2, 0,64% Cr_2O_3, 0.57% MnO with trace amounts of Na, Mg, K. *Leucoxene* contains 4.40% FeO, 80.44% TiO_2, 7.15% Al_2O_3, 6.55% SiO_2, 0.10% MgO and 1.35% P_2O_5. Leucoxene compared to ilmenite has higher

Table 3. Chemical analysis of bulk samples in the study area

Oxide	Content (%)		
	Minimum	Maximum	Average
SiO_2	94.82	97.34	95.95
TiO_2	0.40	1.33	0.88
CaO	0.02	0.13	0.09
MgO	0.04	0.11	0.08
ZrO_2	0.09	0.29	0.18
Al_2O_3	0.68	1.33	1.00
FeO	0.010	0.03	0.02
Fe_2O_3	0.45	1.07	0.73
Cr_2O_3	0.002	0.006	0.004
MnO	0.010	0.05	0.03
P_2O_5	0.030	0.090	0.053
V_2O_5	0.001	0.003	0.002
SO_3	0.18	0.29	0.22

amounts of Ti, Al, Si and lower amounts of Fe. The higher contents of Al_2O_3 and SiO_2 in leucoxene may due to external sources during the complex alteration process [6]. *Anatase* has 92.65% TiO_2, 0.97% Al_2O_3, 0.45% SiO_2, 0.38% P_2O_5, 0.32% MgO, 0.17% CaO, 0.79% Cr_2O_3, 0.78% MnO and 3.5% FeO. SEM-EDS confirms the presence of Zr, Si in zircon and La, Ce and Th in monazite (Fig. 3, Table 4).

Table 4. Chemical analysis of heavy minerals in the study area

Oxide	Content (%)					
	Ilmenite	Rutile	Leucoxene	Anatase	Monazite	Zircon
Na_2O	0.21	0.38	0.00	0.00	4.55	1.70
MgO	0.08	0.09	0.10	0.01	–	–
Al_2O_3	0.70	0.87	7.15	0.97	3.57	1.94
SiO_2	0.43	0.55	6.55	0.45	3.02	35.47
P_2O_5	0.30	0.44	1.35	0.38	35.03	–
K_2O	0.23	0.19	0.00	0.32	–	–
CaO	0.22	0.34	0.00	0.17	–	–
TiO_2	58.02	95.12	80.44	92.65	–	–
Cr_2O_3	0.51	0.64	0.00	0.79	–	–
MnO	1.97	0.57	0.00	0.78	–	–
FeO	37.33	0.81	4.40	3.50	3.47	–
ThO_2	–	–	–	–	6.08	–
La_2O_3	–	–	–	–	16.63	–
Ce_2O_3	–	–	–	–	27.64	–
ZrO_2	–	–	–	–	–	60.89

4.4 Variation of Ore Body Thickness

Titanium-zirconium ore placer body lies horizontally, exposes on the terrain surface and spreads over the entire study area. Sand layer containing ore consists mainly of small to medium-sized grains which are dark yellow, yellowish-gray to light yellow in color. The results of hand drilling and sample analysis indicate that orebody thickness varies from 2.0 m to 15.0 m with the average thickness of 8.3 m. The orebody is relatively stable in thickness with the coefficient of variation of 39.28%. In parallel with the coastline, the thickness of orebody is less variable and tends to gradually decrease from north to south. As perpendicular to the coastline, the thickness of orebody appears to decrease from center to edge (Fig. 5).

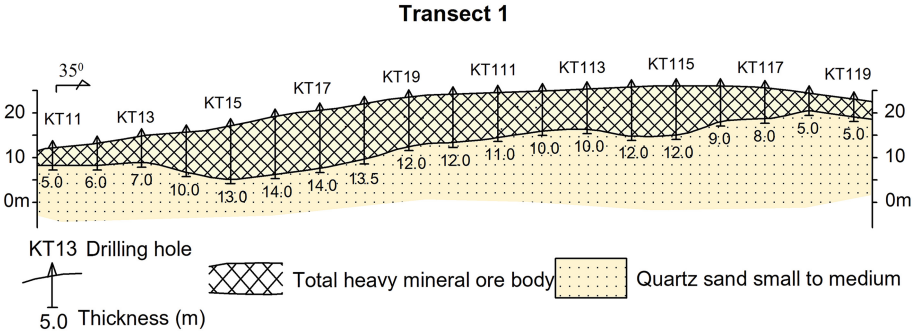

Fig. 5. Variation of orebody thickness in a representative transect 1

4.5 Distribution of Total Heavy Minerals

Research results show that valuable minerals in coastal placer at Quang Ngan area are mainly consist of ilmenite and less zircon, rutile, leucoxence, anatase and monazite. In general, the total heavy mineral contents considerably vary from low to medium grade with value of 0.251% to 3.35%, and the average of 1.17%. The total heavy mineral content varies unevenly with the coefficient of variation of 49.0%.

The results indicate that placer mineral contents vary considerably. These minerals also show quite clear distribution pattern. In general, mineral contents highly vary along the coast and perpendicular to the coastline. In parrallel with the coastline, heavy mineral contents tend to gradually decrease from center to northwest and southeast.

As perpendicular to the coastline, the contents of the total heavy minerals and heavy minerals normally appear to decrease from the continent to the sea. However, within the study area, this trend slightly changes with rich ores concentrating in the center in the form of strips and decreasing toward the two sides (Fig. 6). With depth, the results of hand drilling, sampling and sample analysis indicate that total heavy minerals are mainly distributed at the depth of 0–15 m with a cut-off of 0.25% THM (Fig. 6).

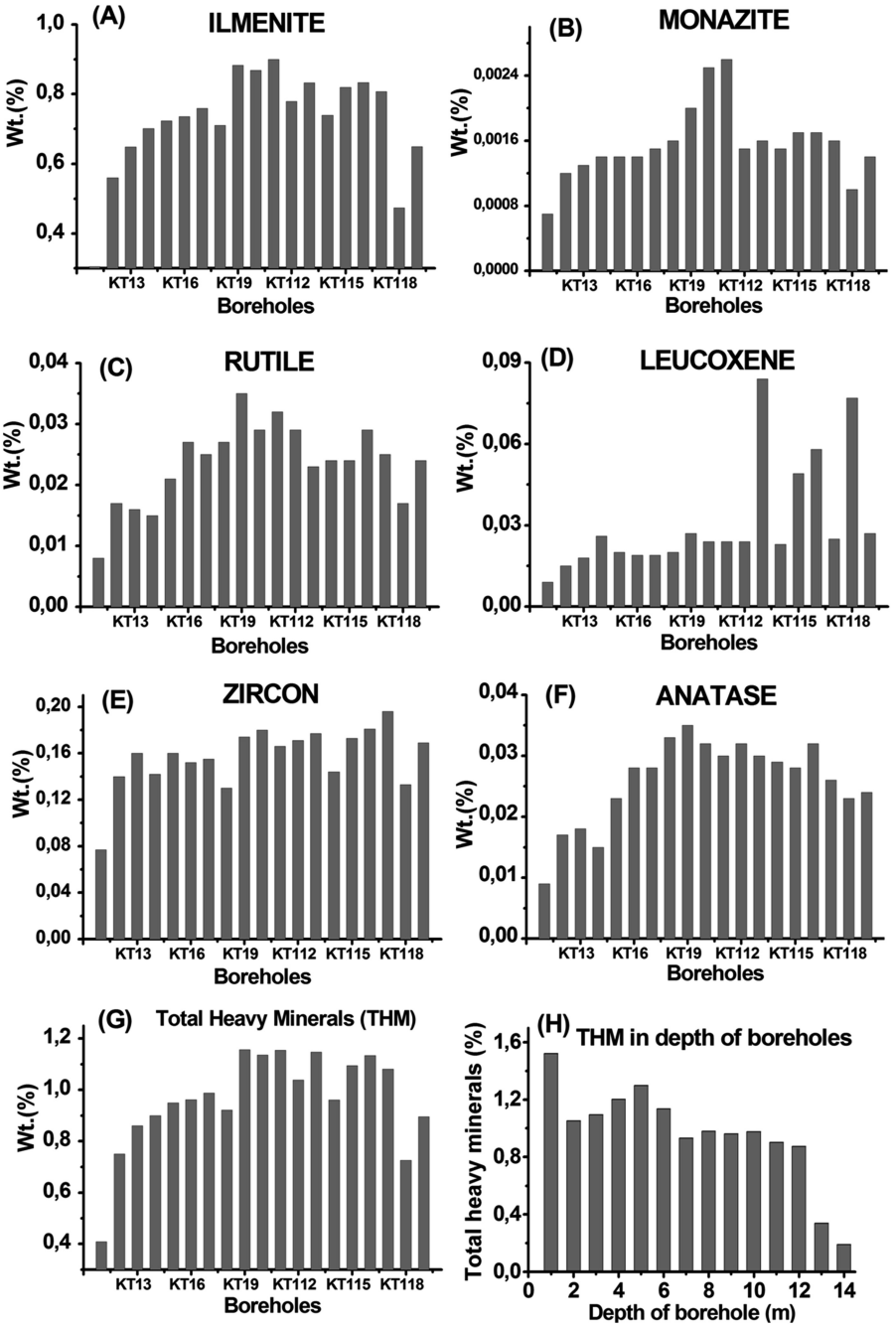

Fig. 6. Distribution of total heavy minerals in a representative transect 01

4.6 Reserve of Heavy Minerals

The parameters were selected for calculating the measured and indicated reserves of total heavy mineral in the study area including: a cut-off of 0.25% total heavy minerals in single sample and 0.50% in the block. The minimum thickness of the ore body is 1.0 m. The maximum thickness of waste sand is also 1.0 m.

Because the ore body in the study area is horizontal and its thickness is quite stable. All drilling holes were cut through the thickness of the ore body. Therefore, the method using to calculate reserves of total heavy minerals is the geological block method. Bourdary of block is connected by drilling grid patterns of 100 m × 20 m and 200 m × 40 m for level 121 (the measured mineral reserve) and 122 (the indicated mineral reserve), respectively (Fig. 2). The study area is divided into seven blocks (one block of level 121 and 6 blocks of level 122) and the proven reserves are shown in Table 5.

Table 5. Proven reserves of total heavy minerals in Quang an area

Block	Square (m^2)	Thickness (m)	Content of THM (%)	Dry weight (ton/m^3)	Proven reserve (1000 tons)
1–121	404700	9.19	1.207	1.52	68.177
Level 121					***68.177***
1–122	330000	9.51	1.328	1.52	63.301
2–122	392300	7.06	1.209	1.52	50.855
3–122	378900	6.60	1.109	1.52	42.116
4–122	431700	7.72	1.215	1.52	61.447
5–122	504100	7.81	1.139	1.52	64.092
6–122	432400	7.96	1.083	1.52	56.607
Level 122					***338.418***
Sum (121 + 122)					***406.595***

The calculated results indicated that the proven reserves of total heavy minerals in Quang An area, Thua Thien Hue province, Vietnam were about 406.595 thousand tons, of which the level 121 is 68.177 thousand tons and the level 122 is 338.418 thousand tons.

5 Discussion

Quang An is located in Quang Ngan and Quang Cong Communes, Quang Dien District, Thua Thien Hue Province, about 15 km to the north of Hue City (Fig. 1A). It is one of the areas with great heavy-mineral potential. The whole area is covered by marine-eolian sedimentary formations (mvQ_2^{2-3}) at Late Holocene (Fig. 1B). Mixed marine sediments form sand strips and dunes distributed on high elevation terrain with uneven surface. Typical components are small to medium-sized dark yellow, brownish-yellow quartz sand showing yellowish-gray color in the surface, containing

many black heavy minerals. The heavy-mineral ore body is along the beach with the width of 300–800 m and the length of about 6,100 m. It has maximum thickness of 15 m, minimum thickness of 2 m and average thickness of 8.3 m. As perpendicular to the coastline, the thickness of orebody appears to decrease from center to edge because of sea waves and wind actions. Results indicate that the useful heavy minerals in the study area are mainly ilmenite, zircon, rutile, anatase, leucoxene and monazite. Close relationships between heavy minerals were referred to drive from the same source. Moreover, small and rounded to sub-rounded grains also indicate that these heavy minerals had been moved a long way along the rivers. The rivers in the region are important factors for carrying heavy minerals from the land to the beaches. After that, these heavy minerals had suffered from tectonic and neotectonic activities and other influences such as geomophology, sea waves, tides, winds and currents. In order to precisely identify the source rock and understand the depositional history of the placer deposit, detailed studies should be carried out.

In the bulk samples, the average total heavy minerals (THM), TiO_2 and ZrO_2 contents are 1.172%, 0.88% and 0.18%, respectively. These contents are not so high comparing with other coastal areas such as in Binh Thuan province [9–11]. The average content of TiO_2 in ilmenites of of 58.02% and ZiO_2 in zircons of 60.89% indicate that titanium-zirconium heavy minerals in Quang An area have relatively good quality. Heavy mineral grains in the Quang An area are small with mainly in the size of 0.05–0.25 mm. The average thickness of ore body is about 8.3 m, however, its variation is relatively stable with the coefficient of 39.28%. The proven reserves in Quang An area are determined reliably in accordance with the Regulations of Minister of Natural Resources and Environment of Vietnam with THM of about 406.595 thousand tons. This is important information for enterprises to invest in mining and processing heavy minerals in the study area.

6 Conclusion

- The results indicate that the ore body is in marine-eolian sediments at Late Holocene (mvQ_{23}) with an average ore body thickness of 8.3 m.
- Useful heavy minerals were ilmenite, rutile, leucoxene, anatase, zircon and monazite and grains are well liberated, rounded to sub-rounded. The average total heavy minerals (THM) content of the bulk samples is 1.172%.
- The ilmenites contain the average TiO_2 content of 58.02%. The zircons contain the average ZiO_2 content of 60.89%. Distribution of the total heavy minerals are mainly in the size of 0.05–0.25 mm.
- The proven reserves of total heavy minerals in study area were about 406.595 thousand tons, of which the level 121 is 68.177 thousand tons and the level 122 is 338.418 thousand tons.
- Although the distribution of grain size, orebody thickness, characteristic of mineralogy, mineral chemistry and mining conditions are relatively favorable for exploiting, environmental impacts should be carefully researched. High technology of mineral processing has to be selected to improve the content of heavy minerals effectively.

Acknowledgements. The authors would like to thank the Center for Excellence in Analysis and Experiment (CEAE), Hanoi University of Mining and Geology, Vietnam for allowing us to use the SEM-EDS analyzer - Quanta 450.

References

1. Decision No 06/2006/QD-BTNMT: Regulations on classification of solid mineral resources and reserves. Minister of Natural Resources and Environment of Vietnam (2006)
2. Acharya, B.C., Das, S.K., Muralidhar, J.: Mineralogy, mineral chemistry and magnetic behaviour of ilmenite from Chhatrapur coast, Orissa. Indian J. Earth Sci. **26**, 45–51 (1999)
3. Acharya, B.C., Nayak, B.K., Das, S.K.: Heavy mineral placer sand deposits of Kontiagarh area, Ganjam district, Orissa. India Res. Geol. **59**(4), 388–399 (2009)
4. Acharya, B.C., Nayak, B.K., Das, S.K.: Mineralogy and mineral chemistry of placer deposit around Jhatipodar. Odisha J. Geol. Soc. India **86**, 137–147 (2015)
5. Acharya, B.C., Panigraphy, P.K., Nayak, B.B., Sahoo, R.K.: Heavy mineral placer deposits of Ekakula beach, Gahiramatha coast, Orissa, India. Res. Geol. **48**, 125–136 (1998)
6. Bradley, S.V.G, Donald, I.B.L, George, M.B., Karl, J.E., Anjana, K.S.: Heavy mineral sands. Coastal deposits of heavy mineral sands; Global significance and US resources. Mining Engineering, pp. 36–43 (2016)
7. Choudry, M.A.F., Nurgis, Y., Hussain, A., Abbasi, H.N.: Distribution and percentage of heavy minerals along makran coastline of Pakistan. Am. J. Sci. Res. **11**, 86–91 (2010)
8. Frost, M.T., Grey, I.E., Harrowfield, I.R., Mason, K.: The dependence of alumina and silica contents on the extent of alteration of weathered ilmenites from Western Australia. Mineral. Mag. **47**, 201–208 (1983)
9. Le, V.D., Pham, S.D., Dang, Q.D., Nguyen, P.T., Nguyen, V.H., Le, X.N., Nguyen, V.Q., Nguyen, V.S.: Report on surveying and assessment of heavy mineral potential along coastal line from Thanh Hoa to Thua Thien Hue. North Central Geological Division (2008)
10. Luong, L.H., Mai, T.N., Tran, D.Q., Hoang, V.T., Quach, M.D., Nguyen, D.H., Nguyen, T. T.: Characteristics of marine environmental geochemistry from Ha Tinh to Quang Nam (60-100 m water depth). Vietnam J. Earth Sci. **38**, 217–230 (2016)
11. Luong, Q.K., Khuong, T.H.: Distribution and potential of the titanium, zircon and rare earth minerals in the coastal placer, South Suoi Nhum, Binh Thuan province. J. Min. Earth Sci. **54**, 56–65 (2016)
12. McLemore, V.T.: Distribution, origin, and mineral resource potential of Late Cretaceous heavy mineral, beach-placer sandstone deposits, San Juan Basin, New Mexico. In: 61st Field Conference, Four Corners Country, pp. 197–212 (2010)
13. Nguyen, T.D., Tran, T.V.A.: Heavy minerals along coastline in Thua Thien Hue province and its influence to drilling grid pattern. J.Min. Earth Sci. **37**, 13–22 (2012). (in Vietnamese)
14. Nguyen, T.T., Karl, S., Daniel, U., Charles, N., Phung, V.P., Paul, L., David, D., Bui, V.D., Le, D.A., Mai, D.D.: Surface sediment grain-size distribution and sediment transport in the subaqueous Mekong Delta, Vietnam. Vietnam J. Earth Sci. **39**, 193–209 (2017)
15. Nguyen, T.D., Nguyen, C.D., Vu, V.S., Nguyen, G.N., Nguyen, Q.T., Dang, V.L., Le, V.P.: Report on exploration of titan-zircon heavy minerals in Quang Ngan commune, Quang Cong commune, Quang Dien district, Thua Thien Hue province. Thua Thien Hue one member limited liability Company (2011)
16. Tyler, R.M., Minnit, R.C.A.: A review of sub-Saharan heavy mineral sand deposits: implications for new projects in Sourthern Afica. J. South African Inst. Min. Metall., 89–99 (2004)

Application of Land Subsidence Inversion for Salt Mining-Induced Rock Mass Movement

Ryszard Hejmanowski(✉) and Agnieszka A. Malinowska(✉)

AGH University of Science and Technology,
Al. Mickiewicza 30, 30059 Cracow, Poland
{hejman, amalin}@agh.edu.pl

Abstract. Modelling of strains and deformations in salt mine areas encounters considerable difficulties because of the varying strength properties of salt, complex morphological formation of dome deposits and rheological properties of salt. Due to such properties the impact of salt extraction increases over hundreds of years and accurate determination of strains at a given moment and place is burdened with high uncertainty. Numerical modelling is useful when the model is reduced to one or several chambers. A broader range considerably lowers the accuracy and efficiency of calculations in such models. Stochastic models allow for 3D modelling of an entire mining complex, provided the model has been parametrized in detail. The process of strain and deformation modelling was presented on the example of one of the biggest salt mines in Europe, where the volume of over 21 million m^3 of salt deposit was extracted. The stochastic model could be parametrized thanks to the documented measurements results of panel convergence and levelling on the surface. The use of land subsidence inversion in the least squares method allowed to estimate the optimum values of the model parameters. The correctness of the evaluation was qualitatively and quantitatively confirmed graphically by comparing modelled and measured values of subsidence. The presented model can be applied in the future extraction projects for predicting strains and deformations for an arbitrary moment

Keywords: Rock mass movement modeling · Salt mine · Stochastic model · Subsidence and convergence measurements · Inversion method

1 Introduction

The prediction of strains and deformations of areas located above extracted salt deposits is necessary for a number of reasons. Firstly, mining contractors are obliged to submit maps with predicted subsidence and deformation areas along with the concession document. Secondly, salt rock with its rheological properties tends to show its impact on the surface with certain delay, even up to hundreds of years [1]. Therefore, prediction of movements is important for spatial management and urban development in the mine neighborhood. Rock mass and surface movements can be modelled with the use of mechanics-based numerical models or stochastic models based on the theory

© Springer International Publishing AG 2018
D. Tien Bui et al. (eds.), *Advances and Applications in Geospatial Technology and Earth Resources*, https://doi.org/10.1007/978-3-319-68240-2_21

of randomness of strains in uniform and loose medium [2, 3]. Regardless of the applied strain modelling method, a basic research problem occurs, i.e. that of model parametrization. This was frequently dealt with by solving the inverse equation interpreting the generated strain field as a known value, to which theoretically tends towards the strain field, calculated for given and approximate values of parameters [4, 5]. The objective function is distance between both strain fields, which in the course of minimization allows to determine optimum corrections for approximate–initial values of parameters. The weakness of the model is that it has too many parameters and they depend on one another. Such systems are hard to solve due to a lack of functional dependences between parameters (apparently independent), making the reduction of their number impossible [6]. The presented method allows to assess the parameters of the stochastic model with partial stabilization of parameters. It was based on a theoretical solution of inverse problem with the use of convergence and surface subsidence measurement results. In this way ambiguous solutions could be omitted and full parametrization of the model optimized. The evaluation method was adapted to rock salt and potassium salt mine where the panel structure is extensively developed.

2 Mining and Geological Setting

The salt dome located in central Poland is one of the biggest rock salt and potassium salt mines in Europe (Fig. 1). The deposit consists of Zechstein sandstone petering out through a thick complex of Mesozoic-Cenozoic sediments. Ten or so salt domes of complex geological formation, 5 to 7 km high, can be found in central Poland. Owing to strong tectonic deformations it is predominantly rock salt and potassium salt which are deposited inside the dome structure forming small and irregular cumulation. The experiments were conducted in the Klodawa salt dome, which belongs to the central part of the Izbica Kujawska–Klodawa-Leczyca salt dome. In the planar projection this dome is ellipsoid in shape and is oriented from North-West to South-East (Fig. 2).

The production of salt in Klodawa started in the mid 20th century and has been mined in 6 fields (P1 to P5 and P6, Fig. 2, Table 1) with the chamber-pillar system. In the first field extraction was conducted at five shallowest levels. The majority of the deposit was extracted in field 2, at levels corresponding to the relative depth of 450 to 600 m b.s.l. and in field 3, where part of the pink rock salt is being extracted (final stage) between levels 450 and 750. In field 4 over 20 chambers were mined at levels 538, 572 and 600, in a typical regular room-pillar system with chamber axes perpendicular to the length of the deposit. In field 5 pink rock salt deposit started to be cut and extracted between levels 600 and 750. Field 6 is a new region of dome extraction where chamber extraction has not been conducted yet except recognition with panels and boreholes. Field 7 is a small area where potassium salt is extracted from the dome, where the extraction was conducted in several chambers at levels 575 and 600, in a regular room-pillar system (the room and pillar 15 m wide). On average the rooms were 12 to 30 m high and about 15 m wide. The length of the chamber depended on

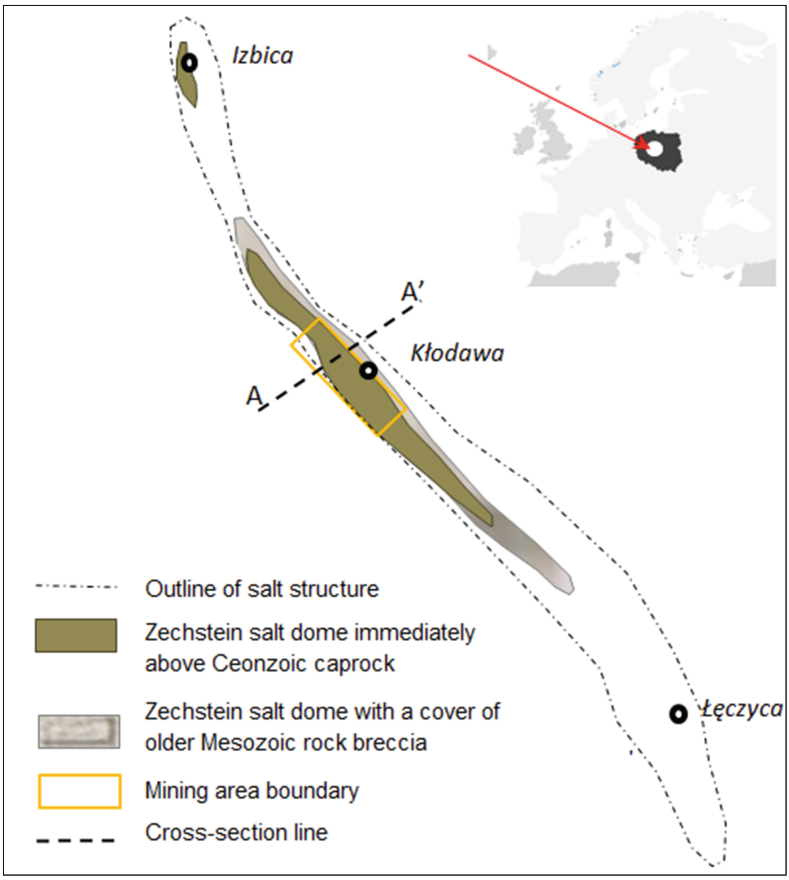

Fig. 1. Izbica Kujawska–Leczyca salt structure (after [7])

the geometry of particular parts of the deposit (Fig. 2). On the whole, since 1959 extraction has been conducted in 1310 chambers and about 21,005,800 m^3 of salt have been produced in Klodawa deposit. Presently production of a maximum of 26,597,500 m^3 of salt is being planned (Table 1). In the future the mine will be closed and filled with brine. This means that the voids will never fully contract.

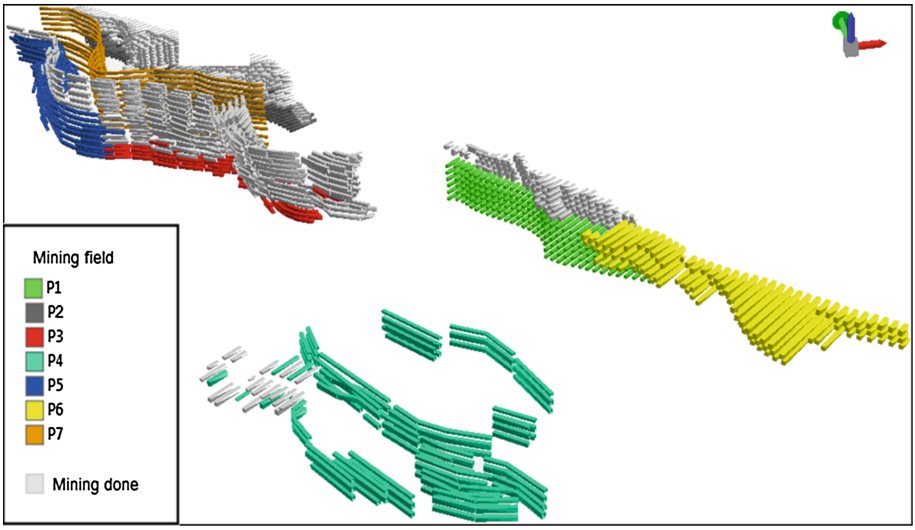

Fig. 2. Spatial distribution of mining panels done and planned in all fields (P1 ÷ P7)

Table 1. The volume of the extracted seam

Mining field No.	Panels done	Volume [m^3]	Panels left	Volume [m^3]
P1	143	1 957 802	210	3 374 640
P2	562	9 513 812	130	9 532 021
P3	461	6 540 183	93	3 950 935
P4	96	1 984 474	30	2 739 700
P5	38	698 060	205	2 799 061
P6	0	0	104	4 072 362
P7	10	311 520	201	128 784
Σ	**1310**	**21 005 851**	**973**	**26 597 502**

3 Measurement of Rock Mass and Surface Deformation

The salt dome is located immediately beneath a town (7,000 inhabitants). In order to ensure safety of extraction and to protect the surface in the dome area, underground and surface geodesic surveys have been conducted.

3.1 Measurement of Land Surface Subsidence

Owing to the considerable extent of strain fields and small annual alterations of the height of terrain over the salt mines, the measurements of vertical strain have been related to scattered benchmarks of guaranteed stability. This increases the number of levelling errors in long height series. Hence the exploration works focus on the height

differences between two neighboring points or groups of points in the levelling network. Levelling with the double levelling method may be an interesting solution [8]. The present impact of the K.S. Klodawa salt mine was determined on the basis of classic geodesic surveys. The benchmark network was stabilized in 1952 before mining of the salt deposit begun. The first levelling series were performed in 1978. Successive measurements were conducted in 1979, 1780, 1999, 2005 and 2011. Presently the measurement network consists of 282 benchmarks (Fig. 3). The benchmark levelling completed in 1978–2011 could be used to determine total subsidence troughs. Two local subsidence troughs can be distinguished in the mining area. The first formed over the second field. The maximum surface subsidence in the center of that trough amounted to 200 mm. The center of the trough shifted to the North-East in relation to the extraction fields (Fig. 4).

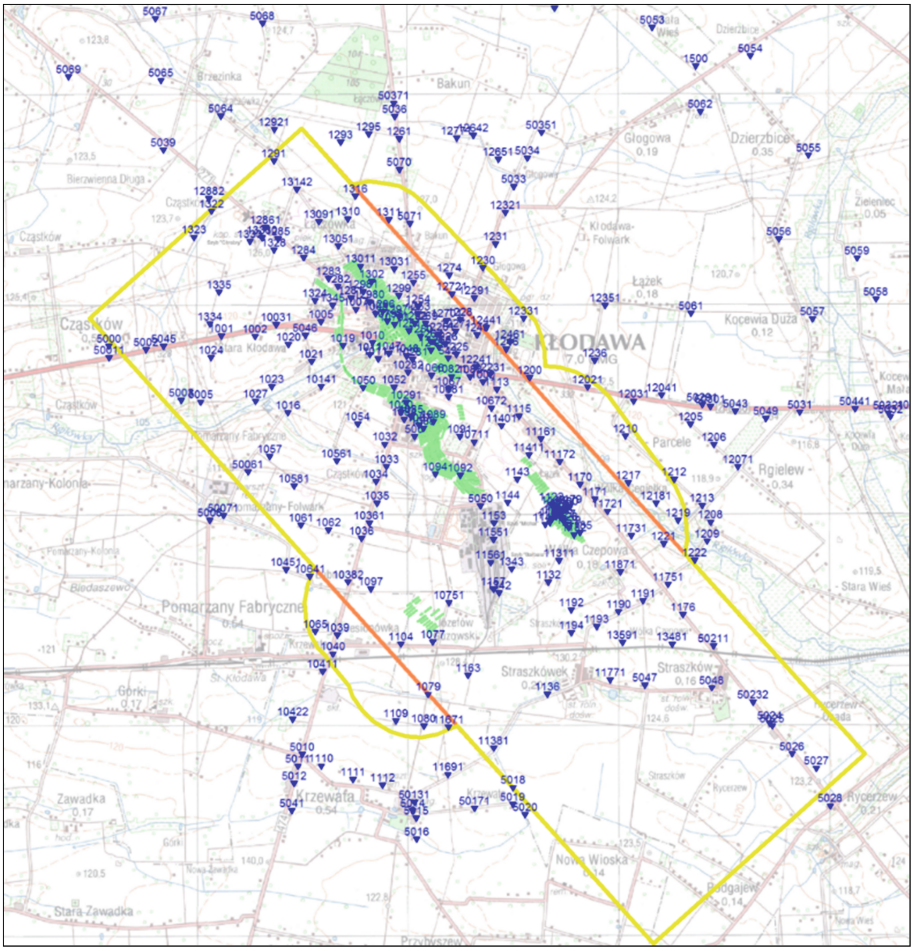

Fig. 3. Measurement network in KS Klodawa salt mine area

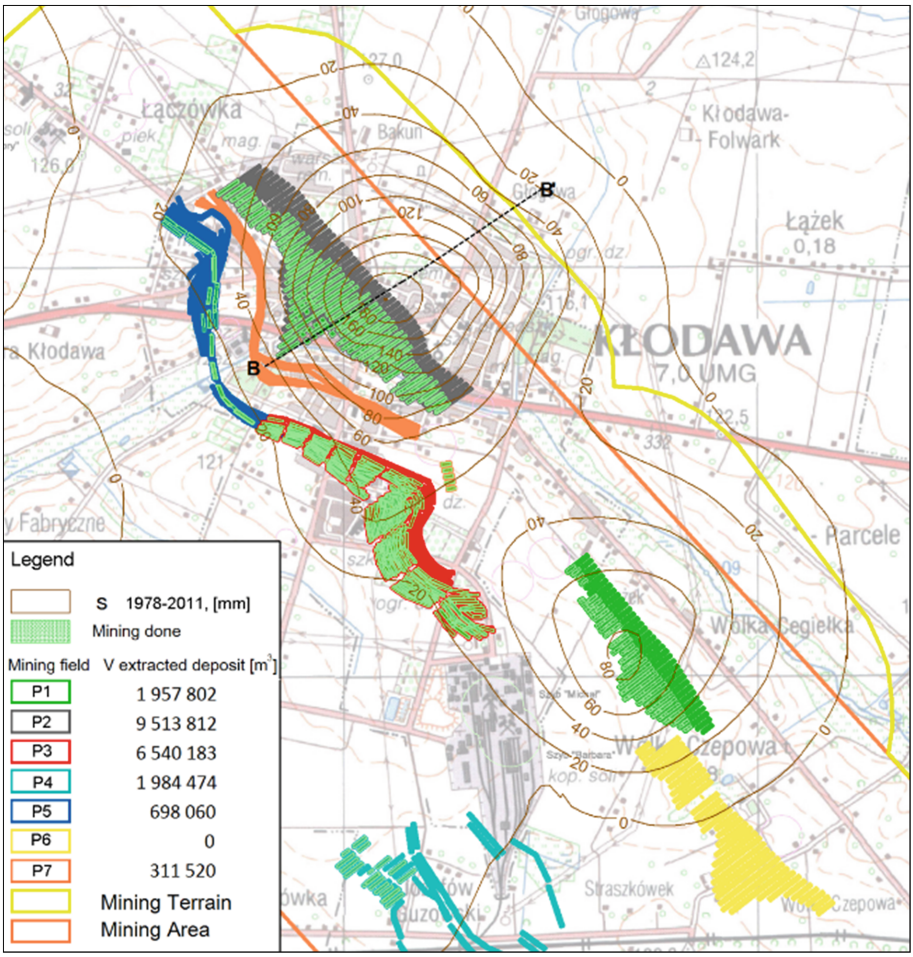

Fig. 4. Surface distribution of surface subsidence troughs

The other local subsidence trough formed above the first field. The maximum subsidence in the center of the trough was about 80 mm. An analysis of selected deposit volume in the light of subsidence observed on the surface reveals that:

- the biggest deposit volume was extracted in fields 2 and 3,
- the biggest subsidence was observed over the fields 2 and 1,
- extraction conducted in field 3 caused slight subsidence up to about 50 mm,
- the shift of the center of the trough in relation to the extraction field 2 may prove the presence of subsidence trough deviation caused by inclination of the dome layers over the deposit.

To conclude, the extraction works conducted in fields 1 and 2 had a decisive impact on the strains in the Klodawa salt dome area.

3.2 Convergence Measurements in Salt

Movements of salt rock mass disturbed by mining operations depend on a number of factors. Among the most important ones are the structural formation of the deposit and the surrounding rock mass, type of salt in the deposit, depth of deposition, method of extraction and geometry of panels, size of shelves between chambers and deposits. As a consequence, the movement of rock mass is very complex and convergence of panels in various parts of the deposit has decisive impact on the surface movement. The only efficient means of determining the convergence is its measurement.

The concluding results of complex and time-consuming convergence measurements in various Polish mines have been presented in Fig. 5 [9]. Thanks to these results the so-called relative bulk convergence may be determined, and on this basis the convergence parameter in the process of inverse estimation. There is a clear dependence of convergence rate on the depth of deposition (Fig. 5).

However, local variability has to be accounted for within the same deposit as it depends on the geological-mining conditions and determines the accuracy of model parametrization. This, in turn, has effect on the accuracy of surface strain and deformation predictions.

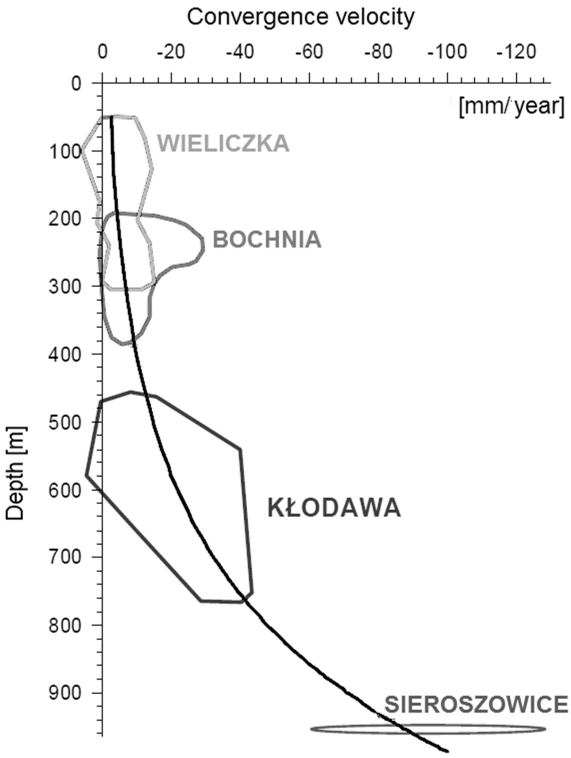

Fig. 5. Average convergence rates determined on the basis of measurements performed in Polish salt mines (after [9])

For instance, in the analysed Klodawa salt mine the convergence rate varies between a depth intervals of 460 m–770 m (Fig. 5). At a depth of 600 m the annual range of possible convergence rates oscillated between +5 mm/year and −50 mm/year. This depended on the location of the chamber in relation to the remaining ones in a given field or thickness of pillars between chambers or the area of the deposit.

4 Surface Subsidence Model

Modelling of such complex conditions in salt rock mass made up of many types of salt of varying mechanical properties, deposited in a dome of varying inclination, is very complicated. Two modelling solutions exist, i.e.

- numerical models with elasticity-plasticity assumptions, or plasticity conditions of modelling, or
- stochastic models.

4.1 Mining Elements and Elementary Subsidence Bowl Modelling

The implemented approach has been developed by the Author in a prediction model for oil and gas reservoirs based on the division of the reservoir into reservoir elements [10]. In the case of raw materials this model may be introduced by dividing the whole salt chamber system into mining elements [10]. In this case subsidence of an arbitrary point caused by mining operations may be expressed as:

$$\Delta s_{z_{i,j}}\left(d_{i,j}, t_i\right) = V_{s_i}(t)\varphi_z\left(d_{i,j}, H_i\right), \tag{1}$$

and mining-induced subsidence of the entire mining lot or part of the reservoir is a sum of elementary impacts:

$$s_{z_j}(t) = \sum_{i=1}^{N} \Delta S_{z_{i,j}}\left(\mathrm{d}_{i,j}, t_i\right) \tag{2}$$

where:

N – number (quantity) of mining elements,
i – number of a subsequent mining element,
j – number of an individual calculation point,
$V_{s_i(t)}$ – volume of elementary subsidence bowl at time t, due to mining of the layer volume in i^{th} mining element,
H_i – local mining depth in [m],
t – time difference between extraction date of each mining element and date of the prediction in [years],
$d_{i,j}$ – horizontal distance between calculated point, and the centre of the mining element in [m],
$\varphi_z\left(d_{i,j}, H_i\right)$ – influence function, expressed by the Eq. (3):

$$\varphi_z(d_{i,j}, H_i) = \frac{1}{r_z^2}\exp\left(-\pi\frac{d_{i,j}^2}{r_z^2}\right) \tag{3}$$

where:

r_z – radius of major impacts in Knothe's model, at a level 'z' over the mined deposit. For z = H this will be dependence of the angle of major impact zone β and mining depth H:

$$r_H = H\,ctg\beta \tag{4}$$

then:

$$r_z = r_H\left(\frac{z}{H}\right)^n \tag{5}$$

where:

H – mining depth [m],
β – angle of major impact zone [grad],
n – rock mass parameter, characterizing propagation of deformations in the space above the deposit. The 'n' value does not have impact by the prediction on the terrain surface, n < 1.0.

4.2 Two-Grade Modelling of Time

The Sroka-Schober two-grade time model was used in the analyses to describe terrain deformation caused by salt domes [11]. In the first phase the salt panels undergo convergence in time, in the next phase a convergence-induced subsidence trough is formed. This model was adapted by Hejmanowski firstly for oil and gas deposits [12], then to the conditions of coal, salt and copper ore extraction, taking into account the deviation of impact on the surface [13, 14]. In the first phase of description of the rock mass strain, the convergence rate of salt deposit was defined by proportionality to the difference of post-extraction void and bulk convergence at an arbitrary time t. This relation may be expressed by a differential Eq. (6):

$$\frac{\delta K(t)}{\delta t} = \xi \cdot [a_0 \cdot V(t) - K(t)] \tag{6}$$

where:

$\frac{\delta K(t)}{\delta t}$ – rate of bulk convergence in time t,
V(t) – volume of depletion at moment t,
K(t) – bulk convergence at moment t,

ξ – relative rate of convergence in time [1/year], convergence coefficient characterizing retarding properties of roof rocks in the workings area, [1/year],

a_0 – extraction coefficient, for salt = 1, i.e. the whole volume of the chamber changes (excluding loss) after infinite time into volume of converging rock mass.

The description of the deformation through the caprock has been expressed by an analogous differential Eq. (7):

$$\frac{\delta V_S(z,t)}{\delta t} = \vartheta(z)\left[a_1(z)\,K(t) - V_S(z,t)\right] \tag{7}$$

where:

$\frac{\delta V_S(z,t)}{\delta t}$ – momentary rate of volume increase of subsidence trough at level 'z' over the deposit, in time t,

$V_S(z,t)$ – momentary volume of subsidence trough volume at level 'z' over the deposit,

a_1 (z) – coefficient describing volume loss above the caving zone to level 'z', on the assumption that the dilatation of the rock mass equals zero,

$\vartheta(z)$ – coefficient characterizing delaying properties of the cap rock, [1/year].

Solving Eqs. (6) and (7) for boundary conditions, i.e. immediate extraction of each element of the deposit, a dependence for elementary volume of an elementary trough at moment t may be obtained in the following form (8):

$$V_S(t) = 1 + \frac{\xi}{\vartheta - \xi}e^{-\vartheta t} - \frac{\vartheta}{\vartheta - \xi}e^{-\xi t} \tag{8}$$

Equation (8) can replace Eq. (1) and then prediction of elementary subsidence in time will be possible.

The author's above solution was implemented in 'Modez' system for predicting continuous deformations. Obviously one should not forget about the limited applicability of this model in such systems. The strains of the converging chambers acting on the resistance pillars and interlevel shelves cannot be accounted for in this model. The strains in the roof shelf of the deposit cannot be modelled either, which is disadvantageous as this is how the potential hazard to this natural protection barrier of the dome could be evaluated. This type of calculation should be performed with the use of numerical methods, e.g. finite element method (FEM). With these limitations, the applied methodology of strain and deformation modelling allowed to develop an efficient 3D calculation model. Parameters were defined in this model and then the subsidence and deformations of ground surface could be determined for specific moments of time. This was the purpose of the experiments because of the necessity to specify possible surface hazards in the future.

5 Model Parameter Estimation Based on the Inversion Method

The parametrization of the model was based on the results of geodesic surveys which were used to define spatial distribution of subsidence troughs measured in 2011. The iterative terrain subsidence for varying parameters was modelled using the two-stage function of transition time. Optimum model parameters were obtained by minimizing the distance between these two vectors. The raster representing the time-and-space distribution of the measured subsidence points in space R^3 is described by set S^m:

$$S^m = \left\{ S^m_{ij}(x_i, y_i, t_j), i = 1, 2, \ldots, n, j = 1, 2, \ldots, q \right\} \tag{9}$$

where:

S^m_{ij} – subsidence in the i^{th} mesh of the raster in j^{th} time moment, in which the surface subsidence was defined,
x_i, y_i – coordinates of the gravity centre of i-th pixel in time moment t_j,
n – number of meshes in the raster,
q – number of analysed time moments.

The raster representing the time-and-space distribution of predicted subsidence points in space R^3 for varying parameters, was described by set S^p:

$$S^p = \left\{ S^p_{ij}(x_i, y_i, t_j), i = 1, 2, \ldots, n, j = 1, 2, \ldots, q \right\} \tag{10}$$

where:
S^p_{ij} – predicted subsidence in the i^{th} mesh of raster in j^{th} time moment.

The optimization criterion was worked out on the basis of the least squares method in the successive iterations:

1^o

$$F(\alpha) = \Sigma^n_{i=1} \Sigma^q_{j=1} \left(S^m_{ij} - S^p_{ij} \right)^2 \tag{11}$$

where:

α – set of parameters of the objective function $\alpha = \{S_{Az}, S_{An}\}$,
S_{Az} – dip azimuth of geological layers,
S_{An} – dip angle of geological layers. A constant set of remaining parameters {a, tgβ} was also assumed.

The approximated value of parameters S_{Az}, S_{An} was determined on the basis of a detailed analysis of geological conditions. In the profile running through the anticline

from the two North-East walls of the salt dome visibly stick to the Triassic and Jurassic formations. The tilt angle of the salt dome at the North-East boundary and the azimuth of the tilt angle equals $\alpha = 45°$. Accordingly, this angle was used in further simulations. The coefficient of deviation angle was empirically assumed as $\mu = 0.7$.

For asymptotic distribution: a = 1, tgβ = 1.00, ξ^{m} – the parameter responsible for the convergence rate worked out on the basis of convergence measurements (approximated parameter). The parameter of bulk relative convergence ranged from 0.001 [1/year] to 0.005 [1/year]. In deeper layers, where the pressure is higher, the convergence takes place faster as proved by the results of linear convergence measurements. Minimization of optimum solution for parameters S_{Az}, S_{AN}:

$$(S_{Az}, S_{An})_{opt} = (S_{Az}, S_{An}) : F(\alpha) \rightarrow min \tag{12}$$

minimization stop criterion was assumed as admissible fitting error σ

$$(S_{Az}, S_{An})_{opt} = (S_{Az}, S_{An}) : F(\alpha) < \sigma \tag{13}$$

A raster of predicted subsidence is obtained on the basis of the above solution, with optimum parameters S_{Az}, S_{AN}. Further analyses rely on the resultant raster from the first iteration $S_{ij}^{p'}$.

The second iteration referred to the optimization of solution in reference to parameter ξ:

2^{o}

$$F(C) = \Sigma_{i=1}^{n} \Sigma_{j=1}^{q} \left(S_{ij}^{m} - S_{ij}^{p'} \right)^{2} \tag{14}$$

where:

C – set of parameters of objective function,
$\alpha = \{\xi\}$, ξ – parameter referring to the rate of convergence (optimum parameter value).

The following set of remaining parameters was assumed: $\{a, tg\beta, S_{Az}, S_{An}\}$.

Subsequently simulation calculations were performed thanks to which the best parameter values which best describe deformations in the salt rock mass in Klodawa mine could be selected.

6 Results and Discussion

As a result of an iterative simulation of subsidence for the assumed minimization of deviations between measurement and prediction data, a surface distribution of predicted subsidence in 2011 was obtained (Fig. 6). For the optimum solution i.e. minimum impact, the fitting error standard deviation of predicted to measured subsidence raster, amounted to $\sigma_{So-Sm} = \pm 0.29$ mm.

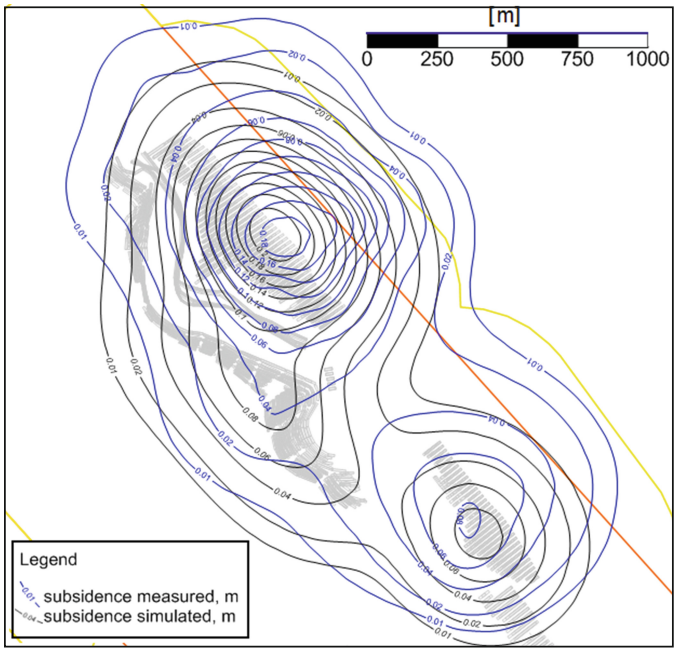

a)

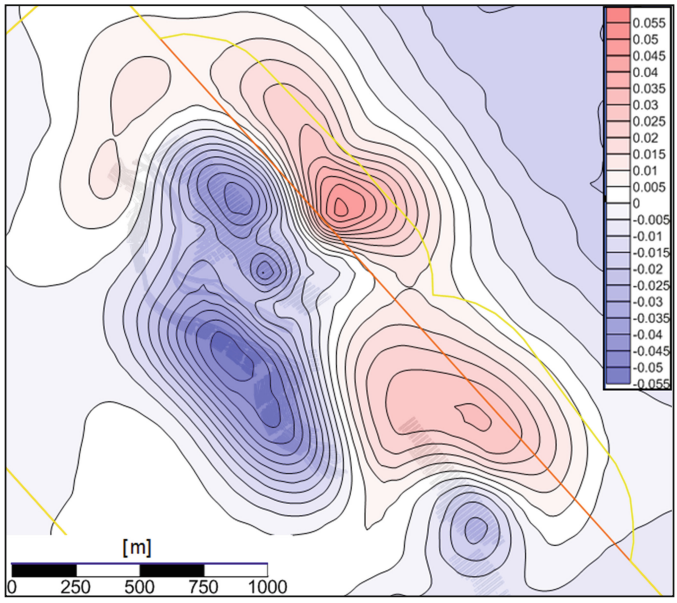

b)

Fig. 6. Predicted and measured distribution of surface subsidence in the year 2011, [m] (a) Difference between measured and predicted subsidence, [m] (b)

The measurements show to smaller subsidence than in the model in the South-West section of the analysed model. The maximum discrepancy between the measured and predicted subsidence reaches ±55 mm. The results of predicted subsidence are underestimated in the North-East sections of the mining area. An optimum solution was obtained for the following parameters:

$tg\beta$ = 0.7, tangent of mining impact angle (0.726),
μ = 0.6, parameter describing deviation of subsidence trough (tilt of rock mass layers),
r_s. = 50 m, major impact radius on the roof level of the extracted deposit,
a = 1.0, parameter depending on the extraction system (roof system),
ξ = 0.0007 ÷ 0.002 [1/year], bulk relative rate of convergence,
ϑ = 3.0 [1/year], coefficient of time for caprock.

Numerical modelling of subsidence over the mine where the total extracted volume in chambers is over 20 mln m^3 would require computation capacities and high cost to work out a 3D model. Attempts made regarding particular chambers or small parts of the mine brought positive results. However, no such numerical model has been developed for the FEM for the entire salt rock mass. The applicability of the analyzed stochastic model which is based on a normal distribution of impacts, has been verified and proved by successful estimation of model parameters. The values determined in the course of calculations are different than the initial values, nonetheless stability of calculations was maintained through the use of an iterative estimation algorithm.

The anisotropy of the rock mass was not analyzed. The distribution of theoretical and observed subsidence isolines indicates the existence of directional variability of mining impact dispersion. This is a potential field for future investigations to enhance the prediction model. The efficiency of the proposed solution could be improved by introducing coefficients of mining impact dispersion to the prediction model equations.

Acknowledgment. Research was financed from a Grant for Statutory Research AGH University of Science and Technology in Kraków, no. 11.11.150.195.

References

1. Marketos, G., Govers, R., Spiers, C.J.: Ground motions induced by a producing hydrocarbon reservoir that is overlain by a viscoelastic rocksalt layer: a numerical model. Geophys. J. Int. **203**(1), 228–242 (2015)
2. Fokker, P.A., Orlic, B.: Semi-analytic modelling of subsidence. Math. Geol. **38**(5), 565–589 (2006)
3. Cui, X., Miao, X., Wang, J., Yang, S., Liu, H., Hu, X.: Improved prediction of differential subsidence caused by underground mining. Int. J. Rock Mech. Min. Sci. **37**, 615–627 (2000)
4. Sroka, A., Schober, F., Sroka, T.: General relations between chosen volume of extracted cavity and a volume of subsidence surface, using a time function. Ochrona Terenów Górniczych **79**(1) (1987). (in Polish)
5. Fokker, P.A.: Subsidence prediction and inversion of subsidence data. In: SPE/ISRM Rock Mechanics Conference, 20–23 October, Irving, Texas (2002)

6. De Waal, J.A., Roest, J.P.A., Fokker, P.A., Kroon, I.C., Breunese, J.N., Muntendam-Bos, A. G., Oost, A.P., van Wirdum, G.: The effective subsidence capacity concept: how to assure that subsidence in the Wadden Sea remains within defined limits? Netherland J. Geosci. **91** (3), 385–399 (2012)
7. Poborski, J.: The Upper Permian Zechstein in the Eastern province of Central Europe. In: Third Symposium on Salt, Cleveland, pp. 24–29 (1970)
8. Fokker, P.A., Van Thienen-Visser, K.: Inversion of double-difference measurements from optical leveling for the Groningen gas field. Int. J. Appl. Earth Obs. Geoinf. **49**, 1–9 (2016)
9. Bieniasz, J., Wojnar, W.: History and selected result of Convergence studies in underground excavations within stratiform slat deposit. Gospodarka Surowcami Mineralnymi **23**(1), 133–142 (2007). (in Polish)
10. Hejmanowski, R.: Modeling of time dependent subsidence for coal and ore deposits. Int. J. Coal Sci. Technol. **2**(4), 287–292 (2015)
11. Schober, F., Sroka, A.: Die Berechnung von Bodenbewegungen über Kavernen unter Berücksichtigung des zeitlichen Konvergenz und Gebirgsverhaltens. Kali und Steinsalz Bd.8, Heft 10 (1993). (in German)
12. Hejmanowski, R.: Prediction of surface subsidence due to oil-or gasfield development. In: Proceedings of the Fifth International Symposium on Land Subsidence FISOLS, pp. 291–300 (1995)
13. Sroka, A., Hejmanowski, R.: Subsidence prediction caused by the oil and gas development. In: 3rd IAG/ 12th FIG Symposium, Baden, 22–24 May 2006
14. Hejmanowski, R., Kwinta, A.: System for prediction ground deformation - Modez. In: Proceedings of X Mine Surveying and Land Protection, Kraków (2009). (in Polish)

Study on the Coupling Effect Between Surrounding Rock and Support Structures of Tunnels

Pham Thi Nhan[1(✉)], Guangsheng Zhang[2], Viet-Nghia Nguyen[3], and Viet Huy Le[1]

[1] Department of Construction Techniques, Faculty of Civil Engineering, Hanoi University of Mining and Geology, Hanoi, Viet Nam
nhanthipham.humg@gmail.com
[2] JSTI GROUP, 2200, Chengxin Road, Jiangning Hightech Industrial Park, Nanjing, China
[3] Department of Mine Surveying, Faculty of Geomatics and Land Administrator, Hanoi University of Mining and Geology, Hanoi, Viet Nam
nguyenvietnghia@humg.edu.vn

Abstract. A coupling analysis system was built considering the interaction between surrounding rock and tunnel support structures. Three indexes including the utilization coefficient of overall performance of the supporting systemη, coupling efficiency of support structures W, and deformation characteristics of tunnel support structures B, were taken into account in this research. The corresponding weight values was obtained using Analytic Hierarchy Process (*AHP*). In addition, the quantitative analysis method was used to evaluate the influence of degree of coupling between surrounding rock and support structures with the aim of effectively controlling the movement of surrounding rock. The 3D software ANSYS was used to analyze the Yang Ling tunnel in Wu Xi province, China as an example of the coupling analysis system. As the grade level of surrounding rock in Yang Ling tunnel increases from type *III* to type *V*, it can be seen that under the condition of type *IV* the coupling efficiency of surrounding rock and supporting structure was the highest. The obtained results indicated that the method is appropriate for design optimization of tunnel support and studying the interaction between surrounding rock and support structures.

Keywords: Tunnel · Rock support · Coupling effect · Analytic Hierarchy Process (*AHP*)

1 Introduction

The infrastructure construction in China has been rapidly developed since the 21st century, especially railway and highway construction. Because of the special requirements of lines and slopes, tunnelling through mountain has become popular due to short traffic routes and less time consumption. Tunnels have became the optimal scheme for mountainous highways [1] as well as an important component of a

© Springer International Publishing AG 2018
D. Tien Bui et al. (eds.), *Advances and Applications in Geospatial Technology and Earth Resources*, https://doi.org/10.1007/978-3-319-68240-2_22

high-grade highway network. The increase in both scale and quantity of highway tunnel, i.e., larger quantity, longer length, bigger section, and deeper depth would be the trend of China's tunnel project development in future [2]. However, a phenomenon of non-coupling between surrounding rock and support structures is easy to appear due to some reasons, such as design and construction of the tunnel. Due to differences in both stiffness and strength of support structures compared to that of surrounding rock, the stability of tunnel can be significantly affected [3]. As a result of this phenomena, the instability of tunnel might somewhat occur at a certain part with a specific magnitude, then start spreading the whole support structures [4]. The current concept of coupling support was mainly used in roadway excavated in soft rock [5–11]. Unfortunately, there have been few researches about the coupling effect between the surrounding rock and support structures in mountain tunnels.

There are not clear definitions for some problems, such as how to achieve coupling, whether or not to be coupled and controllability of coupling mechanism between support structure and surrounding rock. Therefore, this paper aimed to establish a coupling analysis system to quantitatively determine the coupling effect between the surrounding rock and the support structure, forming a quantitative index for coupling analysis which can be used to optimize the design of support structure.

2 Coupling Support Mechanism and Evaluation of Its Performance Index

Recently, the objective of coupling mechanism is applied to control the deformation caused by the development of joints/crack in rock mass and help to make distributed loads acting on the tunnel support [12]. Three evaluation indexes including the utilization coefficient of overall performance of the supporting system η, coupling efficiency of support structures W, and deformation characteristics of tunnel support structures B [13] were considered using available data of previous experiments and data analysis [14–17]. The evaluation factors were determined by the analytic hierarchy process method. The corresponding weight value was used to quantitatively analyze the coupling effect between the surrounding rock and the support structures.

The deformation of tunnel was used to evaluate the effect of the support structure on the behavior of surrounding rock. As the deformation is smaller, the control effect of support system on surrounding rock is better.

$$B = \sum_{i=1}^{n} B_i W_{Bi} \tag{1}$$

where B_i is the component deformations, including that at tunnel vault, arch and inverted arch (bottom heave); W_{Bi} is the weight of corresponding deformation; and n is the number of evaluation factors, $n = 3$.

The utilization coefficient of overall performance of the supporting system η structure is defined as the combination of utilization index of each support component Q_i, i.e. η index is obtained by summation of performance utilization ratio of each

support component such as shotcrete, anchor, steel riband reinforced concrete lining with steel rib. The η index can be expressed as follows:

$$\eta = \sum_{i=1}^{n} Q_i W_{Gi} \tag{2}$$

where Q_i is the performance utilization index of each support component; W_{Gi} is the weight value corresponding to the support component; n is the number of evaluation factors, $n = 4$.

As η value increases, the better overall performance of the support system could be achieved. The utilization coefficient of overall performance of the supporting system η should not be too small. If η is too small which indicates that the support system cannot effectively play its supporting performance, which leads to the waste of material; the overall performance utilization ratio of η should not be too high. The performance utilization index of each support component is the ratio of internal forces induced in the structure component (S_a) over its ultimate capacity (S_l):

$$Q = \frac{S_a}{S_l} \tag{3}$$

S_a is the maximum value of bending moment in shotcrete ($M_{l\text{-}p}$) or in steel rib, bolt, shotcrete and reinforced concrete lining with steel rib ($M_{l\text{-}e}$), the maximum axial force (F_l) in the rock bolt, and the maximum stress (σ_l) in the steel rib. S_a values can be estimated on the basis of numerical simulation or the actual monitoring data taken at the steady state.

S_l is the ultimate value of bending moment in shotcrete (M_{pmax}) or in reinforced concrete lining with steel rib, the maximum bearing capacity (F_{max}) of the bolt and ultimate strength σ_{max} of steel arch structures is taken, too. The ultimate bearing capacity of each support structure can be determined using highway tunnel specifications and other relevant specifications.

The coupling efficiency of the support system is an index which reflects the combined performance and coupling effect between components of support system. As this index is larger, the combined performance and coupling effect of components in support system are better which means the higher performance utilization ratio of each support system component. The coupling efficiency of composite components in support system for mountain tunnels is calculated based on the following equation:

$$W = \frac{2}{\pi} \arctan \frac{1}{30S^2} \tag{4}$$

where S is a standard deviation and determined as follows:

$$S = \sqrt{\sum_{i=1}^{n} (Q_i W_{Gi} - \sum_{i=1}^{n} Q_i W_{Gi}/n)^2 / n} \tag{5}$$

where Q_i is the performance utilization ratio of each support component; W_{Gi} is the weight value of the support component; n is the number of evaluation factors ($n = 4$).

3 Case Study of Yangling Tunnel

Yang ling tunnel [18], located in Yi xing City, Jiangsu Province, is 1080 m in total length, 160 m in the maximum depth. It is a single tunnel with two ways two lanes and used as the case study. This study was performed considering a section of tunnel from chainage 3 + 287 to chainage 3 + 892 which is divided into three sub-sections as mentioned below.

The first section from chainage 3 + 287 to chainage 3 + 509 mainly composed of middle-weathered quartz sandstone, cracked and broken rocks with low stability. Ground water was mainly consisted of water existed in fissures, rainfall or gushing. Due to the existence of groundwater, a large scale collapse was occurred during tunneling process. According to the classification system [19–21], rock mass in this section was classified as rock type *V*.

The second section from chainage 3 + 509 to chainage 3 + 721 was located in fault zone. The main compositions of rock mass were quartz sandstone, silty clay, and gravel. The faults were very close to tunnel and almost intersect with the tunnel. Rock mass in this section was classified as rock type *IV*.

The third section from chainage 3 + 721 to chainage 3 + 892 was mainly lightly weathered mudstone limestone with little amount of groundwater and classified as rock type *III* of rock.

The mechanical parameters of different rock mass were shown in Table 1. This study is performed using ANSYS numerical simulation. Surrounding rock mass was assumed to be homogeneous, isotropy and continuous medium, using failure criterion of Drucker-Prager. Dimensions of model are of 100 m, 80 m and 30 m in width, height and length, respectively, as shown in Fig. 1. Horseshoe shape tunnel was in the middle of the model, dimensions of tunnel are of 14.66 m and 9.25 m in width and height, respectively. Its area is 86.25 m^2. Once the model is established, rock mass inside the tunnel was excavated and supporting structure is immediately applied on the tunnel boundary. The 3D numerical model consists of 70486 zones and 69396 nodes. In order to simplify the calculation, the weight of the rock mass above the model was taken into consideration using distributed loads applied on the top of the model.

Table 1. Mechanical parameters of rock masses.

Rock type	Density ρ (g/cm^3)	Elastic modulus E (GPa)	Poisson's ratio μ	Cohesion C (MPa)	Internal friction angle φ (degrees)
V	1.96	1.0	0.4	35.4×10^{-3}	17.5
IV	2.00	3.2	0.32	1.5	43.5
III	2.10	8.0	0.3	1.6	60.5

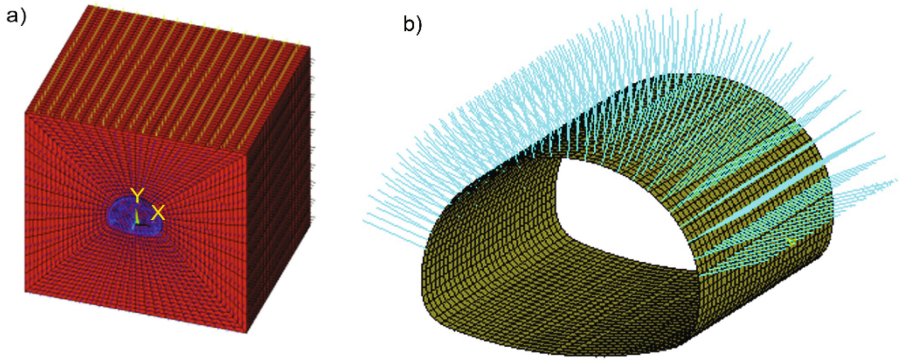

Fig. 1. The full numerical model (a) and tunnel support structures (b)

Two lateral sides of the model were fixed in horizontal direction while the bottom of the model is restrained in vertical direction and the top is free. The numerical model is shown in Fig. 1.

3.1 Stress and Strain Distributions in Surrounding Rock

As indicated in Fig. 2, the displacement of surrounding rock around the tunnel boundary was found during the excavation process. Vertical displacements of around 3.64 ÷ 16.71 mm toward the tunnel center are observed. The lateral displacement mainly occurred at side-walls with magnitude of about 0.12 to 0.78 mm, indicating that after tunnel excavation the main deformation of rocks around the tunnel was in vertical direction. When the tunnel was excavated in rock mass grade *V*, the final deformation at steady state was the largest due to the low stresses induced in weak rock (Table 2).

According to a large number of theoretical analysis, engineering practice, numerical simulation and 9/9–9/1 scale method of AHP, deformation induced in rock mass surrounding mountain tunnels is represented by using three order matrix (n = 3) as follows:

$$p = \begin{bmatrix} 1 & \frac{9}{6} & \frac{9}{5} \\ \frac{6}{9} & 1 & \frac{6}{8} \\ \frac{5}{9} & \frac{8}{9} & 1 \end{bmatrix} \tag{6}$$

The weight indexes of deformations induced at tunnel top (B_1), shoulder (B_2) and inverted arch (B) are of 45%, 30% and 25%, respectively, which were obtained by using normalization processing and *AHP* with a satisfactory consistency.

The deformation of tunnel under different type of surrounding rock can be observed. As shown in Fig. 3, the deformations of tunnel excavated in rock type *V* are largest which means that the effect of support structure on controlling the deformation in surrounding rock is inconsiderable. The deformations of tunnel excavated in rock type *IV* and *III* were lower. Over the tunnel boundary in a cross section, the

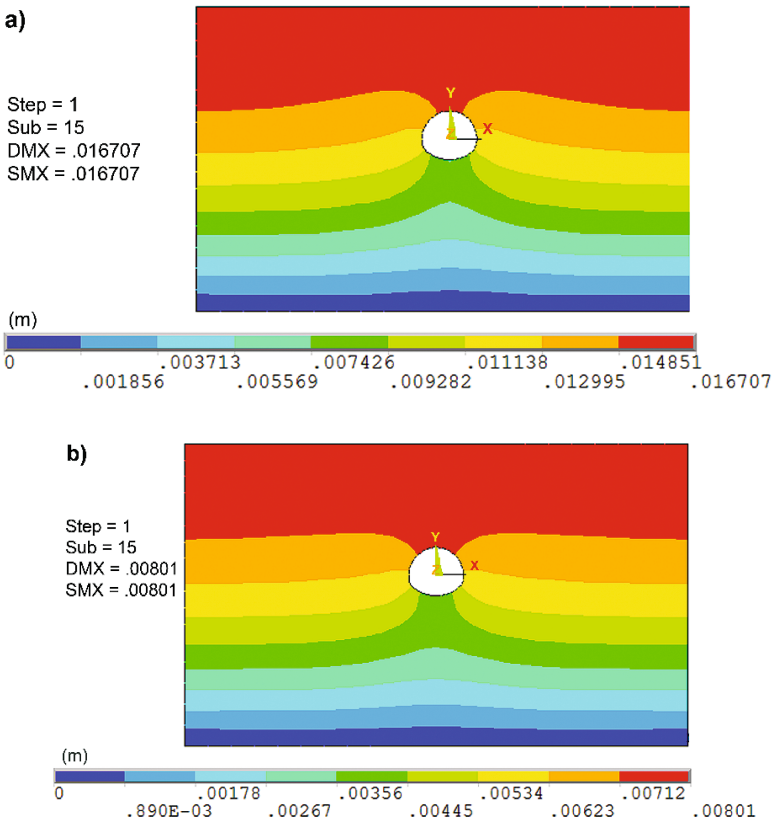

Fig. 2. Displacements in rock mass rock type *V* (a); rock type *IV* (b); rock type *III* (c) (DMX - displacement max; SMX - solution max; Sub - incremental solutions within a load step).

Table 2. The final displacement in rock mass surrounding the tunnel

Rock type	Location		
	Vault (mm)	Arch (mm)	Inverted arch (mm)
V	16.7	11.1	7.43
IV	8.01	5.34	3.56
III	3.64	2.42	1.61

deformation at the vault of the tunnel is largest, followed by deformation of tunnel's arch and that at inverted arch of tunnel is smallest.

3.2 Stress Characteristics In The Support Structure

As shown in Fig. 4, the maximum positive bending moment of structure was observed at the arch and side walls of tunnel. The maximum negative bending moment was however occurred on the spring line of the tunnel. As surrounding rock grade level

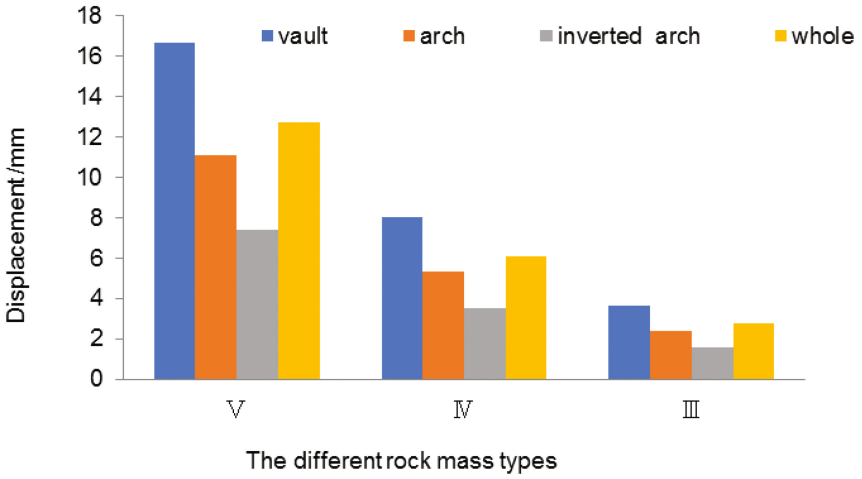

Fig. 3. Displacements in the tunnel boundary in different rock mass types

increased, i.e. from rock type *III* to *V*, the bending moment values were changed from negative to positive. As shown in Fig. 5, in the case of rock type *III*, the distribution of axial force in the bolt bar is uniform, axial force at the vault of tunnel is smallest, while the maximum axial forces are observed at the tunnel's arch. In the case of rock type *V*, the axial force was quite large, the maximum axial forces are observed at side walls and the minimum axial forces are occurred at the vault of the tunnel.

The weight value, W_{Gi}, of each member in the composite support structure is determined by analytical hierarchy process (*AHP*). The main components of support structure in mountain tunnels such as steel rib, rock bolt, shotcrete, reinforced concrete lining with steel rib are considered to estimate the weight value, W_{Gi}.

According to a large number of engineering examples, theoretical analysis and numerical research, by using the 9/9–9/1 scale method, the structure of judgment matrix ($n = 4$) was obtained such as:

$$Q = \begin{bmatrix} 1 & 2 & 3 & 5 \\ \frac{1}{2} & 1 & 2 & 3 \\ \frac{1}{3} & \frac{1}{2} & 1 & 2 \\ \frac{1}{5} & \frac{1}{3} & \frac{1}{2} & 1 \end{bmatrix} \tag{7}$$

Through the normalization process with satisfactory consistency, the weight value of steel rib, bolt, shotcrete and reinforced concrete lining with steel rib are 49.18%, 24.59%, 16.39% and 9.84%, respectively.

By using the numerical simulation performed in ANSYS software, the stress state of each support component indifferent type of surrounding rock was obtained and the ultimate load capacity of each supporting could be found in highway tunnel standard and other relevant standards. The utilization index of each support component was calculated using the weight value (see Fig. 6).

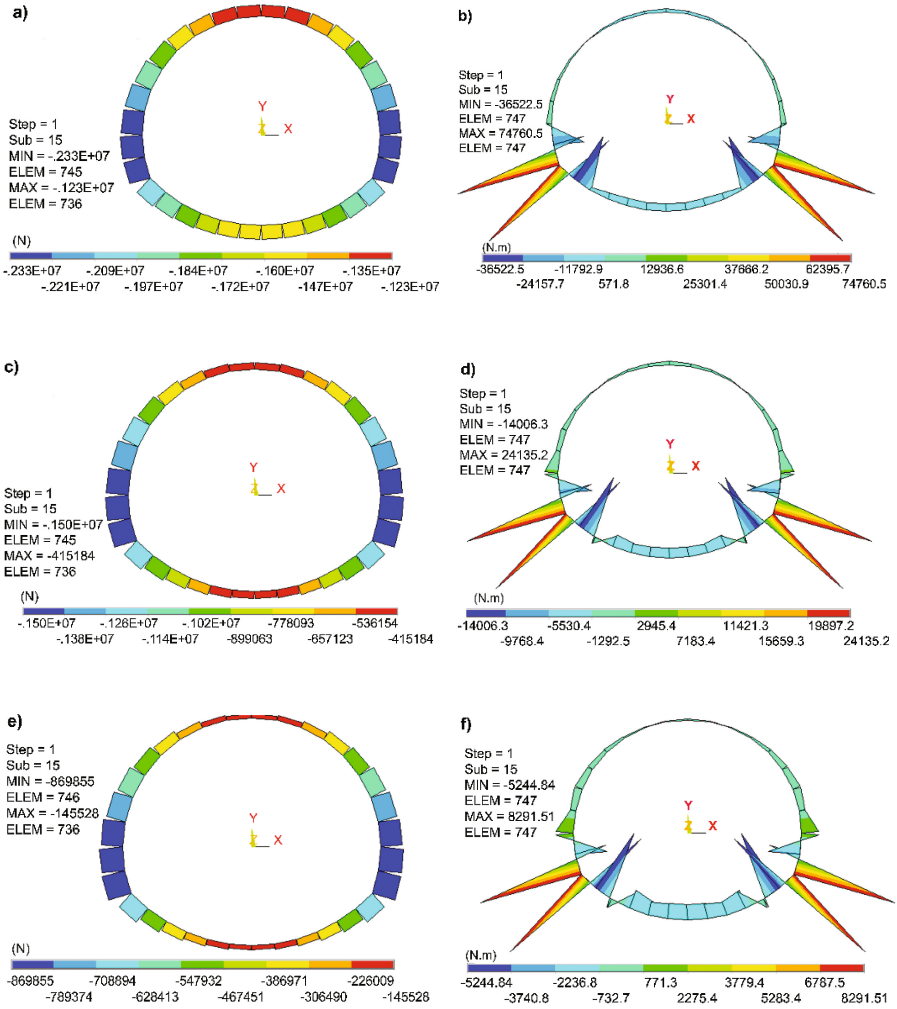

Fig. 4. Axial forces (a), (c), (e) and bending moment (b), (d), (f) in Rock type *V*, *IV*, *III*, respectively

The utilization index steel arch is highest and followed by of that of rock bolt and shotcrete. Whereas, that of the composite lining of concrete and steel rib is lowest. The utilization index of the support structure used in rock type *V* is the highest, followed by the case of rock type *IV* and its value is smallest in the case of rock type *III*.

From point of view of reserve strength and safety, it can be seen that the efficiency and economic of support structure in the case of rock type *IV* are both high, so it can be used as optimized case.

Figure 7 shows the coupling efficiency of support and rock mass obtained for three kinds of surrounding rock. The coupling efficiency obtained in case of rock type *IV*

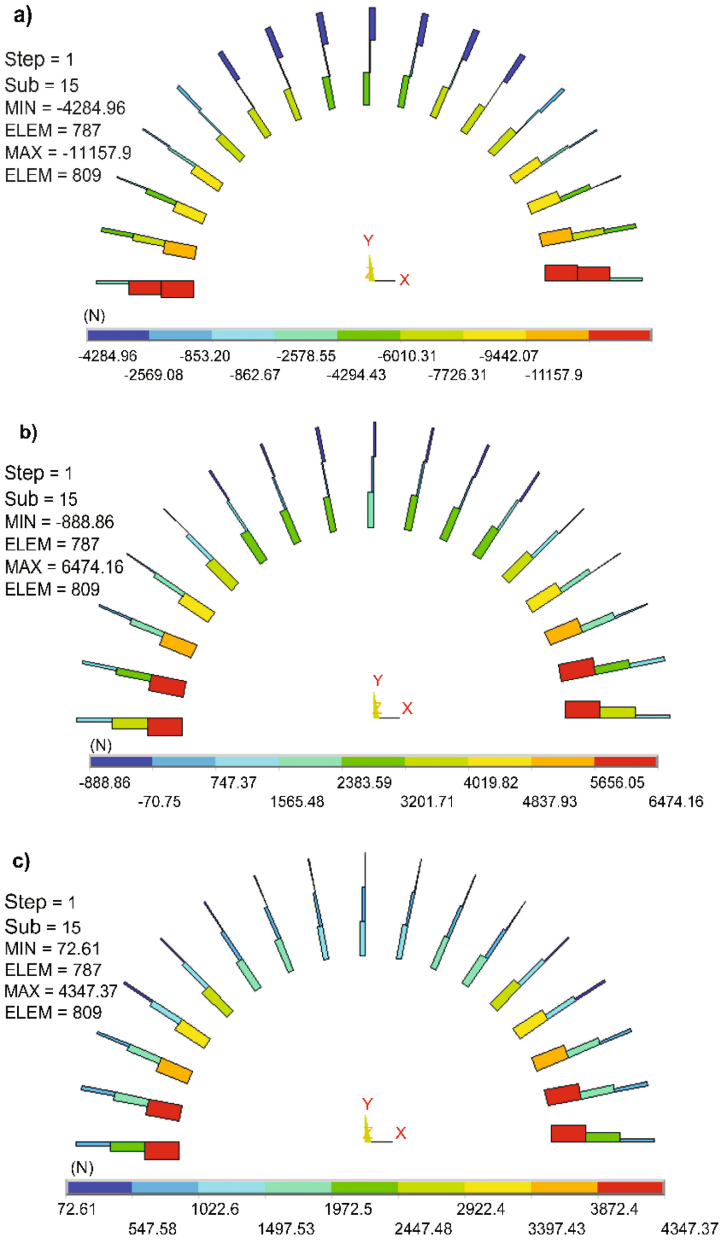

Fig. 5. Axial forces in bolt under different rock mass types (a) rock type *V*; (b) rock type *IV*; (c) rock type *III*, respectively

when using the reinforced concrete lining is the best. It means that choosing this kind of support structure not only ensures the controllability of deformation induced in surrounding rock, but also improve the bearing capacity of surrounding rock.

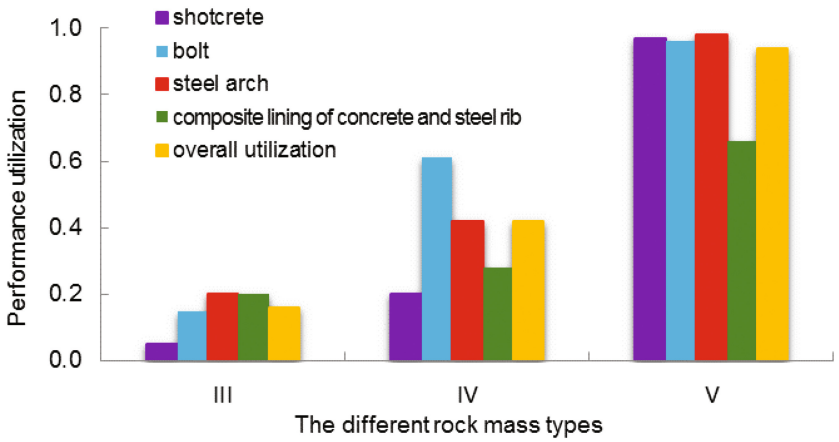

Fig. 6. The utilization ratio for performance of each support component on support system in the different plan

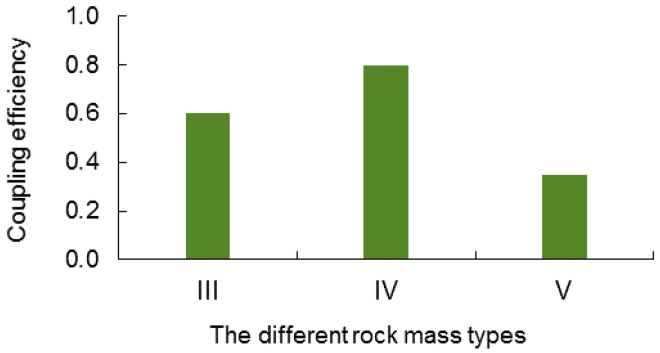

Fig. 7. The coupling efficiency of composite members in different rock mass types

While the overall performance ratio of rock type *V* surrounding rock was the highest, the coupling efficiency of surrounding rock and the support system was however small. In other words, the high overall performance ratio does not always mean that the deformation can be acceptable.

In the case of rock type *III*, the efficiency of each support component cannot be completely mobilized. Consequently, the coupling effect of support structure and rock mass is also affected.

4 Conclusion

On the basis of studying the coupling effect between surrounding rock and support structure in tunnelling through mountain, the following conclusions can be drawn:

- Through evaluation indexes, coupling efficiency of support structure and rock mass was quantitatively determined. These indexes can be used to optimize the design of support structure in mountain tunnels and to study the interaction between surrounding rock and support.
- The evaluation index was effectively applied for a highway tunnel excavated in hilly areas in the eastern of China.
- Through the numerical simulation analysis, it can be seen that under the condition of rock type *IV* surrounding rock the coupling efficiency of surrounding rock and supporting structure is the highest. It shows that choosing the appropriate support is not only to ensure the deformation of surrounding rock, but also to improve the carrying capacity of surrounding rock.

Acknowledgement. This research was funded by JSTI GROUP company (China), the Department of Construction Techniques and the Department of Mine Surveying, Hanoi University of Mining and Geology (Vietnam).

The authors declare that there is no conflict of interest.

References

1. Zhao, C., Hu, X.: Discussion on supporting concept of underground cavern project. Yunnan Water Power **29**, 5–8 (2006)
2. Xiao, Q.: Study on interaction of surrounding rock and support structure in high-speed railway tunnel. Logist. Eng. Manag. **31**, 16–29 (2014)
3. Zhu, W., He, M.: The Stability of Surrounding on the Complex Condition and the Dynamic Construction Mechanics of Rock Masses. Science Press, Beijing (1996)
4. Li, Z., Wu, T.: Interaction between tunnel surrounding rock and support. Nat. Sci. J. Xiangtan Univ. **31**, 716–729 (2010)
5. Sun, X., He, M.: Research on bolt/mesh/anchor combined support technology for deep soft and broken seam gateway. Coal Sci. Technol. **33**, 47–50 (2005)
6. Hou, C., Guo, L.: Coal Roadway Bolt Support. China University of Mining and Technology Press, Xuhou (1999)
7. Wang, J.: Principle and Design of Bolting and Shotcreting in Underground Engineering. China Railway Press, Beijing (1980)
8. He, M., Qian, Q.: A Summary of Basic Research on Mechanics of Deep Rock Mass. In: The Proceedings of the Ninth Symposium on Mechanics and Engineering, pp. 49–62. Science Press, Beijing (2006)
9. He, M., Zou, Z.: Introduction of Soft Rock Roadway Engineering. China University of Mining and Technology Press, Xuzhou (1993)
10. Ma, N., Hou, C.: Pressure Theory and Application of Mining Roadway. Coal Industry Press, Beijing (1995)
11. Wang, Y.: Tunnel Engineering. China Communications Press, Beijing (2000)
12. Shu, H.: Study on the interaction between tunnel surrounding rock and early lining. HIGHWAY **31**, 6–9 (2011)
13. Wang, Q., Li, S.: Analysis of combination components coupling of pressure relief anchor box beam support system and application. Rock and Soil Mechanics **25**, 15–19 (2012)
14. Yu, B., Wang, H.: Study on the Method of Pressure Arch Theory and Tunnel Submergence. China Railway Press, Beijing (2008)

15. Fan, J.: Study on the mechanism of coupling support technology and the parameter optimization in soft-rock roadway, vol. Master, pp. 8–10. China University of Mining and Technology, China (2014)
16. Qi, L.: Study on optimization of initial support design method and timing of secondary lining, vol. Master, pp. 25–27. Shijiazhuang Railway University, China (2014)
17. Wang, Q.: Research on control mechanism of surrounding rock failure in deep roadways with thick top-coal and contrast of new support systems, vol. Ph.D., pp. 45–48. Shandong University, China (2012)
18. Ran, J.: Study on mechanism and control technologies of Yangling tunnel surrounding rock collapse in Filling Karst, vol. Master, pp. 25–60 (2015)
19. Guo, B.: Key points of tunnel engineering design, pp. 14–34. China Communications Press (in Chinese), Beijing (2010)
20. Chinese code for design of road tunnel (JTG D70-2004), pp. 124–134. China Communications Press (in Chinese), Beijing (2004)
21. Song, B.: Tunnel construction technology higher education twelfth five year plan materials (Chinese). China Water Power Press (2014)

Numerical Simulation of CFRA Pile Subgrade Reinforcement Based on Recycled Aggregate of Demolition Waste

Huanda Gu[1], Cong Lu[1(✉)], Guoqiang Xue[1], Huilong Wu[1], Nguyen Chau Lan[2], and Qiang Tang[3]

[1] School of Civil Engineering, Suzhou University of Science and Technology, Suzhou 215011, China
lc2361806@163.com
[2] Geotechnical Engineering Laboratory, Civil Engineering Faculty, University of Transport and Communications, Hanoi, Vietnam
[3] School of Urban Rail Transportation, Soochow University, Suzhou 215131, China

Abstract. There is a large quantity of construction waste with low utilization in China. The construction and demolition (C&D) waste can be manufactured into recycled aggregate instead of natural aggregate, made into cement fly-ash recycled aggregate (CFRA) pile for foundation reinforcement. This study investigated the building demolition waste and construction waste production in Suzhou. The laboratory test was conducted to explore the unconfined compressive strength of CRFA pile samples with different condition, and the strength of samples met the design strength. The CFRA pile composite foundation is simulated to explore the relationship between influence factors (pile length, pile spacing, pile diameter, pile modulus) and settlement. The results indicate that the building demolition waste and construction waste production increases year by year, and waste concrete accounts for over 50% of building demolition waste. The length of pile has a great influence on the surface settlement of subgrade and foundation, and the settlement reduces effectively due to the strong bearing capacity of the pile in the soft soil layer. When the pile spacing is 3 times diameter of pile, the surface settlement at the center of the foundation is minimum. The increase of pile diameter and elastic modulus of pile yield to the decrease of the surface settlement of subgrade. The settlement of CFRA pile composite foundation meets the general control requirements (the post-construction settlement in the first-grade highway should be less than 300 mm).

Keywords: C&D waste · Recycled aggregate · CFRA pile · Laboratory test · Subgrade reinforcement · Numerical simulation

1 Introduction

With the economic development and urbanization process, the construction and demolition (C&D) waste generated in process of construction, renovation or demolition of structures and others [1, 2]. According to statistic, about 1.5 to 2.4 billion C&D

© Springer International Publishing AG 2018
D. Tien Bui et al. (eds.), *Advances and Applications in Geospatial Technology and Earth Resources*, https://doi.org/10.1007/978-3-319-68240-2_23

waste was generated annually in China, while the recycling rate was less than 5% [3]. Compared with that, the recycling rate of New Zealand, Germany, Japan and other countries were more than 75% [4–6]. In addition, C&D waste occupies large areas of land, which was also regarded as precious resource, especially in urban areas [1, 7]. Furthermore, since the existence of cement, the migration of fly-ash-contaminant can be effectively restricted due to the adsorption, etc [8–13].

The conventional treatments towards C&D waste includes landfilling, incineration, reuse/recycle and composting [2, 14, 15]. According to Akash et al. and Li et al.'s research, C&D waste could become recycled aggregates after treatment, instead of natural aggregate [6, 16]. Akash et al. presented a summary of the use of recycled aggregates from C&D waste. Meanwhile they described the salient properties of recycled aggregate and recycled aggregate concrete, especially in relation to strength and durability [6]. Instead of natural aggregate, Li et al. used recycled aggregate to produce cement fly-ash recycled aggregate (CFRA) pile and explored the characteristics of the material [16].

Considering all above, this paper investigates the production of C&D waste in Suzhou and explores the variation trend of the main components. In the laboratory test, the unconfined compressive strength of CFRA pile sample with different condition was tested. In addition, the settlement of CFRA pile composite foundation is simulated by the finite element software. The influence factors taken into account in this study include pile length, pile spacing, pile diameter and pile modulus.

2 Investigation Towards C&D Waste in Suzhou City and Laboratory Test

2.1 Investigation Towards C&D Waste in Suzhou City

The composition of C&D waste is affected by the various types of buildings and their auxiliary facilities for the construction, renovation, decoration, demolition, laying [17]. Figure 1 shows the C&D waste production over the years in Suzhou [18–20]. As shown in Fig. 1, the production of C&D waste kept increasing, in which demolition waste amount was much larger than that of construction waste. The composition of demolition waste (e.g., waste concrete, brick, stone, wood, metal, glass, asphalt) is influenced by different forms of construction and different years of the building [21]. The composition of the demolition waste in different areas and its proportion are displayed in Fig. 2. It is obvious that the composition of the demolition waste is roughly the same in different areas, and the proportion of waste concrete is more than 50% [21, 22]. In term of waste concrete in Suzhou, the production increased with the years, as shown in Fig. 3. Waste concrete could become recycled aggregates with different particle after treatment, as shown in Fig. 4. Based on the above investigation, the production of demolition waste is large and increasing, which could provide aggregate for CFRA pile.

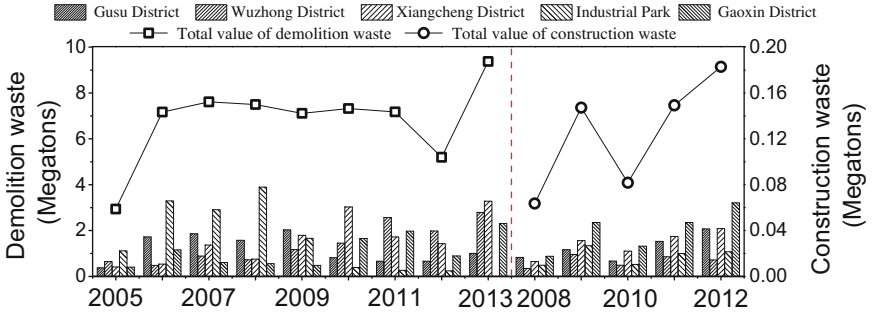

Fig. 1. The demolition waste and construction waste production over the years in Suzhou

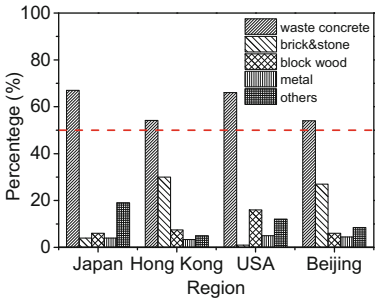

Fig. 2. Demolition waste composition in different areas and its proportion

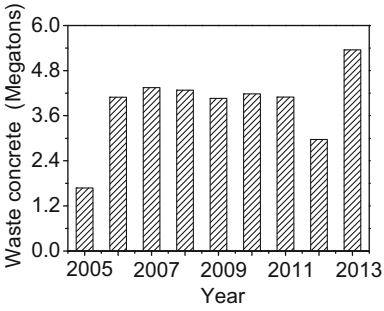

Fig. 3. Waste concrete production over the years in Suzhou

(a) Recycled coarse aggregate (b) Recycled fine aggregate

Fig. 4. Recycled aggregate

2.2 Laboratory Test

According to the investigation and the characteristic of composite foundation, the design strength of CFRA pile sample was 2.5 MPa (C2.5), 5 MPa (C5), 7.5 MPa (C7.5). The proportions of CFRA pile sample and their ratio are shown in Table 1.

Table 1. The material ratio of CFRA pile

Design strength	Cement	Water	Fly ash	Recycled fine aggregate	Recycled coarse aggregate
C2.5	2.5%	12.1%	3.7%	28.2%	53.5%
C5	4.7%	12.1%	3.7%	27.8%	51.7%
C7.5	5.9%	11.9%	3.7%	27.5%	51.0%

Cement, fly ash, recycled fine aggregate and recycled coarse aggregate were oven dried at 105 °C for 24 h (101-A, Leao, China) to ensure the accurate quality during the experiment. Subsequently, they were cooled to room temperature in a desiccator. According to Table 1, the materials of CFRA pile sample were mixed evenly. And the mixture was transferred into the moulds (150 mm × 150 mm × 150 mm, Jianyi, China). To avoid severe dehydration, the moulds were sealed with a polyethylene membrane. Afterwards, the mixtures were left undisturbed for 24 h at room temperature (23 ± 2 °C). After the period of the initial setting, the samples were demoulded and cured (≥ 95% humidity, 20 ± 2 °C) for 7, 14, 28, 60 and 90 days in a curing box (HBY-15B, Donghua, China). Six replicates were analyzed for each trial.

Microcomputer Controlled Electronic Testing Machine (LDS-50, Chenda, China) was used to obtain the unconfined compressive strength of samples. Figure 5 shows the unconfined compressive strength of CFRA pile samples with different condition. The unconfined compressive strength of CFRA pile samples met the design strength after 90 days' curing.

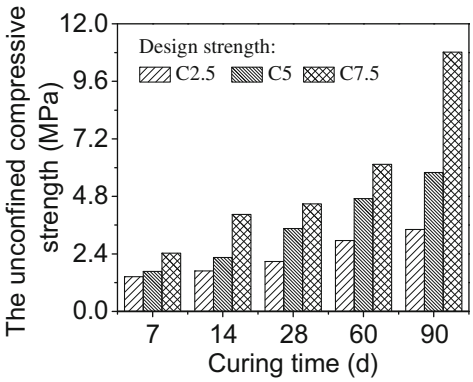

Fig. 5. The unconfined compressive strength of CFRA Pile samples

3 Numerical Analysis

3.1 Establishment of the Model

In this study, finite element software was used to simulate the CFRA pile composite foundation. As Fig. 6 shows, the model consists of an embankment fill supported by a CFRA pile composite foundation. The soil profile consists of some layers as follows: 14.6 m of saturation muddy soil, 4 m of gravel sand, 2.7 m of loess-like soils, 2.4 m of silt, 10.1 m of gravel, 6.2 m of sandstone. According to Zhu et al.'s research, the saturation muddy soil, gravel sand, loess-like soil, silt were modeled as mohr-coulomb materials [23]. While the embankment, cushion, gravel, sandstone, CFRA pile were assumed to be elastic materials [23]. The material properties of the various components are shown in Table 2.

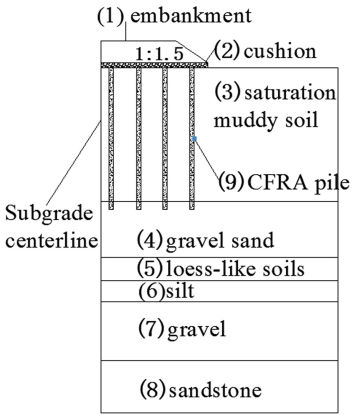

Fig. 6. The model of CFRA pile composite foundation

Table 2. The calculation parameters of model.

Material	Thickness	Elastic modulus	Cohesion	Internal friction angle	Poisson's ratio
	m	MPa	kPa	°	
Embankment	2.0	20	–	–	0.30
Cushion	0.5	22	–	–	0.30
Saturation muddy soil	14.6	3.6	10	18	0.40
Gravel sand	4.0	35	33	–	0.28
Loess-like soil	2.7	8	23	25	0.35
Silt	2.4	10	–	–	0.30
Gravel	10.1	3100	–	–	0.20
Sandstone	6.2	2540	–	–	0.20
CFRA pile	15	100	–	–	0.30

Due to the symmetry of the subgrade, only half of the finite element model needs to be built [23–25]. The dimensions of CFRA pile composite foundation are as follows: CFRA pile – diameter = 0.5 m, length = 15 m, pile spacing = 2.0 m, elastic modulus = 100 MPa; cushion – width = 10 m, height = 0.5 m; embankment – crest width = 7 m, height = 2 m, gradient of side slope = 1.5 on side, bottom width = 10 m, as shown in Fig. 6. The CFRA pile is in square form.

The side boundary of the foundation should be located at a distance of more than 3 times of the bottom width from the embankment. And bottom boundary should be set more than a depth of 2 times of the length of CFRA pile. The width and depth of the model are 40 m.

Model boundary conditions: the bottom boundary is completely fixed; the side boundary is horizontal fixed; the plane strain problems are considered in the model. Grid size is 0.25 m.

3.2 Calculation Results and Discussions

In this study, CFRA pile composite foundation is simulated to explore the relationship between influence factors (pile length, pile spacing, pile diameter, pile modulus) and the settlement [26, 27]. The maximum surface settlement of the subgrade and the foundation mainly appears at the centerline.

Analysis of The Influence of Pile Length

Since the piles in the composite foundation have different bearing capacities and stiffness, the lengths of piles are also different in most cases. Considering the soil conditions, the length of the pile is 9 m, 11 m, 15 m, 17 m, 19 m, with other dimensions kept constant. Figure 7(a) and (b) shows the relationship among the distance from the centerline, the pile length and the surface settlement of the subgrade and foundation.

The surface settlement of subgrade and the foundation decreases with the distance from the centerline of the subgrade. The maximum surface settlement of the subgrade and the foundation appears at the centerline of the subgrade, and the minimum surface settlement is at the outer edge. Compared to the settlement at the centerline, the settlement of the subgrade and the foundation at the edge decreased by 57.1% and 50.0%, respectively.

With the pile length increasing, the surface settlement of the subgrade and the foundation decreases. Compared to the pile length of 9 m, the surface settlement of the subgrade and the foundation with the pile length of 11 m decreases by 10.2% and 6.6%; the surface settlement of the subgrade and the foundation with the pile length of 15 m further reduced by 88.1%, 274.4%. In term of the surface settlement of the foundation, an increase of the pile length beyond 15 m, results in progressively smaller decrease in settlement. When the pile length is more than 15 m, the pile has passed through the saturated muddy soil into the gravel sand, which could reduce the settlement effectively [23]. In short, the settlement of CFRA pile composite foundation meets the general control requirements (the post-construction settlement in the first-grade highway should be less than 300 mm) [26].

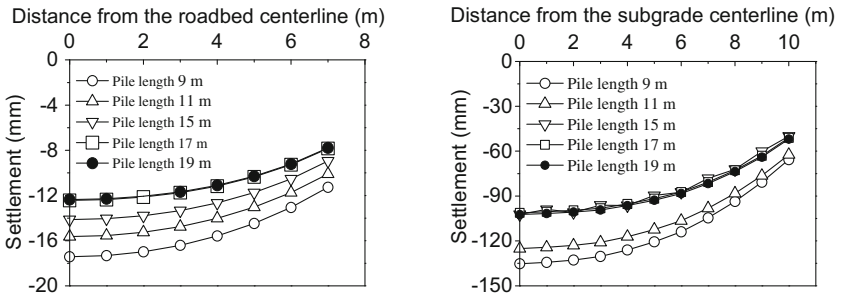

(a) The surface settlement of subgrade (b) The surface settlement of foundation

Fig. 7. The surface settlement of the subgrade and the foundation with different pile length

Analysis of The Influence of Pile Spacing

According to the study of Zhu, Li et al. [23, 28], the CFRA pile spacing in the composite foundation model is 2 d, 3 d, 4 d, 5 d, 6 d (d is the pile diameter), with other dimensions kept constant. The surface settlement of subgrade and the largest surface settlement of foundation at the centerline are shown in Fig. 8(a) and (b).

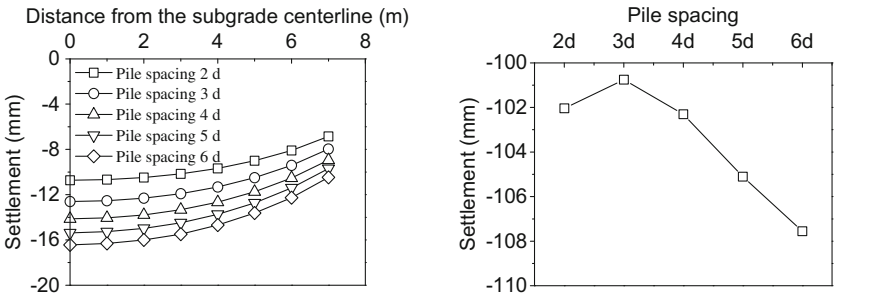

(a) The surface settlement of subgrade (b) The maximum surface settlement of the foundation

Fig. 8. The surface settlement of subgrade and the maximum surface settlement of the foundation with different pile spacing

The surface settlement of the subgrade decreases with the distance from the centerline of the subgrade increasing, and increases with the increase of the pile spacing. Compared to the center of the subgrade, the surface settlement of the subgrade (3 m away from the center) decreased by 5.6%; the settlement at the edge is reduced by 554%. Compared to the surface settlement of the subgrade with the pile spacing (6 d), the surface settlement of the subgrade with other pile spacing (5 d, 4 d, 3 d, 2 d) decreased by 6.6%, 14.0%, 23.2% and 34.3%, as shown in Fig. 8(a).

Figure 8 (b) shows that when the pile spacing is larger than 3 d, the settlement of the foundation increases with the increase of the spacing of the pile. When the pile

spacing decreases from 3 d to 2 d, the surface settlement of the foundation increases. Due to the certain squeezing effect of the CFRA pile, when the pile spacing is too small, the pile could be squeezed and tilted [27]. Therefore, when the pile spacing is 3 d, the surface settlement of the foundation is the smallest. The result is consistent with the pile spacing of the composite foundation in the practical application (3–5 times the pile diameter) [28]. In short, the settlement of CFRA pile composite foundation meets the general control requirements (the post-construction settlement in the first-grade highway should be less than 300 mm) [26].

Analysis of The Influence of Pile Diameter

According to Zhu et al.'s study [23], the CFRA pile diameter of the composite foundation model is 0.4 m, 0.5 m, 0.6 m, 0.7 m and 0.8 m, with other dimensions kept constant. The surface settlement of subgrade, the maximum surface settlement of the subgrade and the foundation with different pile diameters are shown in Fig. 9(a) and (b).

From Fig. 9(a), the surface settlement of the subgrade decreases, with the increase of the pile diameter. Compared to the surface settlement of the subgrade with 0.4 m pile diameter, the settlement of other pile diameters (0.5 m, 0.6 m, 0.7 m, 0.8 m) decreased by 13.3%, 23.2%, 30.3%, 35.5%, respectively. From Fig. 9(b), when the pile diameter is 0.4–0.6 m, the surface settlement of the foundation at the centerline decreases with the increase of the pile diameter. In the actual engineering, the pile diameter of composite foundation is generally 0.35–0.6 m [28]. When the pile diameter are 0.5 m or 0.6 m, the settlement of subgrade and foundation can be controlled effectively. In short, the settlement of CFRA pile composite foundation meets the general control requirements (the post-construction settlement in the first-grade highway should be less than 300 mm) [26].

Analysis of The Influence of Pile Modulus

According to Li et al.'s study [29], the CFRA pile modulus is 50 MPa, 100 MPa, 200 MPa in the model, with other dimensions kept constant. The surface settlement of the subgrade and the foundation are shown in Fig. 10(a) and (b).

As shown in Fig. 10(a) and (b), with the increase of the elastic modulus of the pile, the surface settlement of the subgrade and the foundation decrease. Compared to the surface settlement of subgrade with the pile modulus (50 MPa), the surface settlement of subgrade with other CFRA pile modulus (100 MPa and 200 MPa) decreased by 19.1%, 35.5%. Compared to the surface settlement of foundation with the pile modulus (50 MPa), the surface settlement of foundation with the pile modulus (100 MPa) decreases by 19.4%, and the surface settlement of foundation with the modulus (200 MPa) decreases by 46%. In short, the settlement of CFRA pile composite foundation meets the general control requirements (the post-construction settlement in the first-grade highway should be less than 300 mm) [26].

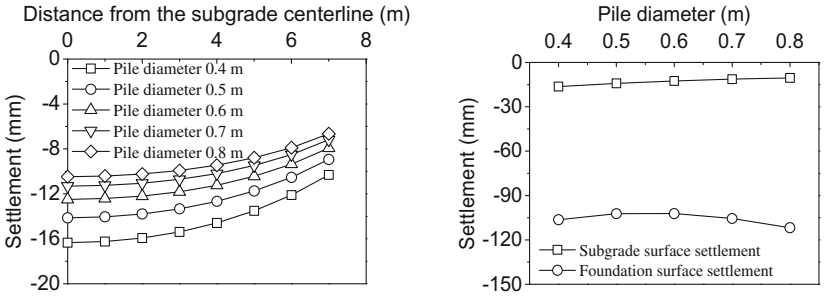

(a) The surface settlement of subgrade

(b) The maximum surface settlement subgrade and foundation

Fig. 9. The surface settlement of subgrade, the maximum surface settlement of the subgrade and the foundation with different pile diameter

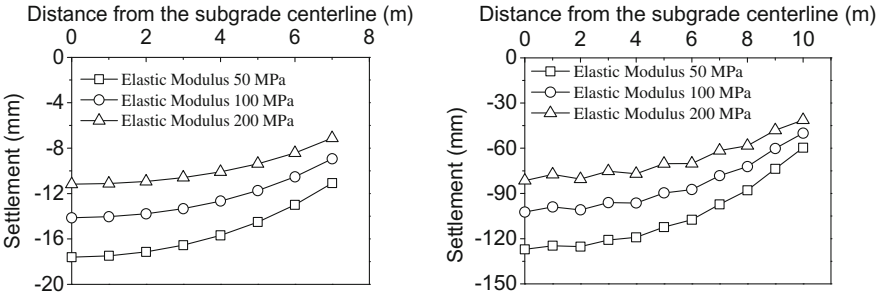

(a) The surface settlement of subgrade

(b) The surface settlement of foundation

Fig. 10. The surface settlement of subgrade and foundation with different pile modulus

4 Conclusion

In different countries, the composition of the demolition waste is roughly the same, and the proportion of waste concrete is more than 50%. The waste concrete can be manufactured into recycled aggregate instead of natural aggregate, made into CFRA pile for foundation reinforcement. In the laboratory test, the unconfined compressive strength of CFRA pile samples with different condition was tested. And the unconfined compressive strength of CFRA pile samples met design strength after 90 days' curing. Numerical analysis results show that the pile length has great influence on the surface settlement of the subgrade and the foundation. When the pile run through the soft soil into the hard bearing layer, it can effectively reduce the settlement. With the increase of pile spacing, the surface settlement of subgrade increases. And when the pile spacing is 3 d, the surface settlement of the foundation at the centerline is minimum. With the increase of pile diameter, the surface settlement of subgrade gradually decreases. And when the pile diameter are 0.5 m or 0.6 m, the settlement of subgrade and foundation

can be controlled effectively. With the increase of pile modulus, the surface settlement of subgrade and foundation gradually decreases. The settlement of CFRA pile composite foundation meets the general control requirements (the post-construction settlement in the first-grade highway should be less than 300 mm).

Acknowledgments. The research presented herein is supported by the National Nature Science Foundation of China (50879023, 41630633), China Postdoctoral Science Foundation funded project (2016M591756), Jiangsu Planned Projects for Postdoctoral Research Funds (1601175C), and project from Jiangsu Provincial Department of Housing and Urban-Rural Development (2016ZD18). The research is also supported by Jiangsu Provincial Transport Bureau (2016T05), Six Talent Peaks Project in Jiangsu Province, China (2015-JNHB-018), and Bureau of Housing and Urban-Rural Development of Suzhou.

References

1. Zheng, L., Wu, H., Zhang, H., Duan, H., Wang, J., Jiang, W.: Characterizing the generation and flows of construction and demolition waste in china. Constr. Build. Mater. **136**, 405–413 (2017)
2. Tang, Q., Kim, H.J., Endo, K., Katsumi, T., Inui, T.: Size effect on lysimeter test evaluating the properties of construction and demolition waste leachate. Soils Found. (JGS) **55**(4), 720–736 (2015)
3. China Strategic Alliance of Technological Innovation for Construction Waste Recycling Industry (CSATICRI): China construction and demolition waste recycling industry development report 2014 (2014). (in Chinese)
4. Tam, V.W.: On the effectiveness in implementing a waste-management-plan method in construction. Waste Manag. **28**(6), 1072–1080 (2008)
5. Tam, V.W.Y., Tam, C.M.: A review on the viable technology for construction waste recycling. Resour. Conserv. Recycl. **47**(3), 209–221 (2006)
6. Rao, A., Jha, K.N., Misra, S.: Use of aggregates from recycled construction and demolition waste in concrete. Resour. Conserv. Recycl. **50**(1), 71–81 (2007)
7. Tang, Q., Liu, Y., Gu, F., Zhou, T.: Solidification/stabilization of fly ash from a municipal solid waste incineration facility using Portland cement. Adv. Mater. Sci. Eng. **2016**, 10 (2016). Article ID 7101243. doi:10.1155/2016/7101243
8. Tang, Q., Wang, H.Y., Tang, X.W., Wang, Y.: Removal of aqueous Ni(II) with carbonized leaf powder: kinetic and equilibrium studies. J. Cent. South Univ. **23**, 778–786 (2016)
9. Tang, Q., Liu, W., Wang, H.Y., Cheng, R., Qian, Y.F.: Membrane behavior of bentonite-amended Fukakusa clay under K, Na and Ca solutions. J. Cent. South Univ. **23**, 3122–3131 (2016)
10. Tang, Q., Chu, J.M., Wang, Y., Zhou, T., Liu, Y.: Characteristics and factors influencing Pb (II) desorption from a Chinese clay by citric acid. Sep. Sci. Technol. **51**(17), 2734–2743 (2016)
11. Tang, Q., Katsumi, T., Inui, T., Li, Z.Z.: Membrane behavior of bentonite-amended compacted clay towards Zn(II) and Pb(II). Membr. Water Treat. **6**(5), 393–409 (2015)
12. Tang, Q., Tang, X.W., Li, Z.Z., Wang, Y., Hu, M.M., Zhang, X.J., Chen, Y.M.: Zn(II) removal with activated firmiana simplex leaf: kinetics and equilibrium studies. J. Environ. Eng. (ASCE) **138**(2), 190–199 (2012)

13. Tang, Q., Tang, X.W., Hu, M.M., Li, Z.Z., Chen, Y.M., Lou, P.: Removal of Cd(II) from aqueous solution with activated firmiana simplex leaf: behaviors and affecting factors. J. Hazard. Mater. **179**, 95–103 (2010)
14. Tang, Q., Katsumi, T., Inui, T., Li, Z.Z.: Membrane behavior of bentonite amended compacted clay. Soils Found. (JGS) **54**(3), 329–344 (2014)
15. Tang, Q., Katsumi, T., Inui, T., Li, Z.Z.: Influence of pH on the membrane behavior of bentonite amended Fukakusa clay. Sep. Purif. Technol. **141**, 132–142 (2015)
16. Li, T., Jiang, Y., Wang, D., Chen, S.: Experimental study on material properties of construction waste low- strength cfg pile. Fly Ash Compr. Util. **2015**(2), 19–22 (2015). (in Chinese)
17. Tang, Q., Heejong, K., Kazuto, E., Takeshi, K., Toru, I.: Size effect on lysimeter test evaluating the properties of construction and demolition waste leachate. Soils Found. **55**(4), 720–736 (2015)
18. Seongwon, S., Yongwoo, H.: An estimation of construction and demolition debris in seoul, korea: waste amount, type, and estimating model. J. Air Waste Manag. Assoc. **49**(8), 980–985 (1999)
19. Apotheker, S.: Construction and demolition debris–the invisible waste stream. Resour. Recycl. **9**(12), 66–74 (1990)
20. Suzhou City Wall Materials Reform Leading Group Office: Investigation report on the utilization of construction waste in Suzhou (2013). (in Chinese)
21. Cui, S., Xu, Y.: Present Situation and Resource Utilization of Construction Waste Disposal in Beijing. The Chinese Ceramic Society (Building Material Sub-Committee) (2006). (in Chinese)
22. Ruan, G.: General evaluation in geotechnical engineering and research on soil improvement with construction waste. Guangdong University of technology, Guangdong, China (2006). (in Chinese)
23. Zhu, Y., Tang, W.: Analysis of settlement of CFG pile composite foundation with different parameters. J. Gansu Sci. **27**(2), 49 (2015). (in Chinese)
24. Gu, F., Zhang, Y., Droddy, C.V., Luo, R., Lytton, R.L.: Development of a new mechanistic empirical rutting model for unbound granular material. J. Mater. Civ. Eng. **28**(8), 04016051 (2016)
25. Gu, F., Luo, X., Luo, R., Lytton, R.L., Hajj, E.Y., Siddharthan, R.V.: Numerical modeling of geogrid-reinforced flexible pavement and corresponding validation using large-scale tank test. Constr. Build. Mater. **122**, 214–230 (2016)
26. Ministry of transport of the People's Republic of China.: Technical Guidelines for Design and Construction of Highway Embankment on Soft Ground (JTG/TD31-02-2013) (2013). (in Chinese)
27. Tang, T.: Study on the Composite Foundation with CFG-pile improve thick and soft ground. Nanjing Hydraulic Research Institute, Jiangsu, China (2007). (in Chinese)
28. Li, C., Wang, B., Zhou, S.: Reinforcement technique for subgrade in soft soil zone by composite structure of CFG pile-net and its application. J. Railw. Eng. Soc. **1**, 27–31 (2006). (in Chinese)
29. Li, T.: Application research on key technology of construction waste drainage CFG pile. Soochow University, Jiangsu, China (2015). (in Chinese)

Worthiness Assessment of New Mining Projects: The Case of Potash Mining in Bamnet Narong, Thailand

Kridtaya Sakamornsnguan[1(✉)] and Jürgen Kretschmann[2]

[1] Institute of Mineral Resources Engineering, RWTH Aachen University, Aachen, Germany
kridtaya.sakamornsnguan@rwth-aachen.de
[2] TH Georg Agricola, Bochum, Germany
juergen.kretschmann@thga.de

Abstract. During these recent years, there have been efforts to develop new potash mining projects in Thailand. However, society doubts whether these projects are worth developing. The government cannot respond well to this question since it has no tool for evaluating new projects and providing concrete answer on the issue. The purpose of this study is to establish a framework to assess the worthiness of new mining projects and apply it to one of the new potash mining projects to find answers for the society. The new assessment framework determines the project's worthiness by a matrix of the necessity of project development and the negative impacts. The worthiness is presented in terms of development priority. The project in Bamnet Narong, Chaiyaphum province is selected as a case study. The project was classified as a moderate development priority. The results provide useful information for supporting governmental decisions, communicating with stakeholders, and identifying suitable management measures during the life cycle of the project.

Keywords: Mining project assessment · Necessity-impacts matrix · Risk assessment · Potash · Thailand

1 Introduction

Thailand has an abundant resource of potash. It was estimated that the probable resources of potash was approximately 407,000 million tonnes [1]. The recent efforts to obtain the mining leases for new potash mining projects have attracted public attention. There have been movements showing concerns about their impacts and opposing some of these projects. The Department of Primary Industries and Mines (DPIM), the governmental agency responsible for granting mining leases and regulating mining operations in Thailand, encounters difficulties in making decisions and making its decisions accepted by the public because it cannot provide a concrete explanation why the projects need to be developed and how critical their negative consequences the projects will be. To mitigate conflicts, DPIM needs to find reasonable answers for the

© Springer International Publishing AG 2018
D. Tien Bui et al. (eds.), *Advances and Applications in Geospatial Technology and Earth Resources*, https://doi.org/10.1007/978-3-319-68240-2_24

aforementioned questions and be able to measure how worthy the mining projects are. This paper aims to assess the worthiness of a new potash mining project in Thailand from the government perspective. A new assessment framework was developed for this purpose, and the underground potash mining project in Bamnet Narong district, Chaiyaphum province, is selected for the assessment because of its forerunning status in Thailand and data availability. The assessment of this project should provide useful information to DPIM for communicating with stakeholders and regulating the project. The assessment concept and method could be used for the consideration of other mining projects.

2 Project Information

The Bamnet Narong underground potash mining project is located in Bamnet Narong district, Chaiyaphum province, Thailand, approximately 300 km northeast of Bangkok. According to the company's document [2, 3], the mining-related activities in Bamnet Narong began when the Department of Mineral Resources (DMR) conducted an exploration and identified key deposits of rock salt and potash in Northeastern Thailand in 1973. In 1989, the project was approved by the Cabinet to be an ASEAN industrial project. The ASEAN Potash Mining Co. Ltd. (APMC) was established in 1991 as a joint-venture of Thailand, Malaysia, Indonesia, the Philippines, Singapore, and Brunei Darussalam and later converted to a public company. In February 2015, the mining lease, which is valid for 25 years, was granted to ASEAN Potash Mining PLC, which was later renamed to ASEAN Potash Chaiyaphum PLC [4].

According to the mining plan and the environmental impact assessment report [2, 3], the deposit of this project is a carnallite deposit, situated at the level of 80–300 m below ground. The mining lease covers an area of around 3,800 acres in three sub-districts, within which approximately 132 acres will be the area for two access shafts and facilities. An additional area of 1,098 acres will be used to construct a waste storage facility. The indicated resource within the mining lease area was estimated at 67.7 million tonnes KCl (potassium chloride) at an average grade of 15.78% and 211.95 million tonnes NaCl (sodium chloride) at an average grade of 43.78%. The extraction will take place at the depth between 100 and 300 m from surface. The extraction will apply a room and pillar method and drilling and blasting techniques. At full production, the annual extraction of carnallite and NaCl should be 7.8 and 3.1 million tonnes, respectively. The run-off mine will be processed by hot crystallization, which should recover more than 90% of KCl. The plant capacity is 1.1 million tonnes of 95% KCl. Together, NaCl and $MgCl_2$ (magnesium chloride) by-products will be generated at the rate of 3.3 million tonnes and 2.0 million cubic meters annually. Approximately 0.4 million tonnes of the NaCl will be sold. The rest will be stored underground or in the waste storage facilities during the operation and will later be backfilled together with $MgCl_2$ to prevent ground subsidence.

3 Assessment Framework

3.1 Limitations of the Available Assessment Tools

The key tool the government currently applies when a new mining project undergoes the project approval process is impact assessment, especially environmental impact assessment (EIA). The EIA is a tool to identify and predict the impacts of proposed activities on the bio-geophysical environment and human well-being and is also helpful for data interpretation and communication [5]. It should be carried out at the early stage of a project to allow effective management of anticipated impacts [6, 7]. The EIA helps the government to assess mining projects during the approval procedure. It provides a neutral understanding of the actual conditions of the environment, health, and/or society since it is based on factual or scientific data. However, it cannot provide concrete, objective information about the project's worthiness because it aims to identify the foreseeable impacts and deal with them rather than describes the development value of a mining project. Moreover, the impact measurement and data accumulation can misguide the understanding of the result-users. For example, the use of monetary values to represent the level of impacts requires assumptions to convert of real value to monetary value, which involve judgments on how the values are defined, the extent to which market prices represent public interest, and the inclusions of intrinsic values, and the aggregation of positive and negative impacts in terms of monetary cost and benefit can make people overlook the real value of impacts such as lost functions that cannot be compensated with the gain of other positive consequences.

Other important tools frequently applied for assessing mining projects are feasibility studies, risk assessment, and sustainability performance indicators. These tools also contain limitations and cannot serve the required application purposes, i.e. determining the worthiness of new mining projects.

A feasibility study is a methodology for evaluating comparable financial opportunities of investment of a mining project. Borquez and Thompson [8] explain that a feasibility study mainly contains the technical designs and planning and economic analyses. Its evaluation criteria depend on the investment objectives, but the comparison of investment alternatives is mostly based on profitability in terms of non-discounted (such as payback period and accounting rate of return) and discounted cash flow (such as net present value (NPV), internal rate of return (IRR), profitability index (PI), and benefit-cost ratio). Although it contains technical data as well as market- and management-related information, a feasibility study aims to identify the economic viability of a project under specified conditions. Accordingly, it contains underlying assumptions and provides a limited perspective on information.

Risk assessment is a process of assessing the effects of uncertainty on identified objectives, consisting of risk identification, risk analysis, and risk evaluation [9]. It is applicable to a wide range of issues, can be carried out at every stage of the project, and can be used as a complementing part of an impact assessment. Risk assessment is an important process to evaluate uncertainty. Backed by scientific facts and able to return quantifiable and comparable results make risk assessment an interesting option for the assessment of project's worthiness. However, data uncertainties and limited knowledge are the key limitations, of which users should be aware.

Sustainability performance indicators are tools for evaluating changes in specific issues. An important set of indicators applied in the mining sector is the one launched by the Global Reporting Initiative (GRI) as a part of the sustainable reporting guideline. The framework consists of performance indicators in economic, environmental, and social categories and is linked to widely-accepted international practices [10]. Despite the consideration of multiple aspects, the GRI guideline is criticized for failing to comprehend the holistic view of sustainability and camouflaging unsustainable practices [11, 12]. Moreover, these indicators are inclined towards the weak sustainability approach [12] and characterize how an organization affects stakeholders interacting economically with the organization rather than the actual impacts. These characteristics limit the potential to apply these indicators to the assessment of the worthiness of new mining projects.

The limitations of the current tools result not only from the characteristics of the assessment methodologies but also from the background values, i.e. how worthiness is defined. The worthiness from the governmental perspective should be characterized by public interests rather than the interests of an individual. However, most of the assessment approaches, especially the economic ones, are influenced by the mainstream economic concept characterized by the pursuit of self-interests of rational men. Therefore, the information obtained from these approaches might not be a good representative of the government views and require adjustments if they are to be used for assessing a project's worthiness.

3.2 New Assessment Framework

To overcome the limitations of the available tools, a new assessment framework is established to assess the worthiness of new mining projects. Buddhist principles, which are the basic value of Thailand, are chosen as the foundation of the new assessment framework since they value neutral understanding, the interconnectedness of beings, and the well-being of oneself and others. These characteristics should refine the background values and the ideas about the worthiness of mining projects. Together, the useful attributes of the available methods are integrated into the framework to combine their strengths. With these, the new assessment framework should be able to serve the requirements and application purposes of the government.

In the new assessment framework, the worthiness of a mining project is assessed from a matrix of the necessity of project development and negative impacts. The idea of determining the value of a project from the necessity and negative impacts is derived from the idea of the evaluation of product worthiness proposed by Mitsuru Tanaka and mentioned in Inoue [13], in which the worthiness of a product is ranked in a matrix of the necessity to consume and the negative environmental impacts caused by the product. The original idea reflects Buddhist values that one should respect the environment. This idea, however, has been extended to capture Buddhist economics characteristics identified by Inoue [13] as "*(1) an economics that benefits oneself and others; (2) an economics of tolerance and peace; and (3) an economics that can save the earth*", which correspond to the governmental duties in maintaining social order and environmental well-being. The worthiness is determined in terms of development priority ranking as low, medium, or high as shown in Fig. 1. High priority means the

project has higher value from the public viewpoint and is worth developing. That means, the project is essential or could contribute positively to society and will have low to medium negative impacts. Medium priority means the project is worth developing if the negative impacts and the positive contributions can be properly handled. The project of this priority level could benefit society, but it is not vital. On the other hand, they do not create critical negative impacts on society and the environment. Low priority means the project does not significantly contribute to public well-being and brings about many negative impacts. This project category is least appealing and its development requires careful attention and stringent measures for controlling the negative impacts.

Necessity of project development	Negative impacts of the project		
	Low	Medium	High
High (vital for the society)	High priority	High priority	Medium priority
Medium (not absolutely necessary but can positively contribute to the society)	High priority	Medium priority	Low priority
Low (not very necessary)	Medium priority	Low priority	Low priority

Fig. 1. Necessity-impacts matrix.

The ratings of the necessity of project development and the negative impacts on humans and the environment used in the matrix are obtained from two separate assessments. Each component is assessed from a set of parameters, defined based on a literature review and structured into a hierarchy to systemically arrange the criteria.

3.3 Necessity of Project Development

The necessity of project development indicates the extent that the assessed project can contribute to socio-economic and environmental well-being. It is determined by two parameters: service provision and positive contributions to society. Service provision concerns the genuine function of mining activities, i.e. supplying raw material to society. It is determined by the contribution of the mining project to domestic demand, the contribution to end use, and resource availability. The mining project fulfils its function if it can serve domestic demand, reduce imported mineral, does not unnecessarily stimulate mineral export, and does not cause too rapid depletion. Positive contributions to society are determined by the company's contributions to workers, communities, and the environment. The project is necessary if it contributes to a better livelihood of people and the ecosystem by employing local people, providing access to water, forest, financial resources, infrastructure, healthcare, and education to its neighboring communities, and creates habitat gain. Shareholders are not included here but considered partly in the negative impacts and partly indirectly in other topics. Figure 2 summarizes the assessment parameters of the necessity of development.

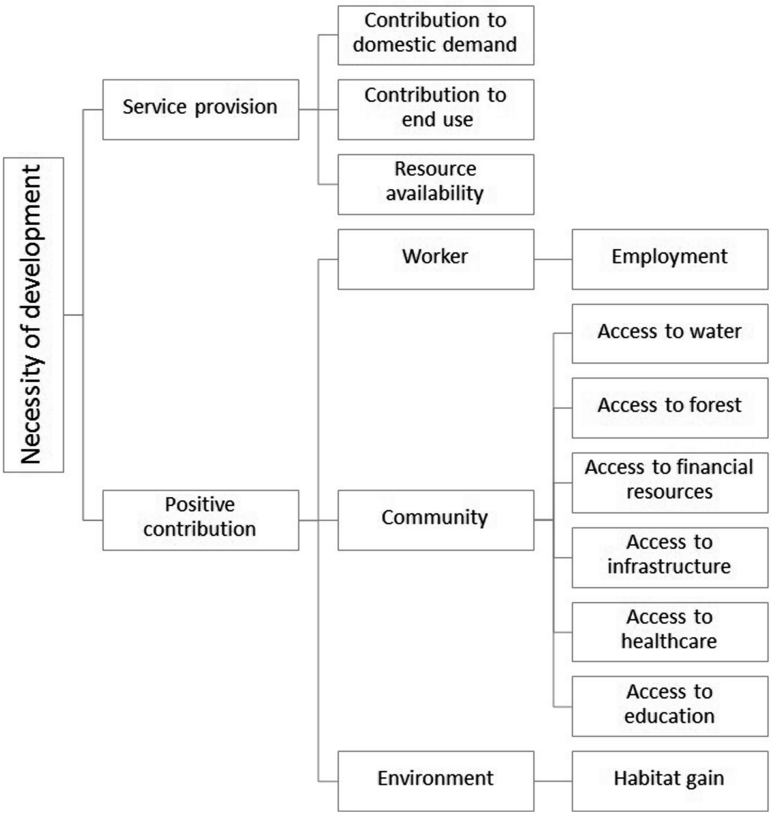

Fig. 2. Components and structure of necessity of mining project development.

3.4 Negative Impacts of the Project

The negative impacts of the assessed mining project are determined by those affecting the well-being of workers, community, the environment, and shareholders. The project's negative impacts on workers are represented by its effects on worker's health and safety, including occupational diseases, harmful working conditions, and accidents. The impact of occupational diseases is assessed from that of respiratory diseases, noise-induced hearing loss, and musculoskeletal disorders, which are the most frequently found occupational diseases in mining [14]. The impacts of harmful working conditions and accidents are identified in reference to the key critical forms of safety hazards in mining specified in the ILO's Safety and Health in Mines Recommendation [15]. The former is characterized by exposure to heat and the lack of oxygen. The latter consists of fire and explosions, gas outburst, rockburst, an inrush of water or semi-solids, and ground failure.

The impacts on communities are determined by the project's direct and indirect influences on the livelihood of local communities, characterized by health and safety, access to livelihood assets, and vulnerability to external changes.

The project's impacts on community's health and safety are determined by the effects of accidents and pollution. The types of accidents included in this assessment are defined according to the key types of large-scale accidents caused by mining found in literature such as that of Blight and Fourie [16] and Whyatt and Varley [17]. Two forms of accidents are used in the assessment, namely, waste storage facility failure and sinkhole. The effects of pollution on human health are confirmed in a number of literature such as CCSG Associates [18], Cronjé et al. [19], and Stephens and Ahern [20]. This assessment considers pollution in three main media, air, water, and soil. Air pollution is determined by direct releases of air pollutants. Water pollution is assessed from both a planned discharge and undesired releases of pollutants into water, including mine drainage, seepage from the storage facility, and failure of the waste facility. Soil pollution is determined by both direct disposal and indirect releases of pollutants through dust deposition.

The project's impacts on community's access to livelihood assets are determined by two main groups of assets, of which the effects are most apparent in case of mining, namely, natural and physical assets. According to literature such as International Institute of Environment and Development [21], Northey et al. [22], Kemp et al. [23], and Kaushik and Kaushik [24], the key natural assets, of which the community's access can be affected by mining projects, are water, land, and forest. Consequently, the competing use of these three kinds of natural assets is used to represent the impacts on community's access to natural access. The project's impacts on community's access to physical assets indicate the competing demands for public infrastructure and public services. Based on the literature such as International Institute of Environment and Development [21] and Petkova et al. [25], the types of physical assets included in this assessment are road, rail, healthcare, and education. The effects of degradation are not included in this subject but in other parts of the framework.

The project's impacts on community's vulnerability to external changes are determined by the vulnerability to natural hazards and to economic changes. They are assessed from vulnerability to floods, vulnerability to droughts, and dependency on mining, all of which are the issues connectable to mining.

The impacts on the environment are considered in relation to biodiversity loss since it emphasizes the services of biotic and abiotic resources and their interdependency. They are determined by habitat loss and habitat degradation due to pollution. The former comprises both terrestrial and aquatic habitat losses. The latter is characterized by three main environmental media: air, water, and soil. The impacts on air pollution are determined by the direct releases of air pollutants. The impacts on water pollution are assessed from both a planned discharge and undesired releases of pollutants into water through mine drainage, seepage from the storage facility, and failure of the waste facility. The impacts on soil pollution are determined by the indirect releases of pollutants through dust deposition.

The project's impacts on shareholders are represented by a business failure, which results mainly from economic, financial, and managerial factors. In this assessment, the impact is determined by the project's return on investment.

Figure 3 summarizes the assessment parameters of the negative impacts of the concerned project.

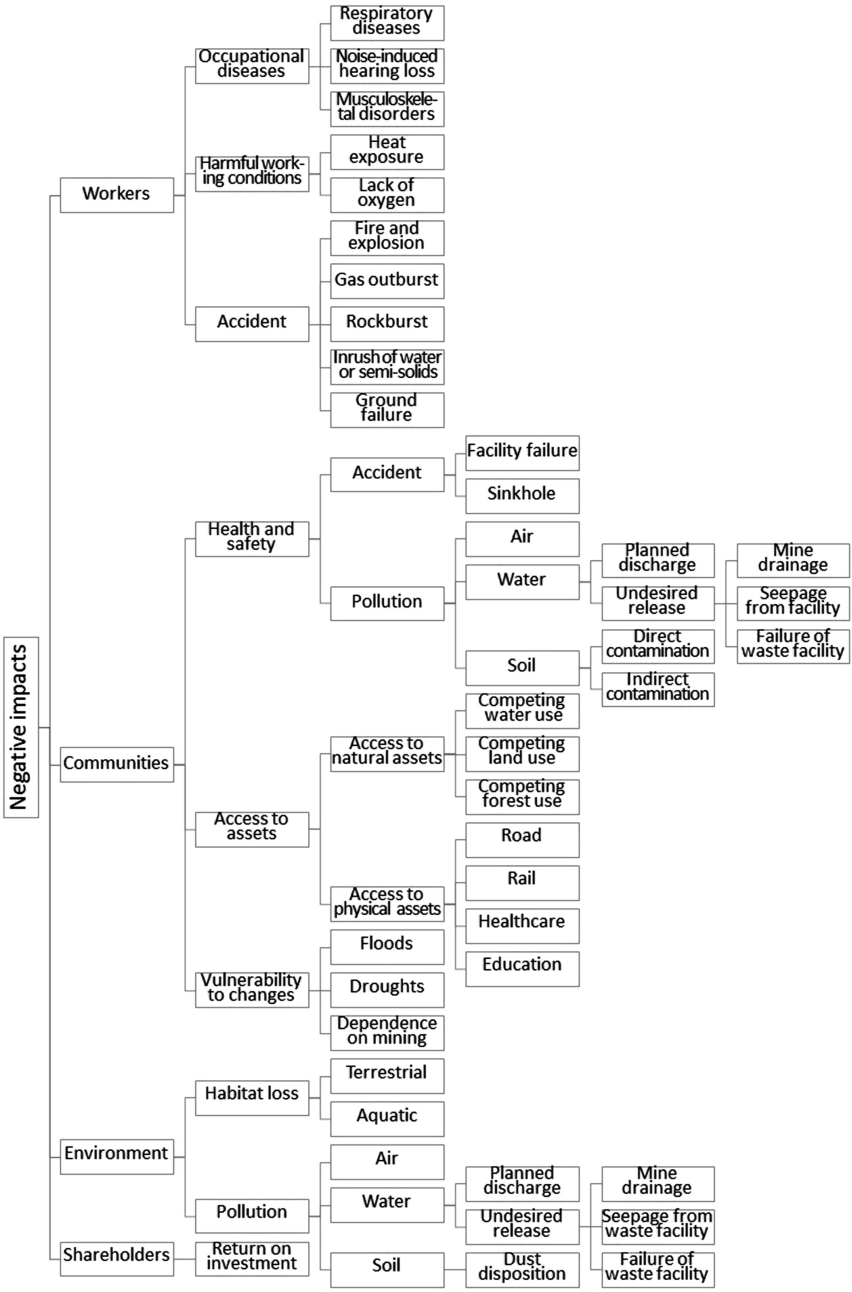

Fig. 3. Components and structure of negative impacts.

The impacts of the aforementioned parameters in the hierarchy are identified as the levels of anticipated impacts or the level of intentional or unintentional risks derived from a risk assessment process. Since this assessment takes place at an early project development stage, it is unable to measure most of the actual changes and the impacts must be considered through risks. Therefore, the concept of risk according to the ISO 31000:2009 standard is applied to identify the impacts of these parameters. The magnitude of risk of each parameter is determined by likelihood (i.e. chance of something happening) and consequences (i.e. the outcome of an event which affects objectives) [9]. Both parameters are assessed from a set of identified factors and rated into three levels: low, medium, and high. The ratings are then combined in a 3 × 3 risk matrix to identify the level of risk (low, medium, or high risk) as shown in Fig. 4. Insignificant or low risk refers to the risk that do not require or require minor actions to improve the likelihood or consequence conditions. Medium risk is the risk that might be tolerable in the short term but efforts to mitigate the risk are required. High risk represents the level of risk that mitigation measures are required before activities start. If the mitigation of risk is not achievable, the activities should not be carried out.

Likelihood	Consequence		
	Slightly harmful (score = 1)	Harmful (score = 2)	Very harmful (score = 3)
Least likely (score = 1)	Low risk (1)	Low risk (2)	Medium risk (3)
Likely (score = 2)	Low risk (2)	Medium risk (4)	High risk (6)
Most likely (score = 3)	Medium risk (3)	High risk (6)	High risk (9)

Fig. 4. Risk matrix.

The risk level of the parameters in the similar hierarchical level, represented by different scores, are aggregated by a weighted sum and the results are aggregated up the hierarchy to obtain the final ratings of the necessity of project development and the negative impacts of the project. An equal weight is applied unless stated otherwise.

4 Assessment Results

The assessment is carried out using the information from the mining plan and the environmental impact assessment report that company officially submitted to the governmental authority [2, 3] and some statistical data as the main data sources. The necessity of project development is determined by the flows of potash-related substances in the country and their changes due to the project development, carried out under this study, and by the development and operation plans stated in the company's documents. The ratings of parameters under the necessity of project development and their aggregated ratings are shown in Table 1. A medium rating is assigned to the necessity of project development, which means the project is not essential but could contribute positively to society.

Table 1. Summary of the ratings of the necessity of project development of the potash mining project.

No.	Components	Rating aggregation (specified in topic no. and weight)[a]	Rating[b]
1	Service provision	(1.1 + 1.2 + 1.3) × 0.33	Medium
1.1	Contribution to domestic demand		Medium
1.2	Contribution to end use	(1.2.1 + 1.2.2) × 0.5	Medium
1.2.1	Status of current end use		High
1.2.2	Increase in mineral export		Low
1.3	Resource availability		High
2	Positive contribution of the mining project to society	(2.1 + 2.2 + 2.3) × 0.33	Medium
2.1	Workers: employment		High
2.2	Community	(Sum of 2.2.1 to 2.2.6) × 0.17	Low
2.2.1	Access to water		Medium
2.2.2	Access to forest		High
2.2.3	Access to financial resources		High
2.2.4	Access to infrastructure		Irrelevant
2.2.5	Access to healthcare		Irrelevant
2.2.6	Access to education		Irrelevant
2.3	Environment: habitat gain		Medium
Aggregated rating		(1 × 0.67) + (2 × 0.33)[c]	Medium

Remarks:

[a]An equal weight is applied to components in the same hierarchical level unless stated otherwise.

[b]Irrelevant means no positive contribution since the consequence is negative. The negative consequence will be considered in the assessment of negative impacts.

[c]The weight of the service provision is twice as much as that of the positive contribution because service provision represents the unique function of mining activity which is difficult to replace by other activities.

The negative impacts of the mining project are determined by a wide range of factors influencing the effects of mining on workers, community, the environment, and shareholders. These factors, comprising, for example, geological characteristics of the deposit, facility and process designs, work plans, machinery list, meteorological data, demographical data, and biodiversity survey, are used in the risk assessment to identify the risk ratings of each component. The ratings of parameters under the negative impacts of the project and their aggregated ratings are shown in Table 2. A medium rating is assigned to the project's negative impacts, indicating the impacts could be significant but manageable.

The rating of the necessity of the potash mining project development and that of the project's negative impacts are put together in the necessity-impacts matrix to identify the development priority. According to the results above, both of them are assigned a medium rating. As a result, the development priority of the project is classified as a medium priority (see Fig. 5).

Table 2. Summary of the ratings of the negative impacts of the potash mining project.

No.	Components	Rating aggregation (specified in topic no. and weight)[a]	Rating[b]
1	Negative impacts on workers	(1.1 + 1.2 + 1.3) × 0.33	Medium
1.1	Occupational diseases	(1.1.1 + 1.1.2 + 1.1.3) × 0.33	Medium
1.1.1	Respiratory diseases		High
1.1.2	Noise-induced hearing loss		Medium
1.1.3	Musculoskeletal disorders		Medium
1.2	Harmful working conditions	(1.2.1 + 1.2.2) × 0.5	High
1.2.1	Exposure to heat		Medium
1.2.2	Lack of oxygen		High
1.3	Accidents	(Sum of 1.3.1 to 1.3.5) × 0.2	Medium
1.3.1	Fire and explosions		Medium
1.3.2	Gas outburst		Medium
1.3.3	Rockburst		High
1.3.4	Inrush of water or semi-solids		High
1.3.5	Ground failure		Medium
2	Negative impacts on communities	(2.1 + 2.2 + 2.3) × 0.33	Low
2.1	Health and safety	(2.1.1 + 2.1.2) × 0.5	Low
2.1.1	Risk of accident	(2.1.1.1 + 2.1.1.2) × 0.5	Medium
2.1.1.1	Waste facility failure		Low
2.1.1.2	Sinkhole		High
2.1.2	Pollution	(2.1.2.1 + 2.1.2.2 + 2.1.2.3) × 0.33	Low
2.1.2.1	Air pollution		Medium
2.1.2.2	Water pollution	((1) × 0.67) + ((2) × 0.33)[c]	Low
(1)	Planned discharge		Irrelevant
(2)	Undesired release	((2.1) + (2.2) + (2.3)) × 0.33	Low
(2.1)	Leaching and contamination from mine drainage		Irrelevant
(2.2)	Seepage and leakage in waste facility		Medium
(2.3)	Failure of waste facility		Low
2.1.2.3	Soil pollution	((1) + (2)) × 0.5	Low
(1)	Direct contamination		Irrelevant
(2)	Indirect contamination		Medium
2.2	Community's access to livelihood assets	(2.2.1 + 2.2.2) × 0.5	Low
2.2.1	Access to natural assets	(2.2.1.1 + 2.2.1.2 + 2.2.1.3) × 0.33	Medium

(*continued*)

Table 2. (*continued*)

No.	Components	Rating aggregation (specified in topic no. and weight)[a]	Rating[b]
2.2.1.1	Competing water use		Medium
2.2.1.2	Competing land use		Low
2.2.1.3	Competing forest use		Low
2.2.2	Access to physical assets	(Sum of 2.2.2.1 to 2.2.2.4) × 0.25	Low
2.2.2.1	Road		Low
2.2.2.2	Rail		Medium
2.2.2.3	Healthcare		Low
2.2.2.4	Education		Low
2.3	Vulnerability to external changes	(2.3.1 + 2.3.2 + 2.3.3) × 0.33	Low
2.3.1	Floods		Low
2.3.2	Droughts		Medium
2.3.3	Dependency on mining		Low
3	Negative impacts on the environment	(3.1 + 3.2) × 0.5	Low
3.1	Habitat loss	(3.1.1 + 3.1.2) × 0.5	Low
3.1.1	Terrestrial habitat loss		Medium
3.1.2	Aquatic habitat loss		Irrelevant
3.2	Pollution	(3.2.1 + 3.2.2 + 3.2.3) × 0.33	Low
3.2.1	Air pollution		Medium
3.2.2	Water pollution	((1) × 0.67) + ((2) × 0.33)[c]	Low
(1)	Planned discharge		Irrelevant
(2)	Undesired release	((2.1) + (2.2) + (2.3)) × 0.33	Low
(2.1)	Leaching and contamination from mine drainage		Irrelevant
(2.2)	Seepage and leakage in waste facility		Low
(2.3)	Failure of waste facility		Low
3.2.3	Soil pollution		Low
4	Negative impacts on shareholders		Medium
Aggregated rating		(1 + 2 + 3 + 4) × 0.25	Medium

Remarks:

[a]An equal weight is applied to components in the same hierarchical level unless stated otherwise.

[b]Irrelevant means unrelated since so such activities are planned or expected.

[c]The weight of the planned discharge is twice as much as that of the undesired release because the former is to be carried out and its consequence is anticipated while the latter is an uncertain event being prevented but possible to occur.

Necessity of project development	Negative impacts of the project		
	Low	Medium	High
High (vital for the society)	High priority	High priority	Medium priority
Medium (not absolutely necessary but can positively contribute to the society)	High priority	Medium priority	Low priority
Low (not very necessary)	Medium priority	Low priority	Low priority

Fig. 5. Necessity-impacts matrix of the potash mining project.

5 Conclusions and Recommendations

In this paper, a new framework for assessing the worthiness of new mining projects is established, and the worthiness of the Bamnet Narong potash mining project in Chaiyaphum province, Thailand, is assessed. The assessment framework is characterized by a necessity-impacts matrix. The necessity of project development and the negative impacts of the project are determined by related parameters structured in hierarchies. The impact of each parameter is assessed in terms of risk and is represented by a risk rating of low, medium, or high. The ratings are then aggregated upwards the hierarchy and the final ratings are used in the matrix to determine the development priority of the project. The results show that the development priority of the Bamnet Narong project is moderate, resulting from the medium rating of both the necessity of project development and the negative impacts.

The assessment results provide DPIM objective information about the value of the project from the public viewpoint. The ranking of the development priority indicates possibilities for increasing the project's values by enhancing the positive contributions and reducing the negative impacts of the project. The ratings of the assessment parameters provide useful information for regulating the project. In this case, the parameters under the necessity of development indicate that the project can reduce the raw material import moderately but will simultaneously increase export while the expected contribution to communities and the environment are not high. This can be improved by, for example, a concrete social investment plan on infrastructure and basic services. The parameters under the negative impacts indicate the issues likely to cause damages and requiring special attentions. In this case, nearly all categories related to worker's well-being are rated as moderate to high risks. Therefore, the measures to prevent safety and health problems should be defined and strictly implemented to avoid, prevent, or mitigate the short- and long-term effects on worker's welfare. The key parameters able to affect the livelihood of communities are sinkhole-related accident, health problems from air pollution, polluted water resource possibly caused by seepage from the waste storage facility, polluted soil from dust deposition, competing water use, competing use of railway at a specific section, and enhanced drought problem. The parameters concerning biodiversity loss that require the authority's attentions are terrestrial habitat loss and environmental degradation from air pollution. The key determinants of these problems can be the design and management of the process or the characteristics of the location. The authority should consider the details

of the assessment to identify the factors they or the company can influence and implement the measures that help preventing these potential problems. Applying risk management can be a helpful approach. In terms of the shareholder's investment risk, the project's return on investment rate is moderate. However, the company is subject to a high-risk condition, especially from social conflicts, so the authority should emphasize on communication and collaboration between the company and other parties to enhance trust and reduce the project's risks.

The results of the worthiness assessment of the Bamnet Narong project can facilitate the governmental decision-making and administration of mining activities. Similar assessments should also be carried out for other mining projects, and the assessment should be added to the current mining lease approval procedure to help the authority ensures the quality of its decision and make its regulation of mining projects more effective.

In terms of methodology, the merits of the proposed framework for assessing the worthiness of new mining projects lie in its ability to provide objective, neutral information to support government's decisions and communication with stakeholders. It considers the interests of different stakeholders as well as the positive and the negative aspects equally. A hierarchical structure and the information from the impact assessment allow a systemic and reliable evaluation, whereas the use of risk assessment concept allows efficient uses of scientific data to identify possible impacts and makes the results easy to understand and comparable. The overview and detailed ratings act as indicators of related issues, which provide a basis for identifying management measures. However, the framework contains some weaknesses that project assessors should be cautious. Data uncertainty and availability are important weaknesses. Since the framework involves a large set of criteria and information, uncertainties can be caused by many factors such as the inconsistency of data from different sources or different time frame and the uses of foreign reference data. The availability of data can also become problematic because the assessment will be carried out at an early stage of the project and some data might be unavailable. Moreover, the projects of smaller scale or applying simple methods might not have all the data required for the assessment. To prevent these problems, the government might consider collecting and compiling statistical or empirical data of mining projects in Thailand to develop a set of reference values. This is a recommendation for a future study which would strengthen the effectiveness of the implementation of the assessment framework. Another weakness involves the aggregation of ratings. The weighted sum method has a disadvantage on its assumption of cardinal utility function [26]. It presupposes that criteria are neutral and that different alternatives have comparable, substitutable values, so their values can be summated. Thus, the rating aggregation is influenced by compensation effects. Although the intermittent aggregation of the ratings at each level of the hierarchy has reduced these effects, the data users need to be aware when interpreting the results. To prevent any misunderstanding caused by the reductionism, the data users should always consider the aggregated ratings together with the detailed ratings in the hierarchy. In fact, the weighted sum method is one of the options for data aggregation. Experimenting with other methods to find better approaches is recommended for future studies.

References

1. Department of Mineral Resources: Geological and Georesource Status Report 2015 (2015)
2. ASEAN Potash Mining PLC: Underground Mining Plan, Mining Lease Application No. 1/2547, Mining Lease Mark No. 31708, ASEAN Potash Mining PLC (2014)
3. ASEAN Potash Mining PLC: Environmental Impact Assessment, Bamnet Narong Potash Project (2014)
4. Department of Primary Industries and Mines: Thailand's Mining Lease Database (2015)
5. Munn, R.E.: Environmental Impact Assessment. Scientific Committee On Problems of the Environment (SCOPE) (1979)
6. Senécal, P., Goldsmith, B., Conover, S., Sadler, B., Brown, K.: Principles of environmental impact assessment best practice. International Association for Impact Assessment Institute of Environmental Assessment, UK (1999)
7. Environmental Law Alliance Worldwide: Guidebook for Evaluating Mining Project EIAs. Environmental Law Alliance Worldwide, Eugene (2010)
8. Borquez, G.V., Thompson, J.V.: Feasibility studies. In: Kennedy, B.A. (ed.) Surface Mining, pp. 396–423. Society for Mining, Metallurgy, and Exploration, Inc., Littleton, Colorado (1990)
9. International Standard Organization: ISO 31000:2009 Risk Management - Principles and Guidelines (2009)
10. Global Reporting Initiative: G4 Sector Disclosure: Mining and Metals (2013)
11. Fonseca, A., McAllister, M.L., Fitzpatrick, P.: Sustainability reporting among mining corporations: a constructive critique of the GRI approach. J. Clean. Prod. **84**, 70–83 (2014)
12. Moneva, J.M., Archel, P., Correa, C.: GRI and the camouflaging of corporate unsustainability. Account. Forum **30**, 121–137 (2006)
13. Inoue, S.: Putting Buddhism to Work: A New Approach to Management and Business. Kodansha International Ltd., Tokyo (1997)
14. University of Gothenburg: Occupational Safety and Health in Mining: Anthology on the Situation in 16 Mining Countries, Gothenburg (2013)
15. International Labour Organization: Safety and Health in Mines Recommendation. International Labour Organization (1995)
16. Blight, G.E., Fourie, A.B.: A review of catastrophic flow failures of deposits of mine waste and municipal refuse. In: Proceedings of International Workshop "Occurrence and Mechanisms of Flow-like Landslides in Natural Slopes and Earthfills", pp. 19–36. Patron, Bologna
17. Whyatt, J., Varley, F.: Catastrophic failures of underground evaporite mines. In: Proceedings of the 27th International Conference on Ground Control in Mining (ICGCM), 29–31 July 2008, pp. 113–122. West Virginia University (2008)
18. CCSG Associates: Overburdened: Understanding the Impacts of Mineral Extraction on Women's Health in Mining Communities (2004)
19. Cronjé, F., Reyneke, S., Van Wyk, D.: Local communities and health disaster management in the mining sector. Jàmbá J. Disaster Risk Stud. **5** (2013)
20. Stephens, C., Ahern, M.: Worker and community health impacts related to mining operations internationally: a rapid review of the literature (2002)
21. International Institute of Environment and Development: Breaking New Ground: Mining, Minerals and Sustainable Development. Earthscan, London (2002)
22. Northey, S.A., Mudd, G.M., Saarivuori, E., Wessman-Jääskeläinen, H., Haque, N.: Water footprinting and mining: where are the limitations and opportunities? J. Clean. Prod. **135**, 1098–1116 (2016)

23. Kemp, D., Bond, C.J., Franks, D.M., Cote, C.: Mining, water and human rights: making the connection. J. Clean. Prod. **18**, 1553–1562 (2010)
24. Kaushik, A., Kaushik, C.P.: Perspectives in Environmental Studies, 280 p. (2006)
25. Petkova, V., Lockie, S., Rolfe, J., Ivanova, G.: Mining developments and social impacts on communities: Bowen basin case studies. Rural Soc. **19**, 211–228 (2009)
26. Pomerol, J.-C., Barba-Romero, S.: Multicriterion decision in management: principles and practice (2000)

Author Index

A
An, Do Manh, 326
An, Tran Dang, 293

B
Bac, Bui Hoang, 326
Buczek, Michał, 1
Bui, Dung Tien, 17
Bui, Luyen Khac, 1
Bui, Quang-Thanh, 166
Bui, Xuan-Nam, 1, 17

C
Cao, Xuan Cuong, 65

D
Dang, Trung Hoai, 34
Deroin, Jean Paul, 65
Duc, Dao Minh, 202
Duc, Do Minh, 202
Dung, Nguyen Tien, 326

G
Gu, Huanda, 367

H
Ha, Doan Thu, 293
Hai, Nguyen Van, 293
Hejmanowski, Ryszard, 340
Hoang, Nhat-Duc, 239
Hoang, Thanh Tung, 134
Hoang, Tuan-Anh, 166
Huynh, Khoa Dat Vu, 1

K
Kaida, Naoko, 103
Katagi, Jin, 134
Kretschmann, Jürgen, 378
Kristoffersen, Bjørn, 17

L
La, Hien Phu, 89, 119
Lan, Nguyen Chau, 315, 367
Le, Cuong Anh Van, 34
Le, Ha Thu Thi, 119
Lê, Thu Trang, 152
Le, Viet Huy, 355
Long, Nguyen Quoc, 1, 17, 52
Lu, Cong, 315, 367

M
Malinowska, Agnieszka A., 340

N
Nasahara, Kenlo Nishida, 134
Ngo, Huong Thanh Thi, 186
Ngo, Phuong-Thao Thi, 17, 52
Ngo, Van-Liem, 186
Ngoc, Do Minh, 202
Nguyen, Minh Quang, 89
Nguyen, Nam Van, 119
Nguyen, Quoc-Phi, 52
Nguyen, Quoc-Huy, 166
Nguyen, Thang Phi, 1
Nguyen, Thuan Van, 34
Nguyen, Trung Van, 119
Nguyen, Van Cam, 52
Nguyen, Van Thanh, 34
Nguyen, Viet-Nghia, 17, 52, 355
Nguyen, Viet-Tien, 186
Nhan, Pham Thi, 355

P
Pan, Lingling, 315
Pham, Binh Thai, 186, 224, 255
Pham, Ha Thai, 152
Pham, Thi Lan, 65

© Springer International Publishing AG 2018

D. Tien Bui et al. (eds.), *Advances and Applications in Geospatial Technology and Earth Resources*, https://doi.org/10.1007/978-3-319-68240-2

Pham, Tien Dat, 103
Phu, Vo Le, 293
Prakash, Indra, 224, 255

R
Revhaug, Inge, 52

S
Sakamornsnguan, Kridtaya, 378
Son, Le Hoang, 166

T
Tang, Qiang, 315, 367
Tien Bui, Dieu, 17, 52, 119, 186, 239
Tong, Si Son, 65
Tran, Hai Thanh, 270
Tran, Van Anh, 152
Tran, Xuan Truong, 152
Trinh, Phan Trong, 186
Tsujimura, Maki, 293

V
Van Anh, Tran Thi, 326
Van Le, Canh, 1, 17
Van Pham, Chung, 17
Vo, Lieu Nguyen Nhu, 34
Vo, Triet Minh, 34

W
Wu, Huilong, 367

X
Xu, Mengyi, 315
Xue, Guoqiang, 367

Y
Yoshino, Kunihiko, 103

Z
Zhang, Guangsheng, 355
Zhang, Yu, 315